The DIPAC (Diagnostics and Instrumentation for Particle Accelerators) has seen in June 2005 its 7th edition. This workshop aims at an active exchange of the latest experiences in the field of accelerator beam diagnostics and instrumentation with a program of oral presentations, poster sessions and discussion groups.
The seventh DIPAC has been organized by members of the beam instrumentation group at CERN in Geneva (Switzerland). About 150 participants from almost all continents have found their way to the conference Hotel Metropole in Lyon (France).
It was a great pleasure to receive this community during the three workshop days, in particular 5 participants, for whom it has been made possible to attend the conference through generous fellowship grants provided by two industrial partners of the beam instrumentation world (BERGOZ Instrumentation (France) and Instrumentation Technologies (Slovenia).

The program committee organised an interesting agenda with invited and contributed presentations and poster sessions of two hours at every day of the workshop. This program was the baseline for the event, which was completed by two additional activities. Like in previous DIPAC workshops the participants were given the opportunity to contribute their own experience to previously selected topics in discussion sessions. Since the topics were communicated before and the chairmen took an enormous effort to prepare the discussion sessions, these events produced lively and interesting communication. Secondly two of the workshop days were ended with so called “Happy

Hours", each day two hour long receptions in the hotel foyer, during which the participants exchanged individual information concerning what they had been presented during the day. Due to these happy hours, the traditional conference banquet was not organised and people used the free evenings in order to profit from gastronomical experiences downtown Lyon.
The workshop was rounded up by the presence of four industrial exhibitors, who produce commercial products close to beam instrumentation activities.

Such a successful event is the result of long preparation work by many people.
I want to thank the program committee members, who invested their time in many email exchanges and two preparation meetings in Lyon and at CERN. The other team was the so called local organising team, which assured all logistics questions of the event ranging from detailed preparations in the hotel up to a reserve of medicaments in order to help the effects of long and stressful nights. The local organising team was composed of six members of the CERN beam instrumentation group, from which I want to highlight the investment of the group secretary Mme Madeleine Catin, who for almost six months was mainly occupied with preparation work. It was very nice to see that Brigitte Azzara (GSI) was given by her management the opportunity to assist to the workshop and help out in the local secretariat. The third team has invested his efforts into the work of preparing the workshop with a splendid abstract booklet and by producing valuable proceedings. All this work has happened in the JACOW software framework and I want to mention Volker Schaa (GSI) as driving force for this activity.

Last not least, no workshop produces co-memorable results without good scientific contributions from all speakers and poster exhibitors as well as from all workshop participants. Many thanks again to all these valuable contributions.

And "the show will go on" with the next DIPAC workshop in 2007, which will be organised by a team from ELETTRA in Trieste (Italy).
I am looking forward to meeting most of you during this upcoming event.

Sincerely Hermann Schmickler

Chairman of the DIPAC 2005 program committee)

Contents

Conference Chair

Hermann Schmickler (Chairman)	CERN AB-BDI, Geneva

Program Committee

Hermann Schmickler (Chairman)	CERN, Geneva
Peter Cameron	BNL, Upton, N.Y.
Mario Ferianis	ELETTRA, Trieste
Eiji Kikutani	KEK, Tsukuba
Alex Lumpkin	APS
Andreas Peters	GSI, Darmstadt
Uli Raich	CERN, Geneva
Kees Scheidt	ESRF, Grenoble
Volker Schlott	PSI, Villigen
Mario Serio	LNF, Frascati
Tom Shea	SNS, Oakridge
Kay Wittenburg	DESY, Hamburg

Local Organizing Committee

Hermann Schmickler (Chairman)	CERN AB-BDI, Geneva
Madeleine Catin (Secretary)	CERN AB-BDI, Geneva
Ivan Andrian	ELETTRA, Trieste
Brigitte Azzara	GSI, Darmstadt
Christian Boccard	CERN AB-BDI, Geneva
Enrico Bravin	CERN AB-BDI, Geneva
Jean-Jacques Gras	CERN AB-BDI, Geneva
Stephen Jackson	CERN AB-BDI, Geneva
Uli Raich	CERN AB-BDI, Geneva
Volker RW Schaa	GSI, Darmstadt


MONTE-CRISTO


DIPAC 2005
Time Schedule Overview


Luminosity


bergoz


WIENER


Libera
Family
Libera electron beam position processor
Libera bunch by bunch feedback processor
Libera hadron beam position processor
We shape the future of the accelerator community...
Libera

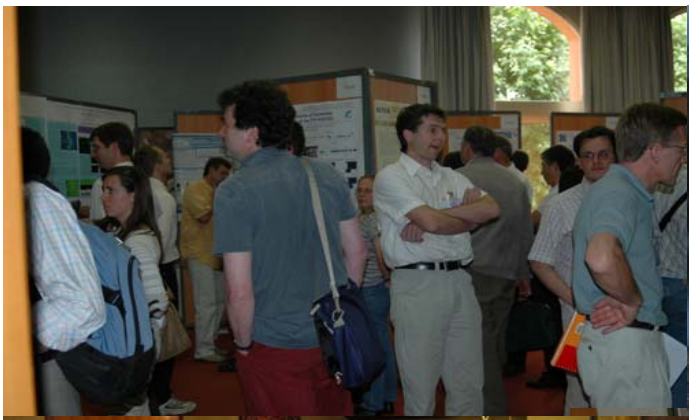
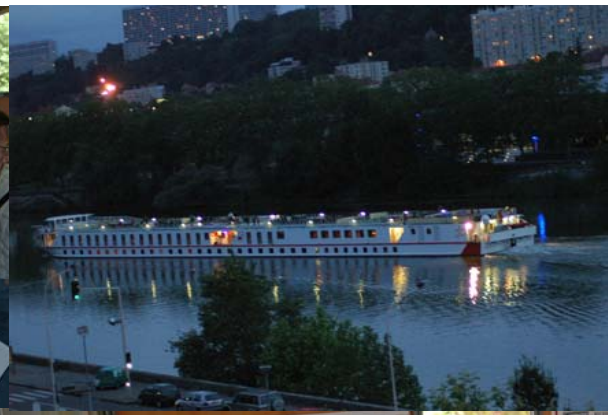

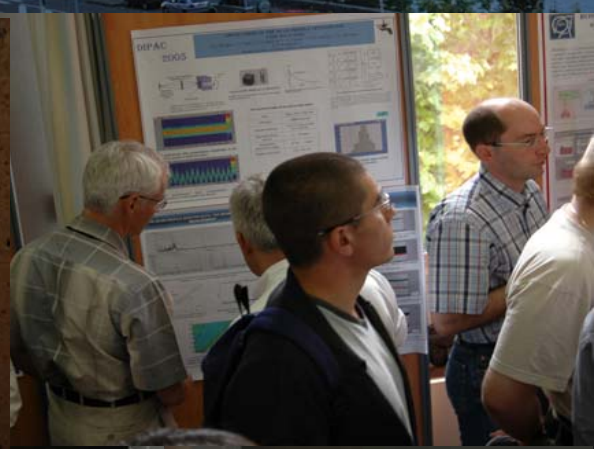
DIPAC
2005

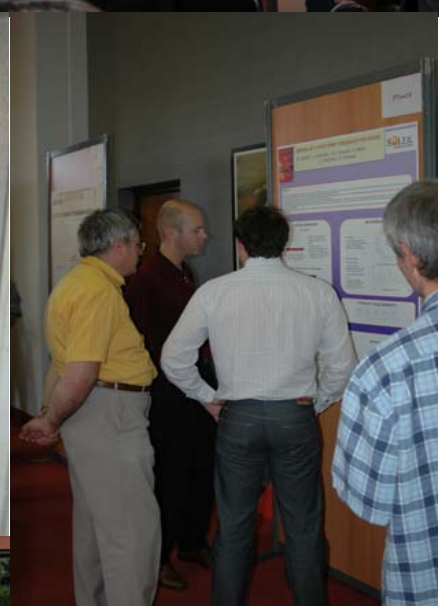


WIENER
WIENER

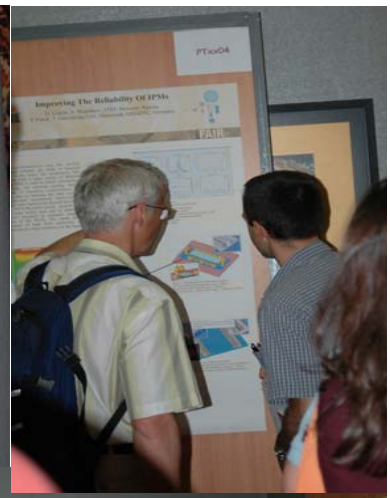


Control Panel for Contribution Submission
Title
Author
Monday

INSTRUMENTATION IN SMALL LOW ENERGY MACHINES

U. Raich, AB Dep. CERN, Geneva, Switzerland

Abstract

Low energy particle accelerators are used either as injectors for higher energy machines or as dedicated machines for special purposes. These may be industrial, medical or prototype machines for testing new accelerating schemes. Low energy beams open measurement possibilities not available at higher energies due to the low magnetic rigidity of the particles, due to their small penetration depth and due to rather big beam spot sizes. On the other hand these beams also represent special challenges due to their high energy deposition in matter, space charge problems etc. which are not seen at higher energies. Measurement principles typical for small accelerators will be presented and explained with the help of example implementations.

INTRODUCTION: THE LHC

The Large Hadron Collider (LHC) is without any doubt CERN's biggest project and one of the most gigantic scientific endeavours ever undertaken in high energy physics. For this reason all eyes of the physics world are focused on it. But… what has the LHC to do with instrumentation in small and low energy machines? The quality factor for a collider is its luminosity L:

$$L \propto \frac{k_b N^2}{\varepsilon_n}$$

where k_b is the number of bunches, N the number of particles per bunch and ε_n the normalised emittance.

In electron-positron colliders like LEP the synchrotron radiation emitted by electrons at high energy inhibits the move to even higher energies but it is also responsible for Landau damping of the beam emittance. The beam quality is to a good fraction determined by the highest energy machine. In hadron machines however, due to the much higher mass of hadrons, synchrotron radiation is very much suppressed and the beam brightness is essentially determined in the injector chain.

This shows the importance of being capable to measure the beam characteristics in the low energy machines well enough.

Acceleration of ions, foreseen for LHC, poses additional constraints. At low energies ions are only partially ionised and they further ionise through stripping when interacting with an intercepting sensor. In addition energy deposition in matter is at a maximum.

Small machines are however not only used as injectors. There are many industrial applications (e.g. material tests) and medical applications (cancer therapy) which need accelerated particles of rather low energy.

INTENSITY MEASUREMENTS AT LOW ENERGIES

FARADAY CUPS

At energies of up to a few MeV and low intensities Faraday cups are used for intensity measurements. Figure 1 shows a very simple cup design [1]. The sensor itself (2) consists of a stainless steel cone which is connected to a vacuum feed-through. Another feed-through is used for the supply of a polarisation voltage to a cylindrical repeller electrode (1) pushing secondary electrons, created when the beam touches the sensor surface, back into the cup.

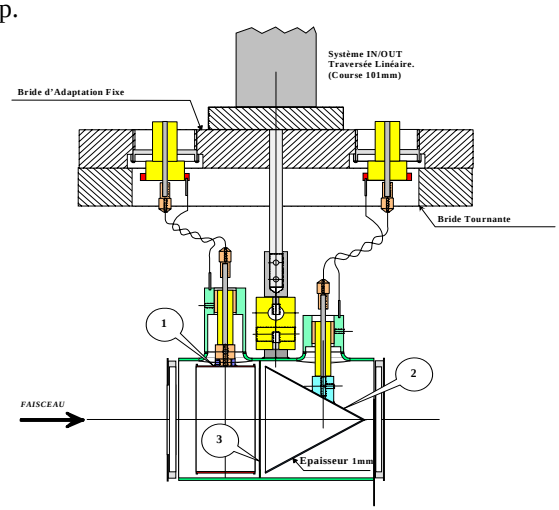

Figure 1: A simple Faraday Cup

Secondary electrons leaving the sensor would of course result in wrong intensity measurements. Since secondary electrons have very low energies of less than 20 eV a polarisation voltage of some 100V is sufficient. Figure 2 shows the current on the sensor with increasing polarisation voltage. At ~30V increasing the voltage further has no more effect on the measured current.

A typical application of Faraday Cups is the measurement of charge state distributions after the ion source. A whole range of different ion charge states is created of which only a single one can be accelerated through the following accelerator chain.

A spectrometer in conjunction with a slit is used to filter out this state. Before doing this however the full charge state spectrum is measured by ramping the spectrometer magnet and measuring the beam current passing though the slit into a Faraday Cup.

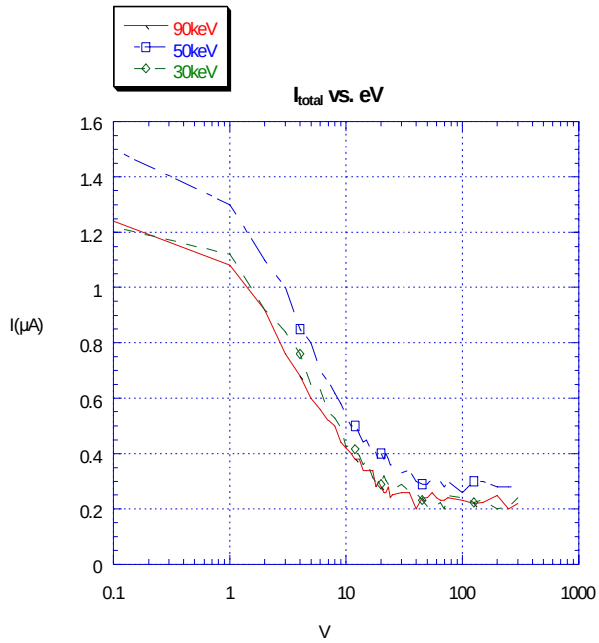

Figure 2: Suppression of secondary electrons

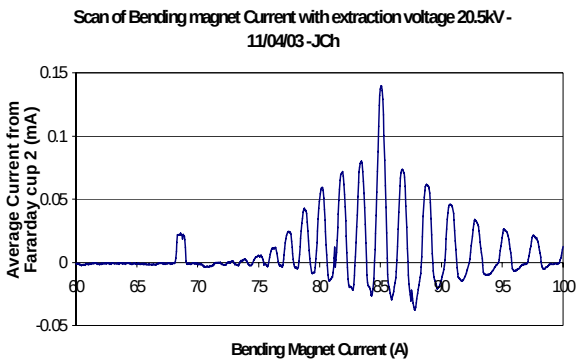

Figure 3: Ion Charge State Spectrum

BEAM CURRENT TRANSFORMERS

In order to produce high beam intensities as required by high energy storage rings, the particle sources produce long pulses in the order of several hundred μs length, which are pre-accelerated in linear accelerators (rfq + Alvarez Linac or IH structure) before being transferred through multi-turn injection into the first circular machine.

During acceleration the physical emittance of the beam is shrinking through adiabatic damping (between the exit of the CERN Linac (50 MeV) and the injection into LHC (450 GeV) the emittance shrinks by a factor 1500!), which means that at the level of the pre-accelerators large beams with particles having large angles must be expected. The mesh of quadrupole magnets used for focusing must therefore be rather narrow and the space for installing equipment is very limited.

For intensity measurements using fast beam current transformers (BCTs) this has two consequences:

- The pulse length is long enough to be sampled with fast industry standard ADCs
- Software based signal treatment on the digitized transformer signals can be used to correct baseline shifts and other aberrations induced by nearby pulsing magnets.

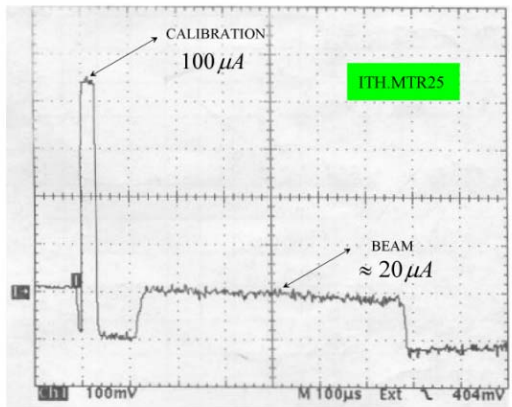

Figure 4: Signal of a low intensity ion pulse from a AC current transformer

Figure 4 shows a typical signal of a 20 μA lead ion pulse as measured by a BCT. A calibration pulse is injected into a separate calibration winding of the transformer shortly before the arrival of the beam. Please note that the total pulse length is 600 μs and that the baseline is inclined. Additional timing pulses are used to determine the start and end injection timing for the multi-turn injection such that the total number of charges injected into the first accelerator ring can be determined.

SCINTILLATING SCREENS

Long beam pulses of some 20μA current cannot easily be measured with beam position monitors and scintillating screens may be used as a fallback solution.

Looking at the Bethe-Bloch curve, describing the energy deposition of hadrons in matter, one can easily see that at very low energy and high charge states the energy deposition is at a maximum. This is the typical case for heavy ions at low energy. The estimated penetration depth of lead ions with 4 Mev/n is ~10 μm, which means that all the ion energy is deposited in an extremely small volume leading to massive heating of the material.

Tests have shown [3] that Al_2O_3:Cr (chromium doped aluminum oxide, chromox) screens used for higher energy protons will quickly burn when used with low energy ions. In addition to the thermal load the evacuation of electric charges represents a problem.

The scintillation material of Table 1 has been exposed to 1 Hz ion beam pulses at 4 MeV/n for several hours and their scintillation properties have been examined.

Table 1: Scintillation material and its properties

Material	ρ g/cm3	C_p at 20ºC J/gK	k at 100ºC W/mK	Tmax ºC	R at 400 ºC Ω.cm
Al2O3	3.9	0.9	30	1600	10^{12}
ZrO2	6	0.4	2	1200	10^{3}
BN	2	1.6	35	2400	10^{14}

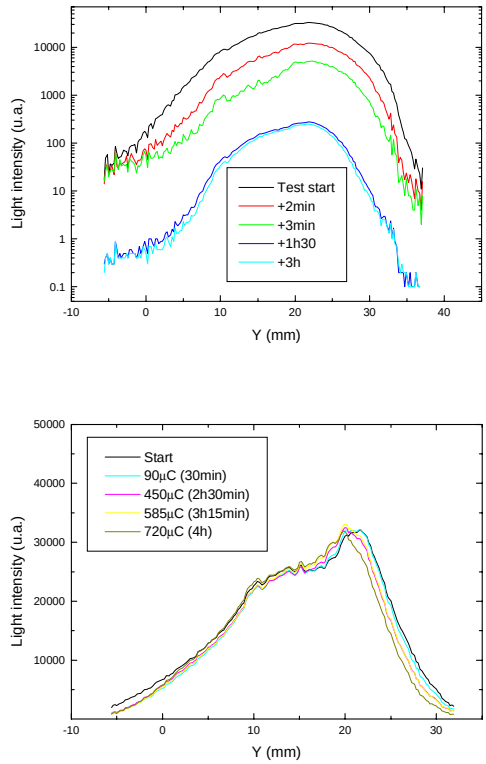

Figure 5: Emission efficiency after bombardment with low energy heavy ions
upper graph: AL_2O_3
lower graph: ZrO_2

While all screens show clear signs of deterioration (see Figure 6) the light emitting properties of ZrO_2 was least affected (Figure 5).

Figure 6: Screen damage

BEAM PROFILE MEASUREMENTS

When thinking about emittance or beam profile measurements in circular machines the wire scanner is the most commonly used device. A thin carbon of beryllium wire is quickly moved through the beam and secondary particles created by the interaction of the incident beam with the wire are detected with a scintillator and photomultiplier assembly outside the vacuum chamber. At beam energies of less than 150 MeV, the minimum energy needed to create pions, hardly any secondary particles are seen on the scintillator [4].

Figure 7 shows a measurement of the secondary particle shower intensity as a function of the primary particle energy where the pion threshold is clearly visible.

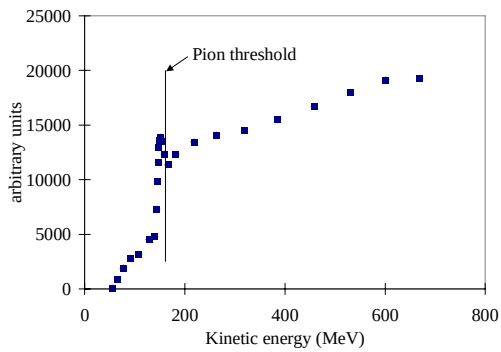

Figure 7: Shower intensities at low energy

If however the wire is mounted electrically isolated the secondary emission current from the wire can be measured. In this case the low energy of the primary beam particles is not an issue. As Figure 8 demonstrates very clean profiles can be measured with secondary emission, while the photo-multiplier signal becomes very noisy and asymmetric due to the bad statistics and due to geometrical effects of placement of the scintillator.

Profiles of partially stripped ions cannot be measured with such a wire scanner because the interaction of the ion with the wire will induce stripping (one or more electrons will be removed from the ions atomic shell) and the ion will be lost.

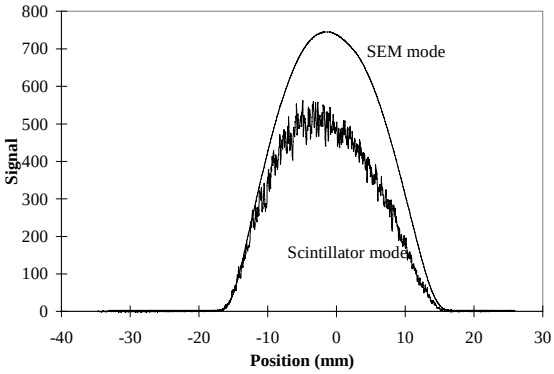

Figure 8: Wire profiles at low energy

One can however use the stripping effect to measure the betatron amplitude distribution. In this case the wire scranner (or a scraper) is used to scrape off the beam starting from the outside of the particle distribution and finishing as soon as the core of the beam has been reached. The losses are observed on a DC current transformer. Figure 9 shows a typical loss curve from which the betatron amplitude distribution can be determined by differentiation.

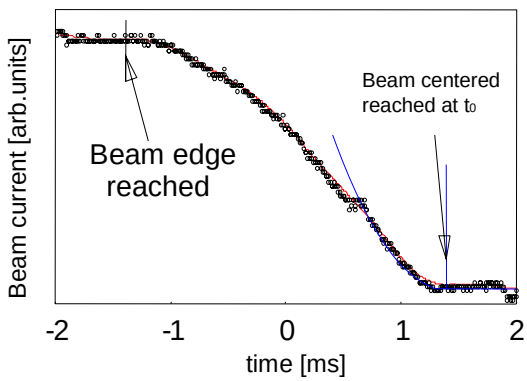

Figure 9: Beam losses due to stripping

TRANSVERSE EMITTANCE

During acceleration the transverse emittance of the beam shrinks due to adiabatic damping. The effect is large: a factor of 1500 for protons between 50MeV and 450 GeV. For this reason beam sizes expected at low energy machines are rather big (as can be seen in Figure) and it is at low energy that phase space cooling must be applied increasing beam brightness as may be required by a high energy collider.

Because of the big beam sizes phase space scans are often applied to measure the beam emittance e.g. at the exit of hadron sources Figure 10 and 11). A fine slit is moved through the beam and the particle angles at the slit position are converted into positions through a drift space and measured with profile measurement devices, often secondary emission or collector grids.

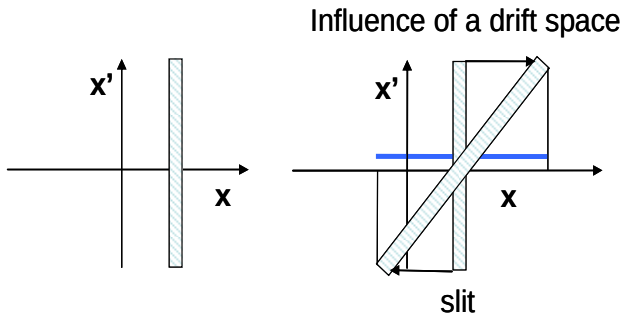

Figure 10: Principle of phase space scan

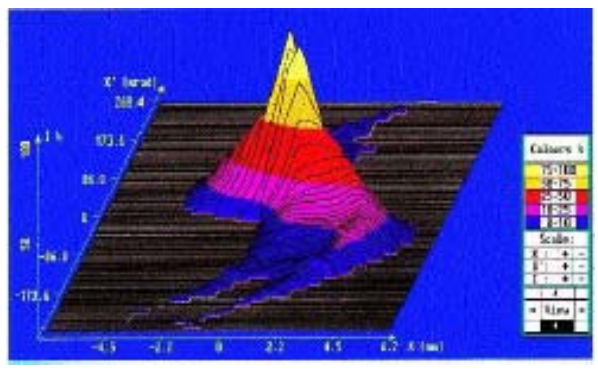

Figure 11: Results of a phase space scan

Advantages and disadvantages of this method are obvious: On one hand the position resolution can be made very fine by moving the slit only for very short distances. On the other hand the slit must be displaced before each measurement which means that scanning the full phase space can take several minutes when applied to a beam with low pulse rate (1Hz is a typical rate). Beam instabilities from one pulse to the next will result in measurement errors.

This problem can be solved by moving the beam with kicker magnets in front of a non-moving slit. Typical kicker rise times and the small magnetic rigidity of particles at low energies allow performing a phase space scan within a single beam pulse. In this case the angle distribution must be sampled in very short intervals (typical ~ 1μs).

Another way is the use of multiple slits. Again, this is only possible if the beam-spot is large enough. Here the number of slits determines the spatial resolution and a high resolution profile detector is needed since now the angle resolution of each slit must be measured in a single measurement. Generally scintillator screens are used. In order to measure horizontal and vertical emittances in a single measurement the pepperpot method is applied in which the multiple slits are replaced by small holes (Figure 12).

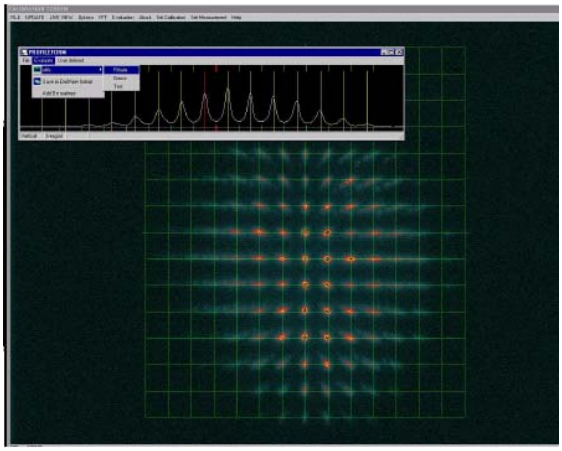

Figure 12: Pepperpot result

LONGITUDINAL PHASE SPACE SCAN

While transverse phase space scans are widely known longitudinal scans are much less common. The canonical parameters in this case are the particle energy and its time of arrival which is equivalent to its phase angle relative to the radio frequency.

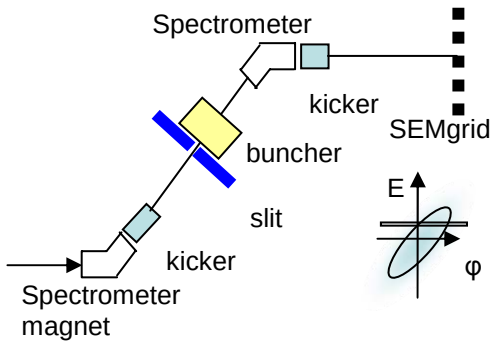

Figure 13: Longitudinal phase space scan

The conversion of particle energy to position can b obtained through a spectrometer magnet which selects a horizontal slice in phase space. As in the transverse case a kicker is used to scan along the E axis. The rotation in phase space of the slice selected is done by means of a buncher which converts the phase distribution into an energy distribution which in turn is converted to position by a second spectrometer (Figure 14).

CONCLUSIONS

Low energy beams from small accelerators present opportunities for instrumentalists which are not seen at higher energies. These are mainly related to big beam sizes, low magnetic rigidity of the particles and the possibility to entirely stop the beam in intercepting material.

On the other hand low energy beams also present problems mainly due to their low penetration depths in matter and due to their high energy deposition in very small material volumes leading to high thermal loads. In addition large emittances correspond to large displacements and angles with respect to the nominal orbit. This means that the beam must be re-focused very frequently leaving very little space for beam diagnostics instruments and bringing them very to close to pulsed elements causing electro-magnetic interference which must be cured by sophisticated shielding.

ACKNOWLEDGEMENTS

Many thanks go to E. Bravin, V. Prieto, T. Lefevre, P. Forck who allowed me to use their illustrations, tables or photographs.

REFERENCES

[1] G. Molinari, V. Prieto, Test d'une Coupe de Faraday avec la Source Duoplasmatron du PS, CERN internal Note PS/BD/2001-001

[2] P. Forck et al. Comissioning of IH-RFQ and IH-DTL for the GSIO high current Linac, 20th International Linac Conference Monterey, California, p. 166.

[3] C. Bal, E. Bravin, T. Lefèvre, R. Scrivens, M. Taborelli, Scintillating Screens Study for LEIR/LHC Heavy Ion Beams, this conference

[4] M. Arruat, C. Carli, A. Jansson, M. Lindroos, M. Martini, J. Olsfors, H. Schönauer, A comparative Study of fast Wire Scanners, Beamscope and SEM-Grids for Emittance Measurement in the PS Booster, DIPAC 1997

COMMISSIONING OF SNS BEAM INSTRUMENTATION

T.J. Shea, ORNL, Oak Ridge, Tennessee

Abstract

The Spallation Neutron Source (SNS) is an accelerator-based neutron facility under construction in Oak Ridge, Tennessee. The project is a collaboration of 6 partner laboratories: Lawrence Berkeley (LBNL), Los Alamos (LANL), Argonne (ANL), Brookhaven (BNL), Jefferson (Jlab), and Oak Ridge (ORNL). To achieve the performance goals, the SNS accelerator facility must deliver over one megawatt of beam power to a mercury target. This talk will describe the beam diagnostic instrumentation required to commission and operate such a facility at high beam power. Status of the SNS construction and recent beam commissioning results will also be presented.

NO SUBMISSION RECEIVED

BEAM HALO OBSERVATION BY CORONAGRAPH

T. Mitsuhashi, KEK, TSUKUBA, Japan

Abstract

We have developed a coronagraph for the observation of the beam halo surrounding a beam. An opaque disk is set in the beam image plane to block the glare of the beam image. We succeeded in obtaining a signal to background ratio of $6x10^{-7}$. As a test, we tried to observe the beam halo at the Photon Factory storage ring. We succeeded in observing the tail of the beam, which has an intensity range of 10^{-4} to 10^{-6} of the peak intensity.

INTRODUCTION

The beam tail or halo is one of the significant problems in proton machines and future Linac-based machines such as LC and ERL. To develop an apparatus to observe the beam tail or halo, we used the concept of the coronagraph. The coronagraph is a spatial telescope observing the sun-corona via artificial eclipse [1]. The concept of this apparatus is to create an artificial eclipse by blocking the glare of the sun's image and thereby observe the weak image of the sun's corona. We applied this concept to the observation of the halo surrounding a beam. In the coronagraph, the diffraction fringe surrounding the sun image is eliminated by a re-diffraction system with a mask (Lyot stop). Since the background mainly comes from scattered light from defects in the objective lens, such as scratches and digs on the surface, the key point to realize good performance of the coronagraph is to reduce scattering light from the objective lens. We used a very well-polished lens for the objective lens, and succeeded in obtaining a signal to background ratio of better than 10^{-6}. We observed the beam halol by coronagraph at the Photon Factory storage ring. We succeeded in observing the halo of the beam which has an intensity range from $1/10^4$ to $1/10^6$ of the peak intensity. The use of the words beam halo or beam tail can introduce some confusion: I use the word "halo" to mean both beam halo and beam tail in this paper.

BEAM HALO OBSERVATION WITH NORMAL TELESCOPE

Let us consider the observation of the sun's corona with a normal telescope. To create an artificial eclipse, we can set an opaque disk on the focal plane of the objective lens to block the glare of the sun image as shown in Fig. 1. In the normal telescope setup, the objective lens aperture makes a bright diffraction fringe surrounding from the sun image. The ratio of intensities between the diffraction fringes to the peak of the Airy disc is approximately 10^{-2} at the first peak of the fringe. These intense diffraction fringes inhibit the observation of the weak image of the sun corona which has an intensity range of 10^{-5}.

In the case of beam halo observation with typical beam profile monitor using the visible synchrotron radiation in the particle accelerator, we have the same difficulty as in the sun corona observation. Let us consider the observation of beam halo at the Photon Factory. As shown in Fig.2, the second diffraction fringe has the same intensity as the geometrical image of the beam. The beam halo near the third diffraction fringe has a weaker intensity than the diffraction fringe, and we cannot observe it by a normal imaging method as in the SR profile monitor.

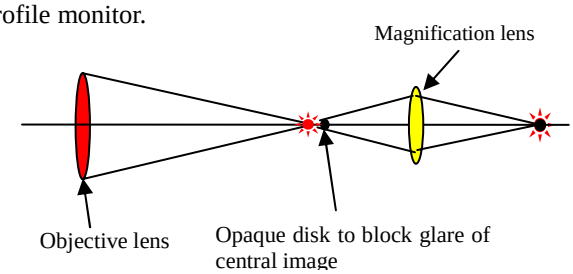

Figure 1: Set up of normal telescope with opaque disk.

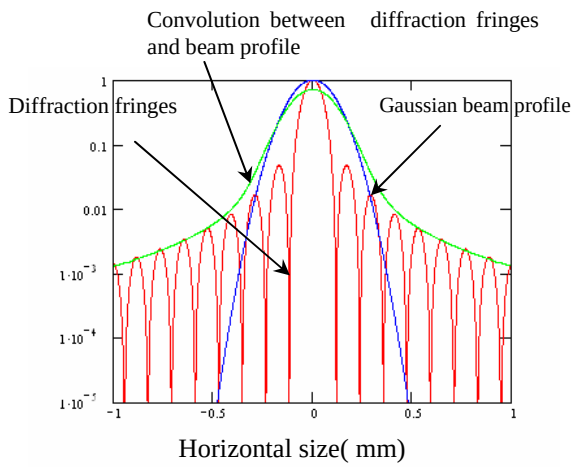

Figure 2: Comparison of the beam profile and point spread function (PSF). The solid red line denotes the PSF, and the blue line denotes the Gaussian horizontal beam profile at the Photon Factory.

CONCEPT OF THE CORONAGRAPH

The optical layout of the coronagraph is illustrated in Fig.3. The first lens (objective lens) makes a real image of the object (beam image) on to a blocking opaque disk which creates an artificial eclipse. A second lens (field lens) is set just after the blocking disk. The focusing length of the field lens is chosen to make a real image of the objective lens aperture onto a mask (Lyot Stop). The diffraction fringe in the focal plane of the objective lens is not blocked by the opaque disk, and is re-diffracted by the field lens aperture. Then the re-diffracted light makes another diffraction fringe around the geometrical image of

the objective lens aperture in the focal plane of the field lens. Lyot's brilliant idea for the coronagraph is to remove this diffraction fringe by a mask, and relay the hidden weak image by a third lens onto the final observation plane [1]. The background light on the final observation plane now mainly come from the scattering of the input light by the objective lens. By utilizing a very well polished lens as the objective, we can reduce the background light to less than 10^{-6} of the main image.

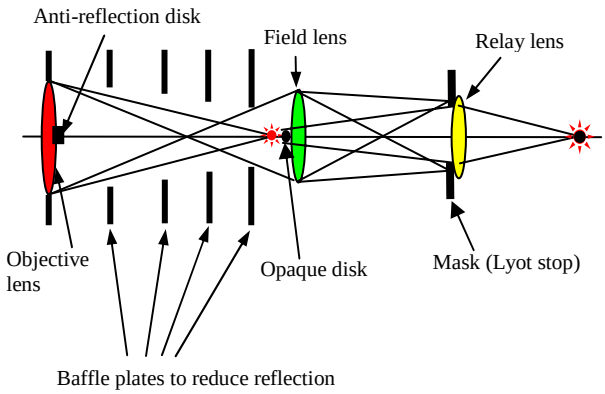

Figure 3: Layout of optical system of the coronagraph.

FUNCTION OF RE-DIFFRACTION SYSTEM TO ELIMINATE DIFFRACTION FRINGE

To eliminate the intense diffraction fringes, a re-diffraction optics system is used in the coronagraph. In the optical system of the coronagraph, the disturbance of the light to the field lens aperture is diffracted again, and produces re-diffraction fringes onto its focal plane. By this reason, the second field lens in the system is called the re-diffraction system. The function of the re-diffraction system in eliminating diffraction fringes in the coronagraph is illustrated in Fig 4. As illustrated in Fig. 4 (a), the aperture of the objective lens makes diffraction fringes in its focal plan. The glare of the central image is blocked by the opaque disk as illustrated in Fig. 4 (b). The entrance pupil of the next field lens is the aperture of the lens pupil with a stop, with the diameter of the opaque disk. Then the input disturbance of the light is diffracted again with this aperture, making diffraction fringes on the focal plane of the field lens. Letting F(ξ) denote the disturbance of the light on the imaging plane of the objective lens, the disturbance of the re-diffracted light u(x) on the imaging plane of the field lens is given by,

$$u(x) = \frac{1}{i \cdot \lambda \cdot f} \int_{\xi 1}^{\xi 2} F(\xi) \exp\left\{ - \frac{i \cdot 2 \cdot \pi \cdot x \cdot \xi}{\lambda \cdot f} \right\} d\xi \ ,$$

where λ denotes the wavelength of the input light, $\xi 1$ denotes the radius of the stop, $\xi 2$ denotes the radius of the aperture at the pupil of the field lens, and f denotes the distance between the field lens and its imaging plane. An example of the simulation of the intensity distribution $u^2(x)$ using an input square aperture at the objective lens is shown in Fig. 5. From this figure, we can see two diffraction sets of rings located in the inside and outside of the geometrical image of objective lens edge. As illustrated in Fig.4 (c), by hiding this diffraction ring with a mask (Lyot Stop), the light from the diffraction fringe will not come to the later stage of the coronagraph.

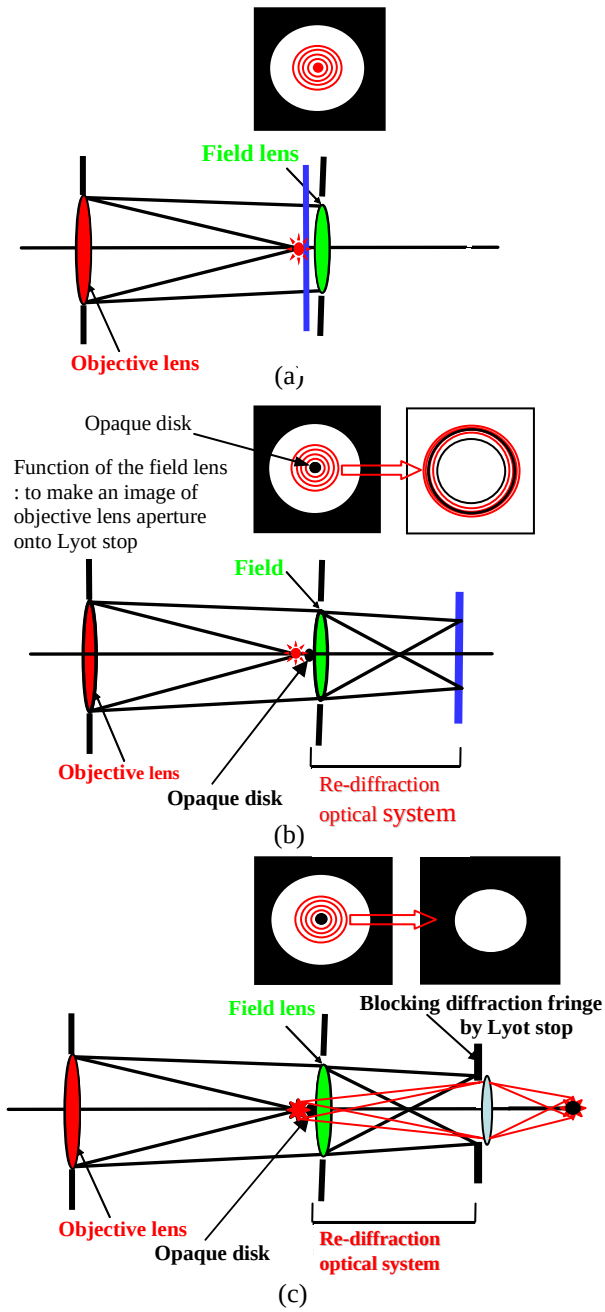

Figure 4: Function of re-diffraction system to eliminate diffraction fringes in the coronagraph. (a) Diffraction by objective lens. (b) The field lens makes an image of the objective lens aperture onto the Lyot stop. Re-diffraction fringes appear inside and outside of the geometrical image of the objective lens aperture. (c) Re-diffraction fringes are blocked by the Lyot stop. The surrounding weak image will be relayed to the final focusing point.

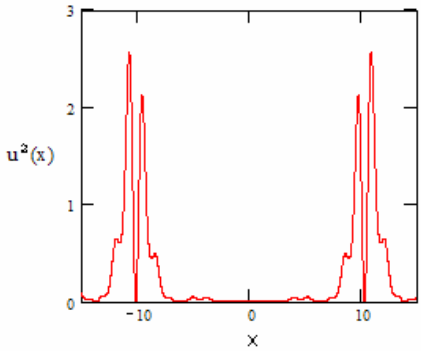

Figure 5: A simulation of the intensity distribution $u^2(x)$ using a square input aperture on the objective lens. The valley between the diffraction peaks corresponds to the position of the geometrical image of the aperture edge of the objective lens.

BACKGROUND FROM THE OBJECTIVE LENS

The glare of the central image is blocked by the opaque disk, and the diffraction fringes are eliminated by the re-diffraction system with the Lyot stop. The remaining measured background is scattered light from the defects in the objective lens such as scratches and digs on its surfaces. This scattered light intensity can reach 0.1% of the input light intensity. To eliminate this scattering background, we must polish the lens carefully to remove such scratches and digs on the lens surfaces. Figure 6 shows a microscope image of a well-polished surface for the object lens compared with a typical surface with optical polishing to scratch & dig 60/40. In these figures, surfaces are illuminated from the side (dark field illumination method). The surface of the lens with optical polishing to scratch & dig 60/40 still has many digs (small spots in the photograph). The surface of the objective lens using careful polishing has almost no digs.

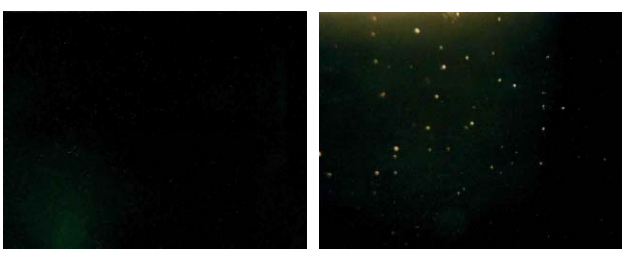

(a) (b)

Figure 6: Microscope image of the digs on the surface of lens illuminated from the side. (a) Surface of objective lens for coronagraph. (b) Surface with optical polishing to scratch & dig 60/40. The side of this picture is 5mm.

OBSERVATON OF BEAM HALO AT THE PHOTON FACTORY

To investigate the performance of the coronagraph, we observed the beam halo at the Photon Factory.

Design of Coronagraph

A well-polished singlet lens made of BK7 having a diameter of 150 mm is used as an objective lens. To reduce spherical aberration, the shape of the lens is chosen to be concave-flat. The focal length of the objective lens is chosen to be 2000 mm to obtain a sufficient size of the beam image on the blocking disc. A square aperture is set just in front of the objective lens to define the entrance pupil. We prepared cone-shaped opaque disks as shown in Fig. 6. The opaque disk is set on a 3-d movable stage for the adjustment of the transverse and longitudinal positions of the disk relative to the beam image. The opaque disk assembly is set in front of the field lens to block the glare of the central beam image. The diameter of the opaque disk is chosen to block 4 σ of the beam size.

Figure 7: Photograph of the opaque disk to block the glare of central image.

An ED achromatic lens having a focal length of 500 mm with a diameter of 50 mm is used as the field lens. A quadratic slit is set in the imaging plane of the field lens as the Lyot stop. A band-pass filter of 550 nm with a bandwidth of 10 nm and dichroic polarization filter are set before the Lyot stop. We used two ED achromatic lenses for the final image relay system. A high-speed gated camera (Hamamatsu photonics C2925-01) is used for the observation of the final image.

Low-noise mirror for the light transport line

The SR monitor has a light transport line between the source point and the observation system such as the coronagraph. The visible SR is extracted by a water-cooled mirror made of beryllium. Then the visible SR is relayed to the dark room by three mirrors made of fused silica. The surface scattering of the Be mirror is rather large due to many digs on the surface. But this Be mirror is located near the source point, and far from the coronagraph. The estimated contribution of background noise from the Be-mirror is about 5×10^{-7} due to the distance between the mirror and the coronagraph. We have a final mirror in the light transfer line in 2 m front of the coronagraph, and the contribution to the background from this mirror is estimated to be 6×10^{-5}. This background is too strong for beam halo observation. We replaced this mirror with a newly made low-noise mirror. As a low noise mirror, we used a well-polished optical flat of the same quality as that of the objective lens of the

coronagraph having a backside Al coating as shown in Fig. 8. To eliminate a ghost image from surface reflection, we applied a small wedge angle (10 arcsec) between both surfaces as shown in Fig. 8. Since the arrangement of back side coating and quasi-parallel surfaces will easily produce interference fringes, this small wedge angle is also important to eliminate the contrast of interference fringes in the ray.

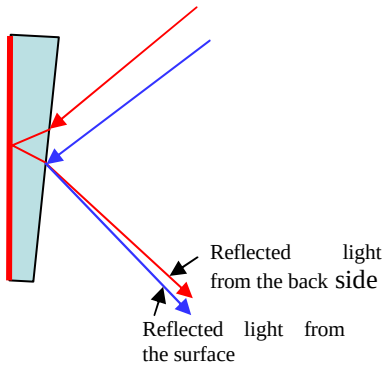

Figure 8: Low-noise mirror for light transport line.

Observation of beam halo

At first, we observed an image of the stored beam profile without the opaque disk and Lyot stop. The result is shown in Fig. 9.

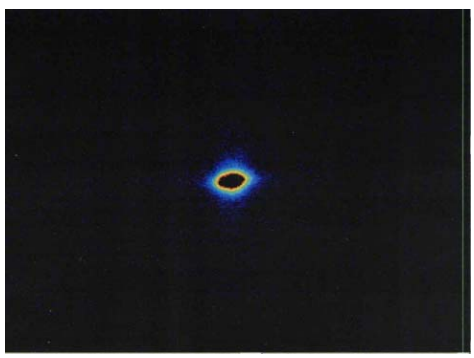

Figure 9: Image beam profile without the opaque disk. Exposure time of CCD camera is 10μsec.

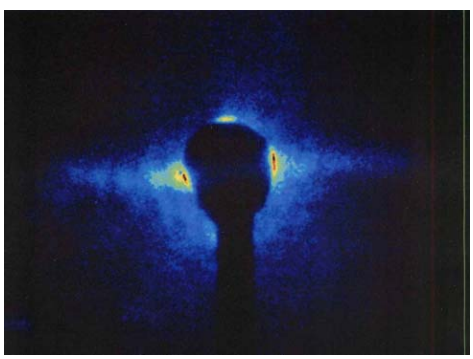

Figure 10: Image of beam halo with the opaque disk. Transverse magnification is same as in Fig. 9. Exposure time of CCD camera is 10 msec.

The exposure time to catch this image was 10 μsec. Next, we observed an image of the beam halo by applying the opaque disk to blocking the central beam image and Lyot stop. Since the intensity of the beam halo image is very weak, we increased the exposure time of the CCD camera. An example of the beam halo image is shown in Fig. 10. The exposure time was 10 msec. Considering the differences in exposure time, the intensity scale in Fig.10 is 1000 times smaller than the intensity scale in Fig 9.

Observation of beam halo with diffraction

On trial, to investigate the effect of diffraction in the halo observation, we observed an image with opaque disk and without Lyot stop. An example is shown in Fig.11. In this figure, we rotate the square entrance pupil by 30 deg for the easy discrimination of the diffraction effect. We can see the tilted diffraction halo in this figure.

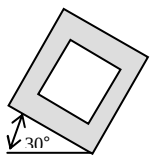

Entrance pupil is intentionally rotated by 30° to recognize diffraction tail easily.

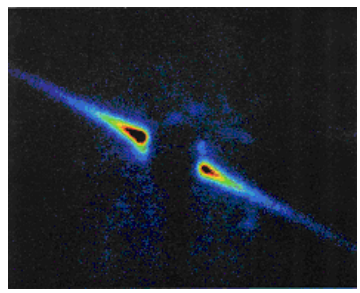

Figure 11: Halo with diffraction observed with opaque disk and without Lyot stop.

A comparison of intensities of halos measured with and without opaque disk and Lyot stop are shown in Fig.12. Both intensities are normalized by the peak intensity of the central beam image. As discussed in Section 1, the beam halo image with diffraction observed without Lyot stop has an intensity range of 10^{-2} of the peak.

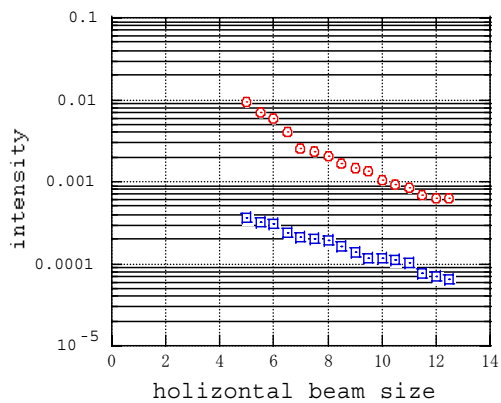

Figure 12: Comparison of beam tails; circles denote beam halo without opaque disk. The red circles denote halo with diffraction. The blue squares denote beam halo measured with opaque disk and Lyot stop. The horizontal axis is normalized by 1σ of the beam size.

Observation of beam halo at different ring currents

The beam halo images are observed at several ring currents in the single bunch operation of the Photon Factory. Results are shown in Fig. 13. For an example at small beam current, the beam tail image which is observed in the multi-bunch operation is also shown in Fig. 13. The corresponding bunch current is 1.4 mA. The intensity of the beam halo becomes stronger as the bunch current is increased. Not only the intensity, but also the two-dimensional distributions of the beam halo are changed in this figure. Particularly in the vertical axis, the area of the beam halo is enlarged as the beam current increases.

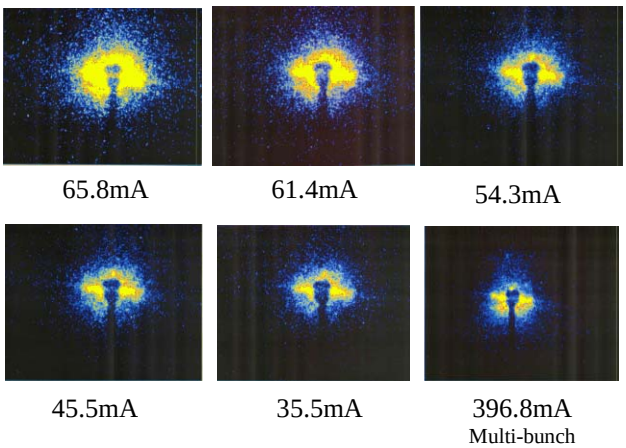

Figure 13: Beam halo observed at different ring currents in the Photon Factory.

Observation of far outside beam halo

As seen in Fig.13, the area occupied by the beam halo does not increase in the horizontal direction as the beam current increases. To investigate the beam halo far outside in the horizontal, we block the strong halo area. This time, an opaque stick was used instead of the opaque disk. An example is shown in the lower picture of Fig.14.

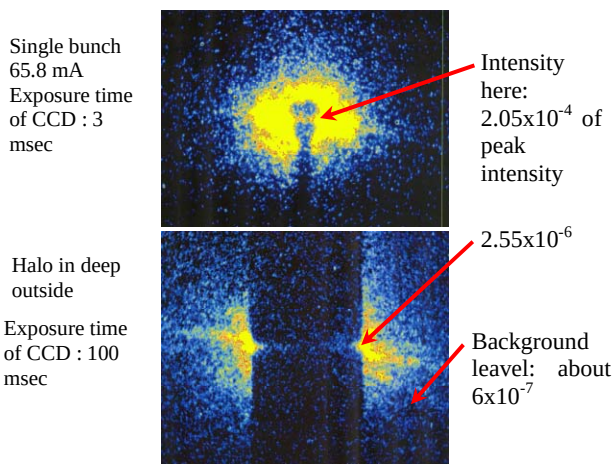

Figure 14: Observation of far outside halo at the Photon Factory.

The exposure time for this observation was increased to 100 msec. This exposure time is about 33 times longer than that in Fig.13. The projection of the horizontal distributions of the beam halos in Fig.14 is shown in Fig. 15.

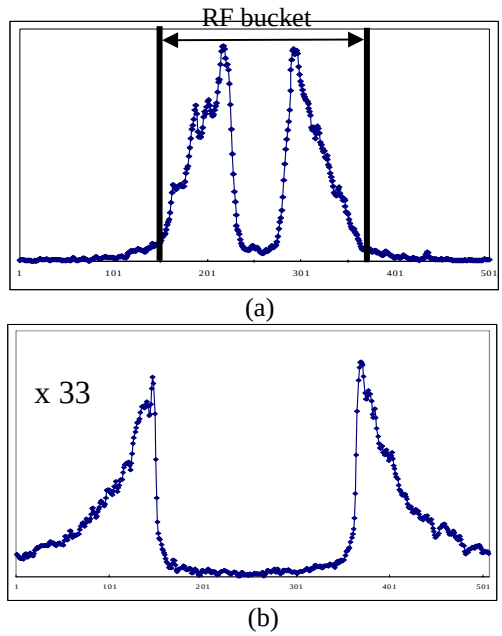

Figure 15: The projection of horizontal distributions of beam halos in Fig.14. (a) Strong beam halo. (b) Weak beam halo far outside.

From the lower picture of Fig. 15, the background level is 6 x 10^{-7} of the peak intensity. This background level is almost the same value as the estimated background from the Be-mirror as discussed in Section 5-2. We see two types of beam halo in Fig.15 (a). One is a strong halo having an intensity range of 10^{-4} in inside the area which corresponds to the separatrix of the RF bucket scaled by the value of the dispersion function at the source point. The other is a weak halo having an intensity range of 10^{-6} outside of this area.

CONCLUSION

We developed and constructed a coronagraph for the observation of the beam halo surrounding the beam. The optical polish of the objective lens is a key point in achieving a good S/N ratio, and we succeeded in obtaining a signal to background ratio 6x10^{-7}. To investigate the performance of the coronagraph, we measured the beam halo at the Photon Factory. As results, we observed a strong beam halo inside the RF bucket and a weak halo outside the RF bucket. The coronagraph is applicable not only to observing the beam halo, but also has many possibilities such as the observation of an injected beam under the presence of intense stored beam.

REFERENCE

[1] B.F.Lyot Month. Notice Roy. Ast. Soc, p580, **99** (1939.)

LARGE DYNAMIC RANGE BEAM PROFILE MEASUREMENTS *

A. P. Freyberger,
Thomas Jefferson National Accelerator Facility, Newport News, VA 23606, USA

Abstract

Large dynamic range ($Peak/Noise > 10^5$) beam profile measurements are routinely performed in the Hall-B beamline at Jefferson Lab. These measurements are made with a 1 to 10nA electron beam current with energies between 1 to 6 GeV. The electron beam scatters off of a thin W or Fe wire and the scattered particle/shower is detected via scintillation or Cerenkov light several meters downstream of the wire. This report describes results on increasing the dynamic range by using multiple wires of varying diameters. Profile measurements with this large dynamic range are of use for accelerators with large amount of stored energy (e.g. energy recovering linacs [ERL]) where small beam loss represents a significant amount of beam power. Results on measuring the transverse profile with large dynamic range during the CEBAF energy recovery experiment is also presented.

INTRODUCTION

Transverse beam profile measurements are typically performed to extract the transverse width of the beam. Such measurements place a modest demand on the signal to noise of the technique. Typically a signal to noise ratio of 100 is more than sufficient for such measurements. This paper describes the large (greater than 10^5) dynamic range beam profile technique used at JLAB. The technique has been used for two experiments, beam acceptance for the CLAS detector in end-station B and for measuring the width of the energy recovered beam during the JLAB energy recovery [ER] experiment. Transverse beam profiles with five to six orders of magnitude dynamic range represent a challenge for the diagnostics. The technique described in this paper is similar/identical to several other efforts summarized in the recent HALO2003 conference[1].

CLAS Experiment

Experiments with the CLAS detector [2] in end-station B at Jefferson Lab (JLAB) place strict requirements on the beam halo due to the small diameter target window (2 to 4mm). The target frame represents a large amount of material when compared to that of the target. Beam particles outside of target window interacting in the target frame can result in an event rate comparable to that of interactions in the target proper. The transverse beam profile measured with sufficient dynamic range provides a mechanism for determining the acceptability of the delivered beam and minimizing or eliminating completely the background from non-target interactions.

Energy Recovery Experiment

Presently there is interest in constructing energy recovery linacs [3, 4] for different applications. A feature of ERLs is the amount of stored energy in the beam. Small loss of beam will result in energy deposition in the beam pipe and possible loss of vacuum. Continuous operation of an ERL requires that the beam loss from injection to energy recovered beam dump be typically less than 1ppm. The JLAB Energy Recovery [ER] experiment is a test of the energy recovery concept using a large number of RF cavities[5]. The electron beam is injected with 55MeV(20MeV) of energy, accelerated to 1GeV and the phase shifted 180° and energy recovered through the RF section back down to the injected energy. One of the issues of interest is the beam shape of the energy recovered beam. The dynamic range that the transverse beam profile after energy recovery retains a Gaussian shape provides information on how much of the beam is retained [ie not lost] in the Gaussian core.

TRANSVERSE PROFILES FOR THE CLAS EXPERIMENT

The beam profile is measured by correlating a wire scanner position with count rates in photomultiplier tubes [PMT] located downstream of the wire scanner. The wire scanner assembly consists of a linear actuator which moves the horizontal and vertical wires through the beam. The actuator is driven by a stepper motor, which drives the wire support structure into the beam axis. The wire support is driven at a 45° with respect to the horizontal axis, which enables both the X and Y profiles to be measured with one axis of motion.

The PMTs [6] which detect the resulting scattered electron or shower are located downstream of the wire scanner. The distance between the wire scanner and PMTs is optimized for symmetric Møller scattering at beam energy of 5 GeV. Four 2" diameter PMTs are installed outside of a 3" diameter beam pipe, located in the following configuration: top, bottom, beam left, and beam right. The top-bottom PMT pair uses Cerenkov light in the quartz window to detect the scattered/showering particle(s). The left-bottom PMT pair has 0.5" scintillator in addition to the quartz window for detection of the scattered/showering particle(s). Due to the low operating beam current in Hall-B, typically 1 to 10nA, the PMTs can be operated in "count

* This work is supported by the Southeastern Universities Research Association (SURA) which operates the Thomas Jefferson National Accelerator Facility (JLAB) for the United States Department of Energy under contract DE-AC05-84ER40150.

mode". The PMT signals are discriminated and counted via a VME scaler. In addition to counting the individual PMT rates, the top-bottom and left-right coincidence rates are also fed to the scaler. These coincidence rates have a much lower background than the individual rates. In addition to the PMT rates, signals proportional to the beam current are also scaled and are used to normalize the PMT rates to the beam current.

Both the stepper motor controller[7] and PMT scalers[8] are VME modules contained within the same VME crate. EPICS controls[9] are used for both devices and state code is used to synchronize the motor motion and scaler readout. During a wire scan the motor position and scaler values are written to a file for further analysis. The minimum time between scaler reads is $\sim \frac{1}{60}$sec and is determined by the maximum update rate on the motor position. The motor speed and time between scaler reads are configurable at the beginning of each scan.

There are two wire scanners at the end of the transport line, upstream of the experimental target. One wire scanner [CLAS wire scanner] uses 50μm W wires and routinely measures the beam profile over five orders of magnitude. A second wire scanner [Integrating CLAS wire scanner] uses wires and integrating plates and is used for increased sensitivity.

The CLAS Wire Scanner

The CLAS wire scanner is located 12m upstream of the PMT bundle and scans 50μm X and Y wires through the beam. The scan speed is configurable and typically speeds of 1mm/sec are used, but slower speeds result in better sensitivity. This wire scanner measures the beam profile with a $Peak/Noise > 10^5$ response. Figure 1 shows a beam profile obtained with a wire speed of 0.25mm/sec and the bottom PMT. Figure 2 shows the same profile but using the coincidence signal between the top and bottom PMTs. The coincidence data is background free, and requires an unacceptably long integration time in order to determine the background level. The end result is that the coincidence signal has an indeterminate signal to noise level.

The achieved dynamic range of 10^5 satisfies the experimenter's requirements, and often the beam profile is Gaussian over the complete dynamic range. To observe and measure beam width with more sensitivity the integrating CLAS wire scanner is used.

THE INTEGRATING CLAS WIRE SCANNER

The wire configuration and support frame for the integrating wire scanner are shown in Figure 3. The wire configuration consists of 25μm diameter X and Y wires, 1mm diameter X and Y wires and a 1mm x 10mm X plate. All wires are made out of Fe for consistency and the plate is stainless steel for convenience. This wire scanner is 5m upstream of the PMT bundle.

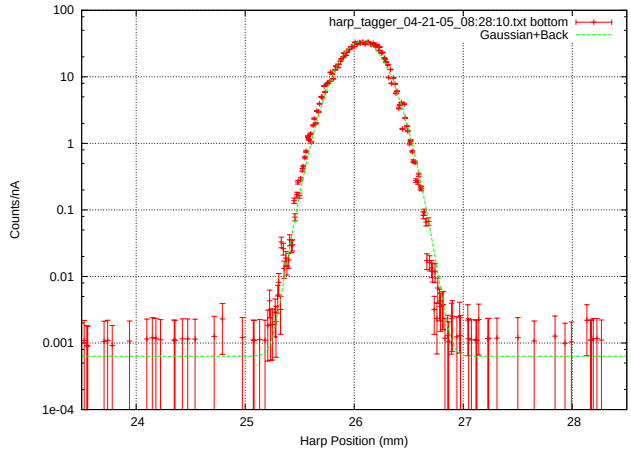

Figure 1: Beam profile [X] using a 25μm wire and PMT readout. The green curve is the result of a fit to the data using a Gaussian plus constant background as the functional form. The data for scan is taken simultaneously with that in Figure 2.

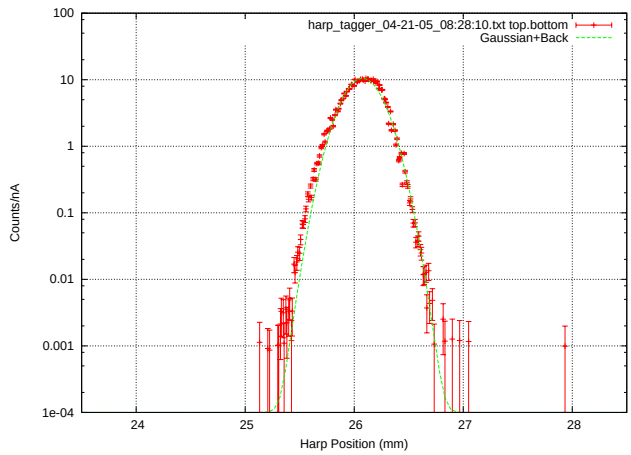

Figure 2: Beam profile [X] using a 25μm wire and the coincidence signal between the top and bottom PMTs. The data for scan is taken simultaneously with that in Figure 1.

Scans were taken in Hall-B with a 1 GeV electron beam with 6 nA of beam current. Scans were taken periodically over several days, while trying to optimize the motor speed and scaler acquisition rate. A slow motor speed results in a high number of data points that allow better matching between the 25μm and 1mm wire or plate data. However, a slow scan speed (0.125mm/sec) often resulted in an incomplete wire scan due to a beam trip. During these scans CEBAF was delivering beam ($1 - 40\mu$A) to the other two experimental halls (Halls A & C).

Integrating Wire Analysis

Once a scan file has been written to disk, offline analysis must be performed to combine the 25μm wire data with the 1mm wire or plate data. The technique used is similar to that found in Ref. [10]. The beam size is small com-

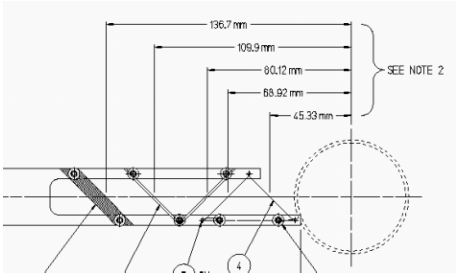

Figure 3: Mechanical schematic of the wire/plate support structure. The thin wire is 25μm in diameter. The thick wire is 1mm in diameter. The plate is 1mm by 10mm. The wire frame is moved into the beam along a 45° axis with respect to the horizontal axis.

pared to the 1mm wire diameter and the X plate. Therefore this data must be differentiated before combining with the 25μm wire data. In order to determine the scale factor and position alignment a χ^2 minimization is performed to match the 25μm data with the differentiated data. The two data sets need to overlap by at least two orders of magnitude [after scaling] in order for the procedure to converge. Noise is suppressed on the 25μm wire data sample, by only using data with more than 10 counts.

Naively one expects a scale factor of 1600 for the 1mm wire, based on the square of the ratio of the wire diameters. The scaler factor for the match between the 1mm wire data and the 25μm wire data had a range between 1400 and 1900 for the scans that were taken. On each individual scan there are four matches that need be performed, two sides of two profiles. The minimum scale factor of the four (1400) is used to match the 1mm data with the 25μm data.

The scale factor for the X plate data will depend on the extent of the beam in the X dimension. Again a χ^2 minimization is performed and scale factor is found to be ~ 1750.

Once the data has been combined it is fitted to the following functional form

$$F = b + G(A_{core}, \sigma_{core}, mean) + G(A_{halo}, \sigma_{halo}, mean) \quad (1)$$

where the G represents a Gaussian function and b is a constant background term. Both the core Gaussian and the halo Gaussian have the same mean.

RESULTS

Figure 4 shows the X and Y beam profile obtained using a motor speed 0.125mm/sec. A small second Gaussian component is observed with the 1mm wire data, which is too small to be observed with the 25μm wire. The parameters determined by the fit are listed in Table 1. Figure 5 shows the X profile for the same scan using the $1 \times 10\text{mm}^2$ plate data. The parameters determined by the fit to the plate data agree with those obtained with the 1mm, see Table 1 suggesting that the scale factor is properly determined.

Figure 6 shows the X and Y beam profile obtained using a motor speed 0.250mm/sec. These parameters determined by the fit for this scan and others not shown here are tabulated in Table 1.

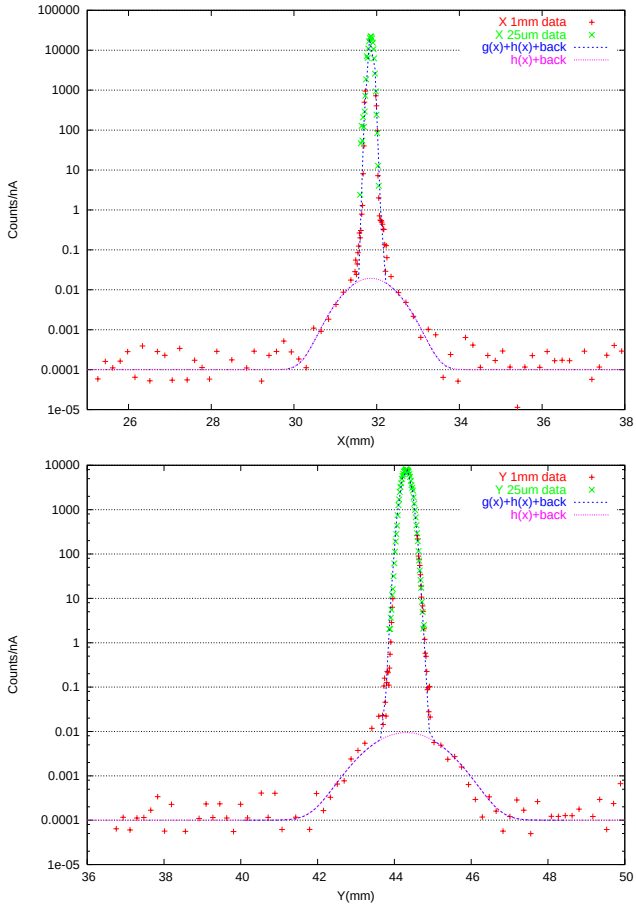

Figure 4: Beam Profile combining the 25μm and 1mm Fe wire data. The top(bottom) plot shows the X(Y) data and results of the fit to the data. The red points represent the 1mm wire data, the green points the 25μm wire data, the blue curve is the overall fit to the data and the red curve is the halo portion of the fit. The ordinate is plotted with a log-scale and the count rate is normalized to the beam current.

The figures show a signal Peak/Noise ratio of $\sim 10^8$ which is an improvement over the existing system. With this increased dynamic range a small second Gaussian component of the beam has been observed in the Hall-B end-station. The source of this second Gaussian is unknown. Scans taken within of few minutes of each other yield consistent results, while scans taken a few days show that the size of the second Gaussian component is changing.

Table 1: Profile parameters obtained by fitting the data to the sum of two Gaussian functions with a common mean for all the scans.

	scan1	scan2 (Fig. 6)	scan3 (Fig 4)	scan3-X plate (Fig 5)	scan4
Date	Dec. 5 17:09	Dec. 9 14:45	Dec. 9 14:51	Dec. 9 14:51	Dec. 10 18:22
$\sigma_{core}[\mathrm{X}](mm)$	0.045	0.053	0.052	0.052	0.106
$\sigma_{halo}[\mathrm{X}](mm)$	0.380	0.470	0.494	0.476	0.656
$\sigma_{core}[\mathrm{Y}](mm)$	0.104	0.111	0.110		0.085
$\sigma_{halo}[\mathrm{Y}](mm)$	0.949	0.855	0.771		0.617
$\frac{A_{halo}}{A_{core}}[\mathrm{X}]$	$4.2 * 10^{-5}$	$1.1 * 10^{-5}$	$8.0 * 10^{-6}$	$7.3 * 10^{-6}$	$3 * 10^{-4}$
$\frac{A_{halo}}{A_{core}}[\mathrm{Y}]$	$1.3 * 10^{-5}$	$4.8 * 10^{-6}$	$5.8 * 10^{-6}$		$< 7 * 10^{-5}$
Motor Speed	0.250mm/sec	0.250mm/sec	0.125mm/sec	0.125mm/sec	1.5mm/sec
Wires	25μm/1mm	25μm/1mm	25μm/1mm	25μm/1x10mm^2 plate	50μm

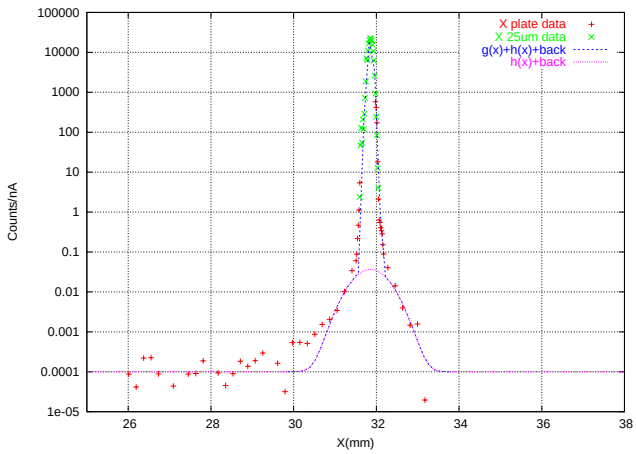

Figure 5: X Beam Profile combining the 25μm and 1×10mm^2 steel plate data. The red points represent the 1mm wire data, the green points the 25μm wire data, the blue curve is the overall fit to the data and the red curve is the halo portion of the fit. The ordinate is plotted with a log-scale and the count rate is normalized to the beam current.

ENERGY RECOVERY TRANSVERSED PROFILES

Large dynamic range beam profile measurements of the energy recovered beam are made with a wire scanner located upstream of the energy recovered beam dump. The wire scanner mechanism is a standard JLAB wire scanner which holds two 25μm W wires.

The wire scanner is only 2m upstream of the dump, limiting the choice of locations for the PMTs. Additionally the proximity of the dump causes some concern about high levels of background originating from the beam dump. Three PMTs are located on the beam pipe [beam left, top and right]. The distance between the PMTs and the wire scanner is chosen to maximize acceptance of Møller scattered electrons, just in case the background from the beam dump is an issue. In order to make use of the Møller electrons, the PMTs are operated in "count mode" and the left-right PMTs are used in a coincidence circuit. Background from the beam dump turned out to not be an issue, and the coincidence signal is abandoned.

Figure 7 shows the profile for the 55MeV ER configuration and the profile for the 20MeV ER configuration in shown in Figure 8. The 55MeV profile shows a clean beam distribution over almost five decades of amplitude, with a small distortion on the left of the X profile. The wide horizontal beam profile in the 20MeV ER configuration is what limited the CW beam current delivery during this part of the experiment. In an attempt to measure the profile with beam currents greater than 1μA, one the PMTs is operated in "current mode" during the 20MeV portion of the experiment. The current mode data and count mode data are merged using similar technique as that used for the CLAS integrating plate data.

SUMMARY

Transverse beam profiles with dynamic range of five orders of magnitude are performed regularly in the end-station B transport line. Using integrating plates and wires the dynamic range can in extended another two to three orders of magnitude. Such sensitive profiles show a small second Gaussian component. The diameter of the 1mm integrating wire is comparable to the width of the second Gaussian term and is not fully integrating this source. This might account for the some of the data to prefer a lower scale factor [1400] then the geometric factor [1600]. On the other hand the 1mm$\times$10mm plate is more then sufficient. Changing the X/Y 1mm diameter wires to X/Y 1mm$\times$5mm plates is planned.

The energy recovered transverse beam profile measured in a similar method the routine end-station B shows a well behaved Gaussian shape over five orders of magnitude. In order to achieve the desired six orders of magnitudes, integrating plates are needed. Beam heating of the integrating plates is an issue as the beam currents of the ER experiment range from 1μA to 100μA. Experiments with chemical vapor deposited Silicon Carbide (CVD SiC) suggest that this material can withstand intercepting such beam currents[11] and would make a good choice for an integrating plate.

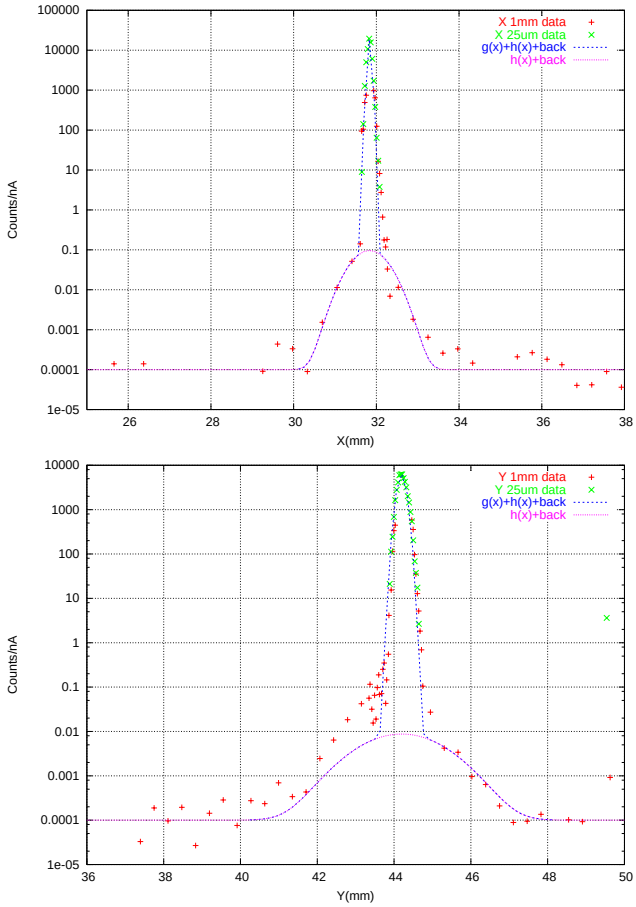

Figure 6: Beam Profile combining the 25μm and 1mm Fe wire data. The top(bottom) plot shows the X(Y) data and results of the fit to the data. The red points represent the 1mm wire data, the green points the 25μm wire data, the blue curve is the overall fit to the data and the red curve is the halo portion of the fit. The ordinate is plotted on a log-scale and the count rate is normalized to the beam current.

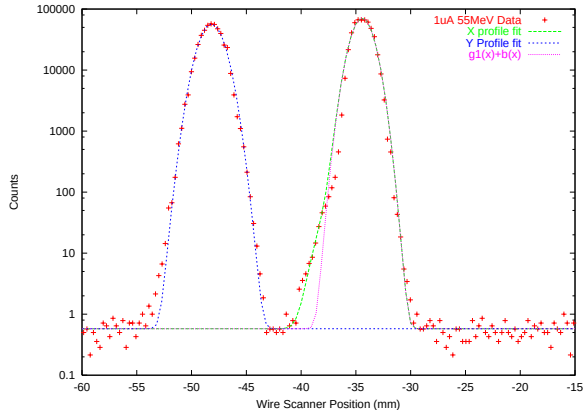

Figure 7: Beam profile after energy recovery for the 55MeV injection configuration.

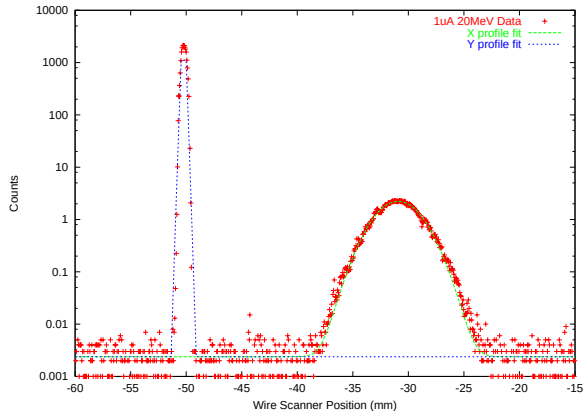

Figure 8: Beam profile after energy recovery for the 20MeV injection configuration.

ACKNOWLEDGMENTS

The author thanks the Hall-B colleagues and CLAS collaborators for beamtime to perform these measurements. Thanks also to M. Zarecky, P. Hemler and D. Kashy for engineering and design support. The CEBAF operations staff efforts to delivery stable beam during these measurements is also greatly appreciated.

REFERENCES

[1] Proceedings of the Beam Halo Dynamics, Diagnostics, and Collimation, edited by J. Wei, W.Fisher and P. Manning, AIP proceedings CP693.

[2] B. Mecking, *et al.*, "The CEBAF Large Acceptance Spectrometer (CLAS)", to be published in NIM-A 2003.

[3] L. Merminga, D. Douglas, G. Krafft, "High Current Energy Recovery Electron Linacs" Annu. Rev. Nucl. Part. Sci., **53**, 387 (2003). f

[4] See the slides of the recent ERL 2005 conference at `http://www.jlab.org/intralab/calendar/archive04/erl/index.html` Proceedings to appear in NIM-A, editted by L. Merminga and S. Chattopadhyay

[5] A. Bogacz, *et al.*. "Cebaf Energy Recovery Experiment", in *Proceedings of the 2003 PAC*, `http://accelconf.web.cern.ch/accelconf/p03/PAPERS/TOAC006.PDF`.

[6] XP2622 photomultiplier tubes from Photonics Corporation (formerly Phillips), www.photonics.com.

[7] VME VS4 stepper motor control from Oregon Micro Systems, www.omsmotion.com.

[8] VME scaler, VSC16, from Joerger Electronics, www.joergerinc.com.

[9] Experimental Physics and Industrial Control System (EPICS), http://www.aps.anl.gov/epics.

[10] J.H. Kamperschroer, *et al.*, "Analysis of Data from the LEDA Wire Scanner/Halo Scraper", Proceedings of the 2001 Particle Accelerator Conference, Chicago.

[11] P.V. Degiarenko, *et al.*, "Radiation-Hard Beam Position Detector for Use in the Accelerator Dump Lines", These proceedings.

DESIGN AND TESTING OF THE MIT-BATES STERN-GERLACH POLARIMETER CAVITY

P. Cameron, N. D'Imperio, A.U. Luccio, W.W. MacKay, BNL, Upton, Long Island, New York
M. Conte, INFN Genova, Genova
W.A. Franklin, E. Ihloff, T. Zwart, MIT, Middleton, Massachusetts
D.A. Goldberg, LBNL, Berkeley, California

Abstract

Historically, beam polarization measurement has been accomplished by scattering experiments, with the attendant complexity of target and detector installation and operation, and smallness and uncertainty of analyzing powers. The purpose of the present effort is to accomplish fast and accurate polarization measurement not as a scattering experiment, but rather as conventional beam instrumentation, with a resonant cavity pickup. This requires that the coupling of the beam magnetic moment to the pickup be enhanced to bring the signal above the noise floor, and that coupling of the beam charge to the pickup be diminished to reduce the dynamic range problem. We discuss details of cavity design that have been implemented to accomplish these ends. Presently, it is planned to install the cavity in the Bates Ring in early May of this year. Beyond polarimetry, successful polarization measurement will verify the underlying principles, and by pickup/kicker reciprocity will open the serious consideration of the possibility of polarizing the full-energy LHC proton beams in-situ.

NO SUBMISSION RECEIVED

MICRO-STRIP METAL FOIL DETECTORS FOR THE BEAM PROFILE MONITORING.*

V. Pugatch, V. Aushev, O. Fedorovitch, A Mikhailenko,
S. Prystupa, Yu. Pylypchenko, KINR, Kiev, Ukraine
V. Karengin, V. Perevertailo, IMD, Kiev, Ukraine
M. Braeuer, H. Franz, K. Wittenburg, DESY, Hamburg, Germany
Ch. Bauer, M. Schmelling, MPIfK, Heidelberg, Germany

Abstract

The Micro-strip Metal Foil Detectors (MMFD) designed and used for the Beam Profile Monitoring (BPM) are discussed. The results obtained for the MMFDs produced by different technologies are presented. The MMFD deposited onto the 20 μm thick Si-wafer has been used for the BPM of the 32 MeV alpha-particle beam at the MPIfK (Heidelberg) Tandem generator. Another MMFD with totally removed Si-wafer at the working area has been applied for the on-line X-ray BPM at the HASYLAB (DESY).

INTRODUCTION

Current developments in fundamental and applied research require non-destructive 'on-line' profile monitoring of micro-beams. For low intensity beams a proper approach could be realized by using silicon micro-strip detectors successfully progressing last two decades. Manufacturing technology allows for a position resolution at sub-micron level. Yet, radiation hardness aspect makes this approach rather limited. The experience was reported [1] for the high intensity micro-beam profiling by means of fine strips supported by thin membranes. In this paper we present the first results of the beam profiling by the MMFD manufactured by different lithography and etching technologies. The MMFD deposited onto the 20 μm thick Si-wafer has been used for the BPM of the 32 MeV alpha-particle beam at the MPIfK (Heidelberg) Tandem generator. Another MMFD with totally removed Si-wafer at the working area of (8 x 10) mm^2 has been applied for the on-line X-ray beam profile monitoring at the HASYLAB (DESY).

MMFD PHYSICS AND TECHNICAL DETAILS

The general physics and registration principles of the Metal Foil Detector (MFD) are discussed in details somewhere [2]. Charged particles (or photons) hitting a metal sensor-foil initiate Secondary Electron Emission (SEE) at 10-50 nm surface layers, mainly [3, 4]. The electron yield is measured by a sensitive Charge Integrator connected to a sensor. To stabilize the electron yield two accelerating and two grounding foils are surrounding the sensor from both sides, creating complete MFD setup as a 5-layer structure. The first SEE monitor has been built in 1955 [5] and in its later modifications a typical position resolution was in the range of a millimeter. We have applied the technology developed for the silicon micro-strip detector manufacturing to produce metal micro-strip detectors for the purposes of the precise beam profile monitoring. 16 or 32 narrow metal strips(10-50 μm width, 20 - 100 μm pitch) are individually connected through the UHV feedthroughs to Charge Integrators (ChI). ChI designed and built for that purpose by the joint effort of the KINR (Kiev) [6] and Max- Planck Institut für Kernphysik (Heidelberg) have reached a fA level of a sensitivity, also due to the direct conversion of the measured current into the output frequency. Some of the advantages of the Micro-strip MFD BPM are as follows:

- Extremely low mass of the detecting material.
- Simple structure (thin, up to few tens nano-meter, metal strips self-supported in the operating area at Si-wafer).
- Low operating voltage ($\approx$ 20 V), which provides nearly total charge collection.
- Simple read-out electronics (charge integrators and scalers).
- Very high radiation tolerance (at Gigarads level).
- Position resolution of 1 μm is in the reach for the current manufacturing technology.
- Profile monitoring of a bunch train (below thermal electron emission threshold).
- Bunch by bunch profile monitoring possible.

The last two items are prospective for the MMFD connected to the readout microchip [7]. We have built and tested few prototypes of the Micro-strip MFD for the Beam Profile Monitoring (BPM).

MMFD SETUP FOR THE MONITORING OF THE 32 MEV HE-3 BEAM.

The first MMFD monitor has been used for the on-line control, positioning and focusing charged particles beam (32 MeV alpha-particles at the MPIfK (Heidelberg) Tandem generator for SEU (Single Events Upset)studies of the BEETLE chip [7].

* Work supported by the DESY Agreement/Contract

Sensors Preparation and MMFD Layout

The sensors have been manufactured by photo-lithography technology used for the silicon micro-strip detectors production and wet chemical etching. The 32 strips (pitch 30-35 μm) are 1 μm thick, 10 μm wide Al ribbons deposited via masks onto a Si-wafer (460 μm thick) over 0.1 μm thick Si_3N_4. A narrow rectangular window of (6 x 10) mm^2 was made by chemical etching of a Si-wafer in the part to be introduced into the beam. The thickness of the beam window (20 μm thick) has been optimized with respect to the mechanical stability and heat dissipation.The rigid surface of the Si-wafer provides reliable mechanical stability of the thin metal layers (which could be in the range of 0.1 μm resulting in the same physical signal of the SEE), and being still massive carrier of the heat load. Using adapter cable one side of strips is connected to the calibrating current source and the opposite one to the read-out Charge Integrator. This defines well the way of the charge transportation from the beam-strip interaction area. The sensor layer is surrounded from both sides by metal layers (grids) biased by a low positive voltage. The voltage accelerates secondary electrons and provides their efficient removal from sensors resulting in a 5 times larger signal at the Charge Integrator input. This 3-layer structure is finally surrounded from both sides by metal layers which should be well grounded to make an efficient shielding of the device. The above mentioned auxiliary metal layers are 1 μm thick, supported by the Si-wafers etched in a way similar to the sensor's case. Thus, the complete MFD is a 5-layer structure made out of thin metal foils. The sensitivity of the MMFD to the radiation flux is determined by the sensitivity of the charge integrators as well as by fluctuations of the charge at their input due to the leakage currents, temperature/humidity impact, r/f pick-up etc.

There is a big concern with respect to the MFD strip breakage [1]. The 5-layer structure of the MMFD has to prevent microwave heating which was considered as amajor cause of the wire breakage. The complete MFD prototype introduced into the beam 3 μm thick Al and 30 μm thick Si, in total. Connection of both ends of the micro-strip to the Charge Integrator has three-fold task: monitoring of the integrity of the micro-strip; limiting of the current through the strip by introducing serially a 1 GOhm resistor and finally providing a possibility of a correction of systematic error related to a variation of the charge integrator baseline and/or sensitivity. The level of an output frequency fluctuations measured from the stable calibrating current is in the range of +/- 2 Hz. The dynamical range is 1500 with a possibility to adjust the input current to be measured from 10 fA to 10 μA. The charge integrator read-out is provided by the vme-based 32 channel scaler with a software allowing for on-line beam profile monitoring also measured during specified time windows.

This setup has allowed to perform the study of the readout micro-chip BEETLE-128 with respect to the Single Event Upset probability. The He-3 beam intensity distribution over different parts of the chip has been measured by the MMFD and used for the SEU cross-section evaluation [7].

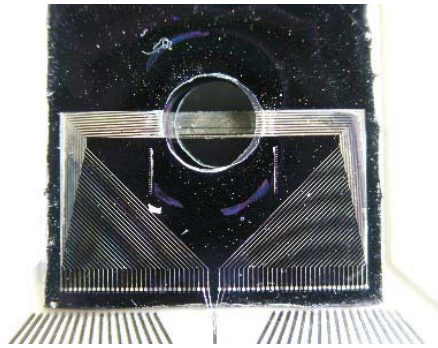

Figure 1: Metal Foil Micro-strip Detector (the HV-layer and sensor layer are visible). The operating window with totally removed Si-wafer (diameter 8 mm) is in the center. The calibrating current feeds through the left/right hand pads and strips.

EXPERIMENTAL SETUP AT HASYLAB

There are considerations to apply the micro-stip MFD for the undulator radiation monitoring at the PETRA facility (similar to the device described in [8]). We expect an improved performance of the MFD detector in comparison with [8] due to its 5-layer structure as well as much better spatial resolution should be obtained.

Sensors Preparation and MMFD Layout

The sensors were prepared by means of micro-electronics technology and plasma-chemistry etching. To isolate a metal film from the wafer the dielectric layers were grown up on both sides of a wafer. At first, the silicon oxide (0.1 - 0.3 μm thick) was grown up covered later by 0.2 μm thick silicon nitride. A thin (0.1 μm) titanium layer was deposited onto dielectric layers. Afterward, nickel (0.5 μm) layers covered finally by silver layers (0.6 μm) served as films for the photo-lithography shaping of the strip pattern as well as contacting lines and pads.

A window from the back side has been created for the plasma-chemistry etching. The KINR plasma-chemical reactor with variable ion energy has been used. The initial etching speed was in the range of 2.5 μm/min at the ion energy of 80 eV and discharge current of 10 A. When the silicon wafer thickness approached 50-100 μm the etching speed was slowed down to 0.3 μm/min by decreasing the current to 4 A and the ion energy to 20 eV. In this way the MMFD (Fig.1) has been manufactured with 30 (out of 32) self-supporting strips (20 μm width, 70 μm pitch) which survived in the operating window with a diameter of 8 mm.

The strips were bonded to the ceramics based pitch adapter and connected by a flexible Kapton isolated cable to the 50 pin-connector and through the additional cable via the UHV feedthroughs to Charge Integrators housed inside

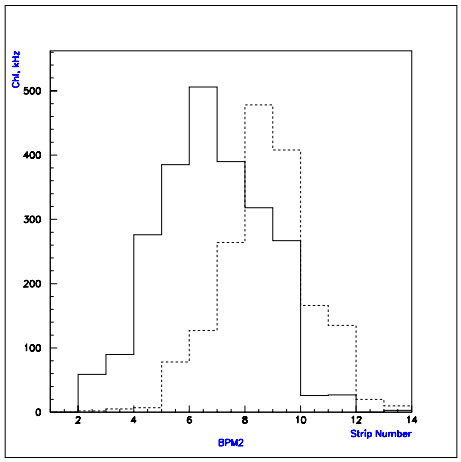

Figure 2: X-ray Beam Profile measured at two MMFD setup positions. The difference between positions is 150 μm.

the NIM crate (3 mm coaxial cables fed the signals from the flange with UHV feedthroughs).

The experiment has been performed at the HASYLAB (DESY) on beam-line BH6. The electron ring PETRA was filled with an injection current ranging from few mA to 40 mA. The beam was monochromated to allow X-ray energies 15 or 18 keV. The beam size was determined by the copper slits and varied from 0.1 to 1 mm in vertical direction while horizontally it was in the range from 1 to 4 mm. The MMFD setup was mounted on a copper cooling table equipped by horizontal and vertical translation stages, allowing positioning and scanning in the plane perpendicular to the beam axis. Fig.2 illustrates a beam profile measured at three fixed MMFD positions (solid and dashed lines) differing by 150 μm. The vertical beam size defined by the slits in that case was 500 μm, which fits well with the width of the intensity distributions shown in Fig.2.
For the X-ray ($\approx$ 15 keV) beam intensity of 4.5 $\times$ 10^{14} photons/second/mm^2) the conversion coefficient (number of photons per single SEE) has been evaluated as (1.5 +/- 0.5)$\times$ 10^4 ph/e. Accordingly to [8] the synchrotron flux of 2 $\times 10^8$ photons/s/100mA/mm^2 with the energy of 8 keV resulted in the SEE-current in their sensors around 0.5 - 1.0 pA. The current we observed in a single strip was in the range of 1 nA. This means that with this setup 3-4 orders of magnitude lower intensity X-ray beams could be well monitored. On the other hand as far as this is very close to the upper limit of the most sensitive charge integrators (1 Hz - 1 fA) to be able to make test at the nominal PETRA current of 50 mA we switched to other charge integrators with a sensitivity of 1 Hz per 1 pA. The preliminary measurements have shown that those charge integrators will provide a reliable beam profile monitoring. Yet, even if the X-ray flux loss inside the MMFD did not exceed 3 % the problem with overheating of the strips has to be solved, as far as some strips were broken during the test at high intensity X-ray beam (average energy 15 keV, total flux 1.7 $\times 10^{16}$ photons/s over the slit of (1 x 0.5) mm^2.
In summary, one may conclude that the developed technology of the micro-strip metal detector manufacturing allows to provide non-destructive measurement of X-ray intensity distribution over area of up to 50 mm ^{2} with an accuracy of 10-20 μm with a possibility of its improvement by factor of 5. A sub-micron position resolution is expectedly in the reach by applying electron lithography for the strip pattern production.

OUTLOOK

The program of the forthcoming tests of the MMFD at PETRA includes:

- Study of the thermal threshold;
- Profile measurements with very high resolution;
- Noise and Higher Order Mode studies;
- Dynamic range;
- Long term stability of the conversion factor;
- Radiation hardness;
- Damage threshold, etc.

ACKNOWLEDGMENTS

We are grateful to N. Tkatch, N. Bulian, V. Wieder and P.Pelikan for designing and building excellent charge integrators for these studies. We appreciate an essential help provided by A. Ehnes and T. Kracht during the MMFD test at HASYLAB.

REFERENCES

[1] C.H. Back et al., Nucl. Instr. and Meth., A435(1999)318

[2] V. Pugatch et al., *NIM*, **A 535** (2004) 566

[3] E.J. Sternglass *Phys.Rev.* **108** (1957) 1

[4] H. Rothard et al., *in: Springer Tracts in Modern Physics, Springer, Berlin*, (1992) 97

[5] Tautfest, et al.,*Rev. Sci. Instr.*,**24** (1955) 229-231

[6] N.M. Tkatch, V.A. Kiva, *Scientific Papers of the Institute for Nuclear Research*, **No. 2(4)** (2001) 72

[7] N. van Bakel et al., *The Beetle reference manual*, Version 1.0, LHCb Note 2001-046 (2001)

[8] C. Schulze-Briese et al., *Nucl. Instr. Meth.*, **A 467-468** (2001) 230

DETAILLED EXPERIENCE OF SYNCHROTRON LIGHT EXTRACTION SYSTEM WITH SLOTTED MIRROR AT THE ESRF

B.K. Scheidt, ESRF, Grenoble, France

Abstract

A slotted, non-cooled, mirror was implemented for the extraction of synchrotron light to feed an Infra-Red spectrometer and microscope in a new laboratory. The slot lets the energetic part of the synchrotron light go through and is kept vertically centred on the heart of the X-ray beam in a slow feed-back loop. This paper reports the experience obtained on : 1) The quality and stability of an imaged light spot that demonstrates the entire system being free of wave-front distortion and vibrations. 2) Elastic deformation study on the Aluminium mirror. 3) Mapping of edge radiation, produced by the interference of light emitted by the edges of up- and down-stream dipoles. 4) UV induced mirror blackening with dependence on the choice of the mirror material.

PRINCIPLE & OPERATION MODES

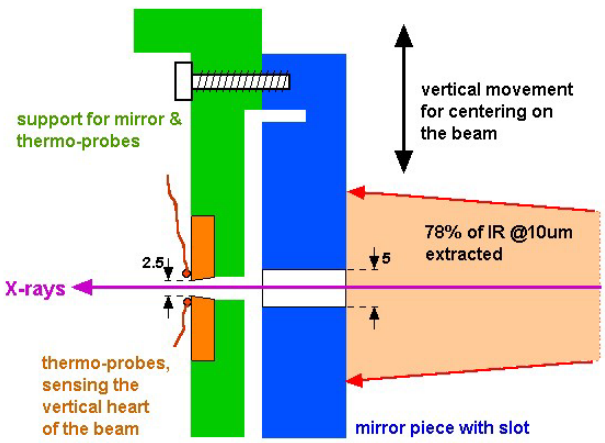

Figure 1: Slotted mirror vertically centred on photon-beam.

The concept of a slotted mirror was adopted for the extraction of InfraRed light from the cell-23 down-stream dipole for reasons of maximum flux extraction and minimum wavefront distortion to preserve the high brightness quality of the source. Although 22% of the lightflux (λ=10um) is lost through the 5mm high slot of the mirror, at 3.2m from dipole entrance, the extracted light is free of any distortion if the upper and lower parts of the mirror surface can be manufactured to good flatness (1um peak-valley) upto a negligible distance (0.1mm) from the slot-edge. The diamond milling technique employed allowed meeting these requirements on the 10mm thick single block aluminium mirror [1].

The 2nd requirement is to keep this slot centred on the photon beam heart under all circumstances and in a highly reliable way so to avoid the occurrence of the high energetic (155W/mrad hor.) X-ray beam hitting any part of the mirror surface and inflicting permanent deformation. This is achieved by thermoprobes (each made up of 3 individual thermocouples) above and below the heart of the beam. At a 1.25mm distance from the beam (at 200mA ESRF current) each probe absorbs at total of ~0.8W which results in a steady-state temperature of 70C. A slight off-centre results in a differential temperature between the upper and lower side, which is then corrected for in a software control loop that keeps the 2 readings equal within a hysteresis value of a few degrees.

Although the control loop is slow it is to be noted that the ESRF electron beam is surveyed by 2 different types of vertical beam machine interlocks. In case of either a sudden large vertical step (>0.7mm), or a fast vertically oscillating beam (amplitude >0.4mm) around a normal average position, these interlocks would cut the stored beam quickly. Therefore the control loop for the mirror does not have to provide itself for a total protection against all sorts of abnormal electron beam behaviour. Nevertheless, for an ultimate protection, a hardwired interlock is triggered directly and independently by the device if any temperature reading exceeds 100C.

The mirror assembly is also equipped with a thermoprobe at the extreme lower end so that it can be operated in a so-called 'half-mirror mode'. Furthermore the mirror can be also be totally extracted, or fully inserted so the deflect all the impinging dipole light (see fig.2). In the latter case, used only for specific studies reported here below, the thermal deformation is avoided by operation under low (<1mA) electron beam current.

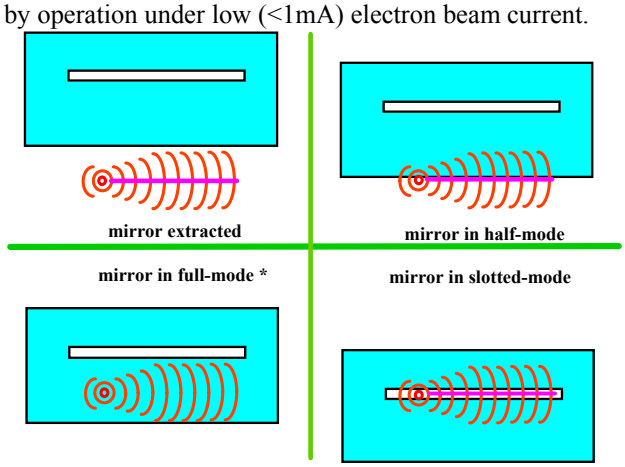

Figure 2: Mirror in 4 vertical positions & operation modes.

Note the absence of cooling to the mirror assembly so to avoid the introduction of any vibrations by a (water) cooling circuit, while allowing keeping the system light, compact and simple. The X-rays going through the slot are absorbed 2.5m downstream by a standard beamport

absorber, with a 400litres Ion vacuum pump adjacent to it. There is no specific pump for the mirror assembly.

THERMAL DEFORMATION STUDIES

The complete transferline of the Infra-Red light is shown in fig.3. It shows that the light is first deflected horizontally at 90deg. (M1) after which it is directed upwards (M2) to leave the Storage Ring tunnel through the roof slabs. The emitted light cone (~10mrad, limited by 35mm optical aperture of the CVD window) is divergent up to 6.4m where it meets the first focussing element M3. It is to be noted that at the first commissioning stage (Jan.2004) of this transferline only the M1 & M2 were installed and the light, at this 6.4m distance from the source point, was simply projected (for mapping measurements reported further below) or imaged (for here reported deformation studies) with a 1.5m achromat and 400nm bandpass filter onto a CCD camera. Also a quartz window replaced the CVD window at that time.

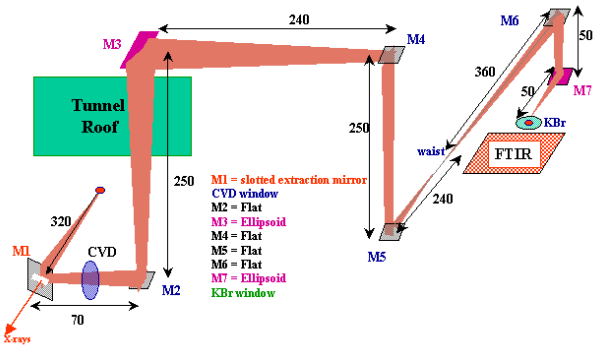

Figure 3: Schematic overview of the full transferline.

In the imaging system an aperture selected the light from the 0.4T flatfield only (P=0.37W/mrad·mA). The beam current was first limited to only 0.1mA, and images were recorded and analysed to verify that their measured dimensions in both planes agreed to the theoretical values from the electron beam and the diffraction at 400nm. Then the current was gradually increased to 5mA and the first signs of vertical beam splitting were apparent at 2mA. These disappeared completely after reducing the current to 1mA. A 2nd cycle was carried out with the beam current ramped up to 20mA : The fig.4 shows the initial image at 1mA (A), the images at 10 and 20mA (B & C), and the subsequent image after reducing again to 1mA. With this last current of 1mA the image fully retrieved its initial shape and dimensions.

The conclusion from this is that, for our 10mm thick aluminium at 45deg. incidence to the beam, the mirror surface deformation is negligible upto 86mW per mm horizontal mirror, and symmetric after that, and reversible upto at least 1.7W per mm horizontal mirror. Knowing the vertical power profile of the X-ray beam these values can also be expressed at 0.25W/mm2 and 4.9W/mm2 respectively.

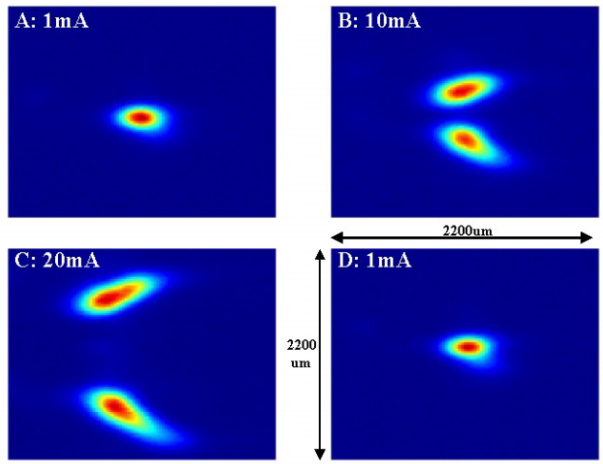

Figure 4: beam images under subsequent beam currents .

MAPPING OF EDGE RADIATION

The possibility to insert the mirror fully at low current and to directly project the undistorted light at low beam current now also allowed to 'map' precisely in both planes the angular intensity distribution. It is known that this intensity distribution around the axis of the electron beam dipole entrance is substantially different from the classical synchrotron inside the flat-field part [2]. This is because of the existence of fringe (or edge) fields at this point and the interference between the light emitted from the up- and down-stream dipoles.

The left image in fig.5 shows the measured intensity distribution as projected directly, after a 500nm bandpass filter, onto a CCD camera at 6.2m distance. The right image shows the result of the distribution calculated with the SRW code, both images have a ~13x9mm scale (HxV).

The large consistency between the measured and calculated values is also true for the full (10mrad) horizontal extracted light that shows the strong peak intensity of the edge region with respect to the flat-field region. The images in fig.6 show this projected light for 2 different colour-scales. The total image (60mm wide) was formed by assembling numerous individual CCD images recorded from the camera on a scanning translation stage.

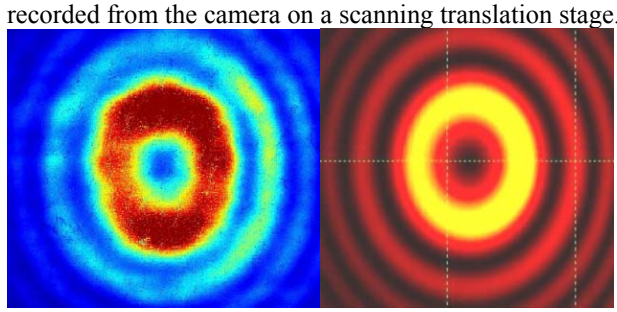

Figure 5: Images of edge radiation at 500nm wavelength : measured (left), calculated with SRW (right) .

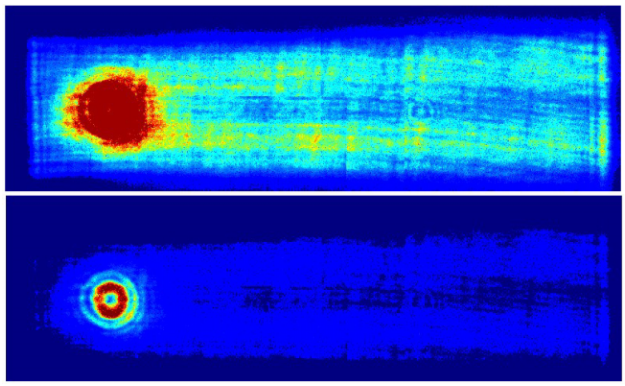

Figure 6: images of full horizontal light extraction.

BLACKENING OF MIRROR & WINDOWS

During the first months in 2004 the mirror was operated in its foreseen slotted mode. During the May shut-down, when the transferline construction was continued with the installation of M3-M6 mirrors and the installation of the CVD window, a severe blackening was observed at both the slotted mirror and on the vacuum-side of the quartz UHV window (30cm downstream the mirror) that had been utilised until then.

Both the mirror and the window have a similar pattern of this blackening with varying intensity depending on horizontal and vertical position (fig.7). The analysis of this particular pattern reveals that a certain spectral range of UV light (i.e. λ=20-200nm) is causing this phenomenon (referred to as 'Carbon-cracking') that is notably known to exist on certain type of soft X-ray synchrotron beamlines. [3]

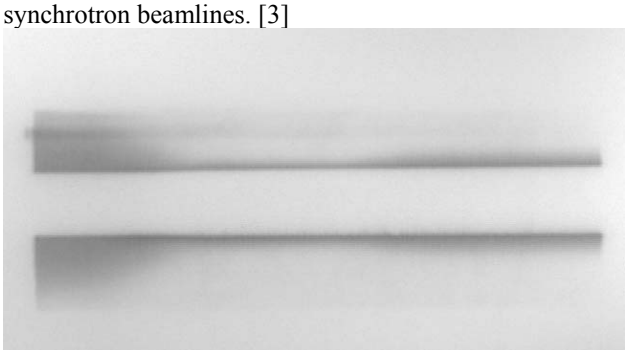

Figure 7: Blackening pattern on a quartz window.

While initially the quality of the vacuum (~4E-9mbar) was suspected it was found that another mirror (a 'half-mirror' for light extraction in cell-5 dipole for diagnostic purposes) in very similar conditions (light exposition, temperature, vacuum quality) did not show such blackening, even after many years of use. The mirror is made out of a Cu-Al alloy (Glidcop) with a nickel coating. Also the sapphire UHV window just down-stream did not show any blackening signs either.

The relative easy access to these components in the system at cell-5 have made it possible to undertake a few practical experiments here to verify if indeed the choice of material for both the mirror and the window are determinant. These experiments will be concluded in summer 2005 after having exposed a single mirror with 3 distinct zones of different coatings (aluminium, gold and nickel) to the synchrotron light. Preliminary results clearly suggest that aluminium is very prone to the blackening phenomenon while gold and nickel are not. Presently it is unknown if the CVD window is affected or not by this blackening.

CONCLUSION

The slotted mirror is now in continuous operation service since January 2004, and has not given rise to any interference with the machine operation or with the local machine vacuum quality. The concept of the slotted mirror not only avoids the mirror surface deformation from X-ray heatload, but also allows to realise a simple, compact and straightforward design that functions reliably without additional water-cooling or vacuum pumps.

The flexible way of vertical mirror positioning also allowed in the commissioning stages to measure the dipole light characteristics, to assess thermal heatload deformation to the aluminium mirror, and to verify the quality of stability and optical wavefront transmission.

The phenomenon of surface blackening on the aluminium mirror is being investigated in more depth, for determining an appropriate coating treatment.

The author expresses thanks to the many colleagues in the ESRF design office, vacuum group, computer services, diagnostic group, alignment group and operation group that have participated in the concept, design, realisation, installation and commissioning of this mirror device. Special thanks are expressed to P.Dumas, O.Chubar and F.Polack of Soleil, and J.Susini of the ID21 beamline for participation in the design elaboration of the light extraction system.

REFERENCES

[1] Kugler GmbH, Salem D-88682 Germany, http://www.kugler-precision.com.

[2] Bosch, R. A. *Nucl. Instrum. Meth. in Phys. Research. A* **1997**, *386*, 525, Bosch, R. A.; Chubar, O. 1997; American Institute of Physics Conference Proceedings 417; 35-41.

[3] J. Susini, P. Dumas and N. Brookes, private communication

DIPOLE LIGHT MONITOR SYSTEM FOR THE ESRF INJECTOR

B.K. Scheidt, ESRF, Grenoble, France

Abstract

The visible part of the synchrotron radiation produced in a total of 9 dipoles of the ESRF injector is now extracted to obtain simultaneously images of the electron beam profile at these locations. This at each injection and in a non-destructive way to the electron beam. The first transferline (180MeV) contains three monitors on the 2 dipoles (0.38T) and the injection septum magnet. The Booster accelerator has one monitor that allows the profile measurement at any moment in its 50ms acceleration cycle by timing the internal camera shutter. In order to equip each of the 5 dipoles (0.9T) in the 2nd transferline (6GeV) with such a monitor, a compact and low-cost light extraction system was added at the end of the (non-modified) dipole vacuum chamber. All systems use low-cost commercial CCD cameras, sufficient light is produced at beam-currents a factor ~100 below nominal values. The video images are displayed to the control room operator at each injection, giving a quick & complete view of injection conditions all along the injector path. This paper describes the mechanics and optics of light extraction and collection, and the results obtained since mid-2004.

OVERVIEW AND TL-1 MONITORS

The position of the total of 9 Dipole light monitors in the injector complex (TL-1, SY, TL-2) is shown in fig.1.

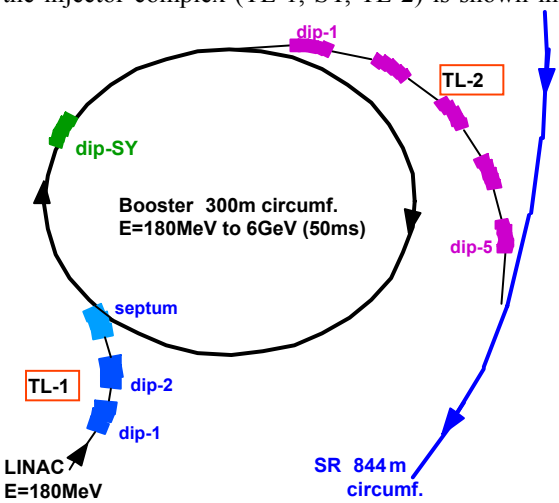

Figure 1: The location of the 9 dipole light monitors.

The 2 dipoles in the TL-1 transferline are of 40cm length with a deflection radius of 1.5m (E~180MeV, B=0.38T). This relative short length and the strong deflection angle (15deg.) permits to equip the simple vacuum chamber with 2 separate vacuum flanges : one for the electron beam exit and another one for the extraction of synchrotron light. The latter, strait aligned on the dipole entrance, uses a sapphire UHV vacuum window (W) to let the visible light through. An aperture directly after the window selects the light from a source point inside the nominal dipole field. A commercial achromat lens of 200mm focal length projects an image on the ½" CCD with a de-magnification factor of 3.1 (fig.2 left).

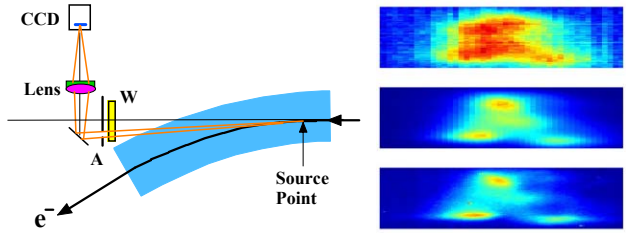

Figure 2: TL-1 dipole light extraction principle and results obtained with it, compared to that of screen monitors.

An existing screen monitor just in front of the 1rst dipole allowed to compare the obtained images from three different devices (fig.2 right): a former screen monitor with an alumina (AF-995-R) screen in air (upper image), a new screen monitor in vacuum (middle), and the dipole light monitor (lower image). [1] The images show several spots that are caused by the emission characteristics of the Linac Gun. The spatial resolution of the dipole light monitor is of superior quality and estimated at <100um, mainly determined by diffraction for 500nm wavelength and 6mrad hor. aperture. The vertical emission angle is ~8mrad. The collected light flux is enough to attain sufficient image quality down to 0.1mA (compared to 5mA nominal TL-1 current).

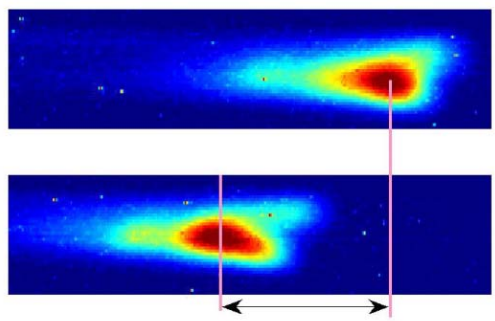

Figure 3: Results from 2nd Dipole Light Monitor in TL-1

The 2nd TL-1 dipole monitor is of similar design, with a 150mm lens offering a larger view area (24x18mm, HxV) so to cover the full excursion of the beamspot. Being at a location of high dispersion it serves the measurement of energy variation & fluctuations from the Linac as shown in the 2 (zoomed) images in fig.3 with a 4mm shift.

For the imaging of the injected beam inside the Septum magnet (injection TL-1 to SY), an 75cm long vacuum chamber had to be added directly after the Septum Tank with an in-vacuum aluminium mirror. Its edge is at 15mm horizontal distance to let the circulation SY beam un-obstructed under all circumstances. The so extracted light

fan is emitted from about 10cm before the septum exit. The fig.4 shows the extraction scheme with two (zoomed) images of same scale (7.3x5.6mm, HxV) : To the right the image of the injected beam, to the left the same image under identical beam condition but of higher sensitivity showing now (to the left of the saturated beam image) the faint light deflected of the septum sheet. In fact this parasitic signal allows to determine the septum position and hence the distance of the beam to it.

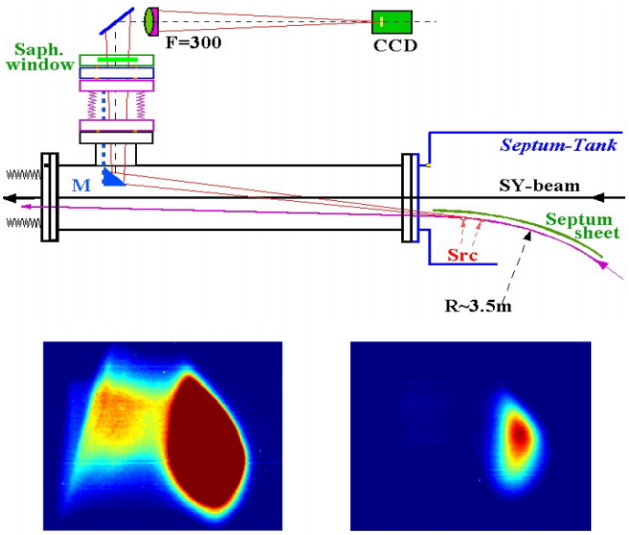

Figure 4: The extraction scheme for the Septum Magnet with images obtained showing the beam, and also the septum sheet.

SY-BOOSTER MONITOR

In contrast to all other monitors, that are compact and inaccessible inside the accelerator, only the SY-Booster system has a permanently accessible laboratory in which the achromat, attenuation filters and camera are installed. The edge of the in-vacuum aluminium extraction mirror has a 13mm horizontal offset to the beam, the light source point lays 70cm ahead of the dipole exit and the achromat (F=1185mm) is at 5.6m distance from this which yields convenient field coverage of 18x13mm (HxV) for the 1/3" CCD camera.

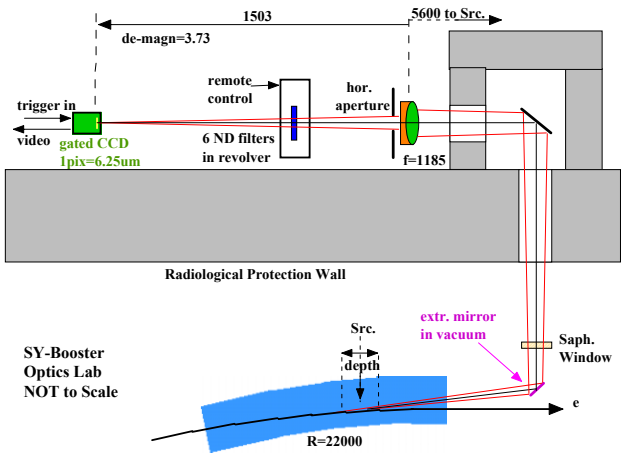

Figure 5: Topview of the SY light extraction to its optics lab

By triggering the internal shutter of this camera with a pulse of variable delay and width, an image at any point in the 50ms acceleration cycle can be obtained.

The light flux at the injection point (E=180MeV B=25mT) is a factor ~100 lower than that from the rest of the 50ms period but still enough to yield good quality images. The minimum shutter-open time of the used camera being 130us means that each image is integration over 130 turns in the 300m SY-Booster. This is of no limitation or disadvantage for its practical use : The two left images here below show the beam-shape at 2ms (both) after injection, the two small ones at the right at respect. 30 and 50ms. The strong fluctuations at 2ms are due to energy fluctuations of the injected Linac beam. The decreasing vertical dimension is consistent with decreasing emittance of the injector, while the horizontal size reaches a minimum at ~30ms before increasing again afterwards, also conform with theoretical predictions [2].

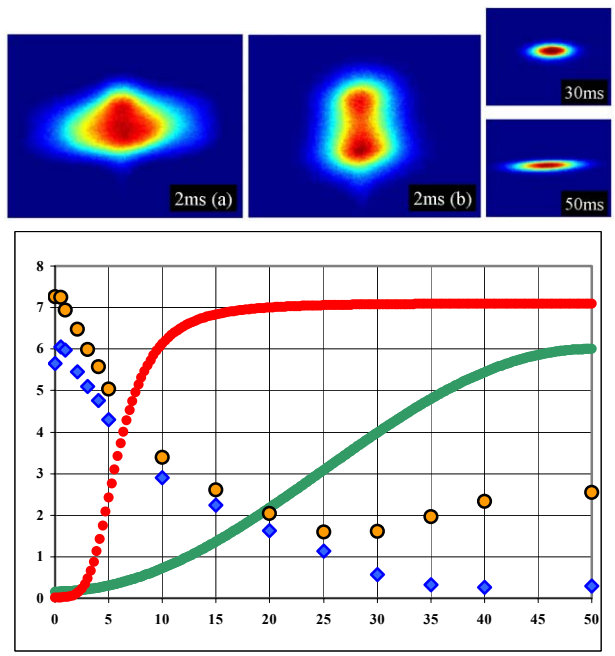

Figure 6: images and beamsize results [mm fhwm] along the 50ms acceleration cycle hor.=orange, vert=blue, red = flux[A.U] , green = Energy[GeV]

TRANSFER-LINE 2 MONITORS

The existing TL-2 dipole chambers are of 2.4m length and could not be modified for practical and cost reasons. The solution was to make place in the drift sections behind each dipole chamber for a small chamber that holds the extraction mirror, sapphire window and optics in a well-aligned position. (see fig.7 for views from 3 sides).

The mirror has a 18mm offset to the chamber centre, this equals the horizontal aperture for the beam imposed by the overall 36mm wide TL-2 vacuum chamber. The mirror deflects the light downwards for reasons of restricted space. An U-bar, rigidly attached to the chamber, provides a support rail for the mounts of the lens, filter and camera. This assembly is pre-aligned in

laboratory before installation to ensure that the optical system will collect & image the light of its theoretical source-point. This point lies 1015mm ahead of the mirror and 1100 from the achromat lens (f=300mm). The ½" CCD covers a 17x12.5mm at the source. The total dimensions of the lightweight assembly measures only 18cm length, 14cm width and 65cm height.

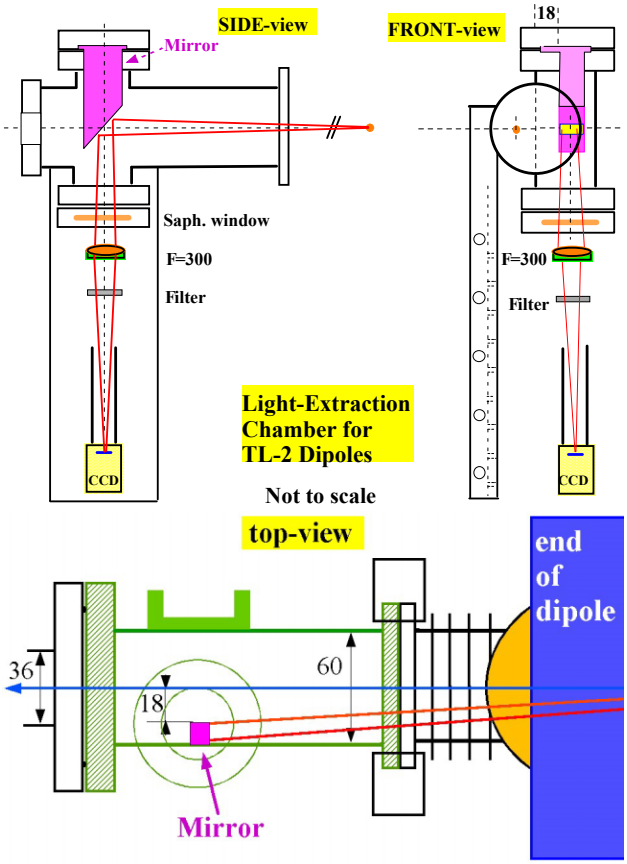

Figure 7: Special light extraction chamber for TL-2 Dipoles.

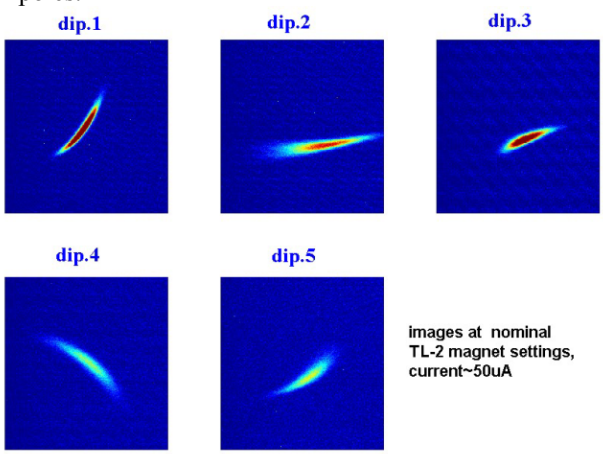

Figure 8: The 5 TL-2 Dipole images (17x12.5mm,HxV)

The obtained images in each of the 5 monitors show, under nominal TL-2 magnet settings, a shape indicative of strong coupling and non-linear distortion. This is caused by a large deviation of the SY beam orbit in the last quadrupole just before extraction. By adjusting the local quadrupoles and steerers in TL-2 it was possible to reduce the beamsize in each dipole individually and so to test the resolution of the whole imaging system. The vertical emission angle is ~4mrad which defines the ultimate resolution at ~120um. For each system the CCD camera is on a single translation stage with remote control for the verification of optimal focussing. This is the only remote control in the system, and has only served once at commissioning.

IMAGE TRANSPORT, ACQUISITION, DISPLAY FOR DAILY APPLICATION

The long distances (up to 200m from camera to acquisition card) and the already available image frame grabbers (incl. software) at the ESRF for the CCIR interlaced 75ohm video standard have determined the choice of the CCD cameras, with the Sony-ST50 (1/2" or 1/3") used for all devices. The NI-1409 frame-grabbers (6 in total) are used in 3 rackable PCs with the 3 output monitor screens directly to the Control Room. The associated timing of the TL-1 and TL-2 system is of great simplicity : only the frame-grabber is triggered with the injection pulse or respectively the extraction pulse. All the TL-1 & TL-2 systems are equipped with a single attenuation filter to select between nominal injector current (5mA) or low current.

CONCLUSION

The injector complex now benefits from a complete system to survey and measure to required precision the transverse beam-shape and dimensions in a routine and reliable way. Being totally non-destructive to the electron beam it is permanently active and thereby giving to the operator a quick & comprehensive view of injection conditions all along the injector path at each injection.

In comparison to traditional screen monitors this non-destructive feature does not only allow this simultaneous data acquisition but also avoids the local generation of radiation from beam interception. In terms of sensitivity and resolution the system is also of superior performance. No effects of degradation on either component have been observed after nearly 18months of operation. The technical simplicity of the light extraction (i.e. no mechanical motion in vacuum) and the system in general is a major advantage in terms of costs and reliability.

The author expresses thanks for the professional help in the realisation of the system, to J.Pasquaud for the mechanical designs, to F.Epaud for the image acquisition, and to the vacuum group colleagues for installation.

REFERENCES

[1] B.K.Scheidt, "Upgrade of the ESRF Fluorescent Screen Monitors", DIPAC'03, Mainz, May 2003.

[2] Y.Papaphilipou et al, "Operational Improvements in the ESRF Injection Complex", EPAC'04, Lucern, July 2004.

ADVANCES TOWARDS THE MEASUREMENT AND CONTROL OF LHC TUNE AND CHROMATICITY*

Peter Cameron, John Cupolo, Christopher Degen, Al Dellapenna, Lawrence T. Hoff, Joe Mead, Robert Sikora, BNL, Upton, NY 11973, USA
Marek Gasior, Rhodri Jones, Hermann Schmickler, CERN, Geneva, Switzerland
Cheng-Yang Tan, FNAL, Batavia, IL 60439, USA

Abstract

Requirements for tune and chromaticity control in most superconducting hadron machines, and in particular the LHC, are stringent. In order to reach nominal operation, the LHC will almost certainly require feedback on both tune and chromaticity. Experience at RHIC has also shown that coupling control is crucial to successful tune feedback [1]. A prototype baseband phase-locked loop (PLL) tune measurement system has recently been brought into operation at RHIC as part of the US LHC Accelerator Research Program (LARP) [2]. We report on the performance of that system and compare it with the extensive accumulation of data from the RHIC 245MHz PLL [3].

INTRODUCTION

Tune Feedback was formally accepted as a LARP task in 2003. For two years prior to that time there existed a bilateral collaboration between CERN and BNL for the purpose of research into the development and refinement of reliable tune feedback, as well as the associated development of means for improved control of chromaticity and coupling. Significant progress has been made as a result of these collaborative efforts.

The LHC Specifications for Tune, Chromaticity, and Coupling Measurement are clearly defined [4]. To meet these specifications requires improvement upon the performance of the present RHIC 245MHz PLL tune measurement system. Limitations of the present system arise from the dynamic range requirements imposed by transition crossing in RHIC, and from the effect of coupling on the tune feedback loop. Recent advances [1,5] are addressing these limitations, and prospects appear favourable for reliable operational tune feedback, both at RHIC and in the LHC.

TUNE MEASUREMENT AND FEEDBACK

We present results from the present RHIC 245MHz PLL and a prototype baseband PLL, as well as plans for the proposed LHC baseband system.

245MHz PLL

The RHIC 245MHz PLL system is mature. It has proven useful for tune and chromaticity measurements, particularly during ramping, as well as for a variety of accelerator physics experiments. Figure 1 shows typical tune data for a RHIC ramp during the 2004 Gold run.

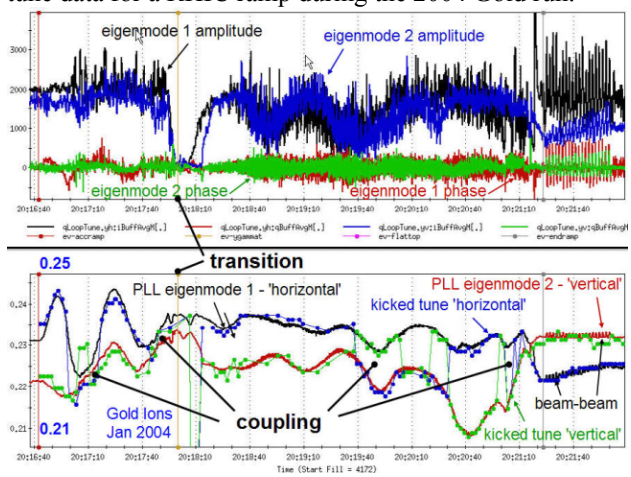

Figure 1: PLL tune tracking during a RHIC ramp.

The lower portion of the figure shows tunes as measured by both the PLL and the conventional kicked tune measurement system during the 5 minute ramp. It can be seen that, as a result of coupling, the kicked tune measurement hops back and forth between the eigenmodes tracked by the PLL. The upper portion of the figure shows the PLL amplitudes and phases. Despite feedback within the PLL on both kicker excitation and signal path gain, the amplitudes are driven to zero around transition. This results from bunch lengths becoming short near transition, which extends the coherent spectrum of the bunches in the 28MHz acceleration buckets up into the passband of the 245MHz resonant pickups. In addition, there are fast orbit changes around transition. These circumstances create a dynamic range problem that frequently results in the failure of PLL tune tracking. This problem is being addressed by the Direct Diode Detection analog front end [5].

Figure 2 shows data from a RHIC ramp with tune feedback on during the 2004 polarized proton run. This was the last of ~25 ramps that were attempted with tune feedback over the course of 3 years. The success rate for ramps with tune feedback was ~50%. Given the great potential benefit of reliable tune feedback during normal operations, this success rate was sufficient to justify continued attempts until the obstacles were fully understood. The first obstacle was the dynamic range problem at transition, as mentioned in the previous paragraph. This problem was understood early on for ion

*Work supported by US LARP and US DOE

beams, and did not prevent attempts with protons, which are above transition at injection.

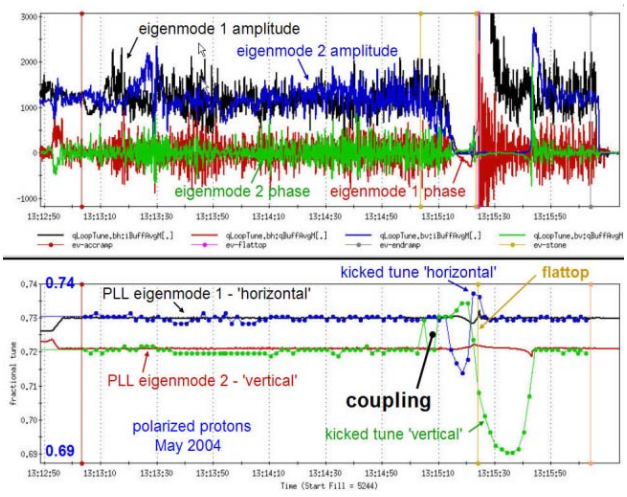

Figure 2: Ramp with Tune Feedback.

Figure 2 makes clear the second obstacle to successful tune feedback. Referring back to Figure 1, it was noted that the PLL successfully tracked the eigenmodes while the kicked tune was hopping between eigenmodes as a result of coupling. In that instance the effect of coupling on PLL performance was relatively benign. In Figure 2 the situation is complicated by the presence of the tune feedback loop, and the effect of coupling in this instance is not benign.

Coupling rotates the eigenmodes. When this rotation is greater than 45 degrees, the tunes are said to have 'crossed'. The PLL is capable of tracking an eigenmode well beyond that point, and feeds this tune data to the magnet control, data which at that point corresponds to the wrong plane. This drives the tune feedback loop unstable. The signature we had expected from coupling was that the tunes would be gradually and uncontrollably driven apart by the coupling. With the data in Figure 2 we understood that we were looking for the wrong signature, that the situation could not progress to that point, but rather that the tune feedback loop would suddenly and catastrophically break the moment the eigenmodes rotated more than 45 degrees. With this understanding, no further tune feedback loops were attempted, and our attention was instead focused on coupling measurement and correction. As a result of that effort, we now believe that the coupling problem is well in hand, as reported elsewhere in these proceedings [1].

It is interesting to note that the behaviour of the amplitudes in Figures 1 and 2 is very similar. During the 2004 run there were large and fast orbit shifts at the PLL pickup during ramping, resulting from beam separation bumps at the IPs to minimize the effects of beam-beam. This contributed to the confusion in understanding the role of coupling in breakage of the tune feedback loop. Our impression was that the orbit shifts were driving the pickups at the revolution line, resulting in suppression of the amplitude by the feedback loop on signal path gain. In reality, the vertical orbit shifts in the sextupoles were introducing the coupling which drove the tune feedback loop unstable.

Prototype Baseband PLL

With the advent of significant improvement in the sensitivity of betatron tune measurement [5], it has become advantageous to work at baseband. Direct Diode Detection analog front ends (3D AFEs) have been designed and fabricated at CERN, and installed in the PS and SPS, as well as the Tevatron at FNAL and RHIC at BNL.

The early experience with these AFEs revealed the presence of harmonics of the mains frequency in the vicinity of the betatron resonance. The origin and effect of these lines is discussed elsewhere in these proceedings [6]. The fact that this excitation of the beam had for the most part gone unnoticed through the entire history of accelerators and storage rings, but was immediately and seriously evident at each of the installations, is a clear demonstration of the excellent sensitivity of this new AFE. The presence of this excitation in the betatron spectrum disrupts PLL operation, and is a serious threat to the implementation of successful tune feedback at RHIC and the LHC.

While the focus on this unexpected problem has slowed the baseband PLL development effort, some progress has been made. Utilizing a commercial lock-in amplifier, a phase loop was closed on the beam. Operation of this system has shown:

- With a given S/N, emittance growth is less with the baseband system.
- The qualitative observation is that tune tracking performance is superior to that of the 245MHz system, even at this early stage. This has not been systematically quantified, due to higher priorities as well as lack of a proper interface to the Control System.
- No bleedthru was observed from kicker to pickup.
- Dynamic range is excellent - no sign of saturation around transition in RHIC

And finally, an observation from the Tevatron:

- S/N of 3D AFE was 10 to 20dB better than that of the 21.4MHz 'Schottky' pickup.

The baseband system at RHIC is presently being moved away from the lock-in amplifier and re-implemented using VME modules. This is expected to provide greater flexibility in system operation, data archiving needed to properly quantify system performance, and other benefits. We expect to have this running before RHIC beam goes off at the end of June.

The LHC Baseband System

There were two primary considerations in the development of the system architecture for the LHC baseband system. The first consideration was to have an architecture with maximum commonality between the implementations at RHIC and the LHC. The primary difficulty here was that the VME operating system at

RHIC is VxWorks, whereas at the LHC it is LynxOS. The second consideration was to have the maximum commonality between the baseband system and other LHC beam instrumentation systems, to minimize the amount of specialist knowledge needed to commission and operate this system.

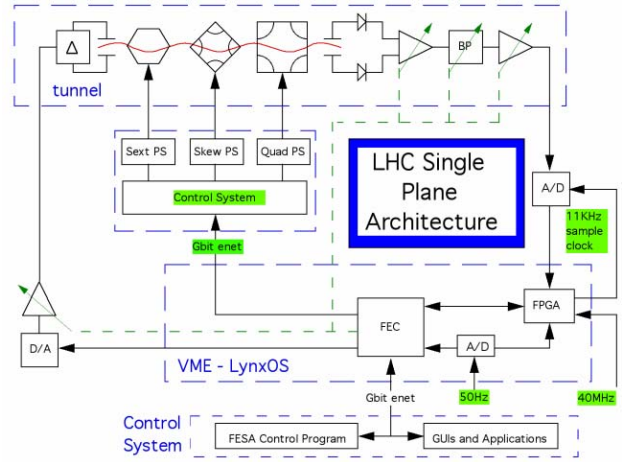

Figure 3: LHC Single Plane Architecture.

With the architecture shown in Figure 3 the gate array code is essentially identical between RHIC and LHC. Similarly, the front-end computers will utilize operating-system independent libraries developed in the C programming language. VME hardware and functionality will either reside on or be implemented in the DAB board [7] utilized in many other LHC instrumentation system.

CHROMATICITY

PLL-based chromaticity measurement during ramping in RHIC is accomplished by measuring the tune modulation resulting from 1Hz modulation of the beam momentum. A momentum modulation depth of +/- 10^{-4} gives a +/- 100μ radial modulation. During RHIC operations neither beam loss nor emittance growth has been identified as resulting from this modulation.

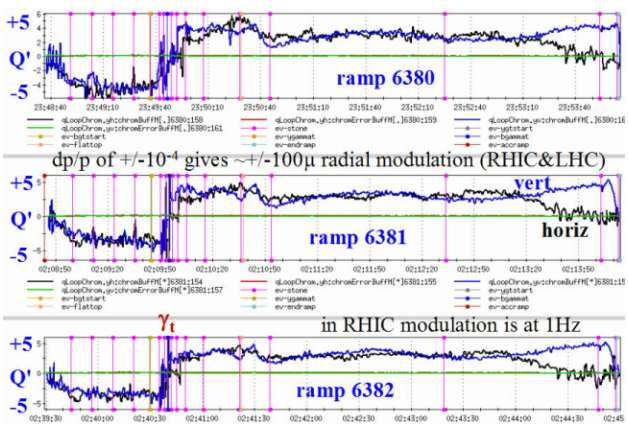

Figure 4: Chromaticity Measurement on the Ramp

Figure 4 shows chromaticity measurements on 3 successive ramps during the 2005 copper run. Understandably, the quality of the data is questionable around transition. Measurement fluctuations for values near zero result from the inability of the chromaticity algorithm to properly determine sign. In principle it should be possible to overcome this difficulty. In its present form, the quality of this measurement approximates that needed to meet the LHC specification at commissioning.

CONCLUSION

The status of the LARP efforts to meet the requirements of the LHC Specification was recently reviewed [7]. The opening summary of the report from that review states "The Collaboration between LARP and CERN has demonstrated prototype hardware and system architecture that has the potential to satisfy the LHC tune tracker/feedback system requirements. Team members have established the rapport that enables a successful collaboration." We reported here on some details of the progress that has resulted in this favourable assessment of the prospects for PLL-based tune and chromaticity measurement and control in the LHC. The most significant progress has been made in two areas - the Direct Diode Detection analog front end and PLL-based coupling measurement and control. With these improvements in hand, we feel that there is a good possibility that the LARP/CERN Tune Feedback effort will make a substantial contribution to the commissioning and operation of the LHC. The problem of mains excitation of the betatron spectrum is now the highest priority.

REFERENCES

[1] R. Jones et al, "Towards a Robust Phase Locked Loop Tune Feedback System ", these proceedings.
[2] see http://www.agsrhichome.bnl.gov/LARP/
[3] P. Cameron et al, "RHIC Third Generation PLL Tune Measurement System", PAC 2003.
[4] S. Fartoukh and J.P Koutchouk, "On the Measurement of the Tunes, Coupling, & Detuning with Momentum and Amplitude in LHC", LHC-B-ES-004, Feb. 2004.
[5] M. Gasior and R. Jones, "High Sensitivity Tune Measurement by Direct Diode Detection", these proceedings.
[6] P. Cameron et al, "The Effects and Possible Origins of Mains Ripple in the Vicinity of the Betatron Spectrum", these proceedings.
[7]http://www.agsrhichome.bnl.gov/LARP/050404_Tune_Feedback/

A FIRST LOOK AT BEAM DIAGNOSTICS FOR THE RHIC ELECTRON COOLING PROJECT*

Peter Cameron, Ilan Ben-Zvi, Jorg Kewisch, Vladimir N. Litvinenko

BNL, Upton, NY 11973, USA

Abstract

High energy electron cooling [1] is essential to meet the luminosity specification for RHIC II [2]. In preparation for electron cooling, an Energy Recovery Linac (ERL) test facility [3] is under construction at BNL. A preliminary description of Diagnostics for the ERL was presented at an earlier workshop [4]. A significant portion of the eCooling Diagnostics will be a simple extension of those developed for the ERL test facility. In this paper we present a preliminary report on eCooling Diagnostics. We summarize the planned conventional Diagnostics, and follow with more detailed descriptions of Diagnostics specialized to the requirements of high-energy magnetized cooling.

INTRODUCTION

The RHIC electron cooler is designed to cool 100GeV/nucleon ions using 54MeV electrons. The electron source will be a superconducting RF photocathode gun. The accelerator will be a superconducting energy recovery linac. The frequency of the accelerator is set at 703.75MHz. The maximum electron bunch frequency is 9.38MHz, with bunch charge of 20nC.

Electron cooling at high energy imposes a variety of unique requirements. Of these many requirements, we mention here those that are relevant to the diagnostics discussed in this paper.

While other coolers use DC electron beams, the only way to make a high quality 54MeV beam is with a super-conducting Energy Recovery Linac. High resolution differential current measurement is needed to monitor the efficiency of current recovery.

In typical ERL applications, considerable effort is devoted to generating the shortest possible bunches. In the present application, the need is to match the electron bunch length to that of the ions, as well as to lower the bunch density to insure that Debye shielding doesn't degrade the cooling efficiency. This requires a bunch stretcher, and diagnostics to confirm that the contribution of longitudinal space charge to transverse emittance during bunch stretching is minimized.

Suppression of the transverse temperature of the electron beam in the cooling region requires the generation and transport of magnetized beams, as well as solenoids in the cooling region. Diagnostics are required to measure the *non-magnetized* transverse emittance of the electron beam at the end of the linac matching section, as well as within the solenoid.

Field errors in the cooling solenoids contribute to the transverse temperature of the electron beam [5]. For efficient cooling, local field errors must be at the level of 10^{-5} or less. This requirement is beyond construction tolerances, and will require beam-based diagnostics to permit local correction of field errors.

A layout of the cooler is shown in Figure 1. The magnetized electron beam from the source is accelerated to 54MeV through four superconducting RF cavities, then passes through the stretcher and a bunch rotation cavity (not shown). A dipole in the bend after the cavity has the option to be operated at high field, functioning as a spectrometer to permit energy spread measurement for cavity phasing. The electron and ion beams enter the solenoid from the right. After the solenoids the electron beam enters a second bunch rotation cavity (again not shown). Between the cavity and the compressor there is the option to divert the electron beam to a diagnostic line, where a matching section similar to that at the end of the linac permits measurement of the unmagnetized emittance. A streak camera situated after the compressor permits measurements before the beam re-enters the linac for energy recovery.

CONVENTIONAL DIAGNOSTICS

Preliminary estimates of types and quantities of conventional diagnostics are shown in Table 1.

Table 1: Conventional Diagnostics

Device	Qty	Comments
Position/Phase		
BPM (button)	~70	Dual plane
BBU/Energy Feedback	1	Sample scope
Beam Transfer Function	1	Include BTF kicker
Energy Spread	~8	Dispersive BPMs
Phase	~16	BPMs w/ I/Q
Loss		
BLM (PMT/ photodiodes)	~40	20μsec and 1sec
BLM (cable ion chamber)	~10	20μsec and 1sec
Current		
Current	1	DCCT
Differential	1	DCCTs w/ null
Profile		
Flags	4?	Phosphor
Wire Scanner - profile	3?	SEM mode
Wire Scanner - halo	3?	BLM mode
Scraper	2?	SEM + BLM
Synch Light	3?	
Streak Camera	1?	Dual sweep

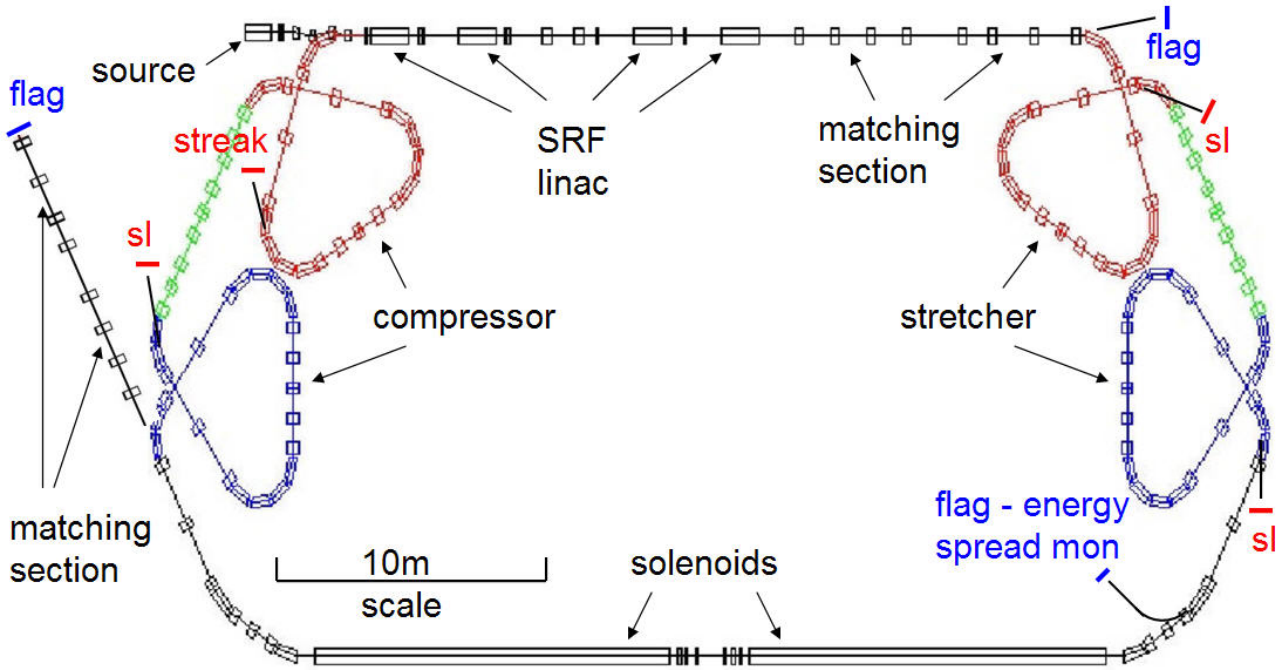

Figure 1: Layout of the RHIC Electron Cooler

Position/Phase monitors

Dual plane button BPMs will be located at every other quadrupole, and at additional locations as needed. BPM electronics will be an adaptation of the SNS electronics [6], modified to the VME form factor. Beam-synchronous digitization and I/Q demodulation will permit phase measurement at any desired BPM location. Pickups at dispersive locations will permit measurement of energy spread.

Possible onset of the BBU instability will be monitored with a stripline pickup. Data acquisition will be accomplished in parallel with a fast (20GHz BW) sampling scope, as well as with a spectrum analyzer. With the addition of a stripline kicker and power amplifier, this pickup will also be used for beam transfer function measurements, and in particular to explore parameters related to the BBU instability.

Loss Monitors

The preliminary plan is to include both local detectors (PMTs and/or photodiodes) for fast high-sensitivity measurements and cable ion to ensure a calibrated measurement and complete coverage.

The loss budget goal is 1uA. The electron beam has enough power to damage the vacuum chamber if it is not adequately protected. The loss monitor system will be able to rapidly shut the beam down when beam loss exceeds a programmable threshold. Shutdown within 10us of beam loss detection is anticipated. The loss signal will be processed using integrating electronics for equipment protection, and a linear and/or logarithmic technique for diagnostics & beam tuning. Similar systems have been used extensively at existing machines such as CEBAF at JLAB.

Current Monitors

The fiducial for current measurement will be a Bergoz Parametric Current Transformer (PCT). By virtue of the BPM processing architecture, current measurement from the sum signals of all BPMs will be available essentially for 'free', and will be calibrated by the PCT.

The differential current measurement (the difference in currents between the accelerated and decelerated beams) will assume increasing importance as commissioning proceeds and beam current increases, both as a measure of the efficiency of current recovery and as an input to the machine protect system. A simple and elegant method is to utilize two toroids in the injection and dump lines, linked with a figure eight winding. The output of one toroid is used to drive a nulling current through the figure eight, and the output of the second toroid is then the differential current measurement. This overcomes the dynamic range problem of measuring a small current difference in the presence of a large current signal. For 100mA beam current the AP specification of 99.9995% current recovery requires measurement resolution of better than 0.5μA. Possible refinements of technique to accomplish this are discussed in detail elsewhere [7].

Profile Monitors

Profile measurements are required to gain information about lattice functions as well as longitudinal and transverse emittance. Preliminary plans for profile monitors include flags, wire scanners, synchrotron light monitors, and a streak camera. Detailed specification of quantities, locations, and measurement requirements is in progress.

SPECIALIZED DIAGNOSTICS

As previously mentioned, electron cooling at high energy imposes several unique requirements upon diagnostics.

Beam-based Alignment

To minimize the contribution to transverse temperature of the electron beam resulting from field errors, beam-based alignment is under consideration. In the proposed method [8] the ion beam serves as the fiducial, is assumed to be perfectly rigid within the solenoid, and is aligned within the solenoid by BPMs at either end. Local dipole correctors and alignment quadrupoles are distributed within the cryostat along the length of the solenoid, at ~15cm intervals. The quadrupoles are designed to permit modulation at a few Hertz, and the resulting position modulation of the ion beam is detected by position monitors located elsewhere in the RHIC ring. The amplitude of position modulation is dependent upon the location of the ion beam in the quadrupole. Application of a swept four-bump of the ion beam position in the solenoid permits locating the magnetic center of that quadrupole relative to the BPMs at either end of the solenoid. The quadrupole can then be modulated in the presence of the electron beam, the position modulation can be detected in the return path of the ERL as a local bump (we note here only that this is non-trivial) is applied to the electron beam position, the position of the electron beam relative to the quadrupole can be determined, and the local dipole correctors can be used to locally align the electron beam relative to the ion beam. Determination of the quality of the alignment is problematic. During studies presently in progress in RHIC the only available means has been measurement repeatability, which is a few tens of microns.

Recombination Monitor

The ion/electron recombination rate is estimated [9] to be ~1MHz for the expected conditions in the RHIC cooling solenoids. The envelope of ions that have captured an electron is shown in Figure 2.

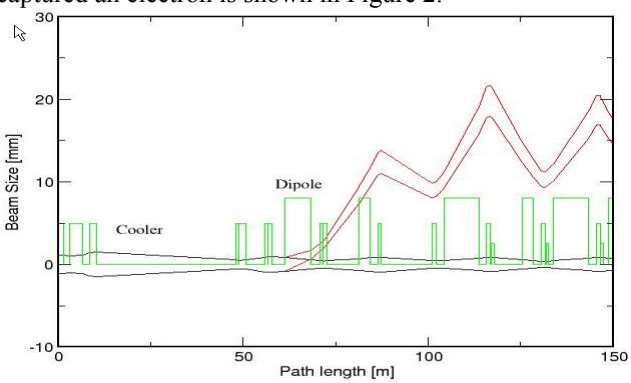

Figure 2: Envelope of recombined ions

Installing a scraper and fast PMT at the location of maximum displacement will permit counting recombined ions. Adjustment of a single in-cryostat local dipole corrector will result in count rate variations approaching 10KHz. This will provide a clean signal for correcting local field errors, and might be used either in combination with quadrupole modulation BBA, or stand-alone. It will also be a useful monitor for matching the longitudinal velocity of the electron beam to the ion beam.

Magnetization Monitor

Adjusting the betatron phase advances in the matching section at the end of the linac to differ by 90 degrees in the horizontal and vertical planes results in a flat beam, which can be observed on the diagnostic flag at the end of that line. From this data one can extract the beam magnetization and the un-magnetized emittance. A similar measurement can be accomplished in the matching section installed in the diagnostic line downstream of the second bunch rotation cavity. The non-magnetized emittance measured here should correspond well to the electron beam emittance within the solenoid, and will permit tuning of the dispersion and phase advance in the stretcher to minimize the contribution of longitudinal space charge to transverse emittance.

CONCLUSION

The diagnostics of a high-energy electron cooling present many challenges: The high-average-current, the energy recovery mode which necessitates non-intercepting diagnostics, the magnetization of the beam and the beam-based alignment requirements in the solenoid. We started the process of defining the various diagnostics for this application and present some new approaches (such as the use of beam-based alignment of the ion and electron beam to the solenoid axis) as well as an outline of our approach to the more conventional diagnostics, adapted to the extreme conditions of ampere-class beams in an ERL.

REFERENCES

[1] I. Ben-Zvi et al, "Electron Cooling of RHIC", PAC 2005, Knoxville.
[2] W. MacKay, et al. “Upgrading RHIC for Higher Luminosity”, PAC 2001. BNL-67939
[3] V. Litvinenko et al, “High Current Energy Recovery Linac at BNL” PAC 2005, Knoxville.
[4] P. Cameron et al, "Beam Diagnostics for the BNL Energy Recovery Linac Test Facility", BIW 2004.
[5] C. Montag and J. Kewish, "Effect of Field Errors on Temperatures in the Electron Cooler", PAC 2003 http://accelconf.web.cern.ch/accelconf/p03/PAPERS/WPAE030.PDF
[6] K. Vetter et al., "RF Beam Position Monitor for the SNS Ring", BIW 2004
[7] P. Cameron, "Differential Current Measurement in the BNL ERL Test Facility", ERL 2005 Workshop. http://www.jlab.org/intralab/calendar/archive04/erl/proceedings.html
[8] P. Cameron et al, "Beam-based Alignment in the RHIC eCooling Solenoids", PAC 2005, Knoxville.
[9] I. Ben-Zvi, “Electron cooling for RHIC”, Beam Cooling and Related Topics Workshop, Bad Honnef/Germany, May 13 - 18, 2001.

THE EFFECTS AND POSSIBLE ORIGINS OF MAINS RIPPLE IN THE VICINITY OF THE BETATRON SPECTRUM *

Peter Cameron, BNL, Upton, NY 11973, USA
Marek Gasior, Rhodri Jones, CERN, Geneva, Switzerland
Cheng-Yang Tan, FNAL, Batavia, IL 60439, USA

Abstract

With the advent of significant improvement in the sensitivity of observation of the betatron spectrum[1], the appearance of spectral lines at harmonics of the mains power frequency has been observed in the PS and SPS at CERN, the Tevatron at FNAL, and RHIC at BNL. **These lines are potentially problematic for accurate tune tracking and the implementation of tune feedback**. We discuss the possible origins of these lines, and present data to support our discussion.

INTRODUCTION

Identification of the source of mains ripple in beam spectra is often problematic. The difficulty is to clearly demonstrate that the observed ripple originates in the beam, rather than entering the signal path spuriously. Recent data collected at the CERN PS and SPS, the Tevatron at FNAL and RHIC at BNL using a newly developed, highly sensitive, baseband tune (BBQ) measurement system [1] suggests that the beam is being excited at the betatron resonance by high harmonics (h > 100) of the mains frequency.

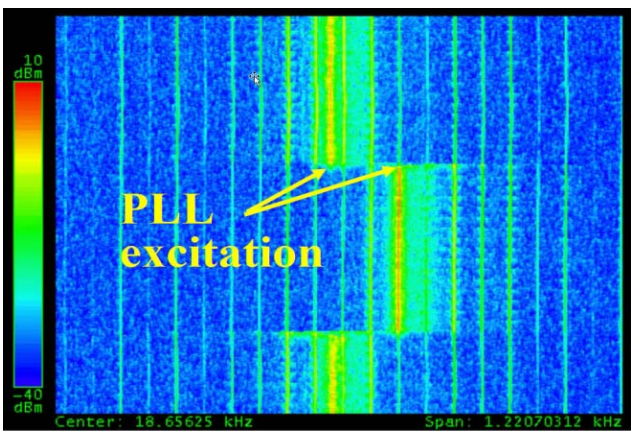

Figure 1: Spectrum with PLL excitation and 60Hz lines

Figure 1 shows the spectrum obtained from a 1m stripline pick-up looking at Copper ions in RHIC, using the Direct Diode Detection (3D) analog front end (AFE) of the BBQ system. The horizontal axis spans ~1.2KHz, centered on the betatron resonance at ~18.65KHz. The vertical axis spans ~30s, with the most recent time at the bottom. The baseband PLL tune tracker [2] is locked on the betatron resonance, which can be seen to shift by ~.002 when the quadrupole currents are changed and then returned to their original values. The 60Hz lines don't move. This illustrates the conundrum - what mechanism might cause high harmonics of the mains frequency to appear in the vicinity of the betatron resonance, yet not be sidebands of the betatron line? The obvious conclusion is that the beam is being directly excited at these frequencies. This interpretation was met with considerable scepticism from accelerator physicists and power supply specialists, the question being what mechanism might generate field ripple at such relatively high frequencies. Some of the means employed to rule out spurious sources included:

- Batteries - AFE electronics were powered from batteries, with no change in the observed spectrum.
- Electronics location - AFE was situated immediately adjacent to the pickup in the tunnel, and then ~70m away in the instrumentation room, with no change in the observed spectrum.
- Isolation transformers - AFE was operated with and without isolation transformers in the signal path, with no change in the observed spectrum.
- High pass filtering - 70MHz high pass filtering was inserted between pickup and AFE, with no change in the observed spectrum.
- Pickup movement - no spectral variation was seen with large (~1cm) changes in the position of a moveable pickup.
- Intensity variation - no spectral variation was seen with large changes in bunch charge.
- Different pickups - mains harmonics were observed from a homodyne detection AFE, a 245MHz resonant pickup, and a million-turn BPM.

All testing indicated that the apparent mains excitation was not spurious and that the beam was truly being excited at the betatron frequency by high harmonics of the mains frequency. The clue leading to the final crucial observation came from the Tevatron, where a change in the relative amplitudes of the observed mains harmonics in the horizontal and vertical planes was seen when the beam separation helix was turned on. The helix is known to introduce coupling. This prompted a brief experiment at RHIC, in which the relative amplitudes of the mains harmonics in the two planes were monitored while coupling was varied. The spectral power of the mains harmonics in the vertical plane was seen to be a linear function of the coupling strength, and was almost entirely absent when the machine was well decoupled. There was no dependence on coupling in the horizontal. From this it was definitively concluded that the observed mains harmonics are indeed on the beam, and that the excitation, at RHIC at least, is in the horizontal plane.

*Work supported by US LHC Accelerator Research Program

OBSERVATIONS

Beam Spectrum during Ramping

There is a lot of information in the beam spectrum during the ramp. Figure 2 shows such a spectrum from Copper ions in RHIC, seen through the 3D AFE. The horizontal axis spans ~2.4KHz, centered at ~17.6KHz. The vertical axis spans ~6 minutes, with the most recent time at the bottom. The baseband PLL kicker was off. The visible betatron signal is some combination of kicked tune excitation, 245MHz PLL excitation, and Schottky.

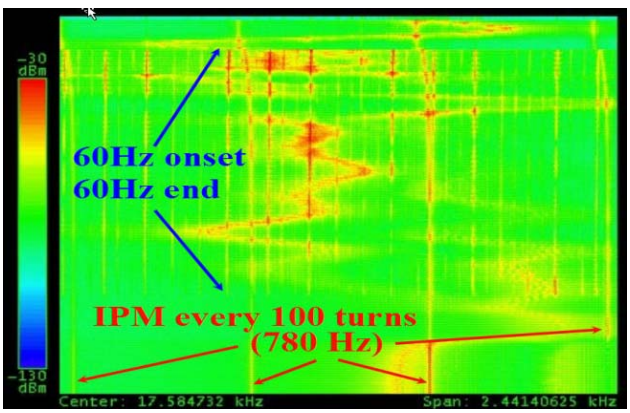

Figure 2: RHIC Spectrum during an acceleration ramp

The onset of strong 60Hz harmonics coincides with the turning on of the ramping power supplies, and the end of the harmonics with their turning off. The harmonics have a pattern that repeats every 720Hz, with 3 strong lines spaced by 180Hz. Their frequency remains constant during the ramp. The spectrum also shows coherence generated by the firing of the IPM sweep voltage every 100 turns. The frequency of the IPM signal tracks the revolution frequency up the ramp. This data suggests that the source of the ripple is the ramping power supplies.

Homodyne Detector

In the effort to confirm that the mains frequency harmonics were not due to the interaction of some spurious source with the 3D AFE, a comparison was made with spectra obtained from other pickups.

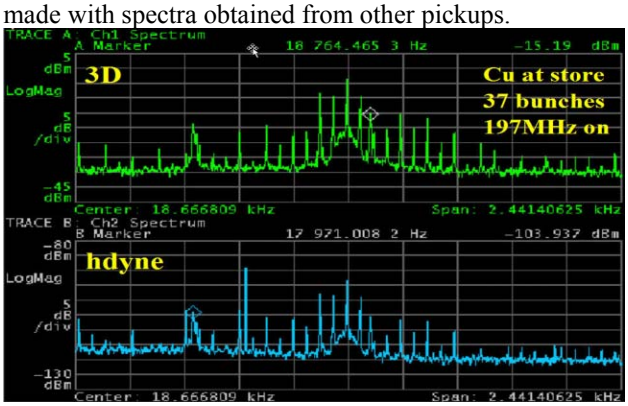

Figure 3: Spectra from 3D and homodyne AFEs

The upper portion of Figure 3 shows the spectrum in the vicinity of the betatron line as seen by the 3D AFE, while the lower portion shows the same beam as seen by a homodyne detector. The homodyne signal was obtained using the sum signal from a H9 hybrid to mix down the difference signal from the same hybrid. The instantaneous power levels were such that saturation of the hybrid or mixer was unlikely. The spectra shown in figure 3 are clearly very similar, which reinforces the notion that the mains harmonics are not an artifact somehow generated by the 3D AFE.

245MHz Resonant Pickup

Simultaneous data was also taken with the 245MHz resonant pickup used in the operational RHIC PLL system, and is shown in Figure 4.

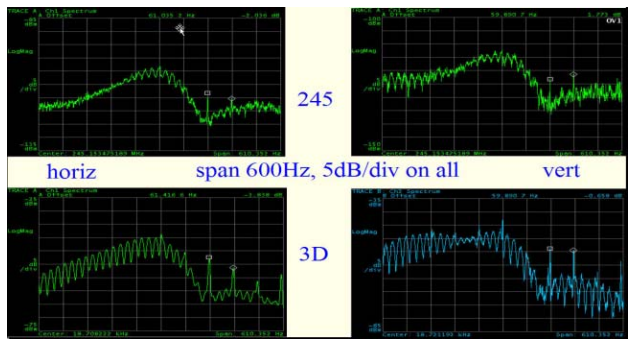

Figure 4: Spectra from 3D and 245MHz resonant pickup

The upper images show signals from the 245MHz pickup, and the lower from the 3D AFE. RHIC was at store and the gap cleaner was operating when this data was taken. The broad peak which occupies the left 2/3 of the images results from beam excitation by that kicker. Mains harmonics are clearly visible in both planes and in the signals from both detectors, in the right 1/3 of the images. These harmonics had never been noted in the 245MHz signal during the many earlier years of RHIC running. It requires some effort to observe them, as they are present only when the 197MHz storage cavities are on and produce shorter bunches, so extending the coherent spectrum up to the 245MHz pickup frequency. In this circumstance it is difficult to avoid saturation of the sensitive front-end electronics. This data again reinforces the notion that the mains harmonics are not an artefact somehow generated by the 3D AFE.

Million Turn BPM

Several of the RHIC BPMs have added memory to permit acquisition of turn-by-turn data for one million turns. These BPMs were used in the study of transition

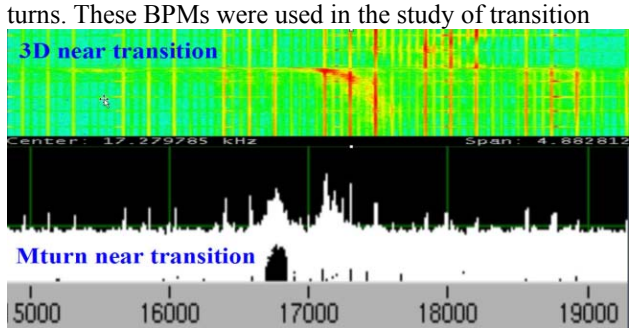

Figure 5: Spectra from 3D AFE and MTurn BPM

instabilities during the Copper run. With its excellent sensitivity and immunity to saturation, the 3D AFE also proved an excellent tool for these studies. Figure 5 shows data taken at the same time near transition (but on different ramps, with slightly different tune values). The pattern of the mains harmonics (repeating every 720Hz, with 3 strong lines spaced by 180Hz) is essentially identical for these two systems. This data once again reinforces the notion that the mains harmonics are not an artefact generated by the 3D AFE.

Coupling Scan

Motivated by the Tevatron observation that the spectrum was altered by the coupling introduced by the separation helix, a single RHIC skew quad was scanned from zero to ~10^{-3} m^{-2}. The result is shown in Figure 6.

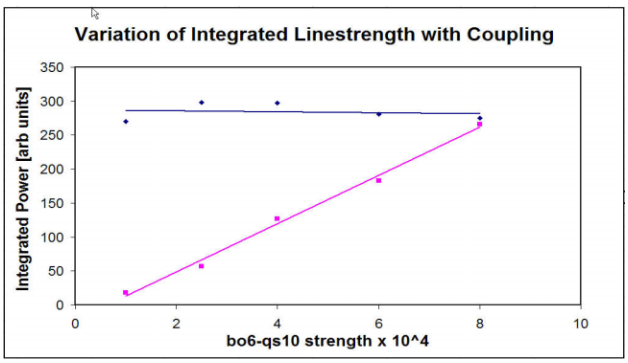

Figure 6: Power in the mains harmonics as a function of coupling strength

Power in the horizontal plane is uncorrelated with coupling strength, and strongly correlated in the vertical plane. This conclusively demonstrates that the mains harmonics are on the beam, and further that the excitation is in the horizontal plane. If the excitation originates in the ring dipoles, a field variation of a few parts in 10^{11} would be sufficient to cause the observed effect. We estimate the magnitude to be several hundreds of nanometers at injection and store, and tens of microns during ramping, and the 3D noise floor to be ~10nm.

EFFECT ON PLL

The excellent sensitivity of the 3D AFE is a major step forward in realizing reliable operational tune feedback in large hadron colliders. However, the mains harmonics revealed by this sensitivity have the potential to disrupt efforts to utilize it to full advantage. Figure 7 shows the tracking performance of the Baseband PLL in the vicinity of mains harmonics as the reference phase is manually swept. The lower portion of the figure shows that the PLL excitation is ~12dB to ~18dB above the adjacent mains harmonics. The upper portion shows that, despite this significantly greater excitation power, the PLL still locked to the mains lines at times of close proximity.

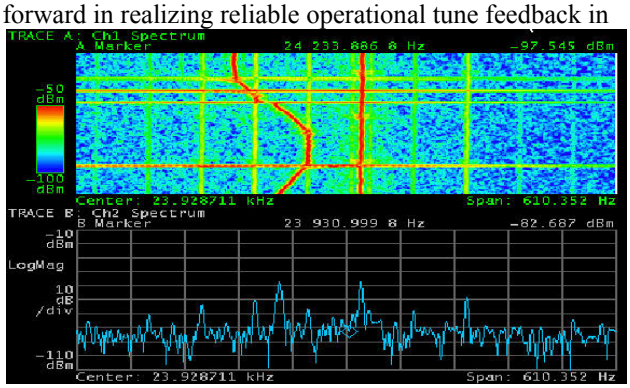

Figure 7: Baseband PLL with 100msec time constant

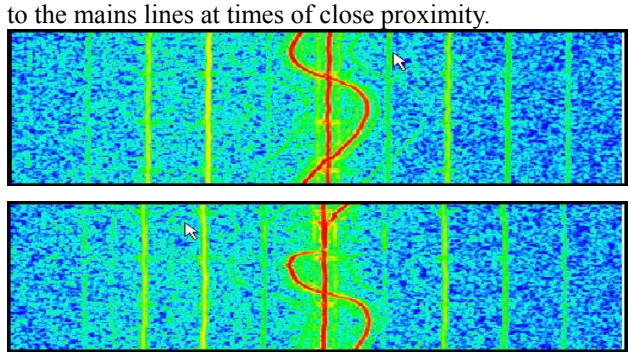

Figure 8: Baseband PLL with 1sec (upper half) and 300msec (lower half) time constants

Our expectation had been that this problem might be avoided by increasing loop gains to cause the PLL to sample a large band around the mains harmonics. The data in Figure 8 reveals that the actual behaviour is the exact opposite. As the time constant is increased (equivalent to lowering the loop bandwidth) the susceptibility to locking on a mains harmonic diminishes.

CONCLUSION

It has been demonstrated that the betatron spectrum is excited by harmonics of the mains frequency, and that this excitation is seriously detrimental to PLL tune tracking. This has been seen at the PS, the SPS, the Tevatron, and RHIC. One might expect that it will also be seen at the LHC, and that given the much lower betatron frequency it has the potential to be more severe. **It is essential that causes and cures of these harmonics be investigated as quickly as possible.** At RHIC there exists, as yet un-commissioned, a 12-phase balancing circuit for the main magnet power supply. Our hope is that spectra from the 3D AFE might be used to tune this balancing circuit, and that a similar solution might be applied at the LHC. The alternative to fixing the problem at the source is filtering in the PLL. This approach looks complicated and difficult, and is likely to adversely affect PLL reliability.

REFERENCES

[1] M. Gasior and R. Jones, “High Sensitivity Tune Measurement by Direct Diode Detection”, these proceedings.

[2] P. Cameron et. al., “Advances Towards the Measurement and Control of LHC Tune, Chromaticity, and Coupling”, these proceedings.

ABSOLUTE CURRENT CALIBRATION OF 1μA CW ELECTRON BEAM *

M. Bevins, A. Day, P. Degtiarenko, A.P. Freyberger, A. Saha, S. Slachtouski
Jefferson Lab, Newport News, Virginia
Ronald Gilman
Rutgers University, Piscataway, New Jersey

Abstract

The future experimental program at Jefferson Lab requires an absolute current calibration of a 1 μA CW electron beam to better than 1% accuracy. This paper presents the mechanical and electrical design of a Tungsten calorimeter that is being constructed to provide an accurate measurement of the deposited energy. The energy is determined by measuring the change in temperature after beam exposure. Knowledge of the beam energy then yields number of electrons stopped by the calorimeter during the exposure. Simulations show that the energy lost due to electromagnetic and hadronic particle losses are the dominant uncertainty. Details of the precision thermometry and calibration, mechanical design, thermal simulations and simulations will be presented.

INTRODUCTION

An experiment scheduled for the Hall A end station of the Thomas Jefferson National Accelerator Facility (JLab) CEBAF accelerator requires absolute beam current measurements with 0.5% to 1.0% accuracy for beam currents around 1μA [1]. The beam current monitor is based on a pair of resonant RF cavities which need to be cross calibrated against an absolute current reference. The present absolute current calibration system is designed for currents greater then 50μA and extrapolation is required for lower beam currents [2]. In order to perform a cross calibration of the cavity response at 1μA of beam current, a new calibration device based on calorimetry is being fabricated.

The calorimeter is a slug of material that is inserted on the beam axis for a well defined period of time. The energy deposited in the calorimeter is: $E_{cal}(Joules) = E_{beam}(MeV)I_{beam}(\mu A)\Delta t(sec) - E_{loss}$ where E_{cal} is the energy absorbed by the calorimeter, E_{beam} is the energy of the beam, I_{beam} is the average beam current, Δt is the duration of the exposure and E_{loss} is the energy that escapes the slug via particle loss or thermal loss [radiation and conduction]. It is important that E_{loss} be small so that the average beam current can be extracted without additional uncertainties. The calorimeter is designed to operate with $0.8GeV < E_{beam} < 11GeV$ and $0.1\mu A < I_{beam} < 5\mu A$.

The change in temperature of the calorimeter after a beam exposure is proportional to the energy deposited, $\Delta T = E_{cal}/\mathcal{C}_m$ where $\mathcal{C}_m$ is the specific heat of the slug. Typically heat capacities of materials are not known with the precision required for this application so $\mathcal{C}_m$ must be measured. A resistive heater inserted in the calorimeter, will be used to determine a precise value for $\mathcal{C}_m$. With nominal values of $\mathcal{C}_m$ and a 48sec exposure to a 5kW beam, the expected temperature rise is 30K.

Large copper and silver calorimeters built in the late 1960's achieved precisions of about 1% [3] and influenced the design of this calorimeter. The following sections describe the design of the calorimeter and estimates of E_{loss} and the instrumental error budget.

PARTICLE CONTAINMENT

The incident electron beam interaction in the calorimeter will result in the creation of secondary electromagnetic and hadronic particles. Electromagnetic particle/shower formation and energy leakage was studied using GEANT and EGS4 simulations. Hadronic particle formation and leakage was studied using GEANT/DINREG [5]. The optimal size, shape and material of the calorimeter from these studies is a Tungsten cylinder 16cm in diameter and 16cm long. Most of the losses are backscattered particles, and to minimize these losses the beam strikes the calorimeter within 1cm diameter by 2.5cm deep cylindrical bore. The electromagnetic loss estimate from the simulations is $0.1 \pm 0.1\%$ and the hadronic loss estimate from the simulation is $0.3 \pm 0.2\%$.

MECHANICAL DESIGN AND THERMAL CONTAINMENT

Pure tungsten shapes are typically produced by pressing and sintering tungsten powder followed by an extrusion or swaging operation to reduce porosity. Subsequent operations to reduce porosity are not practical for a part this large. An extensive search for a high thermal conductivity, high density, tungsten composite material identified a tungsten-copper (95:5) produced by OSRAM/Sylvania. This material is produced using a unique process that does not require an infiltration of copper into a sintered tungsten framework. The blended tungsten and copper powders are pressed then sintered producing a very dense (99%), homogeneous, machinable part. Copper infiltration would not be an option for a part this large.

Since the calorimeter must be installed upstream of the

* This work is supported by the Southeastern Universities Research Association (SURA) which operates the Thomas Jefferson National Accelerator Facility (JLAB) for the United States Department of Energy under contract DE-AC05-84ER40150.

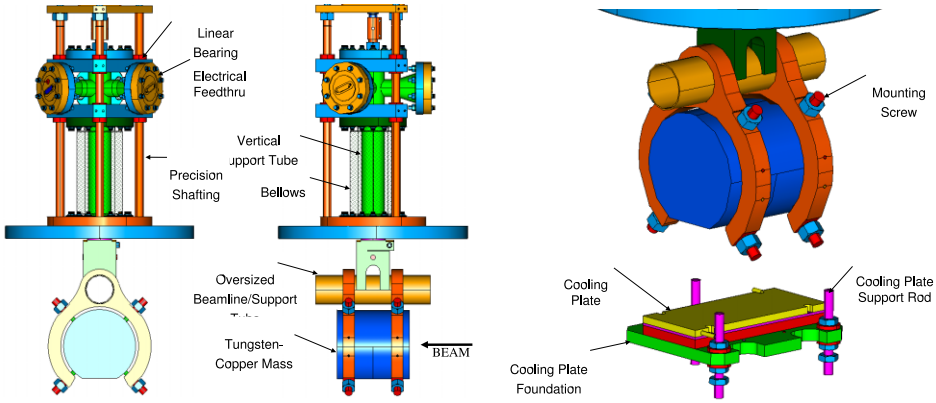

Figure 1: Mechanical drawing the calorimeter and the support mechanism. The calorimeter and cooling plate will reside in a vacuum vessel.

physics target, the tungsten-copper mass must be inserted into the beam-line to intercept the electron beam then removed for normal beam operations to resume. A three position actuation scheme (using a three position air cylinder) minimizes actual beam time required to take a current measurement. The mass support frame incorporates an over sized beamline tube that allows beam to pass through the device in both the equilibrating and cooling positions (see figure 1). Electrical wires for thermometry, charge bleed off, and the calibration heater are routed to the mass through electrical vacuum feed-through, then down the vertical support tube, eliminating the need for a service loop inside the vacuum chamber. The electrical feed through/support tube is guided using linear ball bushings and precision shafting.

Thermal Design and Simulations Heat leaks to and from the mass during exposure to the beam and during equilibration must be minimized, or at least known with sufficient certainty ($<<$ 1% of total absorbed energy). Socket set screws with glass ceramic inserts are used to position and support the mass inside the frame while providing thermal and electrical isolation. The mass is gold coated and the vacuum vessel electro-polished to reduce radiation exchange. The ceramic inserts used in the mounts minimize conductive heat transfer.

Advanced compliant thermal interface materials with good conductance in vacuum at low interface pressures allow the mass to be cooled for subsequent measurements by bringing it in contact with a cold plate rather than embedding or otherwise attaching cooling tubes.

Two-dimensional finite difference (FD) calculations and commercial thermal finite element (FE) [1] models were used to estimate the thermal losses, response time and temperature gradients in the calorimeter. A lumped mass model that assumes minimal spatial variation in temperature was used to estimate the time required to cool the mass to repeat a measurement. This model was used to check the results of the FD code and conduct more detailed analysis that more accurately capture the transient heat flow out of (and into) the tungsten-copper mass during each of the three stages of operation (i.e., charging, equilibrating, and cooling).

[1]The IDEAS TMG transient solver was used to build a finite element model of the calorimeter

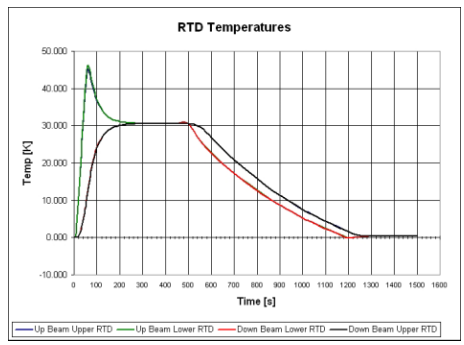

Figure 2: Thermal response of the calorimeter after a 240kJ exposure. Equilibrium is reached about 350seconds after the exposure. After 500seconds the calorimeter is lowered to the cooling plate.

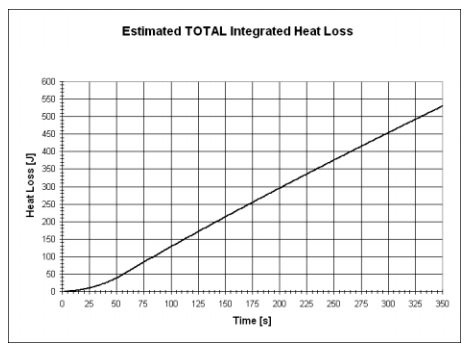

Figure 3: Estimated integrated heat loss through radiation and conduction after a deposition of 240kJ of energy in the calorimeter.

The simulated thermal response of the calorimeter to 48seconds of a 5kW (240kJ) is shown in Figure 2. The calorimeter reaches equilibrium 350seconds after the expo-

sure. Figure 3 is the simulated total energy loss due to radiation and conduction through the wires and mounts. The total energy lost at 350 seconds is 530J which amounts to only 0.2% of the deposited energy. This 530J loss is dominated by radiation losses($\tilde{3}$20J), followed by the mounts ($\tilde{1}$70J) and finally the conduction loss through the instrumentation wires ($\tilde{4}$0J).

Refinements to the FE model could include radiation exchange and a model of the heater cartridge for comparisons between simulated calibration and electron beam heating. Thermal stress calculations are ongoing at this time. Preliminary conservative estimates for higher power exposures show stresses high enough to warrant more refined analysis.

INSTRUMENTATION

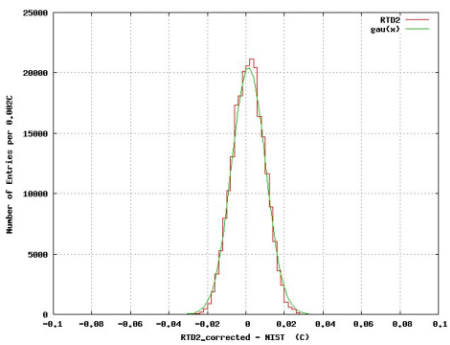

Figure 4: Measured residuals for an industrial RTD after cross calibration against NIST traceable thermometer for temperature range of 20C to 60C. The data is fit to a Gaussian function with $\sigma = 0.008K$ and mean=0.002.

The absolute temperature of the calorimeter needs to measured to better than $\pm 0.025^0$K. The beam current calibration involves measuring a temperature rise,however absolute temperatures are needed for precise determination of the calorimeter's heat capacity. The heat capacity of the calorimeter is a function of temperature. Absolute temperature probes calibrated [NIST traceable] at this accuracy are expensive and bulky. Using inexpensive industrial small RTDs allows multiple and redundant temperature measurements.

The readout of the RTDs will be done by a Sensoray S518 PC104 daughter board and a PC104 CPU. The small PC104 form factor permits the readout electronics to be easily shielded and located near the calorimeter. The PC104 CPU operates Linux operated system and communicates control and monitor signals via EPICS, for ease of integration into the accelerator control system.

Calibration of the industrial RTDs against a NIST traceable thermometer has been performed by uniformly heating an Al slug of roughly the same dimension as the calorimeter and recording RTD and the NIST temperature during the decay to room temperature. The slug is suspended by thin wires in an insulated chamber [cooler]. Care must be taken to slowly heat the slug uniformly to avoid thermal waves in the slug which result in temperature gradients. Both the RTDs and the NIST thermometer are embedded several centimeters into the slug. The default calibration constants for the industrial RTDs need to be modified by a linear correction. The typical slopes and offsets for the correction were less than 3% for the slope and 0.5K for the offset.

After calibration the RTDs measure the temperature within $\pm 0.006^0$K accuracy repeatably for several weeks of testing, see Figure 4. The tests did show that the S518 card does have a temperature dependence which must be included in the calibration constants (mainly the offset term).

SUMMARY

Table 1: Tabulation of energy losses and uncertainties for the calorimeter.

Mechanism	**Loss**(%)	**Uncertainty**(%)
Beam Energy		± 0.01
Radiation	0.13	
Conduction	0.08	
Electromagnetic particle	0.1	± 0.1
Hadronic particle	0.3	± 0.2
Instrumentation		± 0.1
Total	0.61	± 0.24

Estimated losses and uncertainties are shown in Table 1. Escaping particles represent the dominant loss and uncertainty. Thermal and mechanical design limits radiation and conduction losses to the 0.2% level. The design minimizes actual beam time required to take a measurement and allows a measurement to be repeated within 20min. The device is currently in fabrication with initial bench testing (using the heater) expected to begin summer of 2005. Installation is planned for 2006.

REFERENCES

[1] R. Gilman, "Hall A Beam Calorimeter: Overview, Specifications, Operations", JLab internal document, May 6, 2004

[2] J.-C. Denard *et.al* "High Accuracy Beam Current Monitor System For Cebaf's Experimental Hall A", Proceedings of the 2001 Particle Accelerator Conference, Chicago USA `http://accelconf.web.cern.ch/AccelConf/p01/PAPERS/WPAH103.PDF`

[3] G.E. Fischer and Y. Murata, "A Beam Monitor System for High-Intensity Photon Beams in the Multi-GeV Range", Nuclear Instruments and Methods, 1970

[4] P.V. Degtiarenko, "Tungsten Calorimeter Model Calculations and Radiation Issues", JLab internal document, May 14, 2004

[5] P.V.Degtyarenko and M.V.Kossov. "Monte Carlo program for nuclear fragmentation", Preprint ITEP-11, 1-18 (1992), Moscow Institute for Theoretical and Experimental Physics Preprint.

PRELIMINARY TESTS OF A NEW KIND OF BPM SYSTEM FOR SOLEIL

J-C. Denard, L. Cassinari, F. Dohou, N. Hubert, N. Leclercq, D. Pedeau;
Synchrotron SOLEIL; FRANCE

Abstract

SOLEIL is a third generation light source in construction near Paris. Its small emittance requires improving the resolution of existing BPM systems to submicron level up to 100 Hz and stability to the micron level. The same BPM system has also to perform turn-by-turn acquisitions at high rate (846 kHz) with a resolution of a few microns for machine physics studies. SOLEIL entrusted the design of a new digital BPM system to a young Slovenian company, Instrumentation Technologies. SOLEIL defined technical specifications that seemed attainable and proposed a way of improving beam position measurement stability when the current or the bunch pattern of the beam changes. This paper presents the preliminary tests performed in the laboratory with signal generators simulating the electron beam as well as those done with real beam at ESRF in order to evaluate the SOLEIL BPM Electronics.

INTRODUCTION

SOLEIL, a third generation light source being built near Paris (France), will provide users with 24 beam lines [1]. Its small emittance leads to small beam sizes, especially in the vertical direction with 8 µm (at 1% coupling) at the insertion device source points.

The Beam Position Monitor (BPM) system comprises 120 monitors located around the storage ring next to quadrupoles. The system fulfils several important tasks:

- Slow acquisition: the closed orbit is measured at about 10 Hz acquisition rate for stabilizing it with a slow global orbit feedback via the control system and the dipole corrector coils located in the sextupole magnets. The important performances are current and bunch pattern dependences in order to always deliver photon beams at the same spot to the users for all beam currents and bunch patterns they work with.
- Fast acquisition: the closed orbit is measured at a high acquisition rate (> 4 kHz). In addition to the performances previously mentioned a good resolution (rms position fluctuation) is necessary. This mode is used for the fast orbit feedback [3].
- Turn-by-turn: for machine physics applications (machine model, non linear beam dynamic studies) and for tune measurements. High resolution (≤ 3 µm) beam positions are measured at the revolution frequency (846 KHz).
- First turns: this is mainly for the commissioning. The system must accommodate low currents on a single beam passage.
- Interlock: when the beam goes outside a predefined position range at any selected BPM, the BPM electronics gives an interlock signal which is used to prevent possible damage to the machine.
- Post mortem: records the last few thousand turns of beam position data in case of a sudden beam loss.

BPM ELECTRONICS

Each BPM has four button electrodes delivering narrow pulses to an electronic processing unit located outside the machine tunnel, via four coaxial cables. The spectrum line at the RF frequency (352 MHz) is the useful part of the signal processed by the electronics. The BPM electronics requirements for the Storage Ring are shown in table 1.

Table 1: Storage Ring BPM electronics requirements

	Slow acquisit.	**Fast acquisit.**	**First turns**	**Turn-by-turn**
Absolute accuracy	≤ 20 µm	≤ 20 µm	≤ 500 µm	≤ 200 µm
Resolution rms	≤ 0.2 µm	≤ 0.2 µm	≤ 500 µm	≤ 3 µm
Measurement rate	10 Hz	≥4000 Hz	847 kHz	847 kHz
Dynamic range	20 – 600 mA	20 – 600 mA	0.4 – 4 mA	4 – 600 mA
Current dependence	≤ 1 µm	≤ 1 µm	≤ 500 µm	×
Bunch pattern depend.	≤ 1 µm	≤ 1 µm	≤ 500 µm	≤ 500 µm
8-h drift	≤ 1 µm	≤ 1 µm	≤ 500 µm	×
1-month drift	≤ 3 µm	≤ 3 µm	≤ 500 µm	×

The same electronics equips the Booster and the measurement rate reaches 1.9 MHz. Booster resolution and stability requirements are relaxed. A Booster specific mode provides beam positions over the acceleration cycle with a choice of data averaging; it is called Booster Normal mode.

Instrumentation Technologies, a Slovenian company, has been chosen to design and build the electronics. There is one 1U-19" chassis (figure 1) per monitor. It takes its power from the 220 V 50 Hz mains and provides the X and Z positions directly to the control system via an Ethernet port. It also provides the four electrode signals, their sum, and a signal for checking the BPM.

Figure 1: Front and back panels of a Libera chassis

A description of the resulting electronics called "Libera" is found in reference [2]. The processing board includes a powerful FPGA with two imbedded PowerPC™. The FPGA firmware, split in two, can be loaded via Ethernet. One part is for Storage Ring operation, the other for the Booster.

LABORATORY TESTS

Goal

We check the performances of the Libera chassis in the laboratory at their arrival at SOLEIL. The measurements were carried out on 25 Liberas randomly picked from 152 units. Four kinds of measurements were performed:

- Absolute accuracy: measurements of a centered beam (simulated with same signal levels on the 4 inputs)
- Beam Current Dependence (BCD): measurements of an off-centered beam (simulated with unbalanced signal levels on the inputs). The input level covers the –2 to –72 dBm range in 4 dB steps.
- Measurements of an off-centered beam in "First-Turns" mode for the Storage Ring measured in the –44 to –86 dBm range.
- Raw (non averaged) measurements with off-centered beam in the "First Turns" mode for the Booster measured in the –20 to –80 dBm range.

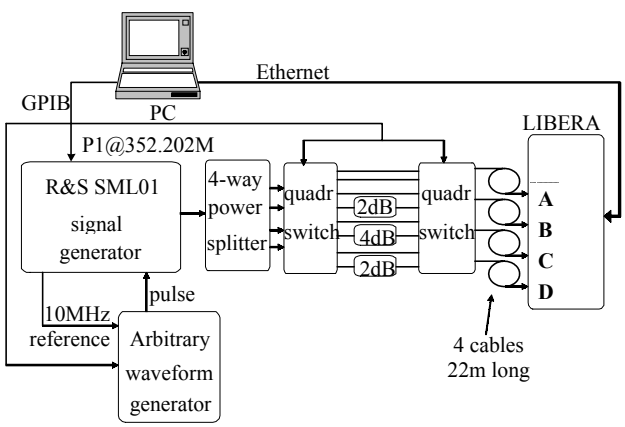

Figure 2: Measurement set-up

Measurement Results

The results are consistent with the end-of-manufacturing tests performed by Instrumentation Technologies:

- Resolution in First Turns mode is better than the 0.5 mm resolution specification, down to – 80 dBm for the SR (~15 µA) and -78 dBm for the Booster (~0.2 mA considering injection bunch length).
- Absolute accuracy is outside the specifications, especially for the vertical position. It is planned to apply a fixed offset correction specific to each Libera.
- Beam Current Dependence (figure 4) and Bunch Pattern Dependence should easily be brought within specifications using correction tables.

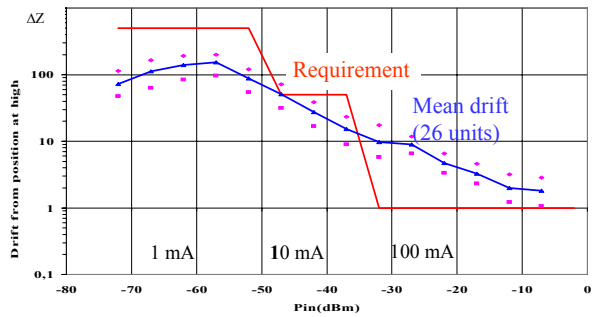

Figure 3: Beam Current Dependence for a simulated beam off-centered by 1.4 mm in X and Z.

Resolution

The resolution of the SOLEIL Liberas has been improved in three steps in order to lower it to an acceptable level. Resolution is an issue for fast orbit feedback. The BPMs must not induce excessive noise on the beam. It is also an issue at revolution frequency for machine physics studies. IT measured the performance of the first few units recently upgraded (figure 4). The acquisition in turn-by-turn mode (846 kHz) is within 3 µm down to 20 mA. Some units are slightly outside the very tight requirement of 0.2 µm rms @ 100 Hz acquisition rate for a -32 dBm input level. However, the whole production of 152 chassis should be within 0.3 µm.

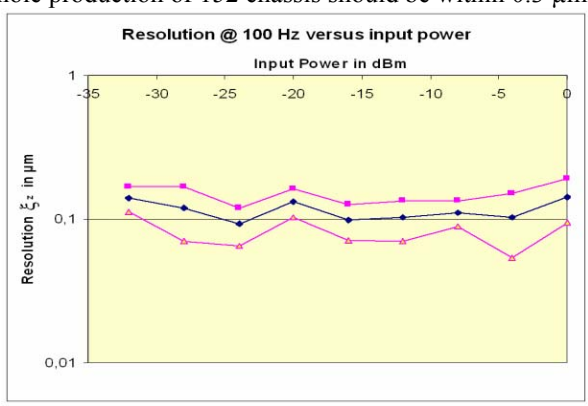

Figure 4: Resolution @ 100 Hz repetition rate

TESTS ON ESRF BOOSTER

Goal

We need to check the behavior of Libera hardware, FPGA firmware, and generic server software with its SOLEIL Device Server on a real machine in order to identify any problems and fix them before the Booster commissioning. A similar test on the Storage Ring will be done when the corresponding FPGA firmware is ready.

Test Setup Characteristics

ESRF and SOLEIL RF frequencies are both 352 MHz. Libera features a VCXO for Booster BPM sampling frequency at 107.19 MHz that combined with the processing, results in one measurement every SOLEIL Booster revolution period of 522 ns. ESRF Booster revolution period being 1000 ns, there is almost two measurements per revolution period for our Libera monitoring the ESRF Booster. A BPM with four striplines is available for the test. Its geometry is different (electrodes on the X and Z axis) from that of SOLEIL Booster BPM (electrodes on the diagonals). The X and Z computation, done in the Tango Device Server, is modified accordingly for the test. A trigger, 190 µs ahead of the injection, can be delayed at will via a pulse generator and applied to the Libera. A laptop computer running the Tango Device Server and another laptop running SOLEIL Tango control system are connected to a same local Ethernet switch as the Libera.

Tests in "turn-by-turn" mode

We record 40 000 position measurements (~20 ms) at a 522 ns repetition period during the acceleration cycle. The signal levels were adjusted from – 44 to -74 dBm with attenuators. It corresponds to currents from 5 to 0.15 mA, the useful SOLEIL Booster dynamic range. The beam trajectory for the first turns after injection are shown in figure 5.

CONCLUSION

The laboratory tests and ESRF tests of the SOLEIL BPM electronics (Libera) gave encouraging results. We think all performances should eventually reach our very tight requirements.

The current dependence should be suppressed and fit the specifications by using correction tables.

The fast feedback mode resolution has being improved via hardware upgrades implemented by IT and we expect all units to be within 0.3 µm.

The tests done on the ESRF Booster showed the Libera operates well with Tango, the SOLEIL control system, and a first version of the BPM Device Server.

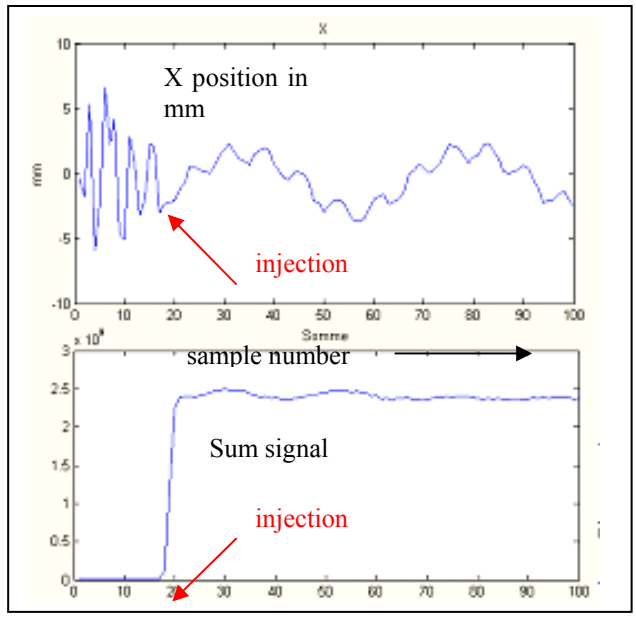

Figure 5: ESRF Booster horizontal position and BPM sum signal for 100 acquisitions.

ACKNOWLEDGEMENTS

We thank the Instrumentation technologies team for their development of the Libera electronics and its software. Many thanks have also to be addressed to P. Elleaume, E. Plouviez, Y. Papaphilippou, and K. Scheidt from ESRF. They greatly helped us for testing the Libera at their facility and in interpreting the results.

REFERENCES

[1] M-P. Level et al, "Progress Report on the Construction of SOLEIL", PAC'03, Portland (OR), May 2003, p. 229.

[2] A. Kosicek, "Libera Electron Beam Position Processor", PAC'05, Knoxville, May 2005, to be published.

[3] N. Hubert et al, "Design of a Fast Orbit Feedback for SOLEIL. This conference.

APPLICATION OF THE BEAM PROFILE MONITOR FOR VEPP-4M TUNING

#O. I. Meshkov, A. V. Bogomyagkov, F. Gurko, A. N. Zhuravlev, P. V. Zubarev, V. A. Kiselev, N. Yu. Muchnoi, A. N. Selivanov, A. D. Khilchenko.

Abstract

A transverse beam profile monitor based on the Hamamatsu multi-anode photomultiplier with 16 anode strips is used at VEPP-4M collider. The monitor is used to study turn-to-turn dynamics of the transverse beam profile during 2^{17} turns. In addition, it provides a permanent measurement of synchrotron and betatron frequencies. The operation of the device for tuning the collider and studying of collective effects is described.

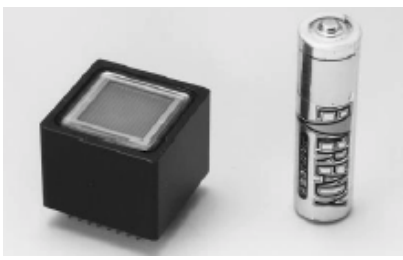

Figure 1. MAPMT R5900U-00-L16 HAMAMATSU

INTRODUCTION

The interest in the study of beam distribution within fast instabilities like beam-beam effects has always existed in accelerator physics. The corresponding diagnostics should provide a one-turn distribution for a few ten thousand turns of the beam. For this purpose we have designed a device based on the Multi-Anode Photomultiplier Tube (MAPMT, Fig. 1). The Fast Profile Meter (FPM) is a part of the VEPP-4M optical diagnostic system [1,2]. It is applied also for determination of synchro-betatron resonances, phase oscillation monitoring and studying of collective effects.

DESIGN OF THE FPM.

The device includes a MAPMT, a 12-byte ADC, a controller module, an internal memory of 4Mb and 100 Mb ethernet interface. It can record 2^{17} profiles of a beam at 16 points. Discontinuity of the records can vary within $1 \div 2^8$ turns of a beam. Revolution time of a beam in the VEPP-4M collider is 1220 ns and the recording time can last between 0.16 s to 20 s. As a result, the device can analyze the frequency oscillation of a beam in range of 10 Hz — 1MHz. The main parameters of the device are listed in Tab. 1

#O.I.Meshkov@inp.nsk.su

Table 1. The technical data of the Fast Profile Meter.

Size	250 x 100 x 100 mm
Interface	100Mb ethernet
Internal memory	~4 M (2^{17} beam profile at 16 points)
Discontinuity of record	1 to 2^8 turns
Analyzable frequency range	10 Hz to 1 MHz
Single anode size	0.8 × 16 mm

The optical arrangement (Fig. 2) allows to change the beam image magnification on the cathode of MAPMT from 6× to 20×, which is determined by the experimental demands.

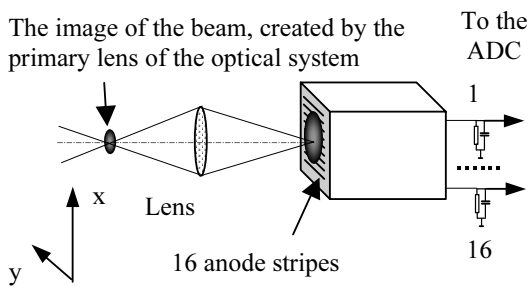

Figure 2. Optical layout of the diagnostics. The lens sets up a beam image on the photocathode of the MAPMT. The radial profile measurement is shown.

The operating cycle of the device is as follows. MAPMT signals are recorded to the ADC after start pulse. The starting moment is either chosen by user or coincides with the beams convergence in the interaction point, “kick”, beam pass by, etc. The ADC triggering is synchronized with the beam revolution frequency. The recorded signals are stored in the internal memory and read out to the PC.

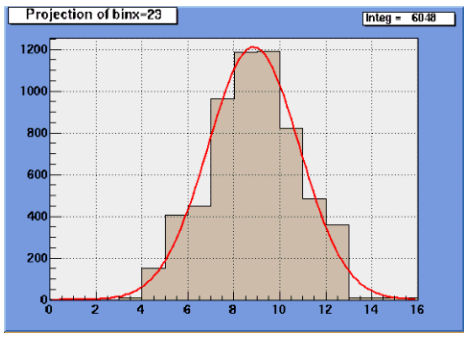

Figure. 3. Example of the single beam profile fitted by the Gauss function.

At present, the signals processing consists in fitting a Gauss function to every single profile and perform a Fourier transformation. The relative sensitivity of the MAPMT channels is taken into account. Typical single profile is shown in the Fig. 3.

EXPERIMENTAL RESULTS

Beam profile behavior during convergence in the interaction point

The standard procedure of the beams convergence is described at [1]. Fig. 4 presents the beam size and position behavior in the case of beam-beam instability. The currents of the beams were restricted by beam-beam effects (Ie^+=3.4 mA, Ie^- =3.0 mA.), and the positron beam is the "strong" one. During evolution of instability taking place, both, dipole oscillations and beam size, increase. Every "flash" of oscillations is accompanied by beam losses.

Frequently beam convergence is accompanied by instability, this looks like beam "twinkling" on the TV screen. The image looks like a small periodical kick applied to the beam. As a matter of fact, this "twinkling" is caused by the oscillation of vertical beam size as Fig. 5 demonstrates.

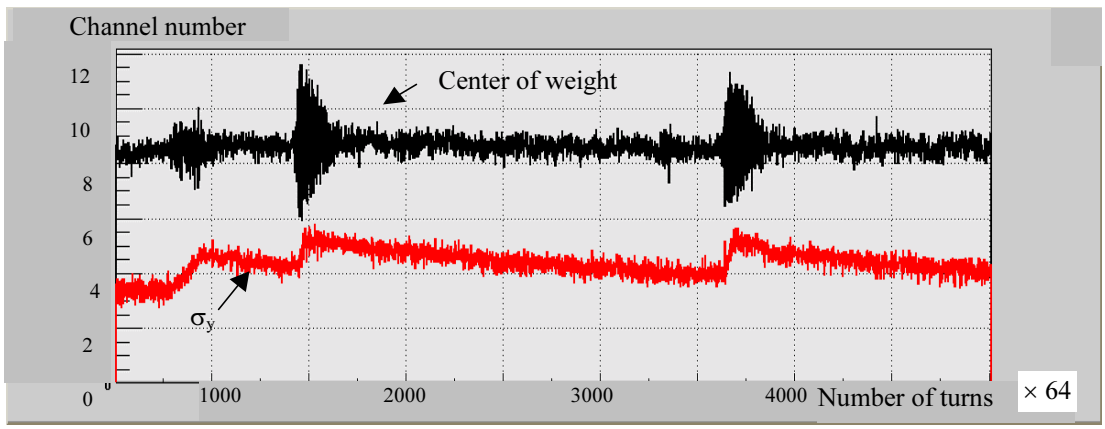

Figure 4. Beam dipole oscillations (black plot) and σ_Y behavior (red plot) during the beams convergence in the interaction point. Duration of the single turn is 1220 ns. Channel constant is 0.12 mm. Ie^+= 3.4 mA, Ie^- = 3.0 mA.

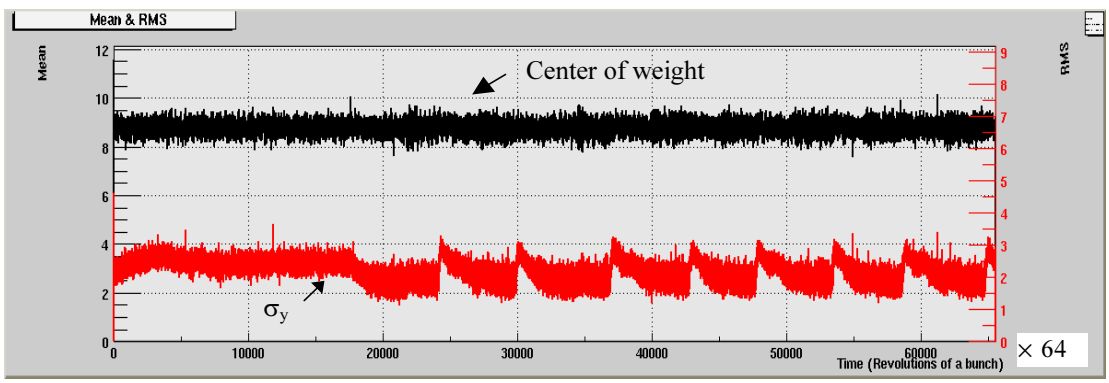

Figure 5. Convergence of the beams with currents of Ie^+=2.4 mA, Ie^- =2.9 mA, accompanied by quadrupole instability.

Measurement of synchrotron frequency and monitoring of phase oscillations.

The experimental program of the VEPP-4M collider and the KEDR detector consists of precise J/ψ -, ψ'-, ψ''-mesons and c-τ lepton mass determination, for which the method of resonance depolarization is applied [3]. This technique requires a storage of a polarized beam as long as possible. The level of polarization can be destroyed by synchro-betatron resonances. The knowledge of synchrotron frequency and its dependence on the accelerating voltage is necessary for the choice of the working point of the collider. The experimental dependence of the synchrotron frequency with respect to the accelerating voltage have been determined by using MAPMT (Fig. 6). Phase oscillations of the electron beam were excited by slightly detuning the accelerating resonator.

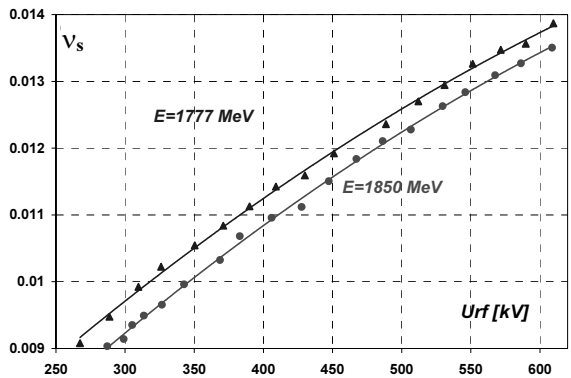

Figure 6. The dependence of the synchrotron frequency ν_s with respect to the accelerating voltage U_{rf}

Parasitic phase oscillations appearing during collecting the data can distort the beam energy and the energy spread. MAPMT is used as a phase oscillations monitor during the collider operation. Monitoring consists in a permanent measurement of the radial position of the beam and Fourier analysis. The maximal value of the Fourier harmonics within an area corresponding to synchrotron oscillations (0.01-0.014 for VEPP-4M) is determined. The KEDR team uses this information (Fig. 7) for selection of the events.

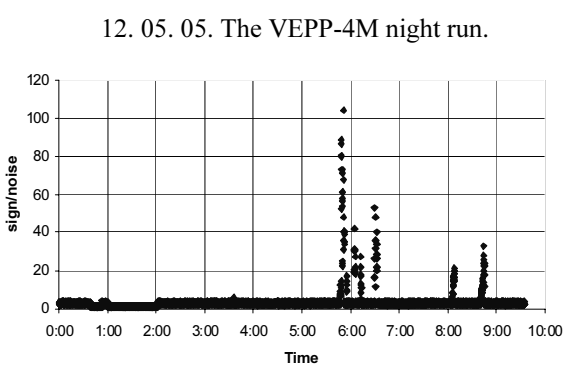

Figure 7. Monitoring of parasitic phase oscillations. MAPMT data are shown.

Tune plane scanning.

The knowledge of betatron resonances is necessary for the determination of the accelerator working point. It is easy to calculate a tune plane, but experimental proof of the resonances manifestation is of immediate interest. Fig. 8 represents the result of betatron tunes scanning around the working point of VEPP-4M. Frequency measurement was made with the help of MAPMT. The beam was kicked with an amplitude of 0.2 $\sigma_{x,y}$ and the ν_x, ν_y frequencies were determined by Fourier transformation. The vertical beam size σ_y was measured permanently with optical system [1] and the resonances appear as an increase of the vertical beam size.

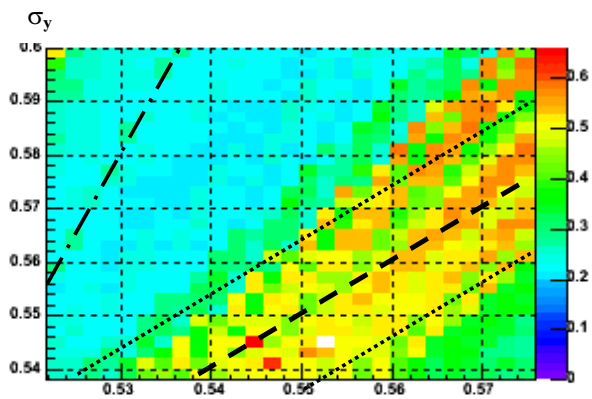

Figure 8. Vertical beam size σ_y with respect to betatron frequencies. The main resonance ν_x-ν_s = 0, two synchro-betatron resonances ν_x-ν_s ±ν_s =0 and 3ν_x-ν_s=1 are shown.

CONCLUSION

The Fast Profile Meter based on MAPMT was designed and applied at the VEPP-4M collider. The device enables the study of the beam profile behavior under diverse experimental conditions and the measurement of beam frequencies within a wide range. The FPM can be used for accelerator physics research and routine machine service.

REFERENCES

[1] O. I. Meshkov et al. The upgraded optical diagnostics of the VEPP-4M collider. Proceedings of EPAC 2004, Lucerne, Switzerland, pp. 2739-2741.

.[2] O. I. Meshkov et al. VEPP-4M optical beam profile monitor with one-turn temporal resolution. Proceedings of EPAC 2004, Lucerne, Switzerland, pp. 2733-2735.

[3] V. E. Blinov et al. Absolute calibration of particle energy at VEPP-4M. Nuclear Instruments and Method in Physics Research A 494 (2002) 81-85.

ROSALI: AN APPLICATION ALLOWING ONLINE/OFFLINE ALGORITHM IMPLEMENTATION TO ASSESS BEAM INSTRUMENTATION PERFORMANCE

M. Moles
CERN, Geneva, Switzerland

Abstract

A software tool called "Rapid Online Software ALgorithm Implementation (ROSALI)" has been developed at CERN. This application is intended to provide instrumentation experts and accelerator physicists with a tool, which allows monitoring and storage of beam measurements and rapid algorithm implementation via specialized actions on the embedded Mathematica kernel. The users are able to build or modify online a sequence of actions implementing their algorithms. Those sequences can subscribe to ongoing measurements from several beam instruments or retrieve data from previous recordings, merge these measurements to obtain correlation diagrams or perform dedicated calculations. This document presents the current state and the foreseen extensions of this application. The application has been tested last year on the SPS and it will be used this year on the new LEIR machine at CERN.

INTRODUCTION

The AB/BDI software section at CERN is responsible for providing all the software necessary to develop, test, diagnose and maintain the different instruments produced by the group. This control software for front-end computers is implemented using the FESA framework [1].

The ***R**apid **O**nline **S**oftware **AL**gorithm **I**mplementation* application; known as ROSALI [2] is an application for the instrumentation experts and accelerator physicists to monitor, store and analyse the beam measurements made by our instruments. As Figure 1 shows, ROSALI can retrieve these measurements directly from the acquisition front-ends or from previously stored data files. The storage of these measurements can be made through a C library following the ROSALI file format (explained later on) directly in the front end software or using the ROSALI application itself. This file format ensures that all data saved from the front-ends or ROSALI will be consistent and readable from the ROSALI application.

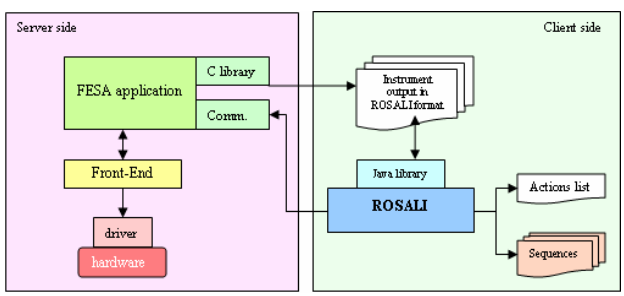

Figure 1: System architecture

ROSALI also provides a rapid and easy way to build and play sequences of actions for testing and assessing the instruments. These actions can subscribe to, store or display ongoing measurements from several beam instruments, retrieve offline data and perform dedicated calculations in the Mathematica kernel [3]...

Another characteristic of ROSALI is to provide harmless access to the instruments. This is achieved by giving full access to the acquisitions and status but restricting the access to the settings to authorized users.

ROSALI FILE FORMAT

To store and share between actions all data coming from the instruments a new file format has been designed based on the following requirements:

- The data files should be human readable.
- This format should be able to handle the main types of data coming from beam instrumentation, i.e lines, XY scatters and surfaces.
- This format should allow the storage in a single file of heterogeneous types of data related to the same acquisition such as 2 profiles, 1 image and the corresponding setting's values.
- This format should be easy to handle in Excel, Mathematica and in-house C/C++/Java programs.

It is composed of tab-separated variables implemented in an XML light format allowing direct use in Excel. Dedicated Mathematica, C and Java libraries [2] have been provided to cover other usages.

ROSALI APPLICATION

As shown in Figure 2, the graphical interface of the application is divided into three main areas together with the toolbar.

- The *Sequence* area contains the list of actions to execute.
- The *Parameters* area contains the parameters of the selected action. These parameters can be used as input (equipment name, target storage directory…) and/or output (result file name,) by the action. The value of an input parameter can also be set as a reference to the value of an output parameter of another action.
- The *Viewer* area shows the result after the execution of the selected action. Each action can have its own viewer (simple table, standard data viewer or custom panel dedicated to beam profile measurements for instance)

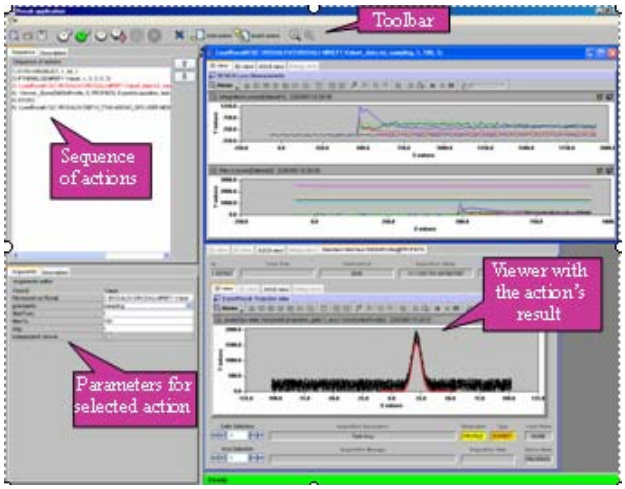

Figure 2: ROSALI user graphical interface

To create a sequence in the ROSALI context, the user has to select the actions from a menu in the *Toolbar*, setting the values for their input parameters in the *Parameters* area; then the sequence will be ready for execution. The result obtained from the execution of a single action will be showed in the *Viewer* at each step of the loop. The user can execute the whole sequence, just one action or a set of actions from the selected one until the end. ROSALI provides users with control statement actions like *if-then*, *repeat*, *goto* or *stop* to create dynamic and/or never ending sequences.

The sequence can then be saved and reloaded for subsequent uses. The sequence saved will contain the list of actions and corresponding parameters together with the creator's contact details, the date of last modification and a brief description of the sequence and how to use it.

ROSALI ACTIONS

An action is a single instruction to execute in the ROSALI environment. Every action has a set of parameters that define its behaviour and the contact information of the developer who gives support to that action. To ensure the harmless objective of the application, every action has a list of users who can see and use the action.

The ROSALI actions can be classified in two groups: the *ready-for-use* actions and the *user-defined* actions that need some development from the user in order to be executed.

Ready-For-Use Actions

For these, the user only needs to set the values for the input parameters. These actions can:

- Subscribe to ongoing measurements from several beam instruments and save them in a file. If selected, the measurements will be displayed in a dedicated viewer depending on the instrument family, being position, profile, intensity or loss monitors.
- Retrieve and display data from previous recordings.
- Merge these measurements to obtain correlation diagrams.
- Execute the different control statement actions.
- Synchronize the sequence execution to machine events.
- …

The action builder tool (see next chapter) allow BDI software expert to upgrade ROSALI with new actions whenever necessary.

User-Defined Actions

The ready-for-use actions can provide standard and common services useful for every user but not linked to a specific evaluation or experiment. To allow users to implement and modify online their data treatment and algorithms, ROSALI also provides *user-defined* actions. The main one currently available is the RosToMath action that gives access to the Mathematica kernel from ROSALI via Mathlink. This action basically includes in its viewer all the power of Mathematica including graphic output. The user can in the viewer edit Mathematica cells, execute them and see the result, being text or graphics. The Mathematica code written will be executed each time the RosToMath action is executed in the sequence.

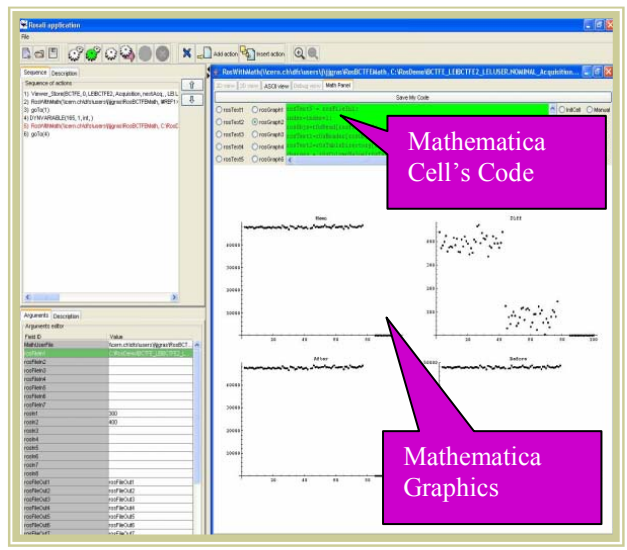

Figure 3: ROSALI / Mathematica Action

Fig. 3 shows the result of a simple use case where a user is testing a scraper efficiency and wants to record every cycle the current evolution and see the evolution of the beam losses before and after scraping of many cycles.

The user built the following sequence of actions:

1. store next BCT acquisition (standard ready-for-use action)
2. add the point corresponding to last acquisition in the loss history graphs via the RosToMath action with dedicated Mathematica code written by the User. This Mathematica code has a direct access on the RosToMath action's parameters (to give the scraping window time in our case) and on

data stored in ROSALI files via a dedicated Mathematica function libray* [2].

3. Goto action 1 (standard ready-for-use action)

The user can build this action in a few minutes without any external interventions, test it immediately and store it for future usage. It will give him in real time the evolution of the scraping efficiency. The user can then add the following actions to the same sequence:

4. increment acquisition index (standard ready-for-use action)
5. add the point corresponding to acquisition number 'index' in the loss history graphs via the RosToMath action with dedicated Mathematica code written by the User.
6. Goto 4 (standard ready-for-use action)

It will give him the same information offline from the files stored during previous tests and also provide the opportunity to implement a new algorithm on these data. The user just has to select action 4 and start the sequence from there.

ACTION BUILDER TOOL

To make easier the ROSALI developer's task of creating a new ROSALI action (being ready-for-use or user-defined), the **ActionBuilder** tool has been provided (see Figure 4).

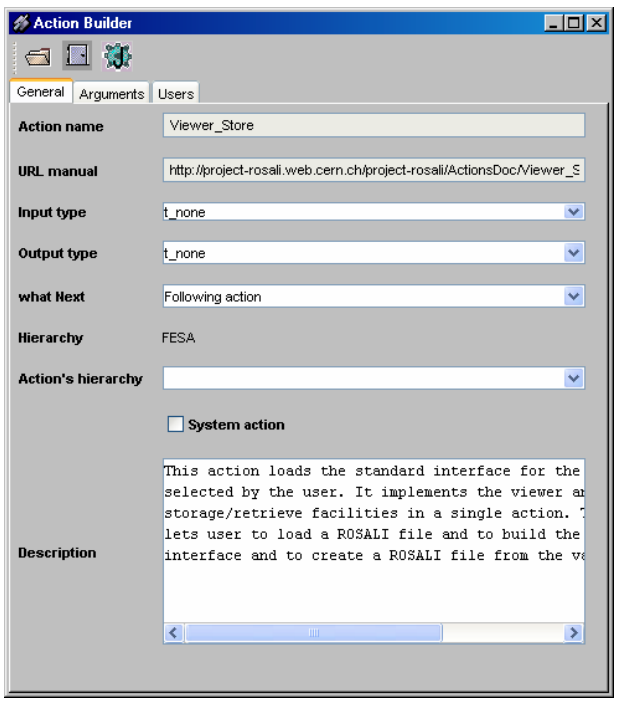

Figure 4: ActionBuilder tool

This application lets developers to specify the action's general information and their input parameters in a visual way. The developer will set the action's name, the URL to the online documentation and a brief description as general information.

For every parameter, he/she will need to specify a name, the order of appearance in the list of parameters and an optional initial value. Once all the information is set, the developer will press the "Generate code" button that will generate the Java code for the action. This code is static, so the developer will need to supply the code to execute when the action is executed inside the ROSALI tool. The developer supplies an *execute()* method in which he/she has a direct access to the input parameters values via the methods *getArg(parameterName)* and *setArg(parameterName, value)*.

PROJECT STATUS

The application described in this paper has been tested last year on the SPS and it will be used this June for the commissioning of the new LEIR [4] machine which is all based in FESA instruments and from where we can take advantage of all ROSALI's features.

The software tools have been developed in Java and are thus platform independent. They are currently used under Linux and Windows 2000/XP.

CONCLUSIONS

The tests carried out on the SPS during the year 2004, show that ROSALI is a very useful application for obtaining and analysing online and offline data from the beam instruments. The non-dependent format of data allows physicists to treat them with different applications such as Excel, Mathematica or ROSALI itself. The dedicated and upgradable actions ensure that the physicists' needs will be always covered, developing new specialized actions if needed.

ACKNOWLEDGMENTS

The development of the ROSALI application was achieved in a short time thanks to the collaboration of many colleagues. In particular, Jean-Jacques Gras helped me in the design of the application, giving to me the practical view of it; BDI Software section who tested the application and supported me in the implementation. Finally, I would like to thank Jean-Pierre Koutchouk who implemented the Mathematica library and supported us with his advice in the use of Mathematica and its features.

REFERENCES

[1] A. Guerrero and al., "CERN Front-End Software Architecture for Accelerator Controls", ICALEPCS'03, Korea, October 2003.

[2] ROSALI web site: http://project-rosali.web.cern.ch/project-rosali

[3] Mathematica web site: http://www.wolfram.com/products/mathematica/index.html

[4] http://project-i-lhc.web.cern.ch/project-i-lhc

* This library also allows direct access to the ROSALI files through pure Mathematica notebooks

MEASUREMENTS WITH A NOVEL NON-INTERCEPTING BUNCH SHAPE MONITOR AT THE HIGH CURRENT GSI-LINAC*

P. Forck, C. Dorn, Ges. für Schwerionenforschung GSI, Darmstadt, Germany, p.forck@gsi.de

Abstract

For bunch length determination in the range of 0.3 to 5 ns at the GSI heavy ion LINAC a novel, non-intercepting device has been realized. It uses the time spectrum of secondary electrons created by atomic collisions between beam ions and residual gas molecules. These electrons are accelerated by an electric field of 420 V/mm toward an electro-static energy analyzer, which is used to restrict the effective source region. Then the electrons are deflected by an rf-resonator running in phase with the acceleration frequency (36 or 108 MHz) to transform the time spectrum into spatial separation. The detection is done with a Ø 70 mm multi-channel plate. The achieved time resolution is about 50 ps, corresponding to 2 degree of 108 MHz phase.

MONITOR OVERVIEW

The determination of the longitudinal density distribution of a bunched beam is an important issue because it is required for an optimal matching between different LINAC-modules as well as for the comparison with numerical calculations. At proton and ion LINACs the bunch structure cannot be determined by capacitive pick-ups due to the non-relativistic beam velocities ($\beta < 20\%$ at the GSI-LINAC) causing a faster propagation of the electric field of the bunches. At most LINACs the bunch structure is determined by secondary electrons emitted from a wire crossing the beam [1, 2]. The wire is biased with about -10 kV to pull the secondary electrons toward a slit outside the beam path. An rf-deflector follows, where the electrons are modulated in transverse direction by an electric rf-field. The deflection angle depends on their relative phases, i.e. the device transforms the time information into a spatial distribution.

For the high current beam operation at GSI with heavy ions and currents up to 20 mA [3], the beam power is sufficient to melt intersecting materials. The described principle is adapted to a non-intersecting device by performing the time spectroscopy of secondary electrons created by atomic collisions between beam ions and residual gas molecules. The electrons are accelerated by a homogeneous electrical field formed by electrodes outside of the beam pass, as usually used for Ionization Profile Monitors. To restrict the source region for the secondary electrons, an aperture system and an electro-static energy analyzer is used. The time-to-spatial transformation is performed with an rf-deflector developed at INR (Moscow) [2].

* Partly funded by EU-FP6-CARE-HIPPI

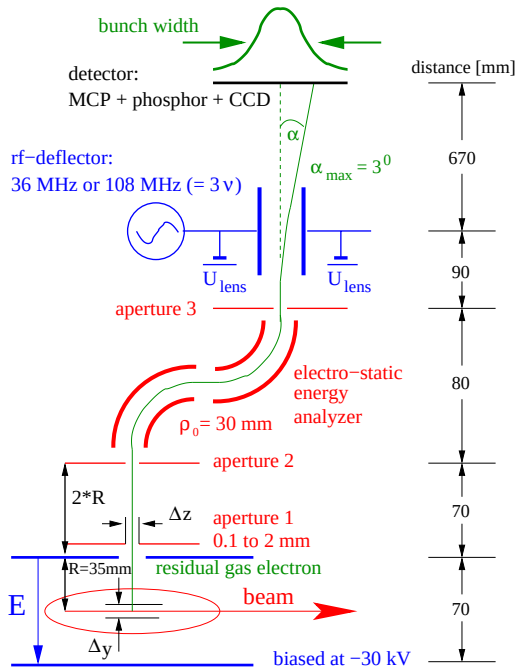

Figure 1: Schematic sketch of the bunch shape monitor.

MONITOR HARDWARE

The schematic layout of the monitor is displayed in Fig. 1: At the detector location, the beam passes a static electric field region generated by a 160×60 mm^2 electrode biased up to -30 kV. With the help of field forming strips, a homogeneous field of 420 V/mm perpendicular to the beam direction guides the secondary electrons toward a grounded plate with a horizontal slit of 1.5 mm in beam direction, see Fig. 2. To shorten the source length Δz in beam direction and the corresponding divergence of the secondary electron beam, two apertures with a distance of 70 mm are used. Their opening can be varied remotely between 0.1 and 2 mm by dc-motors. The second aperture serves as entrance slit of a 90^0 cylindrical electro-static energy analyzer with a bending radius of $\rho_0 = 30$ mm. The nominal voltages are ± 5.5 kV for the opposite cylinder segments. Two similar devices are installed to place the electron detector perpendicular to the beam pipe. A third aperture is located 10 mm downstream from the second cylinder edge to enable a point-to-point focusing from the entrance- to the exit-slit [5]. Using ± 0.25 mm opening for aperture 1 and 2 as well as ± 0.5 mm for aperture 3, the vertical source prolongation is restricted to about $\Delta y = \pm 0.2$ mm [4], which is comparable to the wire thickness in the standard method [1].

After a drift of 90 mm the time information is transferred into spatial distribution by the rf-deflector synchronized

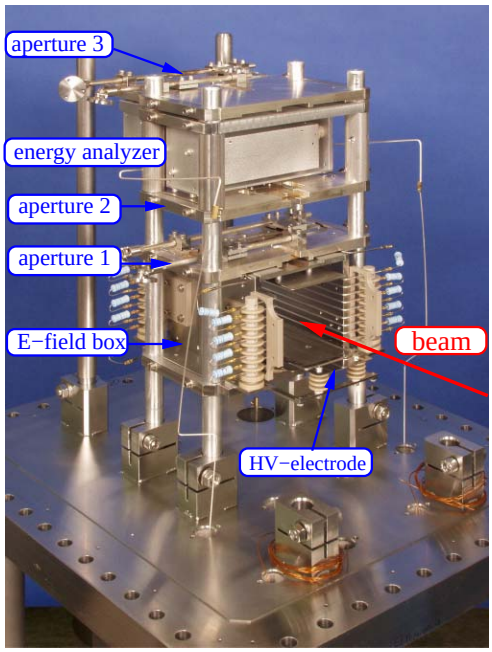

Figure 2: Photo of the electric field box and the energy analyzer. The parts are mounted on a rectangular flange of 340×400 mm^2, which can be mounted to a vacuum chamber. The opening for the beam is 70×70 mm^2.

with the LINAC rf. Two types of rf-deflectors are available, one running at the base-frequency of 36 MHz for the measurement of long bunches and one for short bunches at the third harmonics at 108 MHz. The deflectors are built as 800 mm long parallel-wire $\lambda/4$-resonators [2] having a quality factor of $Q_0 = 290$ and $Q_0 = 370$ for the 36 and 108 MHz device, respectively. The 108 MHz type has straight parallel-wires, while spiraled wires are used for the 36 MHz device. The maximum rf-power fed into the resonator is 100 W and 50 W for the 36 MHz and 108 MHz, respectively. A 6 ms pulse length for the rf-power is sufficiently longer than the maximum macro beam pulse. After this transverse deflection of maximum $\alpha_{max} = 3^0$ and a flight path of 670 mm the single electrons are detected by a Ø 70 mm Chevron MCP (Hamamatsu F2226-24P) equipped with a P20 phosphor screen. The light spots are read out with a 12 bit digital CCD camera (PCO SensiCam) having a 480×640 pixel VGA-resolution and a fiber optic link for digital data communication.

BEAM-BASED MEASUREMENTS

Systematic test measurements at a target location were performed at 11.4 MeV/u for several ion beams. Without applying rf-power to the deflector the optics of the energy analyzer was checked. The parallel wires of the rf-deflector can be biased with maximal $U_{lens} = -7$ kV acting as a electro-static einzel-lens [1]. As shown in Fig. 3 the electron beam can be focused on the MCP and a spot size of 1 mm can be reached corresponding to about 6 pixels.

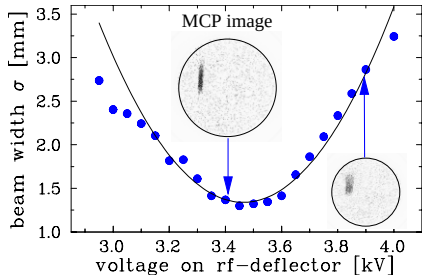

Figure 3: Determination of the monitor resolution by variation of the electro-static lens voltage without applying rf to the deflector for the nominal aperture setting of ± 0.25 mm for aperture 1 and 2 and ± 0.5 mm for aperture 3.

This coincides with the optical calculations for the nominal aperture settings of the energy analyzer. Due to the 70 mm active diameter of the MCP this width contributes by only a few % to the monitor resolution; for the measurements of Fig. 5 and 6 it corresponds to a time resolution of about 50 ps. The beam spot size can be even reduced by a smaller aperture opening, but than also the signal strength decreases.

To illuminate the full MCP the rf-power of the rf-deflector can be varied. Therefore, quite different bunch lengths can be measured. A calibration of the bunch center position at the MCP with respect to the rf-phase is required to achieve an absolute time or phase scale. An example is shown in Fig. 4 using an digital rf-phase shifter with $\sim 0.3^0$ accuracy. In addition, the plots proves the linearity of the transverse deflection as long as the rf-phase difference between deflection voltage and the bunch stays within an interval of $\sim 45^0$. For large phase differences, the non-linear behavior of the sine-wave starts to contribute.

A typical raw image of the bunch as recorded by the CCD camera is shown in Fig. 5. The deflection with a frequency of 108 MHz is displayed horizontally spanning 3.6 ns. The projection of the light intensity on this axis gives the bunch shape. This measurement proves the general functionality of this novel device, where short bunches down to $\sigma = 125$ ps were monitored [4].

It is required to subtract a homogeneous distributed background. This background is only present during beam delivery and is not influenced by the aperture opening. Presently, its origin is not well understood. It might be due

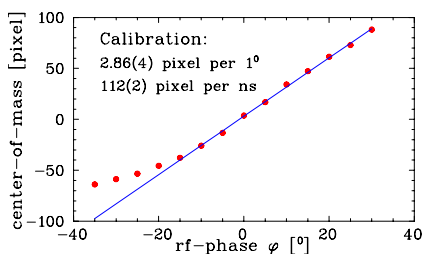

Figure 4: The central position of the bunch as a function of the relative phase shift.

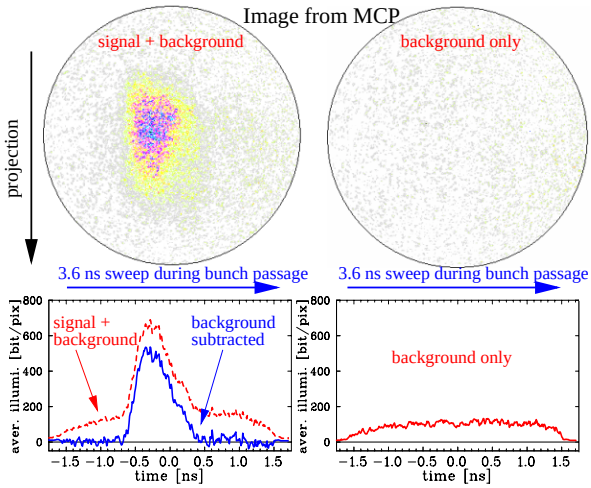

Figure 5: Typical image (inverted color) from the MCP for a 2 mA Ni^{14+} beam averaged over 8 macro-pulses with 0.2 ms duration and a vacuum pressure of $2 \cdot 10^{-6}$ mbar. 15 W had been fed to the 108 MHz rf-deflector.

to x-rays from secondary electrons accelerated by the electric field and hitting the stainless steel plate of the electric field box. But the installation of a 5 mm thick steel shielding behind the energy analyzer for x-ray absorption (maximum energy 30 keV) did not lead to a significant reduction. We will install a biased grid close to the HV-electrode to prevent for secondary electrons entering the interaction region. Other reasons for the background might be neutrons or γ emitted at the nearby beam dump. A nearly background-free measurement is intended to allow single macro-pulse monitoring. Moreover, with an enhanced signal quality the monitor resolution can be increased by a smaller aperture opening and possible non-Gaussian bunch structure contributions can be detected within a single macro-pulse. The image of the bunch can than be spread over the full MCP area and a resolution down to $\sim$ 20 ps would be achievable.

The displayed measurement had been performed with a high current setting of 2 mA Ni^{14+} beam. But the same signal quality can be reached for low current settings [4]. If the amount of secondary electrons does not result in a sufficient statistic, the vacuum pressure can be raised by a regulated gas inlet system. It has been proved, that a local pressure bump up to 10^{-4} mbar in the transfer lines at GSI does not influence the beam properties. Due to the statistical nature, averaging also improves the signal-to-noise ratio leading to a large dynamic range.

An application of the bunch shape monitor is to determine the longitudinal emittance. By varying the voltage amplitude of a buncher cavity and measuring the bunch width, the longitudinal emittance in a linear approximation can be calculated by fitting a parabola through the square of the bunch width, as displayed in Fig. 6.

Compared to the 'standard' method by an intercepting wire a larger contribution for the bunch space charge is expected for the following reason: Close to the wire the electric field for the secondary electron acceleration is large, while for our setup the electric field is constant during the whole acceleration process. Therefore the influence of the beam's electric field on the detected electrons is more important. Model calculations for the measured beam parameters are discussed in [4] proving the applicability for the high current operation at GSI with a bunch length in the ns range.

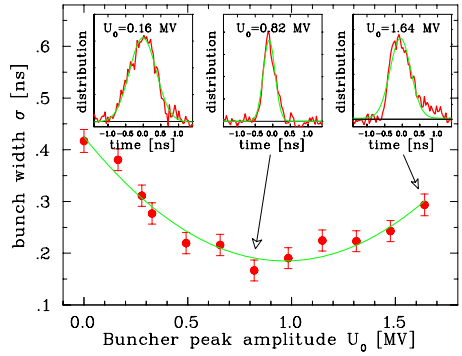

Figure 6: Measurement of the bunch width (one standard deviation) as a function of the buncher voltage 31 m upstream of the detector performed with the same beam as of Fig. 5.

CONCLUSION

A novel, non-intersecting device for the bunch structure determination has been successfully tested. It can be used in a wide current range and offers a direct determination of parameters that are difficult to measure. For high currents and moderate bunch-length in the ns range, the bunch structure is reproduced faultlessly. Presently, the origin of the diffuse background is not well understood and limits the achievable resolution. After its reducing a high resolution single macro-pulse observations seems to be possible.

Acknowledgment: We like to thank, H. Graf, M. Herty, P. Strehl from GSI, A. Feschenko, V. Peplov from INR as well as S. Sharamentov from ANL for valuable discussion and the technical realization. We acknowledge the support of the European Community Research Infrastructure-Activity under FP6 'Structuring the European Research Area' program (CARE contract No. RII3-CT-2003-506359). Photos by G. Otto.

REFERENCES

[1] A. Feschenko, *Proc. PAC 2001, Chicago*, p. 517 (2001) and references therein.

[2] N.E. Vinogradov et al.,*Nucl. Instrum. Meth.*, **A 526**, p. 206 (2004), Y.V. Bylinsky et al., *Proc. EPAC 1994, London*, p 1702 (1994).

[3] W. Barth et al., *Proc. PAC 2001, Chicago*, p. 3281 (2001), W. Barth et al, *Proc. XX LINAC Conf. 2000, Monterey*, p. 1033 (2000).

[4] P. Forck et al., *Proc. EPAC 2004, Lucerne*, p. 2541 (2004).

[5] See e.g. H. Wollnik, *Optics of Charged Particles*, Academic Press (1987).

DESIGN OF THE FARADAY CUPS IN DIAMOND.

A.F.D. Morgan, Diamond Light Source, UK

Abstract

This paper details the work done on the design of the faraday cups for the DIAMOND light source. Diamond has faraday cups in positions covering the complete energy range of the machine from the 90keV gun to the 3GeV storage ring.

The Linac cups were modified from an existing design, while the higher energy designs were done using Monte Carlo code. The Monte carlo led designs achieved an electron capture rate of around 99%, allowing them to be used with reasonable certainty as calibration references.

Due to the modest 5Hz repetition rate of the electron gun, power loading of the structures is minimal and active cooling is not required for any of the cups.

Ablation is also not thought to be a significant problem for these designs.

OVERVIEW

Diamond light source is a 3GeV 3^{rd} generation synchrotron. The electrons are initially ejected from a 90keV gun. A linear accelerator increases the energy of the electrons to 100MeV. A booster ring further increases the energy to 3GeV. Finally the beam is injected into the storage ring to generate the synchrotron radiation [1].

Faraday cups are a basic charge capture device which can be used as reference points for current measurement calibration. Diamond has faraday cups after the 90keV gun and the 4MeV bunching section, in the linac to booster transfer line at 100MeV and at 3GeV in the booster to storage ring transfer line.

An initial design decision was made to make the designs passive to increase reliability and reduce complexity.

Due to the modest 5Hz repetition rate of the electron gun, power loading of the structures is minimal and active cooling is not required for any of the cups.

The 90keV and 4MeV cups were modified from an existing design using analytical formulæ and MathCAD. Monte carlo modeling was used to confirm the new design. The high energy 100MeV and 3GeV designs were done using the EGSnrc Monte Carlo code[1] from the national research council Canada, with MatLAB being used for interfaces and post analysis.

This paper will cover the basic methodologies used to obtain each design as well as the final design details and expected performance.

[1]http://www.irs.inms.nrc.ca/inms/irs/EGSnrc/EGSnrc.html

THE LINAC FARADAY CUPS

The 90keV/4MeV cup is an in vacuum design, based on the SLS 90keV design [2]. The design maintains the coaxial structure as much as possible in order to obtain a high bandwidth (figure 1).

Figure 1: The linac faraday cup assembly

The design changes were calculated using analytical formulæ taking into account collisional losses, radiative losses due to bremsstrahlung, the photoelectric effect, compton scattering and pair production. The final design was verified using the EGSnrc code (figure 2).

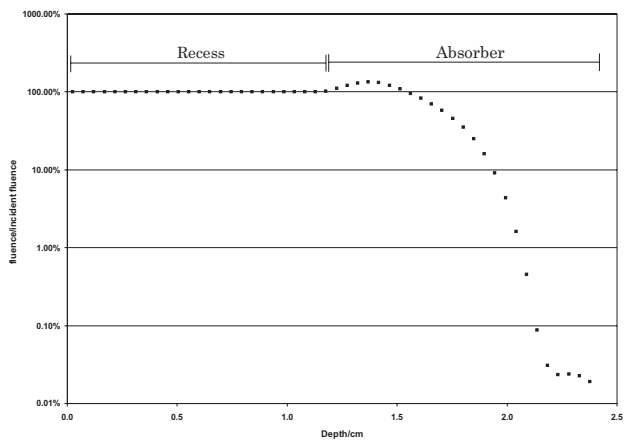

Figure 2: Data from the EGSnrc code

The cup is mounted on an actuator to enable it to be inserted into the beam path of the linac. The main absorber is made from a 24mm aluminium block with a 12mm deep recess cut into it. This enables the design to work at both 90keV and 4MeV.

At this energy the backscatter from the absorber block is the dominant effect. The recess diameter was chosen to be 13mm to accomodate some beam movement while still keeping backscatter low. A carbon cup with 1mm wall thickness was inserted into the recess to act as a soft stop to reduce the backscatter from 12% to 3.5% in the 90keV

case, and from 2.5% to 0.7% at 4MeV (figure 3). Thus we expect the cups to perform with greater than 90% electron capture efficiency.

Figure 3: Close up of the absorber

The cup was tested in the 90keV position during the linac gun tests by PPT. Figure 4 shows the signal from the cup in response to the single bunch output of the gun.

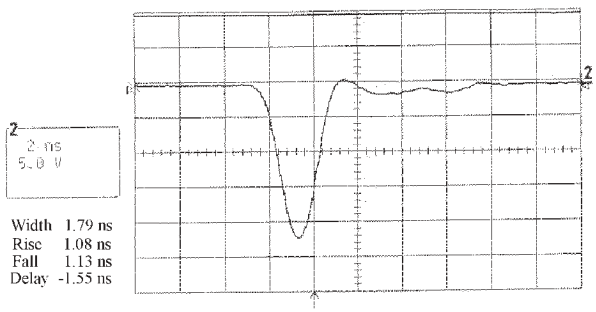

Figure 4: Data from initial test

This shows that the cup behaves as expected.

THE 100MEV DESIGN

The 100MeV faraday cup is an in-vacuum design directly connected to the machine vacuum. A solid block of oxygen free copper was used for the main absorber due to its superior heat conductivity, allowing it to thermalise the heat spikes caused by the electron bunches quickly enough to reduce power loading to negligible levels.

The absorber block is suspended off ceramic washers to give it electrical isolation while a recess and carbon soft stop were used to reduce backscatter (figure 5).

The absorber section is a cylinder with a diameter of 160mm and a length of 250mm, with an additional 100mm for the recess. The total mass of copper used is 84.5kg.

The recess diameter of 63mm was chosen to match the beam pipe diameter in order to ensure beam capture (both

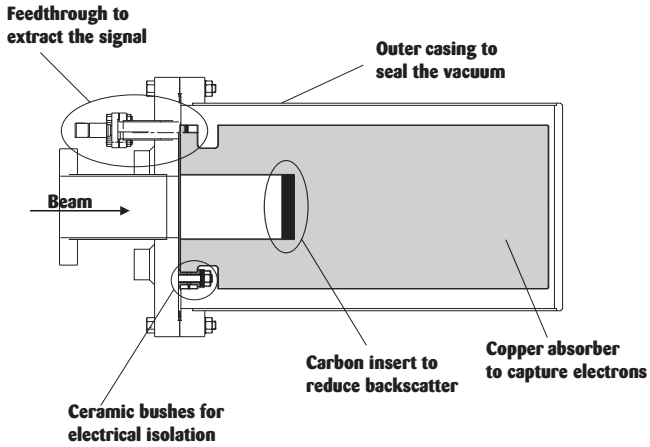

Figure 5: The design of the 100MeV device

high energy designs also act as beam stops). Making the recess opening larger does not have much effect on the capture efficiency as backscatter reduces as the energy increases.

Ablation of the cup was considered but the energy density at the cup is below the surface ablation limit of Copper (10^7W/cm^2) [3]. From the EGS results, this design is expected to have an electron capture efficiency of 99.2%.

THE 3GEV DESIGN

The 3GeV design is also a copper absorber with carbon soft stop. The absorber will be constructed out of several plates. The front plate is made from oxygen free copper and will be braised to the 38mm diameter vacuum tube.

A ceramic break in the vacuum tube gives the electrical isolation needed for the cup to work, while a bellow gives mechanical isolation between the absorber block and the break.

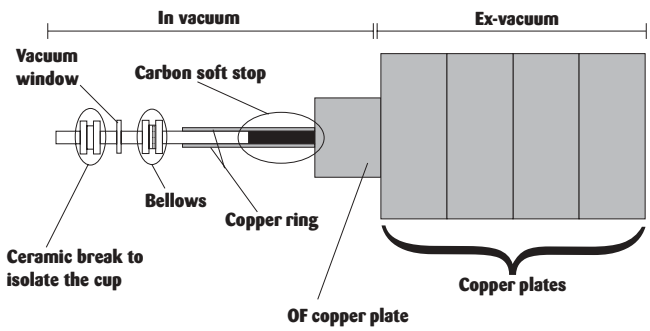

Figure 6: The design of the 3GeV device

The front of the cup is in a vacuum environment to eliminate the problem of ozone generation if the beam were to pass through air. However, it is separated from the main machine vacuum using a vacuum window in order to eliminate the risk from outgassing and from possible ablation.

The rest of the absorber will be constructed ex-vacuum using a stack of additional copper plates. The soft stop to

reduce backscatter in this case is a carbon cylinder inside the vacuum tube, while a ring of copper surrounds the tube to capture the remaining backscatter (figure 6).

From the monte carlo results the design has an electron capture level of 99%.

The total length of the absorber is 500mm. The front plate is 100mm thick in the beam direction and has a 240mm diameter. The ex vacuum plates are 100mm thick in beam direction with a minimum diameter of 500mm.

The thickness of the copper ring was studied and an optimum thickness of 51mm was reached by balancing the secondary electron capture against the number of electrons escaping from the resulting cascade.

The total mass for this design is 957kg.

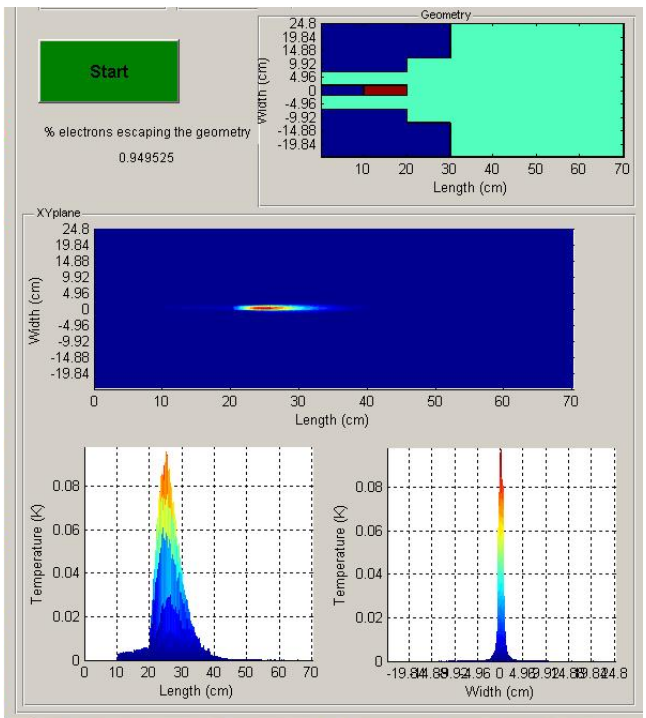

Figure 7: Thermal data for the 3GeV design for a single shot

For this position in the machine the energy density could go above the surface ablation limit of copper if a large portion of the energy was deposited near the surface. However, the majority of the energy was found to be deposited some centimeters into the structure with little deposited near the surface (figure 7). Thus surface ablation effects are not thought to pose a large risk.

CONCLUSIONS

Designs have been developed for all of the faraday cups in the DIAMOND machine. The 90keV and 4MeV designs are expected to exceed 90% electron capture while the results from the EGSnrc code show capture efficiencies of 99.2% for the 100MeV cup and 99% for the 3GeV cup.

Due to their passive designs these capture efficiencies should have a low error on them, allowing all the designs to be used with confidence as calibration sources for current measurements.

Power loading and surface ablation are not thought to be significant problems for these designs.

The linac faraday cup has been tested in the 90keV position and has performed as expected.

References

[1] R. P. Walker Progress with the diamond light source, Proceedings of EPAC 2004.

[2] V. Schlott SLS LINAC AND TRANSFER LINE DIAGNOSTICS, PSI Scientific Report 1999, Volume VII Swiss Light Source.

[3] A. Bogaerts Z. Chen R. Gijbels A. Vertes Laser ablation for analytical sampling: What can we learn from modeling?, Spectrochimica Acta Part B 2003 pp 1867-1893.

DESIGN ALTERNATIVES FOR BEAM HALO MONITORS IN HIGH INTENSITY ACCELERATORS

C.P. Welsch[1], H. Braun, E. Bravin, R. Corsini, T. Lefèvre, D. Schulte, F. Tecker
CERN, Geneva, Switzerland

Abstract

In future high intensity, high energy accelerators it must be ensured that particle losses are minimized as activation of the vacuum chambers or other components makes maintenance and upgrade work time consuming and costly. It is imperative to have a clear understanding of the mechanisms that can lead to halo formation and to have the possibility to test available theoretical models with an adequate experimental setup.

Optical transition radiation (OTR) provides an interesting opportunity for linear real-time measurements of the transverse beam profile with a resolution which has been so far at best in the some μm range. However, the dynamic range of standard OTR systems is typically limited and needs to be improved for its application for halo measurements.

In this contribution, the existing OTR system as it is installed in the CLIC test facility (CTF3) is analyzed and the contribution of each component to the final image quality discussed. Finally, possible halo measurement techniques based on OTR are presented. Later beam tests are foreseen to be carried out in CTF3.

INTRODUCTION

Optical transition radiation is produced when charged particles pass through media with different dielectric constants. It took about 10 years from the first demonstration of its practical application for measuring a wide range of important beam parameters [1] until it was used in a number of accelerators as one of the main diagnostic tools [see for example 2, 3].

Since then, OTR has proven to be a flexible and effective diagnostic method for measuring a wide range of beam parameters like the beam profile, its divergence and the beam emittance. Its fast time response in combination with e.g. a streak camera makes it the ideal tool even for the analysis of the longitudinal beam shape in single shot measurements.

In order to be applicable for investigations of the beam halo, i.e. measurements with large differences in intensity between the beam core and the tail region, a highly optimized diagnostic system is needed, where the influence of all components on the final data is known in detail.

In CTF3, different constraints have to be respected, which directly influence possible measurement techniques: The high radiation level in the machine requires special shielding of the CCD cameras used and the power deposited in the screen limits the type of material of the screens. Either Aluminum or carbon screens are used depending on whether the focus lies on high reflectivity or good thermal resistance.

To get a better understanding of the characteristics and present limitations of the optical systems used in CTF3 at the moment and to find possible improvements systematic measurements and associated simulations were started.

ANALYSIS OF THE LENS SYSTEM

If a charge q hits a boundary surface with an oblique incidence, the emitted electric field has two components: One in the plane of observation and the other one perpendicular to it. The total emitted intensity W of a beam with a given relativistic γ therefore has to be calculated as the sum of these to components [1]

$$\begin{aligned} \frac{d^2W}{d\Omega d\omega} &= \frac{d^2W_{||}}{d\Omega d\omega} + \frac{d^2W_{\perp}}{d\Omega d\omega} \\ &\approx \frac{q^2}{\pi^2 c}\frac{\theta^2}{\left(\gamma^{-2}+\theta^2\right)^2} \end{aligned} \qquad (1)$$

By direct differentiation of equation (1), the maxima of the resulting intensity distribution can be found at angles $\theta_{max}=1/\gamma$. In calculations with the ZEMAX code [4], this opening angle was used as one initial parameter to qualify the lens systems installed at CTF at different energies.

A typical installation consists of a set of achromats as shown in the following Fig. 1.

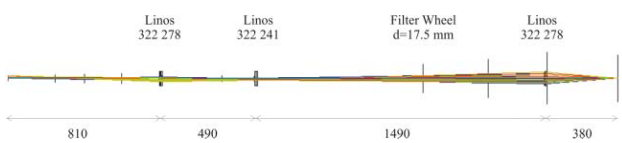

Figure 1: Overview of an optical line as it is presently used in CTF3

With ZEMAX, a detailed analysis of the present installation was performed to find out the main limiting factors.

It was found that, in contrast to the existing systems, the two first lenses should be installed in a so-called confocal arrangement, i.e. where the lens spacing equals

[1]Carsten.Welsch@cern.ch

the sum of the focal lengths, to preserve linearity for both position and angle measurements.

Furthermore, it turned out that, particularly with regard to higher energies, homogenous illumination of the detector is only reached for very small object sizes, Fig. 2 – mainly due to vignetting in the lenses.

This effect clearly limits the performance of the system and needs to be avoided in halo measurements where one is mainly interested in measuring larger distances from the beam center with high accuracy.

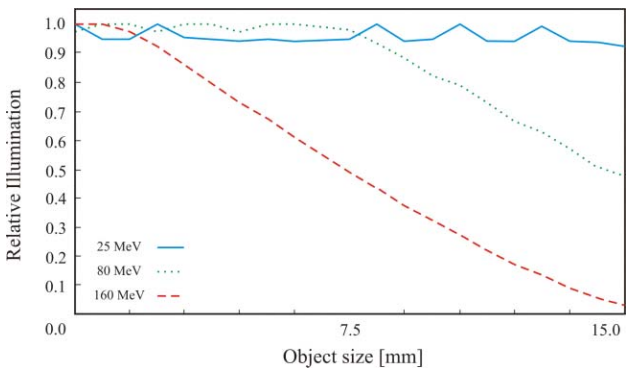

Figure 2: Calculated relative illumination of a standard optical line in CTF3 at beam energies of 25 MeV, 80 MeV and 160 MeV.

These limitations were also found in measurements done at CTF3. The following Fig. 3 shows the measured vertical profiles of a 100 MeV beam as a function of the horizontal dipole magnet current (i.e. center position). In this measurement, the entire width of the screen was scanned and a homogeneous illumination should be expected. The decreasing intensity observed towards the screen boundaries clearly indicates strong limitations of the angular acceptance of the optics.

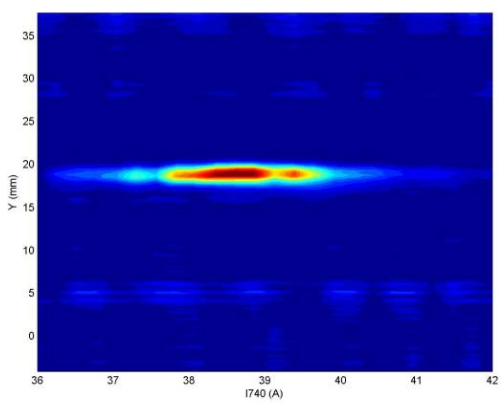

Figure 3: Measured vertical profiles of the OTR light of a 100 MeV beam at different bending fields

SCREEN SURFACE

Different ways to improve the relative illumination of the system are feasible and one way is to modify directly the light emitted from the OTR screen. Since there are strong constraints due t the high radiation level in the machine, the number of usable materials is reduced to a few. The emission distribution of the backward OTR light is proportional to the diffusive (R_D) reflection of the screen surface

$$\theta \propto R_D \qquad (2)$$

Thus one would like to increase the opening angle q while keeping the number of emitted photons as high as possible. The main goal therefore was to find out how well the diffusion of the incident light can be controlled, since this parameter helps to avoid the sharp emission profile of OTR that gives rise to the present limitations.

Table 1: Overview of applied surface treatments

Number	Description of surface treatment
1	Direct illumination of photomultiplier tube
2	Mylar foil + Aluminum
3	Reference plate, mechanically polished
4	Silver-plated
5	Sand blasting
6	Degreasing
7	Degreasing + HNO_3 + HF
8	Degreasing + HNO_3 + HF + NaOH
9	Glass bead blasting
10	oxidation
11	unpolished

In a series of measurements, Aluminum plates were first mechanically polished to mirror quality and then systematically depolished by applying different techniques summarized in Table 1.

Figure 4 shows the measured total reflection of the different screens, measured with a photomultiplier tube type XP2020 and a psec laser pulse.

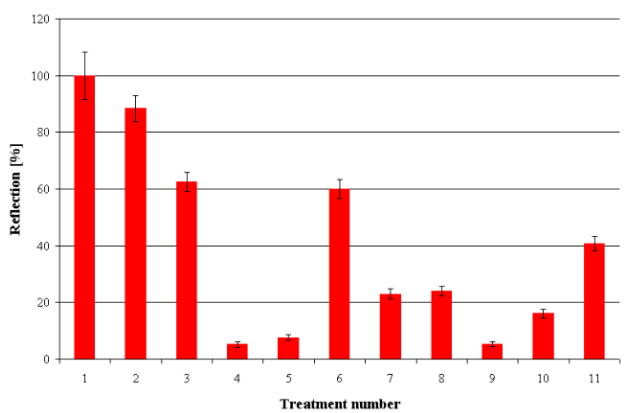

Figure 4: Measured total reflection of different surfaces within the angular acceptance of the PMT

Depending on the applied treatment the absorption of light changes over a wide range. It can be seen from the graph that in some cases not more than 5% of the light is detected, which has to be taken into account during the estimation of the sensitivity of the final detection system.

The angular divergence was measured with a CCD camera and a small cw laser. The resulting angles after reflection can be seen in the following Fig. 5.

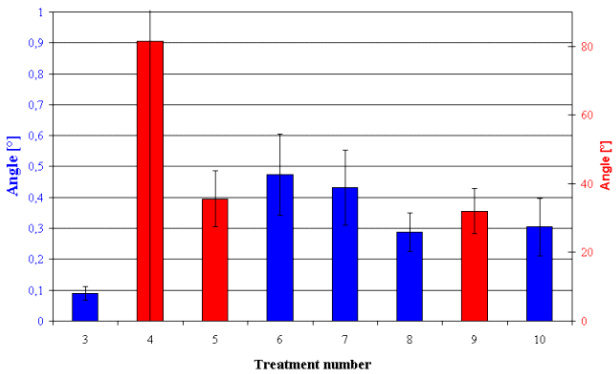

Figure 5: Measured angular divergence of the reflected beam of different surfaces. Either small angles or very large divergences were measured (the color of the bars indicates which scale to use).

The influence of the surface treatment on the diffusion can clearly be seen and these first measurements showed already that it is possible to vary this parameter over a wide range.

Next steps will focus on the properties of different metals and reaching controlled and reproducible effects with different treatments.

Another option is to influence the emitted light by the shape of the screen itself rather than modifying its surface characteristics. Due to the geometrical limitation of the present system especially in the spectrometer lines of CTF3, where the beam is ribbon-like, not all light emitted from the screen surface can be captured with the optical system.

A parabolic foil support could be a possible solution since it might allow capturing more light by the optical system due to the initial focusing of the emitted light. The surface of the screen is described by:

$$z = \frac{1}{4 \cdot f} \cdot x^2 \qquad (3)$$

where z is the vertical surface coordinate, x is the horizontal displacement from the center and f is the desired focal length.

A prototype with a focal length of $f = 500\ mm$ which can hold foils of a thickness of $d = 0.2\ mm$ has been manufactured and is presently under investigation.

MEASUREMENT TECHNIQUES

At present, standard CCD cameras are used at CTF3 for beam profile measurements. To overcome their limitations concerning at the same time spatial resolution and in particular dynamic range, alternatives are being studied.

Beam collimation technique

By putting a mask with only one or a few small holes in an image plane of the optical line and by thus collimating most of the OTR light, measurements with large dynamic ranges are feasible. In such an arrangement, small PMTs are placed right behind these apertures and allow integration of the incident light over variable time periods. By putting the complete setup on a stepping motor, the complete image can be scanned systematically.

Core masking technique

Developed originally for corona measurements in Astrophysics, a core masking technique might also be beneficial for halo studies and a first setup has already been tested at CTF3 [5]. This technique was mainly limited due to the usage of a fixed-size mask and the limited performance of the CCD camera used.

Improvement of the camera system

Since the CCD cameras used in the present installations clearly limit the dynamic range of the measurements, alternatives are being investigated. CID cameras offer the possibility to read out single pixels without deleting the image information and thus allow integration of the measurements over longer time periods and thus increase the sensitivity enormously. Without the need of a mask or collimator, direct image detection with large dynamic ranges might be possible and will be tested.

CONCLUSION

A number of different effects directly affect the results of high resolution OTR measurements: The way how the radiation is created, i.e. the quality and shape of the screen surface determines the initial light distribution. Their control might thus be a way to optimize the final image quality particularly important for halo measurements. Furthermore, the optical imaging system itself, the quality and type of lenses and mirrors influence the final image. All these components and the measurement technique determine the final layout of the halo measurement system.

REFERENCES

[1] L. Wartski et al, J. Appl. Phys. **46**, 3644 (1975)
[2] D.W. Rule, Nucl. Instr. and Meth. B, **24/25**, 901 (1987)
[3] A.H. Lumpkin, Nucl. Instr. and Meth. A, **393**, 170 (1997)
[4] ZEMAX software: http://www.zemax.com
[5] T. Lefevre et al., "Beam Halo Monitoring at CTF3", Proc. EPAC 2004, Lucerne, Switzerland

SCINTILLATING SCREENS STUDY FOR LEIR/LHC HEAVY ION BEAMS

C. Bal, E. Bravin, T. Lefèvre*, R. Scrivens and M. Taborelli, CERN, Geneva, Switzerland

Abstract

It has been observed on different machines that scintillating ceramic screens (like chromium doped alumina) are quickly damaged by low energy ion beams. These particles are completely stopped on the surface of the screens, inducing both a high local temperature increase and the electrical charging of the material. A study has been initiated to understand the limiting factors and the damage mechanisms. Several materials, ZrO_2, BN and Al_2O_3, have been tested at CERN on LINAC3 with 4.2MeV/u lead ions. Alumina (Al_2O_3) is used as the reference material as it is extensively used in beam imaging systems. Boron nitride (BN) has better thermal properties than Alumina and Zirconium oxide (ZrO_2). BN has in fact the advantage of increasing its electrical conductivity when heated. This contribution presents the results of the beam tests, including the post-mortem analysis of the screens and the outlook for further measurements. The strategy for the choice of the screens for the Low Energy Ion Ring (LEIR), currently under construction at CERN, is also explained.

INTRODUCTION

Luminescent screens, ceramics or crystals, have been used widely for the past 25 years for beam observation [1]. Radiation hardness was a major concern and experimental studies led to the development of special Al_2O_3 with Cr_2O_3 as a doping material, known as Chromox 6 [2]. Thermal quenching of fluorescence and the dependence of lifetime on temperature have been studied using a 30keV electron beams [3]. These effects are due to competing radiative and non-radiative decay processes, the latter increasing in probability with temperature. At CERN screens have withstood integrated proton fluxes of up to 10^{20} p/cm^2 at flux levels up to 7 10^{14} p/cm^2/pulse (~500ns). In the SLC linac [4], a phosphorescent deposition (Gd_2O_2S:Tb known as P43) on a thin aluminium foil was used as a screen without any sign of damage after bombardment with 4 10^{18} e/cm^2. Chromium doped alumina has been also successfully used on 10 and 100GeV/u low intensity oxygen ion beams in injection and extraction lines of the SPS machine at CERN [5]. Some investigations were done in the following years in order to find a luminescent material with a better sensitivity [6]. Thallium doped caesium iodide was found to have a 30 times better sensitivity than chromium doped alumina. In low energy ions accelerator, profile monitoring is most of the time done using SEM grids or wire scanners. Some tests were done on low energy lead ions using Chromox [6] screens but their performances were very poor with a strong reduction of the light intensity limiting the life time of the screen to very short time periods [7]. The range of low energy ions in matter is very small, (few tens of µm), so that the ions are stopped in the screen inducing a local charging of the material and the high thermal load.

The Low Energy Ion Ring (LEIR) [8] will start operation at CERN by the end of 2005. Its main task is to prepare the ion beams to reach the required brilliance for LHC. In LEIR 4.2MeV/u ions from the LINAC3 [9] are accumulated, cooled and pre-accelerated up to 72MeV/u. They are then injected into the consecutives accelerator rings PS, SPS and finally LHC.

In 2004 a new study has been initiated with the aim of understanding the degradation mechanism of the screen and finding an alternative for the imaging system needed for the LEIR instrumentation. In this paper we present the test of different luminescent materials irradiated by 4.2MeV/u lead ions.

SETUP AT LINAC3

A sketch of the experimental set-up in LINAC3 at CERN is given in Figure 1.

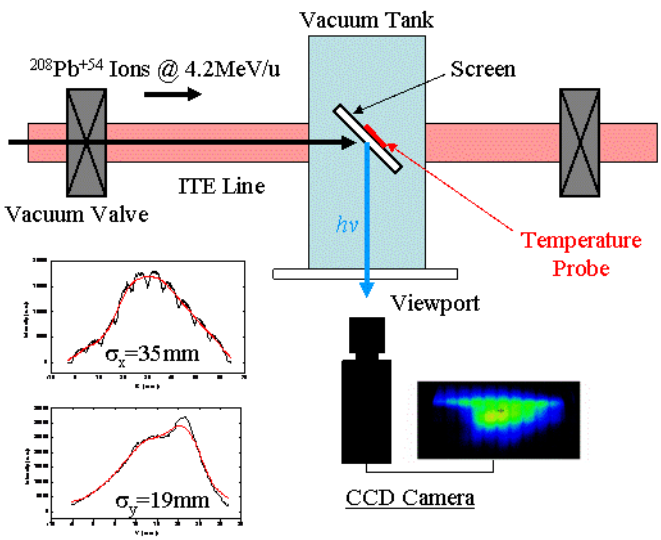

Figure 1: Set-up for the screen test in the LINAC3

The irradiation tests have been carried out in the ITE bypass line with a 100µA, 600µs lead ions beam every 1.2s. This line, normally used for emittance measurements is already equipped with a TV observation tank. The system was slightly modified in order to install 1mm thick and 50mm diameter screens. Mounted on an aluminium support the screen was tilted by 45 degrees with respect to the beam trajectory. The screen was then imaged onto a normal CCD camera using a 50mm focal length camera lens. A temperature probe was installed on the back of the screen through a hole in the support in order to monitor the temperature variations due to the beam impact.

Images were recorded digitally on a near by PC for periods spanning from a few hours to a whole night at more or less regular intervals.

The characteristic of the screens used in the test are summarized in Table 1. They were all bought from the BCE GmbH special-ceramics company in Germany [10]. Alumina was used as the reference material. The two other ceramics were chosen because they were presenting somehow better characteristics either from the thermal or electrical point of view. Boron Nitride (BN) has higher heat conductivity (k) and can be used up to 2400 ºC. Moreover with a higher specific heat (c_p), the local temperature rise would be less. On the other hand Zirconium oxide, actually worse than alumina for thermal properties, was chosen because of its electrical properties. All the ceramics are in general very good insulators at ambient temperature with resistivity (R) between 10^9 - 10^{14} Ω.cm. The resisitivity of ZrO_2 has the interesting feature of decreasing strongly with temperature. At 400 ºC, it has dropped by 5 orders of magnitude.

Table 1: Characteristics of the luminescent screens

Material	ρ (g/cm^3)	c_p at 20ºC (J/g.K)	k at 100ºC (W/m.K)	Tmax (ºC)	R at 400ºC (Ω.cm)
Al_2O_3	3.9	0.9	30	1600	10^{12}
ZrO_2	6	0.4	2	1200	10^4
BN	2	1.6	35	2400	10^9

Four different screens have been tested consecutively, one Al_2O_3, one BN and two ZrO_2 namely the Z700-20A particle reinforced and the Z500 which were corresponding to materials with two different doping and grain sizes, respectively Y_2O_3-0.7µm and MgO-50µm.

EXPERIMENTAL RESULT

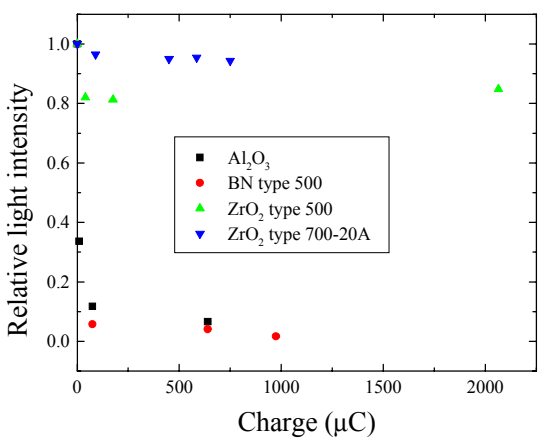

Figure 2: Luminescence yield of the different material as a function of the integrated beam charge

At the screen position, typical horizontal and vertical beam sizes were measured to be respectively 35mm and 19mm as shown in Figure 1. The relative luminescence yield was computed by integrating the pixel amplitudes over the full image. Unfortunately no absolute measurements of the light intensity were performed during this test so that the relative luminescent yield of one material with respect to the others could not be extracted from these data.

The results are depicted shown on Figure 2, plotting the light intensity as a function of the integrated beam charge irradiating the screen. In some cases, the iris of the camera lens was re-opened during the test in order to follow the decrease of the light intensity. For BN and Al_2O_3, the luminescence yield in the irradiated zone dropped rapidly to levels not observable anymore with the set-up used. For ZrO_2, it decreased only by a small fraction (10-20%) in the first minutes and remained constant at least till the end of our test.

When the screens were taking out of the vacuum tank after irradiation, the surface exposed to the beam has turned to a dark-brown coloration. This was the case for all the screens as depicted in Figure 3 with as examples BN and Z500. The coloration seemed to be even stronger for ZrO_2. This could come from the difference in the integrated irradiation time or in the temperature rise of the screen. Since ZrO_2 was performing well, it was tested twice longer than BN. Maximum temperature measured with ZrO_2 was 46°C and only 30°C with BN. Exposed to the same beam conditions, the thermal load on ZrO_2 would be higher than on BN because it has a four times lower specific heat. Moreover ZrO_2 has a factor 17.5 worse heat conductivity. It is important to remind here that the thermal probe, installed on the back side of the screen, was measuring a much lower value than the local temperature on the irradiated screen surface.

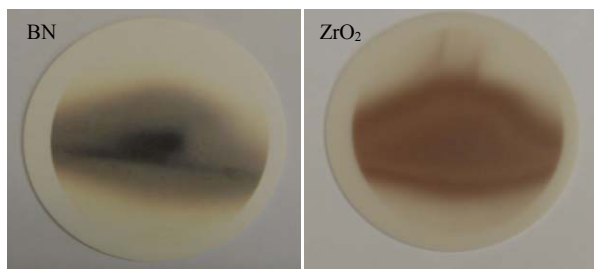

Figure 3: Pictures of the BN and Z700-20A screen after the beam irradiation

For BN heating in ultra-high-vacuum at 350°C during 1hour did not change the colour of the dark area. On the opposite side, Al_2O_3 and ZrO_2 screens were recovering their initial colour by heating the samples in air (some 100-200°C).

As a second step of the test, the screens have been analyzed using x-ray photo-electron spectroscopy (XPS) in order to check if there is any radiation induced surface modification. Both the irradiated and the non irradiated part of the screens were analyzed by the same method. The results are presented in Figure 4. Non-irradiated sides were, in general, more polluted with C and showed a higher amount of "other" contaminants than irradiated

sides. The ion beam irradiation had a surface cleaning effect.

For BN, a large amount of O was found on the irradiated area. In the non-irradiated area the ratio of B to N concentration corresponds to the correct stochiometry of the compound BN, whereas in the irradiated area N has been partially replaced by O. For Al_2O_3 and ZrO_2, no noticeable difference was observed that could explain the colour of the exposed side.

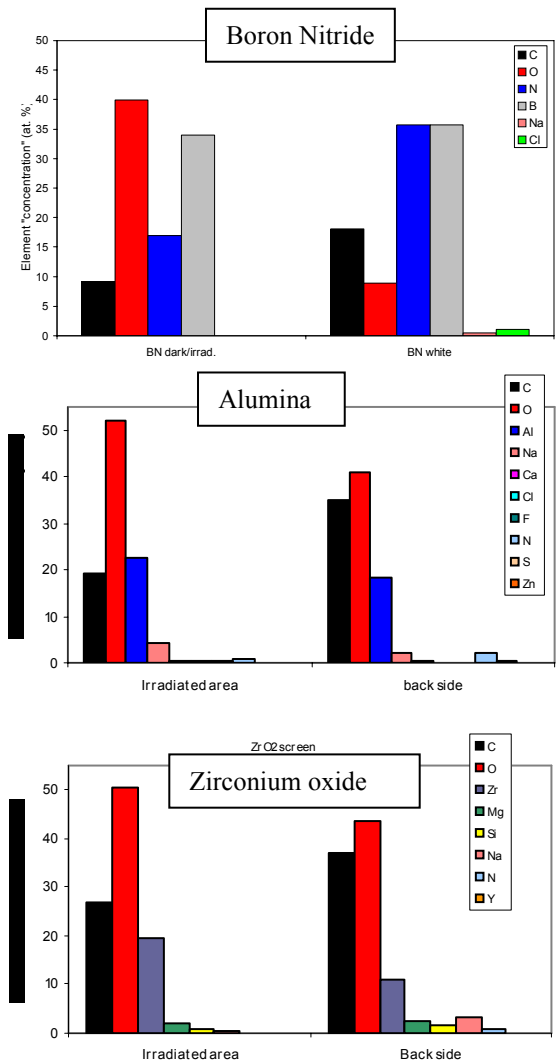

Figure 4: Analysis of the screens composition done by X-ray photo-electron spectroscopy

CONCLUSION AND PERSECTIVES

BN, Al_2O_3 and ZrO_2 screens have been irradiated by 4.2MeV/u Pb^{54+} ions (~ 3 10^{11} ions/s). The screen was imaged by a CCD camera (visible light) and the evolution of the fluorescence light intensity measured as a function of the irradiation time. For BN and Al_2O_3 the light intensity decreased rapidly to very low level making beam profiles measurement impossible. For ZrO_2 the light intensity was just reduced by 10-20% in the first minutes of the test and then remained constant. Beam profiles measurements were not altered at least during 24h conserving the same spatial resolution. The screen surface has been then characterized by XPS. After irradiation the colour of all the materials had turned to a dark-brown colour. For Al_2O_3 and ZrO_2 screens, the modifications induced by the beam were probably a chemical reduction of the oxides at a level which cannot be detected by XPS and were reversible by heating the samples in air (some 100-200°C). No mechanism has been identified so far in order to explain this colour change and the fluctuations of the luminescent yield for alumina. For BN, the colour comes from the large amount of O which has partially replaced N. The re-crystallization of BN have been already observed by others under irradiation with 8MeV protons [11] and was irreversible.

In the context of the ions program for LHC, 10 imaging systems, named MTV, will be installed in the injection line from the LINAC3 to LEIR and in the extraction line from LEIR to the PS accelerator. All the systems will be equipped with 2mm thick 80mm diameter ZrO_2 screens (Z700-20A particle reinforced). Outgasing tests have been performed and they have confirmed that ZrO_2 could be used in a high quality vacuum as foreseen on LEIR (10^{-12} Torr).

Some other tests have been already planned in parallel to the LEIR operation in order to understand the degradation mechanism. High power excimer laser irradiations will be performed with the aim of verifying the influence of a high local temperature increase on the degradation mechanism.

ACKNOWLEDGMENT

The authors would to thank Tobias Hofmann from GSI for suggesting the use of Boron nitride and Zirconium oxide as luminescent screens.

REFERENCES

[1] R.Jung, et *al*, Proceeding of the DIPAC 2003, Mainz, Germany, p10.
[2]http://www.morganadvancedceramics.com/company.htm .
[3] C.D. Johnson, CERN PS note 90-42, 1990.
[4] M. Ross et *a*l, SLAC_PUB_3640, 1985.
[5] J. Bosser et *al*, Proceeding of the Particle Accelerator Conference, Washington, USA, p.732, 1987.
[6] J. Camas et *al*, Proceeding of the Particle Accelerator Conference, Washington, USA, p.2498, 1993.
[7] J.Bosser et *al*, Nuclear Instruments and Methods in Phys. Rev. A 441, (2000), 116.
[8] H. D. Haseroth, Proceeding of the Particle Accelerator Conference, Dallas, USA, 1995.
[9] H. D. Haseroth,, Proceeding of the Linear Accelerator Conference, Geneva, Switzerland, p.283, 1996.
[10] http://www.bce-special-ceramics.de/index.html
[11] O.A. Plaskin et al, Nuclear Instruments and Methods in Phys. Rev. B 193, (2002), 265.

TIME RESOLVED ENERGY MEASUREMENT AT CTF3

H. Braun, E. Bravin, N. Chritin, R.Corsini, C. Dutriat,
T. Lefèvre*, F. Tecker and C. Welsch, CERN, Geneva, Switzerland

Abstract

The high charge (>6μC) electron beams produced in the CLIC Test Facility 3 (CTF3) is accelerated in fully loaded cavities. Leading to a strong transient effect, the time evolution of the beam energy and its energy spread must be measured with at least 50MHz bandwidth. Three different detectors have been installed and tested so far on the three existing spectrometer lines of the machine: a secondary emission wire grid, a segmented beam dump and a segmented photomultiplier tube observing OTR emissions. This contribution describes the three devices and gives a comparison of the relative performances.

INTRODUCTION

In CTF3 an electron pulse of 3.5A and 1.5μs is accelerated using fully loaded 3GHz accelerating structures. The strong coupling between the beam and the cavities induces transient effects such that the head of the pulse is accelerated twice as much as the rest of the pulse. The resulting energy spectrum shows a strong time dependency with higher energies in the first 10-50 nanoseconds of the pulse, followed by 1.35μs of steady behaviour.

Spectrometer lines have been installed to measure the beam energy and its energy dispersion at three different locations, corresponding to 20MeV, 40MeV and 100MeV electrons. Figure 1 gives a schematic overview of the main components of the line. The beam is deflected using a bending magnet and the beam energy and energy spread are monitored by measuring respectively the beam position and size. In 2003 the system was originally composed of an optical transition radiation (OTR) screen (10μm thick Al) observed by a CCD camera for the setting up of the line and a SEM Grid for time resolved measurements. The optical system, composed of some mirrors, two lenses and an optical density filter wheel, is approximately 1.5m long so that the camera can be placed on the floor surrounded by an adequate shielding.

Due to the disappointing performances of the SEM Grid, two other detectors have been developed and installed in 2004 with the aim of providing time resolved measurement with 50MHz bandwidth and sufficient signal to noise ratio. Segmented dump has been installed at the end of the line just before the dump block and multi-anode photo-multiplier tube (PMT) has been installed in parallel with the CCD camera on the OTR optical lines as shown in Figure 1.

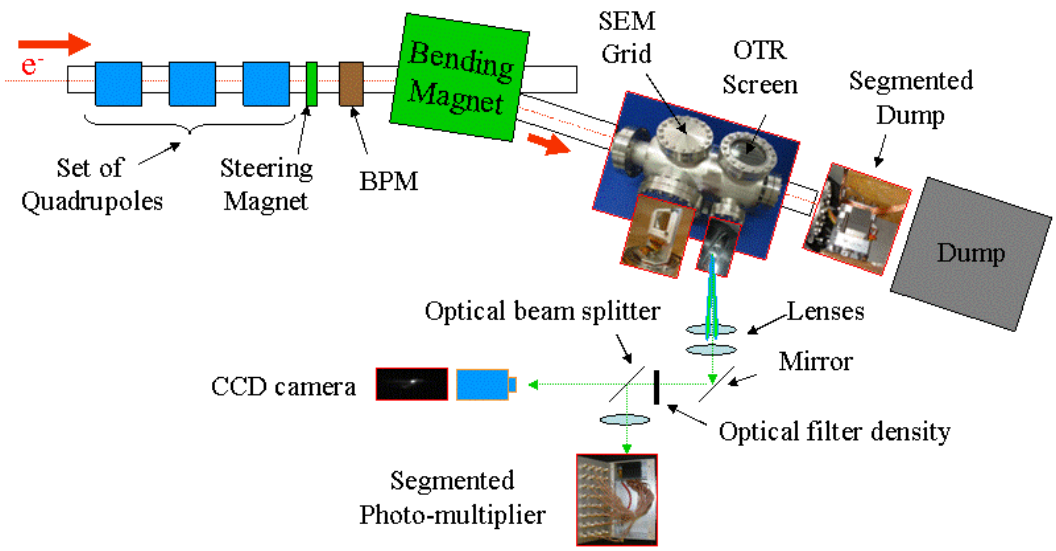

Figure 1: Description of a spectrometer line

SEM GRID

The SEM grids are composed of an assembly of 71 vertical gold plated tungsten wires spaced by 1mm. Each wire, 40μm thick, is mounted on a ceramic support as shown on Figure 2a. When electrons pass through the wires, secondary electrons are emitted and the current induced on the wire is detected using a 100MHz amplifier and fast ADC's. A thin titanium foil, not visible on Figure 2a is mounted upstream of the wire plane and can be polarized in order to help capturing secondary electrons.

For low current beam, below 1A, the SEM grid provides horizontal beam profile as shown on Figure 2b. But noise is already limiting the time resolution and the situation is rapidly degrading with higher beam currents. The signals are not linearly proportional anymore to the beam current. A strong signal is also observed on the SEM grid wires even when the electrons are not deflected into the spectrometer line. The wires, like an RF antenna,

interfere with wakefields or RF resonance in the vacuum chamber.

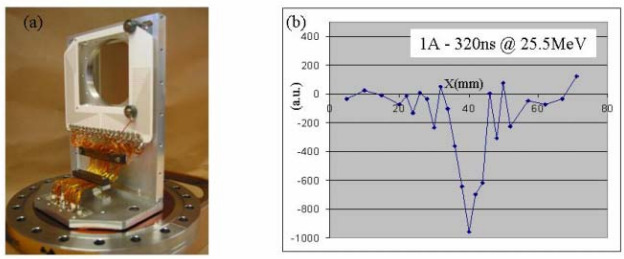

Figure 2: Example of a horizontal profile

An RF shielding has then been developed and installed in 2004. The shielding as shown on Figure 3a consists of two thin titanium foils mounted on a copper support installed on both sides of wires. An example of the time signal measured on few wires is given on Figure 3b. Even if the RF shielding has a positive effect, the signals are still noisy. Moreover the polarization of the collection foil has no effect on the measured signals. For short and intense bunches, the peak electric field of the bunch can be extremely high (>MV/m ~ >10kV) compared to the dc high voltage of the foil (1kV). The dynamics of the secondary electrons and the way they are collected or not by the polarized foil are not well known. The observed signal may be affected by contributions from secondary particles emitted by the foil or the nearby wire. But no experimental evidence has been shown so far.

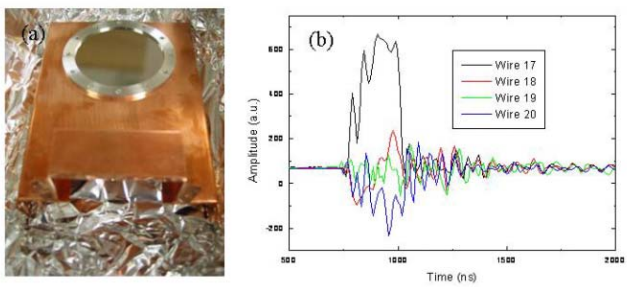

Figure 3: (a) RF shielding implemented on the SEM Grid. (b) Example of the time evolution of the wire signals measured on a 3.5A, 100MeV beam.

SEGMENTED DUMP

A segmented dump is a metallic device in which the particles are stopped and the deposited charge measured. In order to get the horizontal beam profile, it is composed of 24 tungsten plates, 2mm thick and spaced by 1mm using an insulator. Their length must be, depending on the beam energy, long enough to stop the particles. The segment thickness must be big compared to the transverse scattering distance of the electrons. This induces a limitation of their spatial resolution for high energy beams which would need longer distance to be stopped.

Compared to a SEM grid, the segmented dump presents already some steps forward. They are installed outside vacuum thus they are not sensitive anymore to wakefields. The beam induced signal is also higher by a factor 20 since secondary emission yield does not exceed 5% [1]. In our case, no amplifier is needed to fully use the dynamic range of our ADC's (11bits, 0-2V). The beam current is directly converted into voltage through a 1Ω resistance to ground.

On CTF3, the beam power dissipated in the dump is rather large, up to 50kW, depending on the beam energy and the repetition rate of the machine (up to 50Hz). In order to operate the segmented dumps in safe conditions, the repetition rate of the machine must be reduced to 1Hz and the segmented dumps are water cooled to evacuate the heat load.

In 2004 two segmented dumps have been build and installed on the spectrometer lines for 20MeV and 40MeV electrons. An example of the time signal is shown on Figure 4.

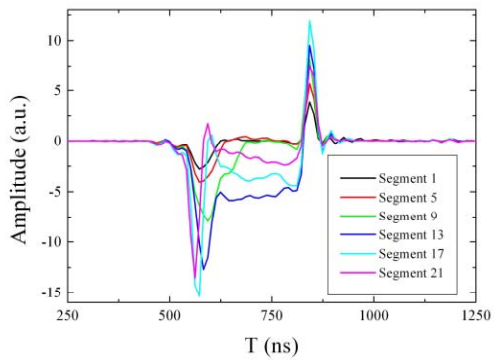

Figure 4: Example of the temporal evolution of the signals from the segmented dump at 20 MeV

Overshoot and undershoot are clearly visible respectively at the beginning and the end of the pulse. That may be the signature of a direct coupling to the beam. This effect limits the bandwidth of the device to 20MHz. An energy spectrum measured with a beam of 3.5A current and 400ns pulse length is shown in Figure 5. A higher energy transient in the first 50ns is followed by a steady state part, characteristic of the operation of fully loaded linear accelerator [2].

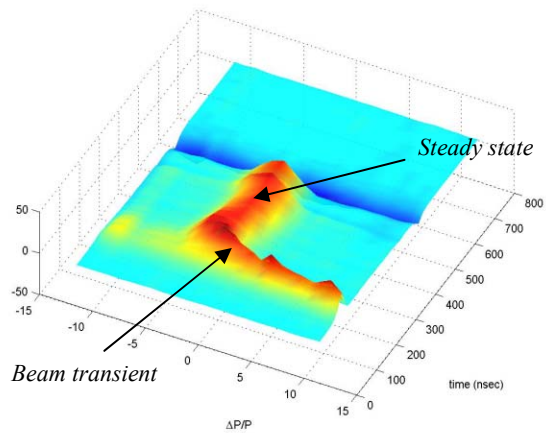

Figure 5: Energy spectrum measured by a segmented dump

The long term radiation hardness of the segmented dump is a concern. After just one year of operation the insulator needs to be replaced.

MULTI-ANODE PHOTO-MULTIPLIER TUBE

In October 2004, another method has been tested. This time we used a 32 channels multi-anode PMT from Hamamatsu observing the light from an OTR screen. A semitransparent mirror is added to the optical system so that the photomultiplier can be used in parallel to the CCD camera. In this test the output signals of the PMT are directly recorded on the ADC channels.

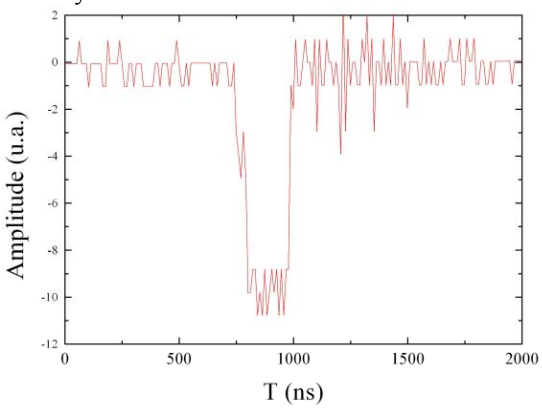

Figure 6: Example of the time signal of one PMT channel

An example of a typical time signal from one of the PMT channel is shown in Figure 6. With its fast time response (0.8ns), the PMT provides measurements with a good time resolution. The total average anode current is limited to few hundreds of µA, so that the amplitude of the voltage signal on 50Ω impedance can not exceed 20mV. The noise seen on the signal in Figure 7 is the intrinsec noise of the ADC's. A fast amplifier (40dB, >100MHz) must be added in order to match the PMT output amplitudes to the ADC characteristic and use the full dynamic range of the system.

A beam energy spectrum has however been measured successfully as presented in Figure 7. This measurement refers to a 3.5A, 600ns, 100MeV electron beam.

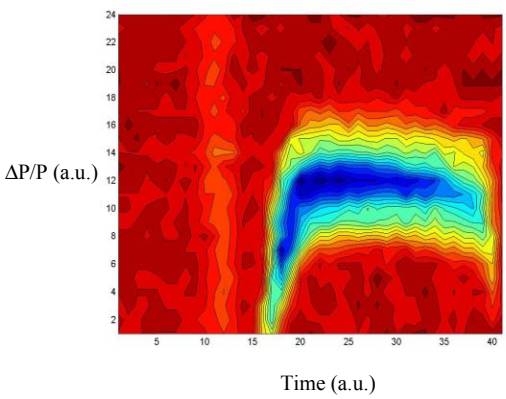

Figure 7: Time evolution of the beam energy spectrum measured by the multi-anode photo-multiplier

Compared to the two previous devices, the photo-multiplier option has the advantages of avoiding any direct coupling to the beam, so that the sources of noise (i.e. RF or electric) are reduced to almost zero. Moreover, the electronic gain of the PMT can be adjusted by the amplitude of the high voltage bias. The energy spectrum can be measured for a wide range of beam currents.

However, a limitation in this technique has already been identified and results in a non homogenous illumination of the PMT channels. This is linked to the small angular distribution of the OTR light and the fixed angular acceptance of the optical system. Described in details in [3], this effect alters the accuracy of the profile measurement. Since the performances of the optical system are already limited by the light intensity and radiation problems, an option for improvement is to modify the surface of the OTR screen. Two possibilities are under investigation at the present time: one using a parabolic screen, the other one trying to slightly increase the diffusion of the screen in a controlled way.

CONCLUSION

In the last two years, three different methods have been developed for measuring the time evolution of the beam size in spectrometer lines: a SEM grid, a segmented dump and a multi-anode photo-multiplier tube.

The SEM grid provides data for low beam current. This device is very sensitive to RF fields and the signals degrade completely for beam currents above 1A. An RF shielding has been added but for high currents the signals are still not usable. At the present time, the development of SEM grids is abandoned.

Segmented dumps have been used on two spectrometer lines and provide beam size measurements with 50ns time resolution. The bandwidth limitation would come from a coupling with the beam. To be improved, their mechanical design would have to be modified to stop all the electrons in the segmented dump. Radiation hardness problems of the insulator must also be solved.

A test has been done using a multi-anode photo-multiplier tube observing the light from an OTR screen. The results are very encouraging, providing a beam size measurement with a time resolution limited by the ADCs to 50MHz. The system has also the advantage of a high sensitivity. However the optical system and the screen surface must be modified to ensure a homogeneous illumination of the PMT channels.

REFERENCES

[1] H. Rothard, et *al*, "Electrons yields from solids: aprobe for the stopping power of swift charged particles", Nuclear Instruments and Methods in Phys. Rev. B 69, (1992), 154.

[2] R.Corsini et *al*, "First Full Beam Loading Operation with the CTF3 Linac", Proceeding of the European Particle Accelerator Conference 2004, Lucern, Switzerland, p39; CLIC note 604.

[3] C.Welsch et *al*, "Design Alternatives for Beam Halo Monitors in High Intensity Accelerators", This conference

SINGLE PHOTON DETECTOR TESTS FOR THE LHC SYNCHROTRON LIGHT DIAGNOSTICS

S. Hutchins, CERN, Geneva, Switzerland
S. Cova, I. Rech, I. Labanca, M. Ghioni, Politecnico diMilano, IT
G. Buller, S. Pellegrini, K.J. Gordon, Herriot Watt Univ. Edinburgh, UK

Abstract

A synchrotron light detector using a Single-Photon Avalanche Detector (SPAD) is planned for the LHC longitudinal diagnostics monitor, an application which requires high count rate, low noise and good time resolution. SPAD detectors have been developed at Milan Polytechnic with active quenching circuits. Initial tests of these detectors and currently available commercial time-to-digital data acquisition equipment were made at the ESRF. We present the results of those tests, an estimation of the performance that can be expected for the LHC case and an analysis of the difficulties, constraints and potential of this type of detector.

THE SPAD MODULE

The advantages of using SPADs[1,2] as opposed to other detectors such as photomultiplier tubes, is that they exhibit high count rates, low timing jitter <50ps, and low dark noise <100 counts per second[3,4].

A thorough experimental characterisation of SPAD devices with active area diameters of 8, 20 and 50 µm was carried out, in order to carefully ascertain the performance of the detectors. All the main parameters, i.e. photon detection efficiency (PDE), dark counting rate (DCR) and timing resolution were measured as a function of excess bias voltage and operating temperature.

The best compromise between PDE and DCR was found by operating the SPAD at an excess bias voltage of 5 V. At room temperature, devices with 8 and 20 µm diameter size met the specifications, while devices with 50 µm size showed too high a DCR (about 2 kc/s for the best devices). On the other hand, a larger active area is a definite advantage in the foreseen experiments, since it makes it possible to relax the optical alignment requirements without sacrificing the photon collection efficiency. Furthermore, fibre pigtailing may be routinely made on these devices. We therefore decided to exploit a 50 µm SPAD device, even though moderate cooling is required to meet specifications. When operated at 5V excess bias voltage the selected device shows: peak detection efficiency 48% at a wavelength of 530 nm (> 30% all over the visible range); 44 ps FWHM time resolution; dark counting rate of 80 c/s with device cooled at –15 °C.

Integrated Active Quenching and Reset Circuit (i-AQC)

The SPTM employs a fully integrated active quenching and active reset circuit (i-AQC), which is the first monolithic circuit of this kind [5]. This circuit had been previously developed at Politecnico di Milano and is covered by US and European patents[6]. After the detection of a photon, the dead time is given by the sum of the quenching delay plus an adjustable hold-off time plus the reset time. The dead time was set to 125ns, corresponding to a saturated photon counting rate of 8 Mc/s. The i-AQC power dissipation is quite low (30 mW at 2Mc/s, 170 mW at 8 Mc/s).

In order to achieve the required time resolution, a patented timing board including a linear network that feeds a fast comparator must be connected to the high voltage terminal of the SPAD [7,8,9]. The purpose of the timing board is to extract the avalanche current pulse at a very low threshold level, corresponding to an avalanche current of a few hundreds µA. The time resolution improves by reducing the threshold voltage of the comparator. By lowering the threshold to 10 mV, the SPTM can achieve a time resolution of about 40 ps FWHM. The TCSPC card used in these measurements was a Becker and Hickl SPC600 photon counting card [10].

In various applications, it is necessary or at least advantageous to operate the SPAD under the control of a gate command [1]. In this case, the SPAD is turned on only in a time window centred on the optical pulses of interest. A standard TTL gate signal can be provided to the SPTM. The minimum duration of the gate-on TTL signal is 20 ns, corresponding to an effective minimum gate-on duration of 10 ns.

Performance evaluation

Preliminary tests of the performance of the SPTM with the selected SPAD sample were carried out on the bench at Politecnico di Milano. The operating temperature of the SPAD was set at –15°C and the dark counting rate was checked to be 80 c/s at +5V excess bias voltage.

Photon detection efficiency (PDE) of the SPTM has a peak of 48% around 530 nm and it stays well above 30% in all the visible range.

Time resolution measurements were performed in a conventional time-correlated single photon counting (TCSPC) setup by using an ultra fast laser diode (Antel MPL-820 laser module) emitting 10 ps FWHM optical pulses at 820 nm wavelength. The unit has a prompt peak with a full-width at half maximum of 44 ps and a clean exponential diffusion tail with 300 ps lifetime. The overall duration of the diffusion tail is less than 2.5 ns. A signal-to-background ratio (SBR) higher than 10^4 is clearly demonstrated.

EXPERIMENT AND RESULTS

The operating mode of the ESRF was 2x1/3 fill, there were two frequency sources available for synchronisation of the light, the orbit revolution frequency of the synchrotron 355 kHz and the RF frequency of 352.2MHz. The RF frequency was too high for the synchronisation input of the TCSPC card allowing only the orbit revolution frequency to be used for data collection. The bunches of light in each batch were separated in time by 2.84 ns.

The synchrotron radiation was filtered by using a mirror before entering the optical inspection laboratory. The remaining beam still had a broad spectrum, which was filtered by using either one bandpass filter centered at a wavelength of 650nm with 35nm bandwidth, or a combination of two identical ones. The latter configuration would reduce the bandwidth of transmission to between 31 and 20nm, depending on the angle of inclination of one of the filters (fig.1).

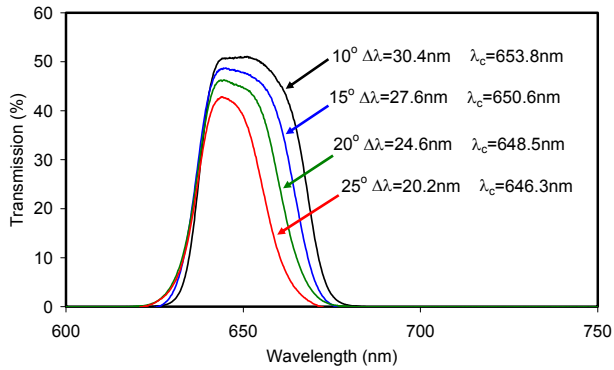

Figure 1: Transmission spectra of two bandpass filters in series, one placed at normal incidence and the other at 10°, 15°, 20° or 25° to the normal.

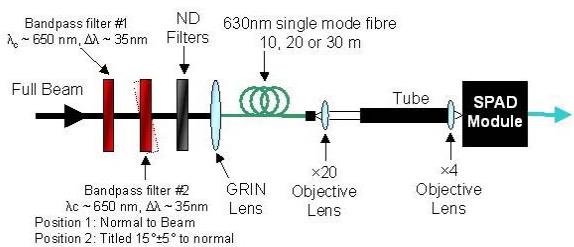

Figure 2: Optical arrangement employed to couple the synchrotron beam into the 4.3µm core fibre (single mode at a wavelength of 630nm) and optically image the photons onto the 50µm diameter SPAD.

Free Running Measurements

The SPAD module was initially operated in free running mode, which simply allows the SPAD to operate continuously. Figure 3 shows the results obtained by measuring the dynamic of the rising edge of one batch. The figure also shows the dark counts obtained from the SPAD during the same measurement time. One can see on the left part of the diagram before the arrival of the pulses, it is evident that there is background radiation, much higher than the intrinsic dark counts of the detector, which could not be filtered in the current experimental conditions.

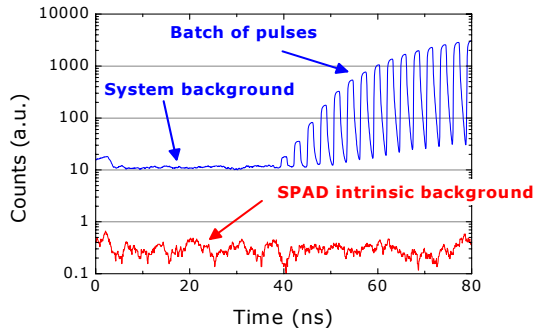

Figure 3: System background between batches of pulses compared to dark noise from SPAD module collected over 10 minutes.

Further experiments were carried out to study the effect of the optical fibre dispersion on the timing resolution. The resolution worsens of approximately 10ps for every 1m of fibre added to the experiment. The temporal profile is increased by ~8ps per metre of fibre for a 35nm bandpass. This means for a 10nm bandpass, we can expect a FWHM of approximately 135ps for the necessary 30m of optical fibre in the LHC, using the same detection system and the same central wavelength.

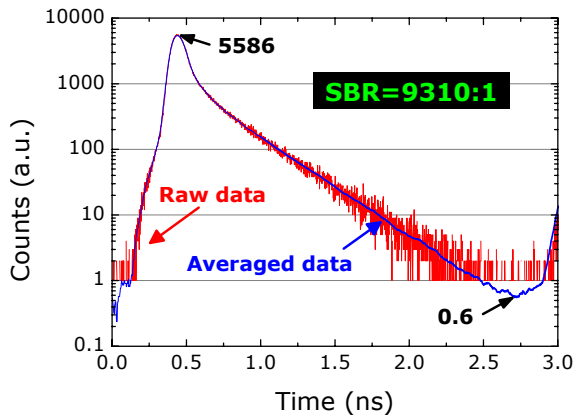

Figure 4: Histogram taken using the setup in Figure 2 employing two BP filters and 10m of Single mode fibre

In terms of signal-to-background ratio (SBR), as mentioned before, our experiments were limited by the scattered background light coming from the synchrotron radiation. Nevertheless we managed to obtain a SBR of approximately 9000:1 as shown in Figure 4.

CONCLUSIONS AND SUMMARY

The timing jitter of the system is lower than that required for the LHC system, but the use of fibres can cause a significant deterioration in the timing resolution. The choice of detection wavelength and spectral detection band will be critical in the final system. From this feasibility study, it can be inferred that a 30m length of single-mode fibre (necessary in the LHC experiment) can be used but only if spectral filtering is employed to limit the bandwidth to approximately 10-20nm.

The signal-to-background ratio at ~2.5ns after the main peak was demonstrated at 9300:1. However, this was affected by background light signal from the synchrotron. We estimate the possible SBR in the LHC experiment – which will have a spatial filter arrangement in place – to be well in excess of 10,000:1. Provided that the background light is spatially filtered, further improvement in the SBR may be achieved by choosing a shorter wavelength (e.g., 450 – 500 nm instead of 650 nm), as it is well known that the diffusion tail that affects the time resolution curve of a SPAD detector is wavelength dependent [7]. Its decay time gets shorter while reducing the excitation wavelength. Figure 5 shows the time resolution curve of the SPAD module measured with a Ti: Sapphire laser providing excitation pulses with a wavelength of 440 nm and a repetition rate of 76 MHz. The slow exponential diffusion tail is not present, since all photons with 440 nm wavelength are absorbed within the depletion layer.

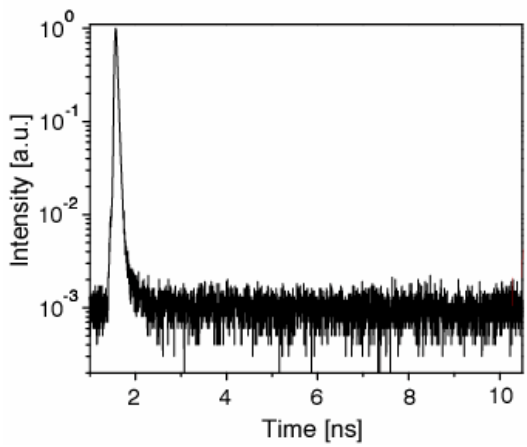

Figure 5: Time resolution curve of the SPAD module as measured at 440 nm excitation wavelength. The diffusion tail is barely visible. Note that the background counts are due to stray light in the experimental set up.

In order to perform the requirements of the Longitudinal density monitor for the LHC, the final detector will have to operate as a sustained counting rate of over 1 Mc/s, which will require attention to the selection of the final devices and optimization of the associated quench and cooling circuits.

ACKNOWLEDGEMENTS

The authors wish to thank Kees Sheidt and Graham Naylor for the kind use of their facilities at ESRF, Grenoble.

REFERENCES

[1] S. Cova, M. Ghioni, A. Lacaita, C. Samori, F. Zappa, *"Avalanche photodiodes and quenching circuits for single-photon detection,"* Applied Optics, **35** (12), Page 1956-1976 (1996)

[2] F. Zappa, A. L. Lacaita, S.D. Cova, P. Lovati, *"Solid-state single-photon detectors,"* Optical Engineering, **35** (4), Page 938-945 (1996)

[3] A. Lacaita, M. Ghioni, S. Cova, F. Zappa, *"Ultrafast single photon avalanche diodes without slow tails in the pulse response,"* IEEE Transactions on Electron Devices, **40** (11), Page 2145 (1993)

[4] S. Cova, A. Lacaita, , G. Ripamonti, *"20-ps timing resolution with single-photon avalanche diodes,"* Review of Scientific Instruments, **60** (6), Page 1104-1110 (1989)

[5] F. Zappa, A. Lotito, A. C. Giudice, S. Cova, and M. Ghioni, *"Monolithic active-quenching and active-reset circuit for single-photon avalanche detectors,"* IEEE J. of Solid-State Circuits, **38**, Page 1298-1301 (2003)

[6] . Zappa, A. Lotito, A. C. Giudice, S. Cova, and M. Ghioni, *"Monolithic active-quenching and active-reset circuit for single-photon avalanche detectors,"* IEEE J. of Solid-State Circuits, **38**, Page 1298-1301 (2003)

[7] S. Cova, M. Ghioni, and F. Zappa, "Circuit for high precision detection of the time of arrival of photons falling on single photon avalanche diodes," US patent No. 6,384,663 B2, May 7, 2002

[8] A.Gulinatti, P.Maccagnani, I.Rech, M.Ghioni, S.Cova: *"35 ps time resolution at room temperature with large area single photon avalanche diodes,"* Electronics Letters, **41**, Page 71-72 (2005)

[9] S. Cova, M. Ghioni, A. Lotito, I. Rech, F. Zappa *"Evolution and Prospect of Single-Photon Avalanche Diodes and quenching Circuits,"* J. Modern Optics, **51**, Page 1267-1288 (2004) and NIST-ARDA Workshop on Single-Photon Detectors, March 31-April 1 2003, NIST Gaithersburg, MD, USA.

[10] Becker & Hickl GmbH, Model number SPC-600, Time-correlated single photon counting module, www.becker-hickl.de/pdf/spc800ps01.pdf Instruction Manual (2002)

[11] G.Ripamonti and S.Cova, *"Carrier diffusion effects in the time-response of a fast photodiode,"* Sol. State Electronics **28**, Page 925-931 (1985)

MEASUREMENT OF THE LONGITUDINAL PHASE SPACE AT THE PHOTO INJECTOR TEST FACILITY AT DESY IN ZEUTHEN (PITZ)*

J. Rönsch†, Hamburg University, 22761 Hamburg, Germany
K. Abrahamyan, G. Asova, J. Bähr, G. Dimitrov, H.-J. Grabosch, J.H. Han,
S. Khodyachykh, M. Krasilnikov, S. Liu, H. Lüdecke, V. Miltchev, A. Oppelt,
B. Petrosyan, S. Riemann, L. Staykov, F. Stephan, DESY, 15738 Zeuthen, Germany
M.v. Hartrott, D. Lipka, D. Richter, BESSY, 12489 Berlin, Germany

Abstract

PITZ generates electrons with an energy of about 5 MeV. To optimize the RF-gun parameters and to fulfill the requirements of the bunch compressor the longitudinal phase space behind the gun has to be studied. A measurement of the longitudinal phase space comprises a correlated measurement of momentum and temporal distribution. The momentum distribution is measured by deflecting the electron bunch using a spectrometer magnet. A subsequent Cherenkov radiator transforms the electron bunch into a light pulse with equal temporal and spatial distribution, which is imaged onto a streak camera by an optical transmission line to measure the longitudinal distribution. The longitudinal phase space was measured for different temporal photo cathode laser distributions, bunch charges and phases between RF field and laser. Physical effects in the dipole magnet, optical transmission line and streak camera, which influence the longitudinal phase space measurements, are taken into account. The measurement results were compared with simulations and with directly measured momenta and temporal distributions.

INTRODUCTION

The main goal of PITZ is the test and optimization of photo injectors for Free-Electron Lasers (FELs). The demands on such a photo injector are a small emittance, short bunches and a charge of about 1 nC. The linac of a FEL incorporates a RF gun, capable of producing a high bunch charge, followed by an acceleration section and a magnetic bunch compressor. For an effective bunch compression detailed studies of the longitudinal phase space have to be performed. Besides the projections of the longitudinal phase space, i.e. temporal and momentum distribution of the electron bunch, the correlation between the positions of the particles in the bunch and their longitudinal momenta has to be understood. The non-linearities of the longitudinal phase space have to be analysed. Typical high energy diagnostics for longitudinal phase space tomography can not be used, therefore a special apparatus for an energy around 5 MeV was developed.

*This work has partly been supported by the European Community, contract numbers RII3-CT-2004-506008 and 011935, and by the 'Impuls- und Vernetzungsfonds' of the Helmholtz Association, contract number VH-FZ-005.

† jroensch@ifh.de

SETUP

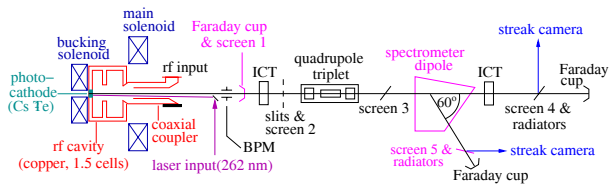

Figure 1: Schematic of PITZ1 setup.

Fig. 1 shows a schematic of the PITZ1 setup. To measure the longitudinal distribution of the electron bunch a Cherenkov radiator (silica aerogel) [1] is used to transform the bunch into a light distribution at screen station 4 in the straight section (SS). This light distribution is imaged by an optical transmission line onto the entrance slit of a streak camera. The momentum distribution is measured with a YAG-screen at screen station 5 in the dispersive arm (DA). To measure the longitudinal phase space both methods are combined. The YAG-screen in the DA can be replaced by silica aerogel using a movable actuator. The light pulse which presents the longitudinal phase space is transported to the streak camera. The momentum axis of the longitudinal phase space measured by the streak camera is scaled using the momentum distribution directly measured at the YAG-screen.

Several physical effects of the main components of the apparatus (as dipole magnet, streak camera and optical transmission line) impact the results of the measurements of the longitudinal phase space. These effects will be described in the following subsections. They have to be corrected successively, but reversely, i.e. starting from the streak camera.

Spectrometer Dipole

The dipole magnet at PITZ1 deflects the electron bunches by 60° in vertical direction to transform the momentum distribution into a spatial one. The vertical position y of an electron behind a hard edge sector dipole is given by the first order transport matrix of a dipole [2]:

$$y = \cos\alpha \cdot y_0 + \rho_{\text{eff}} \cdot \sin\alpha \cdot y_0' + \rho_{\text{eff}} \cdot (1 - \cos\alpha) \cdot \frac{\delta p_0}{< p_0 >}, \quad (1)$$

where α is the angle of deflection, ρ_{eff} is the radius of curvature in the dipole, $\frac{\delta p_0}{<p_0>}$ is the relative momentum deviation, y_0 is the initial vertical position and y_0' is the initial vertical divergence of the electron. To have a good resolution $\cos\alpha \cdot y_0 + \rho_{\text{eff}} \cdot \sin\alpha \cdot y_0'$ should be small in comparison to $\rho_{\text{eff}} \cdot (1 - \cos\alpha) \cdot \frac{\delta p_0}{<p_0>}$. Furthermore, the edge fields of the dipole and drift spaces have to be included into the equation by multiplication of the transport matrices.

Moreover, the field of a hard edge sector dipole shifts the position of an electron inside the bunch by Δl [2] and changes consequently the temporal distribution of the longitudinal phase space:

$$\Delta l = \sin\alpha \cdot y_0 + \rho_{\text{eff}}(1-\cos\alpha)\cdot y_0' - \rho_{\text{eff}}\cdot(\alpha - \sin\alpha)\cdot\frac{\delta p_0}{<p_0>}. \quad (2)$$

To correct the effects due to the finite beam size and divergence a deconvolution has to be performed. The influence of momentum spread on the longitudinal position in the bunch can be rectified by shearing the longitudinal phase space.

Cherenkov Radiator

To measure the bunch length (in the SS) the silica aerogel with a refractive index $n = 1.03$ and a thickness of $l = 2\,\text{mm}$ was used. It has a contribution to the time resolution of 0.13 ps for an energy of 5 MeV. Whereas the full Cherenkov cone is used to determine the longitudinal distribution (SS), for the measurement of the longitudinal phase space (DA) only a segment of the cone is used, because the aperture angle would be too big for the optical transmission line. Due to this, the number of photons is reduced to a small fraction. To reach a sufficient number of photons aerogel with $n = 1.05$ and $l = 2\,\text{mm}$ was installed. The contribution to the time resolution of this aerogel plate is 0.22 ps for 5 MeV. In the energy range of 5 MeV the number of photons produced by aerogel is on the order of 10^3 higher than for optical transition radiation (OTR) [3]. But the disadvantage of aerogel is the danger of outgassing molecules.

Optical Transmission Line

The Cherenkov light distribution produced by the radiator has to be imaged onto the entrance slit of the streak camera. The optical transmission line consists of several mirrors and lenses with a large focal length and a small focal number, arranged as a chain of telescopes [4]. To measure the longitudinal distribution the conservation of the temporal light distribution has to be ensured. For the measurement of the longitudinal phase space the spatial distribution has to be preserved in addition.

There are two different input systems (for SS and DA), which match into a common transmission line. To transport the full Cherenkov cone, the first lens of the optical input system needs a small focal number, to collect a moderate part of the cone. The measurement of the partial cone needs the transport of a quasiparallel bundle of light. The last lenses demagnify the distribution to match with the streak camera slit size. Although achromates are used to minimize dispersion in the transmission line, the pulse length is elongated in the optical transmission line. Fig. 2 shows the mean arrival time of photons with different wavelength produced by the same bunch passing the optical transmission line.

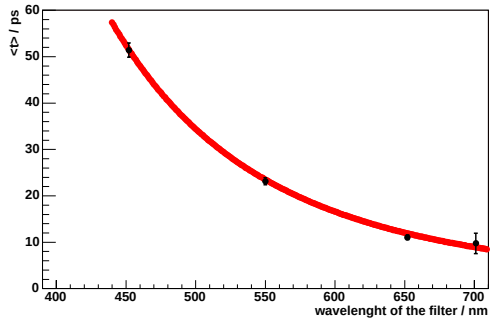

Figure 2: Mean arrival time of photons with different wavelength, measured by using different spectral transmission filters.

This behavior is caused by residual dispersion of the lenses and scattering effects. Narrow spectral transmission filters (10 nm) are used for suppressing the light pulse lengthening.

Rotating Box The dispersive arm is inclined under 60°. Therefore, the image of the momentum distribution is not parallel to the streak camera slit. A rotating box is included into the optical transmission line to rotate the light distribution in such a way, that the image of the light distribution of the momentum spectrum is parallel to the slit. A schematic of the rotating box is shown in Fig. 3, it consists of 11 mirrors. In fact, the rotation is executed by only 3 mirrors (S5-S7). Two light paths lead to mirror S5, one transports the image of the light distribution of the momentum spectrum without rotation (S1-S4) and the other with 180° rotation (S8-S11). The toggle between these two light paths allows the analysis of the influence of the image rotating and the momentum spread to the longitudinal distribution in the bunch. Depending on the path the effects are subtractive or additive.

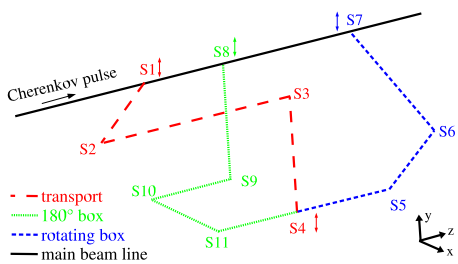

Figure 3: Schematic of the rotating box.

Streak Camera

The streak camera C5680 from Hamamatsu is used to measure the longitudinal distribution and the longitudinal phase space with a resolution of about 2 ps. The streak camera itself shows inhomogeneities in intensity of the signal in the direction perpendicular to the streak direction (horizontal). Furthermore, light entering into the transmission line, stray light and dark current, can produce an unequal background. Therefore, the background has to be determined and subtracted for all measurements.

The streak camera exhibits a non-uniform horizontal sensitivity. Possible reasons are: slight variations of the slit width, of the amplification of the Multi-Channel Plate, of the thickness of the fluorescent material and of the cathode sensitivity, also effects due to internal streak camera optics and the CCD chip as well as a misalignment of the accelerating mesh or of the output optics. The sensitivity for different horizontal positions was determined and corrected.

On the edges of the sensitive area of the streak camera in horizontal direction a temporal delay was observed, when the RF-field was applied on the streak tube. The effect stayed unchanged when the camera was shifted, but without streak RF field it disappeared. It seems that the streak camera does not deflect homogeneously, due to a slightly varying RF-field in horizontal direction. The curvature of mean time value as a function of the horizontal position on the streak image was determined to correct the data.

The smearing of the streak signal in the temporal direction due to slit width and space charge in the streak camera can be described as a convolution, using the signal taken without streak RF-field on the streak tube as response function. To correct these effects the smeared signal has to be deconvoluted.

MEASUREMENT RESULTS

The first measurements were done for flat-top and gaussian temporal laser distributions, bunch charges from 30 pC up to 1 nC and different phases between RF field and laser. The conditions were not optimized to some degree when this data were taken. The vertical divergence and beam size of the bunch were not measured, therefore simulated data had to be used for the corrections of dipole effects. In general the measured and simulated longitudinal phase spaces are similar, but for small longitudinal emittance values the longitudinal phase space could not be fully resolved. Fig. 4 shows the results for 1 nC, phase with the highest momentum and flat-top laser distribution of about 20 ps FWHM pulse length. It displays the measured longitudinal phase space in comparison to the simulated one and their projections compared to the direct measurements.

CONCLUSION

An apparatus to measure the longitudinal phase space for an energy around 5 MeV was successfully developed and tested. This method allows the measurement of the correlations between the longitudinal and momentum distribution, but the elements of the apparatus contribute systematical errors, therefore an extensive data evaluation is required.

Further systematic studies of the longitudinal phase space at 5 MeV are foreseen and improvements of the data analysis are ongoing. In addition, the design of a high energy longitudinal phase space tomograph is ongoing. Another goal is the replacement of the lenses in the optical transmission line by reflective optics.

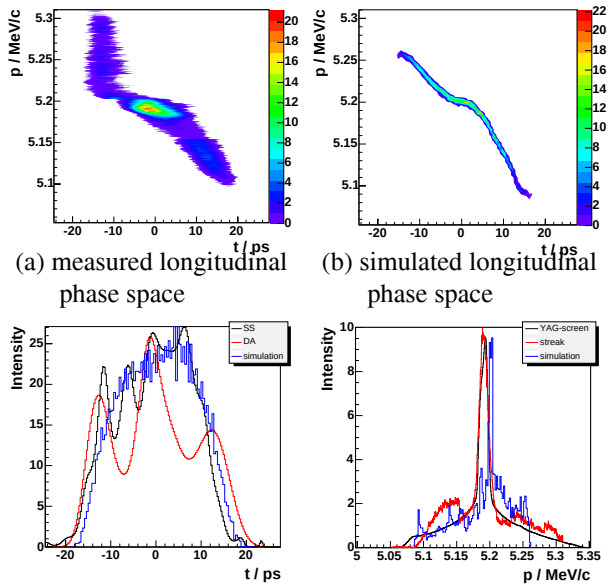

(a) measured longitudinal phase space (b) simulated longitudinal phase space

(c) longitudinal distribution (d) momentum distribution

Figure 4: Measured (a) and simulated (b) longitudinal phase space and their projections: longitudinal (c) and momentum distribution (d) for 1 nC bunch charge, phase with the highest momentum and flat-top laser distribution with about 20 ps FWHM bunch length. In (c) and (d) the black curves are direct measurements, the red ones are the projections of the measured longitudinal phase space and the blue ones are simulations.

REFERENCES

[1] J. Bähr, V. Djordjadze, D. Lipka, A. Onuchin, F. Stephan, "Silica aerogel radiators for bunch length measurements", NIM A 538 (2005) 597-607

[2] D. C. Carey, K. L. Brown, F. Rothacker, "Third-Order TRANSPORT with MAD Input", FERMILAB-PUB-98/310

[3] D. Lipka, "Investigations about the longitudinal phase space at a photo injector for minimized emittance", PhD Thesis 2004 Humboldt University Berlin

[4] J. Bähr, D. Lipka, H. Lüdecke, "Optical transmission line for streak camera measurement at PITZ", Dipac Mainz 2003

REAL-TIME, SINGLE-SHOT TEMPORAL MEASUREMENTS OF SHORT ELECTRON BUNCHES, TERAHERTZ CSR AND FEL RADIATION

G. Berden*, B. Redlich, A.F.G. van der Meer,
FOM Institute Rijnhuizen / FELIX, Nieuwegein, The Netherlands

S.P. Jamison†, A.M. MacLeod,
School of Computing and Creative Technologies, University of Abertay Dundee, Dundee, UK

W.A. Gillespie,
Division of Electronic Engineering and Physics, University of Dundee, Dundee, UK

Abstract

Electro-optic detection of the Coulomb field of electron bunches is a promising technique for single-shot measurements of the bunch length and shape in the sub-picosecond time domain. This technique has been applied to the measurement of 50 MeV electron bunches in the FELIX free electron laser, showing the longitudinal profile of single bunches of around 650 fs FWHM [1]. The method is non-destructive and real-time, and therefore ideal for online monitoring of the longitudinal shape of single electron bunches. At FELIX we have used it for real-time optimization of sub-picosecond electron bunches. Electro-optic detection has also been used to measure the electric field profiles of far-infrared (or terahertz) radiation generated by the relativistic electrons. We have characterized the far-infrared output of the free electron laser, and more recently, we have measured the temporal profile of terahertz coherent synchrotron radiation (CSR) generated at one of the bending magnets.

ELECTRON BUNCH MEASUREMENTS

At the Free Electron Laser for Infrared eXperiments (FELIX) the longitudinal shape of an electron bunch has been measured via electro-optic (EO) detection of its radial electric field. In this scheme, the electric field induces birefringence in an EO crystal placed in the vicinity of the electron beam. The amount of birefringence depends on the electric field strength and is probed at a single radial position by monitoring the change of polarization of a short optical pulse that is focused to the desired 'observation point'.

In the present FELIX setup, the EO bunch diagnostic is situated at the exit of the undulator of the FEL. A 0.5 mm thick ZnTe crystal is used as an electro-optic sensor and is placed with its front face perpendicular to the propagation direction of the electron beam. The probe laser beam passes through the ZnTe crystal parallel to the electron beam. Figure 1 shows a photograph of vacuum flange containing the EO sensor. The electron beam (50 MeV, 250 pC) passes through the rectangular shaped beam pipe (shape is determined by the undulator). The probe laser beam enters and leaves the vacuum pipe through a side window. On the opposite side of the electron beamline, the EO crystal and two small mirrors are mounted on a translation stage.

Several ways have been demonstrated to measure the electric field induced birefringence in the EO crystal using short optical laser pulses (for an overview see e.g. Ref. [2]). At FELIX, high temporal resolution, single-shot bunch profile measurements have been performed using 'temporal decoding' [1, 3]. The probe laser, which is actively synchronized to the accelerator RF clock, delivers short optical pulses with a duration of 30 fs at a wavelength of 800 nm. Each pulse is split into a probe and a reference pulse. The linearly polarized probe pulse is stretched to a length that is longer than the electron bunch, and is passed through the EO crystal. On exiting the beamline, the electric field induced birefringence is translated into an intensity modulation by passing the probe laser through a

Figure 1: Photograph of the vacuum flange containing the EO sensor. The EO crystal together with two small metal mirrors are mounted on a translation stage (visible on the right). The entrance/exit window for the probe laser beam is visible on the left.

* g.berden@rijnh.nl
† also at: University of Strathclyde, Glasgow, UK

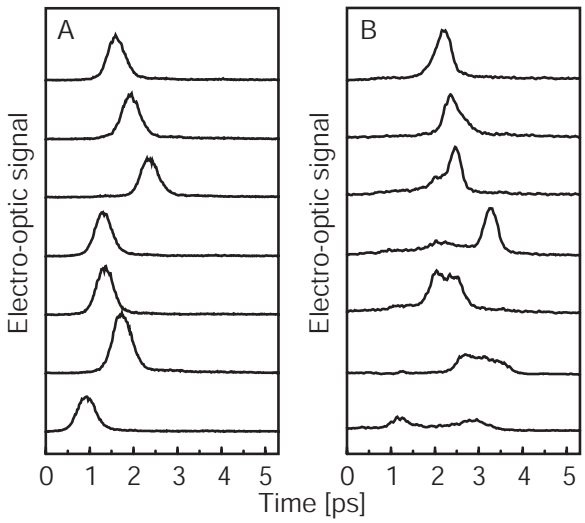

Figure 2: Panel A: a sequence of single shot electron bunch measurements, showing the fluctuations in the arrival time of the bunches. Panel B: single shot measurements of individual electron bunches for different settings of the phases of the buncher and accelerator sections.

polarizer [4]. To measure the ultrafast intensity temporal profile, temporal decoding with a resolution better than 50 fs is performed in a single-shot cross-correlator where the intensity modulated probe pulse is cross correlated with the reference pulse in a BBO crystal. The position dependent emission of the second harmonic light from the BBO crystal is imaged onto an intensified CCD camera.

Examples of single-shot measurements, obtained by binning of the CCD images, are shown Fig. 2. The left panel shows the fluctuations in the arrival time of the electron bunches, illustrating the ability of electro-optic detection techniques to monitor the time jitter introduced by bunchers and accelerators. Furthermore, this method can in principle be used to produce accurate timing information (triggers) for user experiments. Measurements of a sequence of more than 100 bunches shows an rms value of 390 fs for the jitter in the arrival time [5]. Figure 2b shows the dependence of the bunch shape on phase settings of the RF. As data processing is very fast, the diagnostic provides essentially real-time information for optimization of the accelerator settings.

FEL RADIATION MEASUREMENTS

The output from a far-infrared FEL has been characterized with the electro-optic technique using the temporal decoding technique. At a wavelength of 150 μm, a 20 ps long optical pulse consists of 40 optical cycles and is quasi-monochromatic. Since the timing jitter of the electron bunches ($\sim$400 fs, see Fig. 2) is of the same order of magnitude as the duration of one cycle of the far-infrared light, it is evident that one needs a single-shot detection technique to resolve the oscillating electric field.

The laser system, the optical stretcher, and the cross-correlator are identical to those used in the electron bunch measurements. For the experiments described in this section, FELIX produces light at a wavelength of 130 μm at a macropulse repetition rate of 5 Hz. The micropulse repetition rate is 25 MHz, and the micropulse energy is about 1 μJ. In a FELIX FEL user station, the far-infrared laser beam and the 800 nm probe pulse are spatially and colinearly overlapped with an ITO coated glass plate acting as a far IR dichroic mirror. A parabolic mirror with a focal length of 100 mm is used to focus the FEL pulse and the probe pulse onto the ZnTe electro-optical crystal. The FEL induced optical retardation is then measured by the combination of polarisers and a single-shot second harmonic generation cross-correlator.

The second harmonic light (400 nm) emerging from the BBO crystal in the cross correlator is imaged onto an intensified CCD camera. The upper panel of Fig. 3 shows an image obtained by subtracting an image without the presence of an FEL pulse (background) from an image where an FEL pulse was present. The image shows a horizontal line because a cylindrical lens had been positioned in the probe pulse path, just before the BBO crystal. In the horizontal direction, the position in the image is proportional to time. The time axis can easily be calibrated since the duration of one cycle (one oscillation of the electric field) is λ/c and the wavelength is known from an online spectrometer. By vertically binning the image, the electric field profile is obtained and is shown in the lower panel of Fig. 3.

The independently determined electric field oscillation period of the FEL pulse measurements makes it attractive to use such FEL pulse measurements for the quantitative

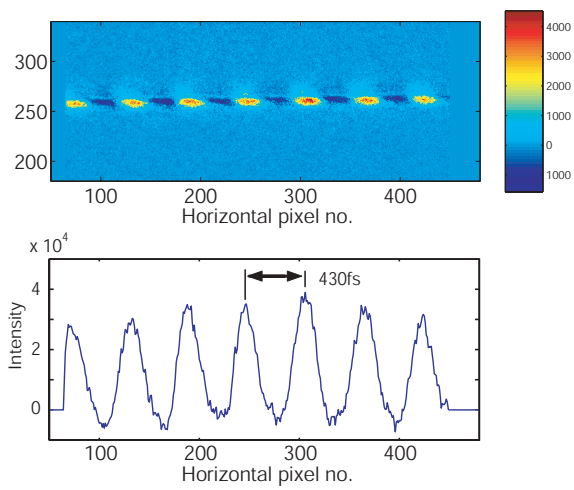

Figure 3: Electro-optic temporal decoding measurement of a quasi-monochromatic FEL pulse. The wavelength is 130 μm, and one cycle therefore corresponds to 430 fs. The image has been obtained by subtracting an image without the presence of an FEL pulse (background) from an image where an FEL pulse was present. The graph has been obtained by vertically binning the image.

study of the capabilities of EO detection. Furthermore, FEL measurements have been performed outside the accelerator vault, making use of the free access, to pre-align the cross-correlator and imaging setup before undertaking electron bunch measurements.

CSR MEASUREMENTS

At FELIX the THz coherent synchrotron radiation (CSR) emitted from the entrance to a bending magnet has also been measured with electro-optic detection. Bunches with a charge of ∼200pC and 45 MeV energy are bent through a 38 cm radius, 45° bend. The CSR radiation is coupled out from the beamline through a crystalline quartz window (see also Fig. 4), collected and focussed onto a ZnTe crystal with a 90° off-axis parabolic mirror. An ITO beam combiner is used to overlap the THz beam and the optical probe beam. The 'spectral decoding' technique [6, 2] is used as the detection scheme. The initial 30 fs probe pulse is linearly chirped to a duration of 20 ps. After passing through a polarizer, the ZnTe crystal, and an analysing polarizer, the probe pulse is coupled into an optical fiber. The other end of the fiber is connected to a spectrometer located outside the accelerator hall. Single-shot spectra of the intensity-modulated probe pulse are measured with a CCD camera.

The spectral decoding signal is obtained by taking the normalized difference between spectra recorded with and without electron bunches present. In Fig. 5, a typical measurement of the electric field profile of the CSR pulse is shown. The energy of this THz pulse, measured at the position of the electro-optic crystal, is on the order of 50 nJ.

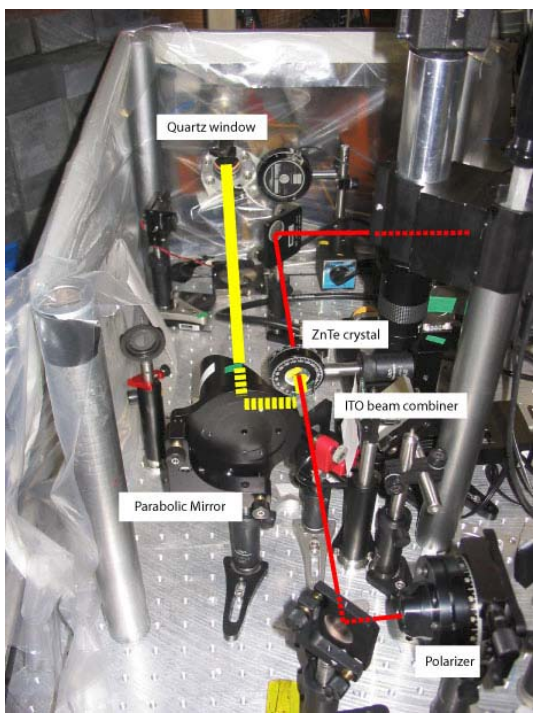

Figure 4: Photograph of the setup for electro-optic detection of CSR pulses.

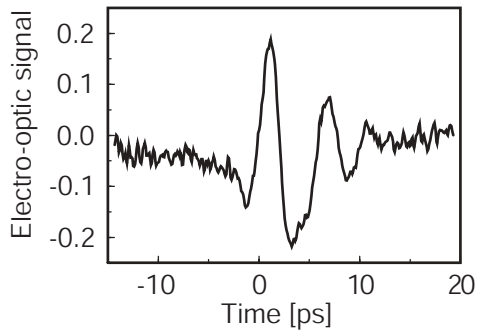

Figure 5: Single-shot electro-optic detection, using the spectral decoding technique, of CSR pulses generated at a bending magnet. Detection takes place outside the vacuum beam line using the setup shown in Fig. 4.

CONCLUSION

This contribution shows that electro-optic detection can be used for real-time monitoring of the shape and arrival time of electron bunches, far-infrared FEL pulses, and THz CSR pulses. This single-shot method for electron bunch characterization is non-destructive; at FELIX lasing of the FEL can be obtained while monitoring the shape of the electron bunches.

REFERENCES

[1] G. Berden, S.P. Jamison, A.M. MacLeod, W.A. Gillespie, B. Redlich, and A.F.G. van der Meer, Phys. Rev. Lett. **93**, 114802 (2004).

[2] G. Berden, G.M.H. Knippels, D. Oepts, A.F.G. van der Meer, S.P. Jamison, A.M. MacLeod, W.A. Gillespie, J.L. Shen, and I. Wilke, *Proceedings of the 6th European workshop on beam diagnostics and instrumentation for particle accelerators (DIPAC2003)*, Mainz, Germany, 2003, p. 20.

[3] G. Berden, B. Redlich, A.F.G. van der Meer, S.P. Jamison, A.M. MacLeod, and W.A. Gillespie, *Proceedings of the ninth European Particle Accelerator Conference (EPAC2004)*, Lucerne, Switzerland, 2004, p. 2697.

[4] The electro-optic signal scales linearly or quadratically with the electric field depending on the actual settings of the optical components controlling the polarization. For the electron bunch measurements in this paper (Fig. 2) the dependence is quadratic. For the FEL and CSR measurements the dependence is linear, allowing observation of the polarity of the signals.

[5] G. Berden, B. Redlich, A.F.G. van der Meer, S.P. Jamison, A.M. MacLeod, and W.A. Gillespie, *Proceedings of the 26th International Free Electron Laser Conference, and the 11th FEL Users Workshop (FEL2004)*, Triëste, Italy, 2004, p. 343.

[6] I. Wilke, A.M. MacLeod, W.A. Gillespie, G. Berden, G.M.H. Knippels, and A.F.G. van der Meer, Phys. Rev. Lett. **88**, 124801 (2002)

OTR BASED MONITOR OF INJECTION BEAM FOR TOP-UP OPERATION OF THE SPRING-8

S. Takano*, M. Masaki, T. Masuda and A. Yamashita
Japan Synchrotron Radiation Research Institute, SPring-8, Hyogo 679-5198, Japan

Abstract

We have developed an optical transition radiation (OTR) based monitor of injection beam at the SPring-8. The monitor has been installed near the injection point of the storage ring downstream of the beam transport line from the booster synchrotron. A screen made of an aluminum coated polyimide film is used as a non-destructive OTR radiator. A CCD camera with an electric shutter is used to observe the OTR image of the injection beam. The electric shutter is synchronized with the external injection trigger signals. At every injection, the image signal from the CCD camera is captured and analyzed by a personal computer, and the position, size and intensity of the injection beam are recorded by the real-time database of the SPring-8 control system. The OTR screen monitor provides real-time and non-destructive diagnostic tool useful for the top-up operation of the SPring-8.

INTRODUCTION

The 8 GeV electron storage ring of the SPring-8 is a third generation synchrotron light source operating since 1997. In May 2004, the so-called top-up operation started to realize practically infinite life time of the storage ring beam [1]. In the top-up operation, continuous beam injections at short time intervals keep the beam current approximately constant. In order to monitor the injection beam to the storage ring non-destructively and continuously in the top-up operation of the SPring-8, we have developed an OTR based screen monitor.

OTR SCREEN MONITOR

The injection section of the SPring-8 storage ring is shown schematically in Fig.1. The electron beam from the booster synchrotron is injected at the full energy of 8 GeV. We have installed the OTR based screen monitor in a vacuum chamber of the beam transport line near the injection septum magnet #5. In the end part of the beam transport line, downstream of the septum magnet #7, the injection beam goes through a vessel filled with helium at atmospheric pressure. We have two fluorescent screen monitors instead of OTR ones there, because intense Cherenkov radiation could disturb observations by contaminating transition radiation. The fluorescent

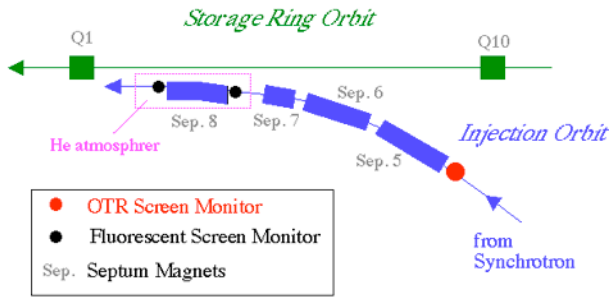

Figure 1: Injection section of the SPring-8 storage ring.

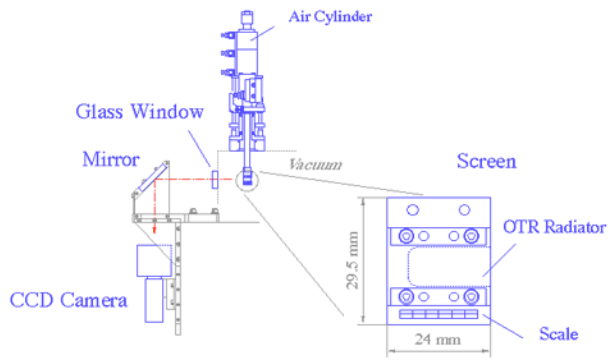

Figure 2: Set up of the OTR screen monitor.

screens are destructive to the injection beam, and they are retracted from the beam orbit during periods of top-up injections.

The setup of the OTR screen monitor is shown in Fig. 2. The OTR screen consists of a frame made of brass and a radiator made of an aluminum coated polyimide film. The thickness of aluminum and polyimide are about 0.5 μm and 50 μm, respectively. Scales for calibration are marked on the lower part of the screen holder. The screen is actuated by an air cylinder, which has three operating positions for 1) beam observation, 2) scale calibration, and 3) retraction. The screen is set at an angle of 45° with respect to beam direction. Backward OTR directed horizontally is transmitted in the atmosphere through a glass window and is deflected by a mirror downward, towards a CCD camera. To protect the camera from radiation damages, it is shielded by a cover made of lead. The OTR image of the injection beam is observed by the camera through a lens (F=1.3, f=75mm). The CCD camera has an electric shutter, which is synchronized

* Email:takano@spring8.or.jp

with the external injection trigger signals. The image signal from the CCD camera is captured and analyzed by a personal computer

PROFILES OF INJECTION BEAM

Fig. 3 shows an image of ordinary (non-collimated) injection beam observed with the OTR screen monitor. The charge in the beam is 6×10^{-10} C. Fig. 4 shows corresponding beam profiles projected on the horizontal (x) and vertical (y) axes of the coordinates of the injection beam as well as fitted Gaussian curves. Here we defined the major axis of the beam as horizontal and minor axis as vertical.

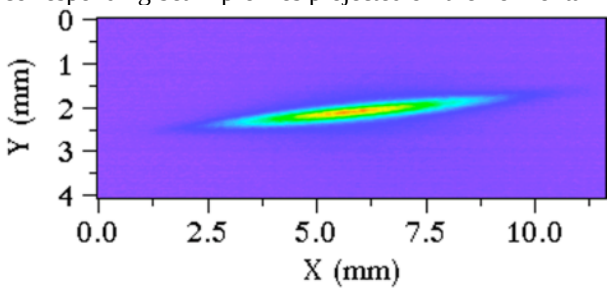

Figure 3: An image of ordinary (non-collimated) injection beam observed with the OTR screen monitor.

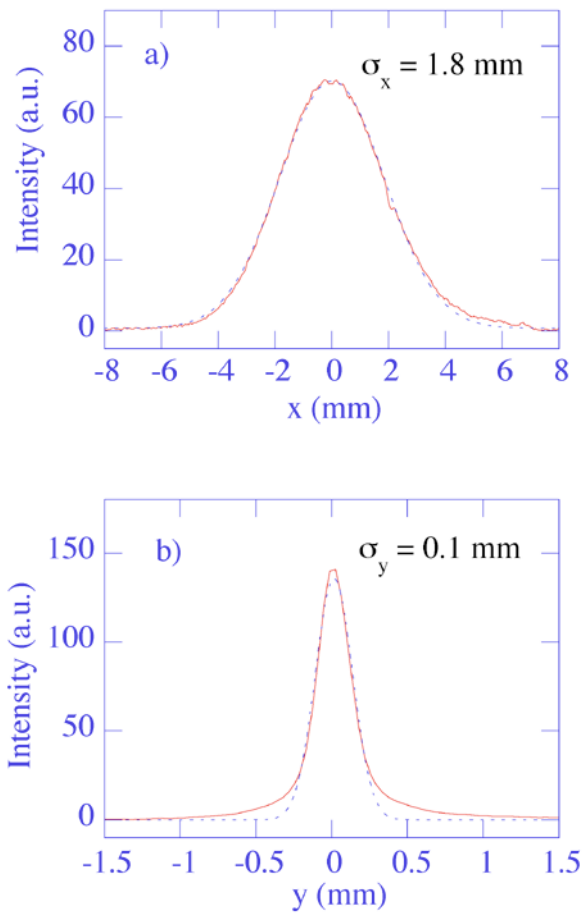

Figure 4: Horizontal (a) and vertical (b) profiles of ordinary injection beam (solid curves) as well as fitted Gaussian curves (dashed curve).

In the top-up operation of the SPring-8, injection beam to the storage ring is collimated horizontally by two scrapers installed upstream of the beam transport line from the booster synchrotron [1, 2]. The two scrapers have orthogonal phase relation in a horizontal betatron oscillation and reduce horizontal emittance of the

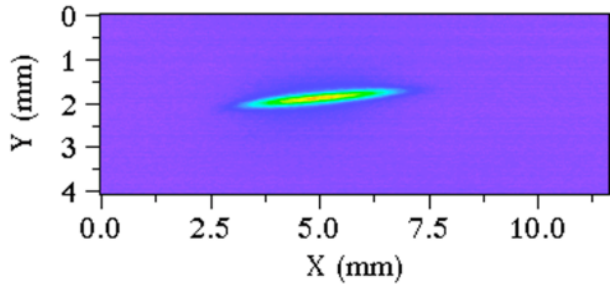

Figure 5: An image of collimated injection beam observed with the OTR screen monitor.

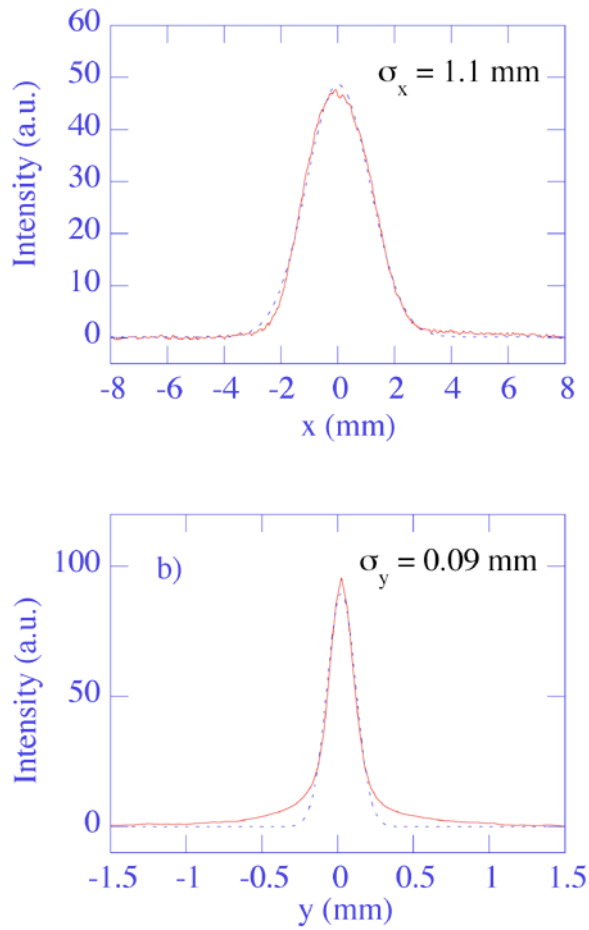

Figure 6: Horizontal (a) and vertical (b) profiles of collimated injection beam (solid curves) as well as fitted Gaussian curves (dashed curve).

injection beam. This enables to bring the injection beam near to the septum wall and to reduce injection beam loss.

Fig. 5 shows an image of collimated injection beam observed with the OTR screen monitor. The charge in the beam is 7×10^{-10} C. Fig. 6 shows corresponding beam profiles projected on the horizontal (x) and vertical (y) axes of the beam coordinates as well as fitted Gaussian curves.

REAL-TIME MONITORING OF INJECTION BEAM

For real-time monitoring of the injection beam, we use an event-driven data acquisition software [3] developed by extending the SPring-8 control software framework MADOCA [4]. At each beam injection to the storage ring, the image signal from the CCD camera is captured and analyzed by the personal computer. Gaussian curves are fitted to one-dimensional beam profiles projected on the horizontal (X) and vertical (Y) axes on the coordinates of the captured image, to obtain intensity I, positions X and Y, and sizes σ_X and σ_Y of the injection beam. Here the sizes σ_X and σ_Y are defined as projections on not the beam coordinates but the image coordinates. The analyzed data are stored into the real-time database [5] of the SPring-8 control system.

An example of time variation of injection beam is shown in Fig. 7 for one week of the top-up operation. The time interval of injections and the charge in the injection beam were one minute and about 2×10^{-10} C, respectively. There were two beam abort events on 6 and 9 Dec. After beam abort, the storage ring was refilled by injecting non-collimated beam, of which the charge was about 7×10^{-10} C.

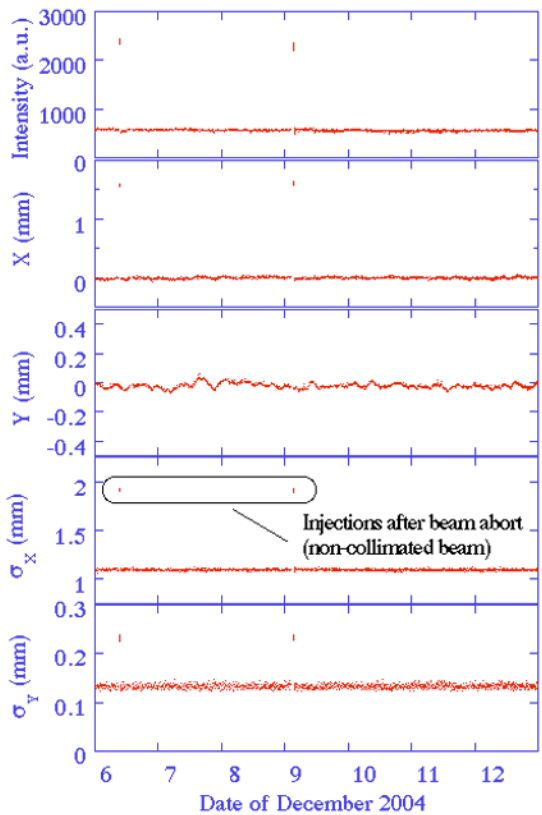

Figure 7: An example of history of injection beam to the storage ring for one week of the top-up operation.

CONCLUSIONS

We have developed an OTR based screen monitor of the injection beam at the SPring-8 storage ring. The profiles of the injection beam were successfully measured with it. At each injection to the storage ring, the intensity, position and size of the injection beam are recorded by the real-time database of the SPring-8 control system. The OTR screen monitor provides non-destructive and real-time diagnostic tool useful for the top-up operation of the SPring-8.

ACKNOWLEDGEMENTS

We thank Drs. S. Matsui and C. Zhang for help in alignment of the OTR screen monitor, and Dr. S. Suzuki for help in preparing the OTR radiator. We also thank Drs. K. Fukami and T. Asaka for valuable discussions on OTR based beam monitors.

REFERENCES

[1] H. Tanaka, et al., EPAC'04, Lucerne, 2004, p.222.
[2] K. Fukami, et al., "Beam collimation system for the SPring-8 Top-Up Operation", APAC'04, Gyeongju, in the press.
[3] T. Masuda, et al., Nucl. Instr. and Meth. A, 543 (2005) 415-430.
[4] R. Tanaka, et al, ICALEPCS'97, Beijing, 1997, p.1.
[5] A. Yamashita, et al., ICALEPCS'97, Beijing, 1997, p.427.

OPTIMIZATION OF BEAM INJECTION INTO THE FIRST ACCELERATING MODULE AT TTF WITH CAVITY DIPOLE MODE SIGNALS

N. Baboi*, H. Schlarb, M. Wendt†, G. Kreps (DESY, Hamburg),
O. Napoly, R.G. Paparella (CEA/DSM/DAPNIA, Gif-sur-Yvette),
J. Frisch, M. Ross, T. Smith, D. McCormick (SLAC‡, Menlo Park, CA)

Abstract

The TESLA Test Facility (TTF) is a user facility for intense VUV-FEL light. The facility is densely equipped with diagnostics, essential in obtaining the necessary beam parameters, in particular the low emittance. However there is no dedicated component for alignment of the beam in the accelerating modules, each containing eight superconducting cavities. Large beam offsets can lead to an increase of the beam emittance. The centering of the beam in these modules is therefore important, mostly at the low energy end. A misalignment of the first TTF module with respect to the gun axis has already been observed using cavity dipole modes. This paper presents the experimental results of the optimization of the beam injection into the first module, based on the monitoring of dipole modes through the couplers installed for wakefield damping. For this we use a spectrum analyzer together with a multiplexer. By scanning the beam position and tilt with two pairs of steerers, we can find the trajectory which minimizes the dipole modes amplitude. The impact of the beam steering in the module on the beam is discussed. A time domain setup is also being presented.

INTRODUCTION

The TESLA Test Facility linac (TTF) at DESY serves as a user facility for intense VUV-FEL light [1]. Each of the five TESLA cryo-modules contains eight 9-cell superconducting cavities, which accelerate the electron beam generated by a photo-cathode to about 450 MeV. Transverse higher-order modes (HOM), resonant fields excited in the cavities by off-axis charged particles, can give kicks on the subsequent beam, leading to emittance growth of the pulse train. In particular, at low energies the effect can be significant. Dipole modes are of main concern. The modes of individual cells are degenerated into 9 modes grouped into passbands.

Although there are various monitors for beam diagnostics in the facility, there is no dedicated device for beam alignment in the modules. Signals suitable for beam alignment are however available, from the HOM couplers with which each cavity is equipped [2]. These couplers extract energy from the HOM, particularly the first two dipole passbands, where most modes with highest impedance can be found. The amplitude of the resonant fields is proportional to the beam offset with respect to the cavity axis and to the bunch charge. Each dipole mode is split into two modes, with different polarizations. The axes of the two polarizations are orthogonal to each other for a circularly symmetrical structure.

From the coupler, the modal energy is normally brought through long coaxial cables to loads. We have disconnected the loads and monitored the amplitude of each mode with a spectrum analyzer. With a multiplexer we are able to choose one coupler out of 16 present in each module, as shown in Fig. 1. Therefore we can monitor the beam position in each cavity individually.

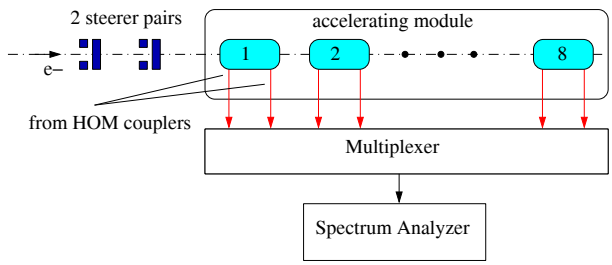

Figure 1: HOM setup for frequency domain measurements

In the next section we describe the procedure used for the alignment on the axis of the first cavity of the first TTF accelerating module. The results are compared to results from studies on beam properties. In the following section a time-domain recorder system is presented, which has recently been installed at TTF. Measurements made with this system are mentioned. There are four modes with high loss factors in the first two dipole bands, which makes them most suited for monitoring[1]. In this paper we have used modes 6 and 7 from the first band, at about 1710 MHz and 1730 MHz.

BEAM ALIGNMENT IN ACC1

The purpose of the measurements was to align the beam on the axis of cavity 1 of the first accelerating module, denoted by ACC1. The beam alignment is most critical here since kicks on the beam are highest due to the low energy of 4.6 MeV given by the gun. We chose mode number 6 from the first dipole passband, with $R/Q = 11$ MΩ/m^2. The

* nicoleta.baboi@desy.de
† currently at FNAL, Batavia, IL
‡ work supported in part by US DOE: DE-AC02-76SF00515

[1] A strong mode in the third passband is not suited, since it is very close to other modes.

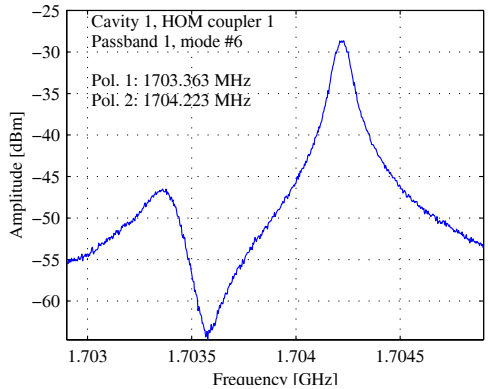

Figure 2: Spectrum of mode nr. 6 from the first dipole passband of cavity 1, ACC1.

two polarizations have in this cavity frequencies of $f_1 = 1703.4$ MHz and $f_2 = 1704.2$ MHz. They can be seen in the spectrum shown in Fig. 2. The split in frequency is caused by the asymmetries in the cavity.

In order to find the center of the cavity, we have moved the beam transversely with steerer pairs such that the angle of the beam in the middle of the cavity is constant. The position of the beam has been scanned. The amplitude of the dipole mode has been recorded. Mode f_2 has proved to respond to horizontal beam movement, while f_1 is sensitive to vertical position [3]. Since it takes a long time to get a spectrum due to the pulse repetitions frequency of 2 Hz, we measure the dipole mode in time domain. A single bunch per train with 1 nC charge has been used.

First a horizontal scan has been made (see Fig. 3-a). The horizontal axis shows the beam position in the middle of the cavity with respect to the starting position for the scan ($x = 0$ mm). A minimum of the amplitude of mode f_2 is seen at -2.7 mm relative position. The beam injection is set to this position and a vertical scan is next made while measuring the amplitude of mode f_1 (Fig. 3-b). The minimum is observed at about the initial beam position. In this way the center of the cavity is localized.

Next, by keeping the beam position constant, we varied its angle to find the cavity axis. The horizontal scan is shown in Fig. 3-c. The minimum dipole amplitude is found at about -90 μrad. A vertical scan (Fig. 3-d) of the beam angle around this position shows an already good alignment in this plane. The beam is now aligned on the axis of the first cavity of the module.

Results and discussion

Time only allowed for measurements to be made in cavity 1. The lowest wakefield effects on the beam from the whole module are expected to be different from this results. However, bringing the bunches on the axis of cavity 1 should provide a good first order alignment in the accelerating module.

Later, studies were made on the steering of the beam generated by module ACC1. The gradient of the accelerating field has been changed and the variation of the beam position has been studied. The injection conditions have been found for which the change in transverse beam position downstream of the module is minimum. The achieved injection was close to the position found with the HOM signals in the horizontal plane: the beam position and angle at the entrance of cavity 1 were within 10 μm and respectively 10 μrad. In the vertical plane the beam injection into the module differed by 0.8 mm and respectively 1.3 mrad.

It has to be mentioned that the beam position after passing an accelerating module is affected by the combined effect of wakefields, coupler kicks, cavity tilt and focusing. No change in deflection while varying the accelerating gradient means that the sum of all these effects cancel at the exit of the module, which does not necessarily match an on-axis beam in cavity 1.

The comparison of the steering study to the HOM beam alignment in cavity 1 seem to indicate a tilt of the cavity with respect to the module axis in the vertical plane, but a good horizontal alignment. This has to be confirmed in the future, by monitoring the HOM amplitude in more than one cavity.

A simple method, is to align the beam through the center of the first and last cavities. Moving the steerers such that the beam angle in the center of the first cavity stays constant, and finding the position for which the amplitude of an excited dipole mode is minimum, brings the beam through the center of the cavity. Starting from here and changing the beam angle such that the position in the middle of the same cavity is kept constant, the mode amplitude is monitored in the last cavity. The minimum will indicate that the beam goes through the middle of that last cavity. A

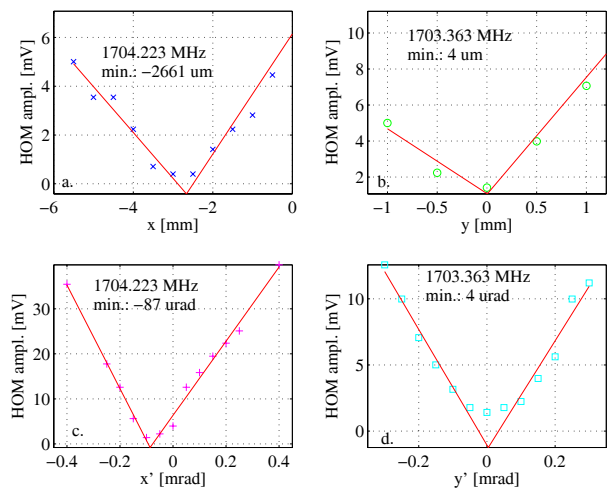

Figure 3: HOM amplitude with the change in beam position and angle in the middle of cavity 1, ACC1: a. horizontal position scan, b. vertical position scan, c. horizontal angle scan, d. vertical position scan. For each scan the position with minimum HOM amplitude from the previous scan is used as reference.

more complex alignment method implies the measurement of the HOM signals from all cavities and minimizing the overall wakefields.

TIME DOMAIN ELECTRONICS

While the frequency domain setup used for the above study is easy and straightforward, it has the disadvantage of being slow and of not providing the phase information. A special electronics has meanwhile been built, as shown in Fig. 4 [4]. The signal from a coupler is filtered around 1750 MHz, i.e. near the frequency of the 7th dipole mode in the first passband with $R/Q = 15.5\,\mathrm{M\Omega/m^2}$. A 1.3 GHz reference signal is used to down-mix the signal, such that it can be displayed with a fast oscilloscope. A 9 MHz signal is used for time reference.

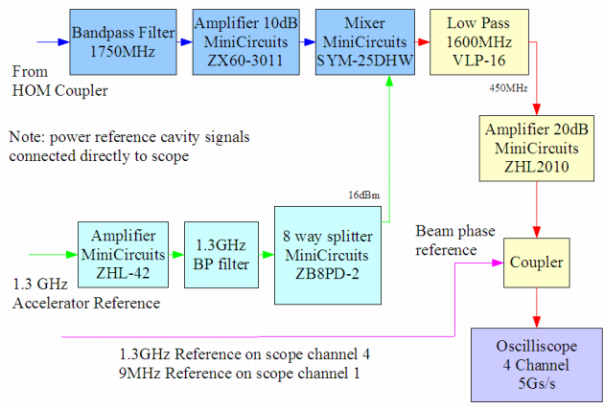

Figure 4: Block diagram of the down-mix electronics

This setup has the potential of measuring both beam offsets and angles with respect to each cavity axis. A calibration has to be made by moving the beam with steerers.

With one oscilloscope, four signals can be recorded in parallel, e.g. from the two couplers of two cavities. Measurements have been made in the fourth TTF module, ACC4. Single bunch beams have been used. The beam has been moved by a pair of correctors for each transverse plane. For more details on the measurement method see [4]. The resolution for beam position monitoring has been estimated to about 3 μm for a single cavity. Theoretically the achievable resolution is under 1 μm.

FUTURE PLANS

A system capable of monitoring simultaneously one or two modes from all 40 HOM couplers at TTF is being planned. The signals will be down-mixed to about 30 MHz and then digitized and send to the TTF control system. With this system a position resolution of better than 2 μm is expected.

Apart from using the HOM signals for beam position monitoring and alignment, the time domain and frequency domain setups are useful for other studies as well:

- The misalignment of the cavities in the modules have been measured at room temperature. The HOM setup can measure the cavity misalignment in the cold modules, providing for a cross-check of the mechanical measurements and cooling models.
- It has been observed that the center of a cavity differs for various dipole mode monitored [3]. A more thorough study of this and its implications is planned.
- The polarization of the dipole modes is not identical for all cavities. The direction of a mode depends on the ellipticity and misalignment of the cells in the cavity. Again a more detailed examination is necessary.

ACKNOWLEDGMENTS We thank the TTF crew for their assistance in performing the measurements described herein.

REFERENCES

[1] B. Faatz, Proc. FEL 2002, Argonne, 2002; P. Piot, DESY-TESLA-FEL-2002-08.

[2] R. Brinkmann et al. (eds.), DESY 2001-011

[3] N. Baboi et al., Proc. LINAC04, p. *117*, Lübeck, 2004

[4] M. Ross et al., PAC05, Knoxville, 2005

NEW TUNE MEASUREMENT SYSTEM FOR THE ESRF BOOSTER

J.M. Koch, J. Meyer, E. Plouviez
European Synchrotron Radiation Facility (ESRF), Grenoble, France

Abstract

The injection of electrons in the ESRF storage ring is performed at full energy, i.e. 6GeV. A linear accelerator provides the booster with a beam at an energy of 200MeV. During the accelerating cycle of the booster, from 200MeV to 6GeV, the tune of the electron beam varies according to the no-proportionality of the magnetic field in the quadrupole magnets as compared to the dipole field. This is mainly due to the harmonic content of the current in the magnets which differs with the load of these systems resonating at 10Hz and their saturation level. In order to measure the fractional part of the tunes all along the accelerating cycle, (50ms) it is necessary to acquire the beam position at a rate of at least one sample per turn, each μs. A set of 48 tune values can be extracted from this record with an accuracy of better than 10^{-3}.

INTRODUCTION

The measurement of the tune of the booster has been made automatic in the last few years, but due to the fact that the beam is excited with short kicks, it is only possible to obtain one measurement per accelerating cycle. To build the curve of the tune, we have to re-construct it point by point by delaying the excitation from the injection time. With an injection rate of one second and an average of a few data per point, it takes a few minutes before the curve for the full cycle can be established and the different points do not belong to the same cycle. Therefore, it was decided to use a white noise excitation present all along the cycle, and an acquisition system that can compute the tunes for the whole accelerating cycle in one go. Although this system is not already in operation, the first tests have shown that it works as expected. In addition to the increase in the tune measurement rate, it will be possible to add new features like the automation of the chromaticity measurement.

SYSTEM LAYOUT

Excitation of the Beam Oscillation

We excite the beam oscillation using magnetic kickers; these kickers are made of 6 coils enclosed in a ferrite box, with a ceramic vacuum chamber surrounding them. The kickers have a 0 to 600 KHz bandwidth when terminated on a 50Ω load and an efficiency of 3 G.m/A. The kickers are driven by a 50W amplifier. The input signal is a white noise in a bandwidth from 0 to 500 KHz.

Analog Front End

The beam position is measured using 2 sets of 4 capacitive pick-ups. The sensitivity of the electrode is improved by using resonant RF transformers to match the pick up capacitance to the 50Ω line impedance. The electrode signals are combined in ΔΣ RF combiners to produce signals proportional to the horizontal and vertical beam offset and beam intensity.

The pick up signals are detected using a 2 stage synchronous detection electronic scheme: The first stage is a 352.2 to 10.7MHz down converter. The second stage is a synchronous vector detection circuit of the Δ signal; the reference signal is the output of a limiting amplifier fed by the Σ signal. This scheme aims at getting the best signal to noise ratio rather than good position accuracy, which is pointless in a tune measurement.

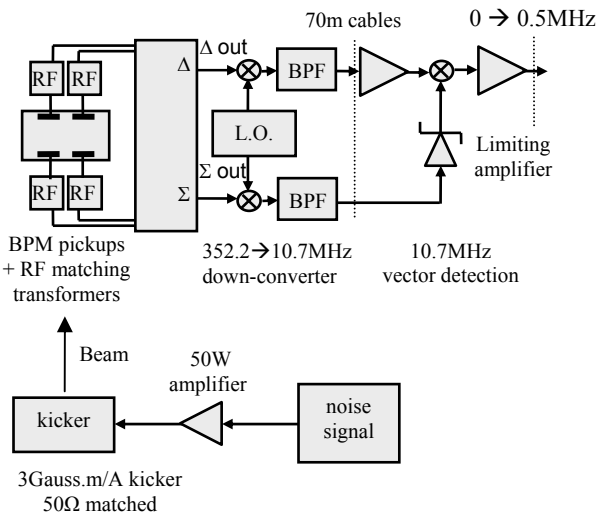

Figure 1: Analog front-end

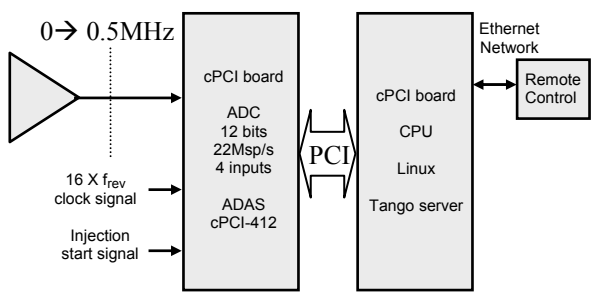

Figure 2: Digital acquisition & processing hardware

Computing

The positions are digitised by using one 12 bit acquisition board able to store a large amount of data at a rate up to 22Msample/s. Over-sampling by a factor 16 is used to enhance the signal over noise ratio. The data buffer is then transferred to a CPU that processes it to produce the results.

A tango server [3] running on a compact PCI CPU under Linux performs all the tasks required for the data processing. New data buffer is available every 2 seconds. A remote application will be developed to access and display the results requested by the operator. The tests have been made with a generic application available for any tango server that allows the commands to be launched and to display the results in several ways:

1) One tune spectrum at any time in the accelerating cycle.
2) A curve representative of the tunes along the accelerating cycle.
3) A three-dimensional picture displaying the spectra amplitude along with the measurements.
4) An array filled with all the data for one cycle.

From the generic application, it is possible as well to set the parameters, averaging number, measurement plane, index for spectrum and a Boolean to position in which part of the spectrum the tunes are, < 0.5 or > 0.5

DATA PROCESSING

Tunes

The method used is based on a Fourier transform of the transverse oscillations of the beam in the booster. The signal from the Beam Position Monitor block representative of the vertical and horizontal position is acquired at the rate of 16 samples per revolution. Whilst one sample per turn is enough to cover the frequency range of Frevolution/2 necessary to analyse the tunes with a full span, we took advantage of the possibility of over-sampling to increase the signal over noise ratio.

The system average the data over 16 samples and group the result in 1024 data long buffers. Then, each buffer is windowed by a Hanning window and processed with a fast Fourier transform. The resulting amplitude spectrum can be averaged with those from the previous cycles. A second-order interpolation is then performed in the area where the signal is maximum; the gain in accuracy depends, however, on the level of noise present on the signal. From each spectrum a peak detection is made, representative of the value of the tune. As the beam oscillation is maintained throughout the energy ramping by a shaker driven by white noise, it is possible to obtain as many points as we need along the accelerating cycle. We found a compromise between the number of points versus the frequency resolution and the choice was made to use contiguous buffers of 1024 data each. The full accelerating cycle is covered with about 48 points for 50ms. A compact numerical result is produced with a set of 48 data per plane and per cycle.

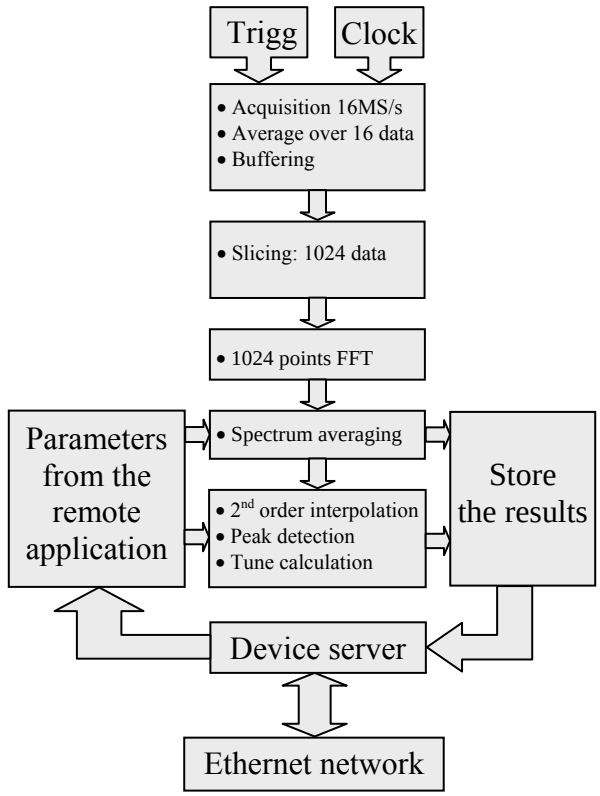

Figure 3: Signal acquisition & processing

Possible Enhancements

The fact of using a system dedicated can be useful in removing spurious frequency lines by including very specific functionalities:

1. Extending the analysis to a span of twice the range required, the frequencies that are not present at the same time on the signal and its image[4] can be disregarded.
2. Subtracting the background obtained without excitation, only the resonance frequency shows-up with a high signal over noise ratio[4].

Another point concerning the oscillation excitation is the rather wide energy range to cover; it can be difficult to find a compromise that gives the right shaker strength for the whole accelerating cycle. Too much strength will induce beam-losses at low energy and a too little will not allow the measurement to reach full energy. Therefore, strength proportional to the energy would be a solution to optimise excitation.

Chromaticity

Automatic measurement of the chromaticity will be envisaged by changing the booster RF frequency between two accelerating cycle and sequentially record the tunes with and without this change.
The averaged results will be processed to give an image of the behaviour of the chromaticity along the accelerating cycle.

MEASURMENT RESULTS

The measurements shown here (Fig.4 & Fig.5) have been plot under Matlab from data arrays (512 x 48) processed by the system.

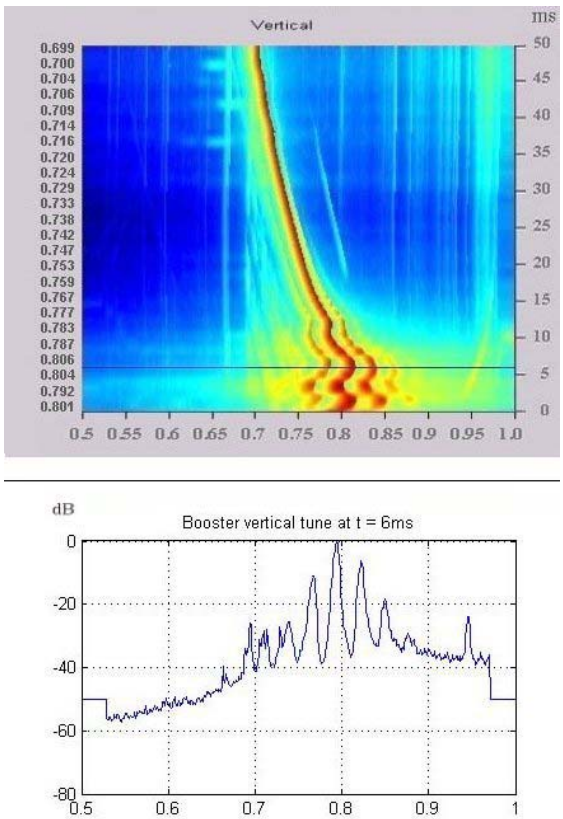

Figure 4: 3-D view of the spectra of the vertical motion during the acceleration cycle and below, one spectrum 6ms after injection

CONCLUSION

By taking full advantage of the use of an acquisition set-up already integrated in the control system and set-up for other purposes, it was possible in a short time to develop the server gathering the functionalities and to demonstrate that the results correspond with the requirements.
As compared with the previous system, the faster measurement rate brought by this system will be a great improvement for all the experiments involving booster tune measurements. A specific application will be developed soon to cover all functionalities in addition of those already available with the generic application.
Both excitation (shaker) and measurement (BPM) planes are switched between horizontal and vertical plane to obtain independent measurements.

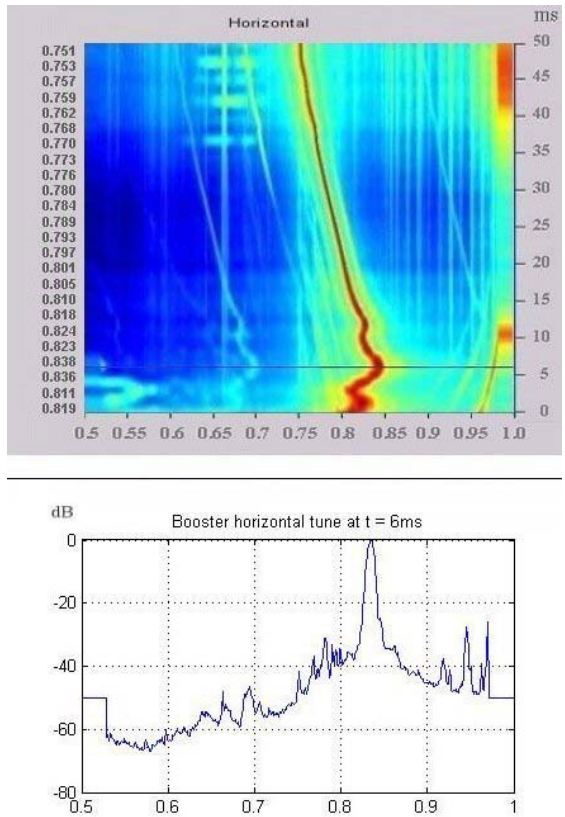

Figure 5: 3-D view of the spectra of the horizontal motion during the acceleration cycle and below, one spectrum 6ms after injection

ACKNOWLEDGEMENTS

We would like to thanks Y. Papaphilippou, N. Michel and our colleagues from the Computing Services.

REFERENCES

[1] J.P. Koutchouk, Advanced diagnostics of lattice parameters in hadron colliders. IT10 Dipac 2003, Mainz.

[2] S. Bassanese et al., Fast tune measurement system for the Elettra booster. PT25 Dipac 2003, Mainz.

[3] TANGO, an object oriented distributed control system.
http://www.esrf.fr/Infrastructure/Computing/tango

[4] J.M. Koch, Use of DSP based systems at the ESRF (2.2 - Fast tune monitor). Dipac 1997, Frascati

MEASUREMENTS OF TRANSVERSE EMITTANCE AT THE TTF VUV-FEL

K. Honkavaara*, F. Löhl, Hamburg University, 22761 Hamburg, Germany
Y. Kim, DESY, 22603 Hamburg, Germany

Abstract

The TESLA Test Facility (TTF) linac at DESY has been extended to drive a new free electron laser facility, the VUV-FEL. The 250 m long electron linac has been commissioned in 2004 and in the beginning of 2005. Characterization of the electron beam is an essential part of the commissioning. The transverse projected emittance has been measured at a beam energy of 127 MeV with the four-monitor method using optical transition radiation (OTR). We describe the experimental set-up and discuss the data-analysis methods. Experimental results as well as simulations are presented.

INTRODUCTION

The TESLA Test Facility (TTF) linac has been extended to drive a new free electron laser, the VUV-FEL [1], in the wavelength range from vacuum-ultraviolet to soft X-rays. The commissioning of the new facility started in the beginning of 2004, and the first lasing was achieved in January 2005.

Figure 1 shows the present layout of the TTF VUV-FEL linac. Electron bunch trains with a nominal bunch charge of 1 nC are generated by a laser-driven RF gun. Five accelerating modules with eight 9-cell superconducting TESLA cavities are installed to provide electron beam energy up to 750 MeV. The electron bunch is compressed using two magnetic chicane bunch compressors. At the location of the first bunch compressor the beam energy is 127 MeV and at the second one 380 MeV. During the commissioning the main emphasis has been on lasing with the wavelength of 30 nm, corresponding to an electron beam energy of 445 MeV. The lasing process requires a high quality electron beam in terms of transverse emittance, peak current and energy spread. The design normalized emittance of the VUV-FEL is 2 mm mrad. A more detailed description of the machine and first experimental results can be found in [2, 3].

At the VUV-FEL, measurements of the transverse projected emittance are performed using a four-monitor method. In this method the transverse beam distribution is measured at four locations along the linac with a fixed beam optics. The emittance is calculated by two different techniques. The first one is based on fitting of the Twiss parameters and the emittance to the measured beam sizes. The second one uses a tomographic reconstruction of the phase space distribution. A detailed description of the emittance measurements and analysis techniques presented in this paper can be found in [4].

* katja.honkavaara@desy.de

EXPERIMENTAL SET-UP

The VUV-FEL has two diagnostic sections dedicated to emittance measurements (see Fig. 1). The first one is located downstreams of the first bunch compressor at the electron beam energy of 127 MeV. This section consists of four OTR monitors combined with wirescanners embedded in a FODO lattice of six quadrupoles with a periodic beta function. A second FODO lattice with four OTR monitors is located upstreams of the undulator. In this paper we concentrate on emittance measurements in the first section using OTR monitors only.

The OTR system is designed and constructed by INFN-LNF and INFN-Roma2 in collaboration with DESY. The system can be controlled remotely, and it provides three different image magnifications (1.0, 0.39, and 0.25). The read-out system is based on digital CCD cameras with IEEE1394 (firewire) interface. The measured resolution of the system is 11 μm rms for the highest magnification. More details of the OTR monitor system are in [5, 6, 7].

EMITTANCE CALCULATIONS

The four (multi) monitor method is based on measurements of the transverse beam distribution (shape and size) at four (or more) locations with a fixed beam optics. The transverse emittance is determined from the measured beam distributions and the known transport matrices between the monitors using two different methods. The first one uses a least square (chi-square) fitting of the Twiss parameters and the emittance to the measured beam sizes. A general description of the least square fitting technique can be found, for example, in [8], and an application for emittance measurements in [9]. The second method is based on a tomographic reconstruction of the phase space distribution using the maximum entropy algorithm [10].

In the error estimation for the fitting method, we take into account both statistical and systematic errors. Statistical errors are caused by fluctuations on the measured beam sizes, and they are calculated as in [9]. Systematic errors are estimated using a Monte Carlo simulation assuming 5% error in the beam energy, 6% error in the gradient of the FODO lattice quadrupoles, and 3% error in the calibration of the optical system. Statistical errors are typically 2-4% and systematic ones 5-6%. For the tomographic reconstruction, no error analysis is performed yet.

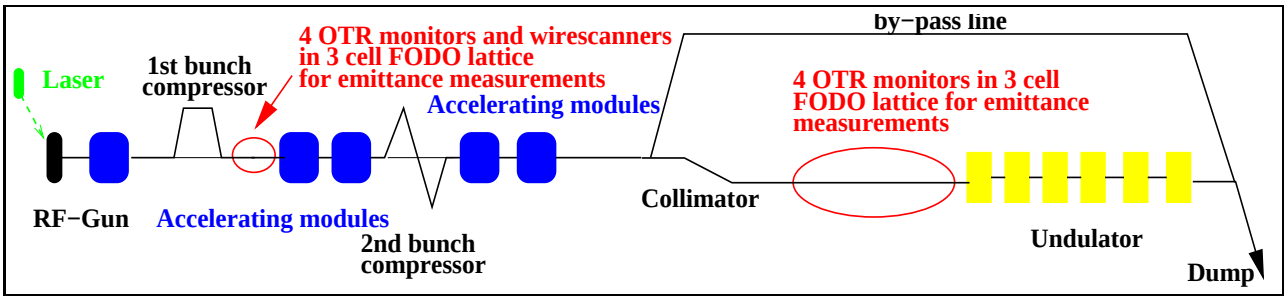

Figure 1: Present layout of the TTF VUV-FEL linac (not to scale). Beam direction is from left to right, and the total length is about 250 m. Locations of the diagnostic sections for emittance measurements are indicated.

IMAGE ANALYSIS

In a typical emittance measurement 20 beam and background images are recorded on each of the four OTR screens. In order to remove the influence of darkcurrent and damaged camera pixels as well as to correct off-sets generated by, for example, noise in the camera system, an averaged background image is subtracted from each beam image. A sophisticated analysis procedure is applied to each image to determine an elliptical region of interest (ROI) surrounding the entire beam. Remaining off-sets are corrected as well. If required, a wavelet filter can be used to reduce the noise further. Horizontal and vertical rms beam sizes as well as projections onto the horizontal and vertical axes are then calculated.

A small fraction of particles in the tails of the distribution can have a significant influence on the measured emittance. Therefore, in addition to the emittance of the entire beam, also the emittance of the high density core is of interest. We determine this core by cutting away 10% (an arbitrary choice) of particles in the distribution tails. After that the horizontal and vertical rms beam sizes of this core containing 90% of the beam intensity are calculated.

The rms beam sizes defined as above are used to calculate the emittance using the fitting technique resulting in the rms emittance of the entire beam (refered here as 'Fit 100%') and the rms emittance of the beam core including 90% of the particles (refered here as 'Fit 90%').

In the tomographic reconstruction an averaged beam profile of the entire beam on each screen is used. In order to avoid broadening of the profile due to a beam position jitter, the measured profiles are rebinned and the center of each profile is moved to the same position before averaging. The emittance of the entire beam is then determined by the maximum entropy algorithm (refered here as 'Tomo 100%'). In order to obtain the 90% core emittance (refered here as 'Tomo 90%'), 10% of the particles in the tails of the reconstructed phase space distribution are cut away.

MEASUREMENTS AND RESULTS

The measurements presented here are performed in the first diagnostic section using OTR monitors. During these measurements the injector was operated with nominal parameters, but it was not tuned to obtain the minimum emittance. The beam energy was 127 MeV, and one bunch of 1 nC was used. The beam was transported through the bunch compressor without compression (on-crest acceleration in the first accelerating module).

Figure 2 shows the normalized horizontal and vertical rms emittances measured ten times during ∼1.5 hours without changing the machine parameters. The results obtained by fitting and by tomography are presented for 100% and 90% beam intensity. We can see that the results by the two techniques agree well, and that the stability of the measurements is good. The rms jitter of the 100% emittance in the horizontal plane is ∼3.5% and in the vertical ∼2%, in agreement with the statistical error estimated above.

In order to reduce space charge induced emittance growth in the RF-gun, the electron beam is focused by a solenoid magnet. Figure 3 shows the normalized horizontal and vertical rms emittances as a function of the current in this solenoid. The beam is matched to the FODO lattice for each solenoid current. This is important, since matched Twiss parameters inside the FODO lattice are required for accurate emittance measurements [4]. The measurement was repeated twice for each solenoid current. The result from ASTRA [11] simulations using normalized projected emittance of 2 mm mrad is shown as a solid line. We can see that the behavior as a function of the solenoid current predicted by the simulations agrees well with the measurements. Both show that the optimal solenoid current, from the emittance point of view, is around 277 A, which corresponds to a magnetic field of 0.163 T.

SUMMARY AND OUTLOOK

The emittance measurement system based on a four-monitor method using OTR monitors is commissioned and in routine use by operators to measure and to optimize the electron beam parameters in the VUV-FEL injector.

Wirescanners in the injector diagnostic section are still under commissioning, but in the near future they will provide a complementary measurement of the beam sizes and the emittance to be compared with the results obtained by the OTR monitors.

Due to present priorities at the VUV-FEL, it has not yet been possible to optimize the measurement conditions in

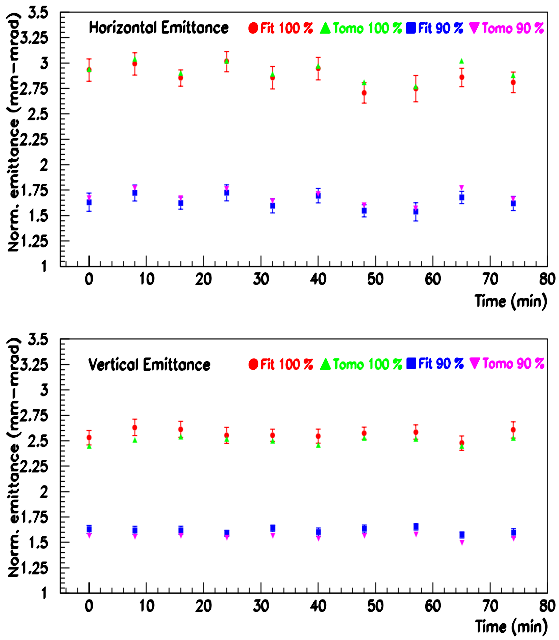

Figure 2: Horizontal (top) and vertical (bottom) normalized rms emittances. The measurement is repeated 10 times during ∼1.5 hours. Results obtained by fitting for 100% (red) and 90% (blue) beam intensity as well as by tomography for 100% (green) and 90% (magenta) intensity are shown. Error is the statistical error only.

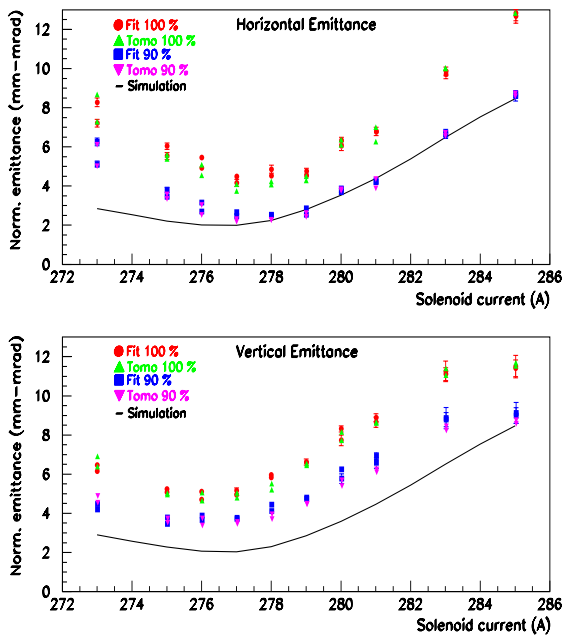

Figure 3: Horizontal (top) and vertical (bottom) normalized rms emittance measured as a function of the solenoid current. Results obtained by fitting for 100% (red) and 90% (blue) beam intensity as well as by tomography for 100% (green) and 90% (magenta) intensity are shown. Error is the statistical error only. The solid line is a prediction from simulations.

the second diagnostic section. Therefore, accurate emittance measurements at the full beam energy have not been done yet. However, when the emittance measurements can be performed simultaneously both in the injector and before the undulator, useful information about the emittance transport through the linac can be obtained.

ACKNOWLEDGMENT

We would like to thank all colleagues, who have contributed in the design and realization of the emittance measurement system and participated in the measurements. Special thanks are to our colleagues from INFN-LNF and INFN-Roma2 for the OTR monitor system, and to S. Schreiber for many fruitful discussions and advice of different aspects of emittance measurements.

REFERENCES

[1] The TTF FEL Team, “SASE FEL at the TESLA Test Facility, Phase 2”, TESLA-FEL 2002-01, June 2002.

[2] K. Honkavaara, “Commissioning of the TTF Linac Injector at the DESY VUV-FEL”, 2004 FEL Conference, Trieste, Italy, Aug 29 - Sep 3, 2004.

[3] B. Faatz, “First Results from the VUV-FEL at DESY”, PAC 2005, Knoxville, Tennessee, May 16-20, 2005.

[4] F. Löhl, “Measurements of the transverse Emittance at the VUV-FEL”, to be published as DESY-THESIS 2005-014 and TESLA-FEL 2005-03, Diploma Thesis, Hamburg University, 2005.

[5] K. Honkavaara *et al.*, “Design of OTR Beam Profile Monitors for the TESLA Test Facility, Phase 2 (TTF2)”, PAC 2003, Portland, Oregon, May 12-16, 2003.

[6] A. Cianchi *et al.*, “Commissioning of the OTR Beam Profile Monitor System at TTF/VUV-FEL Injector”, EPAC 2004, Luzern, Switzerland, July 5-9, 2004.

[7] L. Catani *et al.*, “A Large Distributed Digital Camera System for Accelerator Beam Diagnostics”, PCaPAC 2005, Hayama, Japan, March 22-25, 2005.

[8] W. H. Press *et al.*, *Numerical Recipes in C, The Art of Scientific Computing*, Cambridge University Press, 1993.

[9] M. Minty and F. Zimmermann, *Measurements and control of charged particle beams*, Springer, 2003.

[10] J. Scheins, “Tomographic Reconstruction of Transverse and Longitudinal Phase Space Distribution using the Maximum Entropy Algorithm”, TESLA Report 2004-08, May 2004.

[11] http://www.desy.de/∼mpyflo/Astra-documentation

UPGRADE OF THE GLOBAL FEEDBACK OF THE ESRF STORAGE RING

E. Plouviez, F. Uberto, J.L. Pons, J.M. Koch
European Synchrotron Radiation Facility (ESRF), Grenoble, France
e-mail: plouviez@esrf.fr

Abstract

We have recently upgraded the fast orbit correction system of the ESRF storage ring. We are now operating a global feedback system using 32 BPMs and 24 correctors in the horizontal and vertical planes to compute and apply corrections at a rate of 4.4 KHz from .1 to 150Hz. This new system has greatly improved the damping of the orbit distortion up to 100Hz. It also provides new diagnostics tools thanks to its new data logging capabilities. We report the performance of this new system and some of its applications as a diagnostic.

INTRODUCTION

Until the end of 2004, the damping of the fast beam orbit distortions of the ESRF was done in the vertical plane by a global feedback system using 16 BPM and 16 correctors; in the horizontal plane we were using a set of 4 local feedback systems to stabilize the beam in the 4 most sensitive ID straight sections [1]. This fast orbit correction is working in parallel with a slower correction system using 224 BPM and 96 correctors to perform 2 corrections per minutes with a very good accuracy and long term reproducibility. The goal at ESRF is to keep the amplitude of the fast beam movement time $\beta^{1/2}$ below 2μm inside the insertion devices straight sections (integrated over the frequency span going from .1 to 200Hz). Since the implementation of vibration damping pads on the girders supporting the storage ring magnets in 2001 [2], the beneficial effect of the vertical feedback had become a bit marginal; in the horizontal plane, there was no way to increase the number of local systems, due to the imperfect closure of the local correction bumps at high frequency: with more than 4 systems in operation, the cross talks between the local feedbacks resulted in instabilities. In order to overcome these limitations, we decided in 2001 to upgrade our fast correction scheme and to implement a fast global correction system active in both horizontal and vertical planes. One of the constraint for this upgrade, was to use as much as possible of the components of the old system: BPM, correctors, front end electronics and data links, in order to reduce the cost of the project and to avoid leaving the ring without fast orbit correction during the implementation of the new system. We kept the same approach of separating the slow and fast orbit correction in 2 systems so this new system do not perform any orbit correction below.1Hz.

UPGRADE LAYOUT

The constraint was to achieve an efficient correction in both planes, given the value of the tunes of our storage ring (ν_H=36.44 and ν_V=14.39), the number of BPM and correctors that could be easily integrated in our upgraded system and the frequency range needed for an efficient damping of the orbit distortion.

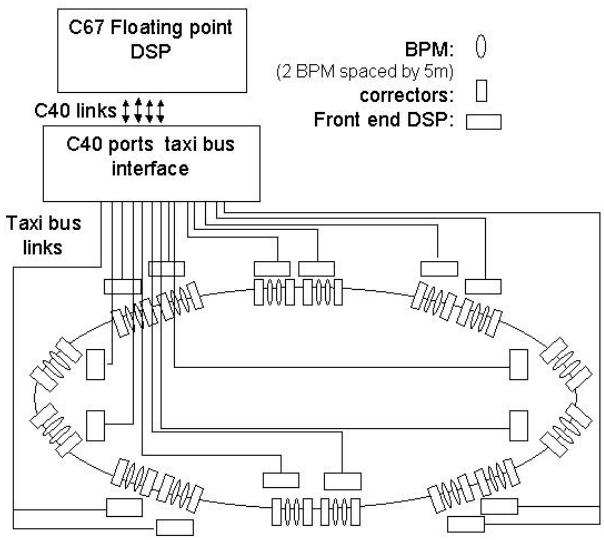

Figure 1: Layout of the global feedback system.

Static correction: BPM and correctors number

The layout of the upgraded global feedback is shown on figure1. The upgrade had to be compatible with some limitation put by the existing hardware. A front end DSP has 8 ADC inputs and 3 DAC outputs so it can handle the data of the 8 electrodes of 2 BPM blocks and drive 3 correctors amplifiers inputs. At the other end of the data link the most convenient interface available for data transmission between a commercially available central DSP board and our data links was the TI C40 port. The central DSP board that we chose can handle four C40 ports and we can concentrate on one C40 port the data stream of four front end DSP; so the size of our system is limited to 32 BPM for both planes and 48 correctors. Presently the correctors output are shared equally by the 2 planes: 24 vertical and 24 horizontal correctors (but this may not be the most efficient repartition). A rule of thumb is that it takes a number of BPM and correctors roughly equal to the tune value to obtain a significant fast

global correction (i.e. leaving less than 30% of residual distortion).

According to simulations the global effect of the correction is efficient enough with 32 BPM, 24 correctors and 16 eigen values for the SVD correction computation, even in the horizontal plane, where the tune value is the highest (36.44). As shown on figure 2 the amplitude of a random static orbit distortion can be reduced by a factor of 5 all over the ring and more than 10 at the feedback BPM location, assuming perfectly accurate horizontal position measurements (simulation plot).

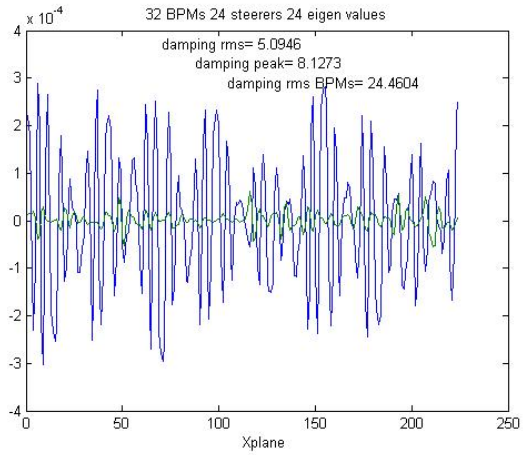

Figure2: initial (blue) and corrected (green) orbit

Dynamic correction: processing power

In order to operate a feedback with a bandwidth of 150Hz without instability or noise increase in the vicinity of the cut off frequency we need, as for the initial vertical feedback, to run the loop at a high enough rate and to achieve a low delay of the signal propagation between the BPM and the correctors, together with a low noise contribution of the BPM. So we aimed at keeping the same figure for the loop rate (4.437 KHz) and loop delay figure (<.6ms) as on the previous systems). This was achieved by using the same type of air cored magnets for the new system, and by replacing the TI C40DSP of the old system by a more powerful DSP.

Choice of the DSP

The choice of the processor board was driven by the need for a sufficient processing power and the possibility to interface this board with the data link already used in the previous system; given these constraints we went for a *TI C6701 DSP* implemented on a *Sundance SMT327* board. Signal processing cannot realistically be coded on such a processor without an adequate programming environment. We used the *3L* real time OS for this project.

BPM resolution

The BPM of our system are dedicated use dedicated BPM pick ups located at both ends of the insertion device straight sections where $ß_x$=36m and $ß_z$=4m; the disadvantage of the low $ß_z$ value is compensated by the possibility to have BPM vacuum chamber with a small 18mm vertical aperture which improves the BPM resolution. The capacitive electrodes are RF matched to the impedance of the cables using resonant RF transformers, which improves the noise figure of the BPM electronics. The BPM electronics is the one used for our previous fast feedback systems and based on a RF multiplexing scheme. They are not designed to achieve any DC position measurement performance since our system does not perform any DC correction but are aimed only at achieving a high frequency resolution. They are definitely a bit outdated, but they still achieve a 10nm/Hz$^{1/2}$ resolution, or .5µm per sample at our sampling rate. This good resolution, combined with the number of BPM available on the upgraded system keeps the contribution of the BPM noise to the beam motion below 200nm when the feedback loop is closed.

Correctors magnets

The correction kicks are produced by air coil steerer dipoles. $ß_z$ value at the steerers location is 35 m and $ß_x$ value is 5m. The stainless steel vacuum chamber at the steerers location is 2mm thick giving a flat frequency response to the magnet field up to 1 KHz. The steerers are powered by wide band power amplifiers and are able to produce up to 40 µradian kicks in a 1 KHz bandwidth. With their amplifiers, they contribute for .3 ms to the loop delay.

CORRECTION ALGORITHM

The flow chart of the feedback loop is shown on figure3

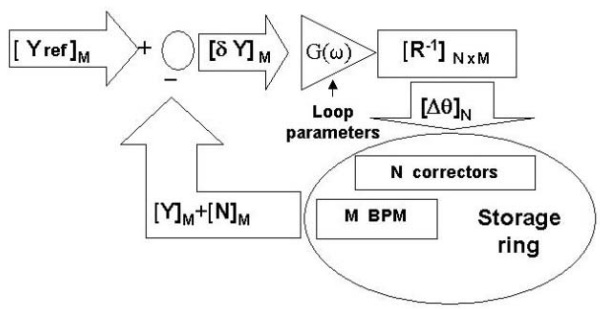

Figure3: flow chart of a global orbit feedback loop

With the 32 positions we calculate a correction vector using a correction matrix. To obtain this correction matrix we invert during a calibration phase, the matrix of the response of the feedback BPMs to each steerer, using the SVD method

PID correction

This correction vector is used to compute the actual correction applied to the beam using the previous correction values and a proportional integral iterative algorithm (PID type). In addition, the correction is

cancelled at very low frequency (10^{-2} Hz) to decouple the fast orbit correction from the slow orbit correction.
These dynamic parameters have been chosen in order to meet the following requirements:

- The cut-off frequency f_c must be at least two times higher than the highest frequency (60 Hz) that we want to damp significantly.
- On the other hand, the propagation delay of the signals in the loop is .6ms; this delay results in a significant amplification of the input signals around the cut off frequency, when this frequency is set above 150Hz.

We found that a cut off frequency of 150Hz was the best compromise between these two requirements

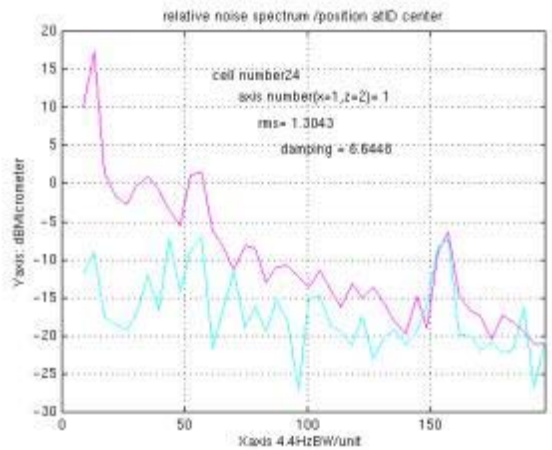

Figure4: spectrum of the horizontal beam motion with PID correction OFF (red) and ON (blue)

50Hz notch filter

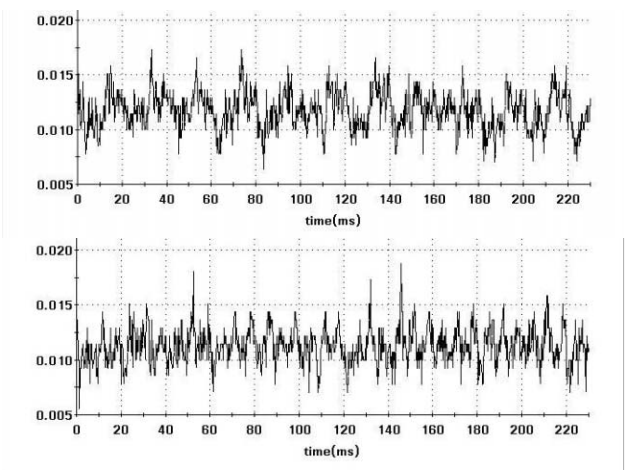

Figure5a and b: time plot of the vertical beam motion with a PID correction only (up) and an additional 50Hz notch correction (down), vertical scale: mm.

In addition to the PID loop, we have added a narrow bandwidth notch filter tuned at 50 Hz to the transfer function of the loop. It further reduces the amplitude of this AC main line by a factor 3. The effect of this notch filter is shown on figure 5. We have implemented it as a recursive filter, with the same high Q second order low pass response as is used at NSLS [3].

ADDITIONAL DIAGNOSTIC FUNCTION

The new feedback allows the data logging of the position measured and corrections computed.by the system. This data logging can be triggered by an external signal, by an alarm in the system (measured position or computed correction exceeding a threshold) or by a request coming from the storage ring control system. 1024 samples of the positions and corrections can be recorded after a trig. A very useful application of this data logging is the possibility to locate the origin of a transient fault on a storage ring component. For instance, in the case of a transient fault of the power supply of one of the 96 slow orbit correction magnets, we compare the data logging triggered by the orbit distortion to the pre recorded responses of the BPM of the global feedback to each of the 96 correctors to locate easily the origin of the problem.

SYSTEM PERFORMANCE

Following the implementation of our new system, we have measured in all the storage ring straight section (equipped with BPM used in the loop or not) a very significant reduction of the fast beam motion as summed up on the table below:

	β at the BPM location	rms motion (.1to200Hz) no feedback	rms motion (.1to200Hz) feedback ON	motion/ beam size
H	36m	5 μm	1.5 μm	<.006
V	6.5m	1.5 to 2 μm	.7 μm	<.1

ACKNOWLEDGMENTS

We would like to acknowledge the contribution of the colleagues of the ESRF Machine Division who participated in the design of this system. Special mention to P. Arnoux for his contribution to the tedious optimisation of the RF circuits, and J. Cerrai and P. Pinel of the Digital Electronics group who implemented the taxi bus data link.

REFERENCES

[1] E. Plouviez, Fast positional global feedback for storage rings, DIPAC1999, Chester, May 1999
[2] L. Zhang, L. Farvacque, J.M. Filhol, E. Plouviez, "E-Beam Stability Enhancement by Use of Damping Links for Magnet Girder Assemblies at the ESRF", PAC2001, Chicago, USA, June 2001
[3] B. Podobedov ``Operation with fast digital orbit Feedback Systems at NSLS", 2nd workshop on beam orbit stabilisation, SPRING8, Japan, December 2002.

RECENT DIAGNOSTIC IMPROVEMENTS FOR THE PSI ACCELERATOR

P. A. Duperrex, U. Frei, G. Gamma, U. Müller, L. Rezzonico, PSI, Villigen, Switzerland

INTRODUCTION

Two recent developments for the PSI proton accelerator are presented: a) a new remote control system that is being implemented for the numerous wire scanner based profile monitors of the proton accelerator, b) a new current monitor as replacement of an older system.

CONTROL SYSTEM FOR PROFILE MONITORS

A new remote control system [1] for the profile monitors has been developed and is being currently implemented on various beam lines of the proton accelerator. The development of this new system was motivated by maintenance difficulties due to an aging system, by some shortcomings related to the old technology and by the better performances offered with the electronics of today.

Shortcomings of the old system

The profile monitor controlling system has been in operation for 20 years. It is made of 3 multiplexed systems controlling all together more than 200 profile monitors.

Several shortcomings motivated the development of a new remote control system. First, the maintenance of this aging system is problematic because some critical electronic components are no more available. Furthermore, the multiplexed nature of the system has a negative impact on the system availability. The wire current measurement of the old system relies on a linear circuit. The correct amplifier gain setting is most of the time requiring several profile measurements. These repeated scans have a negative influence on the longevity of the wire. In addition, the analysis of the raw data is difficult because of the particular ADC used. Indeed, with the old system, the data are sampled at regular position intervals and not at regular time intervals. FFT or time based filtering of the data is then not possible.

Improvements

Improvements addressing these shortcomings are: i) a distributed system structure based on an internally developed CAMAC board controlling up to 8 profile monitors ii) a fixed gain logarithmic measurement of the wire current covering the whole operation range iii) the new control of the DC motor can adjust the motor speed to beam conditions, iv) position and current measurement with a dedicated 14 bit ADC for improved resolution and further off-line processing.

Overview of the new system

Fig.1 gives a conceptual overview of the system. It is made up of 3 subsystems: i) a CAMAC based WIPAM (**WI**re **P**rofilemonitor **A**cquisition **M**odule) including the DASH (**D**ata **A**cquisition module with Hitachi **SH**2 microcontroller) back-end, ii) up to 4 **M**otor **D**rive **M**odules (MDM), iii) up to 8 profile monitors.

Control signals are generated from the CAMAC based electronics (WIPAM). They are then decoded and conditioned for driving the motor in the power stage electronics (MDM). Measurement signals from the profile monitor are first conditioned at the MDM then further processed in the WIPAM. The following sections provide a more detailed explanation of the subsystems.

WIPAM

The DASH back-end has been developed as a standardised universal controller, which can support various front ends. The firmware is responsible for controlling the motors, processing and storing the raw data, calculating the current profile and checking interlock conditions.

The microcontroller 10 bit ADC is used for sampling the DC motor voltage and current. A control program uses these data to drive the DC motor at the required speed. In addition, the scanning wire position is also used to initiate the braking sequence early enough to avoid overshoots. The actual motor speed ranges from 1000 to 5000 rpm. With a 20 gear ratio factor and taking into account the acceleration and deceleration phases, typical time for a run ranges from 0.3 sec to 2 seconds.

The status of the different rest position switches are continuously monitored to make sure that all profile monitors are in their rest position when not in use. The program will otherwise attempt to bring a faulty monitor back into its rest position. If unsuccessful, the program will generate an interlock to avoid any possible damage.

The analogue front-end (AFE) provides correctly conditioned signals for the MDM. In addition, scanning wire current and position signals are filtered and sampled at 10 kHz using a MAXIM 14 bit ADC.

Parameter limits such as beam width or position can be defined so that interlocks may be generated in case the measured parameters go over these limits.

MDM

The MDMs decode the information from the WIPAM, in particular the profile monitor to be activated and the rotation direction of the motor. They provide the necessary power for driving the DC motors, as well as the 10 V reference signal for the position potentiometer measurements. The logarithmic conversion of the current from the scanning wire is also performed in the MDM: 800 mV correspond to a decade with a 0 V output voltage corresponding to 1 μA. Almost 8 decades can be measured this way.

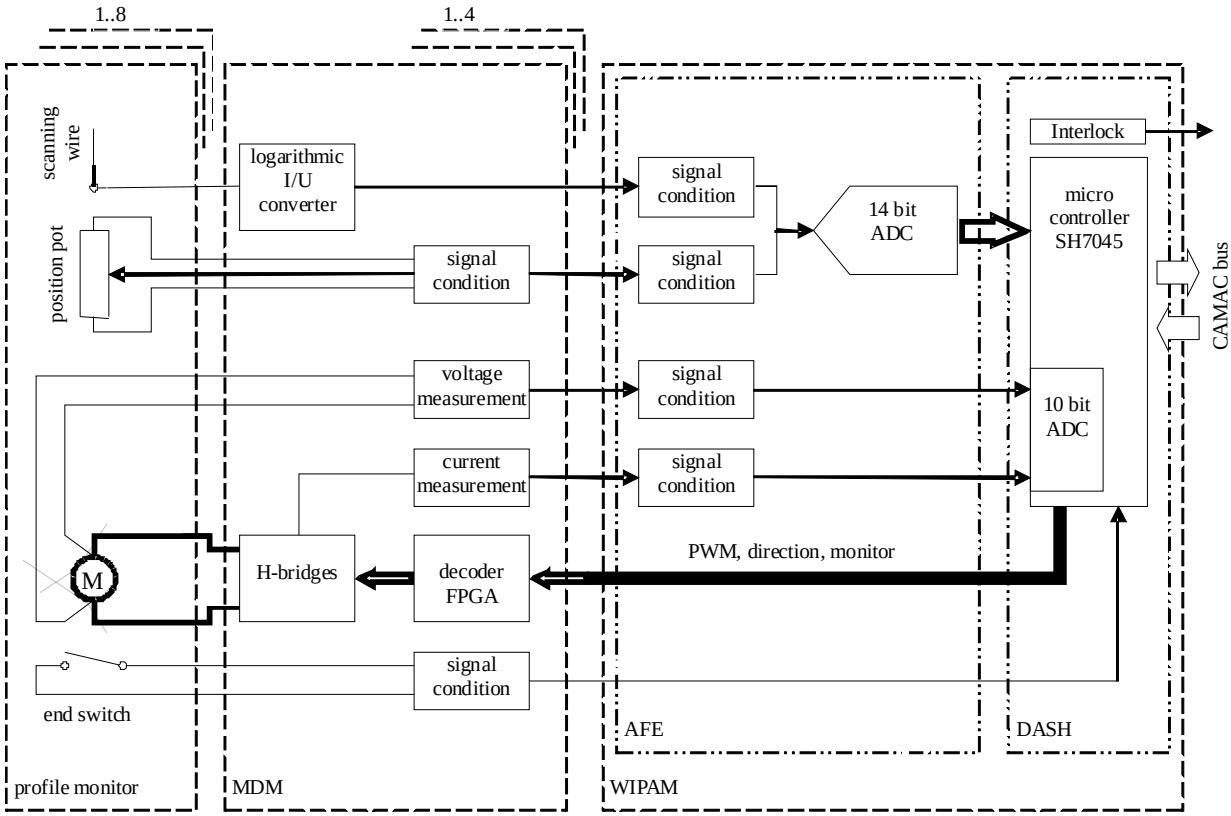

Figure 1: Conceptual overview of the system showing the main system elements.

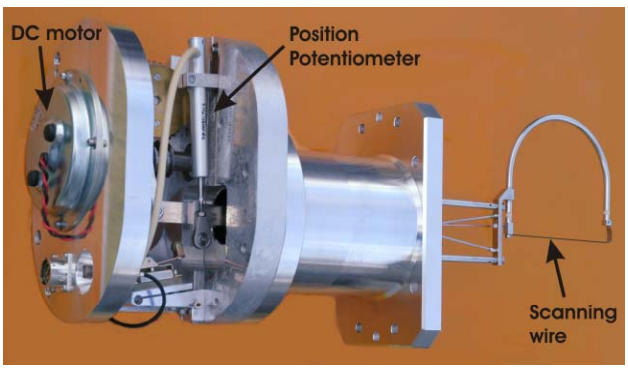

Figure 2: Profile monitor controlled by the system.

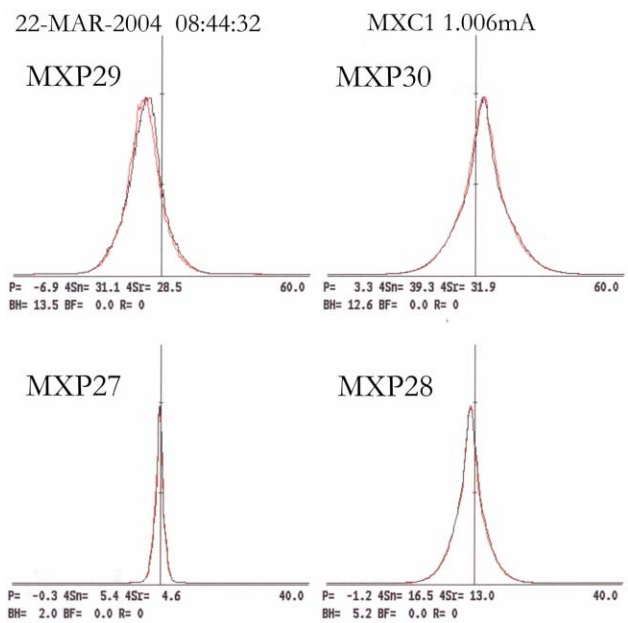

Figure 3: Beam profile measurements with the new electronics showing the beam broadening in the horizontal (MXP29) and vertical direction (MXP30) before the BX2 beam dump

NEWLY INSTALLED CURRENT MONITOR

A current monitor has been built to replace an early prototype installed a few years ago.

Main features

The current monitor consists of a TM01-mode coaxial resonator (reentrant cavity, quality factor Q ~2000). The cavity is tuned at 101.26 MHz, the 2nd harmonic of the proton beam pulse frequency. This frequency is used because of the better signal-to-noise ratio, the RF disturbance components being mainly at the odd harmonics (fundamental, 3rd, …). No significant shape dependency of the 2nd harmonic amplitude for relatively small beam pulses is expected [2]. The magnetic field in the resonator thus provides a direct measurement of the beam current. The monitor is made of aluminium, with a 10µm coating layer of silver to improve the electrical conductivity.

Currents from 0.5µA to 2.5mA can be measured using ~10 kHz analogue output bandwidth electronics. Drifts related to various thermal effects (resonator, cables, electronics) limit the measurement accuracy to ~5%, making almost weekly calibration necessary. The measurement precision is better than 0.5%. With this latest version a test signal can be fed into the cavity to check the integrity of the measurements.

Resonance condition and temperature dependence

For a given resonant frequency, using an external capacitor shunt reduces the actual length of the resonator. The corresponding resonance condition is given by:

$$\tan\left(\frac{2\pi L}{\lambda_m}\right) = \frac{\lambda_m}{2\pi c C_{total} Z_o} \qquad (1)$$

with L. the resonator length, C the capacitor shunt, Z_o the characteristic impedance of the transmission line, and λ_m the resonant wavelength.

Effect of temperature changes on the resonant frequency has been measured. The corresponding frequency drift is 106 kHz for a temperature change of 50°C ($25 \rightarrow 75$°C). These measurements are in accordance with what can be theoretically expected using (1). Indeed, taking into account the thermal expansion coefficient (2.4×10^{-5}/°C), the changes in the resonator length and in the capacitor shunt, the drift was expected to be 105 kHz.

REFERENCES

[1] P.A. Duperrex, U. Frei, L. Rezzonico, "New distributed remote control fort he profile monitors", PSI Scientific and Technical Report 2004, Volume VI, p.18-20.

[2] R. Reimann & M. Rüede, "Strommonitor für die Messung eines gepulsten Ionenstrahls", Nuclear Instruments and Methods 129 (1975) 53.

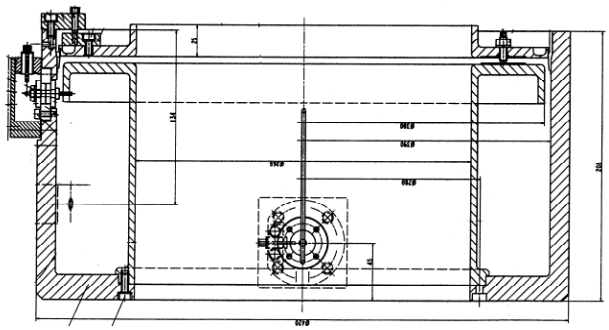

Figure 4: Drawing of the current monitor

Figure 5: Monitor during laboratory tests preceding the installation on the machine

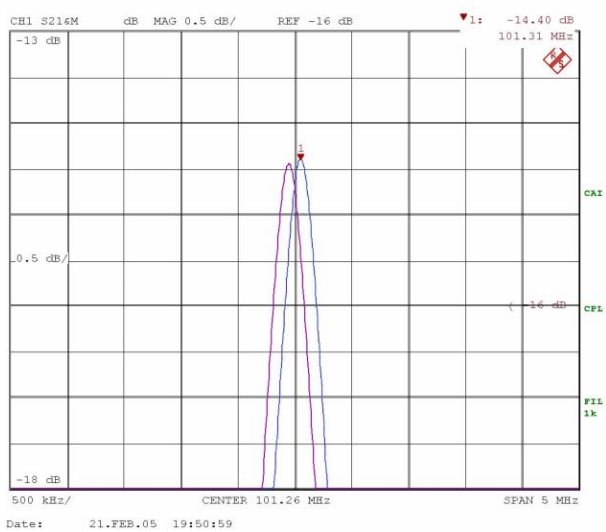

Figure 6: Resonance measurements at two different temperatures ($25 \rightarrow 75$°C) showing a negative frequency shift for increasing temperature.

THE BEAM DIAGNOSTICS FOR SESAME

Seadat Varnasseri *, SESAME -c/o UNESCO Office, P.O.Box 2270, Amman

Abstract

SESAME† (Synchrotron-light for Experimental Science and Applications in the Middle East) is an Independent Intergovernmental Organization developed and officially established under the auspices of UNESCO. SESAME will become a major international research center in the Middle East, located in Allan, Jordan. The machine design is based on a 2.5 GeV 3rd generation Light Source with an emittance of 26 nm.rad and 12 straights for insertion devices. The conceptual design of the accelerator complex has been frozen and the engineering design is started [1]. The completion of the accelerators complex construction is scheduled for the end of 2009. In the following an overview of the electron beam diagnostic system is presented, with special emphasis on the beam position monitoring system and the synchrotron light monitor for the main storage ring.

INTRODUCTION

In SESAME the electrons are injected from a 20 MeV microtron into a 800 MeV booster synchrotron, with a repetition rate of 1 Hz. The 800 MeV beam is transported through the transfer line to the main storage ring and after accumulation, accelerated at 2.5 GeV. Through the path from microtron to and within storage ring both destructive and non-destructive monitoring of beam are performed, consisting of Faraday cup, florescent screen, current transformer, strip line, scraper, beam loss monitor, synchrotron light monitor and beam position monitor pick ups [2].

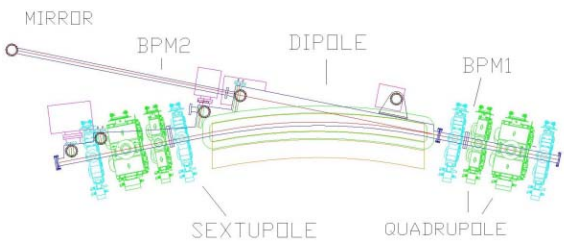

Figure 1 : Arrangements of BPM and light monitor within half cell of the storage ring SESAME.

The aim is to use the destructive monitor instruments mainly for commissioning and first day operation and non-destructive devices for the normal operation of the machine.

Fig.1 shows the half cell of the machine with the proposed diagnostic elements.

* s.varnasseri@unesco.org.jo

† It involves at present the following Member States: Bahrain, Egypt, Iran, Israel, Jordan, Pakistan, Palestinian Authority, Turkey and United Arab Emirates.

Table 1: SESAME storage ring parameters relevant to beam diagnostics and their normal values.

Energy (GeV)	2.5
RF frequency (MHz)	499.564
Natural emittance $\varepsilon_x/\varepsilon_y$ (nm.rad)	25.24/0.2524
Injection energy (MeV)	800
Max. Average current(mA)	400
Harmonic number	222
Revolution period(ns)	444
Bunch length (cm)	1.16
Horizontal beam size (μm) LS/SS/Dipole	794.8/789.7/232
Vertical beam size (μm) LS/SS/Dipole	28.1/16.6/71.5
Horizontal divergence(μm) LS/SS/Dipole	45.3/45.9/260.9
Vertical divergence(μm) LS/SS/Dipole	9/15.2/12.1

The tunnel air temperature for SESAME storage ring will be stabilized at (25±1) ^{o}C. The vacuum chamber temperature gradient per the horizontal distance between the button PUs will not exceed 0.5 ^{o}C. This gives a maximum of 8μm repositioning of button pick ups due to the temperature differential on the stainless steel vacuum chamber.

BEAM POSITION MONITORS [3,4,5]

Overall there are 32 BPM sets, four BPMs in each cell of the storage ring. They will be placed at the exit and entrance of each bending magnet and between sextupoles and quadrupoles, to measure the closed orbit distortion all around the ring. Fig.2 shows the SESAME optical function and 4-buttons BPM arrangements.

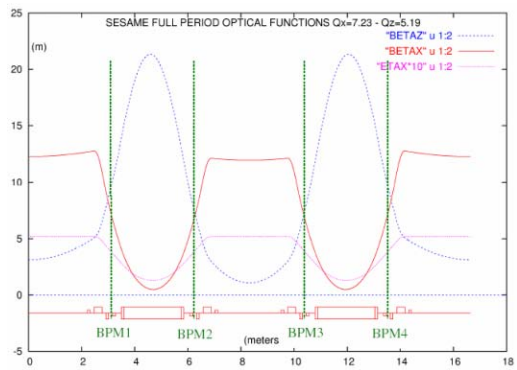

Figure 2: Optical function of SESAME and the BPM arrangements.

The ESRF type capacitive BPM buttons will be used for SESAME electron BPM head. 2D electrostatic sensitivity analysis of the BPM head has been carried out for horizontal and vertical planes and for different relative horizontal positions in the vacuum chamber. Since the vertical distance of the buttons is dictated by the vacuum chamber geometry, the horizontal distance of the buttons should be optimized in order to reconstruct accurately the transverse beam position and recover the nonlinearity of the transfer function.

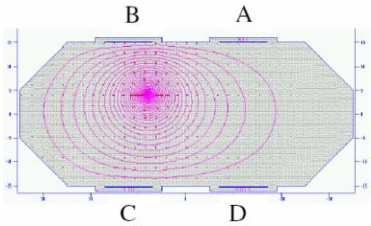

Figure 3: Cross section of the SESAME vacuum chamber, pick up buttons with a non-centered beam.

Figure3 shows the vacuum chamber cross section and the BPM Pick up's. The electrical beam position in the horizontal/ vertical plane is given by:

$$X = \frac{(Q_A + Q_D) - (Q_B + Q_C)}{(Q_A + Q_B + Q_C + Q_D)} \qquad (1)$$

$$Y = \frac{(Q_A + Q_B) - (Q_C + Q_D)}{(Q_A + Q_B + Q_C + Q_D)} \qquad (2)$$

Where Q_A, Q_B, Q_C and Q_D are the induced charges on button pick ups. The position sensitivities in each plane are given by the derivatives of electrical position with respect to x and y, in other words S_x and S_y respectively.

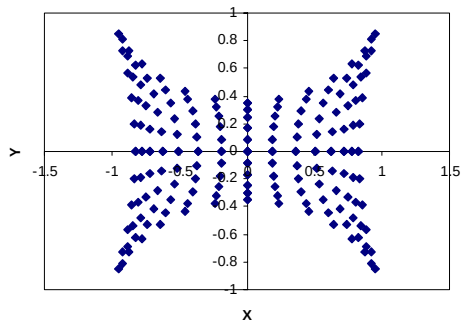

Figure 4: Position map with 30 mm H distance. distance between dots is 2mm.

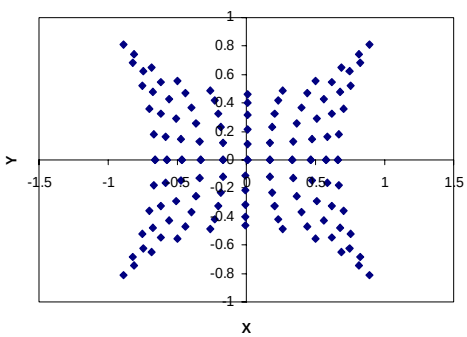

Figure 5: Position map with 24 mm H distance. distance between dots is 2mm.

Figures 4 and 5 show the horizontal and vertical position map for 30mm and 24mm as the horizontal distance between the buttons. The results have shown a better response and resolution for 24mm as the horizontal distance.

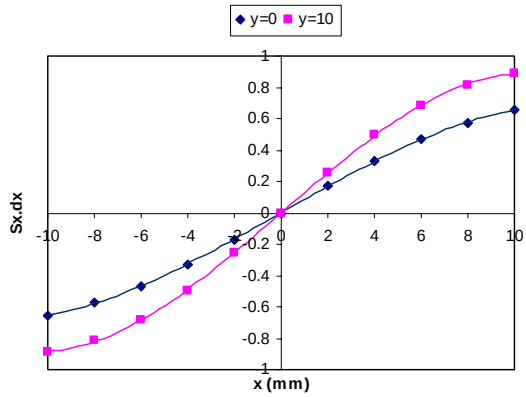

Figure 6: bpm sensitivity curves for x direction.

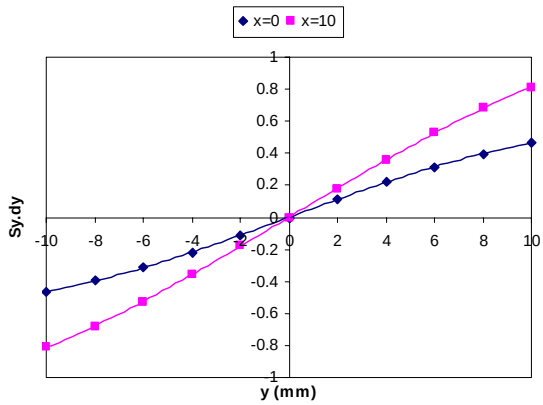

Figure 7: bpm sensitivity curves for y direction.

Figures 6,7 show the sensitivity curves for x-direction and y-direction where the horizontal distance between PUs is 24 mm. The coefficients of the polynomial fitted to the calculated points in x and y direction are as follows:

$$x = 11.73X + 2.63X^3 - 19.66XY^3 + 12.35X^5 + 26.24X^3Y^2 - 2.03XY^4 - 13.77X^7 - 38.02X^5Y^2 + 32.07X^9 \qquad (3)$$

$$y = 17.64Y - 21.17X^2Y + 9.89Y^3 + 16.76X^4Y - 25.29X^2Y^3 + 48.57Y^5 - 14.91X^4Y^3 - 48.55Y^7 + 33.94Y^9 \qquad (4)$$

The sensitivity at the center of the beam pipe is 8.5% per mm for the x-direction and 5.6% per mm for the y-direction.

SYNCHROTRON LIGHT MONITOR

[6,7]

The 2.5GeV electron beam emitting synchrotron light in the 1.455T dipole magnet. It consists of visible light spectrum from 300 nm to 700 nm with a vertical opening angle of 2.3-3.1 mrad. The electron beam sizes in the horizontal and vertical planes are σ_x=232μm and σ_y=71.5μm respectively for 1% emittance coupling.

Electrons moving in the storage ring radiate energy in discrete quanta or photons, each with energy equal to

$\hbar f$. In case of a beam of particles the total continues energy per second radiated, is proportional to the number of particles that pass the observer per second. In this case the angular distribution of total power in (Watts/mrad^2) is given by:

$$\frac{dP}{d\Omega} = 5.42E^4.B.I_b \frac{1}{(1+\gamma^2\psi^2)^{5/2}}\left[1+\frac{5\gamma^2\psi^2}{7(1+\gamma^2\psi^2)}\right] \quad (5)$$

where E, B and I_b expressed in GeV, Tesla and Ampere respectively. ψ is the observation angle in the vertical plane. Therefore in case of observation on off-axis radiation direction, the peak power density is given by:

$$\frac{dP}{d\Omega} = 5.42\,E^4.B.I_b \qquad W/mrad^2 \quad (6)$$

Integration over vertical angle gives the linear power density:

$$\frac{dP}{d\theta} = 4.22E^3.B.I_b \qquad W/mrad\ Horizontal \quad (7)$$

At SESAME ring, the source point is aligned at 6.5^o port of dipole magnet. The first mirror is positioned in a distance of 4.2m from source point. This gives the peak power density and linear power density on the 45 degree positioned mirror as 87 W/mrad^2 and 27.2 W per Horizontal mrad respectively.

Imaging resolution

The visible light wavelength of 500 nm will be used, however shorter wavelength will improve the resolution, but on the other hand the cost of optical elements also will be increased. The resolution of synchrotron light monitor is limited by several fundamental effects. These effects are different in vertical and horizontal plane in some cases.

Table 2: parameters list at 2.5 GeV

Vertical opening angle of light, λ= 500 nm	2.75 mrad FWHM
Slit angular aperture	1mrad horizontal, 7 mrad vertical
Visible light power	2.9 mW (300nm-700nm)
Depth of field error	21.49 μm
Diffraction error	105 μm
Curvature error	2.87 μm
Distance from source point to first mirror	4.2 m
Lattice function values at source point	β_x= 1m , β_y= 19.74m , η_x=0.154m
Bending radius at beam point	5.7296m
Peak power density on the mirror	4.95 W/mm^2
Linear power density on the mirror	6.5 W/mm

The main effect comes from diffraction error and in a less effective factor comes from depth of field error and curvature error. For a simple vertical slit the diffraction resolution is given by:

$$\Delta_{diff} \approx 0.21\frac{\lambda}{\theta} \quad (8)$$

Where λ is the visible light wavelength and θ is the half acceptance angle, This error has a value of 105 μm. Depth of field error is very dependent on the acceptance angle and length of the source as given by:

$$\Delta_{df} \approx 0.5L\theta \quad (9)$$

where L is the length of source and θ is the half acceptance angle. With a half acceptance of 1 mrad, this error will be 21.49 μm. The less effective error comes from the curvature of electron beam as given by(10). It has the value of 2.87 μm.

$$\Delta_{cur} \approx 0.5R\theta^2 \quad (10)$$

where R is the bending radius at the source point. For a particular wavelength the best resolution is obtained by minimizing the sum of squares of the errors. Overview of the light monitor and related optical parameters are given in table(2). With 1 mrad half angle aperture, we will reach a resolution not less than 130μm. The thermal peak power on the first mirror reaches 4.95 W/mm^2 and a sufficient cooling will be arranged to prevent any deformation on the mirror surface.

Transmission outside the ring

The light is reflected out from the first mirror that is positioned 45^o vertically and 4.2m far from the source point into the 1m tube under atmospheric conditions. The second plane mirror brings the visible light into a horizontal (normal to gravity) plane, and into the other side of the SR ring through the 80cm thick concrete shielding wall. All the optical components and tables will be in the other side of shielding wall.

ACKNOWLEDGMENT

I would like to thank the Beam Diagnostics group staffs of INFN, Frascati, Italy for their very helpful informative discussions in the period of my visit.

REFERENCES

[1] G. Vignola, et al. “SESAME in Jordan”, PAC 2005 Proceedings, Tennessee, US, May 2005

[2] S. Varnasseri, et al. “SESAME Beam Diagnostics” Yellow book, May 2003

[3] A. Stella, “Analysis of the DAΦNE Beam Position Monitor with a Boundary Element Method”, DAΦNE Tech Note, Frascati, Dec. 97

[4] T. Shintake et al., “ Sensitivity Calculation of Beam Position Monitor”, Nuclear Instruments and Methods in Physical Research A254 (1987), pp 146-150

[5] S.H. Kim, “Four-Button BPM Coefficients in Cylindrical and Elliptic Beam Chambers”, APS tech. pub. LS-274, March 1999

[6] A.Ghigo, R.Huang, F.Sannibale, “Optical Analysis of the Synchrotron Radiation Monitors in DAΦNE”, DAΦNE Tech Note, Frascati, July 97

[7] R.P.Walker, “Synchrotron Radiation”, CAS, CERN 94-01V1

AN X-RAY PINHOLE CAMERA SYSTEM FOR DIAMOND

C.A. Thomas, G. Rehm, DIAMOND, RAL, Great Britain

Abstract

In this paper we present the X-ray pinhole camera designed for the measurement of the size, the emittance and energy spread of the electron beam at Diamond. The system has been kept as simple as possible. The pinhole and the imaging system are in air, and the X-ray beam from the bending magnet is filtered out through an Al window. The beam is imaged using a fluorescent screen and an IEEE 1394 camera. We describe the system from the problems encountered for the extraction of the X-ray beam, to the optimisation of the imaging system. Taking into account the results of preliminary tests, we estimate the expected performance of the system.

INTRODUCTION

The DIAMOND synchrotron light source is the third generation light source under construction in the UK [1]. The expected performance of the source, in terms of brightness, imposes the electron to occupy a very small phase space volume. To measure the energy spread ($\approx 10^{-3}$) and the emittance ($\approx$ 2.7 nm rad) of the DIAMOND electron beam, an X-ray pinhole camera [2] is probably the most simple and accurate device. The pinhole camera is a known device and the instrumentation very straightforward. However, the adaptation and the optimisation of the camera to the case of Diamond requires to investigate in details the extraction and the imaging of the of the X-Ray beam. For the extraction of the beam, the number of X-Ray photons is an issue, but at the same time, the heat-load of the extraction window has to be considered. To image the electron beam profile, two steps are considered. The first one is to find the best screen that would absorb the X-ray photons and convert them into visible photons. The second step is to investigate the best way to image the fluorescent screen.

In this paper we present the design of the pinhole camera, showing the heat-load taken by the Al window, and then the optimisation of the imaging system.

X-RAY PINHOLE CAMERA

The X-ray pinhole camera, like any pinhole camera, is composed of a source, a pinhole and a screen to image the source. At Diamond, two X-ray pinhole cameras will be installed to measure the beam size in high and low bending magnet dispersive sections. The two systems are identical, as described in figure 1. The X-ray beam from the bending magnet goes through the beam port absorber. The absorber is a copper block, designed to absorb the totality of the X-ray beam, and in our case a modification allows the

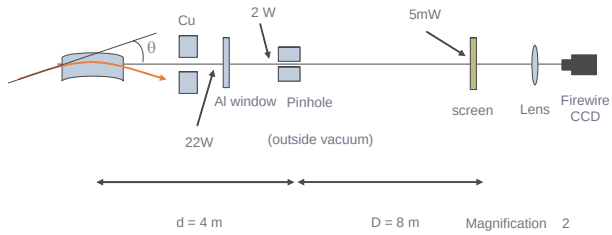

Figure 1: Scheme of the pinhole camera system for measuring the electron beam transverse profile. Electron beam size, emittance and energy spread can be calculating from the image of the beam profile.

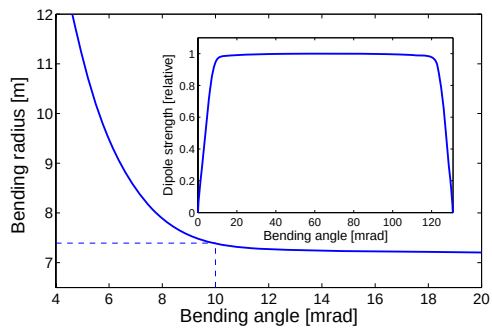

Figure 2: DIAMOND bending magnet radius vs. angle.

transmission of the beam through an aluminium window. The window transmits only the high energy photons from vacuum to air. The position of the window as to be carefully chosen. We show in figure 2 the bending radius as a function of the angle, θ, between the electrons' entering straight direction and the photon beam line. In our particular case, the radiation flux become significant only after 10 mrad (see fig 3). The 25 by 25 μm^2 pinhole is placed behind the window, as close as possible from the source, 4 m in our case. To image the source (2D gaussian, r.m.s 25 by 50 μm^2) we use a fluorescent screen that absorbs X-rays and fluoresces in the visible. The screen is placed at twice the distance source-pinhole, so that the image is magnified by a factor $\approx$ 2. Three different screen have been tested at ESRF, $CdWO_4$ (0.5 mm thick), P43 (5 μm thick) and YAG:Ce (0.1 mm thick). To acquire and measure the size of the source we image the screen with a macro-lens (Componon 2.8/50 from Schneider-Kreuznach) focussing on a compact IEEE 1394 CCD camera (Flea from Point Grey). A Matlab application has been developed to control the camera.

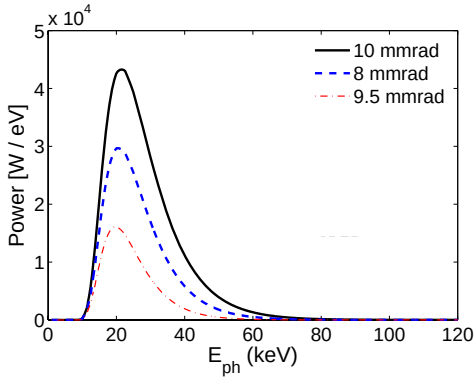

Figure 3: Power radiated from the bending magnet for different angles.

Extraction of the X-Ray Beam

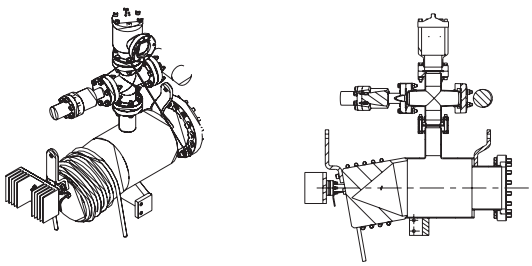

Figure 4: Modified beam-port absorber. The X-ray beam traverses a slit in the absorber and hit the the 1 mm thick Al window. A heatsink is used to cool passively the window.

The scheme of the modified beam-port absorber is shown in figure 4. The X-ray beam traverses a vertical slit in the beam-port absorber before traversing a 1 mm thick Al window. The vertical slit has 1 mm aperture, so that the flux is reduced to a minimum and the heat-load on the window due to the absorbtion becomes acceptable. A heatsink is attached to the window and is able to conduct out 20 W of heat into the air. The aluminium alloy used for the window is AA 6061. Table 1 summaries its properties. The window has to be thin enough to transmit a sufficient radiation flux, and thick enough to be able to sustain the mechanical stress due to the pressure difference and the temperature variation. In addition, the elevation of temperature due to the absorbtion of the radiation should be much less than 500 $^{\circ}$C. Finally, the fatigue strength of the window must be high enough to ensure a the lifetime of the window. In order to ensure for the heat-load and for the mechanical stress, we needed to perform a Finite Element Analysis to simulate the heat flux through the window. The result shows that the temperature at the centre of the window - where the power density of the synchrotron radiation is maximum - rises up to 110 $^{\circ}$C. The mechanical stress induced by the heat-load is, also at the center, 74 MPa. These two results shows that the Al window is able to sustain the thermal and mechanical stress and to transmit enough flux. A previous study [3] showed that with 1 mA current in the ring, and with the 1 mm Al window, 10^9 photons/s could be seen by the CCD camera (to be discussed in the next section).

Imaging system

The role of the imaging system (fluorescent screen, lens assembly, CCD camera) is to take a measurable picture of the X-ray beam profile, in order to measure the electron beam size and calculate the emittance and energy spread of the stored electrons. The fluorescent screen has to convert X-rays in visible light, and the lens assembly focusses the image of the X-ray beam profile onto the CCD camera. The conversion efficiency of the screen, the resolution of the screen, of the lens and of the camera have to be taken into account.

We report here on the results of tests performed at ESRF on the P43 and the $CdWO_4$ screens. The conversion efficiency of the screen parameter determines the image quality, i.e. the number of photons hitting the CCD, as a function of the electron beam current. We have deduced, from the experimental results from the tests at ESRF, the minimum flux at Diamond the imaging system would need to acquire a good quality image. Then we calculated that the minimum current in the DIAMOND storage ring, which generates the minimum detectable flux, would be much less than 1 mA for $CdWO_4$ and and of the order of 1 mA for P43. But, if the P43 screen is relatively less sensitive than the $CdWO_4$, it has a better resolution (10 μm compared to 30 μm respectively). As a consequence we may want to use both two screens. In addition, because the image of the P43 is made from the back through the glass, another problem has to be solved. The glass substrate of the P43 becomes dark after some time in the X-ray beam (see fig 5). This problem doesn't appear with self supported crystals, which is the case for the 0.5 mm thick $CdWO_4$. The P43 can be used then if deposited either on a non marking substrate or on a very thin glass and back illuminated.

PERFORMANCE OF THE PINHOLE CAMERA

The overall performance of the pinhole camera depends on quality of the image given by the fluorescent screen, and on the quality of the optical system imaging the screen. In other words, it depends on the resolution of the full system (pinhole, screen, lens, CCD), and on the quality of the image of the beam. In our case, using the $CdWO_4$, or the P43, the resolution is of the order of 25 μm, and the minimum flux (10^6 photons/s) to make a good image is reached at less than 1 mA. This will allow us to measure the electron beam transverse size with less than 1 % error [3].

Knowing the electron beam size and the Twiss parameters allows to calculate its emittance and energy spread. We need to estimate the error due to the uncertainty in the beam size and in the Twiss parameters. To estimate

the error due to the Twiss parameters we used a statistical approach. Firstly, we generate a distribution set for the Twiss parameters, where the r.m.s values give the incertitude. With the Twiss parameters distribution and using a given energy spread and emittance, we generate then a distribution set of sizes. Finally, we use the set of sizes to recalculate the energy spread and emittance with a least squared method and taking the nominal Twiss parameters. The incertitude in the measure is given by the comparison between the standard deviation of the emittance and energy spread distribution, compared with the nominal values. Table 2 summarises the results.

CONCLUDING REMARKS

This paper presents the design of the pinhole camera for DIAMOND. The system is expected to measure with a very good accuracy the beam size of the order of 25 by 50 (μm), with 1 mA and above current stored in the ring. For that, the optimum X-ray beam flux have been is reached with a 1 mm thick Al window to extract the beam from vacuum to air. The window is robust, passively cooled in air, and is able to sustain the heat-load from the X-ray beam, and the pressure difference.

The image of the beam is obtained with a fluorescent screen combine with a macro-lens and a 'firewire' CCD camera. The best screens identified so far are P43 and $CdWO_4$. They have the best conversion rate, which provides a good quality image at 1 mA and above, and the best resolution. P43 has the best screen resolution (10 μm) whereas $CdWO_4$ has the best conversion rate. We will use these two complementary screen.

In addition, we computed the error in the calculation of the energy spread and the emittance of the electron beam. This computation shows that the Twiss parameters have to be known at better than 1%.

REFERENCES

[1] R.P. Walker. Progress with the Diamond Light Source. In *Proc. of EPAC 2004, (Luzerne)*, page 2433, June 2004.

[2] P. Elleaume, C. Fortgang, C. Penel, and E. Tarazona. Measuring beam sizes and ultra-small electron emittances using an X-ray pinhole camera. *J. Synchrotron Rad.*, 2:209, 1995.

[3] Thomas, C. A. and Rehm, G. DIAMOND Storage Ring Optical and X-ray Diagnostics. In *Proc. BIW 2004*, Knoxville, Tennessee, 2004.

Table 1: Aluminum 6061 properties (Source from http://www.matweb.com)

Mechanical Properties	
Tensile Strength, Ultimate	310 MPa
Tensile Strength, Yield	275 MPa
Elongation at Break	12 % - In 5 cm; Sample 1.6 mm thick
Fatigue Strength	95 MPa - 500 10^6 Cycles
Thermal Properties	
Heat Capacity	0.896 J/g °C
Thermal Conductivity	166.9 W/m K
Melting Point	582 - 652 °C

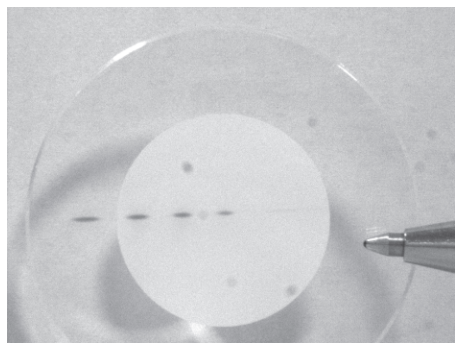

Figure 5: Picture of the P43 screen, from the back, showing the darkening of the glass substrate, image of the 4 pinholes. The glass was exposed for one hour in the ESRF beam.

Table 2: Estimation of the errors vs. the uncertainties on the Twiss parameters (error); we show the relative difference between the initial values and the mean values of the calculated distribution sets of relative energy spread and emittance ($\Delta\sigma_{\epsilon,0}$ and $\Delta\epsilon_0$); the relative uncertainties on the final result ($\Delta\sigma_\epsilon$ and $\Delta\epsilon$) are given by the standard deviation of the distributions.

error	$\Delta\sigma_{\epsilon,0}$	$\Delta\epsilon_0$	$\Delta\sigma_\epsilon$	$\Delta\epsilon$
0.01	0.002	0.001	0.035	0.034
0.05	0.003	0.013	0.164	0.181
0.1	0.067	0.060	0.387	0.358

OPERATIONAL EXPERIENCE WITH BEAM ALIGNMENT AND MONITORING USING NON-DESTRUCTIVE BEAM POSITION MONITORS IN THE CYCLOTRON BEAMLINES AT ITHEMBA LABS *

J. Dietrich, I. Mohos, Forschungszentrum Jülich, Postfach 1913, D-52425 Jülich, Germany
J.L. Conradie, Z. Kormany, P.F. Rohwer, P.T. Mansfield, D.T. Fourie, J.L.G. Delsink, M. Sakildien, A.H. Botha, iThemba LABS, P. O. Box 722, Somerset West 7130, South Africa

Abstract

At iThemba LABS proton beams, accelerated in a K=200 separated-sector cyclotron with a K=8 solid-pole injector cyclotron, are utilized for the production of radioisotopes and particle radiotherapy. Low-intensity beams of light and heavy ions as well as polarized protons, pre-accelerated in a second injector cyclotron with a K-value of eleven, are available for nuclear physics research. Beam position monitors and associated computer-controlled electronic equipment have been developed for non-destructive alignment and continuous display of the beam position in the beam lines for the more intense beams used for therapy and the production of radioisotopes in cooperation* with Forschungszentrum Jülich. The monitors consist of four-section strip lines. Narrow-band super-heterodyne RF electronic equipment with automatic frequency and gain control measures the signals at the selected harmonic. A control module sequentially processes the signals and delivers calculated horizontal and vertical beam position data via a serial network to the computer control system. Eleven monitors have been installed in the beam lines. Operational experience with alignment and monitoring of the beam position is discussed.

BACKGROUND

The design and implementation of a prototype non-destructive beam position monitor and associated electronic module for signal processing in beam lines at iThemba LABS [1] have been reported before [2]. Since then eleven monitors and electronic modules have been manufactured. Four of these monitors, which have been planned for beam intensities of one μA and more, have been installed in the transfer beam line between the light-ion injector and the separated-sector cyclotron and the remaining ones in the high-energy beamlines leading to the neutron therapy and isotope production vaults. The main design considerations and limitation for the monitors, which should measure the beam position in both the horizontal and vertical directions, are that they have to be installed through the beam ports of the diagnostic vacuum chambers in the beam lines and fit into the available space together with the existing other diagnostic components. Since the cyclotrons are in operation for 24 hours per day and seven days a week the diagnostic chambers could not be removed for machining of additional flanges. The electronic modules were designed and built at the Forschungszentrum Jülich-IKP, as part of the work done under a scientific and technological agreement between Germany and South Africa.

*Supported by BMBF and NRF, project-code 39.1.B0A.2.B.

THE POSITION MONITOR

The four electrodes of the monitors are mounted co-axially inside a cylindrical copper housing as shown in Fig. 1. Although the prototype monitor, described before [2], could fit in the diagnostic vacuum chambers installation of the semi-rigid cables inside some of the chambers was difficult. In the final design the overall length of the monitors is therefore 15.5 mm shorter than before and have the dimensions shown in Fig. 1. The length of the electrodes, which are connected through 50 ohm resistors to ground inside the vacuum chambers, remained the same as before.

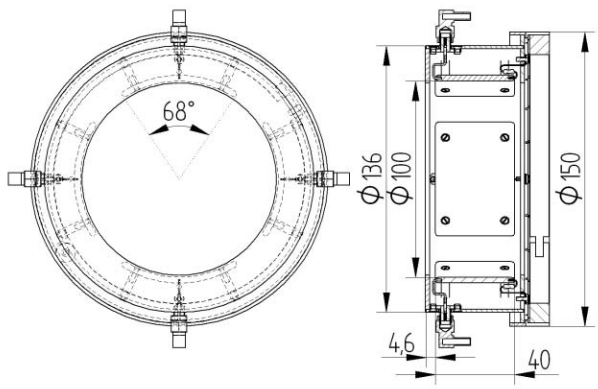

Figure 1: Front view and cross-section drawings of the beam position monitor with 50 ohm terminations on the electrodes.

ELECTRONIC SIGNAL PROCESSING

A block diagram of the electronic equipment used for signal processing of each of the eleven monitors is shown in Fig. 2. A GaAs RF multiplexer switches the monitor signals to the input of the common signal chain. In each acquisition cycle the four signals are sequentially measured before the position data are computed. The RF part, consisting of narrowband super-heterodyne RF electronics, processes the monitor signal components at the selected higher harmonic of the cyclotron RF frequency. The center frequency is programmable between 49 and 82 MHz. Automatic frequency and gain

control tracks the signal changes. The overall bandwidth can be set in 12 steps between 0.18Hz and 1kHz by means of analogue BPF and digital FIR filters. A micro-controller controls the tuning, measuring and filtering functions according to the remotely set parameters. The non-linearity in the strip-line pickup is corrected for each position readout using a 2D stored array, determined by calibration of the monitor on an xy-table with the beam simulated by a conducting rod with an RF voltage applied to it.

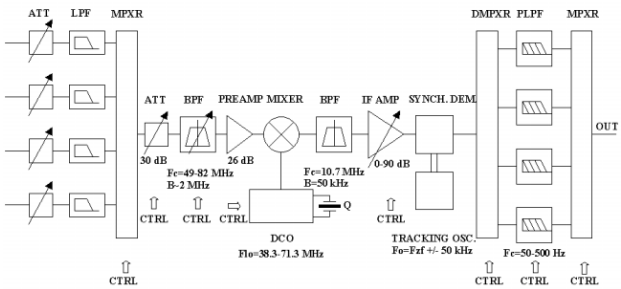

Figure 2: Block diagram of the electronic equipment for signal processing.

HARDWARE IMPLEMENTATION

To avoid radiation damage from the beam the electronic modules were placed outside the cyclotron and beam line vaults. Cable lengths were kept as short as possible by putting each module into the nearest electronic area. As a result, the BPM-stations were arranged in two groups: four units for the monitors in the transfer beam line in the low-energy electronics area and seven units for the monitors in the high-energy beam lines in another electronics area close by. The distance between the two groups is about 50 m.

The electronic modules are equipped with CAN-standard signal interface and use a dedicated serial protocol. They are connected to the serial port of the control computer with a CAN/RS232 converter. Due to the total length of the serial cable an additional bus driver was also installed. All these units with the control PC were placed in the low-energy electronics area.

ELIMINATION OF INTERFERENCE AND SENSITIVITY

Pickup on the electrodes of the beam position monitors at the fourth harmonic of the main RF systems and the second harmonic of the rebuncher, at which it was initially planned to use the monitors could be reduced to below –135 dBm, a level that can also not be detected by the electronic equipment, using cables with solid outer conductors and by proper tightening of the connectors with a wrench, even for monitors installed a few cm away from the rebuncher.

In the diagnostic chambers in which profile grid monitors (harps) are situated RF is introduced into the chambers through the large number of cables connected to the harp wires, leading to pickup on the beam position monitors. The pickup could be eliminated by connecting resistors in series with the harp wires directly outside the chambers to form RC filters with the 30 pF stray capacitance of each harp wire connection inside the chamber.

The slightly wider frequency range than originally planned, in which the electronic equipment can work, also allows the use of the fifth harmonic (81.85 MHz) for the 66 MeV beam. For the 200 MeV beam the third harmonic (78.3 MHz) is used. No pickup could be detected at these harmonics with a spectrum analyzer or the signal processing electronics.

The signal strengths at the input of the electronic equipment are –90 dBm for 1 µA in the transfer beam line and –107 dBm in the high-energy beam line. In the transfer beam line beam alignment worked well at proton beam currents as low as 40 nA, whereas in the high-energy lines beam currents of the order of 700 nA have to be used for alignment. For heavy beams, which move much slower, the charge density in Coulomb per meter in the beam packets is higher and the packets shorter resulting in greater sensitivity of the monitors. A 170 nA beam of 90 MeV carbon ions could be aligned with the monitors in the high-energy lines. By using a monitor without the 50 ohm resistors on the electrodes in the diagnostic vacuum chambers the sensitivity could be increased by a factor of almost two.

SOFTWARE FEATURES

Server-client architecture was chosen for the control programs to provide sufficient flexibility in development and operation. The server that runs on the control PC is the only program that can control the BPM-stations. A driver library was written for the server to perform the low-level communication with the control registers of the modules. The main tasks of the server program are:

1. Checking the status of the stations. It detects any newly connected or disconnected station on the bus. The updated list of the properly operating stations is sent to all clients.
2. Initialization of all available stations according to the actual value of the RF and the harmonics used for the position measurement.
3. Reading measured signal values regularly from those stations that are requested by any client and sending calculated position data to the appropriate client.
4. Forwarding control commands from any client to the requested BPM-station.

Two clients have been developed so far. The first one can be used for the control of a single BPM. It displays the position of the beam centre as measured by the selected monitor in the xy-plane, and displays the distribution of the measured horizontal and vertical position values as well. This client can connect to any BPM, even if the monitor is in an unused beam line or the

beam is stopped at an upstream Faraday cup. This way it can also be used for noise and accuracy test measurements.

The second client works only with monitors installed in the actually used beam line. It gives an overall view about the transport of the particle beam along the line by depicting the measured positions at all monitors and connecting these points with a straight line both in horizontal and vertical planes. The resulting central-trajectory-like curves provide a very good visual measure of beam line settings, displaying the propagation of beam offsets along the transport system. A typical picture of this client is shown in Fig. 3.

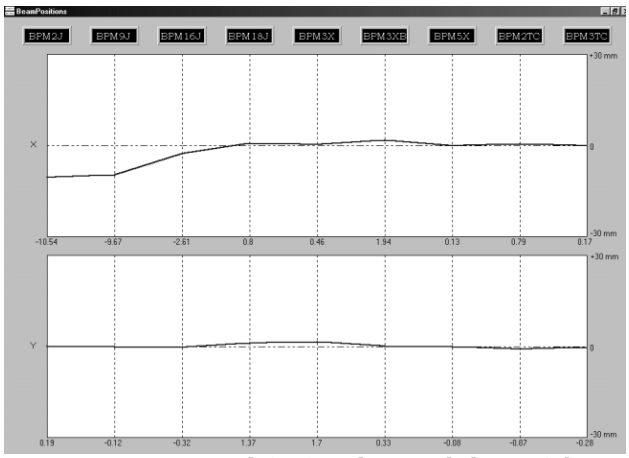

Figure 3: Horizontal (top) and vertical (bottom) beam positions measured along the beam lines from the injector cyclotron to the therapy vault in the high-energy beam line. The scale ranges are from minus to plus 30 mm. Directly downstream from the injector cyclotron the beam is about 10 mm off center in the horizontal direction.

BEAM ALIGNMENT

There are four sections in the beamlines where the arrangement of two BPMs and two steerer magnets can be used for automated beam alignment. This feature has been added to the second client. When using this option, the client program reads the positions measured by both monitors and the actual current of the steering magnets as well. From these data a transcendental equation can be written with just one unknown variable – it is the angular divergence of the central particle at the entrance point of the alignment section. After solving numerically this equation, the required changes in the steerer currents can be calculated to align the beam with the beam line axis downstream of the second steerer magnet. The client then writes the new current values into the appropriate variables of the control system.

A typical result of the automated beam alignment is shown in Fig. 4, where the beam has deliberately been steered off center with a bending magnet upstream of the steering magnets and beam position monitors. The distributions of the measured position values are displayed for both monitors. As can be seen, the beam position at the second monitor (at the bottom), after the second steering magnet, is well centred on the axis. The beam position indications of the monitors agree with those of the harps in the same diagnostic chambers.

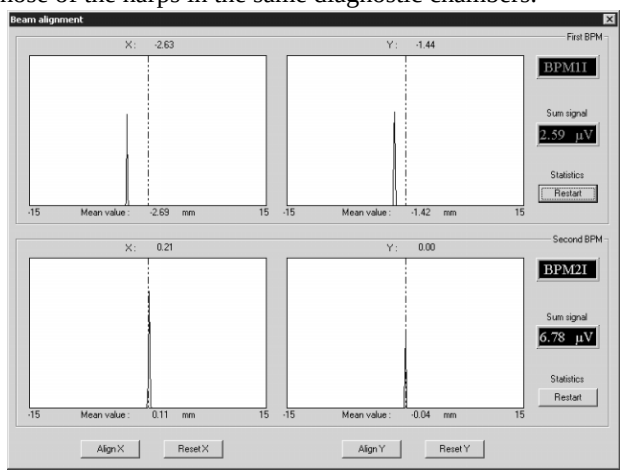

Figure 4: The user interface displayed for beam alignment. The aligned beam is centred at the second (bottom) BPM. The scale ranges are from minus to plus 15 mm.

CONCLUSIONS

Automatic alignment of the beam without mechanical insertion of beam intercepting diagnostic devices and continuous display of the beam position throughout the facility, as well as the fact that the effect of an adjustment to a cyclotron or beam line parameter on the beam position can be directly observed throughout the downstream part of the beam lines, proved to be very useful in the day-to-day operation of the beam lines. Beam alignment can now also be done at high intensities, thereby reducing beam losses and activation of components, since the beam center depends to some extent on the slit settings. Fast variations in the beam position, due to instabilities, could previously not be detected with the harps because of the slow electronic equipment used for current measurement. With the beam position monitors such variations can be instantaneously observed. For these reasons it is planned to install more monitors in the beam lines. The possibility of using the same electronic modules for different monitors by multiplexing between beamlines that are not simultaneously in use will be investigated.

REFERENCES

[1] J.L. Conradie et al, Cyclotrons at iThemba LABS, Proc. of the 17th Int. Conf. on Cyclotrons and their Applications (Cyclotrons'2004), Tokyo, October 2004, to be published.

[2] J. Dietrich et al, Beam Position Monitor Development for iThemba LABS Cyclotron Beam Lines, EPAC'2004, Lucerne, July 2004, p.2589.

PERFORMANCE VERIFICATION OF THE DIAMOND EBPM ELECTRONICS

G. Rehm, M. Abbott
Diamond Light Source Ltd., Rutherford Appleton Laboratory, UK

Abstract

The Electron Beam Position Monitor electronics for Diamond are a newly developed product. As such, extensive testing was carried out as part of the acceptance tests. These tests included measurement of the resolution, beam current dependence, fill pattern dependence, temperature dependence and long term reproducibility in the lab. A setup of signal generators was chosen to simulate the signals from button pickups as realistically as possible. Additionally, tests have been carried out with "real beam" signals at the SRS in Daresbury. Solutions for problems identified during these tests have been developed and their suitability is demonstrated.

INTRODUCTION

Diamond will incorporate 202 *Libera* beam position processors from Instrumentation Technologies for use in the transfer lines, booster and storage ring. The specifications required the resolution to be measured for a range of beam currents and for different acquisition bandwidths and data rates to cater for fast feedback (FFB) and turn-by-turn (TBT) applications (see table 1). Additionally, any systematic offset of the beam position reading correlated with the beam current had to be recorded and within the given limits.

The resolution and beam current dependency test are carried out as part of the factory acceptance test. They were repeated for a sample of the delivered units and additional long term tests were conducted.

LAB TEST SETUP

To facilitate parallel tests of 6 sets of BPM electronics in the lab they were put in one rack and connected to an RF signal generator (Rohde & Schwarz SML01, $f_{RF} = 499.654$ MHz) through a network of power splitters. Additionally, an arbitrary waveform generator (Agilent 33250A) simulated the 2/3 fill of the storage ring by producing a $f_{rev} = 533818$ Hz with 66% duty cycle and delivering this to the fast gate input of the RF generator. This signal was also sent to a custom built trigger fan-out unit, which provided it as machine clock to the BPM units. To phase lock RF and machine clock as well as to ensure frequency stability during long term tests, both generators had their 10 MHz reference inputs connected to a Stanford FS725 rubidium standard. BPMs and the RF generator were connected to Ethernet so that all tests could run completely remote controlled.

Table 1: Specified r.m.s noise and beam current dependence on position readings for different sample rates and beam current ranges

	resolution@bandwidth		beam current
beam current	2 kHz	266 kHz	dependence
60-300 mA	0.3 μm	3 μm	1 μm
10-60 mA	0.6 μm	6 μm	50 μm
1-10 mA	1.5 μm	15 μm	100 μm

DEGRADED RESOLUTION DUE TO HARMONIC FOLD BACK

During the initial resolution tests a strange phenomenon was noted. As long as the sampling frequency of the ADCs is free running, the results are as expected. However, as soon as the machine clock is supplied and the frequency locked loop (FLL) sets the sampling frequency $f_S = 220 f_{rev} = 220/936 \cdot f_{RF}$, the noise on the position readings increases by a factor of 3-5.

An understanding of this phenomenon requires a look at the processing chain (see figure 1). The source for this behaviour is some nonlinearity in the ADCs. This nonlinearity creates the third harmonic of the input signal. In the digital domain, the signal is at $56 f_S$, so the third harmonic will be folded back to $(220 - 56 \cdot 3) \cdot f_S = 52 f_S$. Here, the third harmonic would still be filtered out by the decimation filters in the digital down converter (DDC). However, with the fill pattern square wave modulation at f_{rev}, the signal as well as its third harmonic, carried sidelines at $\pm n \cdot f_{rev}$. The forth sideline of the third harmonic will then come to lie at $56 f_S$, which is the signal frequency. As the FLL locks the VCXO within about 1 Hz, the third harmonic signal will move around and depending on the individual nonlinearities of the four ADCs, create a position fluctuation.

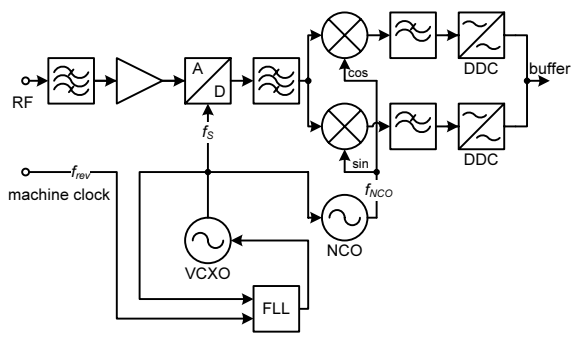

Figure 1: Simplified processing chain for one channel

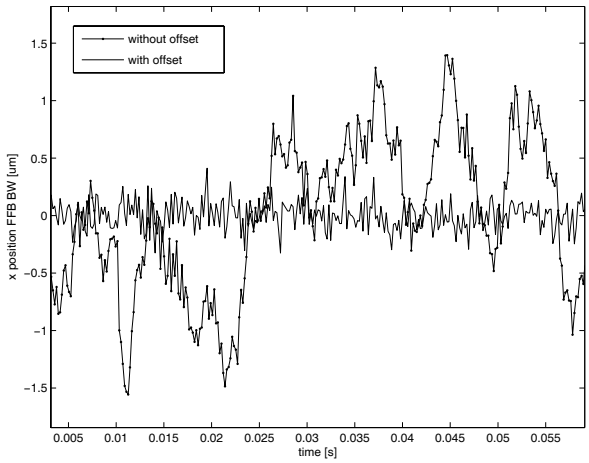

Figure 2: Reduction of position noise by applying an offset to the sampling frequency

The solution to the problem is to offset the VCXO slightly, that is to make $f_S = 220 f_{rev} + f_{offset}$. A few kHz offset are enough to move the detrimental effect of the third harmonic outside the FFB bandwidth. This offset will translate to the signal frequency in the digital domain and is then be corrected by also offsetting the NCO by the same amount. By doing this, the filters in the DDC need not be adjusted. Figure 2 shows a position reading without this offset and after applying the VCXO and NCO offsets.

RESOLUTION MEASUREMENTS

In the lab, the variation of beam current is simulated by changing the power of the RF generator accordingly, taking losses in the power splitter network into account. It has been calculated from the pickup geometry and the cable losses that a continuous (that is un-gapped) stored current of 300 mA would provide a power of -8 dBm to the input of the BPM. However, the peak current at 2/3 fill is 450 mA so the RF generator needs to provide -4.5 dBm peak power to each input of the BPM electronics. All data reproduced in this report has been measured with 2/3 fill and this conversion can thus be applied at all times.

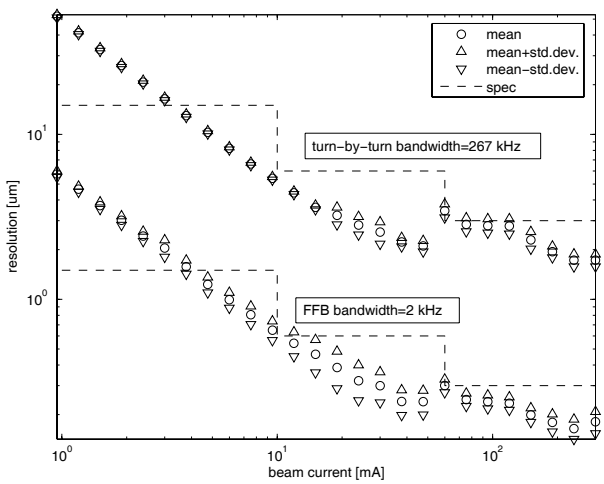

Figure 3: Statistics of resolutions from 48 units

Figure 3 shows the statistics of 48 units measured at DLS. It can be seen that the resolution specifications were met for both bandwidths and for all currents above 4 mA. At this level, thermal noise is the dominant noise source and the "attenuator reserve" has been used up. As a result the product of beam current and resolution is constant. However, no operational implications for Diamond are foreseen due to this, as the FFB is not intended to be operated at such low beam currents.

BEAM CURRENT DEPENDENCE MEASUREMENT

The position reading of a BPMs should ideally be independent of the beam current. With parallel processing channels, unequal nonlinear response or unequal attenuator steps of the individual channels lead to a position offset as a function of beam current. The crossbar multiplexing of *Libera* should eliminate this effect [1].

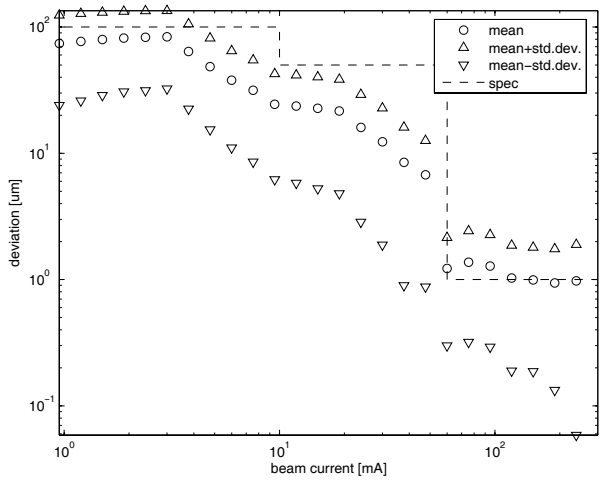

Figure 4: Statistics of beam current dependence from 48 units

Figure 4 shows that on average the goal of a maximum of 1 μm position offset for beam currents between 300 mA and 60 mA has been met. However, that also means that half of the tested units actually showed a higher beam current dependence (up to 2-3 μm). This deviation should be reduced through ongoing efforts to incorporate signal conditioning in the digital signal chain, which will implement linearisation, cross talk compensation and channel to channel phase equalisation.

TEMPERATURE DEPENDENCE

The temperature dependence of the position reading has been investigated by measuring it at different power levels and slowly changing the environmental temperature of the BPM electronics. Temperature coefficients have

Table 2: Statistics of temperature dependence coefficients [μm / °C] for 6 units

	100 mA		10 mA		1 mA	
Unit	x	y	x	y	x	y
5	0.10	0.07	1.7	0.7	3.9	2.8
8	0.12	0.20	1.7	2.4	3.3	7.7
12	0.19	0.01	2.9	2.3	7.7	7.3
14	0.16	0.06	2.4	2.0	5.8	6.3
16	0.13	0.05	4.1	2.1	12	5.5
20	0.15	0.13	2.4	1.8	5.5	5.0
μ	0.114		2.21		6.07	
σ	0.058		0.81		2.47	

been retrieved using linear regression. Table 2 shows a systematic trend of increased temperature dependency at lower simulated beam currents.

LONG TERM STABILITY TEST

The test rack was installed in a temperature controlled environment ($\pm$1°C). A script controlled the RF generator to set different power levels and retrieved the position data from all 6 BPM units. This setup was left to run for 30 days. After some initial dropout due to problems with the BPM internal software and the temperature control of the room, a continuous 21 day run has been achieved. Overall, virtually no drift of the position reading could be observed during this long term test (see figure 5).

"REAL BEAM" TESTS AT THE SRS

One *Libera* has been installed at the SRS in Daresbury. It has been running continuously for 50 days now. Two ways of collecting data are available at the moment: on the one hand, a script can be executed to store the current position readings in a file at an interval (some seconds). On the other hand, an EPICS driver can be started so that data

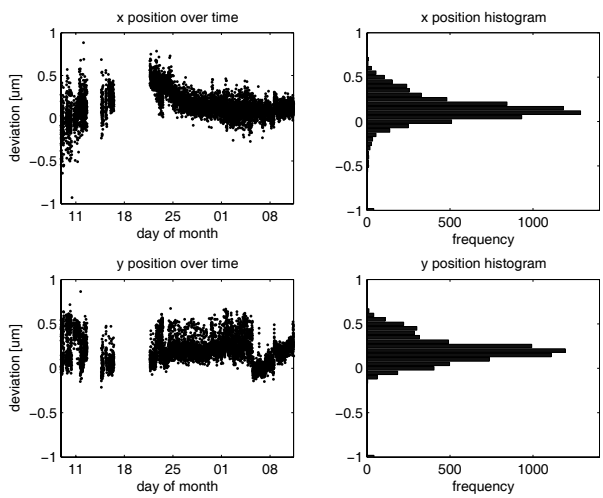

Figure 5: Position stability during one month

can be read directly using Channel Access, for instance into Matlab.

Using the first method, the beam current decay and beam motion during a day has been visualised in figure 6. The second method has been used to capture the kick of the beam during injection (the pickup is within the injection bump). Figure 7 shows the position oscillation and spectrograms which indicate the horizontal and vertical tunes.

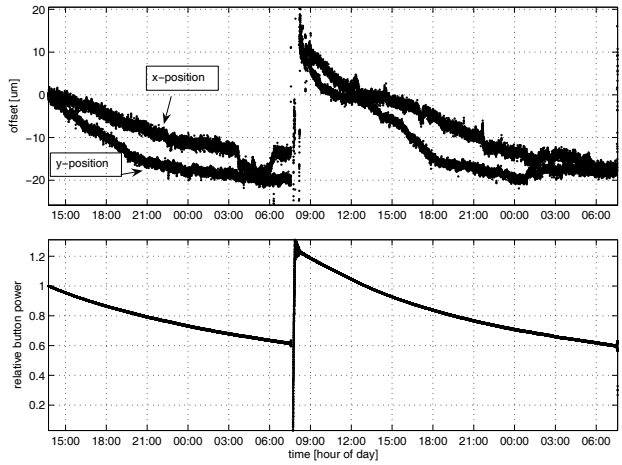

Figure 6: Motion of the beam during decay of the beam current at SRS

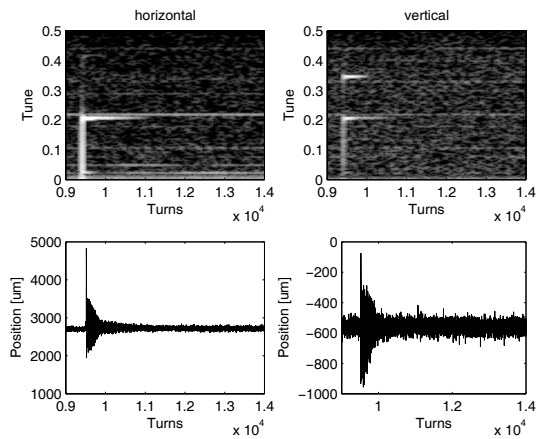

Figure 7: Tune measurement from TBT data of an injection kick

ACKNOWLEDGEMENTS

The authors would like to thank Rob Smith (SRS Daresbury) and the team at Instrumentation Technologies.

REFERENCES

[1] U. Mavric, "Innovative RF Design Unites Benefits of Multiplexed and Multichannel System", in *Proceedings of the 11th Beam Instrumentation Workshop Knoxville 2004*

HIGH DYNAMIC MAGNETIC BEAM CURRENT MEASUREMENTS BY MEANS OF OPTIMISED MAGNETO-RESISTANCE (MR) SENSOR ENGINEERING

Markus Häpe, Wolf-Jürgen Becker, Werner Ricken, University of Kassel (UNIK), Germany
Andreas Peters, Hansjörg Reeg, Piotr Kowina, GSI Darmstadt, Germany

Abstract

A new sensor for the beam current measurement is under design at the department of Measurement Engineering at University of Kassel and GSI Darmstadt. An overview of the commercial available magnetic sensors like AMR- (anisotropic magneto-resistance) and GMR- (giant magneto-resistance) sensors and also the new magnetic GMI-effect (giant magneto-impedance) is given. These sensors have been investigated for their suitability for the clip-on ampere-meter. The results will be discussed and an outlook for further development will be presented.

BASIC IDEA

The GSI-FAIR project (facility for antiprotons and ion research) will comprehend DC currents up to around 1.2 A in the SIS 100 synchrotron and after bunch compression down to 30 ns pulse length the peak currents will reach up to 200 A.

The current measurement device itself will be designed in form of a clip-on ampere-meter, see Figure 1.

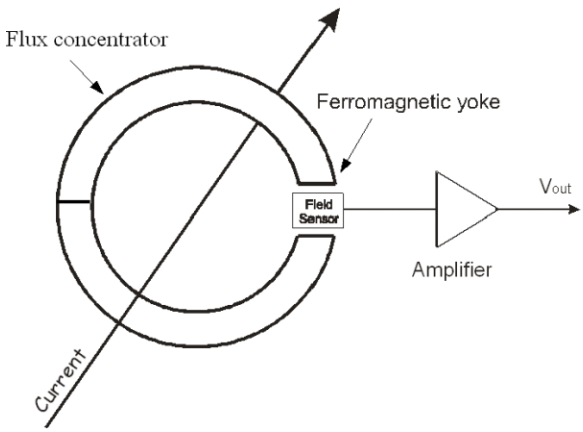

Figure 1: The open loop sensor

This configuration would have big advantages in contrast to a normal DCCT, because it can be dismounted without opening the vacuum due to its separable core. An alternative to a DCCT was looked for because of their problems with the high peak current in the bunch structure of 1 MHz up to 5 MHz. This difficulty was discussed at the 2nd CARE-HHH-ABI-meeting in Lyon end of last year, see Ref. [9] for more details.

To meet the challenging demands of beam current measurements – high dynamics, large current peaks – at the SIS100 new sensor techniques are foreseen, which will be reviewed in this paper.

SIMULATION OF THE MAGNETIC FLUX CONCENTRATOR

The flux concentrator consists of soft-magnetic VITROVAC 6025F. The air gap of the flux concentrator is assumed to be around 5 mm, the inner diameter to be 200 mm (cf. Figure 1). The contour plot of the absolute values of the magnetic flux for an excitation current of 10 A is shown in Figure 2. The simulation has been carried out at GSI.

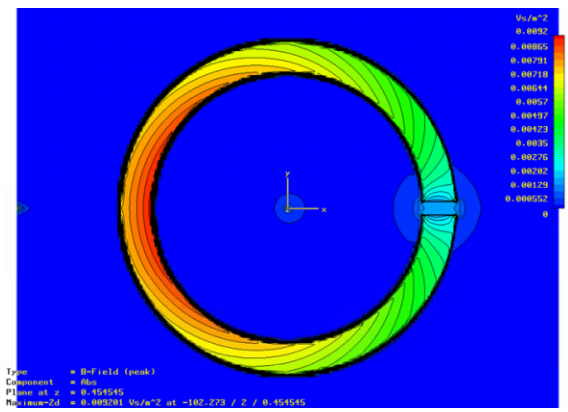

Figure 2: Contour plot of the magnetic flux

The estimated maximal field in the gap is derived to be around 27.4 mT for a beam current of 200 A peak, whereas the magnetic field in the core still keeps away from saturation. The resolution of this device is aimed to be 1 mA (corresponding to only 137 nT in the gap) in beam current, corresponding to a system dynamic of around 106 dB ($2*10^5$). The results of the magnetic flux simulation deliver the input data for the sensor parameters – the range of the detectable fields can only be influenced by the material choice and geometry optimisation.

PRINCIPLE INVESTIGATIONS ON MR-SENSORS

The characteristics like hysteresis, linearity and sensitivity of commercial AMR- and GMR-sensors as well as a GMI prototype sensor have been measured within the magnetic field of Helmholtz coils in a range of +/-4 mT at UNIK (see Figure 9).

The lowest detectable value (S/N) must be determined. Therefore the 1/f-noise, the Barkhausen noise and the thermal noise from the different sensors and the flux concentrator need to be investigated.

AMR- AND GMR-SENSOR CHARACTERISTICS

Five AMR-sensors have been tested, integrated within different external electrical circuits. Modern sensors from Honeywell and HL PLANAR use a set- or reset-pulse to measure correctly. The sensors from Philips use a stabilisation field. The investigated AMR-sensors are:

Honeywell: HMC1001
HL PLANAR: KMY20S, KMY20M
Philips: KMZ10A, KMZ43T

All these AMR-sensors were based on AMR-stripes with barber pole structure (Figure 3).

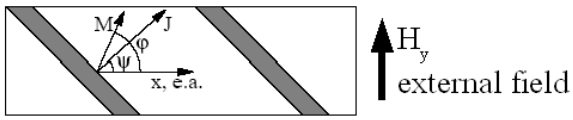

Figure 3: AMR-stripe with barber pole structure [3]

The measured characteristic for the HMC1001 is shown in Figure 4.

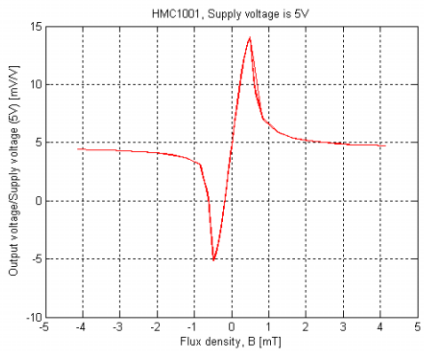

Figure 4: Measurement characteristics of HMC1001

Until now, one GMR-sensor, type NVE AA002 was measured. The multip-layer-structure of such a device is shown in Figure 5, the measurement of its characteristics in Figure 6.

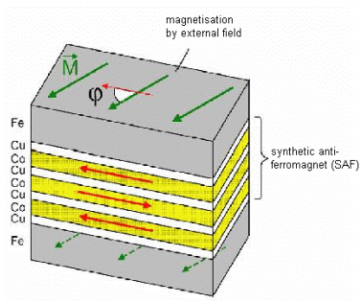

Figure 5: Structure of a GMR-multi-layer sensor [5]

The reproducibility of the measured characteristics in Figure 4 and Figure 6 as well as comparable results in comparison to the data sheets was given. Nevertheless, some measurement problems can occur when using the sensors. The usage of the stabilisation fields, set- and reset-pulses and the needed precision of the orientation in the gap of the clip-on ampere-meter can have effects on the reproducibility of the measured values.

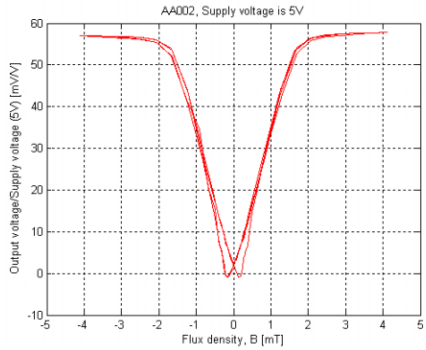

Figure 6: Measurement characteristics of AA002

The measuring range, sensitivity and hysteresis of the investigated sensors were nearly the same as from the datasheet. Therefore only the results of one AMR- and one GMR-sensor are shown:

Sensor	Measuring range	Sensitivity	Nonlinearity	Hysteresis
HMC1001 AMR [1]	±0,2 mT	$25\ldots40\ \frac{V/V}{T}$	1%	0,05%
AA002 GMR [2]	1,05 mT	$30\ldots42\ \frac{V/V}{T}$	2%	4%

Table 1: Table technical data from data sheets [1, 2]

The bandwidth and the dynamics of the commercial sensors are not well published from the manufacturers. Therefore we have to investigate these parameters with a special simulator in the next step.

GMI-PROTOTYPE SENSOR

Up to now commercial giant magneto-impedance (GMI)-sensors are not available. Therefore a GMI-prototype sensor was constructed at UNIK (Figure 8).

GMI is another magneto-inductive effect observed in soft ferromagnetic metals. The ac impedance in a GMI-element has a strong dependence on the applied magnetic field [6 - 8]. This is shown in Figure 7. The effect occurs at high frequencies and can be explained by classical electrodynamics.

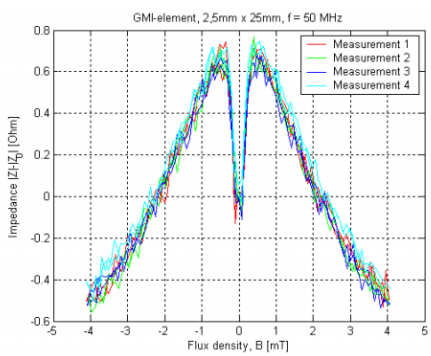

Figure 7: Measurement characteristics of GMI [7], the impedance $|Z_0| = 24.3\ \Omega$.

Radio frequency (RF) current is not homogeneous over the cross section of a conductor (skin effect). The skin depth $\delta = \sqrt{(2 \cdot \rho)/(\omega \cdot \mu)}$ describes the exponential decay of the current density from the surface towards the interior of the conductor. It depends on the circular frequency of the RF current ω, the resistivity ρ, and the permeability μ. In ferromagnetic materials the permeability depends on the orientation of a bias dc magnetic field, the amplitude of the ac magnetic field and the frequency. The high permeability of the soft magnetic metal and its strong dependence on the bias magnetic field are the origin of the GMI effect. At frequencies above 1 MHz, eddy currents heavily damp the domain wall movements, and only magnetization rotations are responsible for magnetic permeability [8].

The prototype sensor itself is a magnetic controlled oscillator that uses the GMI-effect to tune the oscillator's frequency. It is shown in Figure 8.

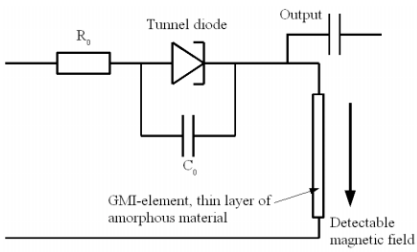

Figure 8: Principle structure of the sensor [6, 7]

The frequency components of the oscillator were measured with a spectrum analyser in the simulation device with Helmholtz coils (Figure 9).

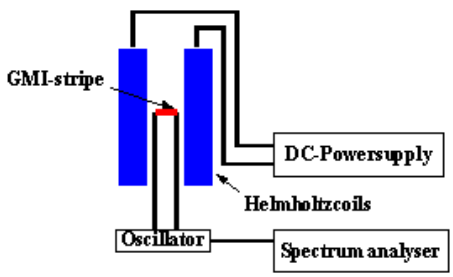

Figure 9: Principle structure of the measuring system with the MCO and spectrum analyser

The measurement characteristics for the GMI-prototype sensor is shown in Figure 10. This investigations have shown that the GMI-stripe is suitable for measurements within a range of ±1 mT. The frequency modulation caused by GMI achieves a peak frequency deviation of 1 MHz, resulting in a measured slope of around 2 GHz/T. The oscillator frequency is 113.1 MHz for this special set-up.

The curve progression from the measurement characteristics of the GMI-prototype sensor (Figure 10) and the GMI-element (Figure 7) are proportional inverted. This effect is given by the formula of the resonant frequency. If the impedance grows it reduces the oscillator frequency.

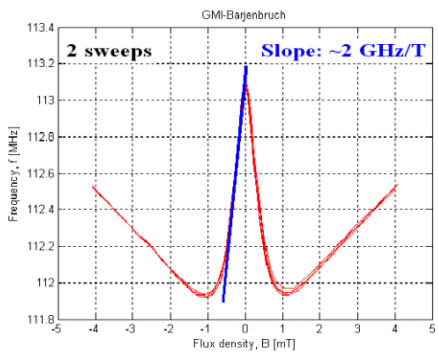

Figure 10: Measurement characteristics of the GMI-prototype sensor

CONCLUSION AND OUTLOOK

The measuring range of all investigated sensors is yet too small, while the resolution of all the investigated sensors is small enough to measure the required beam current of 1 mA. Furthermore other sensors with enhanced parameters must be looked for. Another possibility is to build the clip-on ampere-meter based on a compensation system.

The next steps will be investigations of the sensor parameters in high-dynamic magnetic fields. Therefore a simulation device will be constructed and intensive measurements will be carried out in the next months. In parallel, a first core arrangement will be set up.

REFERENCES

[1] Data sheet, Honeywell, HMC1001/HMC1002.
[2] Data sheet, NVE, AA002-AA006 Series.
[3] Ricken, Werner: *Wegmessung mit magnetoresistiven Sensoren*, Internal Paper, FB 16, Messtechnik, Universität Kassel, Februar 2001.
[4] Mengel, S.: *Technologie-Früherkennung, Technologieanalyse Magnetismus,* Band 2, XMRTechnologie, Hrsg.: VDI Technologiezentrum Physikalische Technologien, Düsseldorf, 1997.
[5] Gross, Rudolf; Marx, Achim: *Grundlagen der Magnetoelektronik - Vorlesungsskript zur Vorlesung im WS 2000/2001*, Walther-Meissner-Institut, Lehrstuhl für Technische Physik, Garching, 2000.
[6] Barjenbruch, Ullrich: *A novel highly sensitive magnetic sensor,* Sensors and Actuators A, 1993.
[7] Häpe, Markus: *Untersuchung des GMI-Effektes und Abschätzung dessen Nutzung zur Strahlstrom-Messung an einer Beschleuniger-Anlage*, Diploma Thesis, FB 16, Messtechnik, Universität Kassel, March 2005.
[8] Hauser, H.; Steindl, R.; Hausleitner, C.; Nicolics, J.; Pohl, A.: *Miniaturized Magnetic Field Sensors Utilizing GMI Effect and SAW Technology, Sensor & Packaging*, ÖVE, Wien, Austria, 2003.
[9] http://desyntwww.desy.de/mdi/CARE/Lyon/ABI-Lyon.htm

SCRAPING FOR LHC AND COLLIMATION TESTS IN THE CERN SPS

M. Facchini, C. Fischer, J.J. Gras, S. Hutchins, R. Jung
CERN, Geneva, Switzerland

Abstract

Scraping of the SPS beam prior to extraction towards the LHC will be important in order to remove the beam tails and ensure clean injection conditions. Scrapers recuperated from the ISR were installed in the SPS for this purpose. The scrapers are associated with a two stage collimation system using collimators previously installed in LEP to reduce the irradiated area in the SPS.

Tests have been performed to demonstrate that with the help of these collimators, it is possible to scrape with very little contamination outside the scraping area. Another issue was whether enough time is left for ejection towards the LHC after scraping, before repopulation of the removed tails. This was investigated with the SPS rest gas profile monitor and synchrotron radiation telescope.

The system is described and the results of these tests are presented and discussed.

INTRODUCTION

Scraping of the beam tails will be required in the SPS prior to extraction in order to maintain clean injection conditions into the LHC, hence avoiding the risk of quench in the cryo-magnets. One horizontal and one vertical scraper, recuperated from the ISR, are installed in the SPS and have been used for various tests. The questions addressed were whether enough time is available after scraping to extract before the tails repopulate and what is the achievable sensitivity of the process. The scrapers are associated with one horizontal and one vertical primary collimator installed at a phase advance of 90 degrees and complemented by two secondary collimators located again at 90 degrees from them. Each collimator consists of two moveable blocks. Photomultipliers and ionisation chambers are positioned close to the scrapers and collimators to watch the losses in comparison to the rest of the machine. Tests were also performed to try to confine the radiation induced from the scraping at these locations.

HARDWARE

Scrapers

A scraper consists in a moveable 30 mm copper jaw (Fig.1) activated linearly by a stepping motor and adjusted with a resolution of about 10 μm at a position which determines the amount of current scraped. It is then moved through the beam at a speed of 0.2 m/s by another stepping motor.

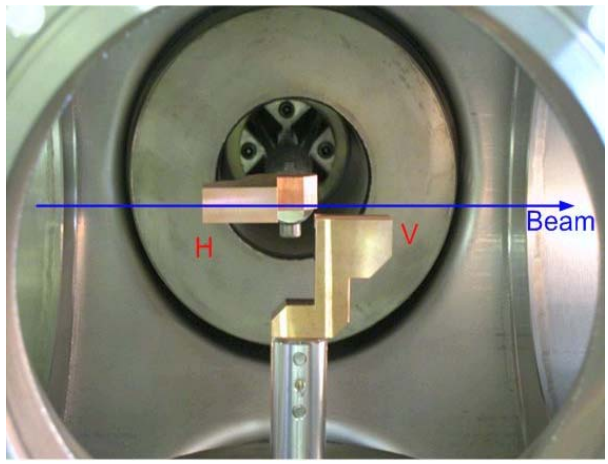

Figure 1: Side picture of the H and V scraper Cu jaws.

Collimators

Each primary collimator block is made of a 100 mm long tungsten core inserted within two transition end pieces made of copper, for RF loss minimization and heat extraction. A block has an overall length of 450 mm and can be positioned with a resolution of 5 μm [1]. The collimator blocks are aligned with respect to the beam axis with an rms precision of 0.1mm. Figure 2 shows a picture of the horizontal and vertical primary collimator assembly.

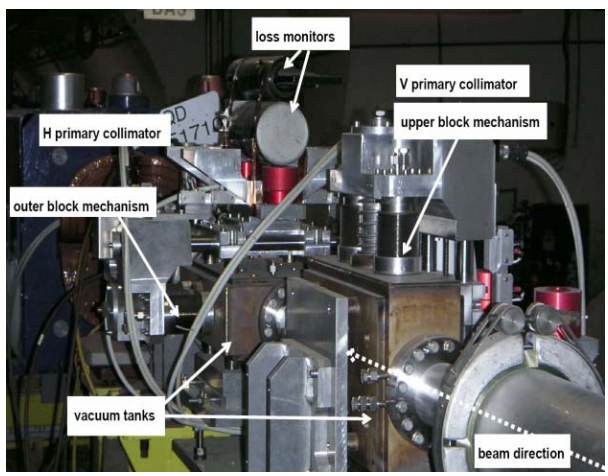

Figure 2: Horizontal and vertical primary collimator tanks and mechanisms with associated loss monitors.

The secondary collimator blocks have shorter copper transition pieces; their overall length is therefore reduced to 250 mm.

RESULTS

Rest gas monitor observations

The effect of scraping the vertical beam distribution was investigated with the SPS rest gas monitor [2].

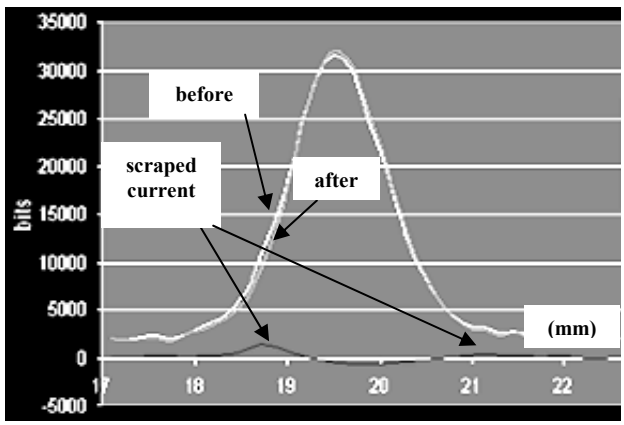

Figure 3: Results of scraping vertically 1% of the distribution of a beam of 2.6 10^{12} protons as seen by the Rest Gas Monitor.

Vertical beam distribution profiles integrated over 20 ms (800 SPS turns) are acquired every 40 ms with the SPS rest gas monitor. For this test the last profile measured before scraping, was compared to the profiles taken after. This was performed for various degrees of scraping, down to 1% of the circulating current, which is the resolution limit of the present current transformers. The results are presented in this last case in Figure 3, showing the distribution before and after scraping, The removed distribution (black curve), obtained by subtraction of these two profiles, although just emerging from the measurement noise, can still be appreciated for this level of scraping.

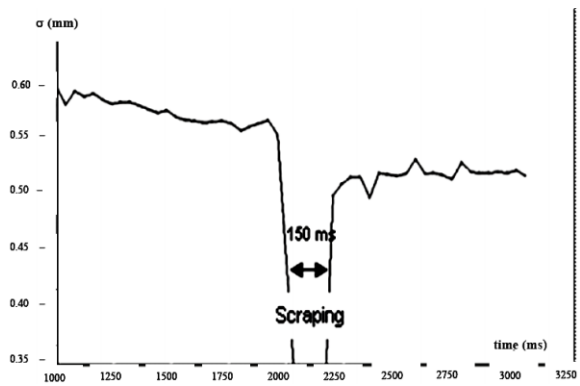

Figure 4: Recording of the vertical beam distribution rms value at a sampling rate of 25 Hz, before and after scraping 7% of the current.

The nominal SPS acceleration cycle to 450 GeV for the LHC ends up with a flat top of 1 second. Scraping lasts typically 100 ms, (Fig.4), on this flat top in order to overcome problems related to instabilities and orbit drifts occurring during the beam acceleration (Fig.5). A repopulation time of 100 ms or less would have been critical, as not enough time would have been left to proceed to the extraction towards the LHC. By increasing the flat top duration at 450 GeV to 2 seconds and by monitoring the beam distribution every 40 ms, the repopulation time constant was investigated. It could be verified that the reduction of the beam distribution rms value resulting from the scraping is kept for at least one second, as shown in Figure 4.

Synchrotron light telescope observations

The Synchrotron Radiation telescope uses the light emitted by the edges of two adjacent bending magnets. This light is extracted horizontally at 14m by a mirror into a telescope equipped with a Peltier-cooled CCD sensor. The CCD can either be operated in TV mode or in digital mode, where a fast projection scheme is available. In this mode, after a chosen integration time, the charges in the CCD are shifted down and compressed in the readout register, where the beam projection is available within 230μs. The register is read out after each projection operation and is digitised over 14 bits. The memory will contain 576 profiles after a sequence. It is a more robust but slower version of the instrument described in [3]. For the scraping application, the integration was chosen to be 5ms, and the acquisition sequence was started at the end of the acceleration ramp to 450GeV, which provided an acquisition time of ~3s covering the whole flat top, including the scraping operation. The CCD was oriented to provide the horizontal projections, complementing the rest gas monitor which measures vertical distributions.

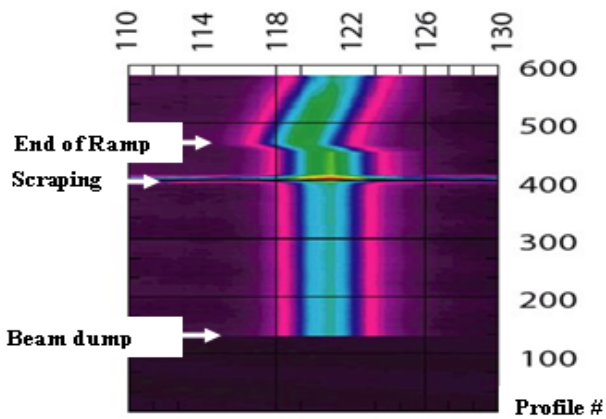

Figure 5: H profile sequence including a 30% H scraping as recorded by the CCD in projection mode.

A typical acquisition sequence is given in Fig.5. The sequence starts with profile #576 taken during the end of the energy ramp, where a position drift is observed. The scraping operation, which is clearly visible due to the production of secondary particles, takes place around profile #400, and is followed by a stable period until the beam is dumped around profile #110. The change in beam size before and after scraping is clearly visible on

this picture of a 30% scraping. To assess the effectiveness of the scraping and check the repopulation of the scraped tails, profiles were compared before and at different times after scraping.

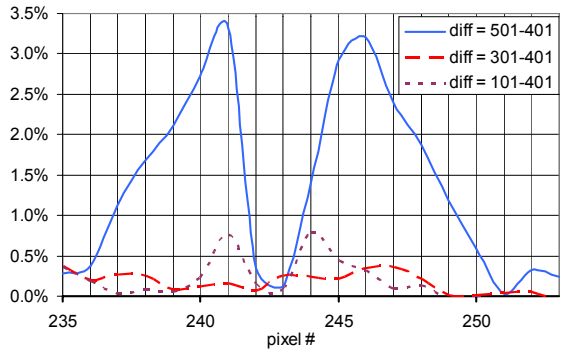

Figure 6: Effect of a 5% horizontal beam scraping as seen by the Synchrotron Radiation telescope.

Such a comparison can be seen in Fig. 6, taken for a 5% scraping and a 5ms integration time. The scraping took place at profile #420 and profiles were compared just before (#501) and just after (#401) scraping to assess the tail scraping effectiveness. To evaluate the tail evolution after scraping, profiles #101 and #301 where compared to profile #401. It can be seen that the tails were effectively scraped (501-401) and that a partial repopulation took place after a relatively long time, as small tails re-appear only after 300 profiles, i.e. 1500ms.

Collimation effectiveness

The achievement of clean scrapings with the help of the associated two stage collimation system was also investigated. The aim was to scrape while confining the losses at the scraper and collimator locations.

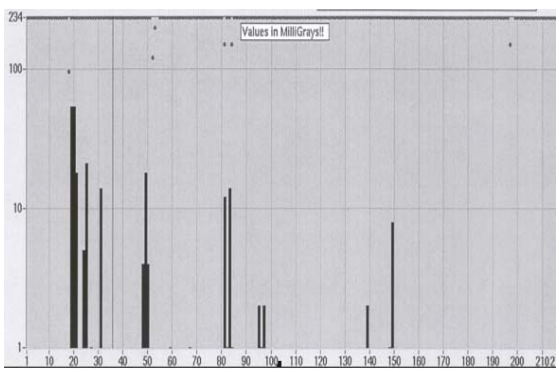

Figure 7: Loss monitor pattern around the SPS without scraping.

Beams of 3 10^{12} protons were injected, ramped in energy from 26 to 450 GeV and then scraped in the last 0.5 second of the cycle flat top. The vertical scraper position was adjusted to remove 10% of the current.

The primary horizontal and vertical collimator jaws were progressively moved IN by steps of 1 mm, and followed by their corresponding secondary jaw retracted by an additional 1 mm opening. During this exercise, the basic criterion was the reading of the beam loss monitors positioned all around the SPS circumference, Figure 7 and 8, trying to concentrate the losses at the scraper and collimator locations and to minimize them elsewhere.

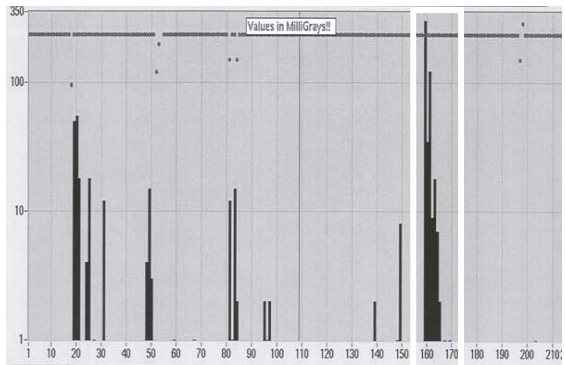

Figure 8: Loss monitors when scraping 10% of beam with collimators adjusted.

Figure 7 shows the loss distribution around the SPS during a normal cycle, without beam scraping. It can be observed by comparison with Figure 8 that additional losses resulting from the scraping are confined at the scraper and collimator locations, white rectangle, and that the loss pattern is unchanged outside these locations, demonstrating the effectiveness of the collimation.

SUMMARY

Scraping tests down to 1% of SPS beams accelerated to 450 GeV have been performed.

The repopulation time constant was measured to be longer than 1 second, long enough to ensure clean extraction conditions towards the LHC.

With a two stage collimation system associated with the scrapers, the radiation induced by the scraping is concentrated at the scraper and collimator locations, without irradiating other parts of the accelerator.

ACKNOWLEDGMENTS

It is a pleasure to acknowledge the help of Gérard Burtin for the preparation of the scrapers, collimators, and telescope and of Jean-Michel Vouillot for the fast projection camera design and data acquisition.

REFERENCES

[1] R. Jung, R. Perret, R. Valbuena: Design of a New Generation of Collimators for LEP 200, Proc. PAC 1993, Washington, DC, p. 2202-2204.

[2] C. Fischer et Al., Design and Tests of a New Rest Gas Ionisation Profile Monitor installed in the SPS, BIW04, May 2004, Knoxville, TE and CERN-AB-2004-031-BDI.

[3] R. Jung: Image Sensor Technology for Beam Instrumentation, BIW 1998, CERN SL 98-061 BI.

SINGLE BUNCH TRANSIENT DETECTION FOR THE BEAM PHASE MEASUREMENT IN SUPERCONDUCTING ACCELERATORS*

P. Pawlik, M. Grecki, DMCS, Technical University, Lodz, Poland
S. Simrock Deutsches Elektronen-Synchrotron, Hamburg, Germany

Abstract

During commissioning and operation of linear accelerators the beam phase must be determined with respect to the accelerating rf fields. It is desirable to perform these measurements at low beam current and with a short beam pulse duration to avoid unnecessary beam loss during start-up when the correct beam phase is not guaranteed. In the case of the European X-FEL and the International Linear Collider the requirements are to measure single bunch transients at a bunch charge of 1nC to 8nC with an accuracy of a few degrees in phase and a few percent in amplitude in presence of accelerating fields up to 35 MV/m. This implies that transients of the order of 1e-3 must be measured with a few percent resolution resulting in a relative resolution of the order of 1e-5. The concept of the transient detector for the X-FEL is based on nulling method, where the cavity probe signal is split into two branches, one delayed by a up to 100 ns and phase shifted by 180 degrees before adding the two signals. The nulled signal is amplified by 60-80 dB with an rf amplifier and the transient induced by a single bunch is detected by a schottky diode based rf vector detector to achieve the required low noise performance. The principle of rf transient detection, the electronics design and measurements at the VUV-FEL at DESY will be presented.

INTRODUCTION

The measurement and adjustment of the phase of the accelerating field with respect to the beam phase is essential for the operation of any accelerator. In the case of vector-sum control of many cavities driven by one klystron it is even more important to guarantee the stability of the vector-sum [1]. For this purpose each individually measured cavity field vector is multiplied by a rotation matrix before adding the vectors to the calibrated vector-sum.

The measurement of the relative phase between accelerating field and beam can be based on the beam induced voltage. The measurement can be realized as a transient measurement or as a steady state measurement. In both cases the beam must be turned on and off to detect the change.

*We acknowledge the support of the European Community-Research Infrastructure Activity under the FP6 „Structuring the European Research Area" program (CARE, contract number RII3-CT-2003-506395), and Polish National Science Council Grant "138/E-370/SPB/6.PR UE/DIE 354/2004-2007"

PRINCIPLE OF TRANSIENT DETECTION

Single bunch running through the cavity induces RF field vector change called transient (Fig. 1) [2]. This transient is very small and for X-FEL and 3nC bunch at gradient 25MV/m is about 3 orders of magnitude smaller then the RF field. The vector model of the RF field without and with beam presence is shown in Fig. 1. The RF field change induced by the beam is subtracted from the vector of accelerating RF field. For maximum acceleration (on crest acceleration) the beam phase is 0° and the transient vector has opposite direction to the accelerating RF field resulting in a maximum decay in the RF field. For other beam phase the transient adds to the accelerating RF field geometrically. Knowing the phase of accelerating RF field and beam induced transient one can calculate the beam phase.

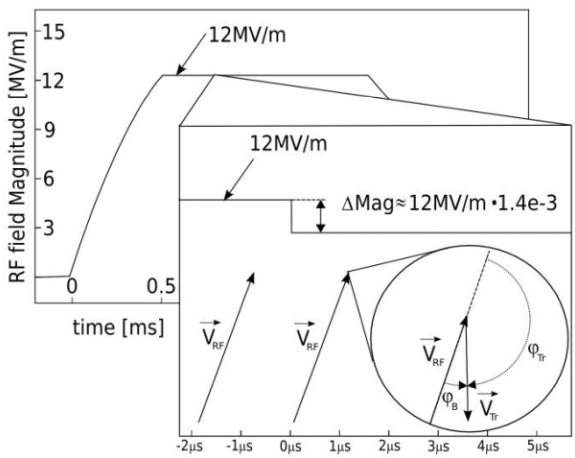

Fig. 1 Single 3nC bunch induced transients

To measure phase of these very small transients it is necessary to reduce carrier 1.3GHz frequency while leaving transients not attenuated. Method that is suitable for this purpose is based on subtracting actual signal from cavity probe from delayed one (Fig. 2) [3]. Short pulse with a width of a time delay is a subtraction result. This pulse carries information about transient.

Subtraction can be realized as a sum of two 1.3GHz signals, where one is shifted by 180 degree with respect to the other one and where magnitudes are the same. Since the exact 180-degree phase shift cannot be achieved one observe also other component between pulses, which is a phase and magnitude adjustment error. To reduce adjustment error to the relevant level one need to attenuate carrier vector below the level of transients, i.e. the attenuation of 100dB is needed since the transients can be 10-4 smaller then the carrier. The phase has to be adjusted with a precision of 0.1° and magnitude 10-5 respectively.

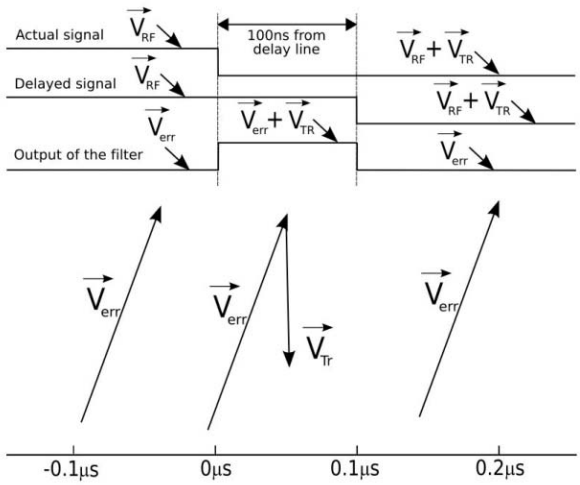

Fig. 2 Subtraction of delayed signal from actual signal

SYSTEM FOR TRANSIENT DETECTION

The block diagram of the system is presented in Fig. 3.

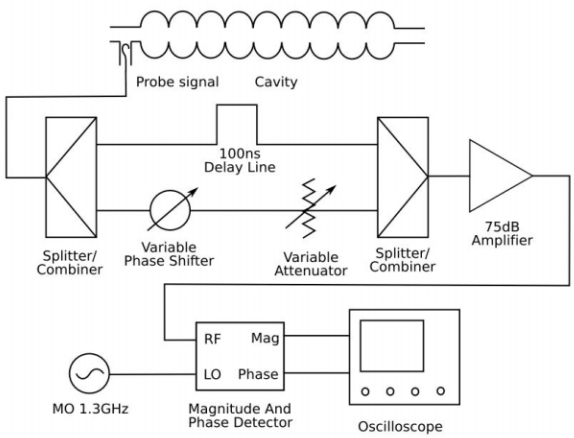

Fig. 3 Block diagram of measurement system.

It consists of cavity probe, nulling circuit, vector detector and digital scope. The probe signal is filtered in a nulling circuit, amplified and detected in vector detector allowing calculation of the real and imaginary part of the signals from the waveforms observed at the scope.

MEASUREMENT OF SINGLE BUNCH TRANSIENTS

The measurements were performed in the VUV-FEL accelerator in DESY. Signals were taken from cavity 3 in module ACC1 that requires phase -10º (that is essential for bunch compression). Gradient was at the level of 12MV/m and measured charges were 1nC, 2nC, 3nC.

Below there are presented measurement results for various beam charges. The beam phase was calculated from phase of transient obtained from change in real and imaginary part values measured on output of the vector detector.

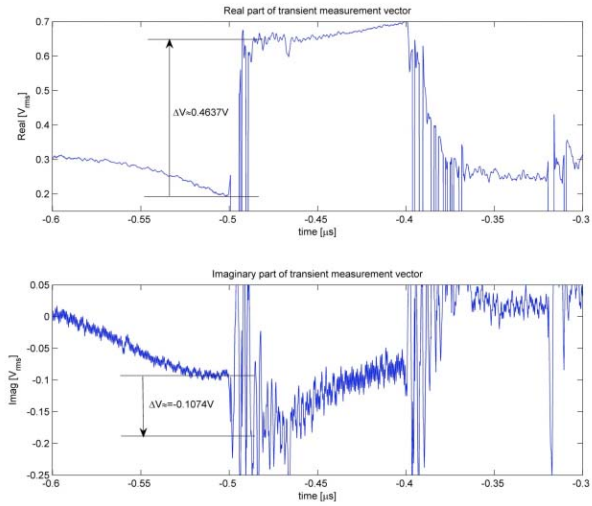

Fig. 4 Measurement of 3nC single bunch transient

Charge [nC]	I [V]	Q [V]	Phase [°]	M.Error [°]
1	0,18	-0,04	-12,33	-2,33
2	0,32	-0,05	-8,53	1,47
3	0,48	-0,11	-12,51	-2,52

Table 1. Results of measurements

Where:

M.Error (measured error): difference between expected and measured values

The differences between expected and measured values do not exceed 2.5°.

PROPOSAL FOR AUTOMATED OPERATION

Since the parameters of the notch filter drifts slowly in time and also depends on temperature the system requires special adjustment procedure before the measurements

start. The amplifiers gain should be set to minimum value for the beginning of adjustment procedure. The signal 1.3GHz is connected to the input of the filter and at the output real and imaginary parts is observed (special Matlab script was designed for computation of complex signal in the real time). For adjustment procedure (input signal is constant) the complex signal should be observed in the complex coordinate system as a single point. By changing attenuation or phase shift the real and imaginary part of the signal changes and point representing signal moves at the screen. When the filter attenuation increases the magnitude of the signal drops down and this point moves towards the beginning of the complex coordinate system. After the point corresponding to the null amplitude is reached the gain of the amplifier should be increased to make higher precision adjustment. This procedure has to be continued until minimum magnitude is achieved with maximal gain (75dB).

This process is annoying and its automation is very useful. It will improve performance of the measurement system. The block diagram of the proposed automated measurement system is presented in Fig. 5

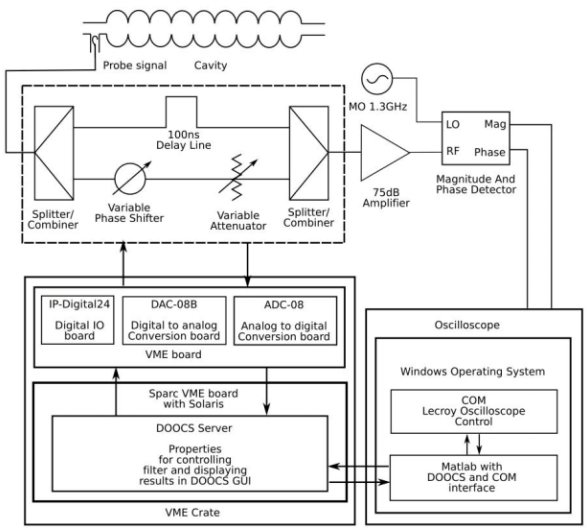

Fig. 5 Block diagram of automatic adjustment circuit

In order to control the adjustment circuit the computer system equipped by ADC, DAC and IO boards are required. For this purpose VME board with three modules is used: IP-Digital 24 module from SBS GreenSpring, DAC-08 and ADC-08 from ACTIS Computer.

The CPU is an embedded VME SPARC computer installed in the same VME crate. It runs under Solaris operating system and DOOCS [4] is used for remote access to the system.

For computation purpose the Matlab scripts running on DOOCS server are used. The scripts get measured waveforms from LeCroy WaveRunner 6100 oscilloscope, compute the required adjustment of the filter and drive DACs and switches that control system motors.

When filter is adjusted properly Matlab script records data with transients for further beam phase calculation. Measured beam phase is available as a DOOCS server property for beam diagnostics.

CONCLUSIONS AND OUTLOOK

From this paper one can figure out that presented method is very promising for amplitude and phase calibration. Filter used for carrier signal nulling achieved its requirements. Transients detected at its output were used to calculate beam phase. Results from this calculations were close to expected values.

Automation of the filter in the future will make measurements more convenient and less time consuming. It will make possible to see beam phase changes in a long term not only for short measurements.

In addition for more accurate and robust measurements filter is planned to be precisely thermally stabilized. Cable which is currently used will be replaced by a semi rigid version with a very high thermal stability. Currently used Amplifonix amplifiers with 1dB Noise Factor will be replaced with Amplitech amplifiers with 0.3dB NF which will further improve measurements accuracy.

REFERENCES

[1] Thomas Schilcher, DESY, “Vector sum Control of pulsed Accelerating Fields in Lorentz Force Detuned Superconducting Cavities” Phd Thesis 1998, TESLA Report 98-20

[2] S.N. Simrock, T. Schilcher DESY “Transient Beam Loading Based Calibration Of The Vector-Sum For The Tesla Test Facility”, DESY http://accelconf.web.cern.ch/AccelConf/e96/PAPERS/THPL/THP025L.PDF

[3] P. Pawlik, S. Simrock, H.C. Weddig “Simulation And Measurement Of An RF Notch Filter For An Electron Beam Single Bunch Detector”, MIXDES 2004, Szczecin 24-26 June 2004 Poland, pp. 430-434

[4] http://tesla.desy.de/doocs/doocs.html

RADIATION-HARD BEAM POSITION DETECTOR FOR USE IN THE ACCELERATOR DUMP LINES *

P. Degtiarenko, D. Dotson, A. Freyberger, V. Popov, Jefferson Lab, Newport News, VA 23606, USA

Abstract

A new method of beam position measurement suitable for monitoring high energy and high power charged particle beams in the vicinity of high power beam dumps is presented. We have found that a plate made of Chemical Vapor Deposition (CVD) Silicon Carbide (SiC) [1] has physical properties that make it suitable for such an application. CVD SiC material is a chemically inert, extremely radiation-hard, thermo-resistive semiconductor capable of withstanding working temperatures over 1500 °C. It has good thermal conductivity comparable to that of Aluminum, which makes it possible to use it in high-current particle beams. High electrical resistivity of the material, and its semiconductor properties allow characterization of the position of a particle beam crossing such a plate by measuring the balance of electrical currents at the plate ends. The design of a test device, and first results are presented in the report.

INTRODUCTION

Some of the new fixed target experiments approved for runtime at the Continuous Electron Beam Accelerator Facility (CEBAF) at Jefferson Lab (JLab) require complicated beam steering efforts to keep the electron beam at its nominal position at the face of the beam dumps after it passes through the experimental targets. The new experiments employ magnetic fields in the areas near the target, which are capable of moving the beam away from the dump face and damaging the dumpline equipment with the few hundred-kW beams. Therefore, the problem of reliable beam position measurement in the dumpline areas has become more critical.

Precise and reliable position monitoring of high energy and high power accelerated particle beams in the vicinity of high power beam dumps has always presented a technical challenge. The beam quality in those areas is often very poor, and any equipment positioned there must be extremely resistant to radiation damage. Methods involving Radio Frequency (RF) beam time structure measurements often do not work in these areas due to the RF disturbances, and the disturbances in the transverse beam profiles, caused by beam scattering in the irradiated targets. The methods involving moving parts to perform beam profile scans, and optical beam viewers all require high reliability of the control and measurement equipment working in the high radiation environment.

Until recently, the only means to see the beam position at the entrance of the beam dump tunnel at JLab was a phosphorescent viewscreen (Refs. [2], [3]) with a video camera readout system. A special optical design was required to bring the image of the viewscreen to a shielded enclosure, in which a camera could survive the radiation. Despite this effort to protect the optical components, cameras typically have a short lifespan in these conditions, and the viewscreens fail after prolonged irradiation. The need for an independent beam position measurement system for the dumpline has brought us to the subject of this work.

NEW BEAM POSITION DETECTOR

The schematic drawing of the device is shown in Fig. 1.

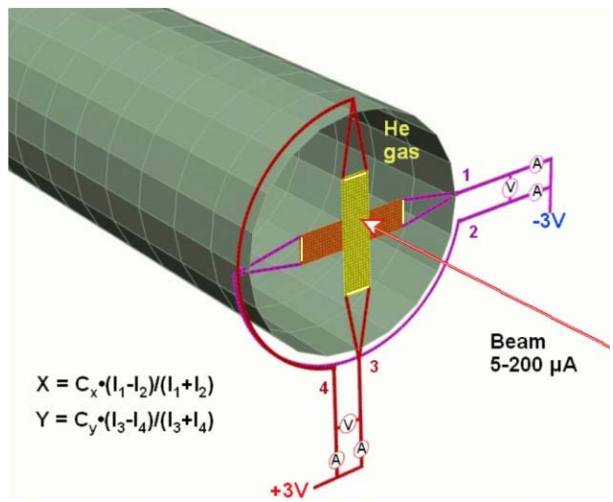

Figure 1: Schematic layout of the BPD.

General Layout and Detector Design

The Beam Position Detector (BPD) consists of the two thin plates (200x50x0.25 mm) made of CVD SiC material of standard (high) resistivity; typical electric resistance between plate ends is 200-600 kΩ. One of the plates is suspended horizontally, and the other one vertically in the middle of He gas - filled pipe leading to the CEBAF high power beam dump. The plate width was determined by the need to measure the transverse beam position within the 5 cm by 5 cm area, determined by the dimensions of the dump entrance window. The plate thickness was chosen to be as thin as technologically feasible, and the plate length was sized sufficiently large to bring the plate endpoints farther away from the center to avoid the beam damage to the end contacts. The vertical and horizontal plates are separated by 5 mm and are orthogonal to the beam direction.

* Work supported by the U.S. Department of Energy under contract DE-AC05-84ER40150; U.S. patent pending

The plates are electrically attached at the ends to the relatively thick ($\approx$ 1 mm in diameter) copper wire, which serves as a mechanical support, and as an additional heat sink for the plates. Placed in Helium atmosphere, the plates are capable of withstanding the CEBAF operational limit of 200 μA electron beam coming through them. The power deposited in one plate by such beam would be $\approx$ 30 W, bringing the conservatively estimated equilibrium temperature of the plate at the ends to no more than 150 ^{o}C. The temperature at the beam center would strongly depend on the beam size, and should be no larger than 500-800 ^{o}C for the extreme operating conditions. Reliable electric contacts at the plate ends are provided by using conductive paint covered by conductive radiation-hard ceramics. The assembly is set up in an aluminum ring inside the pipe with an opportunity for position adjustment. The copper wires are attached to the electrical feedthroughs in the beam tube, and the wires are brought to the control box outside of the dump tunnel in a radiation-safe place.

The control box provides low voltage potential difference between the plates, and is capable of measurement of electric DC currents from/to the plate ends. One plate voltage potential is set at +3 Volts relative to the base ground (chassis, cable electric shield, the beam pipe elements), and the other plate potential is set at -3 Volts. The potential difference causes the electric current between the plates when the beam is present, due to significant gas ionization by the beam. The two-plate assembly works similar to a low-voltage ionization chamber. The sum of currents read from the horizontal plate equals the sum of currents read from the vertical plate with opposite sign. Such current sums are roughly proportional to the beam current intercepted by the sensitive area where the plates are intersecting.

As the plates are resistive, the balance of the currents read off a plate represents beam position information. If an ideal symmetric beam is hitting an ideal plate in the middle, the symmetry requires that the currents read from both ends are equal. The displacement of the beam could be correlated with the asymmetry of the current readings from the two ends. The ideal relation between the coordinate and the currents is as shown in Fig. 1.

The real situation is complicated by the fact that the resistivity of CVD SiC has a very strong temperature dependence, and the heating of the plate by the beam is very non-uniform and dependent on the beam position at the plate. For example, the temperature pattern for the beam hitting the center of the plate is different from the pattern for the beam hitting the edge. Thus the relation between the readout currents and the beam position is non-linear and requires detailed study and calibration. In addition, this temperature sensitivity necessitates waiting until thermal equilibrium is achieved before stable current readings can be obtained. The first experience with beam on the BPD device showed that the characteristic time to reach stable readings is 90-120 seconds after each beam interruption. Once equilibrium is reached, the readings are stable and reproducible with a position resolution of $\approx$ 1-2 mm.

Calibration Procedure

Presently, the BPD device is installed at the entrance flange of the He-filled pipe inside the beam dump tunnel in Hall A at CEBAF. The anodized flourescent screen of the optical viewer is located $\approx$ 10 cm upstream of the BPD. Fig. 2 illustrates results of the calibration run in April 2005. Transverse beam coordinates as measured by the BPD during the calibration (red dots) are plotted on top of the reference beam position coordinates obtained from the digitized image of the optical viewer screen (white dots that are mostly covered by the red dots). The coordinates are

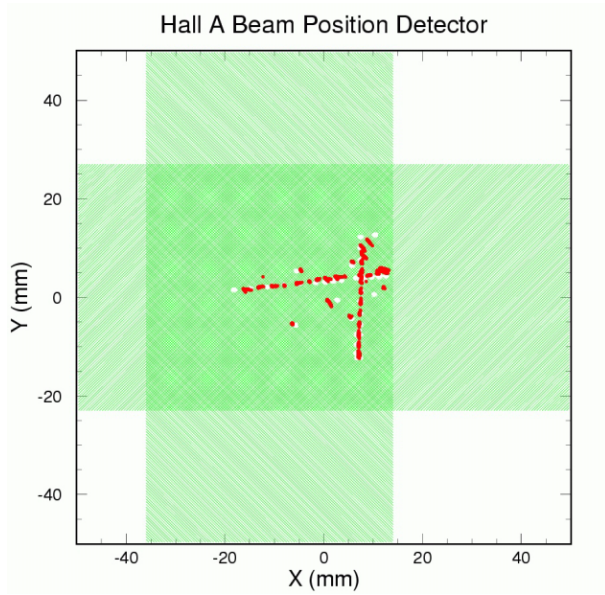

Figure 2: Transverse beam coordinates measured during the calibration. See detailed explanation in the text.

given in the viewer reference frame; the green hatched areas show estimated positions of the vertical and horizontal BPD plates in the viewer frame.

The position of 40 μA, 4.7 GeV electron beam, incident at the BPD, was monitored by the viewer screen; the digitized information on the beam position, and measured current readings from the BPD were recorded once a second by the data acquisition system. The beam steering by the control magnets in the beam line allowed scanning of the sensitive area within a range of $\approx \pm$ 1 cm in X and Y. The correlated readings were used to find the non-linear relations between the BPD current readings and the beam coordinates and subsequently use this information to extract beam coordinate values from the BPD data. Comparison of the viewer and the BPD coordinates after such conversion shows agreement within 1-3 mm in X and Y.

Operation Experience

Fig. 3 illustrates a typical operation of the BPD device. X and Y coordinates are measured every second, and plotted against time. All periods with stable coordinate readings

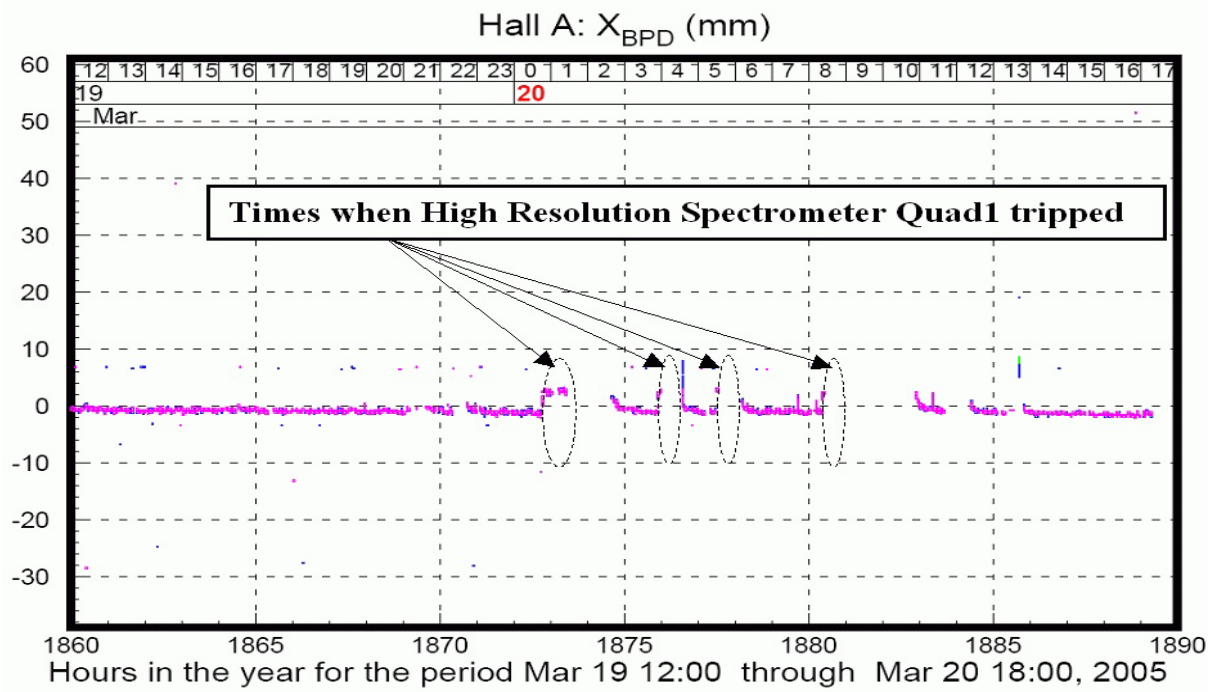

Figure 4: Horizontal beam position plotted against time, measured during March 19-20, 2005 experimental run. Otherwise stable run conditions were interrupted by several trips of a quadrupole magnet in one of Hall A spectrometers in the early morning hours on March 20th. Changes in the magnetic field along the beam path between the experimental target and beam dump tunnel entrance caused horizontal beam position shift of about 4 mm.

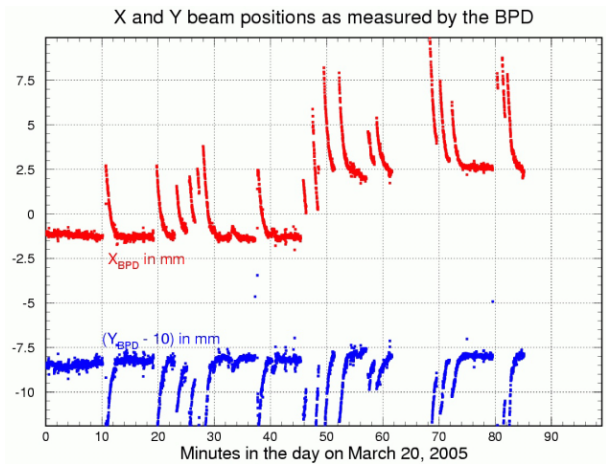

Figure 3: X and Y coordinates measured by the BPD during the experimental run. Y is shifted down by 10 mm to avoid interference.

correspond to the stable 40 μA, 4.7 GeV electron beam crossing the device. The interruptions in the beam correspond to the interruptions in the readings, followed by the characteristic pattern of recovery, delayed by 90-120 sec. The change in X coordinate at around 00:50 is real beam position shift caused by tripping of one of the spectrometer magnets in the Hall not far from the beam line. More extended pattern of X-coordinate readings, covering a period of $\approx$ 30 hours of relatively stable operations, is shown in Fig. 4. The first 120 seconds after the end of each beam interruption are not shown in order to clean up the plot. We see a very stable beam delivery during this period, interrupted by several magnet trips that caused shifts in X.

CONCLUSION

In conclusion, we have demonstrated operation of a new Beam Position Detector device for use in the accelerator dump lines. The first BPDs have survived many hundreds of hours of continuous operation at beam currents up to 100 μA, logging data for more than a year. The stability and reproducibility of the BPD readings allows calibration to within a few mm in position accuracy. We plan to switch from a passive use of the BPD, as a backup to the present beam viewers, to more critical missions for upcoming experiments.

REFERENCES

[1] CVD SILICON CARBIDE® is a registered trademark of Advanced Materials, Rohm and Haas Company, http://www.cvdmaterials.com

[2] A. Silva, “Requirements of the CEBAF beam viewer system”, CEBAF technical document CEBAF-TN-93-035, 1993.

[3] A. Freyberger, CEBAF internal communication.

OPTIMISATION OF "SHOE-BOX TYPE" BEAM POSITION MONITORS USING THE FINITE ELEMENT METHODS

P. Kowina *, W. Kaufmann, J. Schölles and M. Schwickert, GSI, Darmstadt, Germany

Abstract

The enhancements of the sensitivity and linearity of the position determination are the main goals in the optimisation of the Beam Position Monitors (BPMs) for ion synchrotrons. High position sensitivity can be achieved by the reduction of the coupling capacities and the plate-to-plate cross talks. For instance, the insertion of an additional guard ring into the gap between the active plates increases the sensitivity even by a factor two due to reduction of the cross talk. High linearity is typical for the shoe-box type BPM, however, it might be strongly influenced by discontinuities or/and imperfections of the components which are spoiling the fields homogeneity in the BPM volume. This requires a very careful design, especially in the regions close to the edges of the active plates. The BPM response has been investigated in the frequency range from $0 - 200$ MHz. It is shown that the transversal transfer impedance is frequency dependent; however, in the range up to 50 MHz (typical for the BPM applications) it varies only in the order of a few percent. The displayed simulations are performed using CST Microwave Studio.

INTRODUCTION

Motivation for the investigation described in the present work were the optimisations of the BPM's construction for the HICAT synchrotron dedicated for the cancer therapy [1]. The synchrotron will be operated with the maximal bunch frequency of 6.74 MHz (at the maximal extraction energy). The ^{12}C and ^{16}O ions will be accelerated up to $50 - 400$ MeV/u.

The investigations presented in this contribution are based on existing constructions of the shoe-box type pick-ups used at Heavy Ion Synchrotron (SIS) and Experimental Storage Ring (ESR) at GSI. The schematic views of the SIS– and ESR–BPMs are shown in Fig. 1.

The typical bunch frequency of SIS and ESR is in the range from 800 kHz up to 5 MHz at the maximal energy of about 1 GeV/u depending on the charge state of the ions.

The ESR BPM construction differs from the SIS one, since only in the ESR pick-ups the additional ground ring in the diagonal cut has been used, see Fig. 1. This separating ring is supposed to reduce the cross talks between the two close laying signal plates. Both setups are equipped with guard rings, however, the width of the guard rings and the width of the cuts between plates and guard rings for SIS- and ESR-like construction are different.

The main objective of the studies was to investigate how the presence of the certain pick-up's components (like guard rings, separating ring etc.) and their geometrical dimensions influence on the pick-up sensitivity and linearity of the beam position determination.

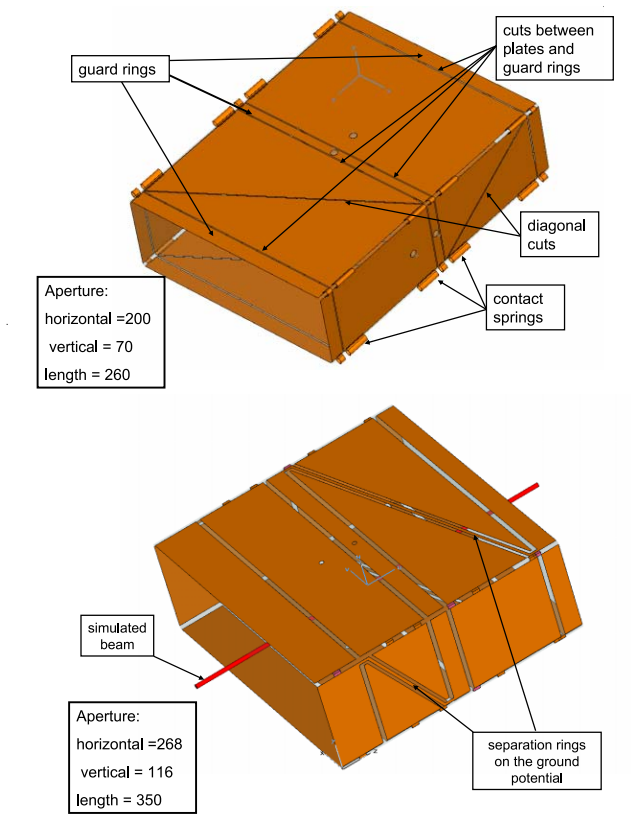

Figure 1: Schematic view of the SIS (top) and ESR (bottom) BPMs— here shown without chassis.

As the simulation tool "CST Microwave Studio" (CST-MW) version 5 has been used. All simulations were performed using the transient solver.

The bandwidth of 0–100 MHz, typical BPM preamplifiers [2], allows to observe up to the 20 harmonics of the bunch frequency. Since it is interesting, how a BPM behaves in frequency range slightly exceeding this limit the frequency regarded in the simulations was chosen to be in the range of 0-200 MHz.

In the present contribution by "horizontal plates" or "horizontal contact" etc. we understand those pick-up components, which are used for the measurements in the horizontal direction. Analogous nomenclature is used for the "vertical" components.

* p.kowina@gsi.de

PLATE–TO–PLATE CROSS TALK

The cross talk between the plates of the BPM influence negatively the amplitude of the output signals. The larger the coupling the smaller is the difference of the output signals for a given beam displacement.

In the CST-MW simulations the BPM without separating ring (SIS-like) was compared to the BPM with the ring (ESR-like). In the last case the width of the ring and the distance from the ring to the plate edges was chosen to be 1 mm. The port impedances were defined to be 50 Ω what reproduces later measurements performed with the network analyser. The coupling for the horizontal (left-right), vertical (up-down) plates and for the mixed pairs like: left-up etc. has been investigated.

The frequency dependences of the S–parameters calculated for the horizontal plates of the BPM with and without separating ring are presented in Fig. 2.

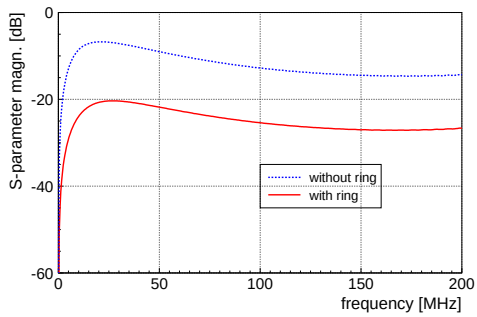

Figure 2: S-parameters for the coupling from one of the horizontal plates to the other obtained in the calculations for the BPMs with and without separating ring.

As indicated in Fig. 2 the coupling for the BPM without separating ring is ~ -8 dB. It means, that about one third of the signal from the one of the plates of the same pair is seen on the other one. In consequence the measured difference of the output signals is strongly suppressed and deteriorates drastically the position sensitivity of the pick-up.

The insertion of the separating ring in the diagonal cut between the plates (see Fig. 1) allows to noticeably reduce the coupling to ~ -20 dB.

The cross talk between orthogonal plates (i.e. right-up etc.) is very weak, in the order of -40 dB due to the guard ring.

Similar results one obtains in measurements for the SIS and ESR BPMs (for ones without and with the separating ring, respectively), performed using a network analyser. In the frequency range up to 100 MHz the absolute values of the plates coupling obtained in the measurements are, with an accuracy better than 1 dB, in line with the results of the simulations.

POSITION SENSITIVITY

The *position sensitivity* is the dependency of the difference between the plate signals (normalised to the sum of the signals) as a function of the beam position in the pick-up. In the following section results of the simulations and measurements of the position sensitivity for the SIS pick-up will be presented.

The ion beam was simulated as a cylinder of a Perfect Electric Conductor (PEC) with the diameter of 1.5 mm and length 10 cm longer than overall dimension of the pick-up. The impedances of the output ports were defined to be 1 MΩ. This corresponds directly to measurements using a setup [3], where the real SIS BPMs were tested using a copper wire mounted precisely parallel to the nominal beam axis. To reproduce the bunched ion beam the wire was connected to a sine wave generator with the frequency of 1 MHz.

In the CST-MW simulations the position sensitivities of the BPMs were extracted from the S-parameters expressed in frequency domain. The output voltages normalised to their sum ($\frac{\Delta U}{\Sigma U}$) were calculated out of the S-parameter values at the frequency of 1MHz applying the following equation:

$$\frac{S_{right\leftarrow in} - S_{left\leftarrow in}}{S_{right\leftarrow in} + S_{left\leftarrow in}} = \frac{\frac{U_{right}}{U_{in}} - \frac{U_{left}}{U_{in}}}{\frac{U_{right}}{U_{in}} + \frac{U_{left}}{U_{in}}} = \frac{\Delta U_{hor}}{\Sigma U_{hor}}, \quad (1)$$

where the S-parameters are given by the output/input voltage ratio [4].

The position of the simulated beam was changed in steps of 20 mm in the horizontal direction within the three planes for the three different and fixed vertical positions, i.e. in the centre of the pick-up high, +20 mm above and -20 mm below the centre plane. For each beam position a full set of the S-parameters was analysed for both horizontal and vertical plate pairs. The results are presented in Fig. 3.

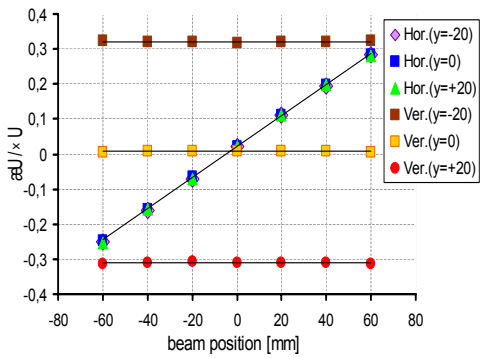

Figure 3: Position sensitivity extracted for the SIS pick-ups for the horizontal beam position shift.

The data points for the position calculation done using the horizontal plates are located on the same diagonal line independently from the vertical beam position (at least for the vertical beam shift of $y \pm 20$ mm). Also in case of the vertical position determination the observed effect is insensitive on the horizontal beam displacement — the data points are located on the three lines parallel to the x-axis where each of these lines directly corresponds to the given y-position. Therefore, the position determination in the

horizontal and vertical direction can be treated as independent.

As seen in Fig. 3 the position sensitivity of the simulated BPMs is extremely linear even for the horizontal beam displacements in the range of ± 60 mm. With the fit to the data for the different beam displacement with a linear function:

$$\Delta x = K \frac{\Delta U}{\Sigma U} + \delta x \qquad (2)$$

the *pick-up constant* K and *pick-up offset* δx can be deduced. For the simulated SIS pick-up the values are:

$$K_{hor} = 226 \text{ mm} \quad \delta_{hor} = -4.8 \text{ mm}$$
$$K_{ver} = 62.7 \text{ mm} \quad \delta_{ver} = +0.39 \text{ mm}.$$

The values obtained in the simulations are 20% larger than the experimental values measured with the test setup [3], since in the simulations the capacities of the feeds-throughs and preamplifiers were not taken into account due to memory and CPU–time limitations.

FREQUENCY DEPENDENCE OF THE POSITION SENSITIVITY

Typically, the position sensitivity is shown at a given frequency (in that particular case 1MHz) which usually corresponds to the bunch frequency of the measured beam. However, due to the bunch structure, higher frequency components enter into the measuring system — if one considers bunches with a Gaussian shape and the bunch frequency of 5 MHz, the frequency spectrum is in order of several tenth of MHz. Therefore the analysis of the frequency dependence of the position sensitivity is of great importance. This can be clearly seen in Fig. 4 (left) where the results of the simulations for the horizontal position determination for the BPM without the separating ring are shown. In this figure the position sensitivity starting at frequency of about 50 MHz shows an extremely nonlinear behaviour.

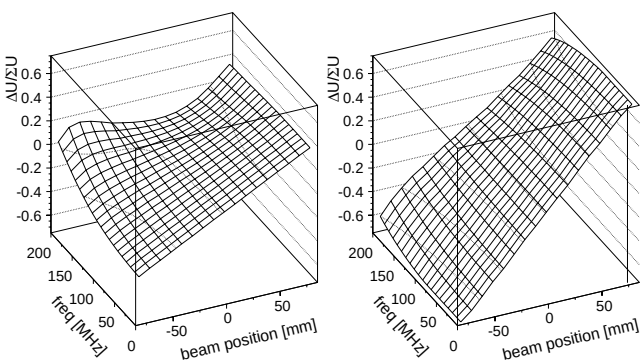

Figure 4: Position sensitivity as a function of the frequency for the horizontal beam displacement obtained in the simulations for the BPM without (left) and with separating ring (right).

The right part of Fig. 4 presents the results of the calculations for the BPM with separating ring. An insertion of the separating ring not only increases the position sensitivity but also makes it much more linear and less frequency dependent.

Projection of the slices perpendicular to the frequency axis taken at a given frequency (for instance 1 MHz) lead to a similar plot as in Fig. 3. By fitting of those slices with a linear function given by the Eq. 2 one can extract both pick-up constant (K) and offset (δ) separately for each frequency point in the investigated frequency range, see Fig. 5.

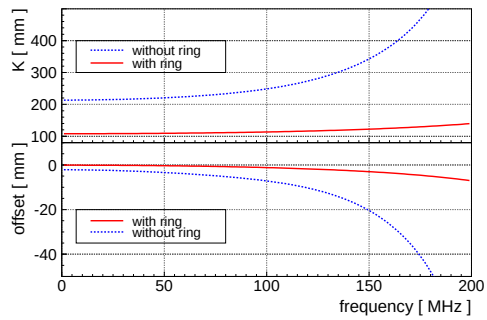

Figure 5: Frequency dependence of the pick-up constant (top) and offset (bottom) for the horizontal beam position determination simulated for the BPMs without and with separating ring.

In the figure it is clearly seen, that the sensitivity of the BPM with separating ring is almost a factor of two larger than for the BPM without the ring [1]. The "BPM constant" K is actually not constant anymore since it varies strongly over the 200 MHz frequency range. For the horizontal position measurement the variation is in the order of 50% for the BPM with separiating ring. The offset in this frequency range drifts from -0.05 mm to -7 mm. In the case of the BPM without the ring the variation of both K and offset is even six times larger. The drop of the BPM sensitivity is caused by the inductive coupling between the plates and the ground which contributes to the coupling impedance strongly at the higher frequencies.

The BPM for the HICAT facility are constructed as a BPM with separating ring since this configuration shows better linearity and much higher position sensitivity than the BPM without the ring. Reducing the bandwidth up to 50 MHz with a low pass filter one can neglect the correction of both pickup constants and offsets since they are constant within an accuracy of 3%.

REFERENCES

[1] H. Eickhoff et al, EPAC'04, July 2004, Lucerne, p. 290.

[2] G. Vismara, BIW'00, Cambridge AIP 564, p. 36.

[3] P. Moritz, GSI-Darmstadt, Private communication.

[4] see e.g. B. C. Wadell, *Transmission Line Design Handbook*, Artech House Boston (1991), ISBN 0-89006-436-9.

[1] The smaller the K in the Eq. 2 the larger is the BPM response $(\frac{\Delta U}{\Sigma U})$ for the same beam shift (Δx).

BEAM LOSS MONITOR SYSTEM FOR MACHINE PROTECTION

B. Dehning, CERN, Geneva, Switzerland

Abstract

Most beam loss monitoring systems are based on the detection of secondary shower particles which depose their energy in the accelerator equipment and finally also in the monitoring detector. To allow an efficient protection of the equipment, the likely loss locations have to be identified by tracking simulations or by using low intensity beams. If superconducting magnets are used for the beam guiding system, not only a damage protection is required but also quench preventions. The quench levels for high field magnets are several orders of magnitude below the damage levels. To keep the operational efficiency high under such circumstances, the calibration factor between the energy deposition in the coils and the energy deposition in the detectors has to be accurately known. To allow a reliable damage protection and quench prevention, the mean time between failures should be high. If in such failsafe system the number of monitors is numerous, the false dump probability has to be kept low to keep a high operation efficiency. A balance has to be found between reliable protection and operational efficiency.

BEAM LOSS MEASUREMENT DESIGN APPROACH

For the design of a safety system, in addition to the standard specifications, like dynamic range, resolution, response time, also a value for the "Mean Time Between Failures" (MTBF) is needed to quantify the level of the protection. The estimate of the MTBF value was based in the case of CERN's LHC on the SIL (Safety Integrity Level) approach [1]. Other approaches like "As Low As Reasonably Practicable" (ALARP) are also often used. For both approaches the MTBF value is estimated by the calculation of the risk of damage and the resulting down time of the equipment [3]. In the case of a failure in the safety system itself, it will fall in a failsafe state with the consequence of making the protected system unavailable.

The design considerations of a beam loss monitor system for machine protection are schematically shown in Figure 1. In the first row the above discussed key words are listed. A risk requires a safety system which provides protection but it also reduces the availability of the protected system. In the risk column the consequences (damage and quench) of a non nominal operation (beam loss) are listed. A further consequence for both is the increase of the downtime of the accelerator. The risk is scaling with the consequences of the proton loss event and its frequency. From the risk the MTBF value is deduced. This main design criterion for the safety system is listed in the safety column as well as the means (failsafe, redundancy, survey, check) to reach the

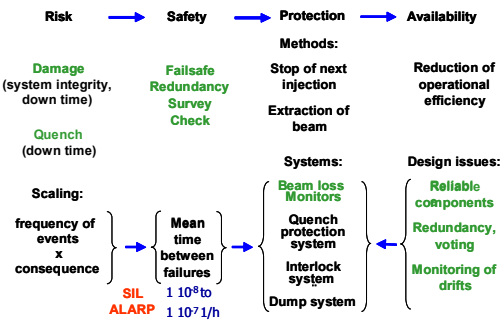

Figure 1: Schematic of the LHC beam loss system design approach (items in green are discussed in this paper).

envisaged MTBF value. In the protection column the methods of protection are listed (stop of next injection and extraction of beam) for a one path particle guiding system (linac, transfer line) and for a multi path system (storage ring). The safety system is consisting of a beam loss measurement system, an interlock system and a beam dump system. In the case of the usage of superconducting magnets, some protection could also be provided by the quench protection system. The availability column lists the means used in the design of the safety system to decrease the number of transitions of the system into the failsafe state. The effect of the components added to the system to increase the MTBF value results in a reduction of the availability of the system. This negative consequence of the safety increasing elements are partially compensated by the choice of reliable components, by redundancy voting and the monitoring of drifts of the safety system parameters (see Figure 1, fourth column). The key words listed in green will be discussed below.

Damage and Downtime

The damage potential at CERN's LHC is over two orders of magnitude higher than at all other existing accelerators (see Figure 2), since the stored beam energy given by the product of the single particle energy and intensity is largest at LHC. The consequence of a dangerous proton loss event was "illustrated" by an accidental loss at Fermi labs Tevatron (200 times lower stored beam energy as at LHC) where the proton beam was lost in a duration of a few revolutions melting some components. The loss was initiated by a moveable measurement instrument. The number of such moveable objects at LHC is also an order of magnitude higher than at Tevatron. This example may indicate the risk associated with the operation of LHC like beams leading to downtimes of months or even years.

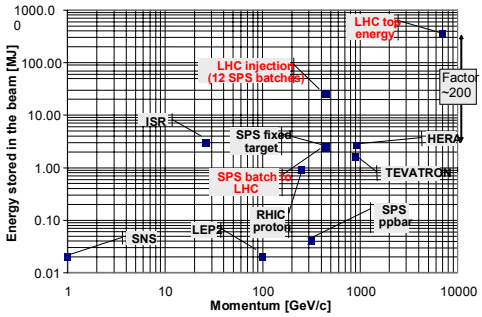

Figure 3: Comparison of the stored beam energy of different high energy physics accelerators as function of the beam momentum.

Quench of Magnets and Downtime

The proton loss initiated quench of magnets is depending on the loss duration and on the beam energy. A quench of a magnet will create a downtime in the order of hours in the case of LHC. To make the operation more efficient the beam could be dumped and a new store prepared. Figure 3 shows the expected loss dependence as

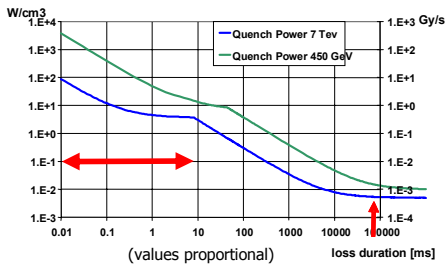

Figure 2: LHC bending magnet quench level curves as function of the loss duration.

function of the loss duration. The two curves indicate the levels for the injection and top energy of LHC. The two arrows indicate loss durations where the quench level of LHC are compared with levels at other storage rings (instant losses, steady state, see Table 1) [6][7]. It can be seen that the expected quench levels at LHC are lowest, resulting also in advanced requirements for the quench level detection.

Table 1: Instant and steady state loss duration quench levels for different accelerators.

instant (0.01 - 10 ms)	J/cm^3	steady state	W/cm^3
Tevatron	4.5E-03	Tevatron	7.5E-02
RHIC	1.8E-02	RHIC	7.5E-02
LHC	8.7E-04	LHC	5.3E-03
HERA	2.1 - 6.6E-03		

The energy dependence of the quench levels is already seen in Figure 3, their dependency as function of energy is shown in Figure 4. The quench levels decrease rapidly with the particle energy leading to the requirement that the quench level threshold need to be decreased during the energy ramp accordingly.

Safety Means

The risk of damage could be reduced by safety means, which are incorporated in the safety system (see Figure 1,

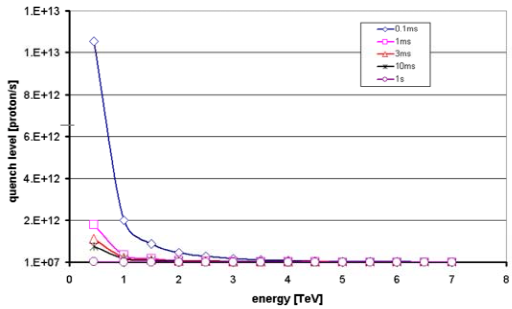

Figure 4: LHC bending magnet quench level curves as function of the beam energy. The parameterisation is for different loss durations.

second column). The most common safety feature of a system is the incorporation of the failsafe mechanism. In case of a failure of the safety system this system falls into a state where the protection is insured. If the system is doubled, redundancy is added, which will reduce the MTBF significantly for short time periods, but tends to reach the same value of the MTBF for long periods (see Figure 5, failure rate = 1/MTBF) [4]. The use of a redundant and surveyed system will decrease the MTBF

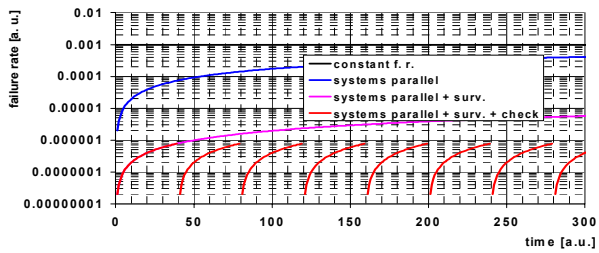

Figure 5: Calculation of the failure rates ranging from a simple system to redundant systems with surveillance and checks.

value for all durations compared to the simple redundant system. An even better result could be reached when a parallel system is not only surveyed but also its functionally is tested during the operation. This procedure will allow to assume that the status of the system after the test is identical to the status of the system as new. The frequency of the test will therefore determine the MTBF value.

Beam Dump Request Distribution

The beam loss measurement system is part of the equipment protection system. The protection as foreseen for LHC is schematically shown in Figure 6 [5]. The number of beam dump request, which reaches the dump system over the machine interlock, is to 60 % operator initiated request (inspired distribution by HERA [7]). The remaining dump requests are to 30 % caused by beam loss initiated dumps and to 10 % by various other reasons. The beam initiated requests are equally subdivided in losses with a duration below 10 ms and above. The short losses can only be detected by the beam loss system. The long losses can be detected in addition with the quench

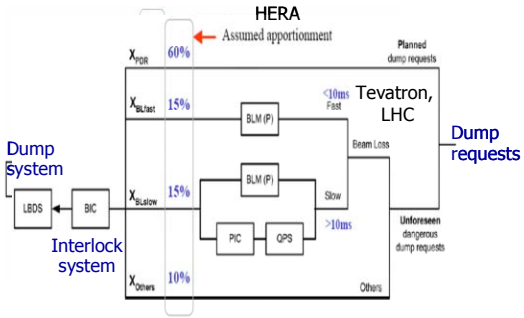

Figure 6: Dump request distribution and the employment of the beam loss system.

protection system (QPS, PIC). In this case two independent systems are available for the detection.

THE BEAM LOSS MEASUREMENT SYSTEM

The last beam loss system design for proton accelerators was done or is under way at SNS, FNAL Tevatron and CERN LHC. These beam systems are used to protect superconducting equipment (cavities at SNS, and magnets at FNAL and CERN). All designs use ionisation chambers as detectors (see Figure 7); however the digitalisation principles are different. The differences

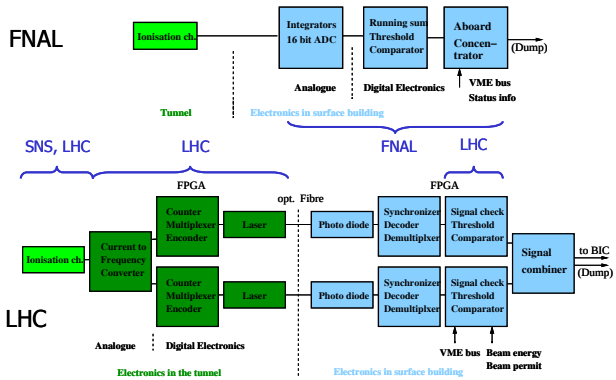

Figure 7: Overview of the beam loss measurement systems at FNAL and LHC. The brackets indicate the discussed subcomponents.

are mainly due to the possible dynamic range. The SNS and FNAL designs use single stage integrators and 24/16 bit ADCs [8][9], whereas the CERN design employs a current to frequency converter (CFC) [10]. The dynamic is about $10^7/10^5$ for the ADCs and 10^8 for the CFC designs. The design of the threshold comparisons in the case of the SNS design is based on analog signal comparisons. The changing thresholds are generated with a DAC. In the case of the FNAL and CERN design the comparison is done digitally in a FPGA. The LHC design is different from the other two in the signal transmission. Due to the extensions of LHC the digitalisation is done near to the detectors and the multiplexed signal from 8 chambers is transmitted over an optical link to the threshold comparator electronic.

Ionisation Chambers

At FNAL, BNL, SNS and CERN mainly ionisation chambers are used for the beam loss detection. At FNAL and CERN chambers are in use which have been designed in the 1970th. For RIC at BNL the FNAL design was copied [11]. For SNS a new design is used, because of the required faster signal response time. A cylindrical stainless steal design with 0.1 litre Ar active volume is used. The signal response limiting ion drift time is reduced from 560 to 72 µs [11]. For LHC a parallel plate design with 1.5 litre N_2 active volume will be used. It is an optimised CERN ISR/SPS design in order to cope with the requested dynamic range of 10^8 and radiation values of 10th of MGy/year in special LHC locations. The lower limit of the dynamic range in the ion chamber is given by the insulation material resistance and the higher limit by the recombination of ions and electrons [12]. The resulting current for the LHC chamber is in the range of a few 10^{-12} to a few 10^{-3} A.

The use of the chamber outside the beam vacuum implies that not only the lost particle species will reach the chambers. The proton initiated shower in the wall materials (cryostats) consists mainly of gammas, electrons, muons, pions, protons and neutrons. The signal response for this entire particle ensemble is not linearly scaling with their energy specifically at low particle energies [13]. The shower development could be seen by scanning a small particle beam across the chamber (see Figure 8). The peaks in the measured and simulated signals are due to the particle shower development in the

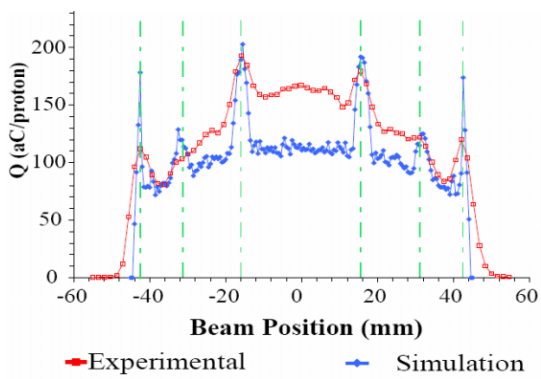

Figure 8: Collected signal charge of a parallel plate ion chamber scanning a proton beam across the chamber.

supporting rots of the parallel electrodes [13].

Another aspect for the usage of ionisation chambers is their high reliability and availability. The chambers used at the CERN SPS operated without failure for 30 years in the ring under an average dose of 0.5 kGy/year and in the injection and extraction areas under a dose of 5 MGy/year. A Cs137 source test of the 142 installed chambers in the SPS ring resulted in a distribution with an average current of 44.7 pA and a width of $\sigma = 1.1$ pA. The 41 injection and extraction areas chambers resulted in an average current of 45.5 with a width of $\sigma = 5.8$ pA [14]. This example may indicate the low degradation of the

chamber parameters under the influence of radiation and long term employment.

Chamber Signal Integration and Digitalisation

The chamber current integration and digitalisation is done in LHC by a charge balanced integrator (see Figure 9). The input current is converted into a proportional

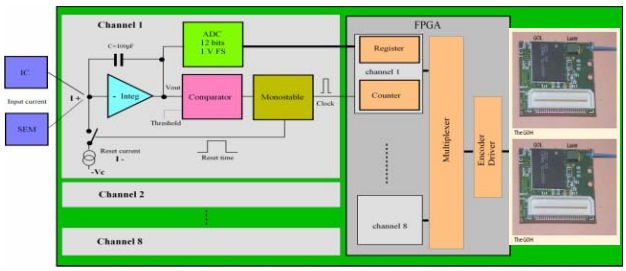

Figure 9: Overview of the LHC chamber signal integration, digitalisation, multiplexing and transmission.

frequency (CFC). To allow a faster response of the CFC for low currents, an ADC was added, which digitalised the integrator output voltage. The CFC frequency is counted over a period of 40 µs and the ADC is read out with the same periodicity. Eight channels are multiplexed, encoded and transmitted using a redundant optical link [10]. The digital signal treatment is done in a radiation tolerant ACTEL FPGA. The whole design is operational up to a total dose of 500 Gy, tested in a 60 MeV proton beam.

Digital Threshold Comparator

The new FNAL and CERN LHC threshold comparators are very similar in their basic design (FNAL see Figure 10). The measured chamber currents are summed over

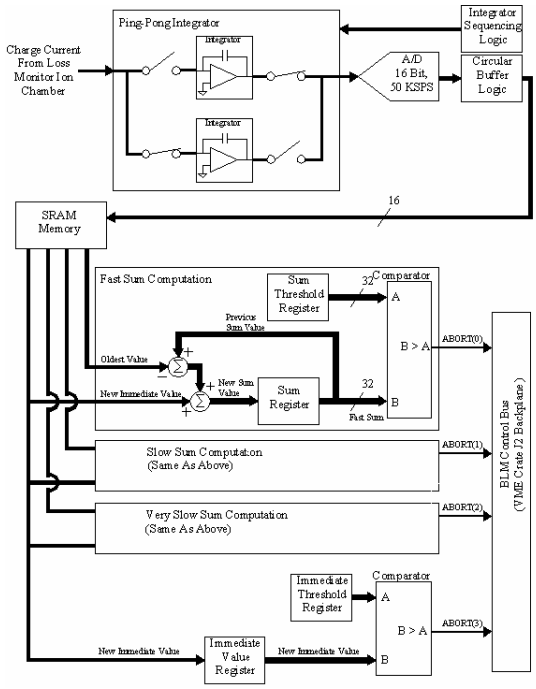

Figure 10: Overview of the FNAL beam loss integration and threshold comparator VME card.

varying periods and compared with corresponding threshold values [9]. The signal from the integrator is treated in different blocks at the same time. In the lower the signal threshold comparison is done for every reading (21 µs) and in the upper a sum is constructed which covers values for 1.4 s (see Table 2). This procedure allows coping with loss duration changing thresholds. Also post-mortem buffers are incorporated in the designs to be able to read out all acquisitions for a certain time period, which were taken before an initialising event (see Table 2).

Table 2: Comparisons of the basic design specifications of the FNAL and CERN LHC threshold comparator cards.

	FNAL	LHC
channels	4	16
Time resolution	21 µs	40 µs
# of running sums	3	11
windows	21 µs to 1.4 s	80 µs to 84 s
thresholds	4	12
Synchronized to machine timing	yes	no
post mortem buffer	4k values	1k values

Redundancy Voting

The redundancy voting procedure allows to increase the availability of a system. An example is the cyclic redundancy check (CRC) comparison of a redundant transmitted signal (see Figure 11). The CRC is calculated

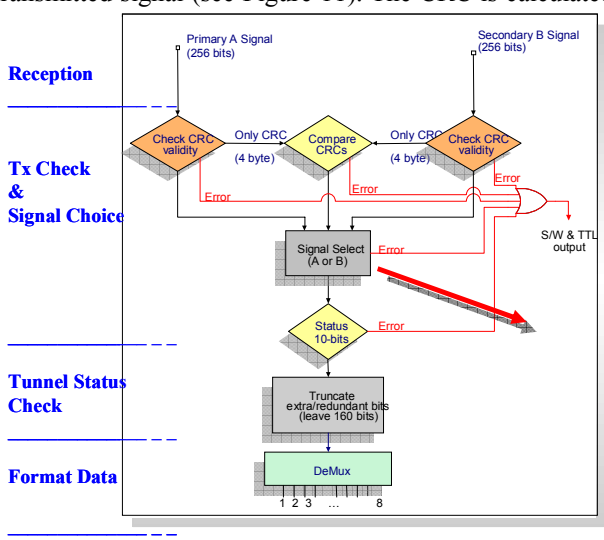

Figure 11: Schematic drawing of the redundant signal transmission comparison for the LHC design.

at the transmitter side and again at the receiver side for each link. For each link the CRCs are compared separately. In addition the CRC of both transmission links, which are calculated at the receiver side, are compared. In case that the comparison of the CRCs of one link is negative, the data of the other link are chosen independently of the result of the CRC comparisons of

both links. The result of the comparison of both links allows to identify the location of the error in the data stream [10].

UNSAFETY OF THE BEAM LOSS SYSTEM

The discussed aim of the beam loss measurement system is the protection of the accelerator equipment to allow an efficient operation. If the detectors are located at the likely loss locations (this aspect is not discussed in this paper), the MTBF value of the beam loss system will indicate the provided safety. This value was calculated for the foreseen LHC beam loss system starting from the single component level and using tabulated or CERN measurements [3][15]. To identify the weakness of safety system components a relative comparison is shown in Figure 12. In the LHC design contributes the ionisation

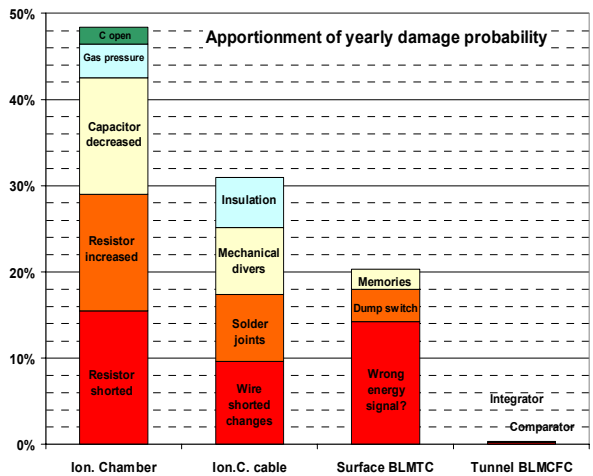

Figure 12: Relative probability of a system component being responsible for a damage to a LHC magnet in the case of a loss.

chambers and their cabling most to the unsafety of the system. Even with no damage in 30 years of the ion chamber operation, systems which are redundant and frequently checked, contribute less to the unsafety. The availability of the system is decreased by false dumps. The components of the beam loss system which are most responsible for this dumps are located in the very front end of the signal treatment chain, which are not redundant. For the LHC design that is the discharge switch of the integrator (see Figure 9).

REFERENCES

[1] "IEC 61508 International Standard", First edition, 1998-12.

[2] G. Guaglio, "Reliability of Beam Loss Monitors System for the Large Hadron Collider", BIW 2004, AIP Conference Proceedings, 10 November 2004 -- Volume 732, Issue 1, pp. 141-149.

[3] G. Guaglio, "Reliability of Beam Loss Monitor Systems for the Large Hadron Collider", Proceeding of ICFA, AIP Conference Proceedings, 8 June 2005, Volume 773, Issue 1, pp. 191-196.

[4] E.B. Holzer, et al., "Design of the Beam Loss Monitoring System for the LHC Ring", 9th European Particle Accelerator Conference EPAC 2004 , Lucerne, Switzerland , 05 - 09 Jul 2004.

[5] R. Filippini et al., "Reliability Assessment of the LHC Machine Protection System", Particle Accelerator Conference PAC 2005, Knoxville, TN, USA, 16 - 20 May 2005.

[6] N. Mokhov, "Protecting Superconducting Magnets from Radiation at Hadron Colliders", Workshop, "Beam generated heat deposition and quench levels for LHC magnets", CERN, 3.-4. March 2005.

[7] K. Wittenburg, "Quench levels and transient beam losses at HERAp", Workshop, "Beam generated heat deposition and quench levels for LHC magnets", CERN, 3.-4. March 2005.

[8] R.L. Witkover and D. Gassner, "Preliminary Design of the Beam Loss Monitoring System for the SNS", AIP Conference Proceedings, 18 December 18 2002, Volume 648, Issue 1, pp. 345-352.

[9] C. Drennan, et al., "Development of a new data acquisition system for the Fermilab beam loss monitors", Nuclear Science Symposium Conference, IEEE, Volume 3, 16-22 Oct. 2004, pp. 1816 – 1819.

[10] C. Zamantzas, et al., "The LHC Beam Loss Monitoring System's Real-Time Data Analysis Card", these proceedings.

[11] R.L. Witkover and D. Gassner, "Design of an Improved Ion Chamber for the SNS", AIP Conference Proceedings, 18 December 2002, Volume 648, Issue 1, p. 337-344.

[12] M. Plum and D. Brown, "Response of Air-Filled Ion Chambers to High-Intensity Radiation pulses", Proceedings of Particle Accelerator Conference, 17-20 May 1993, p. 2181.

[13] M. Hodgson, "Beam Loss Monitor Design Investigations for Particel Accelerators", Depart of Physics, University of Surrey, 15 April 2005.

[14] B. Dehning, "The Beam Loss Monitoring System", 1st LHC Project Workshop, Chamonix 2004, Chamonix, France , 19-23 Jan 2004 – p. 256.

[15] C. Zamantzas, "Beam loss monitors, realisation", LHC Machine Protection Review, CERN, 11-13 April 2005.

DIAGNOSTICS OF ACCELERATOR PERFORMANCE UNDER THE IMPACT OF ELECTRON CLOUD EFFECTS

H. Fukuma#, KEK, Tsukuba, Japan

Abstract

A large number of electrons called electron clouds are observed in many accelerators. The electron clouds produce various effects such as pressure rise, beam induced multipacting, tune shifts, coupled bunch instability, beam size blow-up and so on which often limit performance of the accelerators. Characteristics of the electron clouds are studied not only by direct measurements of the electrons but also by measurements of beam behavior affected by the electron clouds. This paper reviews various diagnostic methods to study the electron clouds with a short summary of the electron cloud effects on the accelerators.

INTRODUCTION

Many electrons are generated and accumulated in accelerators. Primary electrons can be produced by synchrotron radiation or lost particles hitting a chamber wall, or by ionization of the residual gas. If charge of a beam is positive, the primary electrons receive kicks from the beam toward the center of the beam chamber and hit the opposite wall, then secondary electrons are produced. Under some operational conditions of the accelerators rapid growth of the electrons known as beam induced multipacting can occur. The primary and secondary electrons form a group of the electrons called the electron cloud.

Spatial distribution of the electron cloud is strongly affected by magnetic fields as shown in Figure 1 of Reference[1] as an example. In drift space the electrons concentrate at the center of the chamber. In a dipole magnet several strips of the electrons sometimes appear. In a quadrupole magnet eight spots which have large density of the electrons are seen on the chamber wall. In a solenoid magnet most electrons are confined near the chamber wall.

Energy of the electrons is low, typically less than 100eV [2,3,4]. Owing to a low energy nature of the electrons it is possible to measure the energy distribution by applying a manageable voltage to grids as described later.

The electron cloud is built up along a bunch train [5]. In proton rings with a long bunch the electrons produced on the chamber wall are multiplied toward the tail of the bunch and lead to the trailing edge multipacting. Low energy electrons which stay near the center of the chamber before the bunch comes are trapped in the bunch by the beam potential and released at the tail of the bunch [6]. Due to two mechanisms a large number of electrons are observed at the tail of the bunch. The electrons can be trapped in a quadrupole and a sextupole magnetic fields as shown by a simulation [7]. The survived electrons between train gaps would lead to accumulation of the electrons by the passage of many bunch trains. The measurement of the time evolution of the electron cloud is thus important to study the characteristics of the electron cloud.

It is mentioned that the electron cloud can affect electron beams as well as positron beams [2,5,8].

#hitoshi.fukuma@kek.jp

ELECTRON CLOUD EFFECTS AND CURES

The electron clouds produce various effects [9] such as 1) nonlinear pressure rise due to gas desorption by the bombardment of the electrons, 2) electrical noise to instrumentations, 3) beam induced multipacting, 4) heat load to a cold chamber wall of superconducting accelerators such as LHC, 5) tune shifts caused by Coulomb force by the electron cloud, 6) transverse coupled bunch instability mediated by the electron cloud and 7) single bunch (strong head-tail) instability due to the short range "wake" by the electron cloud which causes a beam size blowup. A combined phenomenon of the electron cloud and the beam-beam effect is predicted though it is not yet confirmed by experiments [10].

Various cures have been taken to mitigate the electron cloud effects [9]. Ante-chambers are introduced to reduce the number of the primary electrons from synchrotron radiation. In order to reduce the secondary electrons, processed chamber surface by TiN coating and NEG(TiZrV) coating are used and a grooved surface is considered. The reduction of the secondary electron yield by beam scrubbing is observed. In B factories weak solenoids installed almost all drift space around the ring are very effective to moderate the beam size blowup by the electron cloud. Coupled bunch instability by the electron cloud can be cured by bunch-by-bunch feedback system and Landau damping by nonlinear magnetic fields if the growth rate is not large.

ELCTRON CLOUD DIAGNOSTICS

Many dedicated or standard instrumentations have contributed to understand the electron cloud effects. They also give the data for a benchmark of simulation programs. In this section diagnostics of the electron clouds themselves are reviewed. Diagnostics of the beam behavior under the impact of the electron clouds are discussed in the next section.

Pressure gauge

Pressure rise which is caused by desorption of the gas by the electrons hitting the chamber wall, gives an

indication of the electron-induced multipacting. At PSR [11] a pulse of the ion pump current was measured with HV probe by looking at the voltage across a resistor during beam accumulation. The ion pump pulse correlates well with a retarding field analyzer signal. In PEPII [12] the ion pump current was measured by removing the permanent magnets from the ion pump in order to measure the electrons entering the pump from the beam chamber. Pressure gauge is useful for getting the electron cloud distribution along the accelerator since many pressure gauges distribute around it.

Simple biased electrode

A simple biased electrode was used in many laboratories for evaluating the flux of the electrons. An interesting example is an electron-collecting electrode installed in the ante-chamber at PEPII LER to gather the electrons in the beam chamber [12]. The electrode installed in the pumping chamber close to the synchrotron radiation fan collects the electrons propagated from the beam chamber. The bias voltage of ~ +100 Volts relative to the vacuum chamber is applied to the electrode.

Retarding field analyzer

A biased electrode is simple to implement. But the measurement would be disturbed by several effects [11,13]. Signal is affected by varying the biased voltage since the secondary emission of the electrons from the electrode is a function of the bombardment energy of the electrons which is changed by varying the biased voltage. An area where the electrons are collected will be dependent on the applied bias voltage to the electrode. And the signal comes both from striking electrons on the electrode and from leaving electrons by secondary emission from the electrode. It is difficult to remove the effect of leaving electrons.

A planar retarding field analyzer (RFA) is developed at APS to overcome the disadvantages of the simple biased electrode [2,13]. The RFA measures the electron intensity at the chamber wall. It consists of a shielding grid, a retarding grid (or a repellar) and a collector. The collector is coated by graphite to minimize the secondary emission. By applying the voltage to the retarding grid the energy distribution of the electrons can be measured. The shielding grid shields the retarding grid from the beam to enable the unperturbed measurement of the electrons. The collector current as a function of the retarding voltage V_{ret} gives an integrated flux of the electrons whose energy is larger than eV_{ret} if the electrons are injected perpendicularly to the RFA. The derivative of the collector current with respect to V_{ret} gives the energy distribution of the electrons. If the incident electrons have an angular distribution the energy resolution is degraded since the transmission curve of the RFA depends on the angular distribution of the incident electrons.

The planar RFA based on that at APS is also installed at PSR [11,14]. Information on the time structure of the electron flux can be obtained by a fast electronics connected to the collector. The chassis is placed below the beam line to reduce radiation damage to solid-state components.

The planar RFAs at KEKB [15] are similar to those at APS. Several RFAs are equipped with a multi-channel plate to measure the time structure of the electron flux. An idea is proposed by K. Kanazawa to measure the electron density near the beam position. Energetic electrons are produced near the bunch due to a strong kick from the beam. The retarding bias voltage defines the observed volume around the beam from which observed electrons come. The cloud density near the beam just before the arrival of the bunch can be estimated from the collector current per bunch and the retarding bias voltage.

The planar RFA similar to that at APS is also installed at BEPC [16].

Electron sweeper

An electron sweeper developed at PSR is a variant of the RFA [9]. It consists of a curved electrode subtending an angle of 150° and a RFA with a large aperture which is placed the opposite side of the electrode. A pulse of ~-500V with rise time of ~15-20 ns is applied to the electrode in order to sweep the electrons into the RFA. Thus the low energy electrons remaining in the chamber after a bunch passing through can be measured. The acceptance region calculated by a numerical simulation corresponds to ~30% of the cross sectional area of the beam chamber. After applying HV pulse at the end of the bunch gap a signal with a very fast rise time (~5ns) and a narrow width (~10 ns) was observed as expected from design calculations. A longer tail of the signal is not completely understood yet. The electron sweeper is also used for measuring the decay time of the electron cloud after the passage of the last bunch. The electron sweeper similar to that at PSR is also installed at KEK-PS [17].

Strip detectors

Strip detectors [4,18,19,20] were developed at CERN to study the spatial and the energy distributions of the electron cloud. A collector placed under a beam chamber is composed of 36 channels copper strips with spatial resolution of 1.25 mm. The strips are separated from the beam by the chamber wall which has hundreds of holes (2mm in diameter) to reduce the perturbations to the electron cloud by an excessive collection of electrons. Three versions of the strip detectors were installed in the SPS; a strip detector to measure the spatial distribution of the electrons, a strip pick-up detector for the measurement of the energy distribution and a retarding field strip detector to study simultaneously the energy and the spatial distributions of the electrons. In the strip pick-up and the retarding field strip detector, filtering grids placed between the beam pipe and the collecting strips allow the measurement of the energy distribution. The signal from each channel is integrated using a current integrator with a integrating time from 2 to 255 ms. One version of the strip detector has a variable vertical aperture and another version is operated at 30 K. A measurement by the strip detector in a bending magnet at SPS clearly showed the

appearance of two lateral strips of the electrons which were predicted by a simulation.

Recently a strip detector was installed in a quadrupole magnet to study the spatial distribution of the electrons in a quadrupole field [21]. The result of the measurement shows that two strips appear on a pole of the magnet, which was also predicted by a simulation.

Microwave transmission measurement

The density of the electron cloud would be measured by studying the interaction between the electron cloud and the microwave. A microwave transmission measurement was tried at CERN [22]. TE waves were fed to a wide band button pair then detected by a strip line monitor which was placed 30m downstream of the button pair. The electron cloud in the beam chamber should give a small phase shift of the microwave signal (0.6˚ for the frequency of 2.5GHz and the electron density of $10^{12}m^{-3}$). Since the phase shift is modulated by the bunch revolution frequency, a phase-modulated signal can be observed. Contrary to the expectation an amplitude modulation which couldn't be understood by current electron cloud models was found. Further study is continued.

At PEPII [12], higher order modes (HOMs) generated at collimators in the upstream of a straight section were used as a source of the microwave. A pick-up connected to a spectrum analyzer was located at the end of the straight section. Solenoids of 20 m at the beam chamber between the collimators and the pick-up were switched on and off in order to control the density of the electron cloud. Any noticeable modulation of the HOM amplitudes with the density of the electron cloud was found.

BEAM DIAGNOSTICS

Pickup electrode

A pickup electrode connected to a spectrum analyzer has been used for measuring oscillation modes of the transverse coupled bunch instability by the electron cloud [23,24]. The mode distribution by the electron cloud instability is wide since the "wake field" by the electron cloud has a medium range (typically several to several ten m). The measurement is simple and useful for quickly identifying the threshold current of the instability. It may take long time to obtain the amplitude distribution of the betatron sideband if the harmonic number is large such that at KEKB.

Beam position monitor (BPM)

A bunch-by-bunch beam position monitor measures the beam position of every bunches in a turn-by-turn manner. Oscillation modes and the growth rate of the coupled bunch instability are obtained from the measurement. The data can be taken in very short time (i.e. less than 1 sec). At KEKB [25] Bunch Oscillation Recorder (BOR) which is made by modifying a filter board in the bunch-by-bunch feedback system is used for A/D conversion of the BPM signal, demultiplexing and storing the data to a memory. The BOR was helpful for measuring the effect of the solenoid field on the oscillation modes and the growth rate of the coupled bunch instability at LER [26]. At DAFNE [27,28] a digital oscilloscope Lecroy LC574A was used for storing the data of the BPM with the sampling rate up to 500MHz to observe the fast horizontal instability at the positron ring which is suspected to be caused by the electron cloud.

Synchrotron sidebands caused by the head-tail instability by the electron cloud also can be measured by the BPM. At SPS [29] the synchrotron sidebands were found by SVD analysis of the oscillation data. At KEKB [30] the oscillation of each bunch was processed by Fourier analysis individually, then the power spectra of each bunches were averaged to enhance the peak of the sidebands. As a result a sideband peak appeared in the spectrum. Both observations at SPS and KEKB could be an indication of the head-tail instability by the electron cloud. In such a case the sideband would be used as a diagnostic tool sensitive for the presence of the electron cloud.

Interferometer

An interferometer using synchrotron light from the beam measures the average beam size over the bunches [31]. The principle of the measurement is based on the van Cittert-Zernike theorem. The resolution of the measurement, typically several μm, is not limited by the diffraction effect. Its operation is not as difficult as a fast gated camera or a streak camera which usually require the operation by experts. It has been used to determine the threshold current of the beam size blowup at KEKB LER [32].

Fast gated camera

A fast gated camera measures the transverse size of each bunch. It consists of a photoelectric surface and a multi-channel plate. A gate pulse changes the voltage between the photoelectric surface and the multi-channel plate in order to gate the light of synchrotron radiation. Minimum gate width is typically 3ns. Simultaneous measurement of successive bunches is difficult since the repetition rate is an order of 10 kHz. Resolution of the measurement is limited by the diffraction effect. The fast gated camera was used at KEKB and PEPII for measuring the transverse bunch size along bunch trains in order to observe the buildup of the electron cloud and to measure the effect of train gap and bunch gap on the beam size [33,34].

Streak camera

A streak camera measures the longitudinal and the transverse distribution of the bunch by detection of synchrotron radiation. Simultaneous measurement of several consecutive bunches is possible. Resolution of the measurement of the transverse distribution is limited by the diffraction effect. Head-tail motion by the electron cloud would be detectable. At KEKB [35] the change of

the vertical beam size with and without solenoid field was observed by the streak camera. A tilt of the bunch which indicates head-tail motion was not clearly observed. Increase of the light intensity may be necessary in order to get clearer result. At IHEP the streak camera was used for measuring the effect of solenoids, chromaticity, octupole magnets and clearing electrodes on the vertical beam size [36].

Tune meter

The electron cloud causes betatron tune shifts of the bunches. The tune shifts can be increased along the bunch train due to the buildup of the electron cloud. Comparison between the tunes of the head bunch and those of the tail bunch gives an indirect estimate of the average density of the electron cloud around the ring. At RHIC [37] a beam position monitor in each plane recorded the oscillations of the last incoming bunch at the injection. Typically 1024 turns data were recorded and processed by a fast Fourier transform to obtain the tunes of the coherent beam oscillations. At KEKB [38] another approach was taken to measure the bunch-by-bunch tune shift. A high-speed gate consisted of two GaAs switches was introduced in a standard tracking measurement system. A pair of two switches was used for avoiding a ringing at on/off transition. Results at RHIC and KEKB showed the increase of the tunes along the bunch train.

Bunch-by-bunch luminosity monitor

A bunch-by-bunch luminosity monitor gives an estimate of the transverse size of each bunch because the luminosity is inversely proportional to the cross sectional area of the beam at a collision point. At PEPII [39] gamma rays generated by radiative Bhabha scattering were detected by measuring Cherenkov light which was emitted by the electrons converted from gamma rays. The bunch-by-bunch luminosity monitor was used for determining the optimum filling pattern of the bunches to moderate the electron cloud effect [40]. At KEKB [41] the bunch-by-bunch luminosity monitor called Zero Degree Luminosity Monitor (ZDLM) detects recoil electrons which are emitted by radiative Bhabha scattering at an angle of 0° and then deflected by the quadrupole magnetic field because, after replacement of a vacuum chamber, the intensity of radiative gamma rays largely decreased due to the absorption by the thick chamber wall.

SUMMARY

The electron clouds give various effects on the accelerators as described in this paper. They often limit the performance of existing accelerators and would be a potential threat to under constructing and future accelerators such as intense neutron sources and damping rings of linear colliders.

Many dedicated or standard instrumentations have contributed to understand the electron cloud effects. The efforts to refine and develop the diagnostics should be continued in order to improve the performance of existing accelerators and to predict the influence of the electron clouds on the future accelerators. For example a challenge for experimentalists is the measurement of the electron cloud at the beam location in the magnetic fields. The measurement of the electrons in the magnetic fields is important because a large fraction of the ring is already occupied by the magnets in some machines such as DAFNE, BEPCII, PSR and SPS and most drift space has been covered by the solenoids in B factories. The measurement of the electrons at the beam location is important because beam instabilities, especially single bunch instability, are largely governed by the electron cloud near the beam. The measurement would be difficult because detectors are usually located on the chamber wall while motion of the electrons is affected by the magnetic fields until they reach at the detectors.

ACKNOWLEDGMENTS

The author would like to thank J. M. Jimenez and S. Uehara for providing the materials presented in this paper.

REFERENCES

[1] H. Fukuma and L. F. Wang, “Simulation study of the electron cloud instability in SuperKEKB”, PAC'05, Knoxville, May 2005.

[2] K. C. Harkay and R. A. Rosenberg, "Properties of the electron cloud in a high-energy positron and electron storage ring", Phys. Rev. ST Accel. Beams 6, 34402 (2003).

[3] R. J. Macek et al., “ELECTRON PROTON TWO-STREAM INSTABILITY AT THE PSR ”, PAC'01, Chicago, June 2001, p. 688.

[4] J. M. Jimenez et al., “ELECTRON CLOUD STUDIES AND BEAM SCRUBBING EFFECT IN THE SPS", LHC Project Report 634 (2003).

[5] F. Zimmermann and G. Rumolo, “Electron-Cloud Simulations: Build-Up and Related Effects”, ECLOUD'02, Geneva, April 2002, p. 97.

[6] M. Pivi and M. A. Furman, “Electron-Cloud Updated Simulation Results for the PSR, and Recent Results for the SNS”, ECLOUD'02, Geneva, April 2002, p. 137.

[7] L. F. Wang et al., “Numerical study of the photoelectron cloud in KEKB Low Energy Ring with a three-dimensional particle in cell method”, Phys. Rev. ST Accel. Beams 5, 124402 (2002).

[8] K. Harkay, “ELECTRON CLOUD OBSERVATIONS: A RETROSPECTIVE”, ECLOUD'04, Napa, April 2004, CERN-2005-001.

[9] http://slap.cern.ch/collective/ecloud02/, http://icfa-ecloud04.web.cern.ch/icfa-ecloud04/.

[10] K. Ohmi and A. W. Chao, " Combined phenomena of beam-beam and beam-electron cloud interactions in circular e+e- colliders ", Phys. Rev. ST Accel. Beams 5, 101001 (2002).

[11] R. J. Macek et al., “ELECTRON CLOUD DIAGNOSTICS IN USE AT THE LOS ALAMOS PSR ”, PAC'03, Portland, May 2003, p. 508.

[12] A. Kulikov et al., “SUPPRESSION OF THE BEAM INSTABILITY RELATED TO ELECTRON CLOUD AT PEP-II B-FACTORY”, ECLOUD'04, Napa, April 2004, CERN-2005-001.
[13] R. A. Rosenberg and K. C. Harkey, “A rudimentary electron energy analyzer for accelerator diagnostics”, Nucl. Instr. and Meth. A 453 (2000) 507.
[14] A. Browman, “Electrons at the PSR”, Proceedings of the 8th ICFA Advanced Beam Dynamics Workshop on Two-Stream Instabilities in Particle Accelerators and Storage Rings, Santa Fe, February 2000, http://www.aps.anl.gov/conferences/icfa/two-stream.html.
[15] K. Kanazawa et al., “MEASUREMENT OF THE ELECTRON CLOUD DENSITY AROUND THE BEAM”, PAC'05, Knoxville, May 2005.
[16] Z. Y. Guo et al., "STUDIES ON THE PHOTOELECTRON CLOUD AT THE BEPC", APAC'01, Beijing, September 2001, p. 377.
[17] T. Toyama, “ELECTRON CLOUD EFFECTS IN THE J-PARC RINGS AND RELATED TOPICS”, ECLOUD'04, Napa, April 2004, CERN-2005-001.
[18] J. M. Jimenez et al., “Electron Cloud with LHC-Type Beams in the SPS: A Review of Three Years of Measurements”, ECLOUD'02, Geneva, April 2002, p. 17.
[19] J. M. Jimenez et al., “ELECTRON CLOUD HEAT LOAD ESTIMATIONS FOR THE LHC USING STRIP AND RETARDING FIELD DETECTORS", LHC Project Report 677 (2003).
[20] J. M. Jimenez, “ELECTRON CLOUD AND VACUUM EFFECTS IN THE SPS”, ECLOUD'04, Napa, April 2004, CERN-2005-001.
[21] J. M. Jimenez, private communications.
[22] T. Kroyer et al., “UNEXPECTED RESULTS ON MICROWAVE WAVEGUIDE MODE TRANSMISSION MEASUREMENTS IN THE SPS BEAM PIPE”, ECLOUD'04, Napa, April 2004, CERN-2005-001.
[23] M. Izawa et al., "The Vertical Instability in a Positron Bunched Beam", Phys. Rev. Lett. 74, 5044(1995).
[24] Z. Y. Guo et al., "Experimental studies on the photoelectron instability in the Beijing Electro Positron Collider", Phys. Rev. ST Accel. Beams 5, 124403 (2003).
[25] M. Tobiyama and E. Kikutani, "Development of a high-speed digital signal process system for bunch-by-bunch feedback systems", Phys. Rev. ST Accel. Beams 3, 012801 (2000).
[26] S. Win et al., "STUDY OF COUPLED BUNCH INSTABILITY CAUSED BY ELECTRON CLOUD IN KEKB POSITRON RING", EPAC'02, Paris, June 2002, p. 1592.
[27] A. Drago, "HORIZONTAL INSTABILITY AND FEEDBACK PERFORMANCE IN DAFNE E+ RING", EPAC'04, Lucerne, July 2004, p. 2613.
[28] C. Vaccarezza et al., "EXPERIMENTAL OBSERVATIONS AND E-CLOUD SIMULATIONS AT DAFNE", ECLOUD'04, Napa, April 2004, CERN-2005-001.
[29] G. Arduini et al., "BEAM OBSERVATIONS WITH ELECTRON CLOUD IN THE CERN PS & SPS COMPLEX", ECLOUD'04, Napa, April 2004, CERN-2005-001.
[30] J. W. Flanagan et al., "BETATRON SIDEBANDS DUE TO ELECTRON CLOUDS UNDER COLLIDING BEAM CONDITIONS", PAC'05, Knoxville, May 2005.
[31] T. Mitsuhashi, "Measurement of Small Transverse Beam Size Using Interferometry", DIPAC'01, Grenoble, May 2001, p. 26.
[32] H. Fukuma et al., “Observation of Vertical Beam Blow-Up in KEKB Low Energy Ring”, EPAC’00, Vienna, June 2000, p.1122.
[33] R. L. Holtzapple, "MEASUREMENT OF TRANSVERSE BUNCH SIZE BLOW-UP DUE TO THE ELECTRON CLOUD INSTABILITY AT PEP-II", SLAC-PUB-9222.
[34] J. W. Flanagan et al., "HIGH-SPEED GATED CAMERA OBSERVATIONS OF TRANSVERSE BEAM SIZE ALONG BUNCH TRAIN AT THE KEKB B-FACTORY", EPAC'00, Vienna, June 2000, p. 1119.
[35] H. Fukuma et al., "Recent Observations of Collective Effects at KEKB", e+e- Factories 2003, Stanford, October 2003, http://www-conf.slac.stanford.edu/icfa03/wkgroups.htm
[36] J. Q. Wang et al., "Electron cloud instability studies in the Beijing Electron Positron Collider", Phys. Rev. ST Accel. Beams 7, 094401 (2004).
[37] W. Fischer et al., "Electron cloud measurements and simulations for the Brookhaven Relativistic Heavy Ion Collider", Phys. Rev. ST Accel. Beams 5, 124401 (2002).
[38] T. Ieiri et al., "Bunch-by-bunch measurements of the betatron tune and the synchronous phase and their applications to beam dynamics at KEKB", Phys. Rev. ST Accel. Beams 5, 094402 (2002).
[39] S. Ecklund et al., "A fast luminosity monitor system for PEPII", Nucl. Instr. and Meth. A 463 (2001) 68.
[40] F.-J. Decker et al., “COMPLICATED BUNCH PATTERN IN PEP-II ”, PAC'01, Chicago, June 2001, p. 1963.
[41] S. Uehara, private communications.

ANALOG FRONT-END ELECTRONICS IN BEAM INSTRUMENTATION

A. Boscolo - DEEI Trieste University - Italy. boscolo@univ.trieste.it.

Abstract

The work gives an overview of present and near future technological opportunities for the analog first conditioning and subsequent processing of sensor signal. The interactions between beam sensor capability, their signals characteristics and the system requirements are analyzed from different approaches as: full analog continuous, sampled time discrete, full digital time and amplitude discrete. Special attention will be given to the impact of measurement methods and new devices in circuits and instrumentation architecture design, especially from the metrological point of view

BASIC INSTRUMENTATION STRUCTURE

In order to reach the paper aim it is better to start little bit away, taking in consideration the basic structure of generic monitoring or control system, figure 1. We can identify several sub systems, characterized by specific functionalities, and devoted to collect some aspects of a physical event, modify them in order to allow the comparison with a reference and codify them in order to make easier any reasoning on it. The first reasoning results can be reprocessed with different strategies in order to reach a specific goal, decoded in physical attribute and actuated on the physic domain.

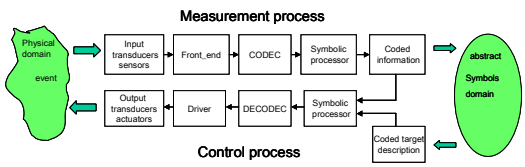

Figure 1. Structure of basic monitoring or control system

From the abstract point of view, in the main loop flow the same information but carried by different physical supports and code figure 2.

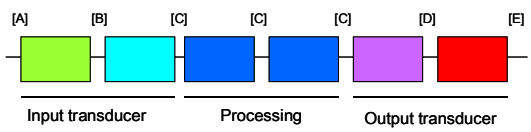

Figure 2. The same information is carried by different physical supports and code.

That is the physical world act as an information source, some of these are captured by a measurement process and converted in to symbols by a coding process, then some actions on the physical world can be performed by reasoning on the coded information and on the activity aim. With this approach we can define a criteria able to identify the transition from the transduction and the processing. We can consider transduction processes where the information carrier change block to block and processing where the physical carrier is stable. Taking in consideration how the information processing can be performed we can identify two different approaches: first based on a physical platform able to modify the carrier by different and controlled phenomena in order to approximate a required model, the analog solution, and the second based on coding processes and symbols manipulations driven by a defined paradigm, the symbolic or numeric solution. Which is the best? It is not easy to answer this question because the best performances or better the suitable performances depend on a large number of aspects as the system aim, the technology state of art, the number of systems required, the available technologies, the time to market, the available design tools, the cost performance ratio, the compliance with specific regulations, without to neglect the designer know-how and habits, his creativity, and his risk propensity etc. and in the end from the functional and technical specifications as accuracy, resolution bandwidth etc..

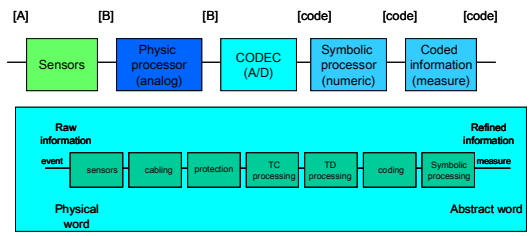

Figure 3. Model of information capture process

The information capture process can be modelled as shown in figure 3 where the coding process can be taken as the border from the physical processing, the analog space, and the symbolic or numeric processing, the digital space, moving this border, basically the A/D converter which perform the measurement process, we can modify dramatically architecture, performance, time delay, cost, knowledge engaged in the design etc. The works aim is to give an overview of some of these aspects and in special manner those related with the analog front end.

SILICON STATE OF ART

The silicon based integrated circuit (IC) industry has followed a strategy of shrinking device geometries for more than 30 years. With the assumption that the basic MOS transistor will remain the dominant switching device and the silicon will remain the dominant substrate material, it is widely believed that this process will continue for at least another ten years. However, there is great uncertainty about the ability to continue scaling metal–oxide–semiconductor field-effect transistor structures due to the considerable increasingly difficult materials and technology problems to be solved. The strategy of constantly shrinking device geometries and

increasing the number of devices per chip produces new technology generations, with deep performance and functionality improvements, every two to three years. This trend is commonly referred to as "Moore's Law". Each new generation has approximately doubled logic circuit density and increased performance by about 40% while quadrupling memory capacity. The increase in components per chip comes from three key factors first identified by Gordon Moore 40 years ago. The factor of two in component density comes from a shrink in each lithography dimension. An additional factor of two comes together from an increase in chip area and from device and circuit cleverness, providing the overall quadrupling in chip capacity. The apparent ease with which all this has happened has led to an expectation that faster and more powerful chips will continue to be introduced on the same schedule for the foreseeable future. In fact, the semiconductor industry itself has developed a "roadmap" based on this idea. The National and the International Technology Roadmap for Semiconductors (NTRS ITRS) now extend this device scaling and increased functionality scenario to the year 2014, at which point minimum feature sizes are projected to be 35 nm and chips with components are expected to be available. The requirements of a very thin thickness oxide is the main troubles source. The practical MOSFET structures generally require the gate dielectric thickness to be a few percent of the channel length. Silicon oxides thinner than about 1.0–1.5 nm, few atomic layers, conduct direct-tunnelling currents at the supply voltages below 1 volt and require a standby power too large for most IC applications. A new higher dielectric constant material system will have to be employed starting with the 100 nm generation. This kind of materials will allow a physically thicker dielectric layer to have a very thin equivalent SiO_2 thickness. Higher, up to 30, dielectric constant materials are also needed for dynamic random access memory (DRAM) storage capacitors. However, the requirements are quite different in this application because only a charge storage function is required. In a logic device because of the difference in permittivity between the silicon channel and the gate insulator, make the dielectric requirements very different and a good solution now does not exist. The gate electrode itself also presents some significant challenges. Polysilicon has been used for more than 25 years as the gate electrode material. However, decreasing its resistivity implies increasing the doping levels in the polysilicon. But this approach is limited by dopant solubility limits and by dopant out diffusion from the poly through the thin gate dielectric and into the silicon. This problem is particularly acute with P gates because boron diffuses rapidly through SiO_2. The likely solution is again new materials metal gate electrodes. But today is not available an optimum material. Ideally, the intrinsic channel resistance limits the current drive in a MOSFET. In practice, all the other parasitic resistances play a significant role and degrade the intrinsic device capability. Normal design procedures require these other resistances to total less than 10% of the channel resistance. Today there are no manufacturable means to reduce the contact resistance. Contacts are almost always made with either TiSi or CoSi contacting heavily doped silicon. The junction depths must keep on to decreasing to minimize short channel effects. Thus, doping levels in these regions must increase in order to keep resistances low. But doping concentrations are limited by dopant solubility and, hence, there are lower bounds on achievable sheet resistances. Today the integrated circuit industry gives some solution for the previous problems such as: Copper as connecting material supported by a low dielectric constant materials in order to reduce the interconnections time constant. This solution reduced the power requirement of 30% and the propagation time of 60% from 25 to 10 pS. SOI Silicon On Insulator, with the same design, speed up the device up to 20 %. Strained silicon. This material is obtained by growing, on a silicon bulk, about 2 μm of silicon-germanium alloy with a graded germanium concentration starting from the top with 20 % of Germanium. Over the silicon-germanium layer is deposited a 20 nm thin layer of pure silicon. The larger silicon germanium lattice strains the last silicon layer, because of the natural tendency for atoms inside compounds to align with one another. This effect gives an improvement of mobility, which can lead to chips up to 35 percent faster without having to shrink the size of transistors. High dielectric constant materials are normally used in memory devices, but are under development for logic application. This approach can delay or reduce in the near future the real problem connected with thinner gate isolator. The great driving force for the huge investments required in the actual technological effort is related to very large scale products as embedded applications in: automotive, medical, personal communication, home automation, and consumer which need, from one side, new high speed low power processors and, from the other side, high speed serial bus (10Gb/s) as the IEEE 802.11, and the IEEE 1394 in order to reduce the chips connections and to improve the system connectivity. Nevertheless 65nm technology is on the market, THz transition frequency transistors are available and 10÷15 GHz bandwidth 40÷80 GSample/s oscilloscopes are presented or announced

SAMPLING STATE OF ART

The high sampling rate is achieved by using the time-interleaved architecture. Here the signal is captured by a parallel array of slow digitizer that is sequentially clocked at a sub-Nyquist rate. The Nyquist criterion is satisfied when the signal is reconstructed in the digital domain. It is well known that the mismatches between digitizers in the array limit the dynamic range, so measured by the ENOB (equivalent number of bit). The process of ADC can be partitioned into two stages: (i) sampling, and (ii) quantization. Given the lack of an efficient digital optical switch, it has been prudently assumed by researchers that quantization is best done in electronic domain, and optics

should be considered as a mean to perform ultra fast sampling. Time-to-wavelength mapping, inherent in chirped optical signals, offers a natural mechanism for sampling a wideband RF signal and to demultiplex the samples into a parallel array of digitizers. In the discrete-time implementation of this approach the spectrum of pulses from an actively mode locked laser are broadened via a nonlinear pulse compression stage (super continuum generation) and sliced to attain discrete wavelength-to-time mapping. The multi-wavelength pulse stream samples the analog signal in an electrooptic modulator. A passive wavelength demultiplexer is then used to perform serial to parallel conversion. An array of slow (20 GSample/s) electronic digitizers quantize each channel. For an N channel system, the aggregate sampling rate would be Nfs, where fs is the sampling rate of individual electronic digitizers. This approach uses photonics for sampling and serial-to-parallel conversion; otherwise, the ADC architecture is identical to that of time-interleaved system. It offers an ultra-high sampling rate, with a resolution (ENOB), which will fundamentally be limited by the mismatch between different channels. A new A/D architecture is the so-called time-stretch ADC, shown in figure 4.

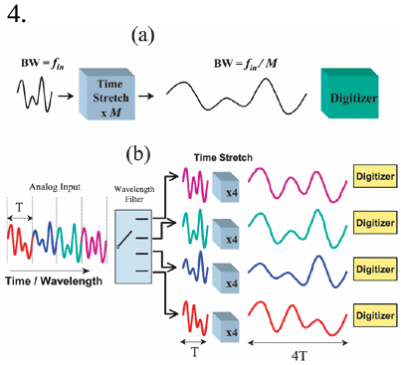

Figure 4. Time-stretch A/D architecture

Here the analog signal is slowed down prior to sampling and digitization by an electronic digitizer. Figure 4a, shown a time-limited input, single channel time-stretch ADC. A continuous-time input could be captured with a multi-channel system shown in figure 4b, where the partitioning of the continuous signal into parallel segments can be performed in the wavelength domain through time-to-wavelength mapping. Slowing down the signal prior to digitization has several advantages: for a stretch factor of M, the effective sampling rate is increased to Mfs. The input bandwidth of the electronic digitizer is also increased by M; the error associated with the jitter in the sampling clock of the digitizer is reduced due to a reduction in the signal slew rate. For a time-limited input, only a single digitizer is needed hence eliminating the inter-channel mismatch problem. For the continuous-time system it has recently been shown that mismatch errors can be corrected using the information available in the signal. This is an important advantage of the time-stretch ADC over the time-interleaved ADC. It exploits a fundamental difference between the two systems: in the former, the signal at each channel is sampled at or above the Nyquist rate, whereas in the latter it is sampled at a fraction of the Nyquist ra

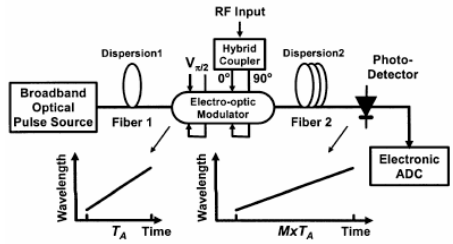

Figure 5. The time-stretch ADC physical implementation

Figure 5 shows the physical implementation for a single channel time-stretch ADC. The input electrical signal is modulated onto a chirped optical carrier. This is followed by dispersion, leading to temporal stretching of the modulation envelope. A single sideband modulation format eliminates the dispersion penalty that would otherwise place a limit on the electrical bandwidth. While the phase distortion remains, the effect is static and can be filtered in the digital domain. The differential scheme, using dual-output Mach-Zehnder modulator, is used to remove temporal distortions caused by the non-uniform power spectral density of the supercontinuum source and noise. A 120 GSample/s real-time digitization of a 20 GHz signal can be achieved by cascading a 6x photonic time-stretch preprocessor with the 20 GSample/s digitizer which has typically a 4 GHz bandwidth. The time-stretch increases the bandwidth to 24 GHz making it possible to capture a 20 GHz signal with the 4 GHz digitizer. The general approach for analog-to-digital conversion is to increase the performance of an electronic digitizer by optical signal pre-processing. Presently, the time-stretch technique appears to be the most promising in enabling ultra wideband analog-to-digital conversion with moderate resolutions 480GSample/s, 96GHz, bandwidth and 5 ENOB has been demonstrated.

INSTRUMENTATION TRENDS

The technological improvements can be seen from the instrumentation designers point of view as the availability of new class of components able to manage high-speed low-level signal in easy and cheaper manner. The availability of good analog switches and the large number of components engaged in the modern integrated circuits allow the implementation of very complex procedure derived from different methods and techniques. They are devoted to maintain the performance of physical processor, as the analog one, typically needed in the first interface with the physical domain for instance in the common mode rejection and low level amplifying with the explicit goal of realizing the whole system in one chip figure 6. The more suitable devices today are:

- Low level differential high-speed ADC
- SSP sensor signal processor
- FPAA field programmable analog array
- PSoC programmable systems-on-chip

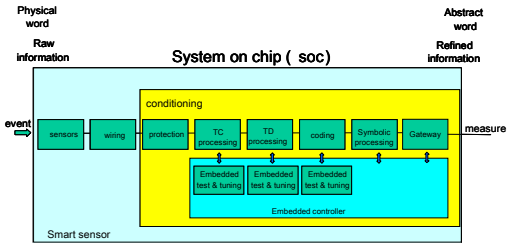

Figure 6. Instrumentation trends is one chip system

Low-level differential high-speed ADC the architecture of this device is more or less always the same: a controlled differential amplifier followed by a track-hold device and a flash analog to digital converter. The innovation is located in a dedicated embedded controller devoted to maintain the overall device performances by a continuous monitoring and adjusting of that. The today performances available on the market are 2.2 GSamle/s and 10 bit resolution. The SSP is a device family able to interface directly the low-level sensors signal today in the medium frequency range but, in the near future, also in the high frequency range. The family main characteristic is the customer availability of a general-purpose programmable microcontroller and/or a digital signal processor. A second important aspect is associated to the capability of those devices to stimulate the sensor and to interface many high-level communication networks. With this devices class is really possible to make one-chip instrumentation. FPAA field programmable analog array and design software introduce two new capabilities to the analog world. The first is the ability to translate complex analog circuits to a simple set of low-level functions, and thus to give designers the analog equivalent of an FPGA. The second is the ability to place analog functions under real-time software control within the system. By providing the analog equivalent of logic gates, FPAAs give designers the ability to describe analog functions such as gain stages and filters without reference to the underlying function. Lifted to this higher level of abstraction, the design process becomes so simple that non-specialists can create sophisticated circuits that would require weeks or months of design work with ASICs or discretes. Dynamic configurability adds to these capabilities by allowing analog functions to be updated in real time using automatically generated C-code. With analog functions under the control of the system processor, new device configurations can be loaded on the fly, allowing the device's operation to be "time-sliced," or to manipulate the tuning or the construction of any part of the circuit without interrupting operation of the FPAA, thus maintaining system integrity. As the physical platform, FPAA architecture is built on the natural precision, generic form, and switching fabric of a CMOS-based switched-capacitor (SC) network. The addition of a programming layer allows designers to implement an extremely wide variety of signal processing functions using digital configuration data. The core of the device is an array of identical Configurable Analog Blocks (CABs). The CABs are enriched with analog-to-digital converters, addressable memory, programmable comparators, references, and dedicated signal interfacing functions. PSoC programmable systems-on-chip developed by Cypress, PSoC mixed-signal arrays are programmable systems-on-chips (SOCs) that integrate a microcontroller and the analog and digital components that typically surround it in an embedded system. Dedicated development tools enable designers to select the precise peripheral functionality they desire, including analog functions such as amplifiers, ADCs, DACs, filters, comparators and digital functions such as timers, counters, PWMs, SPI and UARTs. The PSoC family's analog features are based both on time continuous structure and switched capacitor time discrete architecture and include rail-to-rail inputs, programmable gain amplifiers, low noise, low input leakage and low voltage offset up to 14-bit ADCs. The device digital side typically include flash memory, SRAM, multiplier, long accumulator, power and sleep monitoring circuits, and hardware I2C communications. Very recently has been announced a new component the PROC (programmable receiver on chip) able to support a Direct Sequence Spread Spectrum (DSSS) 2.4 GHz radio system mainly devoted to wireless USB technology.

BEAM POSITION MONITOR (BPM)

The Beam Position Sensor gives four voltage signals proportional to the beam horizontal and vertical positions. The beam position is determined from the ratio between the difference and the sum of two voltages induced in horizontal and vertical electrodes. The information processing can be performed in frequency domain by phase normalization and in time domain by time normalization. Both solutions need high-speed electronics and special care if high resolution is required. This kind of behaviour is quite common in sensor and instrumentation field. A typical example is the linear variable displacement transducers LVDT basically a differential transformer with variable magnetic coupling driven by the position of a moveable iron slug. For this reason a lot of conditioning architectures has been developed in order to improve the performance and the resolution. Some of these can be revised in order to verify if better features can be implemented to BPM. The state of art in BPM is well known and involving DSP, DRX, and FPGA. The four BPS voltage signals are down converted and coded in digital form, and then translated to base-band in the DRX. The DRX bandwidth is user selectable; this allows several measurements modes such as multi bunch, turn-by-turn, closed orbit and tune modes. When set to low bandwidth (typically 10 kHz) it allows following slow aspects of the beam evolution with a resolution of about 1 µm. When the bandwidth is wider (≥ 1MHz) it is possible to look at fast aspects of the beam position with a resolution lower than 20 µm in turn-by-turn mode. If the signal of BPS are combined by a hybrid device and sampled at 500MHz and then processed by multi DSP architecture with suitable firmware it is

possible to perform also bunch-to-bunch measurement. From the metrological point of view it is possible to observe that is quite difficult to obtain good resolution with single end architecture because the common mode weight and amplifier gain mismatching must be always lower than differential one. This condition is quite hard to maintain in the complex field especially if the amplifier gain is variable. The best choice in this situation is to perform an intrinsic difference of signal by a real differential amplifier with high common mode rejection or by a well-matched passive hybrid followed by a variable gain amplifier realized by means of a passive attenuator and a fixed gain amplifier. Today very interesting new devices are available on the market.

FUTURE BEAM POSITION INSTRUMENTATION

A forecast for near future beam position instrumentation goes in direction of wireless autonomous one chip system. A first step can engage a hybrid or a new generation differential amplifier followed by DRX or directly a differential DRX, a PSOC in order to perform the required data processing and continuous performance adjustment based on dedicated procedure and support the external connectivity figure 7a. The second step can be closer to single chip system by exploiting a SSP sensors signal processor where is possible to implement all the procedure needed to perform a good measurement also from the metrological point of view figure 7b.

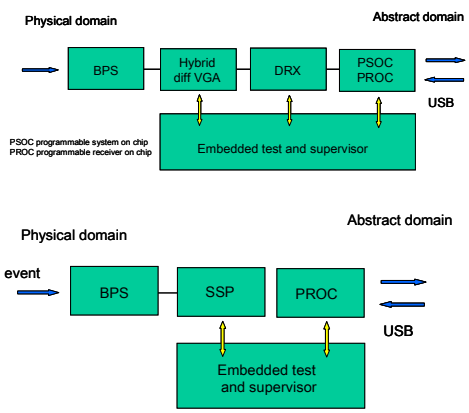

Figure 7. The future of BMP instrumentation

CONCLUSION

At the end of this overview the following statements are widely believable: also the instrumentation is going from module to chip. The new mixed signal array with on chip controller allows a more easy analog hardware practice. A high configurability is achievable by real time programmable physical connectivity. For some aspects more knowledge is required because the result is architecture dependent but good simulators and development tools are available for this purpose. The goal of low development time, low hardware platform dependence, and a suitable cost performance ratio become really more easily achievable.

REFERENCES

[1] Plummer, Griffin, “Materials and Process Limits in Silicon VLSI Technology” IEEE Proceedings Vol.89,N°3, March 2001
[2] Jeffrey, and al. “Interconnect Limits on Gigascale Integration(GSI) in the 21st Century” IEEE Proceedings Vol.89,N°3, March 2001
[3] Randal, and al. “Limitations and Challenges of Computer-Aided Design Technology for CMOS VLSI” IEEE Proceedings Vol.89, N°3, March 2001
[4] Robert, Keyes “Fundamental Limits of Silicon Technology” IEEE Proceedings Vol.89, N°3, March 2001
[5] David, and al. **“**Device Scaling Limits of Si MOSFETs and TheirApplication Dependencies” IEEE Proceedings Vol.89, N°3, March 2001
[6] Yan Han, Bahram Jalali “Time-Bandwidth Product of the Photonic Time-Stretched Analog-to-Digital Converter” IEEE Transaction on Microwave Theory and Techniques Vol. 51 N°7 July 2003
[7] Oleg A. Mukhanov, Deepnarayan Gupta, Alan M. Kadin, Vasili K. Semenov “Superconductor Analog-to-Digital Converters” IEEE Proceeding Vol. 92, October 2004
[8] Yan Han, Ozdal Boyraz, Bahram Jalali “ 480 Gsample/s Time Streatch Transient Digitizer” IEEE LTIMC 2004 Lightwave Technologies in Instrumentation and Measurement Conference New York October 2004
[9] Lechner, M:J: Burbidge, A.M.D. Richardson “Flexible embedded test solution for high-speed analogue front-end architectures” IEE, Proceeding Circuits Devices Systemes Vol. 151, N° 4 August 2004
[10] www.research.ibm.com
[11] www.analog.com
[12] www.anadigm.com
[13] www.intel.com
[14] www.cypress.com
[15] www.maxim-ic.com
[16] www.atmel.com
[17] www.altera.com
[18] www.xilinx.com
[19] www.infineon.com
[20] www.tektronix.com
[21] www.onsemi.com
[22] www.semiconductors.philips.com
[23] www.national.com
[24] www.ti.com
[25] www.fairchildsemi.com
[26] www.zetex.com
[27] www.mitsubishichips.com
[28] www.semicon.toshiba.co.jp/eng
[29] www.lecroy.com

FPGA TECHNOLOGY IN INSTRUMENTATION AND RELATED TOOLS

J. Serrano, CERN, Geneva, Switzerland

Abstract

Field Programmable Gate Arrays (FPGA) have become an alternative to traditional Digital Signal Processors (DSP) in many applications. In some cases, where high throughput is the main concern, an FPGA-based system may in fact be the only solution to fulfil the requirements. In the area of particle accelerators, FPGAs are used in many contexts, ranging from digital feedback loops for power converters and RF cavities to Digital Signal Processing for beam instrumentation. These designs harness the vast amount of logic resources inside FPGA chips to deliver unprecedented performance through parallelism and pipelining. After an introduction to the internal architecture of FPGAs and the design process, including advanced issues such as floorplanning, we look at two important techniques to implement arithmetic in FPGAs: Distributed Arithmetic (DA) and the COordinate Rotation DIgital Computer (CORDIC) algorithm. The goal is not to exhaust the list of Digital Signal Processing techniques for FPGAs, but rather to illustrate ways in which FPGAs are used to maximize performance.

INTRODUCTION

Programmable logic technology has been a central player in the glue logic and bus interface arena since the 1980's. In the last decade, due to the exponential growth in silicon densities and the maturity of the associated software tools, new segments of the digital design market have found solutions in the FPGA realm. One of the most impressive examples is the growing number of Digital Signal Processing (DSP) systems implemented in FPGAs. Accelerator subsystems, where purely digital applications such as those based on counters and state machines have existed for years, are now benefiting as well from the determinism and the speed of FPGA-based DSP solutions.

While this article presents general ideas applicable to any FPGA manufacturer, the examples and specific terminology, when needed, are those of Xilinx [1] products, with which the author is most familiar.

FPGA INTERNAL STRUCTURE

The architecture of an FPGA chip is essentially a rectangular array of Configurable Logic Blocks (CLB) interconnected by a programmable routing matrix. Figure 1 shows the internals of a generic chip from the Spartan IIE family, chosen for purposes of illustration due to its simplicity. CLBs can implement basic combinatorial functions and the result of these operations can either be routed directly out of the CLB or be clocked in internal CLB flip-flops before going out to the routing matrix.

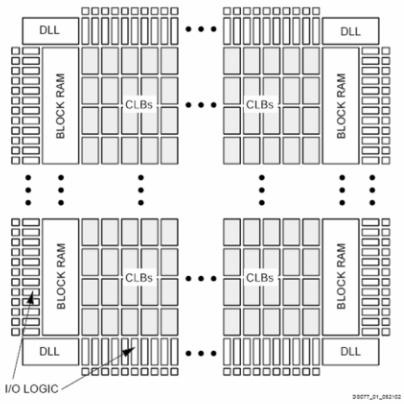

Figure 1. Internal structure of the Spartan IIE family. (Xilinx corp.)

Even in this low-range family, the designer has some extra resources available, namely internal RAM blocks and Delay Locked Loops (DLL) used to manage the phases and frequencies of inter-related internal clocks. Other blocks found in modern FPGA families include, among others, hard-wired Multiply and Accumulate (MAC) units, fast dedicated serial transceivers (useful to cluster several distant FPGA systems in global orbit correction applications) and Digitally Controlled Impedance (DCI) for on-chip high speed signal termination. Figure 2 gives a simplified view of the internals of a CLB.

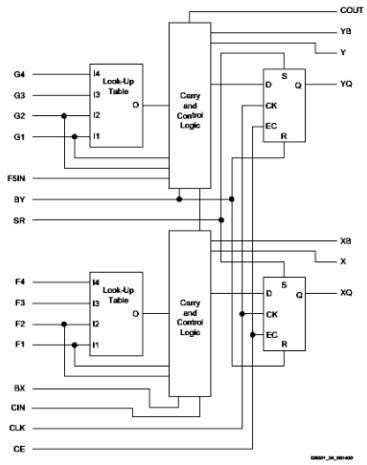

Figure 2. Spartan IIE CLB internal structure. (Xilinx corp.)

The Look Up Tables (LUT) can implement any combinatorial function of four inputs and one output (of the type you would write down using AND and OR operators). An interesting feature is the Carry In (CIN) – Carry Out (COUT) daisy chain, which links each CLB with its two vertical neighbours through dedicated routing

resources, independently of the programmable routing matrix. As its name suggests, this daisy chain is used to implement fast carry logic from one bit to the next in big adders.

For high speed DSP applications, the advantages of FPGA solutions with respect to DSP chips should be apparent from Figure 3. In a DSP with a single MAC unit, a 256-tap Finite Impulse Response (FIR) filter can only accept a new data sample every 256 clock cycles, since this is the time needed to calculate an output. With the pipelined design in an FPGA, input samples propagate through one stage every clock cycle generating a new output value, so the filter can accept one input sample per clock cycle.

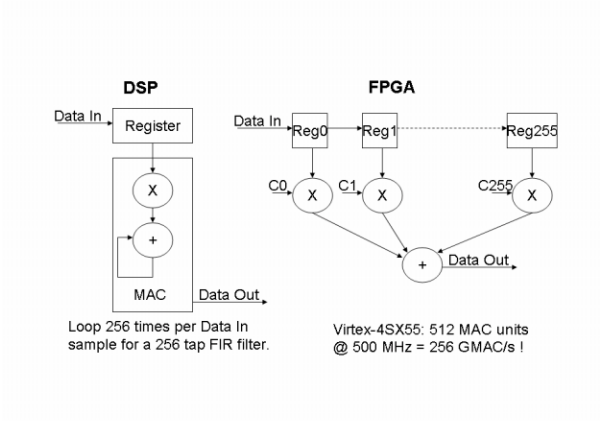

Figure 3. Architectural difference between DSP chips and FPGAs.

If we compare peak performances of top-of-the-line DSP chips against FPGAs (June 2005), in terms of raw GMAC/s without any architectural consideration, we find that the best FPGA can currently deliver 256 GMAC/s (see Figure 3) while the fastest DSP chip can perform 4 MAC operations per clock cycle in each one of its two multipliers, at a clock speed of 1 GHz, i.e. a total of 8 GMAC/s.

FPGA DESIGN FLOW

We now look at how the use of modern software tools helps the designer turn an idea into working hardware. The design flow can be split into three separate phases.

Design Entry

In this phase, the designer uses a software tool to describe the digital system. As circuit complexity increases, traditional schematic drawing methods are replaced by text-based input using a Hardware Description Language (HDL) such as VHDL or Verilog. These text-based methods harness the good design practices coming from the software world, such as code reuse, modular well partitioned designs, comments in the code, etc. For even higher abstraction, some tools can automatically generate HDL from block diagrams where each block represents a complex functional unit such as FFT, PID Controller, FIR filter, etc.

Synthesis

Synthesis tools typically get HDL as input and find out, in a first phase, what the designer is trying to implement. For example, the VHDL statement *DummyOut <= DummyInA when Selector='1' else DummyInB;* would be interpreted by a synthesis tool as a 2-to-1 multiplexer. The whole design is thus translated from text into so-called Register Transfer Level (RTL), a level of abstraction where a circuit is composed of standard combinatorial blocks (multiplexers, decoders, gates, etc.) and registers made of flip-flops. In a second phase, the tool maps the RTL design into the chosen chip. In our example, the multiplexer will end up mapped into a LUT where only three of the four inputs are used.

Place and route (P&R)

The place and route tool takes a netlist output by the synthesis tool, and maps it geographically onto the chip in two steps. In the placement phase, proper CLBs will be chosen to implement the functions described in the netlist. The subsequent choice of interconnection paths between these CLBs constitutes the routing phase.

As we shall see, designs consist very often of groups of combinatorial logic sandwiched between register banks. Every time a clock tick happens, signals propagate from the inputs of the registers to their outputs and then through the combinatorial path generating a result fed to the inputs of the next register bank. This result should be ready by the time the next clock tick comes if we want the circuit to function correctly. Maximum propagation delay through combinatorial logic therefore determines the maximum clock rate at which a design can work.

In this context, the choice of CLBs in the placement stage is critical for timing performance. A clear example is the case of a 16 bit counter, which involves addition and can therefore take advantage of the vertical carry daisy chain between CLBs. A design where only one such counter is instantiated will be an easy task for the placement tool, which will very likely use vertically adjacent CLBs to map the structure. In a more dense design, however, the different bits of the counter might end up in geographically dispersed areas of the FPGA. The process by which the designer constrains the placement tool to use a set of predefined CLBs for certain parts of a design is called floorplanning [2]. The placement tool will start by mapping these parts first and will only have freedom for the rest. Floorplanning is an important technique to achieve timing goals in complicated systems such as those found in typical DSP applications.

PERFORMANCE BOOSTING TECHNIQUES

Besides working on the placement and routing of a design, a designer can also boost its performance by introducing architectural changes. Some of these changes are trivial enough to be delegated to the synthesis tool, for example the automatic insertion of extra internal buffers

in a fan-out configuration to increase the current drive for a signal whose edges are being slowed by too many capacitive loads. If the synthesis tool detects that the output of a buffer is driving too many destinations, it will automatically replicate it. Registers, along with any combinatorial logic downstream, can be replicated in the same way and for the same reasons.

Another family of techniques consists in identifying places where the number of combinatorial logic layers between two register banks is too large. Figure 4 illustrates the technique of retiming, also known as "register balancing".

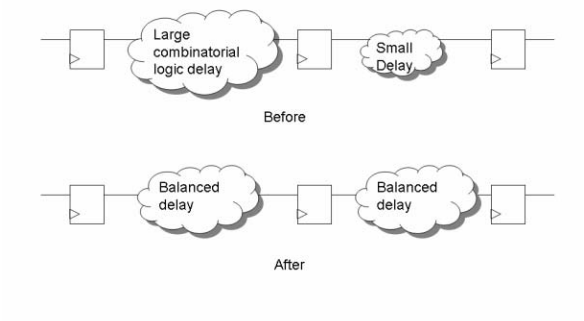

Figure 4. Register balancing.

If a design lends itself to this technique, then some of the logic after the first register bank can be displaced to the second register bank and the resulting system can be clocked at a higher rate. A variation of this theme, if a design can accommodate extra delay cycles from input to output, is to insert one or more register banks to break the large combinatorial block into smaller pieces. This technique is commonly known as pipelining.

Figure 5 illustrates a time-multiplexing scheme to double throughput.

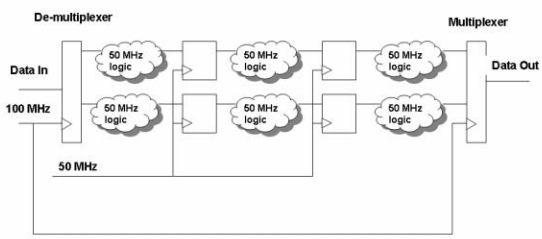

Figure 5. Doubling throughput through time multiplexing.

Time multiplexing and de-multiplexing can be used in conjunction with the other techniques described above to boost throughput by exploiting the inherently parallel nature of FPGA hardware. This is in fact a recurrent pattern in performance boosting schemes: a designer can often trade off speed (throughput) for silicon area. With silicon becoming cheaper and cheaper, there are fewer and fewer systems whose speed requirements cannot be met by FPGAs.

Another technique worth mentioning concerns multiplication of a variable signal by a fixed quantity. It is very often the case that an alternative arrangement can be found to avoid using a full-blown multiplier, saving silicon and increasing speed. As an example, one might want to calculate the product 0.5625M. But notice that 0.5625M = 9M/16 = M/2 + M/16, so a simple adder fed by bit-shifted versions of M will give the correct result. This technique is used for example in a lossy integrator filter that extracts the baseline from a Beam Position Monitor (BPM) signal in CERN's PS.

DISTRIBUTED ARITHMETIC

Digital Signal Processing algorithms often involve the calculation of a Sum Of Products (SOP) of the following type:

$$y = \sum_{n=0}^{N-1} c[n] \cdot x[n]$$

Here the x[n]'s are N input data samples and the c[n]'s are N constant pre-defined coefficients, such as the coefficients of an FIR filter. If we assume x[n] has a width of B bits and we replace x[n] by its bit decomposition, we get:

$$y = \sum_{n=0}^{N-1} \left(c[n] \cdot \sum_{b=0}^{B-1} x_b[n] \cdot 2^b \right)$$

After rearranging the sums (hence the term "Distributed Arithmetic [3]"), we get:

$$y = \sum_{b=0}^{B-1} 2^b \cdot \left(\sum_{n=0}^{N-1} c[n] \cdot x_b[n] \right)$$

Now there seems to be no major outcome of this manipulation until we realise that the term in brackets is easy to implement in a RAM or a LUT: for every possible set of x_b bits (consisting of N elements), we have to assign an output value. The resulting hardware structure is depicted in figure 6.

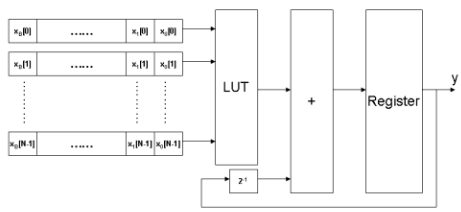

Figure 6. Distributed arithmetic implementation.

Input samples are all presented at the same time, one bit at a time, to the LUT. These N bits act in fact as address lines of the RAM or LUT. The data contained at a given address is the pre-calculated term in the parentheses of the equation above. This data gets scaled by ½ before going to an accumulator. After B iterations, the result of the computation is in the y register.

With distributed arithmetic we have achieved two important results:

- An SOP has been computed using no hardware multipliers. A pre-requisite for this is that the c[n] coefficients be constant.
- The number of cycles necessary to compute the SOP does not depend on the number of input samples but on the number of bits of these samples.

Of course, a larger number of input samples will require a larger RAM, but it will not create bigger delays, illustrating again the area for speed trade-off.

THE CORDIC ROTATOR

The basic arithmetic operations can be implemented in a fairly straight-forward way using digital gates:

- Addition of N bit numbers can be performed cascading N 1-bit full adders, each of them calculating a result bit and a carry to be fed to the next stage.
- Multiplication and division can be performed using a "pencil and paper" approach, i.e. scaling by powers of two and accumulating results under certain conditions.

For more involved operations, such as the conversion of complex numbers from polar to Cartesian coordinates or vice versa, or the calculation of trigonometric functions, the COordinate Rotation DIgital Computer (CORDIC) algorithm [4] provides an elegant silicon-efficient solution.

A CORDIC rotator block takes a vector (x, y) as an input and rotates it by a given angle to give the result (x', y') according to the transformation:

$$x' = x \cdot \cos\phi - y \cdot \sin\phi$$

$$y' = y \cdot \cos\phi + x \cdot \sin\phi$$

These equations are impossible to implement using basic gates. However, if we factor out the cosine term, we get:

$$x' = \cos\phi\left[x - y \cdot \tan\phi\right]$$

$$y' = \cos\phi\left[y + x \cdot \tan\phi\right]$$

Now, the trick is to proceed by angle jumps iteratively, accumulate these jumps and stop when the accumulator value is close enough to the target angle. If we constrain the angle jumps for iteration i to be such that:

$$\tan\phi = \pm 2^{-i}$$

Then, the multiplication by the tangent is a simple shift operation, and the only decision left is the direction of the angle jump for each iteration. The cosine terms are simply fixed multiplicative constants and can be applied at the end since their value does not depend on the jump direction:

$$\cos(\delta_i) = \cos(-\delta_i)$$

The final CORDIC equations are therefore:

$$x_{i+1} = K_i\left[x_i - y_i \cdot d_i \cdot 2^{-i}\right]$$

$$y_{i+1} = K_i\left[y_i + x_i \cdot d_i \cdot 2^{-i}\right]$$

With:

$$K_i = \cos\left(\arctan 2^{-i}\right) = 1/\sqrt{1+2^{-2i}}$$

$$d_i = \pm 1$$

The CORDIC rotator can operate in two modes:

- In rotation mode, we give the required rotation angle as an argument and the CORDIC iterates until the target angle is reached, producing x and y as outputs.
- In vectoring mode, the CORDIC takes an input vector and rotates it until the vector aligns with the horizontal x axis, producing x and the rotation angle as results.

As an example, we can see how to calculate the sine of an angle with the CORDIC. To do this, feed (x=1, y=0) and the desired angle to the CORDIC in rotation mode. After the rotation, the y result is in fact the sine we looked for, since the magnitude of the vector is 1.

CORDIC algorithms generally produce one additional bit of accuracy for each iteration. A typical application with a 16 bit result running at 100 MHz would therefore calculate the sine of an angle in 160 ns.

AN EXAMPLE: RF CAVITY CONTROL

Let's illustrate some of these techniques with a real example. The system described below [5] performs the control of the radio-frequency electric field inside a cavity of CERN's Linac 3. Figure 7 shows a general view.

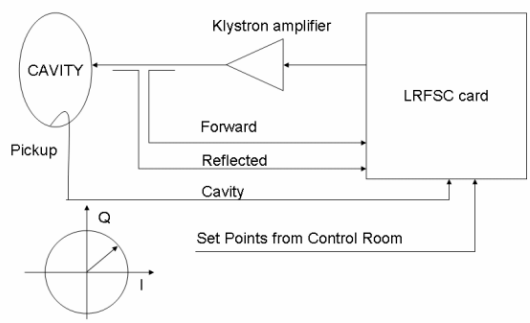

Figure 7. Block diagram of RF cavity control system.

At the fixed 100 MHz frequency imposed by the cavity, the RF signal can be completely characterized by two quantities: amplitude and phase (using polar coordinates

in a phasor diagram) or I and Q if we work in Cartesian coordinates. The goal of the Low level RF Servo Control (LRFSC) card is to maintain a fixed value of I and Q from the cavity despite the imperfections of the klystron amplifier and disturbances due to beam loading.

The main feedback loop measures the signal coming from the cavity and performs the necessary corrections on the signal sent to the klystron. Forward and reflected signals from the amplifier output are also fed back to the card for cavity resonance control and compensation of large phase shifts in the klystron.

The card extracts a 20 MHz sine wave from the 100 MHz RF signal by down-converting with 80 MHz and low-pass filtering. The 20 MHz wave contains all the amplitude and phase information (or conversely I and Q) of the original 100 MHz wave, so we can extract these values from it and use them to determine the feedback. The 20 MHz sine wave is sampled at exactly 80 Ms/s and the samples are sent to an FPGA which implements the loop as well as VME communication and diagnostics.

The reason to sample at exactly four times the input frequency is that the output stream can then be interpreted as I, Q, -I, -Q, I, Q,… So with a trivial de-multiplexer and sign reversal scheme we can extract two 40 Ms/s data steams from the incoming 80 Ms/s stream, as shown in Figure 8.

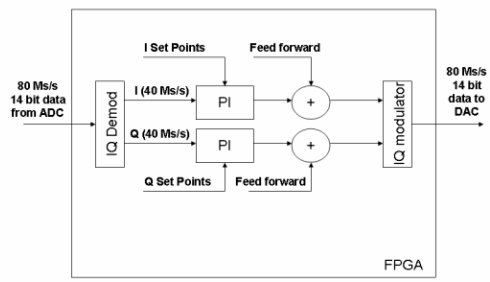

Figure 8. A simplified view of the LRFSC FPGA design.

The I and Q extraction scheme is straight-forward to implement and avoids the need for imperfect analogue components such as power and phase detectors. Once the I and Q streams have been separated, each goes through an independent Proportional-Integral (PI) controller implemented using the hard-wired multipliers of the Xilinx Virtex II family. There are also provisions for injecting systematic feed-forward corrections downstream before the signals go to the IQ Modulator block, where both streams are merged again to generate the samples of a 20 MHz output sine wave with the corrected I and Q values. These are sent to a fast DAC, the output of which goes through a low-pass reconstruction filter before being up-converted with the same 80 MHz local oscillator as the input. Finally the signal is band-pass filtered and amplified before being sent to the klystron, thus closing the loop.

The IQ Modulator/Demodulator pair plays the role of the multiplexer/de-multiplexer pair of figure 5, enabling us to have an 80 Ms/s system by splitting into two 40 Ms/s branches.

A future system enhancement will consist in adding an auxiliary loop to compensate for large phase shifts in the klystron. To implement the phase compensation, the phase will have to be extracted from I and Q, very likely using the CORDIC scheme described earlier.

SUMMARY

After briefly describing the internals of FPGAs and the associated design flow, we have given some tips and techniques commonly used to maximize the performance of a digital design in terms of clock speed. Two important FPGA techniques for performing arithmetic, namely DA and CORDIC have been explained and illustrated, and a real design example of Digital Signal Processing using an FPGA has been presented. The choice of topics has been rather arbitrary, but hopefully enough to give a flavour of the main issues concerning high speed DSP using programmable logic and to trigger design ideas in the field of Beam Instrumentation.

ACKNOWLEDGEMENTS

Many thanks to Wolfgang Heinze, Uli Raich and Tony Rohlev for fruitful discussions and to Bertrand Frammery for letting me set some time aside to delve into this interesting subject.

REFERENCES

[1] http://www.xilinx.com
[2] A basic introduction to floorplanning is available at http://www.fliptronics.com/floorplanning1.html
[3] U. Meyer-Baese, “Digital Signal Processing with Field Programmable Gate Arrays”, 2nd edition, Springer 2004.
[4] See http://www.andraka.com/files/crdcsrvy.pdf for an excellent survey of CORDIC algorithms for FPGAs.
[5] A. Rohlev et al. “All Digital IQ Servo-System for CERN Linacs”, EPAC 2004, Luzern, Switzerland.

A NEW TRAJECTORY MEASUREMENT SYSTEM FOR THE CERN PROTON SYNCHROTRON *

J.M. Belleman, CERN, Geneva, Switzerland

Abstract

We describe the projected new trajectory measurement system for the CERN PS, currently under design, in which the trajectory of each particle bunch is calculated on the fly from a continuous high-rate stream of digitised PU signal samples. The system will store data for a full acceleration cycle. Multiple clients will then be able to select subsets of the data for further treatment and display.

Using a prototype of the projected hardware, raw PU signals have been accumulated during the 2004 run and processed off-line, validating the algorithms for beam synchronisation and calculation of trajectories for all current and known future beam types (subject to pick-up bandwidth limits) in the PS.

Records of the system behaviour, as implemented by the off-line processing chain and using real pre-recorded pick-up signals, will be shown.

THE PS

The CERN Proton Synchrotron (PS) is the oldest particle accelerator still operating at CERN. It was commissioned in 1959 as the world's first alternating gradient, strong focusing machine. Still today, it is the kingpin of the CERN complex of accelerators, in which it now serves as the injector machine to the Super Proton Synchrotron (SPS). Today, the PS accelerates mainly protons (p^+), but in the near future, it will also produce $^{208}Pb^{54+}$ ions for LHC.

PICK-UPS AND SIGNALS

The particle trajectories are measured with forty electrostatic pick-ups (PUs) distributed around the ring.

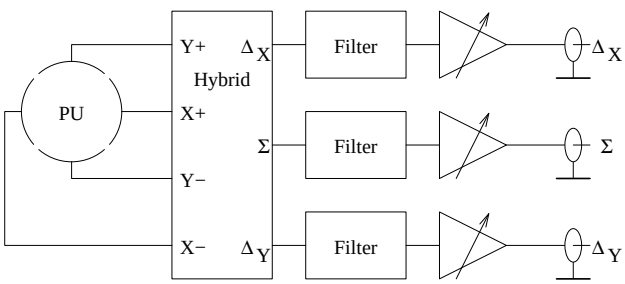

Fig 1 Pick-up analogue signal processing

* We acknowledge the support of the European Community-Research Infrastructure Action under the FP6 "Structuring the European Research Area" programme (DIRAC secondary-Beams, contract number 515873)

Passive hybrids combine the electrode signals into a common sum (Σ) and horizontal and vertical difference signals (Δ_x, Δ_y) (Fig 1). Pre-amplifiers installed near each PU shape and amplify the signals before they are carried over high-quality coaxial cable to the PS central building, where the signals are further treated. A VME-based computer controls the amplifier gains according to the expected beam intensity.

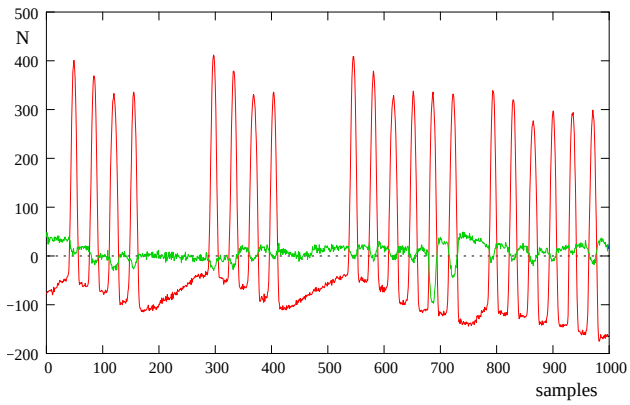

Fig 2 Example of PU signals: LHC beam at 2nd injection. Σ and Δ_x.

The position of the centre of charge of a particle bunch is derived by integrating the three signals, Σ, Δ_x, and Δ_y, over the length of a bunch, and normalising against Σ:

$$x = S_x \frac{\Delta_x}{\Sigma} + E_x \quad (1)$$

Here, S_x is a proportionality constant expressed in mm, and E_x is an additive error correction.

Digital signal processing

The system digitises the analogue PU signals at a constant 125 Ms/s rate. The samples are pre-processed into per-bunch integrals on the fly before being stored in a memory big enough to hold the results for all bunches in the machine for the full duration of an acceleration cycle.

Given that different bunches may follow different trajectories, due, e.g., to being of different intensity, or to being injected at a different time, it is necessary to have a timing reference that can track each bunch from injection all the way through to ejection. The cavity RF is not suitable as a timing reference, because its phase with respect to the beam changes according to whether the beam is coasting or being accelerated, below or above γ-

transition. Also, due to cabling delays, the phase difference depends on F_{rev}.

Further complications are introduced by what are colloquially known as 'RF gymnastics'. These consist of bunch splitting or merging and of changes in the bunch spacing other than through the effect of the changing revolution frequency [2][3].

A simple level trigger algorithm to detect bunch presence quickly runs into trouble because of varying filling patterns, bunch splitting and merging operations, different intensity bunches being accelerated together etc. Thus a more sophisticated approach is needed.

Acceleration

Beams are injected at a magnetic field of 0.1T. Acceleration then takes place up to a maximum field of 1.26T. While p^+ undergo only a small variation of F_{rev} when accelerated from 1.4 to 26 GeV, Pb ions have a variation of over one octave (Fig 3) [1].

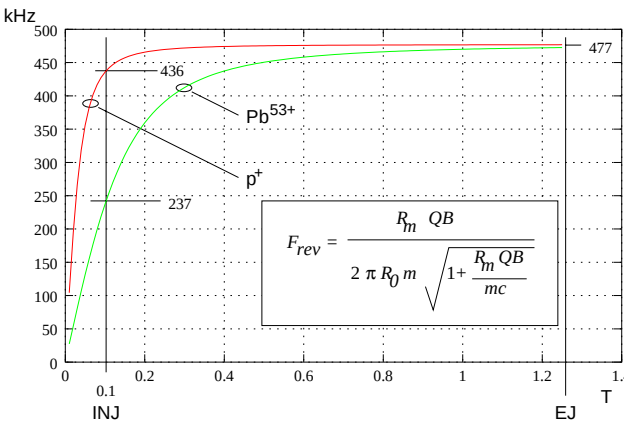

Fig 3 Revolution frequency vs. magnetic field

R_m=70.0789 m is the bending radius of the main magnet, R_0=100 m is the machine radius, Q [C] is the particle charge, m [kg] the particle mass and B [T] the magnetic flux density. The peak dB/dt is about 2.3 T/s, yielding a peak dF/dt of 1.6 MHz/s near the start of acceleration.

SYNCHRONISATION

The core of the synchronisation system is basically a numerical Phase Locked Loop (PLL) (Fig 4). A phase accumulator θ is advanced by f every period of the sampling frequency F_s, making θ overflow at the rate of F_{rev} (Fig 4). The phase accumulator output is used to address the phase table that contains h periods of the Local Oscillator (LO) signal. The LO frequency is thus $h\,F_{rev}$.

The LO is mixed with the incoming PU signal sample stream and the product is low-pass filtered to extract a phase error (ε). The phase error is fed back via a regulator to correct the value of f.

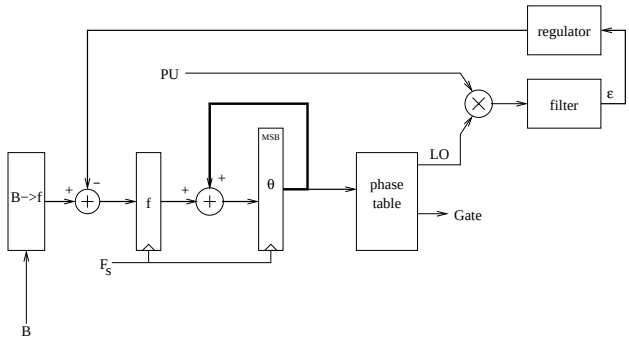

Fig 4 Principle of reference frequency generation

The value of f represents the value of the revolution frequency F_{rev} according to:

$$f = \frac{AF_{rev}}{F_s} \tag{2}$$

Here A is the full-scale value of the phase accumulator. A suitable initial value for f is provided by the block labelled B->f according to Fig 3 and (2). The regulator keeps the phase relation between the PU and LO signals, and consequently the phase accumulator, constant.

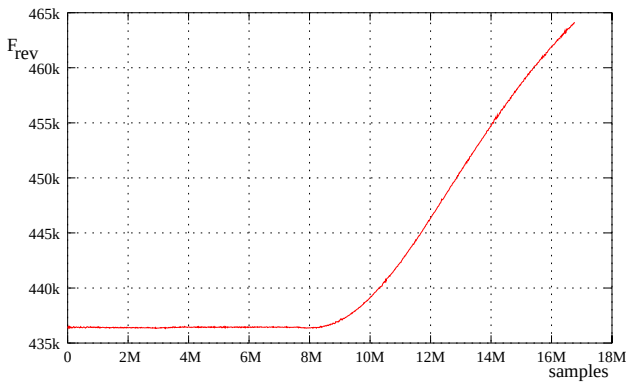

Fig 5 F_{rev} as reconstructed by the PLL

Another column of the phase table is used to produce a 'gate' signal, delimiting the subsets of the PU sample stream that contain a bunch. These samples are added together to get an estimate of the integral over the bunch length, and the results are stored into memory at the end of each bunch.

The actual position calculation (1) can be deferred until data are requested for display on an operator console.

Loop dynamics

The synchronisation loop is a discrete-time feedback system. Its transfer function can be expressed as polynomials in the 'z' domain. The open-loop transfer function is:

$$H_o = \frac{hz^{-1}}{A\left(1-z^{-1}\right)} \cdot H_m \cdot \left(\frac{z^{-1}}{1-0.996z^{-1}}\right)^3 \cdot \frac{\left(1-0.999z^{-1}\right)^2}{1-z^{-1}} \cdot z^{-n} \tag{3}$$

The first factor represents the phase accumulator, modelled as an integrator. Here, A is the full-scale value

of the phase accumulator and h is the accelerator harmonic number. H_m is the mixer, modelled as a pure gain, usually of the order of a few hundreds.

The next factor is a low-pass filter that keeps only the low frequency terms of the phase error. Its corner frequency is a compromise between rejection of F_{rev} and loop settling time.

The fourth factor is the feedback regulator, starting with a pole at +1, i.e., an integrator, to make the static phase error tend to nought. Two real zeroes are needed to make the loop stable. Finally, the last factor, z^{-n}, represents the inevitable pipeline delays of the physical implementation of the loop (n≈6).

The closed-loop transfer function is:

$$H_c = \frac{H_o}{1 + K_R H_o} \qquad (4)$$

K_R is the regulator gain. The stability of the loop can be assessed by examining the root-locus of H_c with the regulator gain K_R as the independent variable. All poles must lie within the unit circle. The optimal setting of K_R depends on the beam intensity and on h, the harmonic number. The loop behaves acceptably over a variation of K_R of more than 20dB.

The algorithm was tested by implementing it in the C-language and feeding it the raw data recorded using the prototype acquisition hardware.

Handling RF gymnastics

For some types of cycle, the beam undergoes manipulations that change the number of bunches, or that change the spacing between them [2][3]. Typically, these operations span several tens of ms on a constant energy plateau. An example is the triple splitting of LHC bunches (Fig 6).

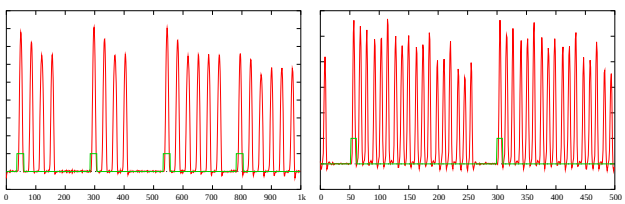

Fig 6 Beam and derived Gate signals before and after LHC triple split

These operations can be dealt with by switching to different phase table columns for the LO and Gate signals at an appropriate instant, e.g., at the end of a splitting operation. The PS machine timing system provides signals suitable for this use. By appropriately initialising the phase table contents beforehand, the change can be made without discontinuity.

Resolution

The position resolution of the system has been estimated by gathering some statistics on position measurements at a quiet spot in an EASTB cycle (single bunch, $10^{11}p^{+}$) (Fig 7). The true beam position was assumed not to vary over this roughly 250-turn interval.

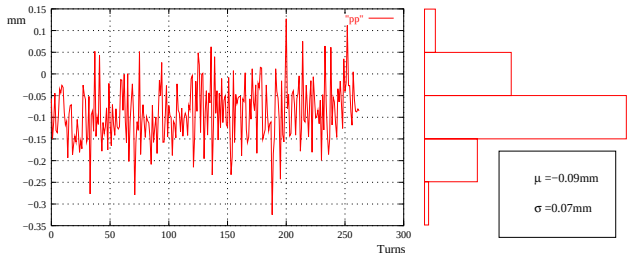

Fig 7 Positions and histogram over 250 turns on EASTB

The RMS resolution is slightly better than 0.1mm. However, the resolution deteriorates on cycles with shorter bunches. This issue remains to be examined in more detail.

CONCLUSIONS

An entirely digital processing algorithm for trajectory measurement of individual bunches in proton synchrotrons, using fast constant-rate digitisers, is described. A C-program, reading real digitised PU data, was used to validate the algorithm off-line. It remains to be implemented in the form of FPGA logic. The design is sufficiently flexible to follow all present and known future RF gymnastics in the PS. The same design has been shown to be usable for other p^{+} or ion synchrotrons, such as the GSI SIS18 and the future GSI SIS100.

ACKNOWLEDGEMENTS

Space here does not allow me to give proper credit where due, but I'd like to thank J.L. Vallet for explaining to me the intricacies of RF gymnastics, M. Gasior for the many discussions on the subject of feedback control and the GSI crew for their help in acquiring PU signals on the SIS18.

REFERENCES

[1] H.H. Umstätter, “Tables of dynamic parameters of the PS”, CERN-MPS-Int-SR 68-7, 1968

[2] R. Garoby, S. Hancock, A. Ozturk, J-C. Perrier, J-L. Vallet, “PS machine development report: Preparation of the nominal production beam for the AD”, PS/RF/Note 99-01 (MD)

[3] R. Garoby, S. Hancock, J-L. Vallet, “Demonstration of bunch triple splitting in the CERN PS”, CERN/PS 2000-038 (RF)

THE PSI "VPC" BOARD - FIRST APPLICATIONS OF A COMMON DIGITAL BACK-END FOR ELECTRON AND PROTON BEAM INSTRUMENTATION AT PSI

B. Keil, R. Kramert, P. Pollet, P. Spuhler, P.-A. Duperrex, G. Gamma, G. Janser,
U. Mueller, V. Schlott, N. Schlumpf, E. Schmid, PSI, Villigen, Switzerland.

Abstract

This report gives an overview of the design concept and applications of the VME PMC Carrier board (VPC), a VME64x board that was developed at PSI as a common digital back-end for beam instrumentation at the PSI electron and proton accelerators. The two Xilinx Virtex2Pro FPGAs of the VPC allow the implementation of the complete digital section of a beam instrumentation system on a single chip ("SOC"), including detector front-end interface, filters, interlocks, feedback links, high-level data analysis like FFTs, and a generic control system interface. In addition to the two on-chip PowerPC processors of the FPGAs, the VPC provides a DSP, RAM, and multi-gigabit fibre optic links for distributed feedbacks and synchronisation. First applications of the VPC include digital proton beam position monitors (DBPMs) and beam profile monitors for the PSI proton accelerators, the readout of several thousand detector channel waveforms for a muon decay experiment, and the integration of photon BPMs into the SLS fast orbit feedback (FOFB). In addition to a status report and first results for these applications, an outlook on possible future applications of the VPC will be given.

INTRODUCTION

A significant number of new projects and collaborations of the PSI diagnostics section for proton, electron, photon and muon beam instrumentation and feedback systems motivated a modular design approach for the required monitor/detector electronics, with customised analog front-ends for each project, and the "VPC" VME64x board as a common digital back-end for all projects [1]. Rapid progress in digital electronics technology allows the digitisation of monitor signals at a very early stage of the signal processing chain, with functions like filters, mixers etc. being implemented digitally in FPGAs (Field Programmable Gate Arrays) or microprocessors rather than with analog components or dedicated ASICs. This allows the design of flexible high-performance beam instrumentation systems with reconfigurable "intelligent" monitor electronics that can relieve the higher control system levels from tasks like data analysis, fit routines or feedback calculations.

In the last decades the ongoing progress in IC integration enabled the reduction of the integration level for the digital part of complex monitor and feedback systems from crate level (e.g. a crate with several VMEbus boards) to board level (one VMEbus board with a large number of ASICs) and finally to chip level. Components like processors, RAM, buses, gigabit serialisers/deserialisers, clock generators, RS232 interfaces and application-specific modules like filters and detector interfaces can now be integrated on a single FPGA. By choosing this SOC approach for the VPC that uses Xilinx Virtex2Pro FPGAs, the number of other components on the VPC could be reduced to connectors etc. and a minimum number of ICs which are not (yet) integrated in FPGAs, like larger amounts of RAM, transceivers for VMEbus and fibre optic links, and non-volatile memory for FPGA configuration and boot software (see Fig. 1). By shifting the system complexity from hardware to FPGA firmware and software written in portable languages like VHDL and C/C++, the dependence on special ICs and their future availability is minimised. Furthermore, the reconfigurability of SOCs allows the use of the VPC for a large variety of different applications and enables upgrades and even complete changes of the system architecture of an SOC within minutes by remote firmware upgrades. A modular generic approach for VHDL firmware and C/C++ software allows the re-use of modules for future designs and future FPGA generations and successors of the VPC with little effort.

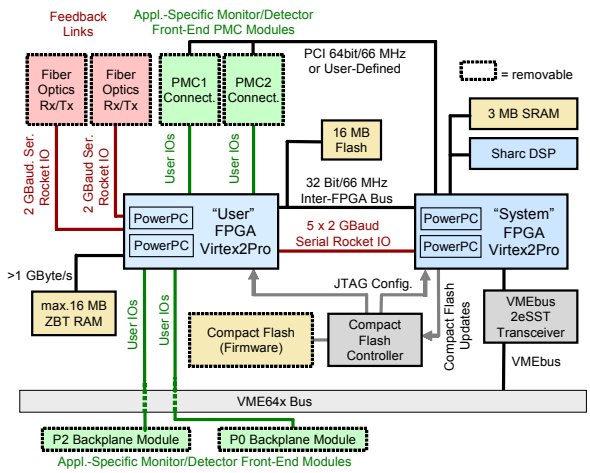

Figure 1: Block diagram of the VPC hardware.

HARDWARE ARCHITECTURE

Fig. 1 shows the main hardware components of the VPC. The core of the VME64x board consists of two Virtex2Pro FPGAs ("System FPGA" and "User FPGA") with two on-chip PowerPC processors each, a floating point DSP, and RAM. The FPGAs can acquire and process measurement data from two application-dependent PMC mezzanine modules or VMEbus P0/P2 backplane modules. Two optional SFP fibre optic

transceivers may also be used to acquire or distribute measurement data at 2.125 GBaud full duplex.

FIRMWARE ARCHITECTURE

Fig. 2 shows the modular structure of the generic System FPGA firmware that is common to all VPC applications. VMEbus, PCI (or user-defined) bus, User FPGA interface, DSP and compact flash controller are connected to an on-chip bus by suitable VHDL modules. So far the modules that are required for the first applications have been implemented (solid boxes). Additional modules (dotted boxes) will be added as required by future VPC applications.

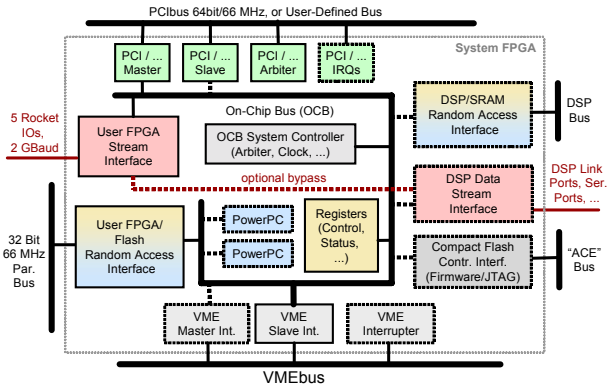

Figure 2: Block diagram of the generic "System FPGA" firmware that is common to all VPC applications.

Fig. 3 shows the typical structure of the application-dependent User FPGA firmware. The interface to the monitor/detector front-end is usually written in VHDL, which allows high-speed parallel data processing and data decimation. The resulting lower data rate can then be handled by the PPCs to perform high-level data analysis (fit routines etc.) in C/C++ code. The results can be transferred to the control system via VMEbus, to other VPCs via fibre links, or to the DSP that has 10 times more floating point power than the PPCs.

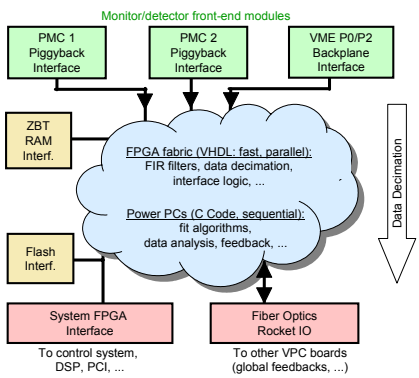

Figure 3: Schematic diagram of the typical structure of the application-dependent "User FPGA" firmware

VPC APPLICATIONS

VPC prototypes are available to users since May 2004, including System FPGA firmware with the features required for the first applications, and example firmware for the User FPGA. An automatic test system for the VPC has been developed in 2004 for simple testing and quality control of several hundred VPCs to be built in 2005/2006.

32-CHANNEL GSA/S WAVEFORM DIGITIZER

In August 2004 a low-cost 4 GSa/s 16-channel waveform digitizer PMC module developed at PSI [2] was successfully tested with the VPC in the lab. About 100 VPCs equipped with two PMCs each will be used to digitize several thousand detector channel signals with 1024 samples and up to 4 GSa/s per channel for the PSI "mu-gamma" (MEG) experiment. The present version of the MEG VPC firmware allows the adjustment of the sample rate, and the triggered acquisition and VMEbus readout of the sampled waveforms. The first particle decays were successfully measured with the VPC in October 2004. The requirements for the final User FPGA firmware version have not yet been defined, but are likely to include pre-processing, calibration and data analysis/decimation of the detector signals on the VPC. 2eVME block transfers will be implemented in the System FPGA until end of 2005 in order to provide VMEbus transfer rates of 60-80 MBytes/s required by the MEG experiment.

DIGITAL PROTON BPMS

Fig. 4 shows the layout of a VPC-based DBPM that was developed as a replacement for the analog BPMs of the PSI Ring Cyclotron transfer lines in order to improve dynamic range and bandwidth [3]. The DBPM consists of two RF front end modules (RFFEs) located close to the beam, a digital downconverter transition module (DTM) that is plugged onto the VMEbus P2 backplane, and the VPC. The RFFEs filter and amplify the 101.26 MHz signal (2nd RF harmonic) of four pickup coils in the beam pipe. Each RFFE also generates a pilot signal that is combined with each beam signal and delivered to the DTM that filters and amplifies the four signals, samples them with four ADCs and delivers them to two digital downconverters (DDCs) with four channels each. This allows to process beam and pilot signals simultaneously. The DDCs deliver the resulting four beam and four pilot signal amplitudes to the VPC via serial links, at a programmable rate of presently 50 kSamples/s.

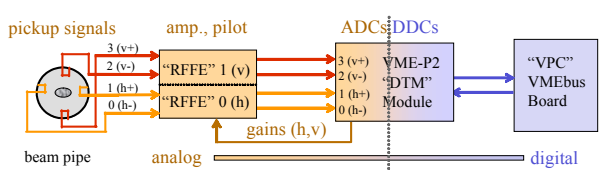

Figure 4: Schematic diagram of the DBPM hardware

Fig. 5 shows the layout of the User FPGA firmware for the DBPM, with green boxes for the application-specific VHDL modules (DTM interface) and other boxes for generic modules that are also used for other VPC applications. The first PowerPC (PPC1) initialises the internal registers and filters of the DDCs using their

parallel bus interface. The DDCs deliver beam and pilot signal amplitudes to the serial interface module of the firmware that stores the data in a cyclic dual-ported internal RAM. This RAM can also be accessed by PPC1 via on-chip peripheral bus (OPB) bridged to the processor local bus (PLB). PPC1 reads and calibrates the BPM data at 50 kSamples/s, normalises beam to pilot signal (optional), calculates beam positions, performs additional averaging, checks interlock levels, and provides oscilloscope-like trigger features with simultaneous storage of waveforms at four different averaging rates (50 kSa/s, 1 kSa/s, 50 Sa/s, 1 Sa/s) in the external ZBT RAM for VMEbus readout. PPC1 also performs automatic gain control (ACG): it reads the DDC input level detectors periodically and sets the gains of DTM and RFFE every 160 µs so that the ADC signal levels are kept in a user-defined window. The amplifier gains of RFFE and DTM (45 dB range each) are controlled by voltages generated by a 4-channel DAC on the DTM. Each RFFE also has an 18 dB attenuator that can be switched by PPC1, resulting in an overall gain range of 108 dB for the beam signals.

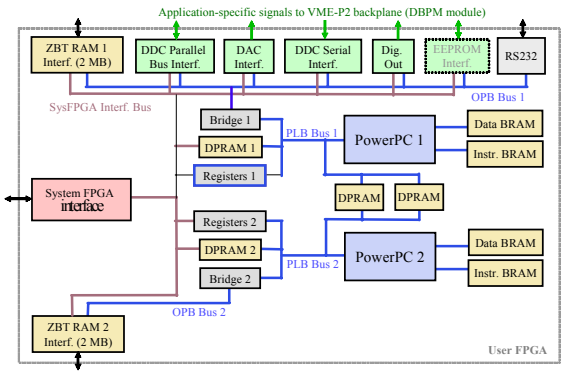

Figure 5: Schematic diagram of the VPC User FPGA firmware for the DBPM

While PPC1 has a fixed software package that provides all features that are vital for the operation of the accelerator, PPC2 is available for any kind of data analysis, and its software may be changed often without risk for the operation of the accelerator. At present PPC2 periodically calculates FFTs of BPM data.

Data transfer between each PPC and the System FPGA (and thus the VME-based control system) is done by internal dual-ported RAMs ("DPRAM1", "DPRAM2" in Fig. 5), by registers, and by the external ZBT RAMs. Dual-ported VHDL interface modules for ZBT RAMs and DTM allow full access to RAMs and DTM both by PPC1/PPC2 and VMEbus.

The complete DBPM (VPC, firmware, DTM, RFFE) was tested successfully in the lab in February 2005. At present the second revisions of DTM and RFFE are being designed, in order to fix minor bugs on the DTM and RFFE PCBs, to improve the dynamic range (presently >80 dB without normalising beam to pilot signal), and to allow direct ADC readout by the VPC, e.g. for future customised additional DDCs in the User FPGA.

PROTON BEAM PROFILE/HALO MONITORS

The VPC is also used for the readout and data processing of beam profile, current and halo monitors [3,4] for the new 250 MeV "PROSCAN" cancer therapy cyclotron that is presently being commissioned at PSI. The monitor front-ends generate currents that are digitised logarithmically by VME P0/P2 "LogIV" backplane modules that have up to 32 channels and a measurement range of 20 pA to 1 mA. The User FPGA firmware has a similar structure as the DBPM firmware, only with different application-dependent VHDL modules (upper green boxes in Fig. 5). PPC1 calibrates the detector currents using lookup tables, calculates a variety of functions like beam size and position, transmission, halo position etc., and provides averages, filters, interlocks and ZBT RAM storage of current waveforms with flexible scope-like trigger features. Firmware, hardware and software are fully operational, and a first series of about 20 VPCs will be installed at the the PROSCAN accelerator in June 2005.

FUTURE APPLICATIONS AND OUTLOOK

In 2005, the VPC will be used to integrate photon BPMs into the SLS FOFB, using the gigabit fibre optic links of the VPC for data transfer to the FOFB, and a newly developed VME-P2 module (currently under development) for the VPC to digitise the currents of the photon BPM blades [5].

The VPC and its FPGA firmware and software may also serve as a platform for future projects such as an upgrade of the SLS BPM and FOFB system, RF control and fast bunch-to-bunch feedbacks for VUV- and X-ray FELs at DESY and PSI, diagnostics for the SLS FEMTO and PSI LEG projects, and for an upgrade of the SLS multibunch-feedback.

REFERENCES

[1] B. Keil et al., "The Generic VME PMC Carrier Board: A Common Digital Hardware Platform for Beam Diagnostics and Feedbacks at PSI", Proc. EPAC´04, Lucerne, Switzerland, July 2004, 2517

[2] S. Ritt, "The DRS2 Chip: A 4.5 GHz Waveform Digitizing Chip for the MEG Experiment", IEEE/NSS Conference, Rome, Italy, Oct. 2004

[3] P.A. Duperrex et al, "Latest Diagnostic Electronics Development for the PROSCAN Proton Accelerator", BIW´04, Knoxville, USA, May 2004, AIP Conf. Proc. 732, 268

[4] R. Doelling, "Profile, Current and Halo Monitors of the PROSCAN Beam Lines", BIW´04, Knoxville, USA, May 2004, AIP Conf. Proc. 732, 244

[5] T. Schilcher et al., "First Steps towards the Integration of Photon Beam Position Monitor Signals into the SLS Fast Orbit Feedback", DIPAC´05, Lyon, France, June 2005, these proceedings

BEAM DIAGNOSTIC DEVICES AND DATA ACQUISITION FOR THE HICAT FACILITY

A. Peters, T. Hoffmann, M. Schwickert,
Gesellschaft für Schwerionenforschung (GSI), Planckstr. 1, 64291 Darmstadt, Germany

Abstract

A set of 92 diagnostic devices for beam diagnostics in the **H**eavy **I**on **Ca**ncer **T**herapy facility (HICAT) at the university hospital in Heidelberg is currently under development at GSI. All beam diagnostic devices will be fully computer controlled and will allow an automated detection of all relevant beam parameters. The HICAT raster scan method with active variation of intensity, energy and beam size requires the exact knowledge of the time resolved and spatial structure of the ion beam. An overview of the integrated devices is presented, particularly the time-of-flight method for energy measurement using electro-static pick-ups in the Linac is described in detail. The real-time PXI data acquisition system is explained as well as the embedding of the diagnostic devices in the timing and control system of HICAT.

INTRODUCTION

A first technical proposal for the HICAT facility had been presented in 1998 [1], a more detailed description of the final HICAT layout is given in [2]. The building is under construction since November 2003 and the installation of the accelerator will start in the last quarter of 2005. Fig. 1 shows the final layout of the accelerator facility. The outer dimensions of the accelerator building are 60m x 70m. HICAT consists of a 7 MeV/u-Linac (including the LEBT – low energy beam transport – and the MEBT – middle energy beam transport – lines), a Synchrotron (magnetic rigidity Bρ=0.38-6.5 T·m), two horizontal treatment stations (H-1, H-2), a Gantry-Section for 360°-patient irradiation and additionally a section for Quality Assurance (Q-A).

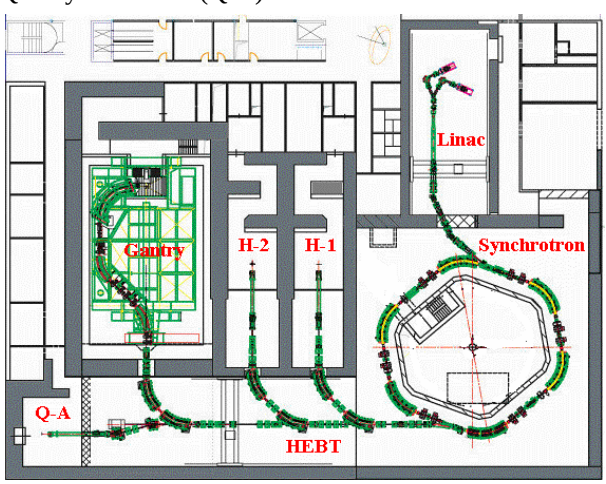

Figure 1: Layout of the first underground floor, housing the accelerator complex [2]

BEAM DIAGNOSTICS AT HICAT

Because no industrial supplier could be found, the beam diagnostics group at GSI was charged with the delivery of all measuring systems. The mechanical parts, such as detectors, linear vacuum feed-throughs, etc. are produced by GSI with sub-contractors. For the software and the electronic devices, however, commercial solutions with industrial partners were preferred.

Table 1: Overview of beam diagnostic devices for HICAT

Device	Qty.	Position	Device class
Faraday-cup (cooled/uncooled)	7	Linac	DC/AC-beam current
Profile grid	8	Linac	Profile measurement
El.-static pick-up	4	Linac	Phase measurement
DC-transformer	3	Lin/Sync	DC-beam current
AC-transformer	4	Lin/Sync	AC-beam current
Position monitor	6	Sync	Beam position
Beam loss mon.	6	Sync	Particle counting
Ioniz. chamber	13	Sync	Particle counting
Viewing screen	12	Linac/Sync/HEBT	Optical diagnostics (2D-Profile-Meas.)
Scintil. Counter	5	HEBT	Particle counting
MWPC	13	HEBT	Profile measurement
Isocenter-diagnostic screen	4	T1-T4	Optical diagnostics (2D-Profile-Meas.)
Slits	4	Linac	Command device
Foil stripper	1	Linac	Command device
Scraper	2	Sync/ HEBT	Command device

The 92 beam diagnostic devices were deliberately assorted to measure all relevant beam parameters (current, energy, beam profile, position and phase information) of the therapy accelerator [3]. Concerning the layout of the electronic hardware the basic idea was to use industrial standards to a maximal degree, in order to achieve a good maintainability of all devices and, as a consequence, to enhance the reliability of the HICAT facility. For example, all data acquisition is uniformly carried out using 11 separate PXI-controllers running LabViewRT [4], as will be described in detail below.

Table 1 summarizes the beam diagnostic devices of HICAT, listed in the order of their position in the accelerator complex and beam transport system – Linac, Synchrotron, High Energy Beam Transport (HEBT). Mainly due to the unification of the software layout, the beam diagnostic systems were subdivided into seven device classes, referring to the measured physical properties of the ion beam. In addition, also passive elements like slits, scrapers and the foil-stripper are included in the list, because these components are mounted on mechanic drives equal to the ones used for the active detector devices. These components build up the 8th device class, labeled as "command devices".

In the following section the electro-static pick-up system for the Linac part is described as an example, where a well-known beam diagnostic component has been redesigned and updated for the use in a commercial therapy facility, with the aim of finding commercial solutions and of unifying the data acquisition process.

ELECTRO-STATIC PICK-UP SYSTEM FOR THE HICAT LINAC

Overview

In the Linac section an RFQ accelerates the 200 µs long macro-pulses to 400 keV/u and the following IH-structure speeds up the ions up to the injection energy of 7 MeV/u, both stages running at 216.7 MHz. The electrostatic pick-up systems are used to determine:

- The energy of the beam at the exit of both accelerating structures within one Linac macro-pulse using the time-of-flight (TOF) method.
- The function of the stripper – a defect of the foil will change the TOF measurement of the beam between the enclosing pick-ups.
- The phase angles of the pick-up signals with respect to the RF tank signals.

The maximum currents in the Linac section are in the order of 50 µA to 1 mA, but due to the intensity variation with I_{max}/I_{min} = 1000 in most cases during normal therapy operation the beam current will be very low. Together with the fact that very small installation space was available, it was decided to design the electro-static pick-ups for phase measurement only. A position monitoring capability would have needed 4 buttons per pick-up with a higher mechanical expense and very cost-intense electronics.

The analog system of the phase pick-ups was determined by the commercially available PXI digitizers from Acqiris (see below) with around 1 GHz bandwidth, which permits the bunch characterization up to the 4th harmonic (5th harmonic at 1.083 GHz attenuated by around 6 dB).

Layout and Properties of the Pick-up

Two different phase pick-up types were built, a special one for the inter-tank section and three identical detectors for the MEBT line between IH-output and synchrotron injection, see Fig. 2.

The phase pick-up is generally designed in 50 Ω geometry and the frequency response up to 1.2 GHz is constant within 0.4 dB. A grounded diaphragm is installed on the entrance side on the pick-up to avoid direct hitting of the beam in case of mismatched optics.

Figure 2: Phase pick-up for the MEBT section

Preamplifier Stage

For amplifying the signals directly behind the pick-up, a commercial amplifier from FEMTO [5], type DUPVA-1-60, is used. It ideally fits the system demands:

- Five gain stages from 20 – 60 dB in 10 dB steps, remote control via optocouplers included
- An analog bandwidth of 1.2 GHz with a flatness of 0.15 dB for all gain stages
- Independent transmission time for all gain settings – necessary for the TOF method

From these preamplifiers the signals are transmitted via coax cables directly to the DAQ stage outside the radiation protected areas.

Data Acquisition and Control System

As already mentioned high speed cPCI digitizer boards from Acqiris, type DC241 [6], were chosen instead of a standard oscilloscope, because it is designed for the integration in a real-time control system. Therefore all 4

Figure 3: 6U PXI crate from EKF with a 3U NI controller and four 6U Acqiris DC241 digitizer modules

digitizer boards were installed in a 6U PXI crate from EKF [7] with additional 3U slots for the NI PXI controller and an I/O board for the amplifier control, which was no problem due to the PXI standardization, see Fig. 3.

From the perspective of the accelerator control system a DAQ system is the abstraction layer for the connected beam diagnostic devices, because one or more detectors are connected to one DAQ system and one or more DAQ systems are in turn logically grouped to “device classes” (cf. table 1). This concept has been developed in collaboration with the company Eckelmann [8], responsible for the whole accelerator control system .

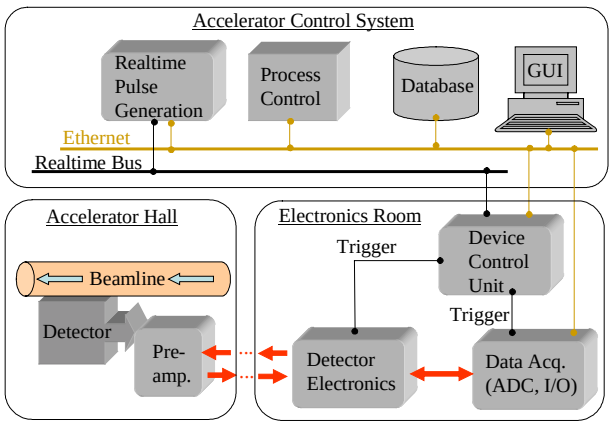

Figure 4: Schematic view of the DAQ systems embedded in the control system

All components of the accelerator control system (e.g. process control, GUI, database etc.) are linked via 100 MBit ethernet. Fig. 4 gives a schematic overview of the beam diagnostic’s integration into the HICAT control system. The DAQ systems communicate with the "process control"-part of the system, which manages the preparation of the DAQ systems to collect data, as well as the transport of the data to the graphical user interface (GUI) or the databases. Timing-signals are transported via a facility-wide real-time bus and are converted to trigger signals for the DAQ systems by so-called timing-DCUs (Device control units) with a precision of better than 1 µs.

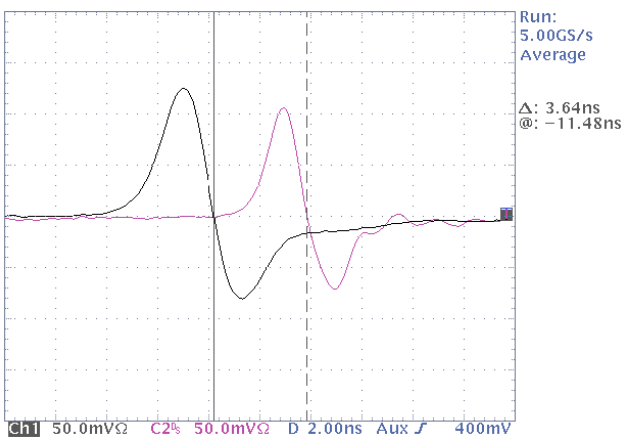

Figure 5: Time-of-flight signal from two pick-ups

Data evaluation and presentation

In Fig. 5 the acquired signals from two pick-ups separated by the distance L of typically some meters are shown. The bunch center-of-mass can be read from the signal data or – more precisely – the correlation function between the two signals can be calculated and evaluated.

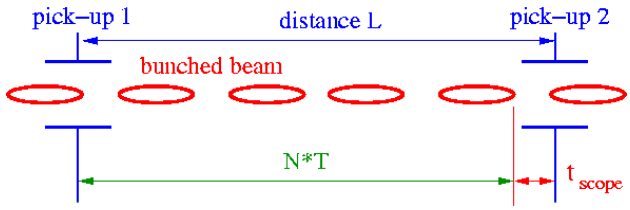

Figure 6: Principle of a TOF measurement using two phase pick-ups

As shown in the schematic (see Fig. 6), several bunches are between the pick-ups and a coarse estimate of the velocity is needed. This is normally known, but in case of trouble, a third pick-up has to be installed much closer to one of the others. The velocity is calculated for the measured time t_{scope} via

$$\beta c = \frac{L}{NT + t_{scope}}$$

with N bunches between the pick-ups and the bunch repetition time of $T = 1/f_{RF}$.

The precision of such a velocity measurement $\Delta\beta/\beta$ is given by the uncertainty of the distance L and the time estimation t to be

$$\frac{\Delta\beta}{\beta} = \sqrt{\left(\frac{\Delta L}{L}\right)^2 + \left(\frac{\Delta t}{NT + t_{scope}}\right)^2}$$

Assuming a precision of ΔL = 1mm and Δt = 100ps, an accuracy better than 0.1% can be reached for the energy spread $\Delta W/W = 2*\Delta\beta/\beta$, if the distance between the two pick-ups is around 4 m like in the HICAT set-up downstream of the IH-structure at 7 MeV/u (β = 0.12). With the energy resolution given above it is possible to detect defects of the stripper foil which e.g. causes an energy loss of 16.2 keV/u for the passing Carbon beam.

Before commissioning of the Linac an intuitive GUI (Graphical User Interface) will be defined for the electrostatic pick system. Tests of the whole system including all software levels are foreseen in the next months at the test stand for the RFQ, which is currently built up at GSI.

REFERENCES

[1] J. Debus et al., 'Proposal for a dedicated ion beam facility for cancer therapy', Heidelberg, 1998
[2] H. Eickhoff, Proceedings EPAC 2004, p. 290-294
[3] A. Peters, P. Forck, BIW2000, AIP Conf. Proc. Vol. 546, 2000, p. 519-526.
[4] http://www.ni.com
[5] http://www.femto.de
[6] http://www.acqiris.com
[7] http://www.ekf.de
[8] http://www.eckelmann.de

BREMSTRAHLUNG DETECTION AND CHAMBER OBSTRUCTION LOCALISATION USING SCANNING RADIATION DETECTORS

G.A. Naylor, B. Joly, D. Robinson, ESRF, Grenoble

Abstract

Radiation monitors consisting of scintillating plastic coupled to photomultipliers are used for diagnostic purposes. By scanning such a detector or a radiation scatterer, two applications are demonstrated:

i) Monitoring of vacuum chamber conditioning by monitoring gas Bremstrahlung from residual gas.
ii) Localisation of beam interception (beam losses) by longitudinal scanning of a radiation detector.

The measurement of gas pressure inside long, small cross section, vacuum vessels is difficult due to the distance between the centre of the vacuum vessel and vacuum gauges (leading to a low vacuum conductance). The narrow beam of gamma Bremstrahlung radiation is intercepted by scanning tungsten blades in the beam line front-end allowing a radiation shower to be detected outside the vacuum vessel proportional to the gas pressure in the corresponding storage ring straight section. A second detector mounted on rails can be moved over a length of 6.5m parallel to the ESRF storage ring so as to localise regions of beam loss. The location of a scraper and narrow chamber entry and exit points are clearly resolved.

NO SUBMISSION RECEIVED

THE INSTRUMENTATION OF THE TI8 SPS TO LHC TRANSFER LINE

L. Jensen, CERN, Geneva, Switzerland

Abstract

The new TI8 transfer-line between the SPS and the future LHC was commissioned during two long machine development sessions in autumn 2004. This paper will present the beam instrumentation linked to the extraction region and along the line from the design and installation up to the tests with beam. After minor modifications copies of these systems will be used for the TI2 transfer-line to be commissioned with beam in 2007.

INTRODUCTION

The LHC Transfer & Injection (LTI) project started for the BDI group in 2002 with the arrival of the functional specifications [1] and the beginning of the official coordination meetings.

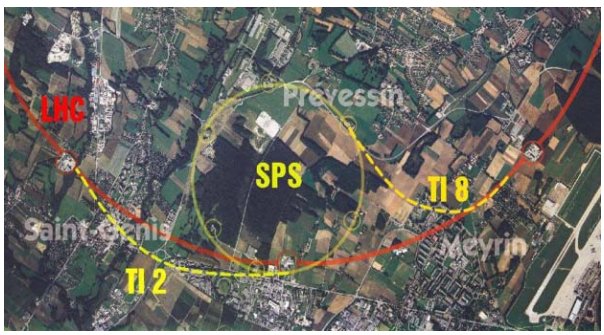

Figure 1: Aerial view of the SPS to LHC transfer-lines

BDI INSTRUMENTS

From the user requirements, the hardware implementation choices for the different systems were made. Some of the systems below had already been tested with beam in 2003 during tests of the extraction system and the first ~100m of the TI8 transfer line (TT40) [2]. The systems involved are:

- A beam position interlock linked to a pickup in the extraction region (named BPCE) that should allow the extraction of the beam only if the bumped position (nominally close to 30mm) is within pre-programmed limits. To acquire the turn-by-turn position data, the existing SPS orbit system (MOPOS) was used. A dedicated real-time action utilising the pickup linearization algorithm described in [3] was developed and the interface to the interlock system took place through the prototype LHC beam interlock controller (BIC) module [4].
- A beam-loss interlock monitoring the losses during the extraction process. If a problem occurs during the slow (~100 msec) ramping of the orbit corrector bumpers, this system should dump the circulating beam to avoid damaging the downstream extraction elements (septa etc). To cover this requirement, 8 dedicated ionisation chambers were installed in the extraction region, with the fast loss detection system [5] connected to the SPS emergency beam dump.
- A total of 15 beam profile monitors (BTVI) (see figure 2) were requested from the SPS extraction region through to the end of the TI8 transfer-line. They are used to acquire the 3D images of the signal produced when the beam passes through a screen made of either alumina (for luminescence) or titanium (for OTR). New mechanisms to select the filter (for signal attenuation) and the screen position were designed and could be controlled from the newly designed BTVI VME acquisition and control card [6]. To avoid signal cable lengths of more than 3km, VME acquisition systems were positioned at either end of the transfer-line. A dedicated PC system with digital video transmission over Ethernet was provided to allow the remote real-time observation of a selected screen.

Figure 2: A TI8 beam profile monitor (BTVI)

- Fast beam current transformer devices (see Figure 3) installed at either end of the TI8 transfer-line to measure the transmission of the beam through the line. Fast 40MHz integrators allow the measurement of individual bunches spaced by a multiple of 25ns. More information about the Fast BCT systems can be found in [7].

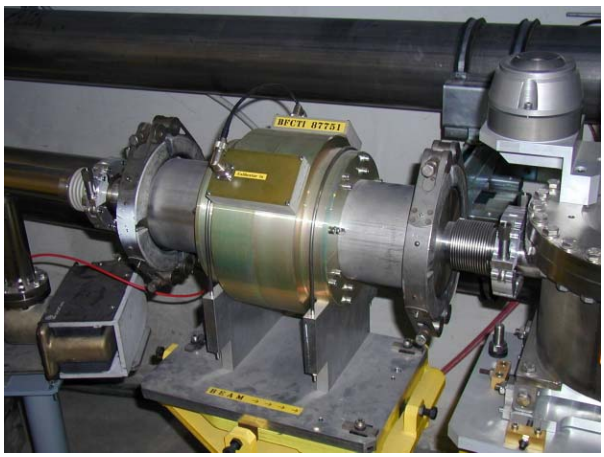

Figure 3: A Fast BCT device on in the TI8 line.

- A total of 44 beam position pickups were installed along the line. These consisted of 4 large aperture strip-line couplers in the first part, followed by 40 button electrode pickups using recuperated LEP buttons. For the majority of pickups, only the measurement plane corresponding to the maximum transverse beta-value was connected. In certain strategic places though, both measurement planes were equipped. Different configurations of the distributed front-end electronics meant that a total of 40 front-end crates (see Figure 4) were installed in the tunnel equipped with power-supply, WorldFIP and WBTN modules. More information about the BPMI system layout can be found in [8].

Figure 4: A BPMI front-end crate before installation in the tunnel. On the top can be seen the optical fibre patch panel.

- Beam loss monitors for detecting of losses produced by the passage of the beam through the line. A total of 28 standard SPS type ionisation chambers were used for this purpose.

INSTALLATION AND COMMISSIONING

The button-type pickups connected to the main transfer-line quadrupoles were aligned and installed before being installed in the tunnel by the vacuum group. All other equipment was installed by members of the BDI group. Priority was given to the equipment under vacuum such that the entire line could be tested for vacuum leaks as quickly as possible. A single leak was found on one of the recuperated LEP buttons. More information can be found here [9][10].

TESTS WITH BEAM

The transfer line was tested with beam during two 48 hour MDs in the autumn of 2004. To keep the induced radiation level to a minimum most of the tests were done using a single LHC bunch at intensities around 5E9 protons. The main problems encountered during the first test period were: a) very noisy downstream BCT readings which meant that the planned transmission tests between the start and end of the line were difficult to do and b) unusable position values obtained for the first two strip-line couplers at the start of the line. It was later discovered that these pickups were incorrectly cabled. Fortunately as the beam went straight through the line this didn't cause any serious problems. It was believed in the beginning, that the beam position system for the upstream part of the line was incorrectly calibrated; giving position readings which were very different from what was expected (see Figure 5).

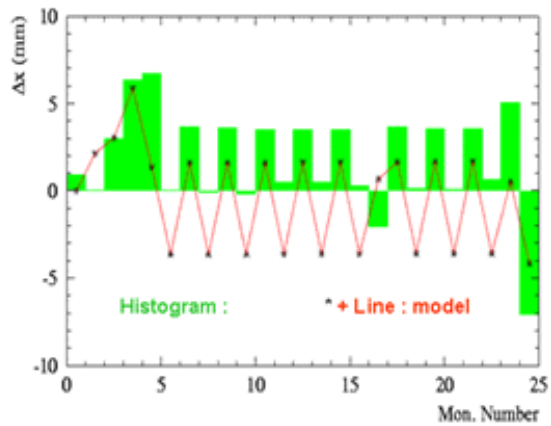

Figure 5: Measured (bars) versus predicted response.

The discrepancy, however, was finally found to come from the wrong current setting in a quadrupole in the beginning of the line. After correcting this problem the entire line fitted the model to better than 10% as expected (Figure 6).

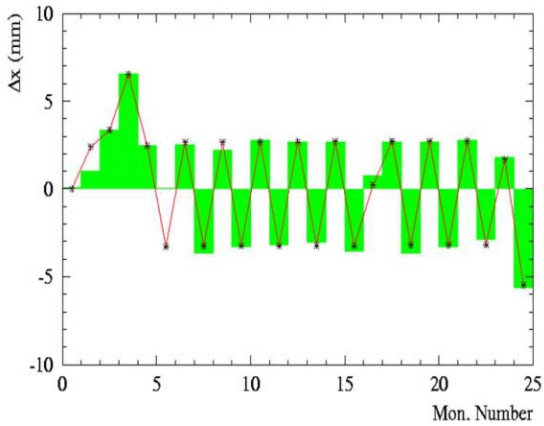

Figure 6: With the quadrupole problem solved the beam response fits the MAD model.

During the second test period some time was spent with a beam of 4 bunches spaced at 525 ns. This beam was used to measure the spread in the bunch to bunch positions and intensities. The operational application to visualize the beam position data in the transfer-line showed the average position rather than that of the individual bunches. However as the spread in the bunch positions were calculated and returned with the data it was possible to get a clear view of the spreads encountered. During these tests, spreads of several 100 microns in beam positions were observed and were judged to come from jitters on the extraction kicker flat-top amplitude. An example of the calibrated intensities acquired in the downstream BCT system at the end of the line can be seen in Figure 7.

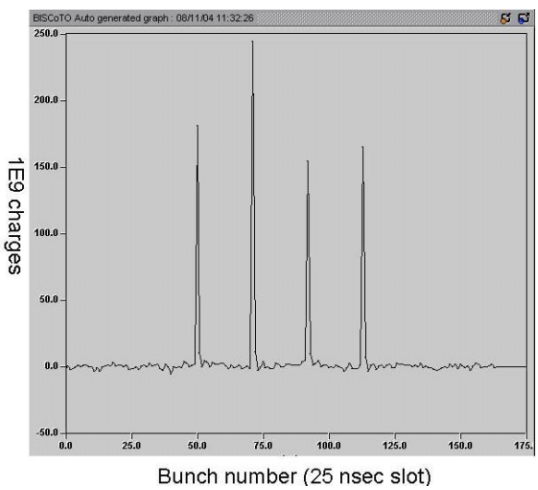

Figure 7: The calibrated intensities of individual LHC bunches spaced by 525 ns.

More information about the results obtained can be found in [9], [11] and [12].

CONCLUSIONS AND THE FUTURE

The instruments installed by the Beam Diagnostics and Instrumentation group allowed the TI8 transfer-line between the SPS and LHC to be thoroughly tested with beam. In addition, since much of this equipment is also destined for the LHC, it provided a first test-bed for LHC instrumentation. Minor design changes were highlighted necessary to make these systems more robust and reliable.

ACKNOWLEDGEMENTS

I wish to thank my colleagues from the OP, BT and BDI groups for the help they provided including photos and information needed to write this paper.

REFERENCES

[1] J. Wenninger et al, “Instrumentation for the TI 2 and TI 8 Transfer Lines”, EDMS Document LHC-B-ES-0004
[2] Chamonix 2004 proceedings, CERN-AB-2004-014-ADM
[3] N. Catalan-Lasheras, et al, “Calibration of BPCE.41801 and SPS extraction bump in LSS4”, AB-Note-2003-046-MD
[4] A. Dinius et al, “Beam Interlocks for LHC and SPS”, CERN-AB-2003-106-CO
[5] L. Jensen et al, “Protection and Diagnostic Systems for High Intensity Beams”, CERN-SL-2000-032-BI
[6] S. Burger et al, “A New TV Beam Observation System for CERN”, proceedings of this conference
[7] H. Jakob et al “A 40 MHz Bunch by Bunch Intensity Measurement for the CERN SPS and LHC”, CERN-AB-2003-056-BDI
[8] D. Bishop et al, “The LHC Orbit and Trajectory System”, CERN-AB-2003-057-BDI
[9] L. Jensen, “Post-mortem of the 2004 LTI project seen from AB/BDI”, AB-Note-2004-079 BDI
[10] J. Uythoven et al, “Commissioning of the LHC Beam Transfer Line TI 8”, PAC2005
[11] J. Wenninger et al, “Optics Studies of the LHC Beam Transfer Line TI8“, PAC2005
[12] J. Wenninger et al, “Beam Stability of the LHC Beam Transfer Line TI8” , PAC2005

IMPROVING THE RELIABILITY OF IPM*

D. Liakin, V. Skachkov , ITEP, Moscow, Russia, P. Forck, T. Giacomini#, GSI, Darmstadt, DE64291, Germany

Abstract

IPMs measure in a non-destructive way the profile of ion beams independent whether the beam is bunched or not. Our application is the heavy ion synchrotron SIS, which can accelerate ions with a large variety of different masses and charges. The IPM is used to obtain information about the beam matching, the electron cooling and to support for any kind of machine experiments. To ensure reliable function and to increase the data accuracy we executed some important mechanical improvements. The resistive E-field plates were replaced by discrete electrodes. We designed a new MCP-Phosphor-screen assembly of rectangular shape and large active area and in addition a module with a filament mounted in meander shape to monitor the degradation of the MCPs. The whole device was planned with respect of high field uniformity and small mechanical dimensions at a large clearance for the beam.

INTRODUCTION

Ionization Profile Monitors (IPM) are used in synchrotrons and storage rings to measure the beam profile. The IPM at the GSI heavy ion synchrotron (SIS) measures every 10ms a full beam profile, horizontal and vertical. At the end of the cycle the data are automatically analysed and the users can view the beams evolution of the whole synchrotron cycle. The beam profile and the beam position provide information about the injection matching and the accelerator setting and adaption. The beamwidth shows the effects of electron cooling and of multiple injections, it also gives a hint of beamlosses during the cycle. The benefit of these measurements is connected to the reliability and long term stability of the IPM and the trustiness of the obtained data. The environmental conditions for IPMs are usually vacuum bakeout and long maintenance intervals. Once installed or modified the IPM is not accessible for a long time, often for several years. These conditions make it necessary to restrict the number of functional parts and to control most parameters from outside the vacuum. The device has to be achieved in a way that it withstands all possible burdens during long term operation. The quality and the long term stability of the electrical field (E-field) that accelerates the ionized particles perpendicular to the beam is most important for a true image of the beam. A rectangular (Multi-Channel-Plate) MCP-Phosphor screen assembly fits best the needs of an IPM. These devices are only in concentric form commercially available. We developed a rectangular device with an active area of 100mm by 22mm. The IPM is designed to have the freedom of detecting residual gas ions and electrons. When detecting residual gas electrons the residual gas ions will produce secondary electrons at the bottom of the E-field box. The resulting signal complicates automatic analysis of the data. Therefor a secondary electron suppression is needed. The amplification of MCPs degrades during operation. Partially the areas of the MCP degrade at most where the density of impacts by residual gas particles is biggest. The degradation must be observed careful to obtain a beam profile correction function. A filament can be used both as secondary electron suppression and to generate a test signal for the MCPs.

ELECTRICAL FIELD BOX

The original E-field design of the IPM was based on resistive side electrodes made of glass coated with germanium [1]. Cracks in the germanium layer occurred probably because of the rough environmental conditions like big temperature changes during multiple vacuum bakeout and the different thermal coefficients of the glass sheet and the coating. The cracks prevented a constant conductivity of the resistive layer. By time the potential difference was equalized by sparks and thus the beamprofiles were strongly deformed. That made it nearly impossible to analyse the IPM data automatically.

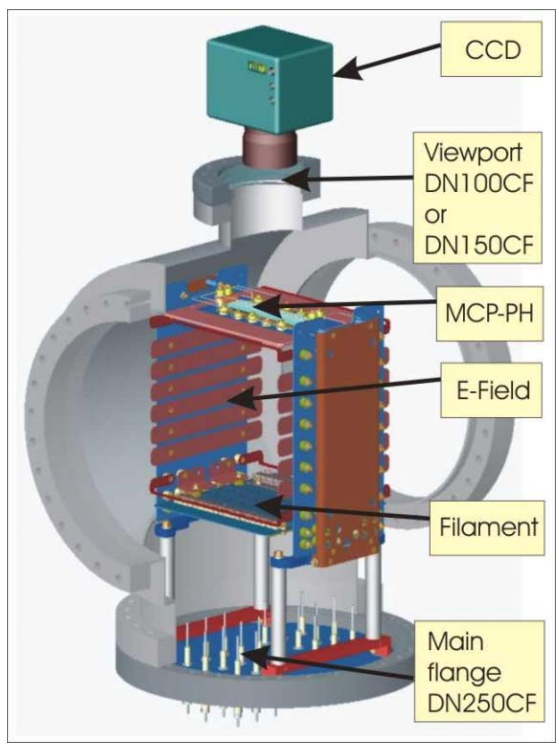

Fig. 1: E-field box vertical side electrodes, double layer filament, corrector electrodes, rectangular MCP-Phosphor assembly.

* Funded by INTAS, Ref. No.: 03-54-3931

T.Giacomini@gsi.de

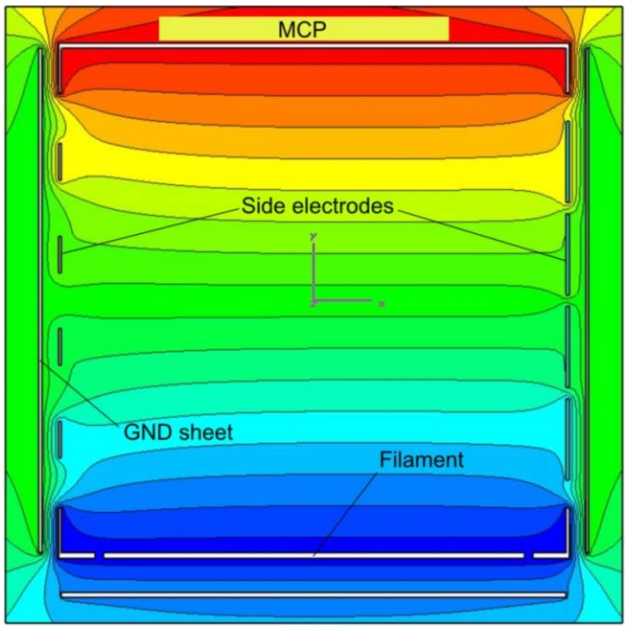

Figure 2: Four discrete side electrodes per side. Left hand side: large gaps between the electrodes, right hand side: small gaps. The y-coordinates of the electrodes are equal also the potentials.

Resistive electrodes are active parts of the E-field contrary to discrete electrodes. We designed and installed an E-field box that uses discrete side electrodes, Fig.1. The potential of each pair of side electrodes can be changed from outside the vacuum. The special alignment of the side electrodes increases the field uniformity if the gaps between the electrodes are small and it reduces the consumption of mechanical space. If the gaps are large the non-uniformity increases, Fig.2. The clearance of the E-field box is about 175mm in square.

The side electrodes increase the field uniformity perpendicular to the beam direction. To increase the longitudinal field uniformity corrector electrodes were applied at the beams entrance and exit of the E-field box, see Fig. 3. The field uniformity is improved significant when the absolute potentials of the correctors are bigger than the absolute potentials of the corresponding top or bottom plate. The relation of the potentials between the corrector and the corresponding electrode depends on the E-field box dimensions.

The fixations of all the electrodes were achieved with standard insulators which are made of glass ceramics due to the UHV conditions.

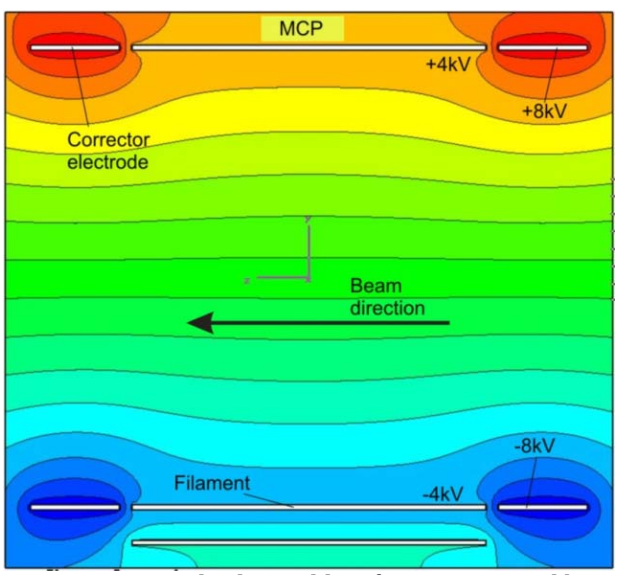

Figure 3: Longitudinal E-Field uniformity increased by corrector electrodes.

SHIELDING

The IPM can measure the horizontal and vertical beam profile simultaneously. In this case the main E-field vectors of the horizontal and the vertical IPM are torn by 90°. To avoid mutual disturbances a shielding is foreseen located between the two IPMs, see Fig.4. The shielding is achieved as a ring at ground potential. This configuration allows also a kick compensation whereby one IPM measures while the second one compensates the kick.

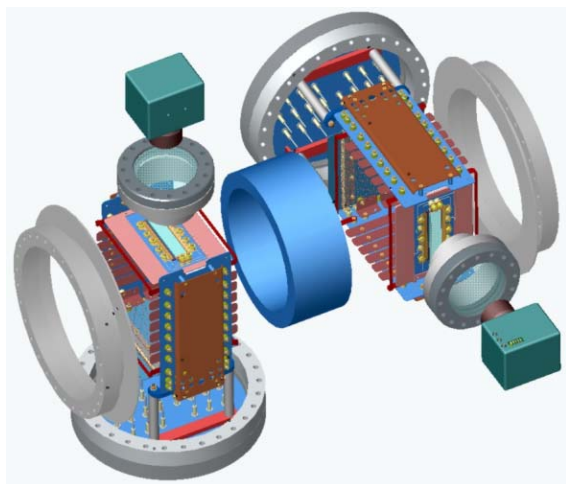

Figure 4: Horizontal and vertical IPM, separated by shielding.

RECTANGULAR MCP-PHOSPHOR ASSEMBLY

The ion beam width in the heavy ion synchrotron is sometimes bigger than 20mm. Additionally the beamposition can be shifted by about 20mm. To detect the ion beam at these conditions we choose MCPs of 100mm by 30mm. The rectangular shape exploits best the conditions of the electrical field. The MCPs are in Chevron configuration with a gap of 0.1mm. The gap between the MCP and Phosphor screen will be about 0.8mm and the potential will be in the range of 6.3kV/mm. The MCPs and the Phosphor screen are not mechanically connected like in commercially available devices. The MCPs are arranged in sandwich style. Two flat springs along the long edges press the MCP Chevron configuration onto the base sheet. The springs are insulated of the base sheet. The electrical power is supplied by the springs to the MCPs. The gap between the MCPs is created by two 2mm wide and 0.1mm thick metal strips. The strips have also electrical connections to

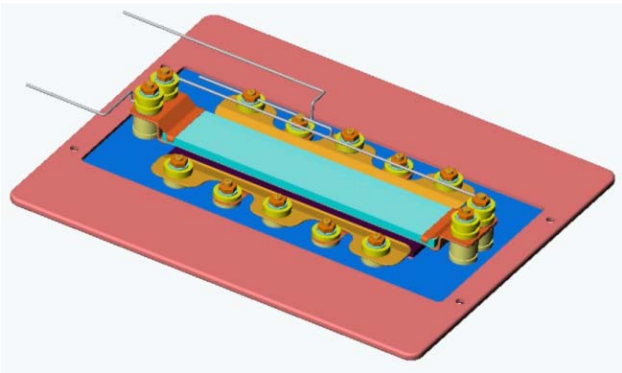

Figure 5: Rectangular MCP–Phosphor assembly. The visible image is 100mm by 22mm.

control the voltage between the MCPs, see Fig 5.
The Phosphor screen is fixed at his short edges on the base sheet and it is lifted 0.8mm above the MCPs. Due to the UHV conditions and no mechanical connection between MCP and Phosphor screen the potential difference of 5kV is not critical. First high voltage tests showed the applicability of this design. The electrical power is supplied by the mechanical fixations. The module provides a detectable image to the CCD of 100mm by 22mm.

FILAMENT MODULE

The tungsten filament is achieved in meander shape to cover the whole MCP, see Fig.6. The center to center spacing of two turns is of about 3mm while the wire diameter is 0.1mm. Each end of the filament is individual connected to an electrical vacuum feed through. To suppress the secondary electrons a proper potential is applied to the filament while the potential of the base sheet is more positiv. To test the MCPs degradation the filament can be used to emit electrons, which are accelerated towards the MCP. On the phosphor screen an image is generated representing the shape of the filament [3]. This can be done by times to keep the correction function up to date. To verify the uniform electron emission a second filament layer of similar function and style is installed. First tests show the feasibility of this technique. The filament was heated for 2 days in intervals of 1hour and there was no measurable change in the resistance. To obtain an uniform electron emission wires free of tinder are required. To compensate the extension of the heated filament every meander turn should be streched by a separate spring. The springs diameter is 0.4mm. A special mounting tool was developed to ensure the accurate assembling and tension of the wires.

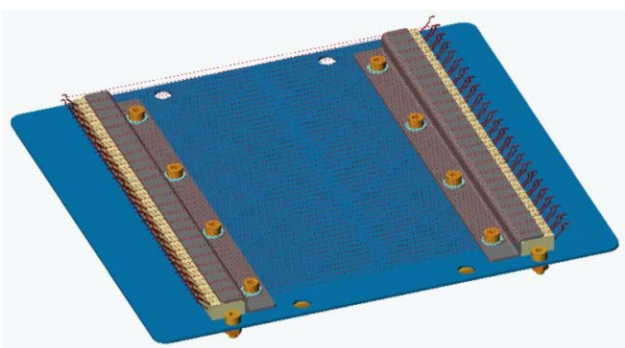

Figure 6: Filament module, the center to center spacing of two wires is 3mm.

Reducing The MCP Degradation

In a Chevron configuration the second MCP degrades usually at first moreover only the rearmost part of the MCP channels [2]. The MCPs degradation can be reduced dramatically when the high voltage is applied only during the measurement. The heavy ion synchrotron of the GSI can control 16 virtual accelerators with different settings for different masses and charges at time. Ions of different masses and charges from several sources can be accelerated alternately. The IPM is used at a time only for one ion mass and charge due to the exact setting of the MCP amplification. Nevertheless the MCPs are reached permanently by residual gas ions of all virtual accelerators. To take care of the MCP it is sufficient to reduce the MCP voltage for a few hundreds of volts outside the measurement. A high voltage relay that bridges a resistor is one possible solution. It can be controlled automatically by timing events of the accelerator. A control mechanism by software is also applied to switch off the MCP amplification completely after a certain time of inactivity.

CONCLUSION

The IPM in the SIS is used more and more for operating purposes. It is permanently improved and upgraded to satisfy the need of reliable data during common operating and at special machine experiments. To ensure an effective and profitable usage of accelerators it is important to make beam instrumentations reliable, long term stable and permanent available.

REFERENCES

[1] T.Giacomini , “Development Of A Residual Gas Profile Monitor With High Resolution And Fast Readout”, BIW 2004, Knoxville, USA.

[2] V.Kamerdzhiev, “Ionization Beam Profile Monitor At The Cooler Synchrotron COSY-Juelich”, DIPAC 2003, Mainz, Germany.

[3] G.Ferioli, “Sensitivity Studies With The SPS Rest Gas Profile Monitor”, DIPAC 2001, Grenoble, France.

DETERMINATION OF BEAM CHARGE USING STRIPLINE SIGNALS AT THE RF FREQUENCY BY FAST SIGNAL PROCESSING IN A FPGA

G.A. Naylor, B. Joly, ESRF, Grenoble

Abstract

Traditional methods of measuring beam charge requires integration of a signal from a fast current transformer. Ultimately the integral of a transformer signal is zero, practical measurements are achieved by taking a finite integration, which leads to some error. In the method proposed here the signal at the carrier frequency (RF frequency) is sampled (from a stripline) and demodulated in an FPGA to determine the total charge. By time multiplexing the stripline signals from different parts of the accelerator complex, cross calibration can be achieved.

NO SUBMISSION RECEIVED

CURRENT STATUS OF THE ADVANCED RESIDUAL GAS MONITOR FOR HEAVY ION SYNCHROTRON APPLICATIONS*

D.Liakin#, Vl.Skachkov, S.Barabin, O.Sergeeva (ITEP,Moscow), P.Forck, T.Giacomini (GSI, Darmstadt), Vic.Skachkov, A.Vetrov (MSU, Moscow), A.Paal (MSL, Stockholm).

Abstract

The challenge and complexity of the advanced RGM requires very careful design of each structural component and special attention to match the properties of different subsystems. In the present paper the status of the high performance readout electronics is discussed. Single optical decoupled profile measurement channel (one of 100) with 14 bit resolution and 10 MHz bandwidth was tested and step-by-step improved. Special attention had been paid to the noise cancellation and digital data processing algorithms optimization.

Another important point is a proper electromagnetic guiding system design. As it is shown, high field homogeneity, which is required for sub-mm spatial resolution, can be achieved despite the presence of the field distorting hole for the light signal transmitting. The low energy (down to 10MeV per nucleon) beam disturbance compensation methods are also discussed. The ionization process and electron dynamics simulations are used for proving this system design.

THE STATUS OF THE FAST PROFILE READOUT ELECTRONICS

The advanced RGM structure was described in details in [1] and [2]. It will cover profile measurements with 0.1 microseconds of time and 1mm spatial resolution. A phosphor coated Microchannel Plate (MCP) is proposed as a wide bandwidth high resolution primary detector. A bundle of 100 optically decoupled from the signal source digitizing channels will allow fast measurement option in addition to the slow profile measurements with a CCD camera. Avalanche photodiode (APD) is used as a light receiver to provide required bandwidth, sensitivity and dynamic range. The saturating of the MCP output basically limits the signals level, therefore low noise operation is mandatory [3]. The structure of the data acquisition channel is shown in Fig. 1.

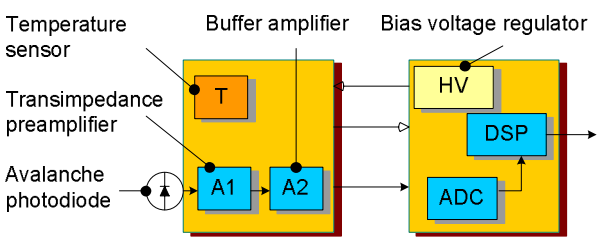

Figure 1: The structure of one photodiode readout channel

A two-module structure was chosen to build a compact, EMI protected head with embedded photodiode and to connect it to a more sophisticated data processing module. To diminish an induced noise and EMI a two-stage preamplifier (A1 and A2) is placed in the head. The sensor T provides the APD temperature which is then used by a digitally controlled high voltage source (HV) to fix the APD multiplication factor. A 14 bits 65MHz ADC sampling rate exceeds the Nyquist frequency, which reduces the requirements to the analog antialiasing filter.

The test setup consists of the readout channel itself, a wide bandwidth LED emitter fed by a signal generator, Hamamatsu's wide band optical receiver and personal computer for control and data presentation. A serial connection was used to communicate with the PC. A dedicated control software had been designed for the DSP and PC to provide a suitable Windows interface with graphical output. A real-time data filtering and decimation algorithms were implemented in C code for fast on-line data processing in the DSP. Three frequency bands were used to cover full frequency range of further applications.

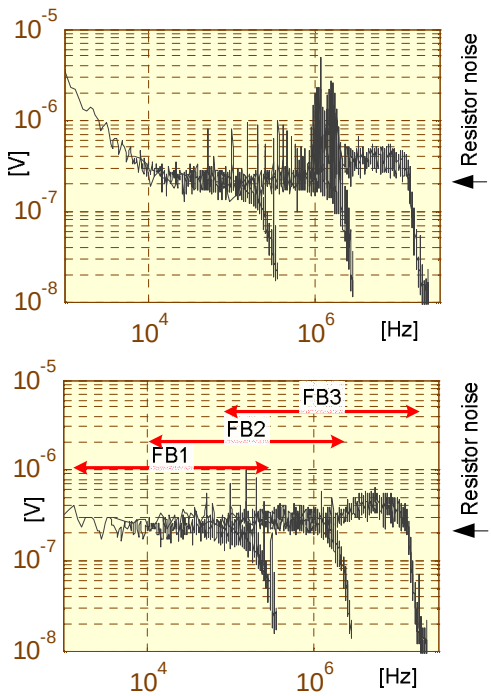

Figure 2: Preamplifier output noise (amplified) before (on the top) and after optimisation

To measure the frequency response of the readout channel the noising properties of the avalanche photodiode were used. The shot noise of a photodiode grows like square root of DC current or incoming light intensity, therefore an illuminated APD can be interpreted as a white noise generator. This APD feature was used to

*Work supported by INTAS, Reg.No.:03-54-3931
#liakin@itep.ru

obtain the frequency response-like spectrum on the amplifier's output.

At the design phase the computer simulation was used to define the estimated output voltage noise on the first stage preamplifier's (A1) output. This simulation gives the value of 40 nV/Hz$^{1/2}$ of the noise power density for the medium frequency range and increases this value for higher frequencies due to the dropping of the operational amplifier gain. The medium frequency range noise consists mainly of the feedback resistor thermal noise and hence can be considered as the lowest achievable theoretical value. The next design phase was dedicated to analysing and suppressing of all extra noise sources. On the top of figure 2 one can see the measured noise spectrum, which still includes a number of external spectrum lines. Some of these lines may be identified with switching power supplies, PC monitor or microprocessor clock frequencies. A few printed board geometries and power supply configurations were tested before the suitable result was obtained. This figure shows the noise spectrum during and after the design optimisation. The resulting noise spectrum is quite similar to the one obtained by the computer simulation.

As it was mentioned above, three frequency regions were used to cover the full frequency range of the future application. The highest frequency band is limited by an antialiasing analog 13 MHz filter while the other two are limited by performing a digital filtering in the DSP. The filtering and decimation of the incoming data were executed as real-time operations by DSP in the data processing module. The performance of the DSP was tested in advance to define the maximum achievable quality of digital filtering. In this test mode the data was acquired by DSP by embedded direct memory access channel. Two switching data banks in the internal DSP memory were used for data reception and evaluation. The required processor time for filtering and decimation was directly measured by a scope and compared to the incoming data rate (acquisition time). As a result, an 80 taps FIR structure has been accepted for the decimation filters of the frequency bands 1 and 2.

ELECTRON DYNAMICS TO MCP

In RGMs an electrostatic field accelerates the ionization products of the beam and residual gas towards a MCP. The fast readout option of our project requires a short drift time and therefore electrons should be used for profile imaging. To compensate the space charge effect and electrons initial velocity spread a guiding uniform magnetic field is applied to allow precise electron positioning on the MCP surface. Detailed requirements to the E and B-fields strength and uniformity were presented in [2]. 100 mT B-field and 50 kV/m E-field are required to cover all proposed RGM applications at GSI. To achieve the desired resolution, the 100 mT magnetic field provides an average cyclotron radius of the electrons smaller than 0.1 mm, as demonstrated in Fig. 3(a). Fig. 3(b) shows the 1D probability P_y as a function of sweep argument y; more than 65 % of the generated electrons hit the circle with radius of 0.1mm.

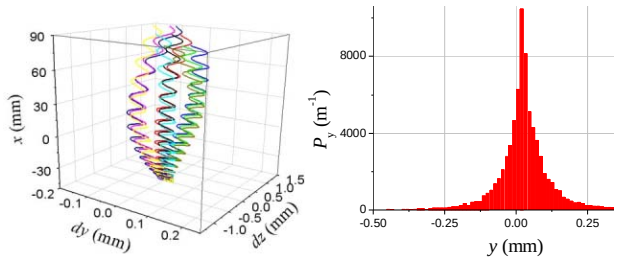

(a) (b)

Figure 3: Electron trajectories – (a) and (b) – integrated distribution at MCP along sweep direction.

The RGM resolution is very sensitive to the orthogonal magnetic field component. To limit the electron deflection with the desired value, this component should be decreased below 0.2 % of the field magnitude. The beam-coincident magnetic field projection is allowed to deviate up to several percents of the field magnitude without affecting the monitor accuracy.

To simulate the ionization process we used a simple model of two interacting point charges. By our code we integrated the electron dynamic equations in the field of a moving ion. After ionization the daughter products (one free electron and one residual gas ion) interact with the external magnetic and electric fields generated by RGM systems and the electromagnetic field generated by the beam.

To present the bunch field the 3D Gaussian charge distribution was used. During electron dynamic calculations toward the MCP our code takes into account the bunch motion up to relativistic velocities.

RGM CHANNELS

E-Field:

A dipole box design with side electrodes supplied with linearly changed potential is used for electric field generation.

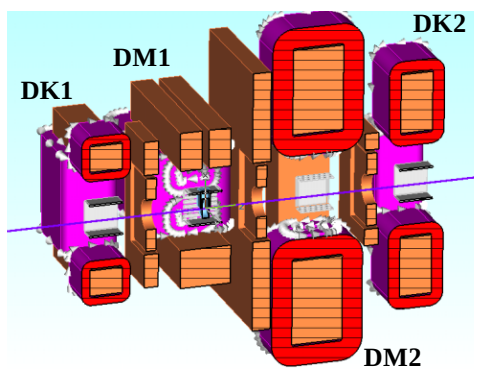

Figure 4: RGM magnetic & electric channels elevation.

Such dipole even of 200 mm long at Ø180 mm aperture provides acceptable field uniformity. A voltage of ±4.52 kV is applied to the bottom and the top electrodes establishing field strength of about 50 kV/m. The main

dipoles are supplemented with a pair of correcting dipoles seen in Fig. 4 to compensate the electric field kick even it is much smaller than magnetic one. Adjacent electric dipoles do not influence each other though steel plates installed into the vacuum chamber for magnetic shielding described below give simultaneously electric shielding reducing electric field superposition.

B-Field:

The magnetic channel shown in Fig. 4 consists of two main dipoles DM1 and DM2, two dipoles DK1 and DK2 for kick compensation, and three steel shields arranged along *z*-axis. The channel sizes are: square of 1024x1024 mm^2 transversely and 2175 mm longitudinally, at an aperture of 481x481 mm^2. The main dipoles and correctors are of "window frame" design. This design provides required accuracy of the field configuration and possibility to assemble/disassemble the dipoles from the beam pipe for high temperature vacuum bake out.

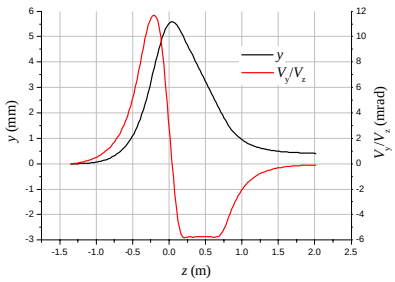

Figure 5: Kick compensation.

We extracted the beam image light from the MCP screen through the slit in the poles of the main dipoles. These 40 mm wide slits are cut-through the whole pole width to reduce magnetic field disturbance near the MCP. A small ratio between the magnet length and the aperture size and a limited permeability of the real steel lead to the field distortion, which we had to neutralize by additional small-power coils attached to the main windings on both sides of the vacuum chamber.

The monitor's *E* and *B* fields result in a transverse kick up to 10 mrad or greater for lower energy ion beam. Beam perturbations should be compensated by magnets with the same field configuration. Such correctors have two pairs of coils exciting both transverse field components. Such channel solution provides transverse kick compensation both in horizontal and vertical planes seen in Fig. 5.

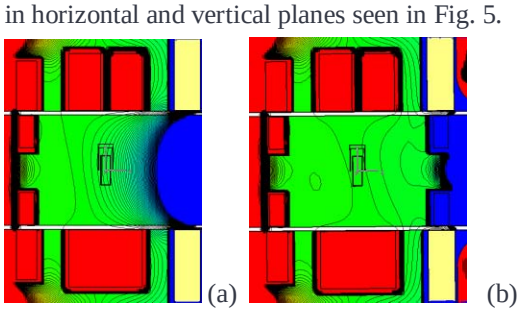
(a) (b)

Figure 6: Sweep direction field component without (a) and with (b) internal steel shield.

We optimised the geometry and potential distribution of correctors to reduce the ion beam shift and its velocity inclination at the channel output down to 1 mm and 1 mrad and smaller.

To shrink the length of the RGM we separated each of two working regions by special steel plates installed between pairs of adjacent dipoles. Practically it was necessary to place some parts of these shields with an aperture hole of Ø180 mm just inside the vacuum chamber. Fig. 6 shows the shielding of the second monitor dipole field penetration into the first dipole working region (10^{-4} T distance between adjacent isolines).

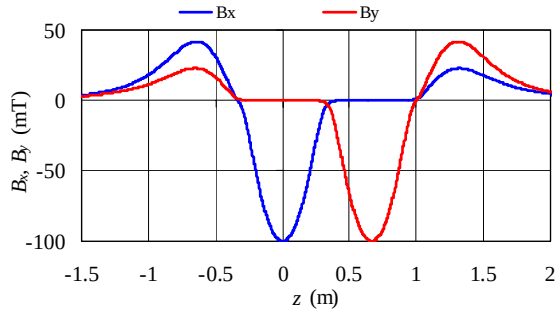

Figure 7: Transverse magnetic field distribution.

As seen in Fig. 7 our channel has symmetric field *x*- and *y*-distributions with required 100 mT in the working region centres and practically suppressed parasitic components on each dipole length.

CONCLUSIONS

The application of an external magnetic field increases both the monitor resolution and detection rate. Our monitor, which is able to operate at two mode regimes, was developed to provide beam diagnostics of any ion types in very wide ranges of ion energy and intensity.

Acknowledgments

The authors are grateful to professor B. Sharkov for encouragement at the monitor design development.

REFERENCES

[1] P. Forck et al. Development of a Permanent Magnet Residual Gas Profile Monitor With Fast Readout, in Proc. DIPAC 2003, p. 134, Mainz, Germany, http://accelconf.web.cern.ch/accelconf/d03/papers/PM17.pdf

[2] T. Giacomini et al, "Development of a residual gas profile monitor with high resolution and fast readout", in Proc. BIW04, Knoxville, Tennessee May 3-6, 2004. http://www.sns.gov/biw04/

[3] D. Liakin et al. Development of a Permanent Magnet Residual Gas Profile Monitor With Fast Readout, in Proc EPAC2004, p. 2724, Lucerne, Switzerland, http://accelconf.web.cern.ch/accelconf/e04/PAPERS/THPLT100.PDF

OPTICAL DESIGN FOR BIPM IMAGING SYSTEM

D. Kramer, B. Dehning, C. Fischer, S. Hutchins, J. Koopman, CERN, Geneva, Switzerland

Abstract

The light imaging system for the Beam Ionization Profile Monitor (BIPM) was designed to allow simultaneous operation of a fast Multi Anode Photo Multiplier and two new types of intensified standard resolution CCD cameras.

The main reason for designing the optics was the poor resolution of the preliminary setup limiting seriously the detectors performance and the need of a second optical path for the Multi (32) Anode Photo Multiplier (MAPMT). An increase of the optical luminosity was also necessary for low intensity beams. Optimization of the optical system was done in the ZEMAX program.

The imaging error was checked by comparing the ionization profile monitor continuous measurements with wire scanner measurements.

INTRODUCTION

The BIPM uses the rest gas in the vacuum beam pipe as ionizing medium where electrons are produced during every beam passage. These electrons are accelerated in a uniform vertical or horizontal electric field and are forced to spiral along the magnetic field lines, which are parallel to the electric field. The Electrons are multiplied by means of an MCP and subsequently hit a phosphor plate get converted into photons.

The density profile of the beam is transformed to the spatial distribution of the photons. The image formed on the phosphor plate has to be properly imaged to a CCD and MAPMT placed outside of the vacuum tank. A new Imaging System (Fig. 1) was designed for the detector.

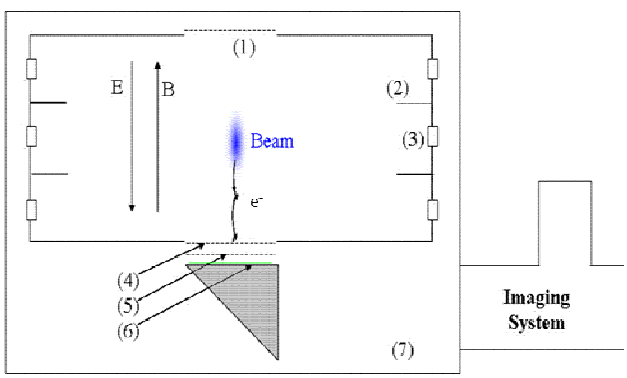

(1)…HV Cathode grid
(2)…Field homogenization electrodes
(3)…Resistors
(4)…Multi-Channel Plate (MCP_{in}) entrance electrode
(5)…MCP_{out} exit electrode
(6)…Phosphor plate deposited on indium tin oxide and fused silica reflecting optical prism
(7)…Vacuum tank

Figure 1: BIPM detector schematics.

DESIGN TARGETS

The main design parameter was the paraxial magnification. It was calculated simply as *m = image size / object size*. Object size was the length of the phosphor screen and for the image, the shortest side of the larger CCD element was used.

Maximal lens diameter was fixed to 50.2 mm due to the width of the viewing port in the IPM dipole magnet where the light path was leading. The overall system length was limited to approx. 70 cm, including the camera's body. The position of the light splitter was defined by the geometry of the mechanics. It was decided not to place any optics inside the vacuum tank.

Two new CCD type sensors were considered: an EM (Electron Multiplied) CCD and an EB (Electron Bombarded) CCD providing light amplification. It was needed to tilt the EB CCD by 90° (see Fig. 2).

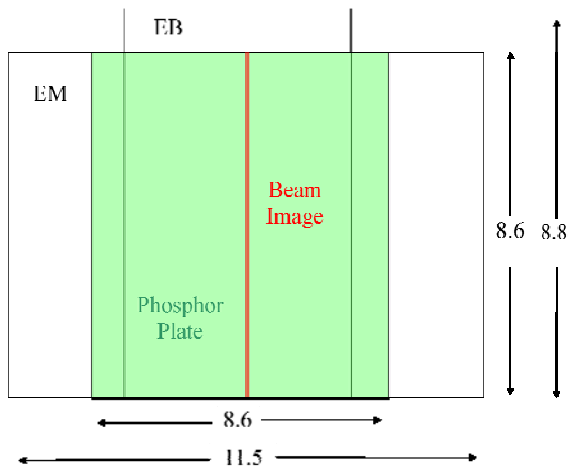

Figure 2: Size and orientation of EM and EB CCDs.

Focusing of the system had to be possible in a reasonable range and the designed optics had to fit inside the C-mount system and have a reasonable cost.

The numerical aperture in the image plane had to be reasonably restricted, because the CCD elements do not accept rays at high angles.

The imaging aberrations should be kept below 1% with respect to the measured transverse beam size.

DESIGN COCNCEPT AND STARTING POINT FOR OPTIMIZATION

Two commercially available doublets are placed between the vacuum window of the detector and the splitting prism with an aperture stop amid. Magnification of this part is matched to the MAPMT and no more lenses are used downstream the splitter. The doublets are optimized for the infinite object position, but as the light

rays are exiting the first lens almost parallel, it has to be used in the opposite direction.

An objective is placed between the splitter and the CCD in the straight path to match the magnification to the smaller square's diagonal of the EM CCD. The objective lenses were supposed to be produced on customer order.

The 150 year old Petzval design with 2 positive power doublets was used as the starting point for the optimization.

OPTIMIZATION AND FINAL DESIGN

Optimization of an optical design required a merit function incorporating target values and constraints of the system. The major part of this function was generated by the ZEMAX program optimizing mainly the RMS spot size for the defined image points and a range of wavelengths 520 – 580nm with a maximum weight at 550nm. A higher number of dimensional constraints had to be carefully set and progressively modified with the optimization evolution. Only reasonable glasses and shapes were used.

During optimization, the first lens of the objective was found not to be crucial for the performance and optimization continued with only three lenses.

The diameter and length of the last element were found to be the major constraint, because it had to fit inside the C-mount and be mechanically hooded outside of it.

Because of mounting difficulties, the front surface of the last element (Fig. **3**) was chosen to be flat without any important losses of image quality. The whole group has a possibility of focalization by its axial movement.

The final design consists of two Optosigma© doublets (200.1 and 169.8mm focal length), a diaphragm almost in the middle of them and an objective (3 elements in one group). Due to supplier stock problems, the first and second elements are made of SK16 glass, the last of SF14.

The main merit target concerned the x component of the RMS image spot; because only one contributes to the resolution of the beam's image (summing the lines along the y coordinate). One can see (Fig. **5**) that the achieved resolution (RMS spot size in the image space) varied from 25μm in the image centre to 37μm at the edges.

Geometrical distortion was also one of the merit function constraints, because it could contribute to the systematic error. One can see a maximum distortion of 2.4%, but actually the beam image should never be in that region. Moreover, this is the maximum deviation from linear imaging and is almost constant for the whole image column (with a small beam) and by summing the lines one gets just a position error.

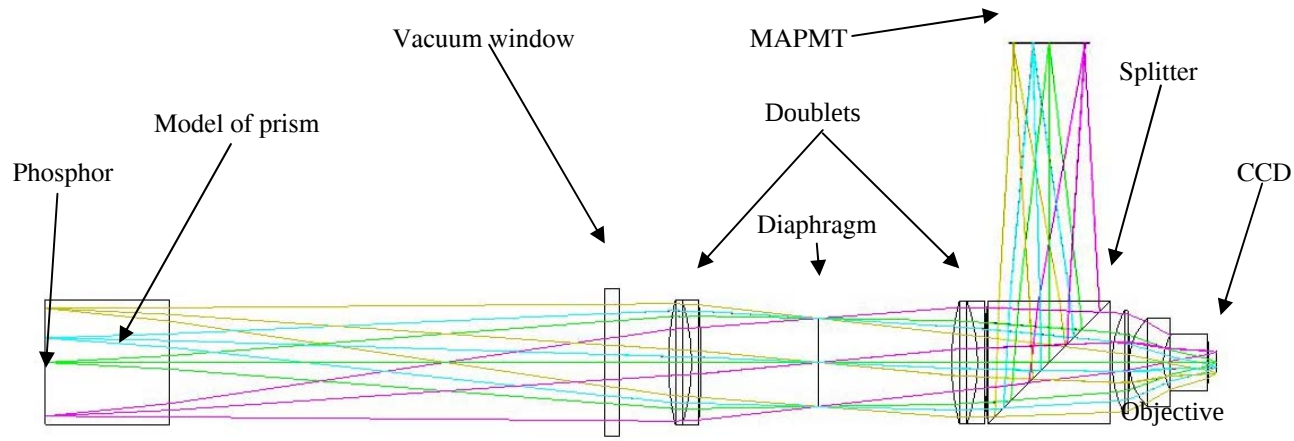

Figure 3: Designed imaging system with optical paths for two separated detectors

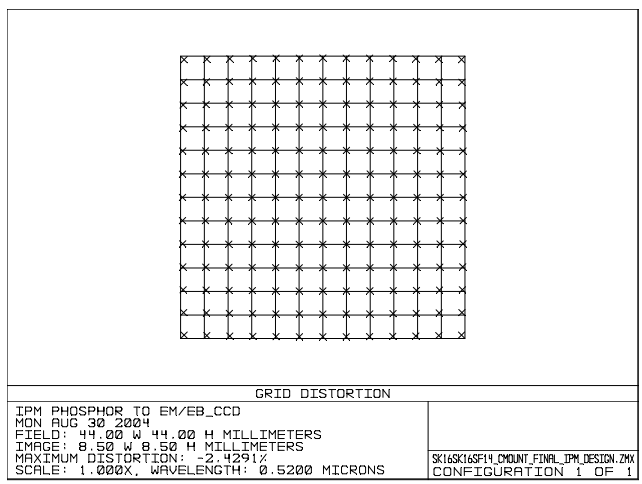

Figure 4: Geometrical distortion of an ideal grid imaged to the CCD.

IMAGING PERFORMANCES AND MEASUREMENTS

Several parameters related with imaging performances were simulated in the Zemax optical CAD program.

The geometrical distortion (Fig. 4) is an important aberration which could have serious impact on the profile measurement precision. The barrel distortion of the system is present mainly in the image corners, where the beam image should normally not be present.

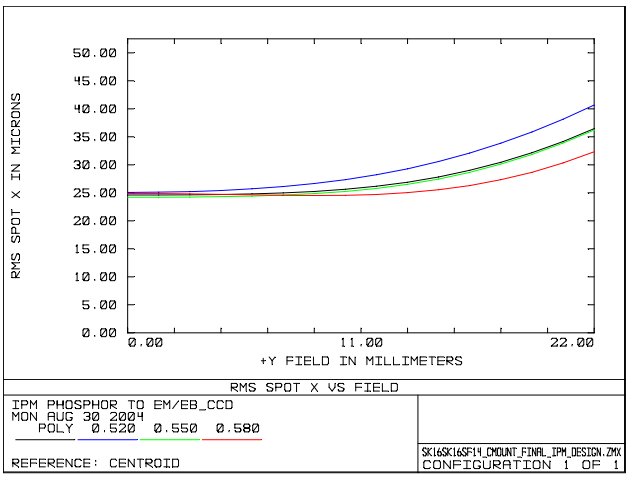

Figure 5: RMS spot size (x component) for different wavelengths.

The spot size of an ideal point imaged to the CCD is the main contribution to the systematic error of the optical part of the detector. It was minimized to a reasonable level (Fig. 5) considering the space requirements. The systematic error caused by the nonzero image of a spot is summarized in the Tab. 1 for different beam sizes and image regions.

Table 1: Calculated systematic errors of measured beam size for different energies.

Average beam size in SPS	**2.3mm (26GeV)**	**0.6mm (450GeV)**
Expected beam size on CCD	439 μm	141 μm
Max RMS spot size	37 μm	37 μm
Measured beam size	441 μm	146 μm
Relative error (max)	**0.36%**	**3.3%**
Min RMS spot size	25 μm	25 μm
Measured beam size	439.7 μm	143.2 μm
Relative error (min)	**0.16%**	**1.5%**

All the elements of the designed system were produced and mounted during the year 2004. The major problem of the optical setup was its very short distance between the last lens of the objective and the CCD's window due to the production tolerances, so the camera's mounting had to be slightly modified.

The BIPM was successfully installed in the LSS5 in the SPS and tested with LHC beams. The measurements showed an important improvement of the detector's accuracy with respect to the previous year (Fig. 6). The measured beam size was compared with the corresponding wire scanner data. The encouraging results were obtained also thanks to the increased transmission bandwidth of the image acquisition chain.

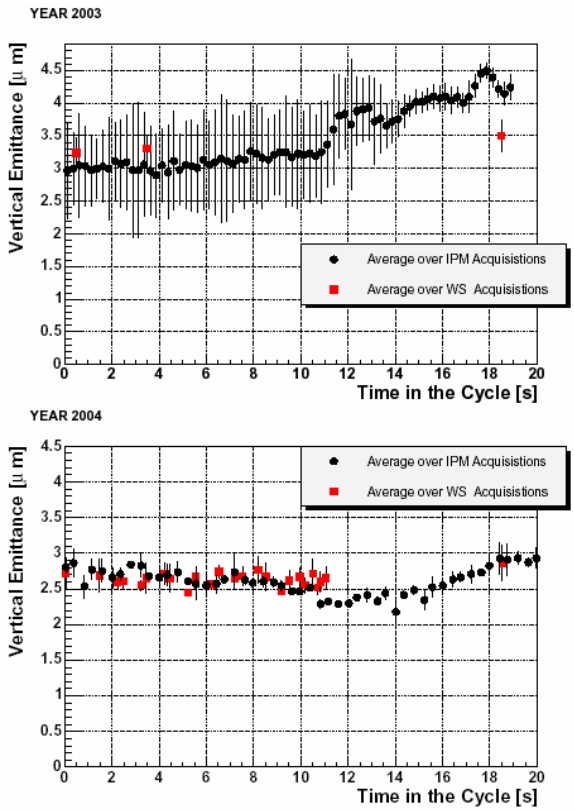

Figure 6: IPM acquisitions with nominal LHC beam and comparison with wire scanners.

SIMULATION OF AN ELECTRON SOURCE BASED CALIBRATING SYSTEM FOR AN IONISATION PROFILE MONITOR

H. H. Refsum*, B. Dehning†, J. Koopman, CERN, Geneva, Switzerland

Abstract

Measurements have shown that the gain of the imaging system of the Ionisation Profile Monitor (IPM) changes over time, in a non-homogenous way. This ageing effect is caused by changes in the Micro Channel Plate (MCP) channel wall secondary emission coefficient, due to electron scrubbing. The MCP is only capable of emitting a limited number of electrons during its lifetime, and after a large number of electrons have been emitted, the gain is gradually reduced. To measure this ageing effect, and to be able to compensate for it, a remote controlled, built-in calibration system was developed. An Electron Generator Plate (EGP) produced by Burle, Inc. was used as the electron emitter for the calibration system. In this paper, computer simulations of the system is presented. Promising results were obtained from these simulations. Results from experiments conducted at low magnetic fields, coincide with the results of the simulations. Both simulations and experiments indicate that the proposed calibration system should not deteriorate the performance of the IPM during beam profile measurements.

INTRODUCTION

The IPM Operation Principle

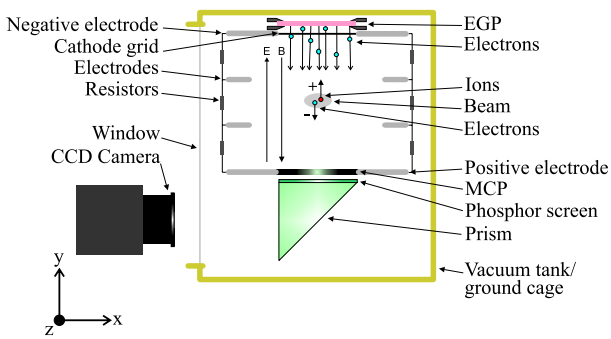

Figure 1: Working principle.

A sketch of the operating principle of the IPM, is shown in Fig. 1. The operating principle of the IPM is based on the ionisation of rest gas atoms and molecules by the passing beam due to the imperfect vacuum. In Fig. 1 the beam is passing in the z-direction, into the paper. Ions and electrons are liberated, and drift up or down respectively, due to the applied electric field. The electric field is created by applying high voltage to the electrodes at the top and bottom of the cage. The voltages applied are typically -1 to -2 kV for the upper electrode (cathode), and +1 to +2 kV for the lower electrode (anode). Consequently the direction of the electric field is in the +y-direction. The distance between the cathode and anode is 84 mm. The lateral electrodes of the IPM, connected through resistors, are included to increase the homogeneity of the electric field. The function of the cathode grid is to prevent secondary electrons, created when ions hit the grounded chamber, from returning into the HV cage of the IPM.

The electron distribution in space, reflecting the transverse density distribution of the particle beam, is forced down to the anode by the applied electric field. A Micro Channel Plate (MCP) measuring 5.08 cm by 5.08 cm is situated at the anode, and this is used to image the distribution. The function of the MCP is to amplify the electrical current from the incoming electron distribution. The amplified electron distribution then hits a phosphor screen. The phosphor screen converts the electron distribution into a photon distribution, which is viewed by a CCD camera, via a prism. A magnetic field of up to 2000 Gauss is added in addition to the electric field. The direction of the magnetic field is in the -y-direction, as indicated in Fig. 1. The magnetic field, together with the initial velocity, cause the electrons to spiral at a small radius, while the electric field forces them down towards the anode.

A New Calibration System

One of the difficulties encountered with the current IPMs, is the too rapid and non homogenous ageing of the MCPs. The ageing mainly affects the area of the MCP where the beam is imaged, causing a local decrease in the gain of the MCP. The reduction of the gain is caused by changes in the channel wall secondary emission coefficient due to electron scrubbing. The MCP is only capable of emitting a limited number of electrons during its lifetime, after a large number of electrons have been emitted, the gain is gradually reduced [2].

Because the MCP images the beam more or less in the same position throughout its lifetime, the gain is reduced more in the centre of the MCP than at the edges. With time, this causes distortion to the images created of the beam. In the LHC the IPM is intended as a continuos beam observation device. The ageing of the MCPs is therefore an important issue, as regularly replacement of the MCPs is both difficult and costly, and would have to be done during machine shutdown.

To measure the ageing effect, and to be able to compensate for it, a remote controlled, built-in calibration system is to be developed. The calibration system consists of an elec-

* helge@refsum.net
† Bernd.Dehning@cern.ch

tron source, placed above the cathode grid, which can emit electrons during periodes where there is no beam present. This electron field can then be used to measure the gain of the imaging system, and improve the images acquired during operation of the IPM. Two electron sources were considered for use in the system, a heated wire grid and an Electron Generator Plate (EGP). EGPs produced by Burle, Inc. [3] are specified to emit homogenous fields of electrons covering the complete area of the MCPs used in the IPM [15, 4]. Based on previous experience with a heated wire grid, an EGP was chosen as the electron source [1]. The EGP was placed 6 mm above the cathode wire grid and 90 mm above the MCP. In this paper, simulations of an IPM incorporating an EGP for calibration purposes is presented.

SIMULATIONS

The computer simulations were split into two main parts: Simulations of the electrical field, and simulations of the paths of the electrons. To compute the electrical fields, the computer program Maxwell 3D Field Simulator (M3DFS) from Ansoft Corporation [5] was used. The program used to calculate the paths of the electrons through the electric and magnetic fields was Garfield [6]. Garfield was originally developed at CERN by Rob Veenhof for simulation of gaseous detectors. The program reads the results of the electrical field simulations created by M3DFS from file, and then calculates the path of the electrons.

The electric field simulations were done using the finit element method for the electrostatic case [7, 8, 9]. The equation which is solved by M3DFS is in general the Poisson equation [10]

$$\nabla \cdot (\epsilon \nabla \Phi) = -\rho_f = 0, \tag{1}$$

where ϵ is the permittivity and Φ is the scalar electric potential. ρ_f is the free charge, which is equal to zero in the electrostatic case.

The path of the electrons through the IPM chamber is calculated by the Garfield program, integrating the expression for the acceleration given by

$$\mathbf{a} = \frac{q}{m}\gamma^{-1}\big(\mathbf{E} + \mathbf{u} \times \mathbf{B} - \frac{1}{c^2}\mathbf{u}(\mathbf{u} \cdot \mathbf{E})\big), \tag{2}$$

where $\mathbf{a}$ is the acceleration, q and m is the charge and mass of an electron, γ is the relativistic constant, $\mathbf{E}$ and $\mathbf{B}$ is the electric field and magnetic field, $\mathbf{u}$ is the velocity and c the speed of light. The numerical method used by the Garfield program is Runge Kutta Fehlberg integration [6].

The resulting field from the electrons present in the drift volume will be negligible compared to the applied electric field in the IPM, even for the highest density of electrons recordable by the MCP [11]. Consequently, the effect of electron-electron interactions can safely be disregarded in the computations. An algorithm that does not take electron-electron interactions into account is therefore chosen to be used in the Garfield simulation program.

To the authors knowledge, no data or theoretical calculations for the energy distribution from single EGPs are published. However, Burle, Inc. has conducted measurements for Z-Stack configuration EGAs [12]. The results are assumed to be similar, but with somewhat lower average energy than for the electrons emitted from a single EGP [13].

The measured results from Burle, Inc. can be fitted to the shape of an *exponential distribution* [14] for the energy U

$$p(U) = \frac{1}{\beta}e^{-U/\beta}, \tag{3}$$

where the parameter β is the average energy of the electrons. For the measured results the average energy is in the range of 34 to 40 eV, however these measurements were done using a Z-Stack configuration EGA, not a single EGP as will be used in the IPM. Since it is expected that the average energy will be lower, an estimate of 30 eV is therefore used in the simulations. This coincides with values obtained from measurements of emittance from single MCPs, where the distribution is reported to be exponential with an average electron energy of 30 eV [2]. The electron current emitted from an EGP is claimed to be more or less parallel with the channels of the EGP [12]. The spatial distribution of the electrons from the EGP is therefore assumed to be equal to the inclinement of the channels of the EGP, which is specified to be $8^\circ \pm 1^\circ$.

The limiting factor for the resolution of the electron path simulations, is the recording of the initial and final position of the electrons. 100 by 100 bins are used, resulting in a bin size of 508 by 508 μm, when the entire area of the EGP or MCP is imaged. In the simulations 10^5 electron paths were computed for each case, resulting in an average of 10 electrons per bin. If the electron distribution is plotted along either the z or x-axis only, an average of 1000 electrons per bin is obtained in one dimension.

RESULTS AND CONCLUSION

The resulting electron distribution on the MCP from Garfield simulations of electrons emitted from the EGP are shown in Fig. 2 (a) and (b) for B=1 Gauss and B=1000 Gauss, respectively. In Fig. 2 (c) and (d) a projection onto the z-axis of these distributions are shown. The figures show that at low magnetic fields the emittace angle of the electrons play an important role, and the electron distribution is distored by both edge effects and shadows from the cathode wire grid. At high magnetic fields, these effects are however negligible. Experiments conducted with no external magnetic field applied, confirm the results. However, experiments with an applied magnetic field is required to confirm the results for B=1000 Gauss and determine the accuracy of the system.

Simulations of the electrical field of the IPM during operation mode, with the EGP implemented, were conducted to confirm that the modification would not decrease the systems performance during actual beam profile measurements.

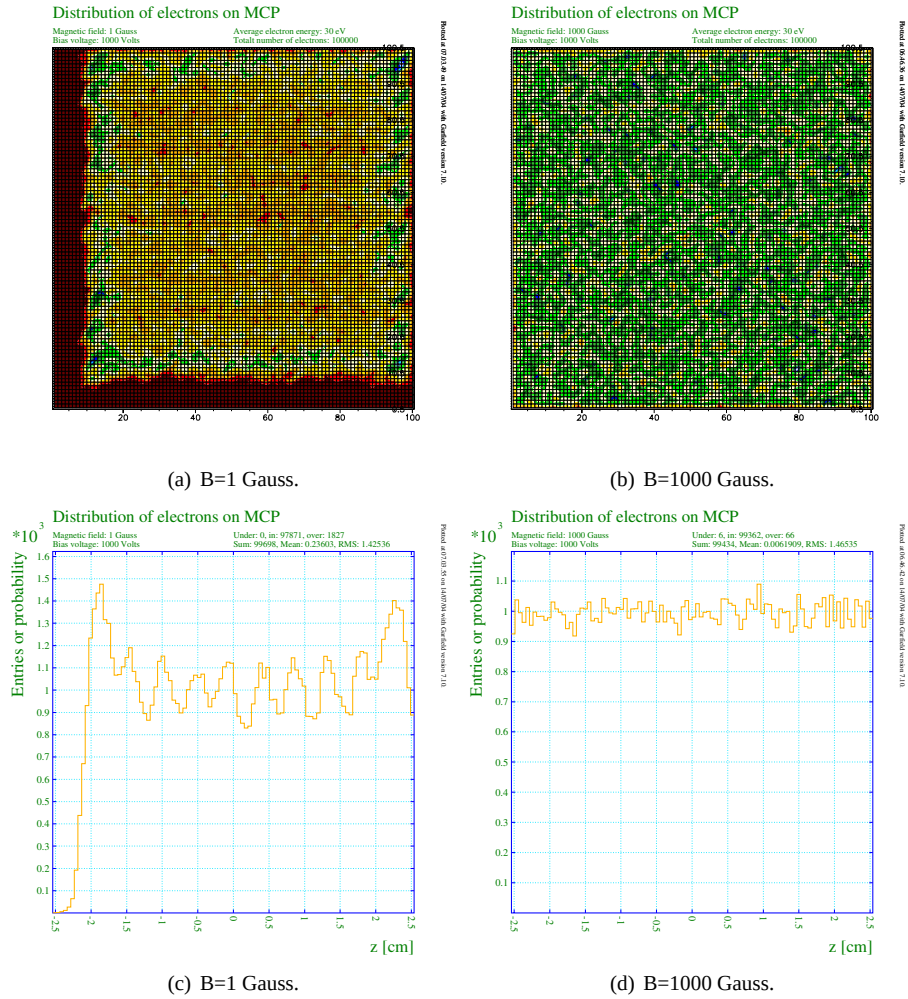

(a) B=1 Gauss. (b) B=1000 Gauss.

(c) B=1 Gauss. (d) B=1000 Gauss.

Figure 2: The resulting electron distribution on the MCP, and the projection onto the z-axis.

REFERENCES

[1] G. Ferioli, C. Fischer, J. Koopman and M. Sillanoli, "Sensitivity Studies with the SPS Rest Gas Profile Monitor", CERN Technical Note SL-2001-026 BI, DIPAC 2001, Grenoble, France.

[2] J. L. Wiza, "Microchannel plate detectors", Nucl. Instr. and Methods 162 (1979), p.587-601.

[3] Burle, Inc. Homepage, 2004, http://www.burle.com.

[4] Burle, Inc., "Procedures and Specifications for MCPs and EGAs, Data sheets, 2004.

[5] Ansoft Corporation Homepage, 2004, http://www.ansoft.com.

[6] R. Veenhof, Garfield Homepage, 2001, http://cern.ch/garfield.

[7] R. Veenhof, "Garfield technical notes, 2004, http://rjd.home.cern.ch/rjd/garfield/notes.html.

[8] N. Ida and J. P. A. Bastos, "Electromagnetics and calculation of fields, 1997, Springer-Verlag New York, Inc.

[9] J. Jin, "The Finite Element Method in Electromagnetics, 2002, John Wiley & sons, Inc.

[10] Ansoft Corporation, Maxwell Manual, 2002, http://wwwce.web.cern.ch/wwwce/ae/Maxwell/documentation.html.

[11] H. H. Refsum, "Design, Simulation and Testing of a 2D Electron Source Based Calibrating System for a Proton Beam Ionisation Profile Monitor, 2004, CERN-THESIS-2004-022.

[12] B. N. Laprade, F. E. Langevin and R. Starcher, "The Development of A Novel, Cold Electron Source, Paper 328, The ASMS Conference, Orlando, Florida, June 2002.

[13] Private communication with R. Cochran, 2004.

[14] V. K. Rohatgi and A. SALEH, "An Introduction to Probability and Statistics, 2001, John Wiley & sons, Inc.

[15] Burle, Inc. "Electrogen^{TM} Electron Generator Arrays, Burle Technical Note TP220, 2002, http://www.burle.com.

SQUID BASED CRYOGENIC CURRENT COMPARATOR FOR MEASUREMENTS OF THE DARK CURRENT OF SUPERCONDUCTING CAVITIES

W. Vodel, S. Nietzsche, R. Neubert, R. Nawrodt, Friedrich Schiller University Jena, Germany
A. Peters, GSI Darmstadt, Germany
K. Knaack, M. Wendt, K. Wittenburg, DESY Hamburg, Germany

Abstract

A newly high performance SQUID based measurement system for detecting dark currents, generated by superconducting cavities for the upcoming X-FEL project at DESY Hamburg, is proposed. It makes use of the Cryogenic Current Comparator principle and senses dark currents in the pA range with a measurement bandwidth of up to 70 kHz.

INTRODUCTION

The linear accelerator technology, based on superconducting L-band (1.3 GHz) cavities, is currently under study at DESY [1]. The two 10 km long main LINACs (linear accelerator) are equipped with a total of nearly 20,000 cavities. A gradient of 23.4 MV/m is required for a so-called superstructure arrangement of couples of 9-cell cavities. To meet the 2×400 GeV/c energy upgrade specifications, higher gradients of 35 MV/m are mandatory.

The dark current, due to emission of electrons in these high gradient fields, is an unwanted particle source. Two issues are of main concern:

- Thermal load: An emitted electron from the cavity surface follows a path along the electric field lines and will most probable hit somewhere else onto the cavity wall. This leads to an additional thermal load in the cryostat, which has to be covered by the liquid helium refrigerator.
- Propagating dark current: If the energy gain is sufficient, the electrons will generate secondary particles when hitting the cavity wall which then also may generate secondaries. In the following avalanche process some electrons may pass through the iris of the cavity cell and will be further accelerated. In this case the dark current along the LINAC would grow exponentially if on average more than one electron passes the complete FODO (focus/defocus lattice) cell.

Recent studies [2] show that the second issue seems to be the more critical one. It limits the acceptable dark current on the beam pipe "exit" of a TESLA 9-cell cavity to approximately 50 nA. Therefore the mass-production of high-gradient cavities with minimum field emission requires a precise and reliable measurement of the dark current in absolute values.

The presented apparatus senses dark currents down to a few nA. It is based on the cryogenic current comparator (CCC) principle, which includes a highly sensitive LTS SQUID as magnetic field sensor. Further on the setup contains a faraday cup and will be housed in the cryostat of the CHECHIA cavity test stand.

REQUIREMENTS FOR DARK CURRENT MEASUREMENT APPARATUS

Electrons can leave the niobium cavity material if the force of an applied external electric field is higher than the bounding forces inside the crystal structure. The highest field gradients occur at corners, spikes or other discontinuities, due to imperfections of the cavity shape. Another potential field emitter is due to any kind of imperfection on the crystal matter like grain boundaries, inclusion of "foreign" contaminants (microparticles of e.g. In, Fe, Cr, Si, Cu) and material inhomogeneity. At these imperfections the bounding forces are reduced and electrons are emitted under the applied high electromagnetic fields [3]. With a series of special treatments the inner surface of the TESLA cavities are processed to minimize these effects. A reliable and absolute measurement of the dark current allows the comparison of different processing methods and a quality control in the future mass-production.

TESLA will be operated in a pulse mode with 5 Hz repetition rate. The 1.3 GHz r.f. pulse duration is 950 µs. During this time the dark current is present and has to be measured. Therefore a bandwidth of 10 kHz of the dark current instrument is sufficient. As field emission is a statistical process, the electrons leave the cavity on both ends of the beam pipe. Thus, half of the dark current exits at each side, and has to be measured on one side only. With the 1.3 GHz r.f. applied, we expect that the dark current has a strong amplitude modulation at this frequency. This frequency has to be carefully rejected from the instrument electronics to insure its proper operation and to avoid a malfunction of the SQUID. This is realized by the help of careful r.f. shielding, appropriate filtering of all leads feeding to the SQUID input coil, and the low pass characteristic of the transformer used.

The use of a cryogenic current comparator as dark current sensor has some important advantages:

- measurement of the absolute value of the dark current,
- independence of the electron trajectories,
- accurate absolute calibration with an additional wire loop, and
- extremely high resolution.

The required working temperature of 4.2 K (boiling temperature of LHe) for the apparatus is unproblematic to provide because the CHECHIA test stand includes the whole cryogenic infrastructure for cooling the niobium cavities. In order to enable the CCC to measure the magnetic field of the dark current only, an effective shielding against external magnetic fields has to be realized.

THE CRYOGENIC CURRENT COMPARATOR (CCC)

In principle, the CCC is composed of three main components (see Fig. 1):

- the superconducting pick-up coil,
- the highly effective superconducting shield, and
- the high performance LTS-SQUID system.

The CCC, first developed by Harvey in 1972 [4], is a non-destructive method to compare two currents I_1, I_2 (see fig. 1) with high precision using a meander shaped flux transducer. Only the azimuthally magnetic field component, which is proportional to the current in the wires, will then be sensed by the pick-up coil. All other field components are strongly suppressed. The very small magnetic flux coupled into the coil is mostly detected by a SQUID.

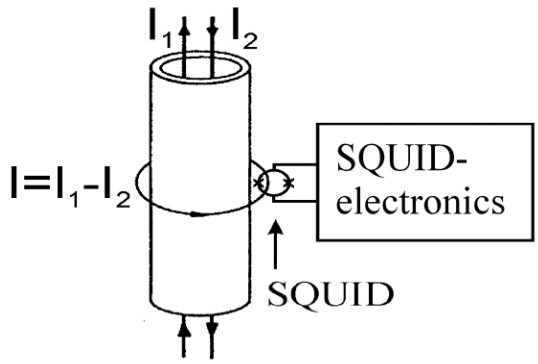

Figure 1: Simplified scheme of a LTS SQUID-based cryogenic current comparator.

The design of the CCC for measuring of dark currents is realized as co-operation of DESY Hamburg, Jena University and GSI Darmstadt. The apparatus will be placed in the CHECHIA cavity test stand and operates at 4.2 K.

Pickup Coil

A single turn pick-up coil is formed as superconducting niobium toroid with a slot around the circumference. It contains a Vitrovac 6025-F core (Vacuumschmelze GmbH, Hanau, Germany) providing a high permeability of about 30,000 at liquid helium temperatures [5]. According to our experience 6025-F cores give the lowest noise level in comparison to other materials tested. The material inhomogeneity of the core is averaged by complete encapsulation of a toroidal niobium coil.

Superconductive Shields

The resolution of the CCC is reduced if the toroidal pickup coil operates in presence of external disturbing magnetic fields. As external fields are in practice unavoidable, an extremely effective shielding has to be applied. A circular meander ("ring cavities") shielding structure (see Fig. 2) allows to pass only the azimuthal magnetic field component of the dark current, while the non-azimuthal field components are strongly attenuated. The attenuation characteristics of CCC shieldings were analytically analyzed in great detail [6-8]. Applied to the shielding of the TESLA CCC an attenuation factor of approximately 120 dB for transverse, non-azimuthally magnetic field components is estimated. This result is based on the superposition of the analytic results for the different shielding substructures, here: coaxial cylinders and "ring cavities" (as shown in [9]).

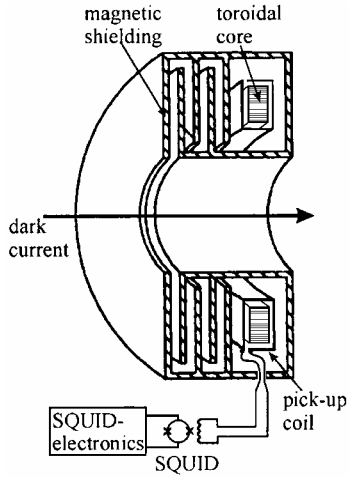

Figure 2: Simplified schematic view of the magnetic shielding, the toroidal pick-up coil, and the SQUID.

SQUID Measurement System

The key component of the CCC is a high performance DC SQUID system developed and manufactured at Jena University. The system makes use of the sensor UJ 111 [10].

The SQUID electronics consists of the low noise preamplifier and the SQUID control and detector unit. The amplification and detection of the SQUID signal is achieved by the state-of-the-art design, i.e. the preamplifier is followed by an AC amplifier and a phase sensitive detector (lock-in) with a PI-type integrator. The output signal returns via a resistor to the modulation coil to close the feedback loop.

For an optimal choice of bias and flux modulation point, a white flux spectral density of $2 \times 10^{-6}\ \Phi_0/\sqrt{\text{Hz}}$ for the SQUID system was found. This flux noise corresponds to an equivalent current noise through the input coil of 0.9 pA/√Hz.

In a DC coupled feedback loop, the field of the dark current to be measured is compensated at the SQUID by an external magnetic field generated from the attached electronics. Due to the superconductivity of all leads in the input circuitry (pick-up coil, transformer, SQUID input coil) the CCC is able to detect even DC currents. For an optimum coupling between the 1-turn toroidal pick-up coil (40 µH) and the SQUID input coil (0.8 µH) a matching transformer is necessary.

The noise current sensitivity of the CCC was calculated to 175 nA/Φ_0. Using a modulation frequency of 307 kHz the measurement system provides an over-all bandwidth of 20 kHz (signal level: 1 Φ_0) or 70 kHz (signal level: 0.1 Φ_0), respectively. Thus, it will be possible to characterize the pulse shape of the dark current beam (300 µs rise time, 950 µs flattop, 300 µs fall time, 10 Hz repetition rate) which is dominated by the r.f. structure applied to the cavities.

Faraday Cup

Because of the fact that the energy of dark current electrons is relatively small at CHECHIA, the design includes a Faraday Cup to have a second measurement system for comparison. The Faraday Cup will be installed at the end of the cavity vacuum chamber. The readout electronics will measure the current to ground. Also it will be needed for stopping the electrons of the dark current in the test facility. This requires a high voltage-screen to absorb the secondaries from the stopper electrode. The simplified scheme of the main component of the CHECHIA's CCC is shown in fig. 3.

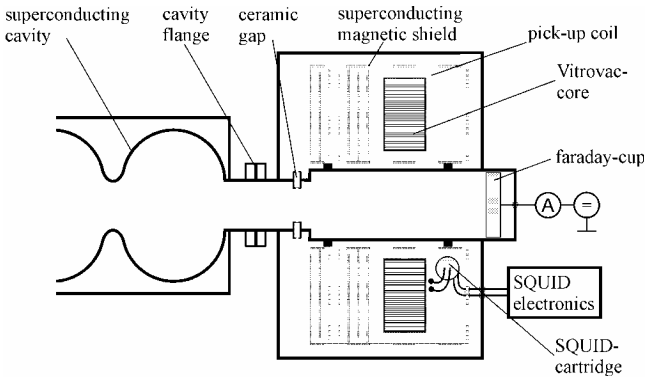

Figure 3: Schematic design of the CHECHIA's CCC.

RESULTS AND OUTLOOK

One of the most sophisticated component parts of the CCC is the superconducting pick-up coil consisting of a one turn toroidal niobium coil including an embedded VITROVAC core for impedance matching and a super-conducting meander-shaped flux transducer to attenuate the magnetic back-ground noise. This important component was manufactured successfully and tested at DESY (see fig. 4).

At 4.2 K an inductance of the pick-up coil of 40.4 μH was found which agrees quite well with the designed value. The inductances of the one turn calibration coil and the feed-back coil have nearly the same values and were determined to 42 and 40 μH, respectively.

Tests of the pick-up coil with connected SQUID system were successfully done in a wide-neck LHe cryostat. Supplying the calibration coil with calibrated current pulses the current sensitivity of the CCC could be measured to (202 ± 4) nA/Φ_0, rather near to the designed value (see fig. 5).

In spite of the rough measurement conditions at DESY the SQUID system worked quite well and the lowest flux noise level of 4×10^{-3} $\Phi_0/\sqrt{\text{Hz}}$ was measured in the frequency range of 30 Hz to 400 Hz. This value corresponds to a noise limited current resolution of the CCC of 0.8 nA/√Hz (see fig. 5).

As the next step the noise limited intrinsic parameters of the SQUID based CCC and the attenuation factor against external magnetic background fields have to be measured under quiet measurement conditions.

At the end of 2005 the whole CCC will be installed in the CHECHIA test stand at DESY.

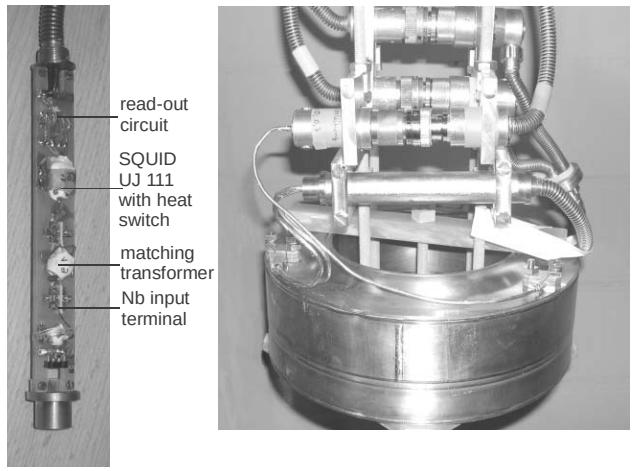

Figure 4: Cryogenic probe with LTS-SQUID (left) and completed niobium pick up coil of the CCC (diameter: 230 mm) with all special cabling for the SQUID (right).

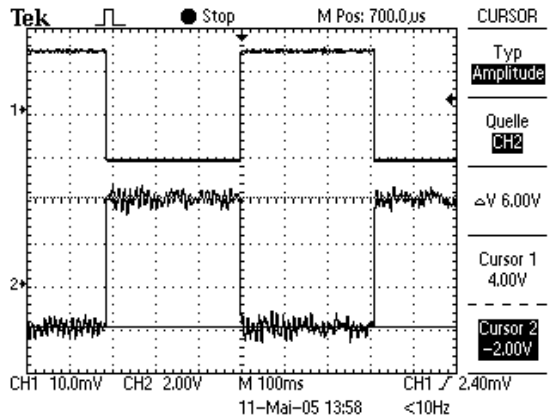

Figure 5: 126.5 nA current pulse through the calibration coil (upper curve) and corresponding 6 V SQUID output pulse (lower curve) at a system sensitivity of 10 V/Φ_0.

REFERENCES

[1] R. Brinkmann; TESLA Technical Design Report.
[2] R. Brinkmann; Dark Current Issues; TESLA Collab. Meeting - CEA Saclay 4/2002.
[3] G. R. Werner, et al.; Proc. of the Part. Acc. Conf. PAC 01, pp. 1071-73.
[4] I. K. Harvey, "A precise low temperature dc ratio transformer", Rev. Sci. Instrum., vol. 43, p. 1626, 1972
[5] Datasheet "Toroidal strip-wound cores of VITROVAC 6025 F" and private communication from Vacuum-schmelze Hanau, Germany.
[6] K. Grohmann, et. al.; CRYOGENICS, July 1976, pp. 423-429.
[7] K. Grohmann, et. al.; CRYOGENICS, October 1976, pp. 601-605.
[8] K. Grohmann and D. Hechtfischer; CRYOGENICS, October 1977, pp. 579-581.
[9] P. Gutmann and H. Bachmair; in V. Kose, Superconducting Quantum Electronics, 1989, pp. 255-259.
[10] W. Vodel, K. Mäkiniemi, "An ultra low noise SQUID system for biomagnetic research", Meas. Science and Technology Vol 3, No 2, pp. 1155-1160, Dec. 1992

PROFILE MONITORS FOR WIDE MULTIPLICITY RANGE ELECTRON BEAMS

B. Buonomo, G. Mazzitelli, L. Quintieri, Laboratori Nazionali di Frascati LNF - INFN
A. Bulgheroni, C. Cappellini, M. Prest, Univ. Insubria e INFN Sez-Milano
L. Foggetta, Consorzio Interunivesitario per la Fisica Spaziale, CIFS
A.Mozzanica, Univ Milano e INFN Pavia
E. Vallazza, INFN Trieste Via Valerio, 2 I - 34127 Trieste- Italia
P. Valente, INFN Sez Roma ,P.le Aldo Moro, 2 - 00185 Roma - Italy

Abstract

The DAFNE Beam Test Facility (BTF) provides electron and positron beams in a wide range of intensity, from single particle up to 10^{10} particles per pulse, and energy, from a few tens of MeV up to 800 MeV. The pulse time width can be 1 or 10 ns long, and the maximum repetition rate is 50 Hz.

The large range of operation of the facility requires the implementation of different beam profile and multiplicity monitors. In the single particle operation mode, and up to a few 10^3 particles/pulse, the beam spot profile and position are measured by a x-y scintillating fiber system with millimetric resolution and multi-anode PMT readout. From a few tens up to 10^{6-7} particles per pulse, a silicon chamber made of two 9.5x9.5 cm^2 wide 400um thick silicon strip detectors organized in a x-y configuration with a pitch of 121um has been developed. Once calibrated, the system can be used also as an intensity monitor. The description of the devices and the results obtained during the data taking periods of several experiments at the facility are presented.

INTRODUCTION

The DAFNE Beam Test Facility (BTF), operational in Frascati LNF since November 2002, is a beam transfer line optimized for the production of a pre-determined number of electrons or positrons. The main applications of the facility are: high energy detector calibration, low energy calorimetry, low energy electromagnetic interaction studies, detector efficiency and aging measurements, test of beam diagnostic devices, etc.

An attenuating target intercepting the primary Linac beam, together with a system of collimating slits (both along the horizontal and vertical coordinate) and an energy selecting dipole magnet, allows to fine-tune the beam intensity, momentum and spot size, according to the users requirements. The characterization of the beam thus requires several diagnostic devices, optimized in the full range of multiplicity and energy. The facility has been operating both in the single particle production scheme and the high multiplicity operation mode almost continuosly since November 2002.

The sensitivity of any standard beam diagnostics (beam current monitors, fluorescence flags, etc.) is not sufficient, especially in the single particle mode, so that several particle detectors have been used and developed to monitor the BTF beam characteristics during the users running periods. These detectors were mainly intended for the measurement of the number of particles in the beam pulses, in a typical momentum range of 20-800 MeV. However, a very important point for the operation of the facility is the measurement of the beam spot position and size. The typical beam spot at the end of the DAFNE Linac is fairly gaussian, with millimetric size in both the transverse (x-y) coordinates, and is efficiently transported by the BTF transfer line. The exit windows of the BTF beam line have been realized with a thin (500 um) Be alloy, so that the beam size is not spoiled by multiple scattering. The required accuracy for a beam profile detector is then of the order of 1 mm or better.

For this purpose, two different beam profile monitors, a scintillating fiber detector and silicon beam chamber, have been designed, built and tested during the last year. The detectors are described together with some details on the construction and the readout of the systems; and some experimental results with the BTF beam are also reported.

BEAM PROFILE MONITOR WITH SCINTILLATING FIBER DETECTOR

In order to have a measurement of the beam spot with millimeter accuracy, we have developed and realized a beam hodoscope, consisting of scintillating fibers coupled to multi-anode photomultipliers. This detector has been in fact designed to cope with the wide range of beam conditions, both in energy and multiplicity, and the typical beam spot characteristics[1].

A detector composed of few layers of 1 mm scintillating fibers should be at the same time fully efficient for single electrons and not saturated at intermediate intensities. We built a two views detector of 48×48 mm^2 active area. Each one of the two planes of the detector, arranged at 90 degrees with respect to each other, is composed of four layers of fibers staggered by a half-diameter (0.5 mm). Three fibers in width and four in depth are glued together with optical glue and are bundled. Each 12 fibers bundle, corresponding to an active width of 3 mm, is coupled to a pixel of two 16-channels multi-anode photomultipliers (Hamamatsu H6568). The analog signal of each pixel is

fed into a channel of 0.1 pC/counts QDC (CAEN 792 V), measuring the collected charge for each fiber bundle [14]. The beam spot, in the transverse plane, can then be reconstructed from the charge-weighted distribution (for each of the two views)
An example of the beam profile transverse distribution, obtained with the fibers running along the horizontal and vertical directions is shown in Fig.1; this has been obtained for a well focused 493 MeV electron beam with an average of one-two particle per pulse.

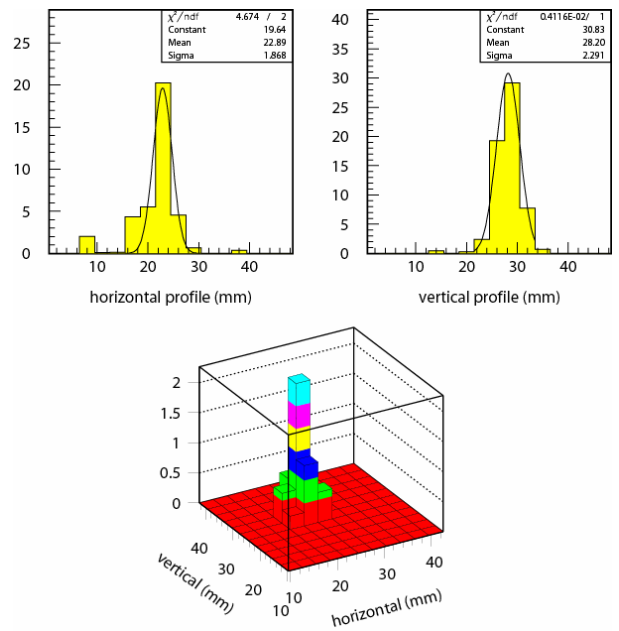

Figure 1: Charge-weighted distribution for horizontal and vertical planes of the scintillating fibers detector (top),and the corresponding two-dimensional beam spot (bottom); focused beam, 493 MeV electrons.

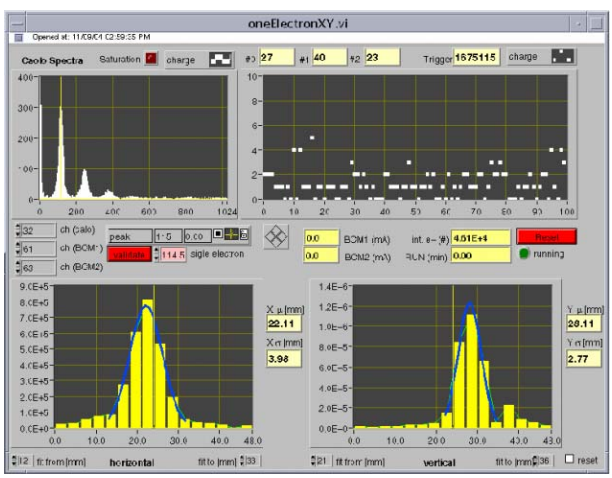

Figure 2: LabVIEW panel showing the calorimeter charge spectrum (up left) and the relative average multiplicity (up right) and the horizontal and vertical profile (down) in a typical BTF run. Each beam profile is obtained by accumulating 2 s of beam (100 hits).

A good accuracy in the beam spot determination can be achieved already with a few hundreds of hits, so that a few seconds of data taking are required at the maximum repetition rate of 50 Hz.
This allows a very useful online monitoring of the beam position and shape, since the measured horizontal and vertical profiles are available in real-time in the control system of the facility, together with the calorimetric measurement of the beam intensity (Fig. 2).

BEAM PROFILE MONITOR WITH SILICON BEAM CHAMBER

Two different silicon based systems have been used for the measurement of the beam profile in low and high multiplicity situations:
-Two x-y silicon chambers each consisting of two 8.9x8.9cm^2 silicon strip detectors (Micron Semiconductor ltd) 400 μm thick and with a pitch of 228μm. Each detector is AC-coupled and readout by 3 TAA1 ASICs (ideas) characterized by low noise, analog readout and self triggering capabilities. The chambers are able to measure the beam profile with a spatial resolution of ~40μm in low multiplicity conditions[2].

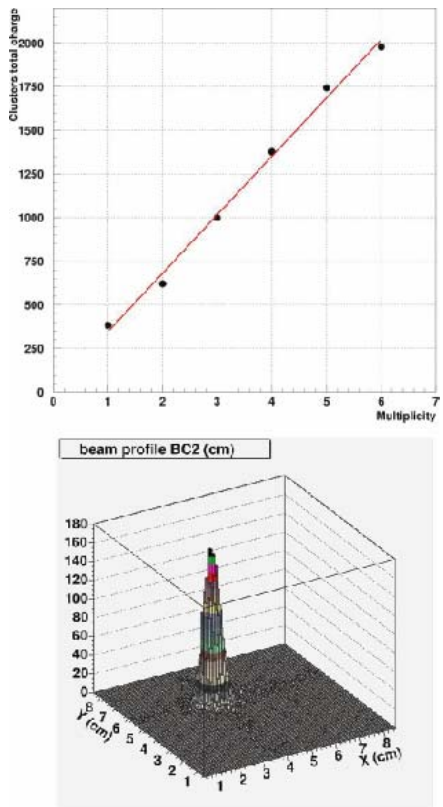

Fig 3: Silicon Beam Chamber: Calibration tests. Top: the beam multiplicity, computed with the number of clusters, is compared with the number of electrons estimated by the NaI calorimeter total energy. Bottom: beam profile for 433 MeV electrons.

Figure 3 shows the results in terms of beam profile, dimensions as a function of energy and linearity with respect to the number of particles impinging on the detector.

-A 9.5x9.5cm2, 400 μm thick silicon strip detector (HAMAMATSU Photonics) developed for the AGILE satellite and used in the SUCIMA configuration[3]. The 121um pitch 768 DC-coupled strips are readout by 6x128 channel charge integrating VA_SCM2 ASICs {ideas} characterized by 4 possible gains (corresponding to a charge range of 400-41000fC/channel) and a double sample & hold circuit enabling deadtime-less data acquisition. This detector can at the same time measure a beam profile and extract from the integral of the profile the beam multiplicity up to very high values.

Figure 4 shows the beam profile obtained in a high multiplicity configuration, and the linearity of the detector response to increasing multiplicity as measured by a NaI calorimeter. All the measurements have been taken using the last but one lower gain. A second set of data taking is foreseen to explore higher multiplicity ranges.

CONCLUSIONS

The Beam Test Facility has showed very good performance operating with very high reliability in the energy range from a few tens of MeV up to 800 MeV, in single electron/positron mode as well as in the high intensity beam.

In order to improve the characterization of the beam quality, we have developed and tested two different beam profile monitors in a wide range of beam conditions, both in energy and in multiplicity. This detectors will be used to monitor the beam conditions and to adjust them to the experimental requests.

REFERENCES

[1] M. Anelli, B. Buonomo, G. Mazzitelli, and P.Valente, *A scintillating-fiber beam profile monitor for the* DAFNE BTF, LNF 04/24P (2004)

[2] G. Barbiellini et al., Nucl. Instr. and Methods A 490, 146-158, 2002.

[3] C.~Cappellini et al., Nucl. Instr. and Methods A 527, 46-49,2004.A.

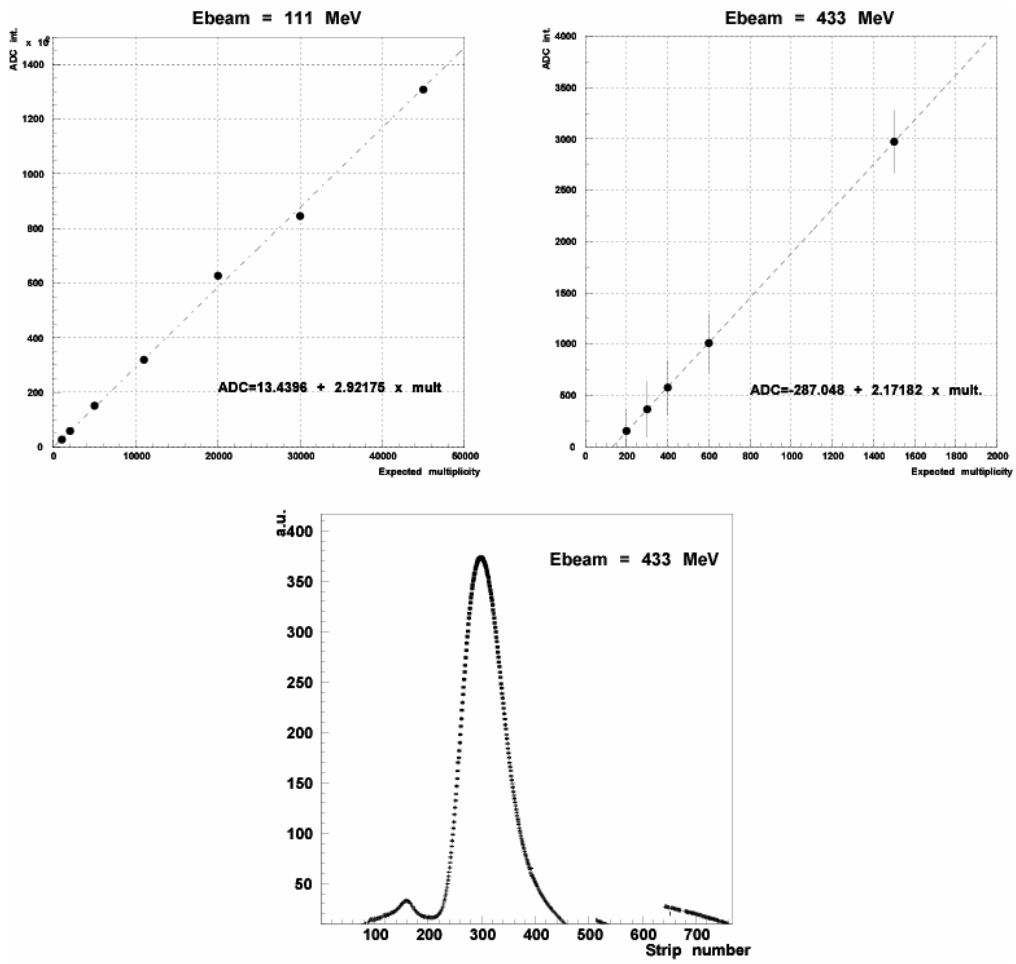

Fig 4: Linearity at two different energies of the detector response with respect to increasing multiplicity (top). The expected multiplicity has been measured with a NaI calorimeter. The y axis units are ADC counts. Beam profile in a high multiplicity configuration (bottom).

THI SAFETY SYSTEM

Christophe Jamet, Thierry André, Pascal Anger, J.L. Baelde,
Clément Doutressoulles, Bernard Ducoudret, E. Petit, Eric Swartvagher
GANIL, BP 55027, 14076 Caen Cedex 5, France

Abstract

For several years, GANIL has been allowed to reach a maximum beam power of six kilowatts (400W in normal mode) thanks to the THI system (High Intensity Transport System). Three modes of running are necessary to accelerate a THI beam ("Injector" mode, "tuning" mode and "surveillance" mode). The "surveillance" mode requires a safety system to protect equipment against beam losses. Inside cyclotrons, diagnostics measure beam-loss currents at the injection and extraction devices. Along beam lines, diaphragms measure beam-loss currents at the input and output of dipoles. Current transformers are used for beam transmission measurements through beam lines and the cyclotrons. The safety system controls beam losses and quickly cuts the beam with a chopper if losses exceed thresholds. These thresholds can be seen and changed by software.

INTRODUCTION

The production of exotic ions at GANIL is performed by fragmentation of the projectile in the target of SISSI [5] or/and by the ISOL method with an acceleration of the exotic beams by the cyclotron CIME [3].

Layout of GANIL

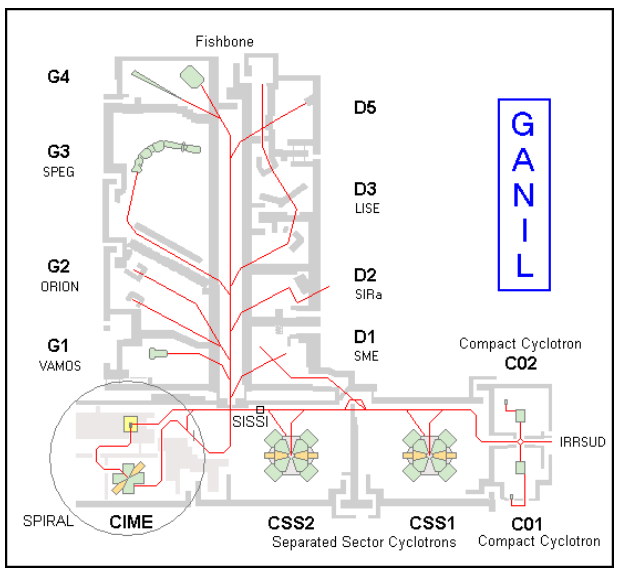

Both devices require high intensity primary beams. Primary beam intensity has been increased up to 15µAe (3kW) for ^{13}C at 95Mev/A and 26µAe (5kW) for ^{36}Ar at 95Mev/A. Therefore, uncooled or unshielded elements can melt very rapidly and must be protect by a safety system.

THI MODES

Three modes of running are necessary to tune a THI beam. C01 or C02 can be chosen to post accelerate the THI beam.

"Injector mode"

This mode permits us to accelerate the beam at the input of SSC1. (Pbeam < 400W)

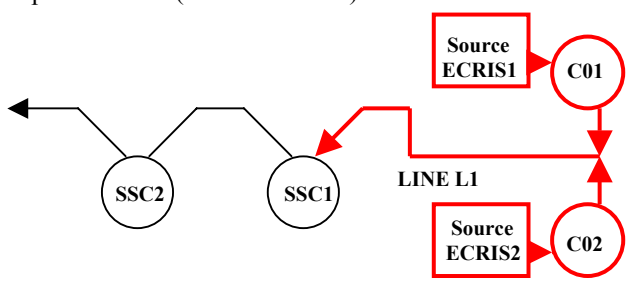

"Tuning mode"

This mode permits us to tune the beam through the accelerators. Beam chopping rates limit the beam power (Pbeam<400W)

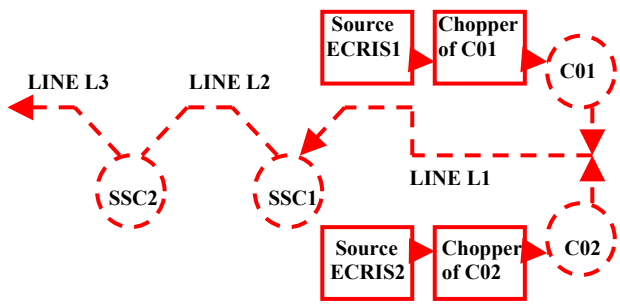

"Surveillance mode"

This mode permits us to tune the beam at a maximum power (Pbeam max = 6kW). Beam current average is increased progressively by changing beam-chopping rates. The safety system controls beam losses.

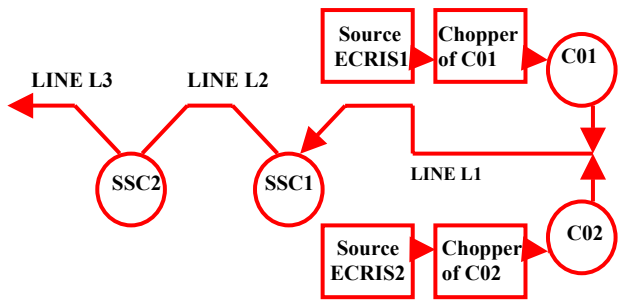

BEAM LOSSES DIAGNOSTICS

Inside cyclotrons, diagnostics measure beam-loss currents at the input of the injection an extraction. Along beam lines, diaphragms detect beam-loss currents at the input and output of dipoles.

Diaphragms used to detect THI beam loses

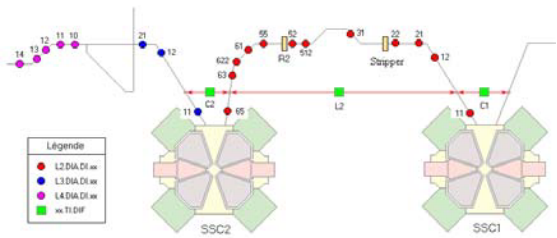

Current transformers (GANIL ACCT) are used to measure the beam transmission through beam lines and the cyclotrons. A change of the efficiency within the accelerators can be detected. The beam is modulated to measure beam currents with the ACCT. The maximum chopping rate is 91%.

Differential Current Transformers used to measure THI beam loses

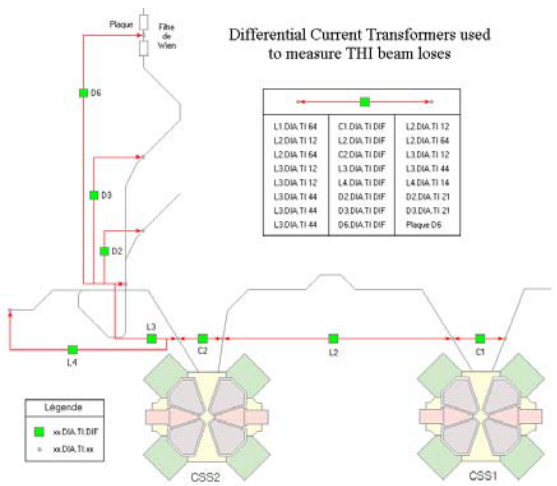

SAFETY SYSTEM

Interceptive beam diagnostics are connected to test boards. Each board is able to inject a test signal (10µA) to the diagnostics and filter the signal from the device. Test signals can be sent by software. Each VME board (PFAIS) measures 4 diagnostic currents with logarithmic I/V converters, which generate a voltage proportional to the logarithm of the current. This voltage is digitised, compared to a threshold and numerically converted into a current.

The signals generated by the current transformers (ACCT) are sent to a differential board. An inhibition board validates the difference between 2 current transformers. Then a VME board digitises, compares to a threshold and numerically converts into a current.

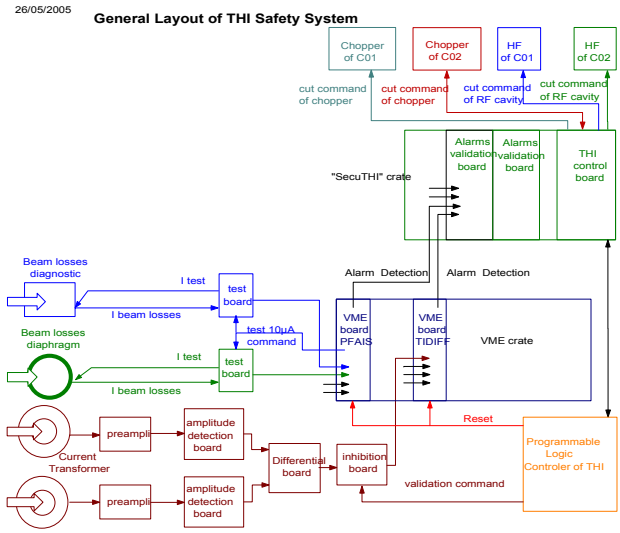

"Alarm detection" signals are generated by VME boards and sent to "alarm validation" boards. "THI control" board collects all alarm signals. A programmable logic controller indicates to the control board different configuration states. If "surveillance" mode is validated for example, when a VME board generates an alarm detection, the THI control board commands the chopper to cut the beam. If a problem is detected on the chopper, the acceleration voltage of the C0 injector is cut.

A reloading system gives us the possibility to restore the beam just after an overshoot. When 3 trigger actions arrive in under 10 seconds, the programmable logic controller passes from "surveillance " mode to "tuning" mode.

CONTROL

Software is used to control and tune the beam.

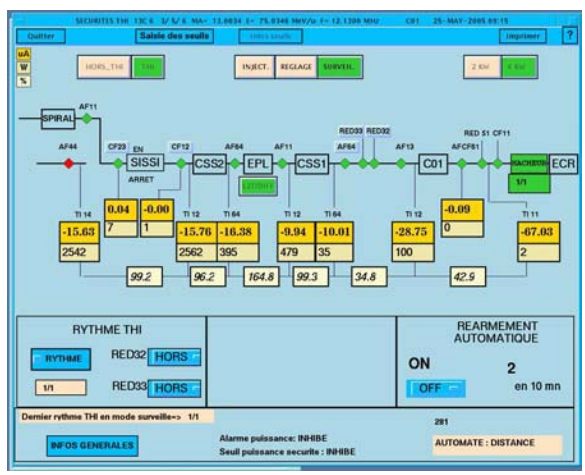

Users can choose various modes of running (normal mode or THI mode and injector, tuning, surveillance mode). Beam current (µA), beam power (W) and efficiency (%) are displayed on the screen. Beam chopping rates can be changed (rythme) and pepper pots inserted in the lines (red32 and red33).

A second program enables us to control and change thresholds of each diagnostic device.

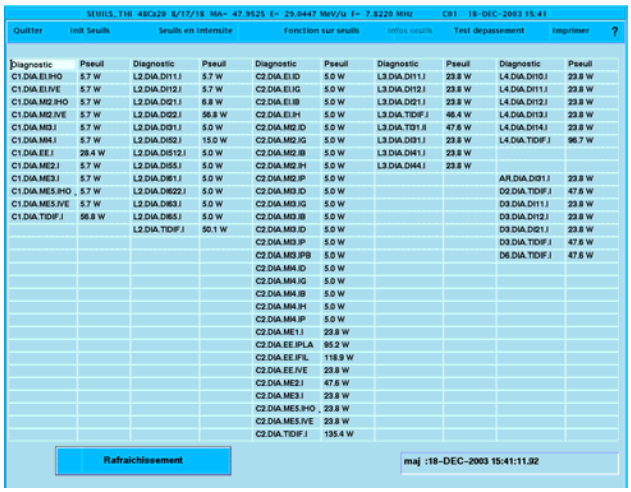

Current or power thresholds can be selected. When a new beam is tuned, we initialise all thresholds in power with beam characteristics. Each value can be displayed and modified. A test command permits sending a test current to each beam-loss diagnostic device and to verify the detection.

RESPONSE TIME

To measure the response time, the beam is tuned to lose 4µAe in SSC1. We cut the beam by the chopper and we set the threshold to 2µAe. The beam is then sent through the cyclotron, and the safety system detects the loss and stops the beam.

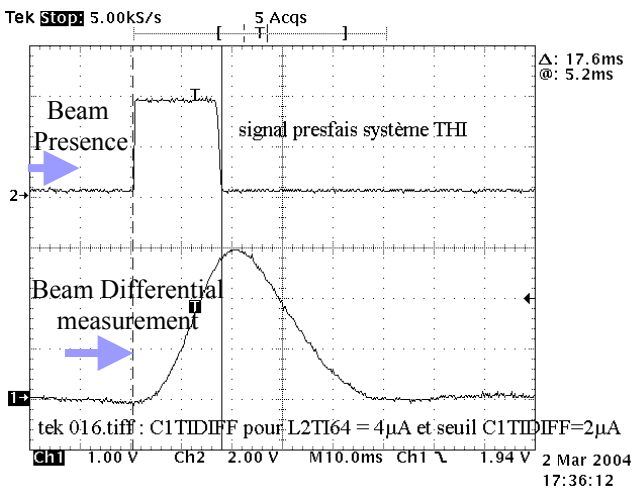

The response time for a beam current of 4µA and a threshold of 2µA is around 18 ms. It depends of the ratio between threshold and loss current.

PHOTOS OF DIAGNOSTICS

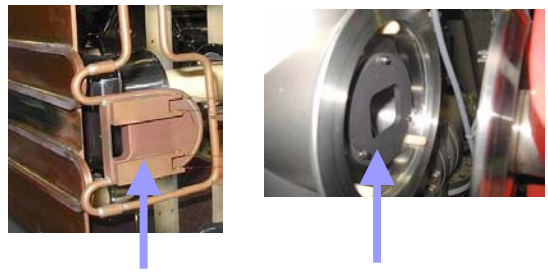

Beam-loss diagnostic inside cyclotron

Beam-loss diaphragm

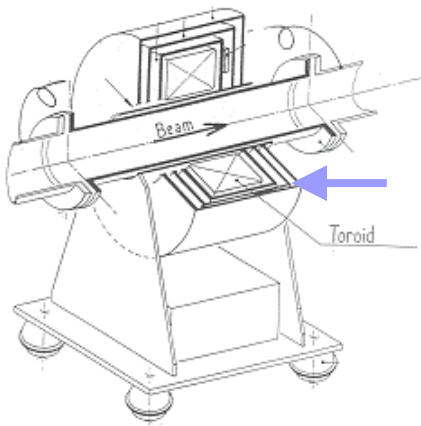

Current Transformer

CONCLUSIONS

The THI Safety System was started in 1995, validated in 1998 and completed in 2001, to give the possibility to send a THI beam into the experimental rooms. The system correctly protects equipment against the beam power loss.

REFERENCES

[1] B. Jacquot et al., GANIL status report, 17th Int. Conf. On Cyclotrons and their Applications. Tokyo, 2004

[2] F. Chautard et al., GANIL status report, EPAC 2004, Switzerland

[3] E. Baron et al., High intensity heavy ion beams for exotic nuclei production at GANIL, 16th Int. Conf. On Cyclotrons and their Applications. Michigan 2001

[4] M. Lieuvin et al., Commissioning of SPIRAL, the GANIL radioactive beam facility, ibid

[5] E. Baron et al., Experience with high intensity operation of the GANIL Facility, 15th Int. Conf. On Cyclotrons and their Applications, 1998

[6] A. Savalle et al, The SISSI facility at GANIL, EPAC 96, Sitges, Spain, June 1996.

[7] E. Baron et al., Upgrading the GANIL Facilities for high-intensity heavy ion beams, 14th Int. Conf. On Cyclotrons and their Applications, 1995

BEAM DIAGNOSTICS INSTRUMENTATION FOR THE HIGH ENERGY BEAM TRANSFER LINE OF I.P.H.I.*

P. Ausset, S. Berthelot, J. L. Coacolo, J. Lesrel, J.N. Maymon, A. Olivier, N. Rouvière, M. Solal, L. Vatrinet, J.F. Yaniche, I.P.N. 91406 Orsay, France
G. Belyaev, I. Roudskoy, I.T.E.P. Moscow, Russia.

Abstract

I.P.H.I. is a High Intensity Proton Injector under construction at Saclay (C.N.R.S/I.N.2P.3; C.E.A./D.A.P.N.I.A and C.E.R.N. collaboration). An E.C.R. source produces a 100 keV, 100 mA C.W. proton beam which will be accelerated at 3 MeV by a 4 vanes R.F.Q. operating at 352.2 MHz. Finally, a High Energy Beam Transport Line (H.E.B.T.) will deliver the beam to a beam stopper and will be equipped with appropriate beam diagnostics to carry intensity, centroïd beam transverse position, transverse beam profiles, beam energy and energy spread measurements for the commissioning of I.P.H.I. These beam diagnostics will operate under both pulsed and C.W. operation. Transverse beam profile measurements will be acquired under low and high duty factor pulsed beam operation using a slow wire scanner and a C.C.D. camera to image the beam-induced fluorescence. The beam instrumentation of the H.E.B.T. is reviewed and preliminary obtained transverse profile measurements at 100 keV are described.

INTRODUCTION

IPHI is a high intensity proton injector (C.N.R.S/I.N.2P.3, C.E.A./D.A.P.N.I.A and C.E.R.N. collaboration) and has been designed to be a possible front end for High Power Proton Accelerator (HPPA) devoted to fundamental and applied research: radioactive beams production, neutron sources, neutrino factories and transmutation. IPHI consists of an E.C.R. proton source SILHI (100 mA, 95 keV), under operation at the present time, followed by a Low Energy Beam Transfer Line (LEBT). A Radio Frequency Quadrupole (length: 6m), operating at 352 MHz will then accelerate the proton beam up to 3 MeV. Finally, the High Energy Beam Transfer line (HEBT) will transfer the beam to a beam stopper. Following the necessary commissioning period, a reliability test (several months) operation of the RFQ will be conducted with the support of EUROTRANS (FP6). In the frame of the SPL (Superconducting Proton Linac) study at CERN, a 3 MeV test stand, designed to become the low energy part of the new linear accelerator "Linac4", is being built. The beam acceleration will be performed by the RFQ of IPHI which will be moved from CEA/Saclay to CERN for this purpose. Downstream the RFQ, a chopper line will deliver the beam to the Linac 4 with the appropriate time structure.

IPHI is planned to work under C.W. operation but during tests and commissioning periods, pulsed mode operation has to be considered.

BEAM DIAGNOSTICS

General considerations

The general layout of the HEBT is shown in Figure 1. The straight section (dipole "off") will be equipped with beam diagnostics in order to:

- Help to the safe transport of the proton beam to a beam stopper able to withstand the full power of the beam: 300 kW in the C.W. mode operation.
- Provide a sufficient characterization of the beam accelerated by the RFQ during the commissioning period and the daily operation.
- Operate under pulsed mode (pulsed mode operation of the ECR source) for machine commissioning or experimental operation, and under the planned CW operation.
- Test and evaluate non intrusive techniques for measuring transverse beam profiles of high average power beams: Due to the large quantity of beam energy deposited in any possible intrusive sensor leading to its destruction and the resulting high activation induced level in the accelerator structure, non interceptive beam diagnostics have to be put on operation in HPPA.

The deflected section (dipole "on") is primarily devoted to energy spread measurements under pulsed mode beam operation (low average beam power operation). For this purpose, an object slit will be located in the straight section before the dipole and an image slit followed by a Faraday cup at the end of the deflected section.

BEAM CURRENT MEASUREMENT

This is probably the most important measurement to achieve. RFQ beam transmission efficiency will be drawn from this measurement:

C.W., Low duty factor pulsed mode operation:

This measurement will be achieved by a DC beam current transformer: a MPCT manufactured by Bergoz Company. It will be housed in a magnetic shielding and placed after the second dipole doublet.

- Resolution reaches 10 µA according to at least a one second integrating signal duration and the bandwidth ranges from 0 to 4 kHz.

Pulsed mode operation:

Under this mode operation, the duration of the beam pulse is expected to be as low as 100 µs and the repetition

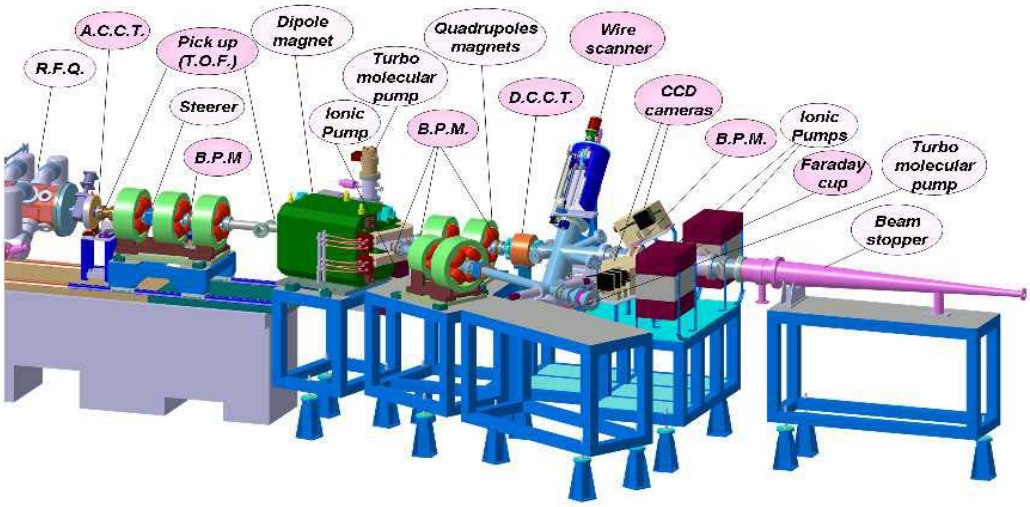

Figure 1: general layout of the high energy beam transfer line of IPHI.

rate 1s. A specific AC beam current transformer has been built and will be located just at the exit of the RFQ.

- The electrical noise is 10 µA rms and the band width ranges from 4 Hz up to 6 MHz.

This beam current transformer is similar to another one which has been put on operation for several years in the LEBT.

BEAM POSITION MEASUREMENT

Six Beam Position Monitors (BPM) are needed to transport safely the beam: 5 designed for a 33 mm chamber radius (3 in the straight section, 2 in the deflected one) and the last one (before the beam stopper) for a 75 mm radius. Electrostatic Pick Up type has been chosen to measure the transverse beam centroïd position.

Electrical signal amplitude :

The amplitude of the signal at the terminals of a load connected to the electrode depends on the charge linear distribution seen by this electrode.

- Due to the space force charge and to the energy spread, simulations show (TRACEWIN code) that the linear charge density decreases as the beam propagates to the beam stopper (rms width: σ_z)
- Due to the low value of β (~ 0,08), the image charge distribution is spread longitudinally along the beam pipe wall (radius a): σ_{wall}rms = $\frac{a}{\gamma\sqrt{2}}$

  with $\gamma = (1-\beta^2)^{-\frac{1}{2}}$
- The current i(t) flowing into the electrode can be expressed versus linear charge distribution λ(z) or current beam and has been computed (table 1). Bench test measurement agrees with the calculated sensitivity: 8.5 mV per mA beam.
- Signals are processed by Log-Ratio Beam Position Monitor electronics module from Bergoz Company.

Error analysis:

- Electrical and mechanical center misalignment lead to offset measurement: 150 µm for the bloc prototype. (mechanical calibration system accuracy : ~ 40 µm)
- The voltage button is obtained by the product of i_{button} by the impedance Zc of the cable seen by the button for low frequencies and by $\frac{Z_c}{1+Z_c C_b \omega}$ for high frequencies.

(C_b : total capacitance electrode / ground: 9,4 pF).

Table 1: Calculated signal amplitude for each B.P.M.

BPM number	$\sqrt{\sigma_{wall}^2+\sigma_z^2}$	**I (fundamental) beam seen by chamber**	**V button in mV** (50 Ω)
1st	25 mm	16 mA eff	136
2 nd	29 mm	2.7 mA eff	23
3 rd	30 mm	1.3 mA eff	11
Last one	57 mm	~0.6 mA eff	~5

- Discrepancy between the characteristic impedance Zc of the cables leads to offset measurements: 400 µm offset deviation has been measured for 1% dispersion of Zc
- Impedance mismatches between Zc and the input impedance of the Log Ratio module increase the Voltage Standing Wave Ratio and induce error measurements. (L/R card input impedance measured: 110 Ω)
- The position sensitivity: 17 µm/mV decreases as the input voltage decreases. After measurements, -80dbm (i.e. 60 µA beam current on the first electrode) at the input of the electronic module is the lower limit.

BEAM PROFILE MEASUREMENTS

Transverse charge distributions and calculation of the emittance of the beam at the exit of the RFQ will be drawn from the transverse profiles measurements.

Wire scanner

A wire scanner, traditionally used for transverse profiles measurements [4], has been built for IPHI and will be located after the dipole.

- A 30 µm diameter carbon fibber has been selected to be moved through the beam. This fibber can not withstand the CW operation. Results of resolution of the "heat equation" leads to limit the pulse duration to 300 µs, rate repetition to 1s (100 mA, 3 MeV)
- The two carbon fibbers, (horizontal and vertical measurements) are mounted in a "V" design on an alumina frame moving at 45 ° to the axis of the beam line. Two biasing wires surround the signal wires.
- The maximum size of the beam to be sensed is 10 cm; the total displacement of the frame is 33 cm and is moved by a stepper motor.
- The transconductance amplifier associated with each signal wire has been designed to exhibit a 1V/ mA gain conversion; 1.5 nA rms noise in a 0-76 kHz bandwidth.
- Measurements have been carried on the LEBT.

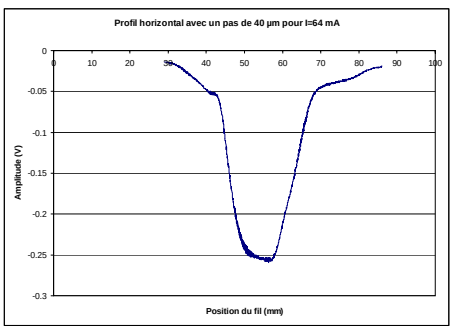

Figure2: LEBT beam profile measurement: Proton beam, 95 keV, 64 mA, pulse 1 ms, repetition 1s, step 40 µm

Fluorescence Beam Profile Measurements

In the L.E.B.T. the moderately relativistic protons interact strongly with the atoms of the residual gas which is mainly hydrogen (pressure: 2.10^{-5} hPa) or additional gaz. A light, visible by the human eye, is emitted by the de-excitation of these atoms. This phenomena looks very attractive and may lead to realisation of non destructive diagnostic for high power beams. This light was studied [3] with an intensified C.C.D. camera working in the 200 nm-820nm range with the aim to measure the transverse beam profiles. Some results have been pointed out:

- The intensity of the emitted light depends on the nature of the gas and increases proportionally to the pressure of the gas.
- Profiles obtained by F.B.P.M. have the same geometrical shape for all gases at the same pressure.

However discrepancies between the width of the profiles obtained by fluorescence and by a grid profiler have been pointed out and further investigations were made. The typical Doppler shift effect of Balmer lines series of hydrogen has been used to sign among the overall light present in the vessel the one produced by the protons accelerated at the nominal energy.

The vacuum vessel of the wire scanner has been equipped with windows to re-conduct these optical experiments at 3 MeV with the aim to compare optical and W.S. profiles.

BEAM ENERGY MEASUREMENT

The kinetic energy of the protons is established by the RFQ through which they have passed. As β =0,08, time of flight technique may be called to measure the time a particular bunch takes to travel between two probes separated by a known distance: two electrodes P.U. will be separated by a distance of 1,3855m ± 0.1 mm. The accuracy on the time measurement must be at least 20 ps. Then an accuracy of 10^{-3} may be reached on energy measurement. Pick Up probes have been built (inner ϕ: 66 mm; length: 10 mm; Capacitance: 26 pF). Their signals will be delivered to a phase meter. One degree accuracy is expected. A third P.U. electrode (8 cm from the first one) has been added in order to discriminate uncertainty on energy measurement if needed.

ACQUISITION AND SUPERVISION

Four PXI chassis (PCI extended for instrumentation) implemented with LABVIEW software, acquire diagnostic data and receive their commands from the supervision system EPICS by an Ethernet connection.

CONCLUSION

Beam diagnostics of the HEBT line will allow the characterisation of the beam accelerated by the RFQ. The wire scanner is under operation and will be our profile measurements reference. Developments on fluorescence induced by the beam will be carried at 3 MeV.

ACKNOWLEDGMENTS

It is a pleasure to acknowledge the constant support of R. Gobin and the SILHI team.

REFERENCES

[1] P. Ausset and al. Optical "Transverse beam profile measurements for high power proton beam". EPAC 2002, June 2002, Paris.

[2] C. Rossi and al, "The SPL Front end: a 3 Mev H- test stand at CERN". LINAC 04, August 2004, Lübeck.

[3] P. Ausset and al, "Optical transverse beam profile measurements for high power proton beams". EPAC 2002, June 2002, Paris.

[4] B. Bouchet and al, Wire "Wire scanner at LEP", Proc. of the I.I.I.E. PAC May 1991, San Franscisco.

A CURRENT MODE INDUCTIVE PICK-UP FOR BEAM POSITION AND CURRENT MEASUREMENT

M. Gasior, CERN, Geneva, Switzerland

Abstract

An Inductive Pick-Up (IPU) senses the azimuthal distribution of the beam image current. Its construction is similar to a wall current monitor, but the pick-up inner wall is divided into electrodes, each of which forms the primary winding of a toroidal transformer. The beam image current component flowing along each electrode is transformed into a secondary winding, connected to a pick-up output. Such sensors are operated in the CERN CTF3 Drive Beam Linac [1]. This paper describes a similar device developed for the CERN Linac 2 to PSB transfer line. To cope with two orders of magnitude longer beam pulses, the new sensor is operated in current mode. The transformers drive transresistance amplifiers (TRA), converting transformer currents into voltages, which in turn are processed by an active hybrid circuit (AHC), producing one sum (Σ) signal, proportional to the beam current, and two difference (Δ) signals proportional also to the horizontal and vertical beam positions. The bandwidth of the Σ and Δ signals spans 6 and 5 decades, respectively. The transformers have an additional one-turn winding to which a pulse from a precise current source can be applied to calibrate the sensor.

INTRODUCTION

The Linac 2 can deliver 50 MeV proton beams of up to some 200 mA in 100 μs pulses to the PSB. The beam position in the transfer line is currently measured with 20 magnetic pick-ups (MPUs) [2] installed 30 years ago, which now show signs of fatigue. Their mechanics is very complex (e.g. 4 layers of magnetic shielding) and in case of a failure, there are no spare parts. To prepare for a future upgrade of the position measurement system, one of the MPUs was replaced by a recently developed IPU [3]. A successful result with this pick-up would allow the new system to be based on this type of sensor, equipped with an acquisition system very similar to that of CTF3 [4]. This solution would require relatively little manpower. In addition, contrary to the old MPUs, the new IPU can measure the beam current, eliminating the need for many of the separate beam transformers.

The IPU cross-section is shown in Fig. 1. Photographs of its components and the installed sensor are shown in Fig. 2 and 3, respectively. The body A, made form alodined aluminium, houses the ferrite cylinder B, surrounding 8 electrodes C. The separate vacuum assembly D with Helicoflex flanges contains a ceramic insert. The insert is titanium coated on the inside with the optimal coating resistance determined by the method described in [5]. The plate E accommodates 8 current transformers F, through which go M5 copper screws, closing the primary transformer circuits. The transformers

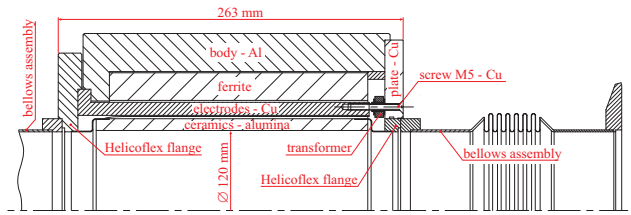

Figure 1: The IPU cross-section.

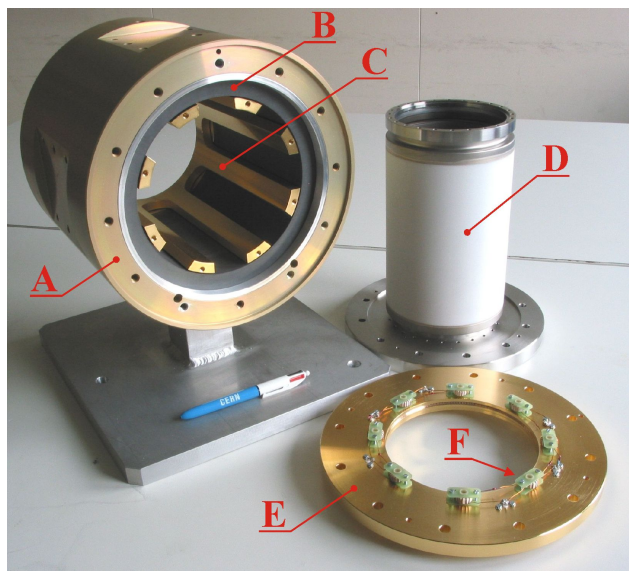

Figure 2: The IPU parts.

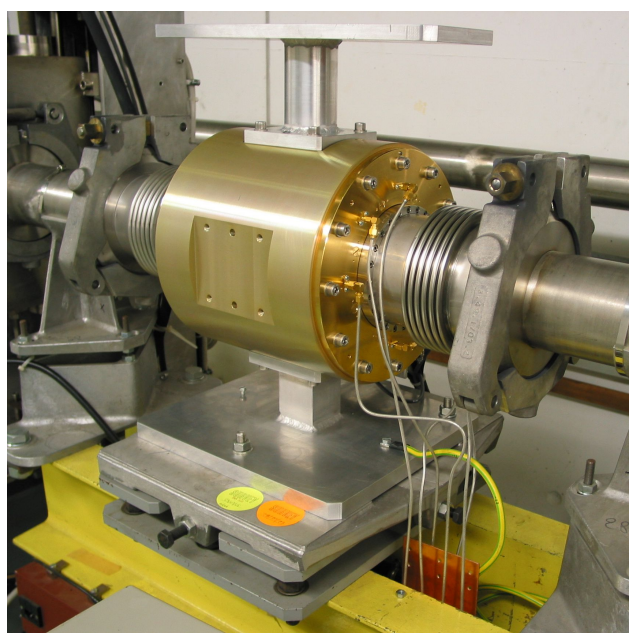

Figure 3: The IPU installed.

are combined in pairs, each of which is connected to a sensor output.

To achieve a good low frequency response, the primary circuit parasitic resistances had to be kept below 0.1 mΩ. Thus the electrodes C and the plate E are made from copper and are gold plated along with the screws. The electrodes and their supporting plate are machined as one piece to minimize primary loop resistances and to achieve good mechanical precision.

Each of the four IPU outputs is connected to one TRA input, representing a low resistance load to the transformers to improve the sensor low cut-off frequency, in order to limit the signal pulse droops. The TRAs convert the transformer currents into voltages, which are then processed by the AHC, producing the Σ and Δ signals.

The whole beam image current must pass through the transformers, so the IPU can be used for absolute beam current measurement. To calibrate the sensor for this purpose, each transformer has a calibration turn, used to inject a current pulse of an amplitude known to 0.1 %, which in addition is independent of parasitic resistances of cables, connectors and the like. Similar pulses are used to test the Δ and Σ channels, calibrate their gains and check the common mode rejection ratio by applying identical signals to the transformers of opposite electrode pairs.

A MODEL AND RESULTS

The low frequency behaviour of two opposite pairs of electrodes, forming one IPU plane, together with two channels of the TRA, can be modelled by the circuit shown in Fig. 4. Its parts are the following:

- Four branches with inductances L_Δ represent two opposite pairs of electrodes with one 1:n current transformer per pair. Resistors R_C are parasitic resistances of electrodes, screws and contacts, while resistance R_P represents the secondary winding load R_S transformed to the primary.
- The current source ΔI_B represents a position signal induced by a beam displacement.
- L_Σ represents the inductance of loops built from electrodes and the pick-up body walls; the inductance is increased by the ferrite filling the loops. L_Σ shunts the beam image current I_B seen by the pick-up.
- The transmission lines represent cables connecting the pick-up with its transresistance amplifier.
- R_S represents parasitic resistances of the transformer windings, cables and connectors.
- R_1 provides the cable termination for high frequencies while for low frequencies it is shunted by L_1 of small value.
- The operational amplifier OA_1 converts the secondary winding current into a voltage, with the value of R_F setting the transresistance.
- Since OA_1 has large DC gain (R_F/R_S is beyond a thousand), an auxiliary op-amp OA_2 is used to provide a very low frequency feedback to compensate for the offset voltage of OA_1. Due to the very small impedance of the OA_1 inverting input, capacitive coupling cannot be used.

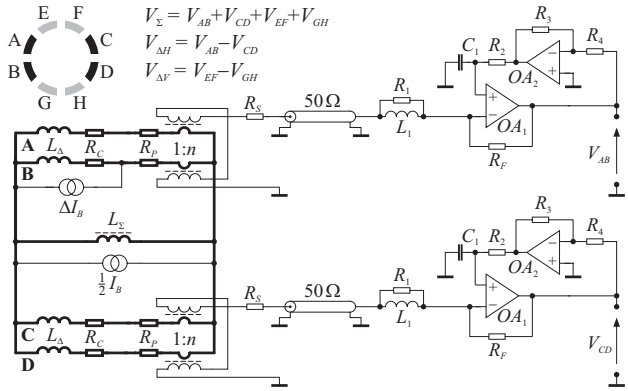

Figure 4: IPU and TRA low frequency model (one plane).

Table 1. Parameters of the IPU and of its electronics.

IPU	Length / body diameter	263 mm / 270 mm
	Overall length with bellows / weight	595 mm / ≈ 50 kg
	Beam pipe / electrode inner diameter	120 mm / 145 mm
	Titanium coating end-to-end resistance	5 Ω (i.e. 9 Ω/□)
	Transformer A_L / turn number n	3 μH / 15
	L_Δ inductance / ferrite μ_r	≈ 250 nH / 100
	Primary parasitic resistance R_C	< 0.1 mΩ
	Secondary winding load R_S	< 50 mΩ
IPU + TRA + AHC	Position sensitivity	30 mm × Δ/Σ
	Electrical center position error	< 0.25 mm
	Linearity error for 20 mm excursions	0.1 % (0.12 mm)
	Min / max measured current	a mA / 300 mA
	Σ low cut-off frequency	50 Hz
	Δ low cut-off frequency	150 Hz
	High cut-off frequency	50 MHz
	TRA transresistance	100 Ω
	AHC Σ channel gain low / high	10 dB / 30 dB
	AHC Δ channel gain low / high	20 dB / 40 dB
Calibration current pulse		100 mA, 0.1 %

Components of the beam image current I_B flow through four 1:n electrode transformers, which are combined in pairs. Each transformer sees half of the secondary winding load R_S. The op-amp OA_1 creates a virtual ground at the inverting input, so the output Σ signal voltage is

$$V_\Sigma = \frac{R_F}{2n} I_B \qquad (1)$$

and decays with the time constant set by $R_P = R_S/2n^2$ and inductance L_Σ. Taking into account parasitic resistances R_C of the primary loops this yields the Σ signal low cut-off frequency

$$f_{L\Sigma} = \frac{1}{2\pi L_\Sigma}\left(\frac{R_S}{2n^2} + R_C\right) \qquad (2)$$

provided that the transformer low cut-off is still smaller.

Similarly, the current ΔI_B resulting from the beam displacement decays with the time constant set by the sum $R_P + R_C$ and electrode inductance L_Δ. The corresponding low cut-off frequency is

$$f_{L\Delta} = \frac{1}{2\pi L_\Delta}\left(\frac{R_S}{2n^2} + R_C\right) \qquad (3)$$

Since $L_\Delta << L_\Sigma$, the more challenging demand is obtaining the desired Δ signal low cut-off frequency $f_{L\Delta}$.

The TRAs have a high gain only for low frequencies. The Δ signal gain G_Δ decays 6 dB per frequency octave, limiting the total noise at the amplifier output. G_Δ is set by the ratio of R_F and the impedance seen from the OA_1 inverting input

$$G_\Delta = \frac{R_F}{2n^2(R_C + R_P + 2\pi \mathrm{j}\, L_\Delta f)} \cong \frac{R_F}{R_S + 4\pi \mathrm{j}\, n^2 L_\Delta f} \qquad (4)$$

reaching unity already at some 300 kHz. The gain for Σ signals is as (4) but with L_Δ replaced by the much larger L_Σ value, resulting in a still smaller gain.

Parameters of the IPU and the channel IPU-TRA-AHC are listed in Table 1. To improve $f_{L\Delta}$, the AHC Δ channels have (6 dB) more gain for low frequencies; the Σ channel has no correction. $f_{L\Sigma}$ was limited by the largest affordable value of series capacitors along the signal chain. The high frequency cut-off is determined by the L R matching circuitry at the TRA inputs.

The IPU linearity error, shown in Fig. 5, was measured by diagonally displacing a 0.2 mm wire across the pick-up aperture. The error is about 0.12 mm (i.e. 0.1 % of the aperture of 120 mm) for excursions up to ±20 mm, which are most important for the transfer line.

An example of a position and current measurement is shown in Fig. 6. No significant signal droops are seen. For this application the 50 MHz high cut-off frequency of the system can be lowered by a decade, as the linac beam does not contain significant components beyond a MHz. This would further lower the system noise.

The pick-up signals contain some components resulting from ground loop currents in the beam pipe, caused by pulsed magnets and power equipment. The components are very slow with respect to the beam signal and only cause a small base line wander. As seen in the measurement, this can easily be removed by a simple base line correction on digital samples and has no significant effect on the measurement quality. Since the pick-up is based on measuring the beam image current, removing the interference could only be achieved at its source, by cleaning up the grounding in the machine.

CONCLUSIONS

An inductive pick-up was commissioned on the CERN Linac 2 to PSB transfer line, replacing an old magnetic pick-up, as a preparation for upgrading the whole transfer line beam position system. The sensor can measure the beam position and absolute current with respectively 5 and 6 decade bandwidths, and can be tested and calibrated in situ with precise current pulses. None of the IPU, TRA and AHC contains adjustable elements. The pick-up has a better performance and a much simpler construction than its old magnetic predecessor, in particular without any magnetic shielding.

Two years of CTF3 experience with some 25 inductive pick-ups have demonstrated that these devices can accurately measure both the beam position and absolute current, and that they are robust and insensitive to beam losses. The new position measurement system for the transfer line can be based on this type of sensor with a relatively small development effort, as many system parts can be copied from the parent CTF3 system. The only different parts are the pick-up itself and the transresistance amplifier. The prototype currently installed can be used for the final system with virtually no modifications.

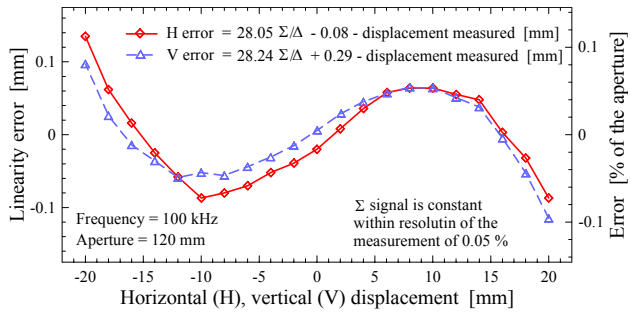

Figure 5: IPU linearity error.

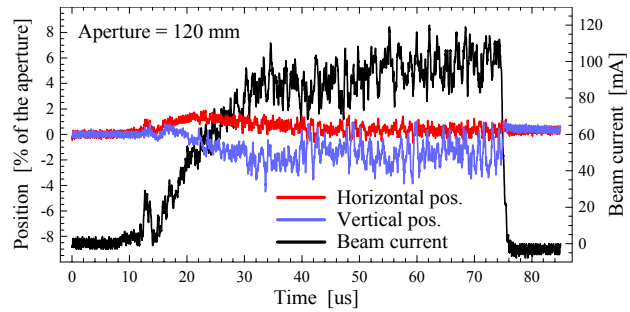

Figure 6: Measured position and current (scope, one shot).

ACKNOWLEDGMENTS

I would like to thank J. Belleman for his help throughout the whole development and U. Raich for supporting the project. I am grateful to Y. Cuvet for the superb mechanical design of the pick-up and to R. Jones for paper corrections.

REFERENCES

[1] M. Gasior, "An Inductive Pick-Up for Beam Position and Current Measurements", Proceedings of DIPAC 2003, Mainz, Germany, pp. 53-55.

[2] K. Schindl, T.R. Sherwood, "Magnetic Position Monitors for the New Linac and the PSB Injection Line", CERN-MPS/BR/LIN/Note 75-12.

[3] M. Gasior, "A proposal for an Inductive Pick-Up for Measuring the Position and Current of Proton Beams in the Transfer Lines between the Linac 2 and the PSB", CERN-AB-Note-2003-082-BDI.

[4] M. Gasior, "Hardware of the CTF3 Beam Position Measurement System", CTF3 Note 053.

[5] M. Gasior, "Limiting High Frequency Longitudinal Impedance of an Inductive Pick-Up by a Thin Metallic Layer", Proceedings of EPAC 2004, Lucerne, Switzerland, pp. 2481-2483.

RESULTS FROM THE SPS 1.7 GHz TRAVELLING WAVE SCHOTTKY MONITOR

M.E. Castro, F. Caspers, T. Kroyer, R. Jones, J.P. Koutchouk, G. Tranquille,
CERN, Geneva, Switzerland

Abstract

A 1.7 GHz waveguide Schottky detector system was recently built and installed in the SPS accelerator following the design of the detectors of the Fermilab Tevatron and Recycler accelerators. The waveguide detector is designed to measure the transverse and longitudinal Schottky signals of the accelerator at a frequency high enough to avoid coherent effects. This paper describes the first tests carried out with the Schottky detector using LHC type beams. The principal goal of these tests was to check whether such a detector can be used for transverse Schottky diagnostics in LHC.

INTRODUCTION

Using a suitable detector, one can detect fluctuations in the instantaneous number and position of particles in a circular accelerator. The frequency spectrum of these signals consists of a set of lines at integer multiples of the particle revolution frequency, and a second set which is shifted in frequency from the first one due to the particles' betatron motion. If the beam is bunched, the synchrotron motion splits each line into a set of satellite lines. One can use Schottky signals to obtain a variety of information on a particle beam without perturbing it [1].

Slow wave slotted waveguide pickups were installed in Tevatron and Recycler accelerators at Fermilab and they are used as a means of non-destructive measurement of betatron tunes, chromaticity, momentum spread (dp/p), transverse emittances and the synchrotron frequency.

First data obtained from the detector installed in the CERN SPS clearly show Schottky betatron lines and even a faint signal with pilot beam without gating.

SCHOTTKY PICKUPS

A travelling wave Schottky pickup consists of a rectangular beam pipe with two waveguides on either side (Figure 1). The wall between waveguide and beam pipe is made of slotted thin aluminium foil for coupling signal into the waveguide. This kind of detector is bi-directional and is used in FNAL to provide both proton and antiproton signals [2].

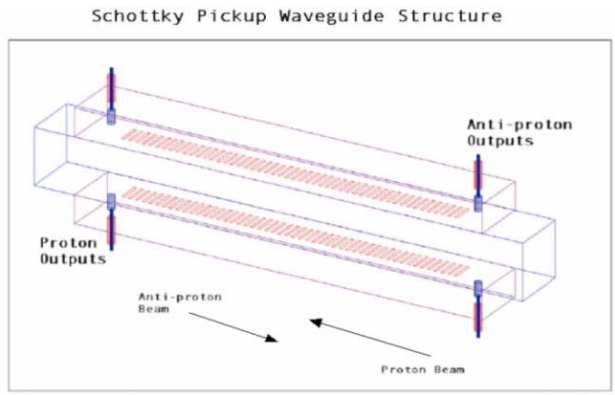

Figure 1: Schottky Pickup design

The designed operating frequency is approximately 1.745 GHz for the DELTA mode and 1.813 GHz for the SUM mode. The Schottky PU at CERN has been used as a vertical detector and tuned for an operating frequency of 1.8 GHz which is a multiple of 40 MHz LHC and 200 MHz fixed target beams harmonics.

EXPERIMENTAL SET-UP

Measurements were taken using both Delta and Sum signals coming out from the arms of the pickup. The Sum signal is an indicator of the longitudinal sensitivity of the detector whilst the Delta signal was used to get the transverse Schottky spectrum.

In the tunnel, Sum and Delta signals were obtained from the pickup by means of a 180° hybrid. Each of the plates was connected to a set of mechanical attenuators in such a way that attenuation for each channel could be varied in steps of different attenuations between 0 and 7.5dB (Figure 2). The objective of the attenuators was to minimize the longitudinal signal (common-mode lines) in the transverse spectrum by trying to electrically center the beam in the pickup. The control of the attenuators was done from the surface. The Delta signal was fed into a narrowband filter installed in tunnel and centered at 1.803GHz. Taking into account the attenuation of the cables carrying signals to surface (~12dB), the Sum signal provided $100V_{peak\text{-}peak}$ and the Delta signal $10V_{peak\text{-}peak}$.

The signal processing was done using a conventional FFT analyzer (SR785 Dynamic Signal Analyzer). The frequency range of the device goes from 195.3mHz to 102kHz and, since signals are expected to appear at frequencies around 1.8GHz, the whole spectrum needed to be shifted to that interval. To do that, a further filtering and two down mixing stages were employed.

Filtering and first down mixing was carried out on a Hewlett Packard spectrum analyzer (SPA). The signal coming from the tunnel was applied to the RF input of the SPA for filtering with the Central Frequency set to 1.8GHz. The SPA has an internal local oscillator placed at 21.4 MHz below the Center Frequency so that the whole spectrum is moved to 21.4 MHz. The IF output of the SPA becomes now the RF input for the next mixing stage where the LO frequency is supplied by a signal generator. Frequencies around 21.45-21.46 MHz were chosen so that the base band signal was at 50-60 kHz in the FFT analyzer (Figure 2).

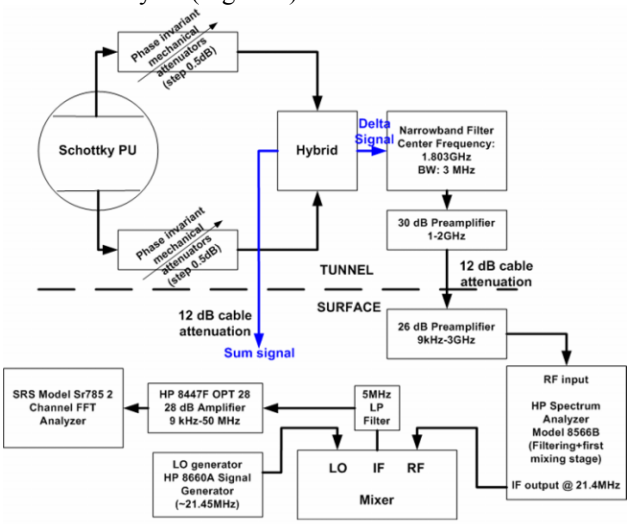

Figure 2: Data acquisition with FFT analyzer

EXPERIMENTAL RESULTS

Data were acquired during several separate SPS runs, all of them with bunched beam, 26GeV coast energy and 40MHz LHC beam pattern (72 bunches spaced by 25ns).

Table 1: Typical SPS beam parameters during data acquisition.

	UNITS	SPS
Coast beam Energy	GeV	26
Momentum	GeV/c	26
Revolution Frequency	kHz	43.347
Betatron Tune, QH		26.13
Betatron Tune, QV		26.19
Intensity per bunch		$1.3*10^{+11}$
Number of bunches		72
Number of batches		Up to 2
Bunch Spacing	ns	25
Bunch Length	ns	4
Normalized r.m.s Vertical Emittance (ε^*_V)	μm	~3.5-3.6
$\Delta p/p$ (r.m.s.)		1×10^{-3}
Beam r.m.s radius (a_{rms})	mm	1.8
(Main) RF Frequency	MHz	200
SPS γ_{tr}		23.4
SPS circumference (C)	m	6911.560387

A spectrum obtained with the FFT analyzer is shown in Figure 3 and illustrates most of the important features of the data.

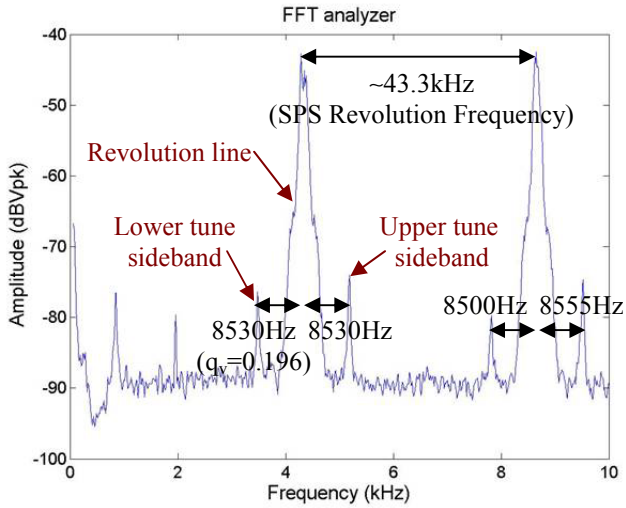

Figure 3: Spectrum of Delta signal from Schottky detector

The large peaks are revolution lines. They repeat at integer multiples of the SPS revolution frequency (43.347kHz at 26GeV) and are due to the residual longitudinal signal. Each peak is a compound peak: a narrow one due to the residual coherent signal at 1.8GHz and a broad peak that is the longitudinal Schottky signal. The two peaks appearing on the right and left of the revolution lines are the betatron signals or the 'upper and lower sidebands'.

According to theory, the distance of the tune lines to the revolution line is equal to the fractional part of the betatron tune multiplied by the revolution frequency ($q_v \cdot f_{rev}$) and the line width is

$$\Delta f_{u,l} = \frac{\Delta p}{p} \cdot f_{rev} \cdot \left[(n \pm q) \cdot \eta \pm Q \cdot \xi \right] \qquad (1)$$

where n is the harmonic number, q is the fractional part of tune, η is the 'slip factor' and ξ is the machine chromaticity.

The fact that the particles have different energies leads to a change in the revolution frequency and a change in focusing strength when particles pass through the quadrupoles. This creates a change in the tune (q) that is related to a change in momentum by the chromaticity. All this together has an effect on the width of the tune lines. Depending on the sign of the chromaticity and the slip factor, either the upper or lower sideband will be wider but since the total power in the two sidebands, independently of the value of the harmonic number, has to be the same, the amplitude of the broader line will be smaller than that of the narrower one.

The longitudinal sensitivity of the detector can be measured using the Sum signal coming out from hybrid. The obtained result in the SPS (Figure 4) shows the

bunched structure of the beam (72 bunches spaced by 25ns) with lines spaced by 40MHz. The best response of the pickup is around 1.7625GHz whilst maximum response for Schottky detector in FNAL is around 1.8GHz; this shift in frequency is due to the convolution of longitudinal bunched beam frequency spectrum and pickup frequency response.

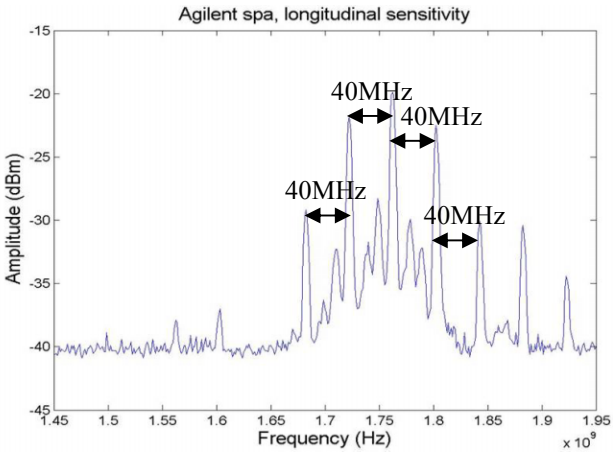

Figure 4: Longitudinal sensitivity of the Schottky detector

SIGNAL TO NOISE RATIO

The level of signal being received in the SPA is consistent with calculations. These calculations are based on the beam power ratio given by

$$g = \frac{P_{beam} - P_{noise}}{P_{noise}} \qquad (2)$$

The power ratio can be extracted from the formula of the difference mode impedance for a slow wave pickup [4]:

$$Z_{\Delta} = (g-1) \cdot \frac{N_f \cdot S_{therm}}{2 \cdot e \cdot I_{dc} \cdot \left(\frac{\sigma}{d}\right)^2} \qquad (3)$$

where Z_{Δ} is the difference mode impedance, S_{therm} the power spectral density of white thermal noise at 300K, e is the charge unit, I_{dc} is the longitudinal DC total current, σ is the beam radius, d is the beam pipe half section and N_f is the noise figure of preamplifier. All these values are known.

Once g has been calculated, and considering thermal noise only ($P_{noise} = 4 \cdot 10^{-21}$W/Hz), the beam power can be extracted from (2). The signal to noise ratio (S/N) is given as follows

$$S/N = 10 \cdot \log\left(\frac{P_{beam}}{P_{noise}}\right) = 10 \cdot \log\left(\frac{1.58 \cdot 10^{-19} W/Hz}{4 \cdot 10^{-21} W/Hz}\right) = 16dB \qquad (4)$$

Result is in agreement with the one observed in the SPA in Figure 5.

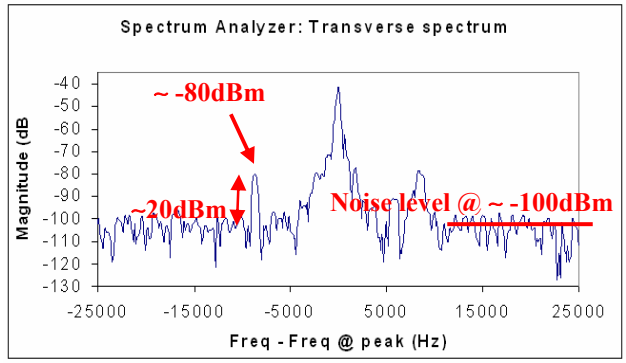

Figure 5: Observed signal to noise ratio

CONCLUSIONS

An extensive signal analysis for static and dynamic beam conditions has been done on different beams from the 1.7-1.8GHz pickup installed in the SPS. Observed signals agree with those predicted by Schottky theory. Vertical tune sidebands could clearly be seen with expected signal level according to calculations. Some signal was even visible with a pilot beam without gating. A passive detector capable of bunch by bunch measurement of tune, chromaticity, momentum spread and emittance would be very interesting for early LHC operation. Such a development is currently underway as part of the US-LARP collaboration.

ACKNOWLEDGEMENTS

This work would not have been possible without the patient and continuous flow of information of R.Pasquinelli from Fermilab, including all the mechanical drawings for the structure.

BDI Group, in particular J.P. Koutchouk, H.Schmickler and R. Jones for support, as well as T.Linnecar and F. Pedersen from the RF Group.

J. Genest and G. Burtin, C. Fischer and the RF group mechanical workshop for preparing and organizing a big part of the mechanical work. G. Tranquille for contributing to the theoretical analysis, J.F. Malo for help and all the others we have not mentioned here...

REFERENCES

[1] D.A. Goldberg and G.R. Lambertson, "Successful observation of Schottky signals at the Tevatron collider", in Proc. 14th Int'l Conf. on High Energy Accelerators.

[2] R.J. Pasquinelli, "A 1.7 GHz waveguide Schottky detector system", PAC'03, Portland, Oregon USA, May 2003.

[3] LHC Design Report, "RF System and Longitudinal Beam Dynamics", CERN, Geneva, 15 December 2004.

[4] D. McGinnis, "Slotted waveguide slow-wave stochastic cooling arrays", PAC'99, New York, March 1999.

[5] D. Boussard, "Schottky Noise and Beam Transfer Function", in Proc. CAS, v.2, 1995.

PETRA PROTON BEAM PROFILING BY VIBRATING WIRE SCANNER

S.G. Arutunian, K.G. Bakshetyan, N.M. Dobrovolsky, M.R. Mailian, L.A. Poghosyan,
I.G. Sinenko, H.E. Soghoyan, I.E. Vasiniuk (YerPhI), K. Wittenburg (DESY)

Abstract

A vibrating wire scanner (VWS) based on the strong dependence of the wire oscillation frequency on temperature was developed and used in the 15 GeV/c proton beam of the proton accelerator PETRAII at DESY. The results show an enormous sensitivity of the scanner and the possibility to use it for weak particle beams and beam halo profiling. Details of the measurements and the results are given. Some investigations of the frequency and the Q-factor of the vibrating wire oscillations dependence on vacuum level are presented.

INTODUCTION

Vibrating wire scanners are based on the extremely sensitive dependence of the wire natural oscillations frequency on its temperature [1-6]. On the other hand, the wire temperature depends on the number of interacting particles/photons with the wire.

In this paper experiments with the vibrating wire scanner on a 15 GeV/c proton beam at PETRA are presented. The dependence of Q-factor of the wire on the vacuum pressure is also discussed. This method might give some additional measuring potential to the VWS.

EXPERIMENT IN PETRA

The experiments in PETRA were done on the proton beam in the bypass, where the electron and proton beams are separated in different beam pipes. Such place was chosen to avoid electromagnetic disturbances induced by electromagnetic wake-fields on the wire, which are much larger for short electron bunches than for long proton bunches.

The vibrating wire resonator consists of a quartz support with a coefficient of thermal expansion of a few 10^{-7} K^{-1} and a beryl-bronze vibrating wire with a coefficient of thermal expansion of 17.5×10^{-6} K^{-1} [7]. Such a ratio of coefficients provides sensitivity to both surrounding media temperature variations and wire heating by the beam. The beryl-bronze vibrating wire passed preliminarily thermal treatment. More details of the experimental setup can be found in [6].

Park Position

The wire of the VWS in its parking position had a distance to the beam center of 6.7 σ. Beam parameters: I = 10 mA, σ_x = 0.6 cm, σ_y = 0.5 cm. The short term frequency stability was 0.01 Hz at a stable room temperature and at absence of the beam.

Fig. 1 represents the typical picture of the scanner frequency change in park position during 30 hours. The proton and electron beams currents in PETRA are also presented. Note that during an absence of both beams the frequency changed smoothly connected with the temperature changes of the whole pickup while during operation of electrons and protons the variations are much larger. The temperature change in the chamber without beam can be estimated from the data to about 7 °C. In the presence of proton beam current the frequency behaviour depends on current intensity. At currents less than 50 mA the wire frequency changes are proportional to the beam current while at higher currents probably the electromagnetic disturbances also have influence on the frequency/temperature by absorbing some modes.

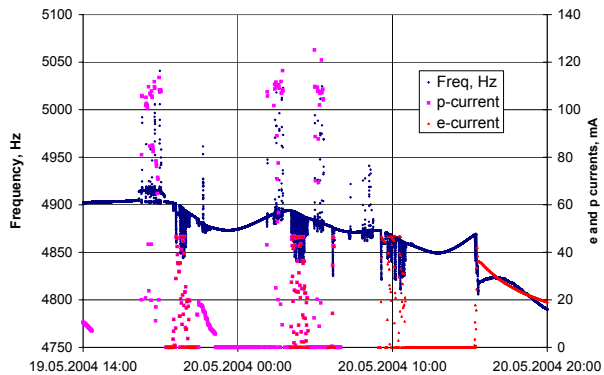

Figure 1: Dependence of VWS frequency on time in park position. Available values of proton beam and electron beam currents are also presented.

Conclusion: Even at a distance of 6.7 σ from the proton beam the VWS has a sensitivity of about 1 Hz/mA.

Scanning

The main mechanism of heat transfer is the thermal conductivity along the wire. The thermal equilibrium time τ can be roughly estimated from the equality of the power scattered due to thermal conductivity ($4\lambda S(T-T_0)/l$ (T is the temperature in the middle of the wire, λ is the coefficient of thermal conductivity, S and l are the cross-section and length of the wire) and power, necessary to maintain the wire at given temperature $\rho Slc(T-T_0)/(2\tau)$ (ρ is the wire material density, c is the thermal capacity). From this equality we obtain $\tau = c\rho l^2/8\lambda$. For beryl-bronze wire of total length 36 mm this time is about few sec. In these experiments the scanning was done at speed 0.5 mm/sec.

Before the scans some vertical and horizontal corrections of the beam position at the scanner were done.

Fig. 2 shows a scan started at a distance of 40 mm from the vacuum chamber center.. Two scintillators with photo-multipliers PM1 and PM2 were installed in the

vacuum chamber to registered protons which are scattered on the wire (and on other parts of the scanner).

The signal from the VWS sensor changes practically from the beginning of movement, while the signals from scintillators start to increase first at distances of 27 mm from the vacuum chamber center.

The scanner was moved from its park position towards the vacuum chamber center up to 20 mm. In this experiment the proton beam was shifted towards the scanner park position by a distance of 4 mm by means of a local beam bump.

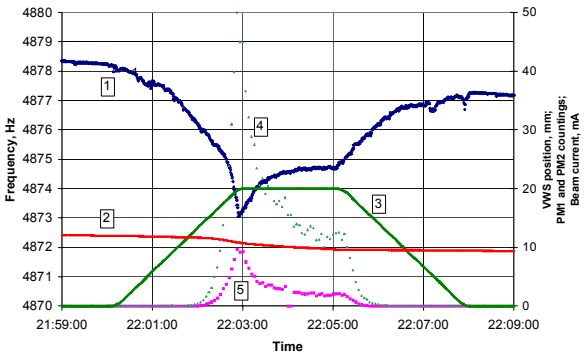

Figure 2: Scan of the proton beam: 1- frequency of the VWS, 2 – beam current, 3 – VWS position relative to the vacuum chamber center, 4 and 5 – PM1, PM2 signals.

As seen from Fig. 2 the signal from VWS appears at distances 27-40 mm from the vacuum chamber center while there is no signal from the scintillators here. Some contribution in wire heating might occur from the influence of electromagnetic higher order modes accompanying the proton beam. These electromagnetic components might be able to heat the wire by absorbing some modes (see [8]). Clarification of this problem and corresponding modifications of VWS require additional efforts.

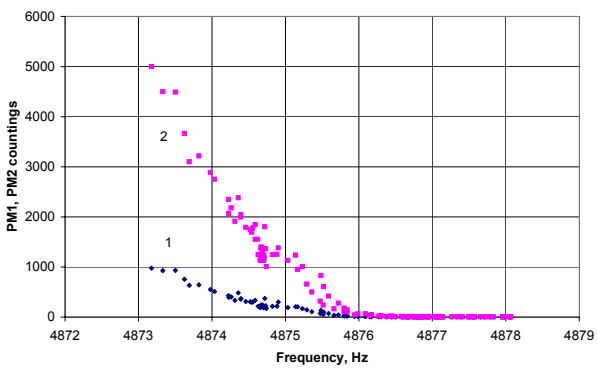

Figure 3: Correlation between signals from VWS and PM1 (curve 1) and PM2 (curve 2).

Despite this effect, the signals from PM1 and PM2 strongly correlate with frequency signal from VWS starting from some scanning depth (Fig. 3). There was some small hysteresis observable connected with different directions of the VWS movement.

The largest shift of the wire oscillation frequency due to heating was about 150 Hz at the distance between the wire and beam center of x slightly less than 20 mm. This value is about a factor 2 less than the calculated value. Three effects might contribute to the uncertainty: 1) the uncertainty of the absolute beam position at the VWS of ±1.5 mm; 2) non-gaussian beam tails; 3) electromagnetic background.

VWS QUALITY FACTOR

In the experiments at PETRA a strong dependence of frequency on the vacuum pressure was observed.

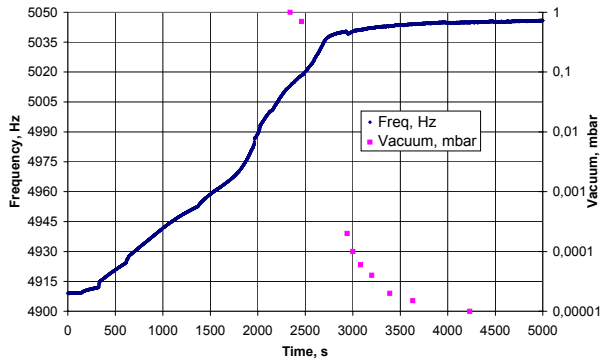

Figure 4: Dependence of frequency of VWS at PETRA chamber vacuum level.

As seen from Fig. 4 the frequency increased with decreasing pressure. The main increment by about 120 Hz occurs in pressure interval 1bar - 1 mbar. At pressures below 0.01 mbar the frequency rate changes its slope and seems to saturate.

The structure of resonant curves was studied by amplitude-frequency characteristics. Fig. 5 represents some such curves for 0.4, 10, 30, 100 and 1000 mbar. The Experiments were done at energomassanalizer EMAL-2 in YerPhI.

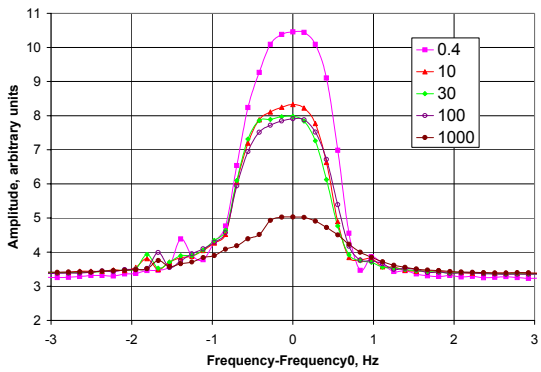

Figure 5: Few amplitude-frequency characteristics for different vacuum levels.

Widths of resonant curves for vibrating wire resonators of different constructions (named A1, A2, A3) are presented in Fig. 6. In all resonators a beryllium bronze wire is oscillating, but different types of wire fixation on the support were used. The above described method requires sweeping of the frequency near the resonance and takes long time. To reduce the time a method for estimation of Q-factor was developed based

on measurement of the signal amplitude in a feedback scheme of the wire oscillations excitation. The voltage on the wire depends on its Q-factor; thus, the magnitude of the feedback signal to support constant amplitude in the generator output can be used for the estimation

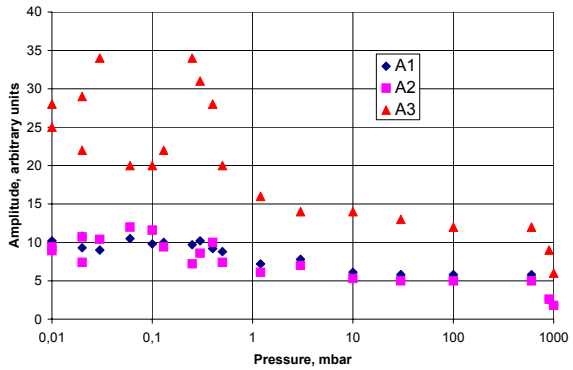

Figure 6: Q-factor measurements of three different resonators depending on vacuum level: A1, A2, A3 different types of VWS construction.

Results of such measurements are presented in Fig. 7. The measurements were done in range of pressures between 0.4-1700 mbar.

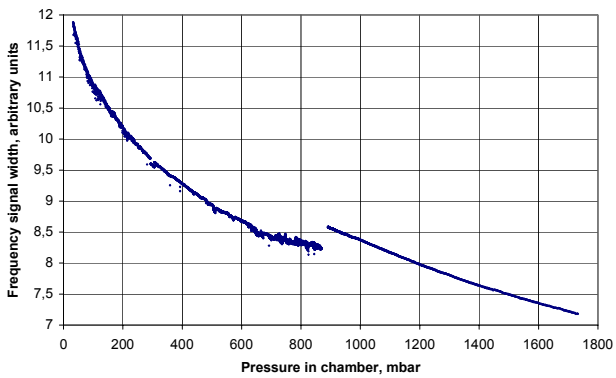

Figure 7: VWS resonator quality dependence on pressure in vacuum chamber.

Experiments in the low pressure range (left part of curve) and at high pressures (right curve) were done at slightly different environmental conditions.

CONCLUSION

Experiments with the VWS show that the system is sensible to changes of the beam current even in park position even at distance of 6.7 σ (here 40 mm) from the beam center. The scans show a strong correlation between scanner position and frequency signal. The accuracy of the frequency measurements achieved 0.01 Hz which corresponds to wire temperature measurement accuracy less than 0.001 K. Comparison of the signal from VWS with a scintillating counter system registering secondary particles/radiation showed that the signal from VWS appears at least 10 mm farther from the beam center than mentioned scintillators.

The obtained data show that the VWS can be used for beam diagnostics in accelerators. Some improvements of the scanner construction to increase the wire operating zone and to diminish the sizes of the wire support of the VWS will be necessary. At very large distances from the beam, the heating of the wire due to higher order mode coupling disturbs the signal. Some more developments are necessary to get rid of this effect. Very perspectives will be the development of sensors on basis of dielectric strings, including new type of oscillations exciting and data acquisition. The area of VWS applications can be enlarged, including profiling and positioning of photon beams from synchrotron light sources and laser beams. In this case the electromagnetic coupling does not exist.

ACKNOWLEDGMENTS

The authors are grateful to PETRA stuff for friendly help during the experiments on PETRA.

REFERENCES

[1] Arutunian S.G., et al. Vibrating wire for beam profile scanning. - Phys. Rev. Special Topics. - Accelerators and Beams, 1999, v. 2, 122801.

[2] Arutunian S.G., et al., Problems of Installation of Vibrating Wire Scanners into Accelerator Vacuum Chamber. - Proc. 8-th Europ. Part. Accel. Conf. (3-7 June 2002, Paris, France), pp. 1837-1839.

[3] Arutunian S.G., et al., First experimental results and improvements on profile measurements with the vibrating wire scanner.- Proc. DIPAC'2003, (5-7 May, Mainz, Germany 2003), pp.141-143.

[4] Arutunian S.G., et al., Vibrating wire scanner: first experimental results on the injector beam of Yerevan synchrotron.- Phys. Rev. Special Topics. - Accelerators and Beams, 2003, v. 6, 042801.

[5] Arutunian S.G., et al., Vibrating wire scanner parameters optimization.-Proc. 9-th Europ. Part. Accel. Conf. (5-9 July 2004, Lucerne, Switzerland), pp. 2457-2459.

[6] Arutunian S.G., Werner M., Wittenburg K. Beam tail measurements by wire scanners at DESY.- ICFA Advanced Beam Dynamic Workshop: Beam HALO Dynamics, Diagnostics, and Collimation (HALO'03) (May 19-23, 2003 Gurney's Inn, Montauk, N.Y. USA).

[7] I.S.Grigor'ev and E.Z.Mewjlikhov in Physical Data Handbook (Energoatomizdat, Moscow 1991).

[8] F. Caspers et al., Cavity model related wire breaking of the SPS wire scanners and loss measurements of wire materials; Proc. DIPAC'2003, (5-7 May, Mainz, Germany 2003).

DIGITAL BEAM POSITION MEASUREMENT AT GSI-SIS AND CERN-PS

A. Galatis, A. Peters, GSI, Darmstadt, Germany
J. Belleman, Uli Raich, CERN, Geneva, Schwitzerland
A. Zoubir, Darmstadt University of Technology, Germany.

Abstract

New, digital BPM techniques needed in hadron machines, accelerating beams with fast varying frequencies, are to be presented. The role of analog electronics is reduced to signal amplification and attenuation as well as bandwidth limitation. This paper explores approaches for the position evaluation of acquired signals, suggesting systems for "free running" estimation as well as machine timing dependent methods. For accurate determining of the transversal bunch position, a good integration window estimation is needed. Two filtering methods will be introduced for this purpose, median and FFT filtering, both methods detecting peaks at bunch signal starting and ending points. Parallel to those a digital PLL approach is discussed in [1].*

PROBLEM DEFINITION

Beam position measurement and monitoring has a significant role in beam diagnostics. It can allow better controlling and regulation of the beam and can be used for estimating global feedback mechanisms. Both need a fast and accurate estimation for obtaining better results. Different approaches have been summarized in [2]. The problem is classified into two different tasks, hard- and software.

Hardware demands:

In order to have sufficient sample data points, while taking into account even short bunches of 30ns FWHM length, a sampling speed of 125MSa/s will be used. ADC resolution has to be large enough to be able to realize observations of transversal position movement in the order of 0.1mm. This fact and considering calculated signal dynamics of the SIS100, a resolution of 14 bit will be needed. The first processing will be done inside an FPGA, which will produce bunch integral data. Due to the high sampling rate and the resulting very short processing time while running the FPGA at sampling speed, complex calculations have to be made off-line and proposed software solutions for first data processing have to be as time efficient as possible to allow bunch-by-bunch resolution. After pre-processing, data rates will decrease to $h*f_{REV}$ (h being the machine harmonic). In order to also be able to use the hardware setup as a fast digitizer to record full acceleration cycles, sufficient RAM has to be provided.

* This project is part of the EU-RP6 SIS100 design study, collaborating members of this subtask being CERN-AB, GSI-SD, I-Tech, TUD and FZ-Jülich.

Software demands:

Fast, online calculation of bunch signal integrals and centre of charge position should be achieved. Since the information primarily needed is the integration over a single bunch and not over all recorded data points, the algorithms determining the limits of a bunch structure will have to be running at full ADC sampling speed. This paper addresses only the software part of the described problem.

PROBLEM SOLUTIONS

As mentioned, integration windows have to be estimated in order to have fixed boundaries on bunch signals. For obtaining those windows, efficient algorithms for online calculation have to be developed. Two methods for determination will be discussed below.

Method 1: Median Filtering

Median filtering introduces a method using a window of N samples length. Data is filtered according to

$$y(n) = \frac{x(n)}{|\ median\ \ (x(n) + \ldots + x(n+N))\ |}$$

The filter smoothes the signal form, filtering out peaks and noise, allowing better estimation of the starting and ending points of a bunch. The variable length of the window indicated by N can be modified to get better results. Since this method is strongly dependent on the used filter window length, different lengths have been tested, with a good estimation level achieved for a length of 16 samples, even for poor SNR. In order to get less falsely detected bunch signals a version will be tested, which adapts the filter window length according to the revolution frequency.

Method 2: FFT calculation and interpretation

The FFT method implements a function that detects variations in the high frequency parts of signal spectra, which correspond to bunch signals emerging from baseline. A short-time FFT (DFT) is taken at consecutive parts of the signal. We again define windows at which we calculate the FFT. We expect to see a rise towards the higher frequency band in a transition from the baseline level to a bunch signal. From the general FFT we can get:

$$x(k) = \frac{1}{N}\sum_{n=1}^{N} X(n)\, e^{2\pi i (n-1)(k-1)/N}$$

$$= \frac{1}{N}\left(X(1)e^{0} + X(2)e^{2\pi i (n-1)/16} + \ldots + 0\right)$$

All X(n) for n>2, when using only two data points, are equal zero. It is obvious that for certain X(n) (X(n) being

the discrete time data values) combinations the maximum will shift towards higher values of k.

We will see that an approach using only a few data points and zero padding up to a length of 16 points is suitable to obtain good results. Nevertheless, other lengths have been tested.

Since both methods can induce false integration window detections, the RF signal is used in parallel to filter those out. False detections in this context mean that a peak was detected even though there is physically no bunch existent. This can happen in cases were the data has a very low SNR.

The data sets for which the results are going to be shown are from a $^{86}Kr^{34+}$ acceleration cycle acquired at GSI-SIS18. The first data set is taken shortly after injection where the bunches are only partly formed and the energy of the beam is low, the second data set while bunches are formed and the third data set after acceleration. Since the signal form coming from the CERN-PS is alike the signal form of the bunched beam at GSI-SIS, no results on the CERN data are exposed here, refer for that to [1].

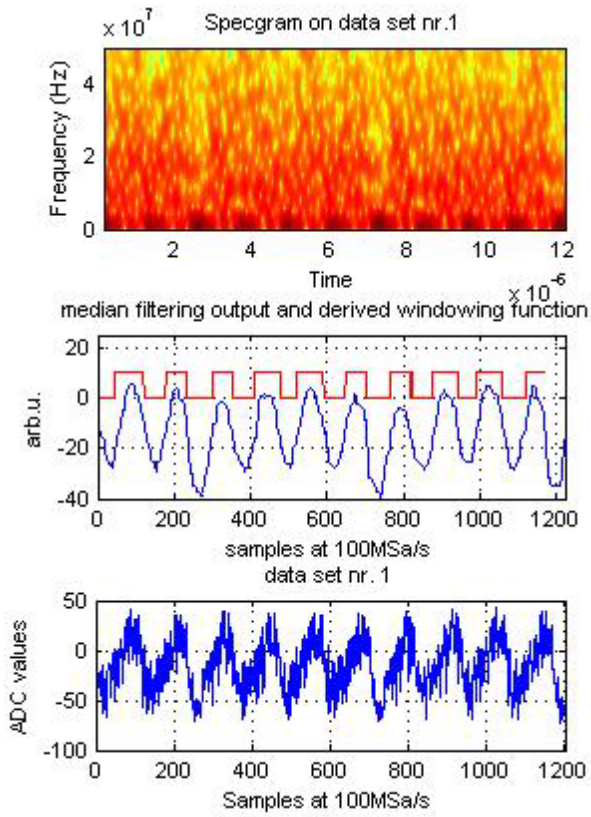

Figure 1: Spectrogram, median filtering of data set nr.1

Top graph of fig. 1 we see the spectrogram of the first data set with peaks at the points where bunches are located (dark red areas in low frequency regions). The time span in the spectrogram is the same as in the time plot of the original data, see bottom plot in Fig. 1.

RESULTS

In order to test both algorithms, the worst-case scenarios were used to prove the method's reliability. The parameters that were used in the FFT approach were a FFT window length of 16 and the number of real data was set to 2. For the case of median filtering the filter length was set to 16 for the data sets at the end of the acceleration, and 64 for the data sets at injection. A tradeoff for the filter length has to be taken into account for any filtering approach, because of the relatively wide span of window or bunch length during an acceleration cycle at GSI. This is starting at about 120 samples (all oncoming number of samples refers to a sampling speed of 100MSa/s) at injection and going down to about 15 samples before extraction.

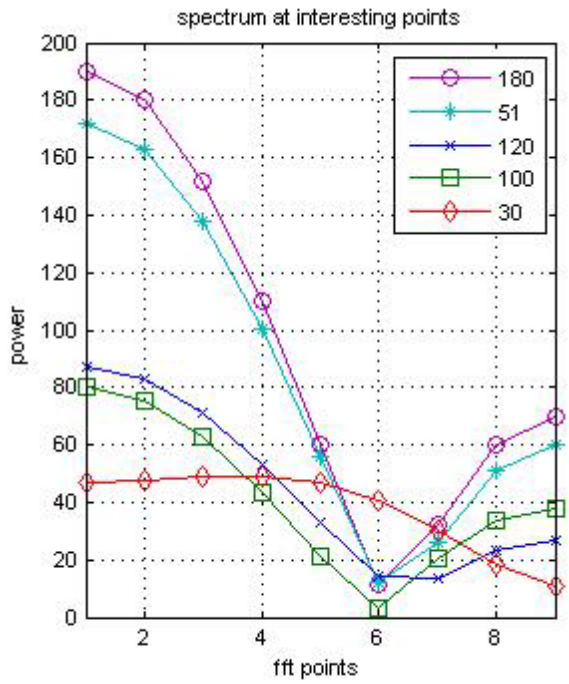

Figure 2: Results obtained by the FFT method, Indices are the time starting points of one bunch structure of fig. 1 bottom graph

In Fig. 2 we see the spectrum of the signal shown in bottom graph of fig. 1 at some points of interest. The indices 51 and 180 of the corresponding graphs are the starting points of the FFT taken from the corresponding time plot. They are the starting and the ending point of an up to that point not well formed bunch structure. The other three depicted graphs are plotted in order to see the differences that can be detected while using that method. The decision bound is, due to the very low signal intensity, very narrow (a factor of two maximum).

The middle blue graph of fig. 1 shows the output produced by the median filtering method. In red we see the derived integration window from the output signal. The

filter length is set to 64, which is about half of the length of a bunch. The estimated window length is, the machine running on harmonic four, almost stable for consecutive turns, with a variation in length of about two samples, therefore an error resulting from noise of one sample as well as one sample jitter error.

In the top graph of fig. 3 we see the spectrogram of data set three. In contrast to Fig. 1 we see a better resolution in the high frequency regions and it is easier to identify the bunches. The better resolution between bunch signals and signal free areas is due to the better SNR. If we look into the low frequency areas, we see points with less energy than others, which we can use as transition points for building an integration window.

As explained earlier, while using the median filtering approach we need to shrink the filtering window length over the acceleration cycle in order to obtain better results. In the case of the middle graph of fig. 3 the length of the window is set to 16. The derived integration window is shown in the red curve. The window length, derived from the filtered signal, is stable for all bunches.

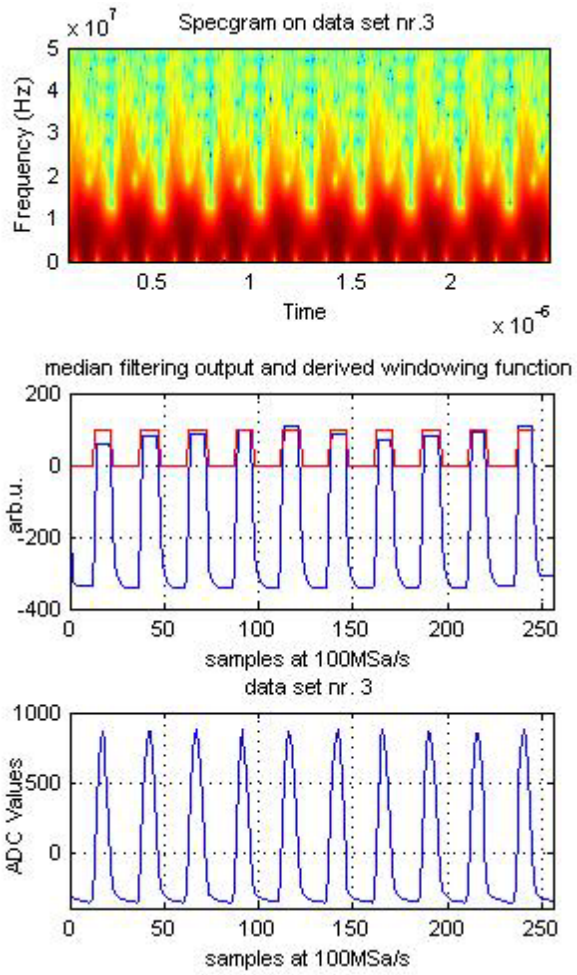

Figure 3: Spectrogram, median filtering on data set nr.3

CONCLUSIONS

Both methods, median and FFT filtering, tend to better results while the SNR, e.g. the bunch forming process completes. At injection levels, they both have their difficulties distinguishing bunches. There have also been made simulations to determine the robustness of the introduced methods. In order to test that the SNR was artificially decreased and the behaviour was observed. The limit was reached at an SNR decrease of about 15-20dB when bunches are completely formed. Both methods will be implemented using the actual RF as a function indicating the actual location of a bunch signal. This information will eliminate false window detections and provide the median filtering method with essential information for the window length variation.

The detection using median filtering works even if we keep the filter window length constant at 16 samples. The FFT method shows a dependency on the FFT length chosen and the amount of data points used. In both cases, a trade off between speed and accuracy has to be made.

The effect of the phase shift between the actual RF master signal and the pick-up signal of up to 25° on the calculated position should be investigated. The jitter should vary between some samples (~10) at injection and about one sample at the end of acceleration. Since both methods will use the RF information as a reference point this jitter should be of no influence.

It is intended to implement both methods in FPGA logic, which directly implies short time factors and very low computational load. Since the FPGA will be running at sampling speed, i.e. 125MHz a calculation time of less than 10ns has to be achieved. From this viewpoint, the median filtering method seems to be the least expensive. First implementations on real hardware should be ready in the next months and tests on efficiency and realisation feasibility will follow.

ACKNOWLEDGEMENTS

We acknowledge the support of the European Community-Research Infrastructure Action under the FP6 “Structuring the European Research Area” programme (DIRACsecondary-Beams, contract number 515873).

REFERENCES

[1] J. Belleman, A New Trajectory Measurement System for the CERN Proton Synchrotron, these proceedings.
[2] G. Vismara, The comparison of signal processing systems for beam position monitors, IT05, DIPAC1999, Chester.

DESIGN OF A FAST ORBIT FEEDBACK FOR SOLEIL

N. Hubert, L. Cassinari, J.C. Denard, A. Nadji, L. Nadolski, D. Pédeau
SOLEIL, Gif-sur-Yvette, France

Abstract

SOLEIL is a third generation light source under construction. Great care is taken at all levels of the machine design in order to reach beam stability at the micrometer level. In particular, a fast global closed-orbit feedback is foreseen for suppressing remaining beam vibrations up to 100 Hz.

The correction uses the computing resource of 120 BPM electronic modules, distributed around the storage ring. Each BPM module includes a powerful FPGA that in addition to its specific BPM task leaves enough room to embed a part of the fast feedback correction algorithm.

All the BPM data (including XBPMs in the future) have to be broadcasted to the 120 modules in order to compute the correction. Broadcasting the data is expected to be fast (around 20 us), thanks to eight multigigabit transceivers per module, and fast links between them. The architecture of the dedicated network is flexible enough to keep the feedback system functional even with a few disabled BPMs.

The correction is applied to 46 dedicated air-core correctors in each plane at a rate of 8 kHz. Simulations will be performed in order to optimize the system in the bandwidth of interest to the machine users.

INTRODUCTION

A third generation light source like SOLEIL has very tight orbit stability requirements. The level of the oscillations of the photon beam must not exceed one tenth of the beam size (see table 1) Great care is taken at all levels of the design to meet these requirements, from building foundations to girders design. The remaining beam motion will be suppressed by global orbit feedback. It is composed of a slow orbit feedback (SOFB) correcting slow beam position drifts and a fast orbit feedback (FOFB) for short term stability. This paper presents the present status of the FOFB system.

Requirements (um)	Long Section	Medium Section	Short Section	Dipole
H	28	18	39	6.2
V	1.7	0.8	0.8	2.5

Table 1: Photon beam stability requirements in each plane for each kind of sources.

SYSTEM COMPONENTS

Both feedback systems use the position measured by the same 120 BPMs in order to compute their correction with a Single Value Decomposition (SVD) algorithm. The SOFB applies its correction at a maximum rate of 10 Hz to 56 correctors in each plane (secondary coils in sextupoles). Those correctors are installed over aluminum vacuum chambers, which limit the correction frequency to ~30 Hz due to eddy currents. For the FOFB, dedicated air-core correctors are installed over the bellows next to the BPMs of the straight sections (fig. 1). Those bellows are in stainless steel and the frequency cut off is greater than 1 kHz.

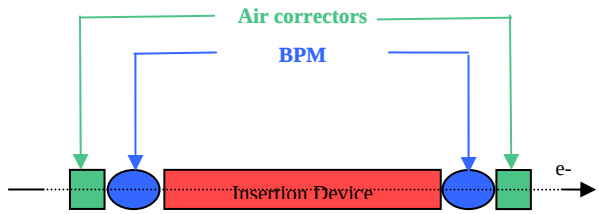

Figure 1: Location of the air correctors on the straight sections. Air correctors are effective in vertical and horizontal planes.

The system is composed of 120 BPMs modules, 46 air correctors in each plane with their power supplies.

Our BPMs are equipped with new electronics modules developed by Instrumentation Technologies [1], [2]. Those modules are based on FPGA technology with high speed communication ports. The large amount of resources of the FPGA allows us to embed the algorithm of correction in the module. In addition to calculating the beam position, the BPM modules perform all the processing of the FOFB. The algorithm computation is distributed on the modules around the storage ring, each one calculating the corrections for its dedicated corrector that is $1/46^{th}$ of the algorithm.

Our power supplies are not yet ordered. They will house 16 bits DACs, power supplies and amplifiers. The command will come directly from a BPM module via its serial RS 485 link.

NETWORKING

Topology

A large amount of data has to be transmitted to all BPM modules as they all need the 120 positions to compute the correction. The high sampling rate of the correction, up to 8 kHz, requires a dedicated network.

The processing is distributed on the modules, and each module has eight multigigabit transceivers. A ring topology for this dedicated network is the most convenient.

This architecture is presented in figure 2. The BPMs are grouped in 16 cells (7 or 8 modules per cell). Two modules in each cell are carrying out the interface between their own cell and the others. In each cell, the 7

or 8 modules are linked together in a ring topology (fig 3).

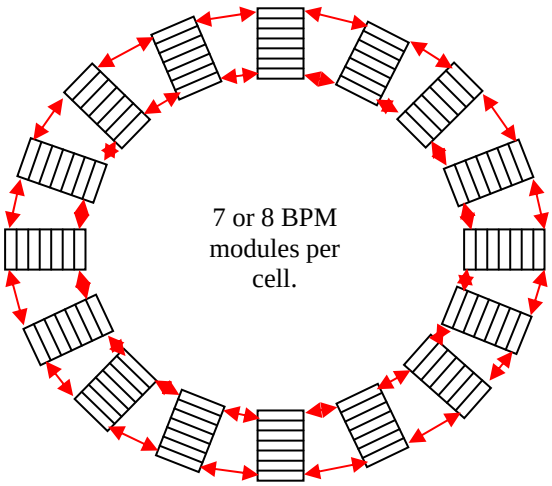

Figure 2: Topology of the dedicated network for the FOFB. Each cell has 7 or 8 BPM modules. The cells are connected with fibre-optic links.

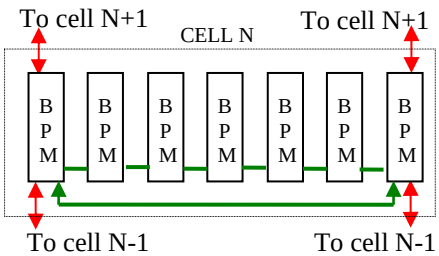

Figure 3: Topology of links in each cell. The BPM modules are connected with copper links.

Data transfer

The data transfer can be decomposed in three steps:

- Recovery of the data from each cell by the two modules carrying out the interface with the others cells. When all the BPM modules of a cell have their position data available, they send it to their two neighbors.
- Those 2 modules transfer data between cells.
- The same 2 modules deliver data coming from the other cells to the modules of their own cell.

Between cells data are transferred over fiber-optic links. Within a cell the data are transferred over copper links. The multigigabit transceivers of the modules allow data transfer up to 2 Gbits/s. That means that data transfer over the network should take around 10 us. This delay will be negligible with respect to the latency of the position processing (few 100 µs).

Modularity

The architecture gives the possibility to easily add or remove modules in a cell. For example, we can later include photon BPMs into the FOFB.

Reliability

The reliability of the system is improved by redundancy. Two modules are interfacing each cell with the others, so even with one failure per cell the system still works. The FOFB system will be down only after two modules of the same cell fail. The Mean Time Between Failure for the whole BPM system is 3 months. This probability is low enough to fulfill our requirements.

Moreover, the correction for each steerer is computed by two different BPM modules. One is chosen to actually apply the correction. A switch will allow to select the other module in case the first one fails.

SIMULATIONS

Two types of simulation can be performed to design and optimize the system: The first one gives us the efficiency of the correction algorithm depending on the number of parameters of the response matrix (number of BPMs and correctors). The number of correctors is fixed by the number of straight sections, but the number of BPMs has to be optimized. In the second one, the behavior of the system loop has to be modeled. Each step or element taking part in the system influences the response because of their delay or bandwidth.

Correction algorithm

The purpose is to determine how many BPMs to include in the FOFB in order to meet stability requirements. The correction algorithm is based on an SVD method. We apply a perturbation on the beam of 10 µm rms, assuming that the value of ground vibration is 1 µm rms and the girder amplification factor is 10. The correction efficiency is compared in two different configurations: 48 and 120 BPMs. For this simulation, we consider that the response of the loop is perfect. The beam displacement is calculated by averaging the result of 100 different machines.

- The first configuration is 48 correctors (2 per straight section) and 48 BPMs (each one is placed just next to a corrector). In this case the system is linear, and the correction for the steerer is calculated with only the position given by its associated BPM. In this case, the beam is perfectly stabilized in straight sections where the requirements are the tightest. This system fits the requirement for the straight sections but not those of the dipoles, where no correction is applied (fig 4).
- In the second configuration, 120 BPMs are used in the algorithm. By including more than 48 BPMs in the FOFB system we will increase the perturbation in the straight sections but gain in efficiency in the dipoles. That's what is shown in fig 5. This configuration suits the beam stability requirements in the dipoles but not anymore for some straight sections (short ones).

The first implementation will be done with 46 correctors (no correctors on the injection section). The number of BPMs and the weight they have in the algorithm will be optimized experimentally in cooperation with the insertion devices users and the dipoles users.

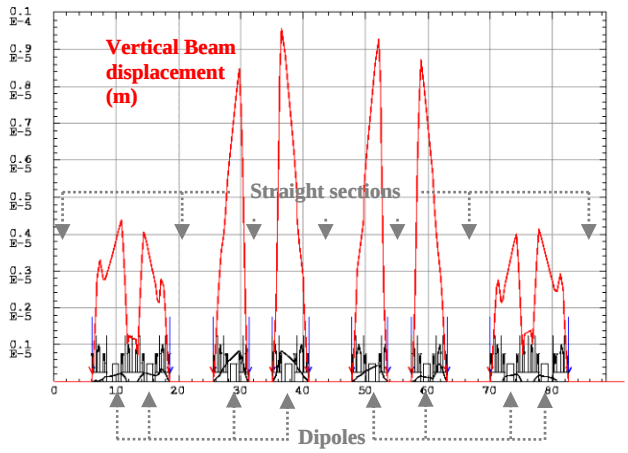

Figure 4: Static simulation of FOFB algorithm with 48 air correctors and 48 BPMs in vertical plane over. 10 µm rms displacement of girders is assumed. Perturbations are perfectly suppressed in straight sections, but the remaining noise in the dipoles does not fit our requirements.

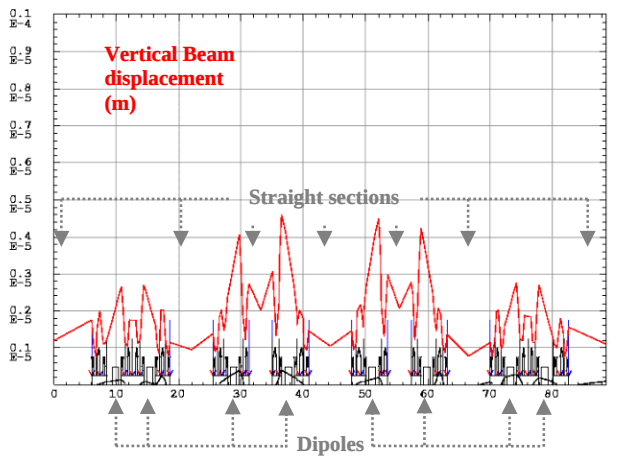

Figure 5: Static simulation of FOFB algorithm with 48 air-correctors and 120 BPMs in vertical plane. 10 µm rms displacement of girders is assumed. Requirements in dipoles are met but not for all straight sections.

Correction loop

The correction loop contains several elements that influence system response. Frequency response of power supplies, vacuum chamber and coils present high enough cut off frequencies to allow corrections to 100 Hz or higher. The correction is computed by a Proportional Integral Derivative (PID) controller. The design of this controller is important in optimizing the efficiency of the loop. The system has been modeled: power-supplies, vacuum chambers and coils are assimilated to low-pass filters (with fc > 1 kHz), and BPMs are assimilated to delays.

The closed loop response shows a damping of the perturbation between 0 and ~100 Hz. But the system also introduces a small amplification of the noise just after this bandwidth. Most of users are very sensitive to beam perturbations at low frequency (<100 Hz).

Nevertheless perturbation above 100 Hz can also be harmful for few experiments. The purpose is to find the best compromise between noise suppression at low frequency and noise amplification at higher frequencies.

The design of the BPM modules and of the dedicated network topology is aimed at minimizing the processing delay. For this simulation, we consider that the efficiency of the algorithm is 100 %.

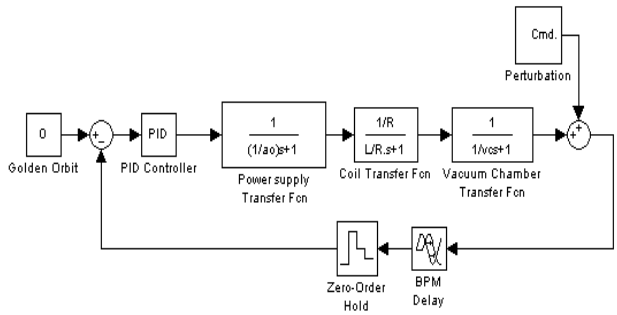

Figure 6: Model of the correction loop.

INTERACTION WITH SOFB

Each feedback system has its own frequency range. In order to avoid any crosstalk between the two systems, one fighting the other [3], and in order to avoid any frequency dead band where none of the systems is efficient, we make them communicate. Based on the ALS system [4], SOFB will update the setpoints of the FOFB system, and will take in charge its DC component.

STATUS

BPMs modules and air correctors are currently under production. Power supplies for the correctors will be ordered soon. The correction loop is under optimization.

ACKNOWLEDGMENTS

We would like to acknowledge E. Plouviez from ESRF for his technical help on simulations.

REFERENCES

[1] A. Kosicek, “Libera Electron Beam Position Processor”, PAC’05, Knoxville, May 2005, to be published.

[2] J.C. Denard, “Preliminary tests of a new kind of BPM system for SOLEIL”, this conference.

[3] C. Schwartz and L. Emery, “Compensating the frequency deadband of the APS real-time and DC transverse orbit correction systems”, Proceedings of PAC 2001, Chicago, p. 1234.

[4] C. Steier et al, “Operational experience integrating slow and fast orbit feedbacks at the ALS”, Proceedings of EPAC 2004, Lucerne, p. 2783.

NEW SINGLE SHOT BEAM POSITION MONITOR OF THE GSI HIGH ENERGY TRANSFER LINE

J.Schölles, W. Kaufmann, GSI, Darmstadt, Germany

ABSTRACT

In the near future, single bunch handling with intensities from 10^7 up to $3{\cdot}10^{12}$ charges/bunch and minimum lengths of 30ns (FWHM) are expected at the GSI high energy transfer line. Thus, the demand of an accurate real-time position monitoring is mandatory. At the moment, a recently developed amplifier optimised for the best common mode amplification covers a dynamic range from nearly -80dBm up to +20dBm and a bandwidth of 200MHz. To gain the required dynamic range of around 130dB, an improvement of the amplifiers will be necessary. The data acquisition shall be done by commercial DSOs which have a sample rate of 2GS/s on each of the four channels for every PU. This DSO based solution is cheap in comparison to the usage of other available sampling units. The data transfer from the DSOs to the operating stuff is foreseen via Ethernet. Amplifier controlling and position calculation happens at the control centre with LabVIEW. First results measured at the GSI synchrotron will be presented.

INTRODUCTION

The purpose of the new single shot BPM electronics is to monitor the position of the injected beam in the high energy beam transfer line (HEBT) and help tuning of machine parameters like the right kicker-timing for fast extraction. Due to the wide dynamic range the development of a complete new PU-electronics was necessary to fulfil the following requirements:

- Dynamic range 10^7 to $3{\cdot}10^{13}$ charges/bunch
- Bandwidth 1MHz-200MHz
- Common mode gain matching better than 0.1dB for each PU-plate pair
- Utilisation of commercially available hardware

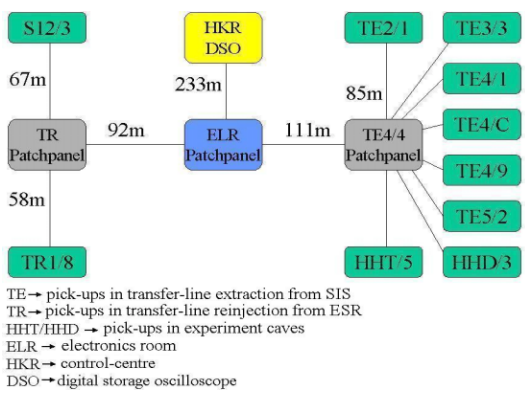

Figure 1: Former setup of the HEBT pick-ups without position measurement capability

A well matched common mode gain for each PU plane is very important for accurate position estimation. Within the scope of the rf-amplifier development it was necessary to find a solution for gain matching. The choosen amplifier concept enables the possibility of digital adjustment of the gain in retracted condition. At the moment there are nine broadband position pick-ups, distributed over the HEBT (and one in the SIS18), installed to supply position information, see Fig.1 for the setup. PUs and infrastructure (rf-signal cables and control-signal-cables) are taken over from a former system that did not fit the needs. The system worked only in a master-mode, an individual parameter based range switching was not possible. Due to the use of electro-mechanical-relays the system did not work reliably for longer times. The next section reports the new system concept and the further development of the remaining hardware. First measurements with a new rf-amplifier will be presented.

SINGLE BPM-SYSTEM

The basic principle (see Fig.2) of the new system is the use of digital storage oscilloscopes for data acquisition instead of conventional A/D-converter-cards. This concept was taken over from the NEWSUBARU-accelerator in Japan [1].

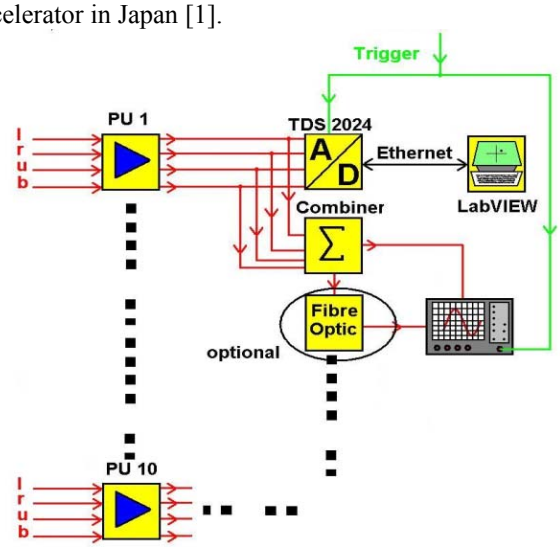

Figure 2: BPM-Overview

This is at the moment a cheap alternative to commercial high speed samplers. The Tektronix TDS 2024 DSO with 2GSa/s, a bandwidth of 200MHz and an 8bit vertical resolution complies the requirements for this project. Since signal magnitudes from µVolts up to several Volts from the given broadband-PU (aperture: 100mm x 50mm)

are expected, a signal conditioning before data acquisition is necessary. The operator at the control room (HKR) sets the gain range depending on the beam intensity. With the help of a clipping detector an overdrive of the amplifier input can be detected. Each of the ten PUs will be equipped with the following electronics (see Fig.3):

- four rf-amplifiers- modules
- combiner-module
- testsignal-generator-module
- digital I/O
- attenuator-control
- fibre-optic links (optional) for the sum-signal
- TDS 2024

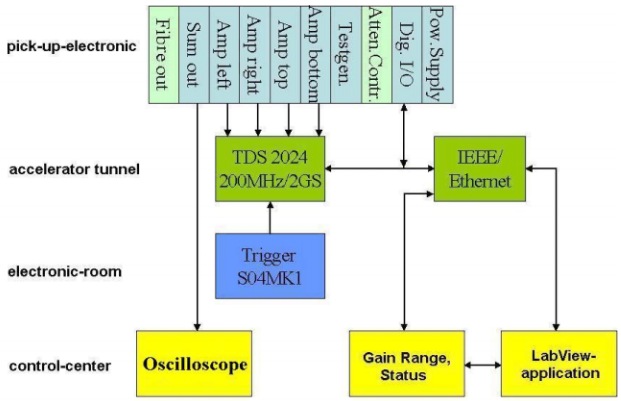

Figure 3: BPM-electronics

Both, control signals and digitized signals will be transferred via Ethernet. A LabVIEW application controls the entire BPM-system and determinates the beam position. A desired feature is to have an additional signal for a qualitative evaluation of the bunch shape in real-time. Hence an analogue sum-signal is available. With the focus on the FAIR project and the expected long signal cable length, it is foreseen in a further step to provide the sum signal via a fibre optical transmission line instead of coax to improve the signal quality.

DYNAMIC RANGE

As mentioned before the data acquisition is based on by DSOs. But with the utilisation of the scope-internal range switching, it also works as an additional amplifier.

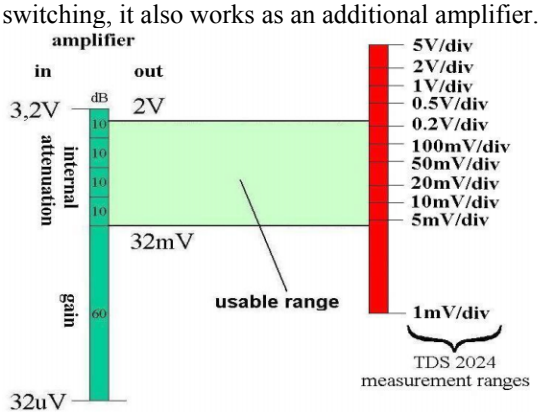

Figure 4: Dynamic range of the BPM-system

Measurements show noise equals -80dBm i.e. a peak voltage of V_P = 32µV. For such low PU-signal levels amplification of 60dB is applied to get the signal in a reasonable mV range of the DSO. This is done by a cascade of the commercial MMIC´s GALI 52 and GALI 4 from minicircuits [2]. The upper limit of the amplifier electronics depends on the design parameters of the used building blocks. In this case, +20dBm i.e. a peak voltage of V_P = 3.2V is the maximum input-level for a linear amplifier work-mode. Hence, an internal accessory attenuator of about 40dB is needed and installed to assure the +20dBm upper limit of the amplifier cascade. Figure 4 shows the usable dynamic range. This means that the PU-signal may vary from 32µV up to 3.2V peak voltage. This equals 32mV up to 2V for the DSO-range. All up a dynamic range of 100dB is reached.

PICK UP SIGNAL AMPLIFIER

Former amplifier installations used several switchable in-line-attenuators to provide miscellaneous gain ranges. A necessary adjustment for a common mode gain matching was exhausting, especially if the matching should be in the range of less than 0.1dB.

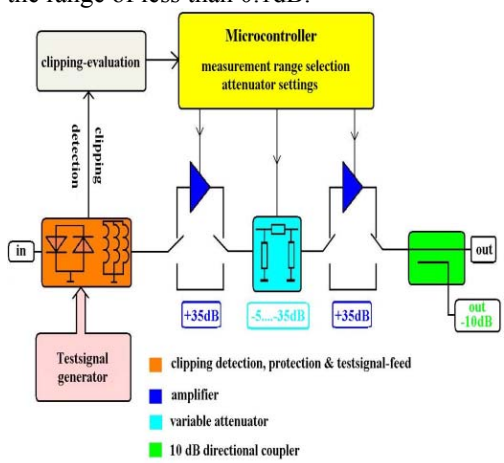

Figure 5: rf-amplifier principle

The now used concept (see Fig.5) works with a stepless 35dB-variable PIN-diode-attenuator between two 35dB-amplifier-stages.

Z_{IN}	50Ω
Z_{OUT}	50Ω
Bandwidth	1MHz-200MHz
gain	> 70dB
min. attenuation	5dB
max. attenuation	40dB
max. input	+20dBm
max. output	+17.5dBm
noise voltage (200MHz)	< 20mV_{RMS}

Table 1: rf-amplifier performance and properties

This assembly enables the individual adjustment of each measurement range. As figure 6 and table 1 shows, more gain than necessary is available. This is the playground

for the gain matching. A PIC controller and a DAC manage the matching in the required range. In combination with a temperature sensor it is also possible to compensate the temperature drift of the PIN-diodes.
Measurements with a network-analyzer demonstrate a only a slight gain versus frequency.

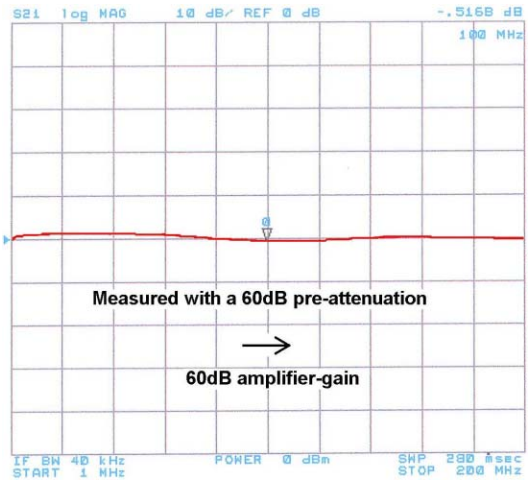

Figure 6: gain versus frequency

The reason is a mismatch between the GALI amplifiers and additional parts like directional coupler, attenuators etc.. Since the nonlinearity is a generally attribute of this amplifier, a calibration process enables the compensation.

MEASUREMENTS

The lower limit of the amplifier resolution is reached with about $1.8 \cdot 10^7$ charges per bunch (see Fig.7). In this case $(S/N)/N \approx 2$ is essential. This means that the worst case of the lower limit with 10^7 charges per bunch is nearly reached.

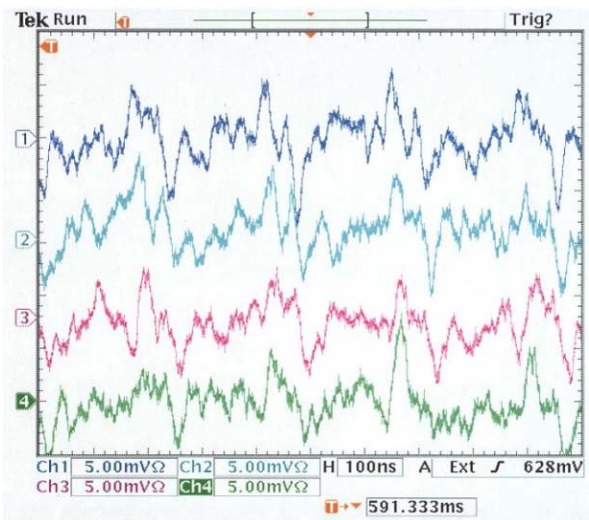

Figure 7: Ar^{+18} 10^6 particle/bunch, 60dB gain

Figure 8 demonstrates bunch signals with $3.4 \cdot 10^8$ charges per bunch. An estimate shows that the amplifier upper limit is reached with about $1.1 \cdot 10^{13}$ charges per bunch.

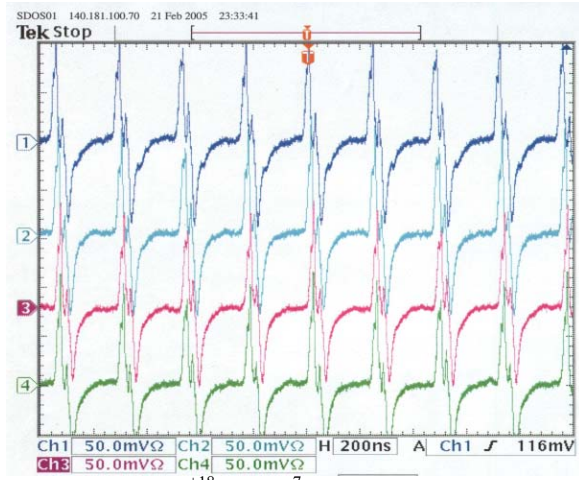

Figure 8: Ar^{+18} $1.9*10^7$ particle/bunch, 60dB gain

CONCLUSION

The rf-electronics achieve nearly the requirements. With a gain greater than 60dB over a bandwidth of 200MHz, a big gain reserve is given. It is also succeeded to provide common mode gain matching for each position plane. An individual gain adjustment is possible to stay in the tolerance range of 0.1dB. This enables by the PIN-diode-attenuator. To get an improvement for the lower limit, an additional low-pass-filtering close to the PU can produce relief. But this is not tested yet. The next necessary step will be testing the interaction between the DSOs, software and electronics. The project will be finished end of 2005 after installation of all components.

REFERENCES

[1]Y.Shoji, A.Ando, S.Hashimoto, "Single pass beam position monitor of NEWSUBARU", Himeji Institute of technology, Proceedings of the 2001 Particle Accelerator Conference, Chicago
[2] minicircuits, GALI broadband amplifier datasheet, http://www.minicircuits.com/dg03-166.pdf

DIRECT MEASUREMENTS OF SPACE-CHARGE-POTENTIAL IN HIGH INTENSITY H⁻ BEAM WITH LASER BASED PHOTO NEUTRALIZATION METHOD

S. Lee[A)], T. Tomisawa[B)], H. Akikawa[B)], Z. Igarashi[A)], S. Sato[B)], T. Toyama[A)], A. Ueno[B)], Y. Kondo[B)], M. Ikegami[A)] and K. Hasegawa[B)]
[A)] KEK, Tsukuba, Ibaraki, 305-0801, Japan
[B)] JAERI, Tokai, Naka, Ibaraki, 319-1195, Japan

Abstract

Laser wire scanner is considered as the most promising method for profile measurements in high intensity H⁻ beams [1]. In order to demonstrate the feasibility of laser wire scanner, a Q-switched Nd:YAG laser (1064nm) diagnostic system has been developed in Japan Proton Accelerator Research Complex (J-PARC) linac [2]. In this paper, first experimental results of laser based beam current profile and space-charge potential measurements in J-PARC medium energy beam transport line (MEBT1) are described.

INTRODUCTION

Wire scanners are presently used to measure transverse beam profile in the J-PARC linac, and observed results agree with calculated rms widths within 20% differences [3]. However, measured beam intensity and pulse width has to be restricted by heat load limitations in the scanner wires. The interaction mechanism between thin wire and H⁻ ions for various beam energies should also be investigated to clarify beam profiles. To avoid these limitations, the photo neutralization method with Nd:YAG laser has been developed as an available candidate for beam intensity profile monitor. Laser stripping technique is also considered as charge exchange procedure for Accelerator-Driven-System (ADS) in J-PARC [4]. An electron of H⁻ beam can be stripped by fast and intense laser beam with non-destructively, and laser system have advantages of maintenance and radiation hardness in high intensity proton accelerators. The photo neutralization method is also expected as an advanced diagnostic technique to measure space-charge-potential in high intensity negative hydrogen ion beams. The kinetic energy of photo detached electron corresponds to the ion velocity and space-charge potential at stripped location.

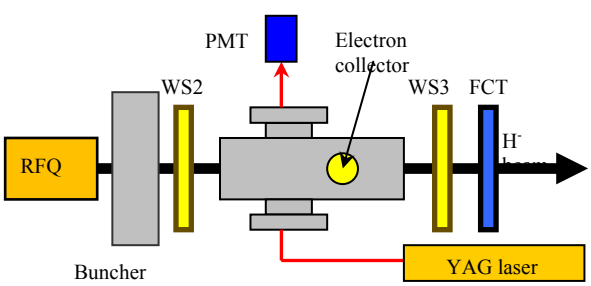

Fig.1: Schematic of laser profile monitor in MEBT1.

EXPERIMENTAL APPARATUS

The 0.5ms long, 30mA pulse beam in the MEBT1 consists of micro bunch of <0.5ns pulse width. The H⁻ ion beam is accelerated by 324MHz radio frequency quadrupole linac (RFQ) up to the beam energy of 3MeV. Laser profile monitor system was installed on MEBT1 transport line and laser light is horizontally injected into the H⁻ beam line and scanned across in the vertical direction (Fig. 1). Commercial Nd:YAG laser can produce pulse width of 20ns long, maximum pulse energy of 500mJ, wavelength of 1064nm at repetition rate of 25Hz. Laser beam size was formed to horizontal width of 6mm and height of 0.8mm at the H⁻ beam line by a pair of 80mm focal length cylindrical lenses. A photomultiplier tube (PMT) observe the laser beam that passing through vacuum chamber after interaction with H⁻ beam, to confirm laser injection timing, pulse width and optical alignment. Stripped electrons were deflected 90degree by a electromagnetic dipole and collected to a Faraday cup.

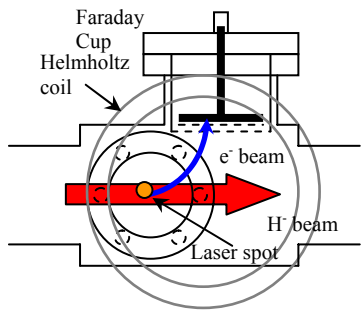

Fig.2: Layout of photo diagnostic box and Faraday cup.

The magnetic field required to deflect 1.63keV electrons is about 50G and its effect on the ion beam is negligible. In order to collect whole stripped electrons diffused by intense space charge, the sufficiently wide area collector plate have been prepared at the nearest location of downstream. The Faraday cup was also designed with electron repeller grid and electrostatic shield mesh (transmission ratio are both 56%, Au coated) in front of the detector. For a high current H⁻ beam, Lorentz stripping and/or residual gas stripping can contribute to a significant amount of activation. It's also being a source of background in laser wire measurement. Although the high energy component of background electron can be neglected owing to the small cross section of

neutralization in the experimental condition of gas pressure of 10^{-6}Pa and magnetic field of 50G, electron cloud like component possibly be a contamination of electron collector. The electron repeller grid can discriminate the background component and also suppress the secondary electron emission from detector plate.

Vertical and horizontal beam profiles at up and downstream of photo interaction chamber are measured by wire scanners, and averaged (30msec) beam pulse signals for each sample positions. The out put signal of WS has been supposed to depend mainly on beam energy, wire diameter and materials. The bias potential have been optimized by measuring the wire signals as a function of bias potential. An expected mechanism of interaction between thin wire and H^- beam is that, as the wire is biased positively, the current component due to the intercepted H^- ion are clearly detected because of a reduction in secondary electron emission. The beam current was also monitored by using a fast current transformer (FCT, ~324MHz) at downstream of laser diagnostic box [5].

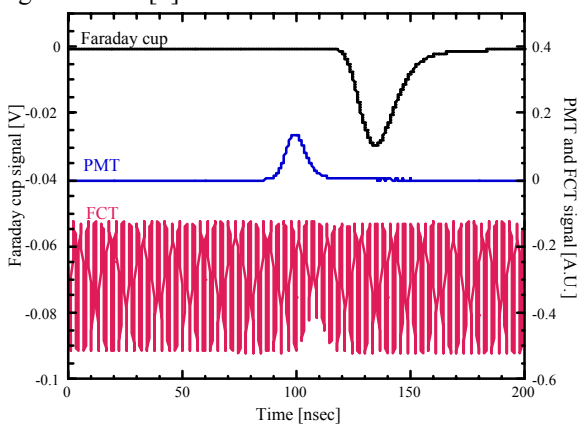

Fig. 3 An example of Faraday cup, PMT and FCT signals during the laser injection timing.

OBSERVATION RESULTS

In Fig. 3, the experimental results are shown as function of time along the beam pulse. Faraday cup signal was passed through 20MHz low pass filter to remove electrostatic 324MHz micro bunch oscillation.

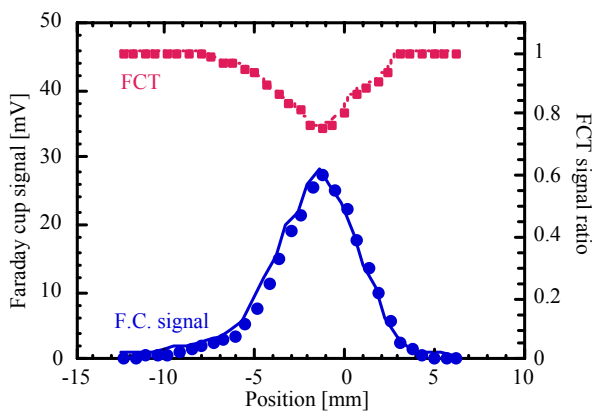

Fig. 4 Faraday cup signal and FCT reduction profile in vertical direction (beam current 15mA). The FCT notch signal corresponds to stripped electron signal.

The signal was clearly observed by averaging 16 pulses, and had about 30nsec delay time from PMT signal due to the difference of cable length and signal transport velocity. The beam current notch was also confirmed in FCT signal at downstream of laser photo neutralization point. The notch depth corresponds to the photo neutralized beam component. For example, about 25% decreasing of 15mA H^- beam equivalent to about 30mV Faraday cup signal by take account of the total 31% transmission efficiency of electron reppeler and shield mesh, 3dB reduction of low pass filter and 50ohm input impedance of oscilloscope. As shown in Fig. 4, the consistent beam current notch level with neutralized electron signal was confirmed.

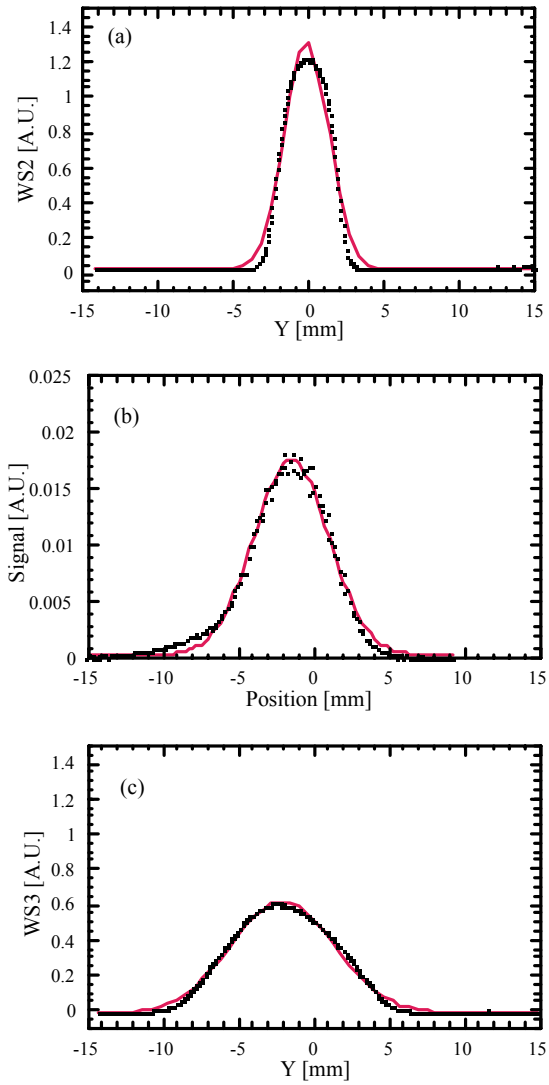

Fig. 5 Vertical beam profiles of (a) upstream at laser injection, (b) laser profile monitor and (c) downstream after photo neutralization for beam current of 20mA. Red thin line shows the Gaussian fitted curve to the measurement.

The radial profile after Abel inversion is also calculated and rms width of the Gaussian fitted vertical profile is σ=2.2mm, the width of the laser beam of 0.8mm intercept

about 25% particles at beam center line. Thus the almost complete photo neutralization fraction for a 130mJ (repetition frequency of 5Hz) 1064nm Nd:YAG laser pulse on a 15mA, 3MeV H^- beam could also be confirmed [6]. Beam profiles measured with laser and carbon wire scanners located in the up and downstream of laser injection port are shown in Fig. 5. The Gaussian fitted curve to the laser and carbon wire data has an rms width of σ_{laser}=2.49±0.02mm, σ_{up}=1.45±0.01mm and σ_{down}=3.45±0.1mm for 20mA beam. The beam divergence and position in vertical direction were consistently observed.

The laser photo neutralization method has a capability of direct measurement of space-charge potential by evaluating the photo detached electrons energy. As shown in Fig. 6, the electron will have the energy of E_0 corresponding to m/M (m, M: electron and ion mass) of H^- beam energy at the stripped point, then the photo detached electron at this point will gain the energy of eϕ at the exit point. Therefore, the space-charge potential is directly measured by scanning the electron reppeler grid potential.

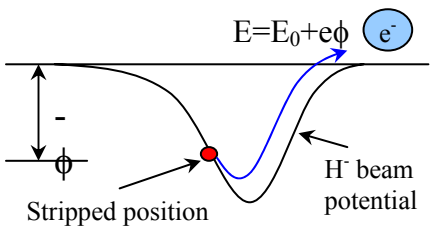

Fig. 6: Principle of space-charge potential measurement.

The bias potential dependence of photo detached electron is shown in Fig. 7. The low energy (<1.63keV) signal component shows that the electron trajectory has finite spread of injection angle into the Faraday cup due to the strong space-charge potential. The main component of electron signals are observed in higher energy region than electron kinetic energy of 1.63keV, and maximum electron energy indicate the space-charge potential at beam center. In the MEBT1 beam line, accelerated particles are confined by micro bunch structure of 324MHz RF potential. The Gaussian profile of 30degree phase width is assumed in longitudinal direction. The maximum space charge potential of about 700V, 500V and 200V are calculated for 20mA, 15mA and 5mA beam respectively by taking into account the experimental results of transverse profiles. Thus, the collected electron will have total energy of 2.3keV, 2.1keV and 1.8keV at the Faraday cup position. The experimental results of bias potential dependence agree with these calculation results.

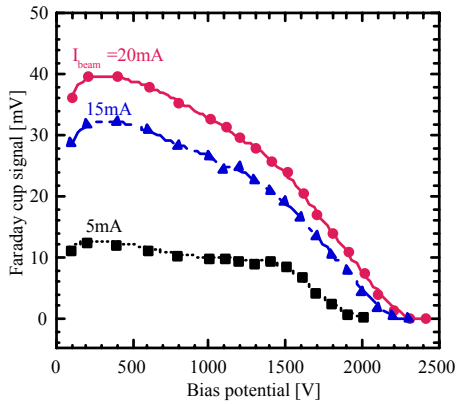

Fig. 7: Faraday cup signals as a function of applied bias potential.

SUMMARY

The Nd:YAG laser based beam profile monitor have been developed to observe the current profile of high intensity H^- beam in the J-PARC MEBT1. It was shown that the photo detached electron signal corresponds to the reduction of H^- beam current. The results of transverse profile measurements also agree with wire scanner signals of up and downstream. The strong space-charge effect is considered as an essential source of emittance blow up for high intensity linac beam. In order to contribute the beam dynamics study, the direct measurement of space-charge potential was also examined. The bias potential dependence is consistent with the calculation results of space-charge potential of micro bunch structure.

REFERENCES

[1] R. E. Shafer, "Laser Diagnostic for High Current H^- beams", Proc. 1998 Beam Instrumentation Workshop (Stanford). A.I.P. Conf. Proceedings, (451), 191.
[2] Y. Yamazaki, eds. *Accelerator Technical Design Report for J-PARC,* KEK Report 2002-13.
[3] H. Akikawa *et. al.,* Proc. of the 1st annual meeting of Particle Accelerator Society of Japan, 6C06.
[4] K. Tsujimoto *et al.,* "Conceptual Study of Transmutation Experimental Facility" JAERI-Tech 2003-085.
[5] S. Lee *et al.,* Proc. of LINAC2004, TUP74.
[6] T. Tomisawa *et al.,* Proc. Of DIPAC2005, POW018.

PRESENT STATUS AND UPGRADE OF BPM SYSTEM IN THE PHOTON FACTORY

T. Obina#, T. Honda, K. Haga, M. Tadano, W. X. Cheng
KEK, 1-1 Oho, Ibaraki 305-0801, Japan

Abstract

In the Photon Factory 2.5 GeV electron storage ring at KEK, the upgrade project of its straight sections is underway. In the project, we improve the beam-position monitors (BPMs) and the global orbit feedback system. New BPMs are designed and installed in the straight sections and the orbit stabilization system is improved. The effect RF phase modulation to the beam position fluctuation is also observed with turn by turn BPM.

INTRODUCTION

The Photon Factory storage ring has been operating since 1982 as a dedicated synchrotron light source. The original beam emittance of 460 nm-rad was reduced twice with the major upgrade of the ring, namely, 130 nm-rad in 1987 and 36 nm-rad in 1997[1]. We started new upgrade project form 2002. Figure 1 shows an outline of the new upgrade project. Goal of this project is to equip new short straight sections and enlarge the existing straight sections[2,3]. The total number of straight section will increase from 7 to 13. The newly installed short straight sections plan to use for short-period and narrow-gap undulators.

In this project, two-thirds of the vacuum ducts those are used over 20 years will be renewed. We also install new quadrupole magnets which is shorter and stronger than the previous one. The replacement will be performed during the shutdown period beginning from Mar/2005.

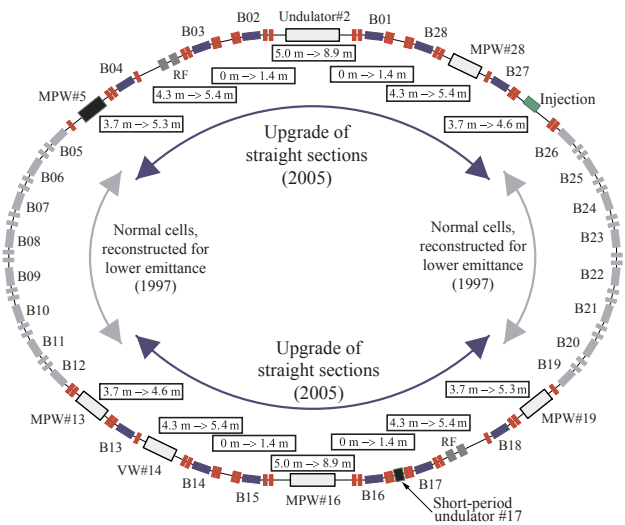

Figure 1: Outline of upgrade project of the straight sections. The arc-sections of the ring (normal cells) remain unchanged.

#takashi.obina@kek.jp

As a part of the project, we improve the beam-position monitors (BPMs), and the global orbit feedback system.

IMPROVEMENT OF BPMS

We install a new arrangement of BPMs electrodes and increase the total number of BPMs. Figure 2 illustrates a cross sectional view of vacuum duct with arrangement of pick-up electrodes. Two different arrangements of the electrodes were used before, a 6-electrode type with BNC feedthroughs (left) and the 4-electrode type with SMA feedthroughs (right upper; type "A"). With the 6-electrode type BPMs, we use two electrodes in upon top and bottom for the detection of vertical position and four electrodes in the side to horizontal detection. With following reasons, we decided to remove 6-electrode type BPMs 1). We have no space to install the 6 electrodes BPMs. 2) 4-electrode type have enough sensitivity for horizontal and vertical. 3) Since we use switching circuit in front of the super-heterodyne detectors [4], we can decrease the readout time if the number of electrode reduced from six to four. We will use four electrodes arrangement for new BPMs.

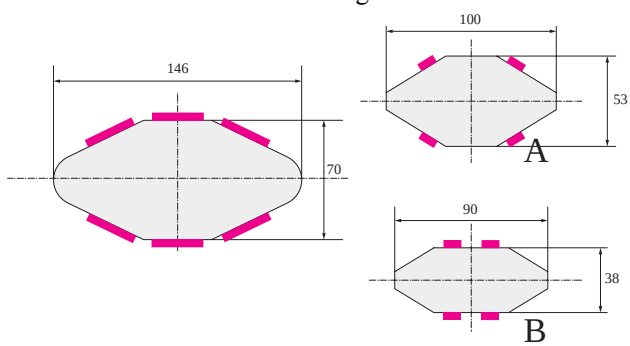

Figure 2: Cross-sectional view of the vacuum duct. The 6-electrode type (left) BPM at the normal cell section was repaced with the 4-electrode type “A” (right, upper) in 1997. We install the new type “B” (right, lower) in the straight section.

We designed a new 4-electrode type BPM as illustrated in Fig.2 (right bottom, type "B") for new vacuum duct of quadrupole magnets. We still have a type "A" in the existing section (from B05 to B12 and B19 to B26). The sensitivity for the vertical direction of type "A" is worse than that for the horizontal direction. The new type "B" has same sensitivity for both planes. We have 77 BPMs in total, and we will use 65 BPMs for the closed orbit measurement. Remaining 12 BPMs are used for feedback of insertion devices and diagnostics, for example, pickup for the bunch-by-bunch feedback system (longitudinal and transverse), turn-by-turn beam oscillation monitor and the phase space monitor.

IMPROVEMENT OF ORBIT FEEDBACK SYSTEM

We currently utilized the vertical global orbit feedback system which consists of DSP and fast-corrector magnets for the users operation [5]. Figure 3 show the block diagram of the system. The signal from electrode is detected by the heterodyne detector, and output voltage of it is sampled by 16-bit ADC and converted into the beam position trough a calculation of DSP. Since the feedback period of the system is 12 ms, we can suppress the vertical orbit fluctuations up to about 8 Hz. With this condition, the system becomes unstable in rarely. For a stable operation, we limit the bandwidth of the system with PID parameters. With previous system, the number of the fast-corrector magnets is 28, and this number is not enough to compensate the drifts of the beam orbit in some place of the ring. We increase the number of fast corrector magnet to 32 in order to perform good orbit stability. Furthermore, we will use of slow corrector previously existing in the ring together with the fast corrector to perform a slow orbit correction for both horizontal and vertical plane. The algorithm for the synchronous operation of fast and slow feedback is carefully designed to avoid the conflicts between two feedback loops. The block diagram of the two feedback scheme is also shown in Fig.3. The feedback period for the workstation-based system is estimated to 10 to 30 second, and this period will be tuned via the beam study.

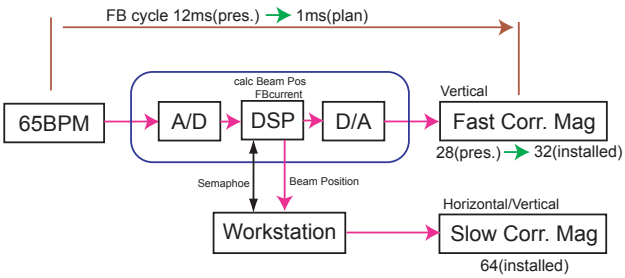

Figure 3: Block diagram of the feedback system.

Since replacing the old controller for switching unit of the 6 electrode BPMs by controller system for 4 electrodes BPMs, total feedback system components can be operated with up to 1 kHz, we plan to increase the feedback cycle. The frequency of coherent synchrotron oscillation in the PF which induced by the longitudinal coupled-bunch instabilities is similar frequency, we mast take care for this influence in this case.

Developments of the fast local feedback system for insertion devices are also in progress. We are evaluating the FPGA-based system that can handle the feedback cycle faster than 1 kHz.

BEAM OSCILLATION OBSERVATION

In order to measure the beam oscillation in variety of frequency range, we installed a beam position monitor named "Digital BPM 2" developed by Instrumentation Technologies Company [6]. We can measure the beam position in turn-by-turn or average of several turns by changing the settings of digital filter. We used the BPM located between B08 and B09. The detected beam position by the system is analyzed in offline.

As a first step, we measured a beam position with the bandwidth of 300 Hz. Figure 4(a) shows a result of power spectral density (PSD) of the horizontal beam position, and 4(b) the vertical, respectively. The numerical integration of the PSD, as shown in Fig. 4(c), represents the corresponding rms beam motion. The range of the integration is from 0 Hz to 300 Hz. In the horizontal plane, oscillation peak around 15 Hz is observed as shown in Fig. 4 (a), and this peak makes a first step in the integrated curvature as shown in Fig.4(c). Previously, we investigated the mechanical vibration of the magnet girder, and we found the source for beam oscillation in 15Hz is mechanical vibration of the girder of the quadrupole magnet [7].

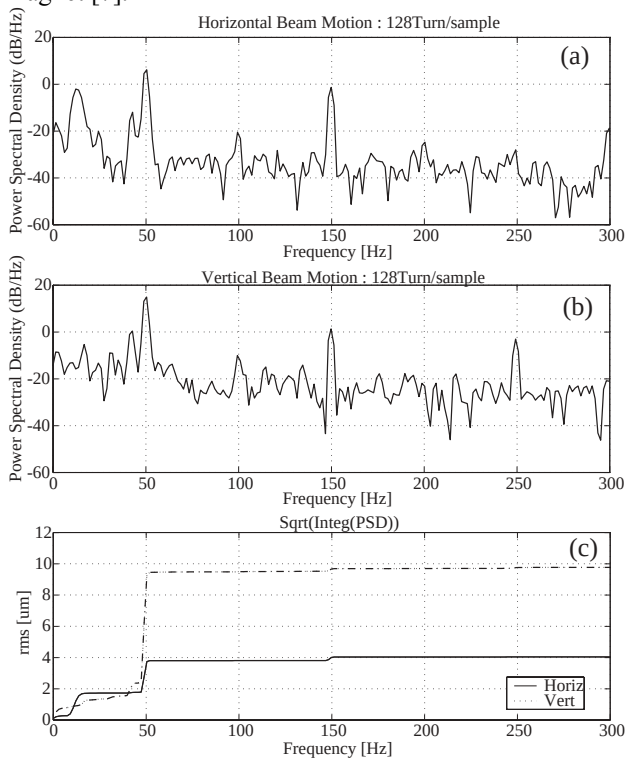

Figure 4: Power spectral density (PSD) of the beam motion in horizontal (a) and vertical (b) direction. The integration from 0 to 300Hz of each PSD is plotted in (c).

The required orbit stabilities from users are at least one-tenth of the beam size. The typical beam size at the bending magnet source is 390μm in the horizontal and 60μm in the vertical. As shown in Fig. 4(c), the fluctuations of beam position below 50 Hz are less than 2μm, and this is small enough for users. As mentioned in the previous section, our global orbit feedback system stabilizes the vertical fluctuation of the beam position. We plan to expand the system to stabilize the horizontal

fluctuation and to extend the bandwidth to suppress the various oscillations up to 100 Hz.

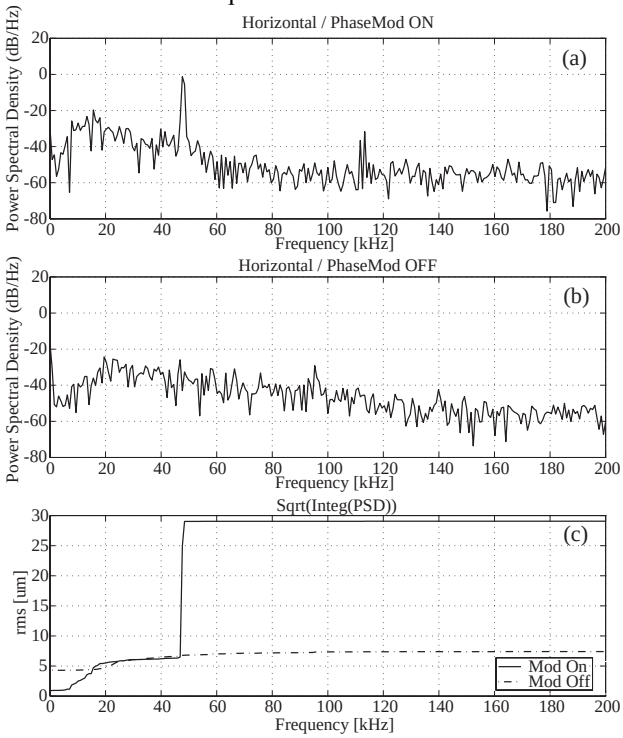

Figure 5: PSD of horizontal beam motion with (a) and without (b) the RF phase modulation. The integration of PSD is plotted in (c).

In the PF, we applied the RF phase moderation with twice of the synchrotron frequency to improve the beam lifetime during the users operation [8]. The phase modulation increases the bunch volume, and in the same time, the increase of bunch volume has an effect to suppress the longitudinal coupled bunch instabilities. We measured the beam motion with turn-by-turn position detection. The revolution frequency of the PF ring is 1.6 MHz and we can analyze the beam motion up to 800 kHz. This measurement is useful to ensure the effectiveness of the RF phase modulation technique. Figures 5 (a) and (b) show the power spectral density of the horizontal beam fluctuations while the RF phase modulation is turned on and off, respectively. The integrations of PSD are shown in Fig. 5(c). The figure shows the results with 200 kHz bandwidth, because there are no significant peaks from 200 kHz to 800 kHz. When the phase modulation is turned on, frequency component at the frequency at twice of synchrotron frequency (48 kHz) is observed in the spectrum. The beam oscillation below 20 kHz is stabilized with the phase modulation as shown in Fig. 5(c).

The effect of the phase modulation to the vertical beam fluctuations are shown in Fig. 6. The rms value of the beam motion without the modulation is about 6 μm and this value is decreased down to less than 2 μm with the phase modulation. In the observation for phase modulation off, the frequency component near by DC is appeared as shown in Fig. 6(b). This component dominates the rms value of the beam motion via integrations of PSD as shown in Fig. 6(c). To investigate this frequency component near by DC in the vertical, we

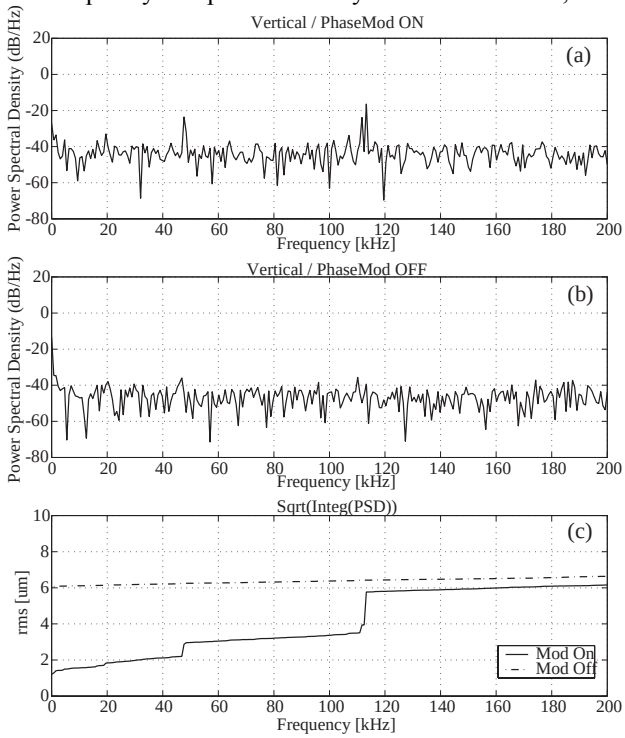

Figure 6: PSD of vertical beam motion with (a) and without (b) the RF phase modulation. The integration of PSD is plotted in (c).

plan to measure the effect of phase modulation on the slow orbit motion below 300 Hz in near future.

SUMMARY

Upgrade project of the KEK-PF is underway. The four electrodes BPMs are installed in straight sections. The total number of BPMs is increased from 65 to 77. The number of fast corrector magnets is increased to inprove the orbit stability. The slow orbit correction based on the workstation will add into the fast global orbit feedback system. We plan a fast local feedback system based on FPGA with the newly installed BPMs. The effect s of the RF phase modulation to the beam position fluctuation was observed in frequency range less than 20 kHz. We plan a further investigation for this effect.

REFERENCES

[1] S. Sakanaka, et al., APAC'01, Beijing, China (2001) 61
[2] T. Honda et al., to be published in Proc. PAC2005, Knoxville, USA (2005)
[3] T. Honda et al., APAC'04, Gyeongju, Korea, (2004)
[4] K. Haga et al., Proc. EPAC'98 (1998)1517
[5] T. Obina et al., Proc. EPAC'98, (1998)1726
[6] www.i-tech.si
[7] K. Haga et al.,Proc. EPAC'00, (2000)2388
[8] S. Sakanaka et al., Phys. Rev. ST Accel. Beams 3, 050701 (2000)

TEST OF NEW DIAGNOSTICS FOR BUNCH LENGTH MEASUREMENT

T. Perron, E. Plouviez, G. Naylor, K. Scheidt, ESRF Grenoble, France

Abstract

Two new diagnostics for bunch length measurements have been recently tested at the ESRF. The first one is based on the spectral analysis of the visible light beam produced by a dipole. The beam is collimated at the input of a photodiode whose output is connected to a spectrum analyzer. The frequency signature is then equivalent to the longitudinal spectrum of the beam. The second device is based on two HF cavities, tuned at two different frequencies, and coupled to the beam wake fields. Their response to the beam passage gives the component of the beam spectrum at the two specified frequencies, from which the beam profile may be reconstructed. Results for these two devices will be presented and compared to measurements made with a streak camera in order to evaluate them. In particular, the reconstruction of the time profile from the information on frequency will be discussed.

INTRODUCTION

For three years, an effort has been made at the ESRF to obtain the bunch length as an operational parameter. For this purpose, a streak camera is already available, and gives precise and reproducible results [1]. However, for reasons of risk of damage to the streak-Tube it is not feasible to operate the streak Camera in an un-manned and permanent mode.

The initial measurement bench is based on the time domain analysis of the visible light produced by a point like source located in a bending magnet [2]. It has shown to be a very practical diagnostic for wide large bunches and is already operational. Nonetheless, due to the reduced bandwidth (5 Ghz) of this device, it is not meant to be operated for short bunches of the order of 15 to 20ps RMS.

We will present the test carried out on two new devices, one also using visible light but processing is done in the frequency domain using a 25Ghz spectrum analyser, enabling measurements at low bunch currents, as well as for large bunches. The other diagnostic is based on two HF cavities measuring the components of the longitudinal beam spectrum at 10 and 16Ghz. Bunch length can then be deduced assuming a Gaussian bunch shape. This device is only relevant for low current per bunch. Both diagnostics obtain information in the frequency domain, and the accuracy of the time domain reconstruction is an important issue, which will be discussed in detail.

SET UP FOR MEASUREMENTS USING THE SPECTRUM ANALYSER.

For this measurement, the visible light beam is focused on the input of a 25Ghz photodiode. The size of the active surface of the diode being rather small (25×25µm), a lens with a short focusing length is used in order to get an image of the source point as small as possible. The output of the photodiode is then directly plugged into a 20Ghz 18dB RF amplifier. The amplified signal is processed by a 25Ghz spectrum analyser. The resulting spectrum is corrected by the impulse response of the measurement chain. The impulse response drawn on figure 2 has been measured using a femto-second laser emitting at 980nm with a repetition rate of 80Mhz.

The schematic set up of the system is basic, care should be taken to avoid cables because of the high frequencies involved. In addition, the use of optical fibber is dangerous because of the chromatic dispersion they induce. It is possible to use them but the light beam should be filtered, resulting in a loss of input power. This was done for the measurements presented in [2], where input power was not an issue, but this is not the case for the spectrum method. The focusing of the visible light beam had to be done directly on the photodiode, without the help of optical fibbers, making the focusing of the image on the optical sensor even more delicate. The set up is pictured on figure 1.

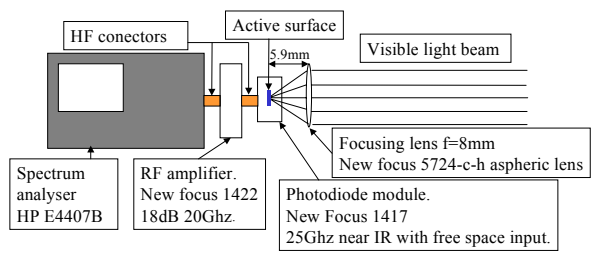

Figure 1: Experimental set up and component references.

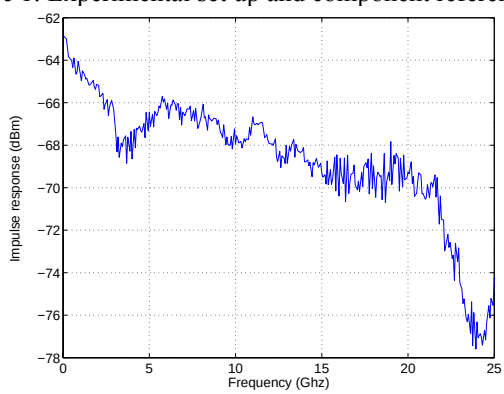

Figure 2: Spectrum of the impulse response of the measurement chain.

If the bunch has a Gaussian longitudinal profile with a standard deviation σ_t, the envelope of the spectrum also is a Gaussian with $\sigma_\omega=1/\sigma_t$. To obtain the bunch length, a Gaussian fit of the spectrum envelope is performed, giving σ_ω. A simple inversion then gives the RMS bunch length σ_t.

This analysis is made assuming a perfect Gaussian shape for the bunch, which is true for an electron bunch at

zero current. It is however well known that, under the influence of longitudinal impedance, the shape of the bunch is distorted and for high current bunches, the Gaussian approximation is no longer acceptable. An estimation of the induced error has been performed.
Concerning the sensitivity of the set up, in order to obtain a signal to noise ratio of 10 at zero frequency (where the signal is maximum), 20mA should be injected in the machine. It is estimated that above 30 mA the sensitivity is good enough. Thus, the device can cover all operational filling patterns at the ESRF as the current is always in-between 40 (4 bunch mode) and 200mA (uniform).

GAUSSIAN APROXIMATION.

Evaluating the error done by considering a Gaussian bunch is of importance. Indeed, both diagnostics give an amplitude spectrum in the frequency domain, but the phase information is missing. The inversion is made considering a zero phase for the entire spectrum, which is true for a symmetric bunch, but false as soon as the bunch distorts in a non-symmetric manner. A non-symmetric distortion is the signature of resistive longitudinal impedance.

The error has been evaluated by comparing results of streak camera profiles processed in two different ways. First a usual FWHM is derived and divided by 2.37 in order to get an equivalent RMS bunch length.

The second bunch length estimation is obtained by doing a Gaussian fit of the Fourier transform of a streak camera profile. Comparing both methods will give the error induced by the Gaussian assumption. On figure 3, It becomes obvious that the error induced by considering a Gaussian shape in frequency is significant even for quiet low current per bunches. The two curves converge, as expected, at zero current, but already at 1mA/bunch, we get an error of more than 10%.

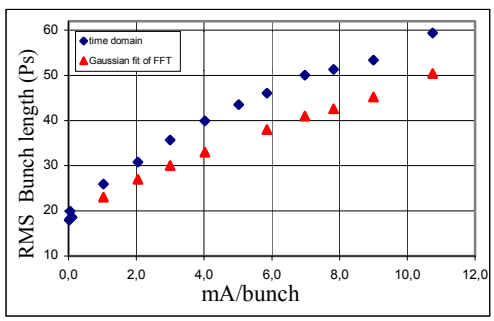

Figure 3: RMS bunch length derived by streak camera time profile (blue squares) and Gaussian fit of the FFT of the same profile (red triangles).

RESULTS USING THE SPECTUM ANALYZER

Zero current measurements

At zero current, the equilibrium bunch profile is a Gaussian, whose width can be calculated. It is the result of the equilibrium between the focussing RF field and the spread in energy induced by the quantum fluctuation of photon emission. All measurements where done with an RF voltage of 8MV leading to a theoretical bunch length of 16ps RMS. As the Gaussian approximation holds in this case, it is possible to compare results for the two new devices with streak camera results in the time domain. Measurements were done at low current (10 to 40mA) uniformly distributed in the 992 RF buckets of the ESRF.

Streak camera gives an RMS bunch length of 18.7±1ps. The Gaussian fit of the frequency spectrum leads to 16.3±3ps for the RMS width of the bunch, corresponding exactly with the theory. The comparison with streak camera measurements shows a relatively good agreement as both values are only separated by 2.4ps. This comparison validates the viability of the new diagnostic for the low current measurements. Nevertheless, the agreement is not perfect. Figure 3 shows the comparison between the recorded spectrum and the FFT of a streak camera profile. There is obviously divergent behaviour of the two diagnostics at low frequency (f<8Ghz).

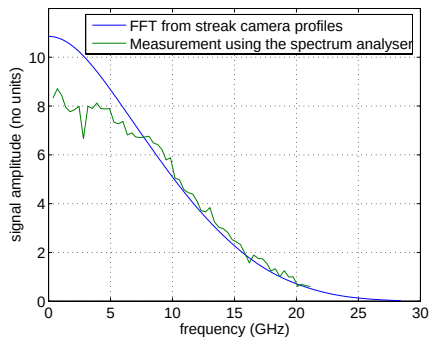

Figure 4: Comparison of the FFT of a streak camera profile (blue) and the recorded spectrum (green). Both measurements are made for I_{bunch}<0.04mA.

High current per bunch

As already stated, at high current, the reconstruction of the time profile from the spectral measurement is no longer possible, because the information about the phase of the Fourier components is missing. In order to evaluate the quality of the new diagnostic, the FWHM of the recorded spectrum will be compared with the FWHM of the FFT of streak camera profiles. Figure 5 shows this comparison for different currents per bunch.

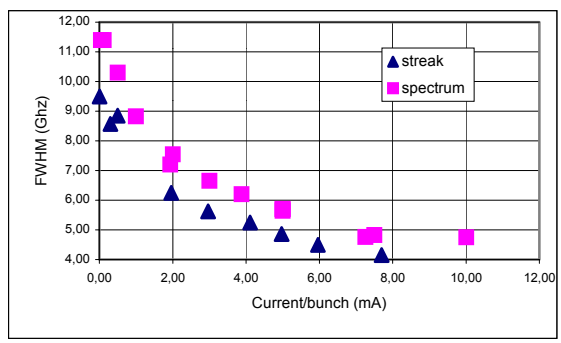

Figure 5: FWHM of frequency spectrums based on streak camera measurements (blue triangle) compared to the measurement using the spectrum analyser (pink squares).

Both curves show the same evolution with current, which is again an encouraging result, but there is a general discrepancy of about 20% between the two curves. Compared to the streak camera spectrums, we already saw that at low frequency, the spectrum tends to underestimate the signal, leading to a smaller maximum and a larger FWHM. As shown on figure 6, it is also valid for large current per bunches. No clear explanation could be found for this behaviour at low frequency, it may be due to an overestimation of the impulse response of the system at these frequencies, which would lead to an underestimation of the signal.

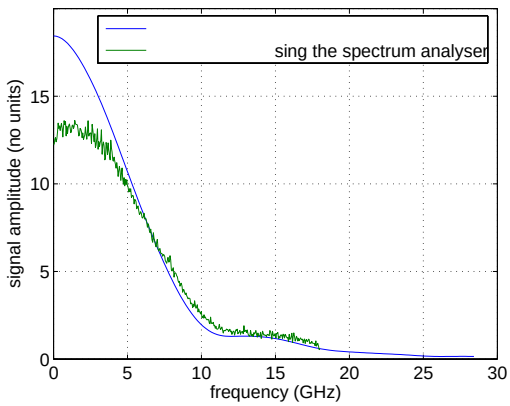

Figure 6: Same as figure 4 but for I_{bunch}=3mA.

MEASUREMENT USING MICROWAVE CAVITY PICKUPS

When the current per bunch is low enough, we can assume that the bunch current pulse shape is Gaussian. In this regime, it is possible to derive the bunch length from the measurement of only two points of the current spectrum, providing the frequencies of these points are far enough from each other to allow an accurate fit of the Gaussian shape of the spectrum. The measurement of a third point in the spectrum will help to assess if the bunch shape is Gaussian or not. Such a measurement was easy to implement for us since we have installed in 2001 on the ESRF storage ring two sets of narrow bandwidth microwave cavities, loosely coupled to the beam; these cavities are used as the pick ups of a general purpose diagnostics for the study of single bunch phenomena [3]. Their central frequencies are equal to 29 x f_{RF} =10.213GHz and 46 X f_{RF} =16.2GHz, with f_{RF} = 352.2MHz, the frequency of our RF system. Their bandwidth is 100MHz. These cavities are equipped with RF front ends implemented in the storage ring tunnel, which down convert the signals excited by the beam from 29Xf_{RF} and 46Xf_{RF} down to an intermediate frequency equal to f_{RF}. The amplitude of these intermediate frequency signals is proportional to the beam spectrum level at 10.213GHz and 16.2GHz and can be detected with any narrow bandwidth detector (RF spectrum analyser or dedicated electronics). The third frequency in the spectrum is 0Hz, given by the average current value. Compared to the full spectrum measurement of the photo diode signal, the measurement of the ratio of the amplitudes of the two cavities signals versus the RF current is much faster; it takes less than one second when a full 0 to 18GHz spectrum measurement takes several minutes. The accuracy of the beam signal detection is also better: because the cavities have a bandwidth of only 100 MHz, the ratio of the peak value versus the average value of the cavity signals is moderate resulting in a high signal to noise ratio. In parallel with the measurement of the photo diode spectrum, we have measured the variation of amplitudes of the signals of the 10GHz and 16 GHz cavities for various values of the current per bunch. Since the sensitivity of the detection of the cavity signals is not precisely known, we have first calibrated the gain of the amplitude detection of the 10 GHz and 16GHz signals using a streak camera measurement of the bunch length as a reference; we did this calibration with 1mA per bunch. Then using this reference measurement we have derived the value of the bunch length down to .1mA per bunch. The σ value that we derived at .1mA per bunch was 17ps when the value predicted by the theory is 16ps. So this method could also allow an easy and accurate monitoring of the bunch length at low current per bunch without requiring the permanent use of a microwave spectrum analyser.

CONCLUSION

Two new diagnostics for bunch length measurements have been tested by comparing them to streak camera results. In the low current per bunch regime, both devices show promising results as the theoretical value for zero current bunch length could be reproduced. In this regime, the microwave cavity offers a faster acquisition time.

Unfortunately, for high current bunches, time reconstruction is no longer possible for both devices, because the Gaussian approximation is no longer valid. The spectrum method accurately describes, the evolution of the longitudinal spectrum with current, but absolute values differ by about 20% from the streak camera measurements.

Nevertheless, it's simplicity, as far as both hardware and software is concerned, make it a good candidate to be routinely operated. A simple calibration using streak camera results would be sufficient to derive time domain values for high current bunches.

REFERENCES

[1]K.Scheidt, 'Dual Sweep Streak Camera at the ESRF', EPAC-96, Barcelona, Spain, June 1996.

[2]G.Naylor, 'Fast DSP Using FPGAs and DSOs for Machine Diagnostics', DIPAC 2003, Mainz, Germany, May 2003.

[3]E. Plouviez, 'Microwave Pickups for the Observation of Multi GHz Signals' Induced by the ESRF Storage Ring Electron Bunches, DIPAC 2001, Grenoble, France, June 2001.

DETAILED RESOLUTION STUDIES OF THE SYNCHROTRON RADIATION PROFILE MONITOR FOR THE HERA ELECTRON BEAM

G. Kube, R. Fischer, Ch. Wiebers, K. Wittenburg, DESY, Hamburg, Germany

Abstract

For the measurement of the electron beam emittance at the proton–electron storage ring HERA (DESY) a monitor is used which is based on the direct imaging of visible synchrotron radiation from a bending magnet. In order to reduce the thermal heating of the light extracting beryllium mirror it is vertically offset. While the resolution of profile measurements by synchrotron radiation is already strictly limited by fundamental effects, the observation in this off-axis geometry modifies the measured vertical angular intensity distribution leading to an increased contribution of the diffraction limited resolution. In order to describe the resolution broadening effects calculations based on near field computation of synchrotron radiation have been performed with the code SRW [1]. The resulting wavefronts have been propagated through the optical elements of the monitor. Taking into account the calculated resolution broadening corrections the deduced beam emittances are in good agreement with the expected design values.

INTRODUCTION

The precise determination of the beam emittance is essential for the understanding of luminosity in colliding beam experiments as the ones at HERA. While the emittance itself is not a directly accessible quantity, the beam width is usually measured from which the emittance can be calculated based on knowledge of beam optic parameters. For the measurement of the electron beam size at HERA a profile monitor is used which utilizes the visible part of synchrotron radiation (SR) from a bending magnet to form an image of the beam. The image resolution of this kind of monitor is affected by inherent effects like diffraction and depth of field.

In the vertical direction the resolution broadening is additionally increased due to off–axis observation, i.e. if a part of the radiation used for image formation is shielded. This is the case for the HERA monitor in order to reduce thermal heating of the light extracting mirror due to absorption of hard X–ray radiation which would result in an image deformation. However, by careful calculations of these resolution broadening contributions, the real beam size can still be derived.

The development of a model to describe these effects has turned out to be nontrivial. Attempts range from rules of thumb to quite elaborate models, see Refs. [2, 3, 4] and the references therein. In these works diffraction and depth of field are treated as independent processes and their broadening contributions are added together quadratically. A more accurate approach is to calculate a Fraunhofer diffraction pattern that includes both the effects of diffraction and depth of field. This accounts for the fact that synchrotron radiation is not actually a spherical wave because of depth of field.

PROFILE MONITOR SETUP

In luminosity operation the HERA electron beam energy is E = 27.6 GeV. According to the beam optical design parameters, in this mode the beam should have a horizontal (1σ) size of σ_x = 1175 μm and a vertical size of σ_y = 260 μm. The task of the optical system is to provide an image of the beam onto the chip of the CCD camera.

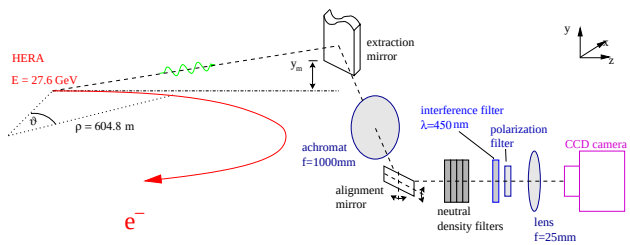

Figure 1: Schematic picture of the profile monitor setup.

In Fig. 1 a sketch of the monitor setup is shown. The emitted SR radiation is extracted out of the vacuum system by a mirror (thickness 4 mm, width 15 mm) which is located 6.2 m away from the central part of the bending magnet. The mirror surface has an inclination angle of 45° with respect to the xy plane, hence the light is reflected out perpendicular to the beam axis. An achromatic lens with focal length f = 1000 mm, located about 6.5 m away from the source point, forms an image at a distance of 1.2 m. The resulting real intermediate image is then magnified by a second lens (f = 25 mm) onto the chip of the CCD camera (*JAI CV–M300E* with 768 × 494 pixels of size 11.6 × 13.5 μm^2). The total magnification factor of the optical system is V = 0.55. The video output of the camera is fed to a commercially available 8 bit PCI framegrabber board (*Data Translation DT3155*) for digitalization and finally analyzed by a standard personal computer.

In order to minimize chromatic errors and to improve the diffraction limited resolution an interference filter (central wavelength 450 nm, FWHM 10 nm) is used together with a polarization filter. The neutral density filters serve to adjust the incoming light intensity to avoid saturation of the camera chip. The alignment mirror which is rotateable about the x and y axis allows to adjust the image onto the center of the CCD.

The light extracting mirror is made of beryllium which has a high thermal conductivity together with a low absorption coefficient for hard X–rays. Additionally, the mirror is cooled by water. However, these precautions are not sufficient to reduce thermal heating down to a level that no mirror surface distortion occurs. Therefore, the extracting mirror bottom edge is placed y_m = 2 mm above the beam axis. In this geometry the X–ray part of SR which is emitted close to the beam axis will not affect the mirror, while the optical SR components which are emitted under larger angles are reflected out of the vacuum system.

RESOLUTION STUDIES

In order to describe the resolution broadening effects in both planes calculations have been performed with the computer code SRW [1]. With this code, the initial SR electric field is computed in the frequency domain using a high–accuracy near–field method. The method is based on the Fourier transform of the retarded potentials which are used to derive an expression for the electric field [5] and it is exact in the sense that the velocity field term is not neglected as it is in the case for calculations based on the Fourier transform of the Liénard–Wiechert fields. The computation preserves all the phase terms that are necessary for further propagation of the radiation through optical components. SR propagation is implemented in the frame of scalar diffraction theory applying the methods of Fourier optics.

For the calculation of the resolution broadening contributions the HERA SR monitor was modelled in a simple way: the influence of the extraction mirror in both planes was described by a rectangular aperture with the corresponding mirror dimensions. For the case of off–axis observation the aperture was shifted in the vertical direction in such a way that the lower aperture boundary corresponded to the lower mirror edge. Finally the beam profile image was calculated at the position of the real intermediate image after propagation through the achromat which was described in thin lens approximation.

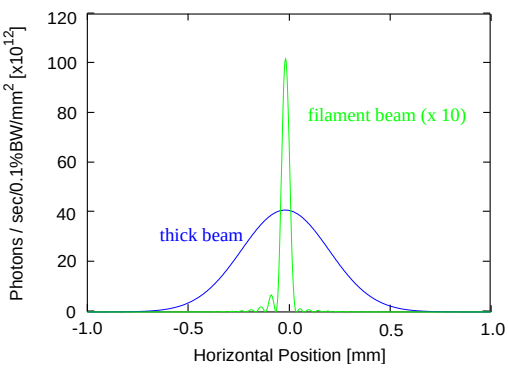

Figure 2: Calculated image of the horizontal beam profile at the position of the intermediate real image for a filament beam with zero emittance and a beam with the HERA design horizontal emittance.

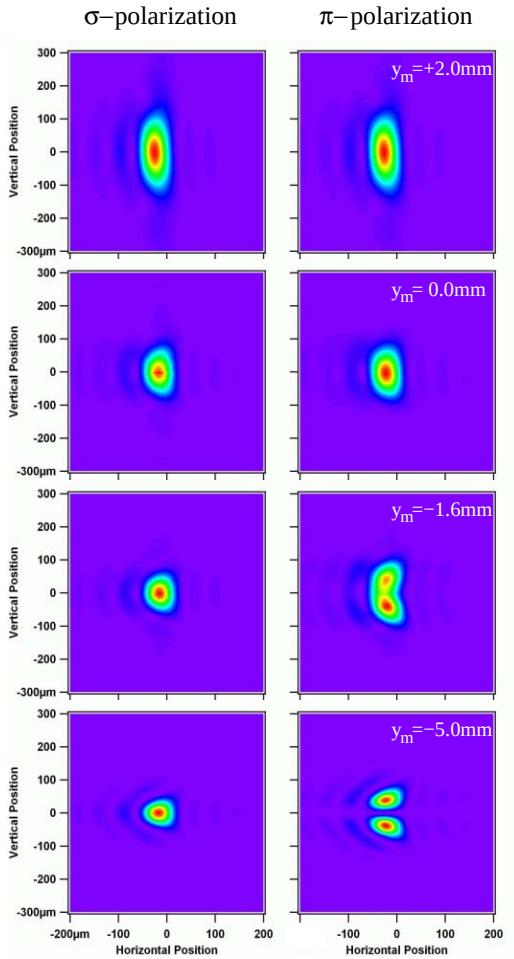

Figure 3: Calculated image of the filament beam profile for both polarization states. Parameter is the light extracting mirror bottom edge y_m.

In Fig. 2 images of the horizontal beam profiles behind the achromatic lens are shown for the case of a filament beam (i.e. with zero beam emittance) and a thick beam with the HERA design emittance. The asymmetry in the filament beam image accounts for the fact that SR is not actually a spherical wave due to the influence of depth of field. The resulting resolution broadening contribution was calculated in a similar way as described in Ref. [4]: assuming an ideal imaging without resolution broadening the thick beam profile was transformed back to the source plane using the geometrical magnification of the optical system, then fitted with a normal distribution, and finally the theoretical horizontal beam size used as input for the calculations was subtracted quadratically, resulting in an "effective" broadening contribution $\sigma_{x,rb}$ = 203 μm. This value is slightly smaller than the one of 333 μm as calculated on the basis of the model described in Ref. [4], and much smaller than predictions based on standard formulas used as rule–of–thumb as pointed out in this reference.

In Fig. 3 calculated imaged filament beam profiles are

plotted for both polarization states as function of the position of the light extracting mirror bottom edge y_m. y_m = -5 mm corresponds formally to the case of on–axis observation, i.e. for smaller mirror positions no appreciable change in the vertical beam shape is observable. y_m = +2 mm corresponds to the standard operation mode of the monitor and is a compromise between a reasonable value for heat load and sufficient vertical resolution. According to Fig. 3 for on–axis observation the distribution of the σ polarization component has a narrow shape while the one of the π component has a minimum on–axis. If the mirror is moved upward, the vertical width of the σ polarization component is continuously broadened. With increasing y_m the on–axis minimum of the π component is smeared out and the shape of both polarization component distributions becomes more and more similar. Applying the procedure to calculate the "effective" broadening contribution results in a value of about $\sigma_{y,rb} \approx 370$ μm for both polarization states. Again this value is smaller than the predictions based on the model of Ref. [4] with $\sigma^{\sigma}_{y,rb}$ = 490 μm resp. $\sigma^{\pi}_{y,rb}$ = 430 μm.

Experiment Fig. 4 shows a monitor screen shot. The measured beam spot is fitted with a two–dimensional normal distribution and based on the theoretical electron beam optics the emittances are evaluated.

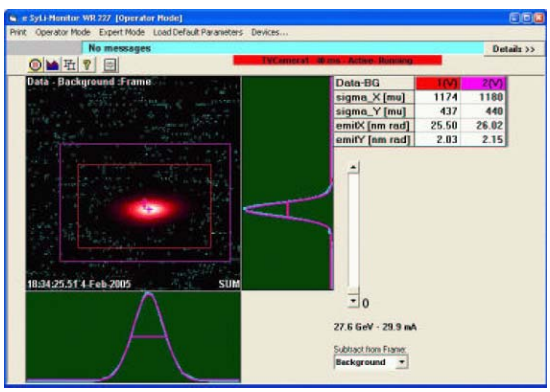

Figure 4: Screen shot of the HERA synchrotron radiation emittance monitor.

For the horizontal plane the deduced beam emittance agrees well with the theoretical design emittance and values expected from measured luminosities. In the vertical plane the monitor beam emittance is smaller than expected. Fig. 5 shows measured vertical beam sizes as function of y_m together with calculated ones, including all resolution broadening effects. From this it is to conclude that the general behavior of the broadening due to off–axis observation is reasonably described. However, the absolute measured beam sizes for both polarization states are about 10% smaller than expected from the design beam emittance and luminosity measurements. The reason for this is still under investigation and may have its origin in the monitor calibration or in a discrepancy with the particle beam design optics. Another discrepancy is the sudden increase in the

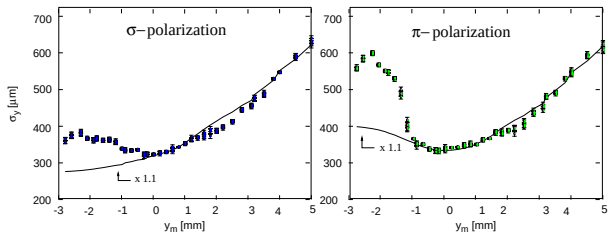

Figure 5: Comparison of measured vertical beam sizes as function of y_m together with calculations based on near field computation of SR and their subsequent propagation through optical elements. The calculated beam sizes are about 10% larger than the measured ones.

measured beam sizes for mirror positions $y_m \leq$ -0.5 mm. The cause may be background light reflection inside the beam pipe but this is also still under investigation.

SUMMARY

The present article summarizes resolution studies for a beam profile monitor system using visible SR radiation from a bending magnet at the HERA electron storage ring. These studies are an extension to the one presented in an earlier publication [4]. Special attention is drawn to the influence of off–axis observation which smears out the vertical resolution additionally. While the measured horizontal beam emittance agrees well with the design values and independent measurements, up to now the measured vertical beam sizes are about 10% smaller than expected. In the meantime the monitor is established for online emittance monitoring and serves as a versatile tool for the study of dynamical beta beating. An example for such a measurement is shown below.

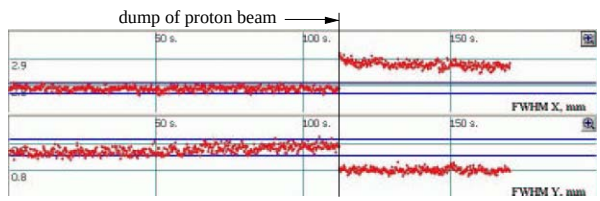

Figure 6: Screen shot of the HERA emittance monitor: temporal evolution of the electron beam size as the proton beam is dumped under collision.

REFERENCES

[1] O. Chubar and P. Elleaume, Proceedings of the EPAC98, Stockholm, Sweden (1998) p.1177–1179

[2] A. Hofmann and F. Méot, Nucl. Instr. Meth. **203** (1982) 483

[3] Å. Andersson and Juri Tagger, Nucl. Instr. Meth. **A 364** (1995) 4

[4] G. Kube, R. Fischer, K. Wittenburg, in Proceedings of BIW2004, AIP Conf. Proc. 732 (2004), p.350–357

[5] O. Chubar, Rev. Sci. Instrum. **66** (1995) 1872

WIRE SCANNERS IN THE UNDULATOR SECTION OF THE VUV-FEL AT DESY

P. Castro, H.-J. Grabosch, U. Hahn, M. Sachwitz, and H. Thom
Deutsches Elektronen-Synchrotron DESY, Hamburg and Zeuthen, Germany

Abstract

The design and implementation of wire scanners for the Vacuum Ultraviolet - Free Electron Laser (VUV - FEL) facility at DESY [1] is presented. In the undulator section of the VUV FEL a set of seven wire scanner stations determine the relative position of the electron beam within few μm and the absolute position related to the undulator axis with a precision better than 50 μm. First results of beam trajectory and beam size measurements along the undulator section are shown.

INTRODUCTION

Wire scanners have been in use for many years in accelerator facilities in order to measure the profile and the position of particle beams [2-4]. The basic working principle of wire scanners is shown in figure 1. A fork equipped with thin wires (10 – 50 μm) passes the electron beam. The beam interaction with the wires produces high energetic radiation which is detected by scintillation counters. Simultaneously monitoring of the wire position allows the measurement of beam profile, and position. Constant wire velocities of up to 1 m/sec (fast scan mode) are needed to scan powerful particle beams.

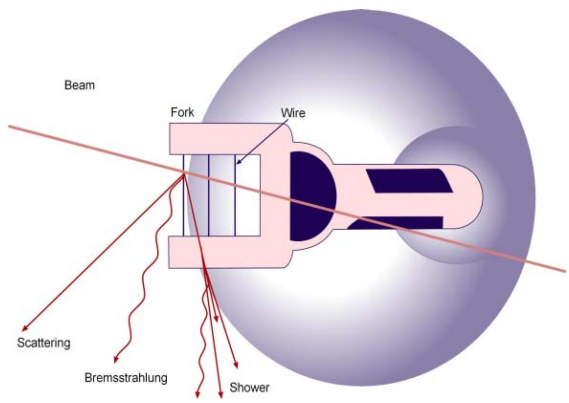

Figure 1: Working principle of the wire scanner. Secondary particles are created when the wire passes through the electron beam.

The VUV FEL at DESY [5] is a 30 m long permanent magnet undulator structure with seven integrated wire scanner stations. The system is part of a test linac operated in superconducting technology. The FEL light (down to a wave length of a few nm) is created by **S**elf **A**mplified **S**pontaneous **E**mission (SASE). The SASE effect takes place when the electron and photon beam overlap better than 50 μm over the whole undulator length. Critical alignment parameters for this interaction are:

- Alignment (< 50 μm) of the electron beam trajectory to the magnetic center of the undulator.
- Electron beam parameters as beam position and beam emittance.

To measure these alignment parameters in the undulator section of the VUV FEL special wire scanners were developed [6].

TECHNICAL LAY OUT OF THE WIRE SCANNER

The essential features of the wire scanner are the stroke of 48 mm combined with high position accuracy (few μm) over a working range of 30 mm. A scanning speed of 1 m/sec has to be realized to avoid destruction of the wire in multi bunch mode operation. In this case the electron beam with up to 7200 bunches within 800 μsec (at 10Hz) will heat up slowly passing wires and destroy them. Three thin wires (10 μm carbon, 10 μm and 50 μm tungsten) are clamped between the two teeth of a ceramic fork with a spacing of 10 mm. The linear movement of the fork is based on a slot winding cylinder transforming the rotation of a stepping motor into a linear motion. The cam of the slot winding cylinder uses the transfer function of a Bestehorn-sinuide. The interaction between the wire and the electron beam takes place in the linear speed range of the transfer function. The position of the wires is measured on axis with an incremental length gauge with a resolution of 0.1 μm.

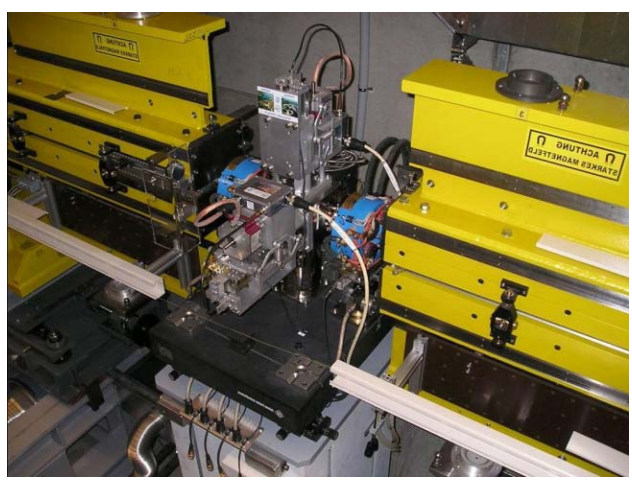

Figure 2: A wire scanner station between two undulators.

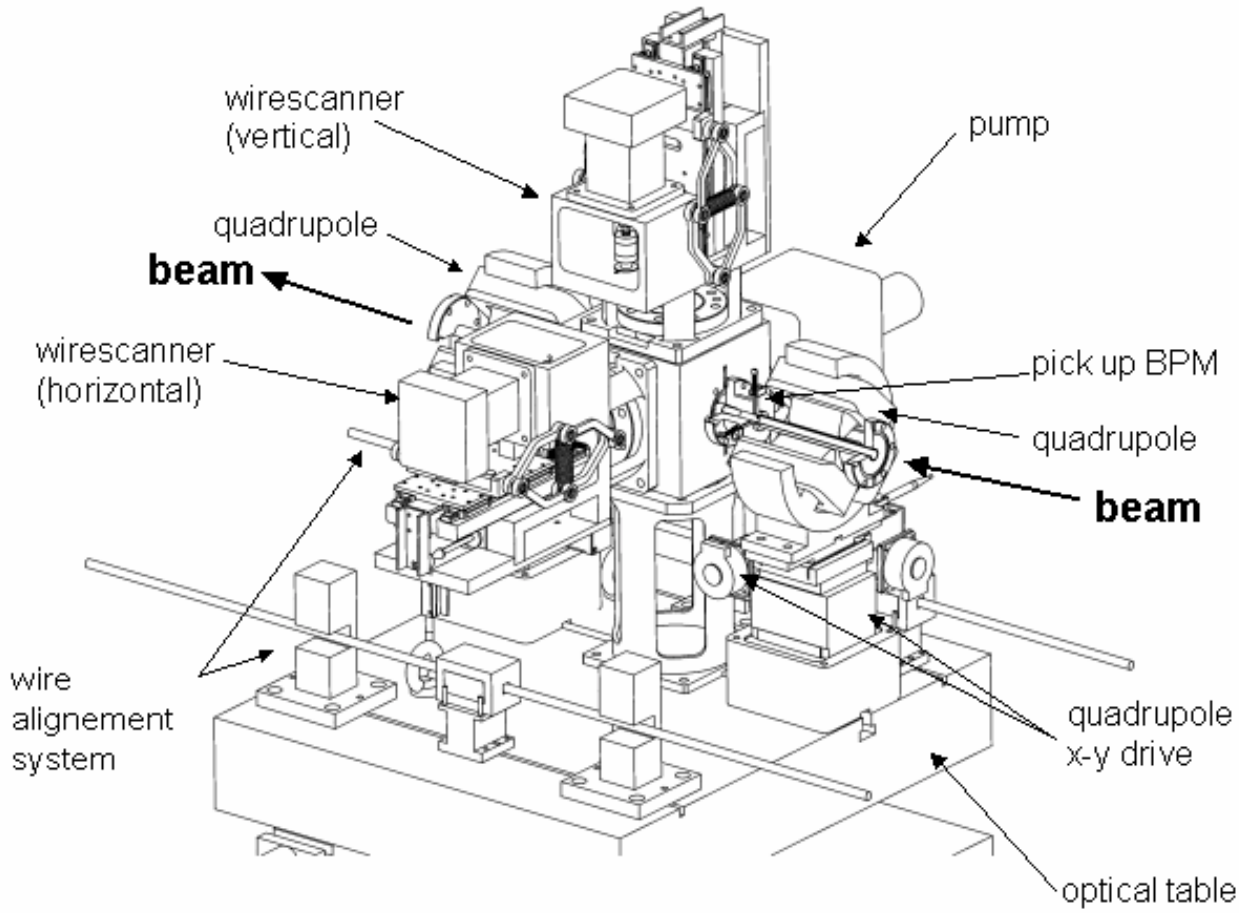

Figure 3: The technical schema shows the different components of the station.

The wire positions relative to the theoretical beam position (undulator axis) is calibrated using the length gauge in combination with an optical calibration tool during the assembly procedure. This allows in combination with a wire alignment tool an absolute beam position measurement related to the undulator axis with a precision better than 50 μm. The whole unit as shown in figure 2 and 3 was assembled under class 100* clean room conditions.

A stepping motor with a torque of M > 2 Nm and 51200 micro steps per rotation is used to drive the slot winding cylinder. To ensure that the motor does not lose steps, a special power supply unit [7] is used. This power supply accomplishes a minimal step resolution of 2.8 μm in the linear range of the slot winding cylinder. For the control of the wire scanner movement an IP-Stepper module [8] is used.

FIRST MEASUREMENTS IN THE UNDULATOR SECTION OF THE VUV-FEL

The described systems were installed in the undulator section in 2004. All units are in operation and in use to align the electron beam.

A complete wire scanner station between two undulators is shown in figure 2. Figure 3 depicts the 3D drawing of the diagnostic set up with the two wire scanners, the quadrupoles with their driving units, and the base plate with the wire alignment system.

Figure 4 shows slow stepwise scans of all seven installed wire scanner stations in the horizontal and vertical plane perpendicular to the particle beam.

* clean room classification according US Fed. Standard 209E

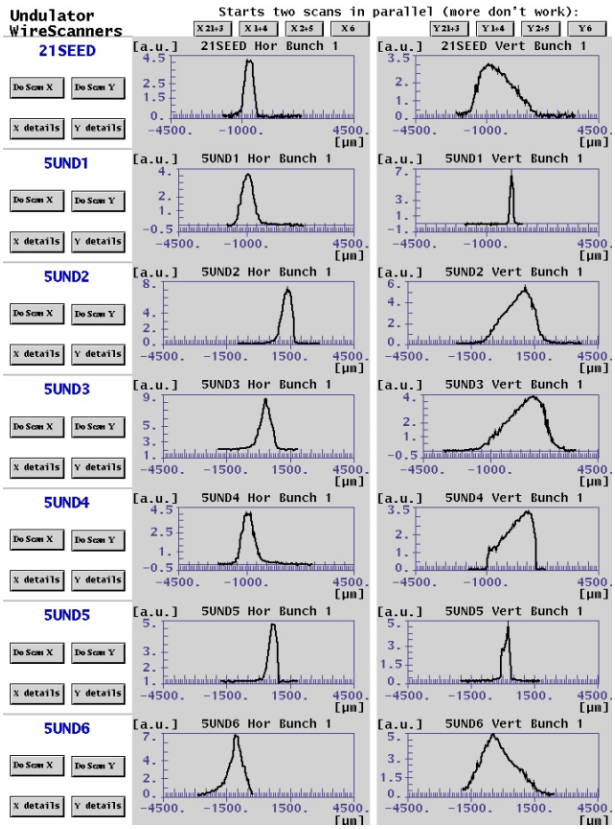

Figure 4: Example of horizontal and vertical beam scans at the seven wire scanner stations.

From these types of measurements the beam trajectory as well as the beam size can be deduced. A different evaluation of beam trajectories and beam sizes in horizontal and vertical direction is presented in figures 5 and 6.

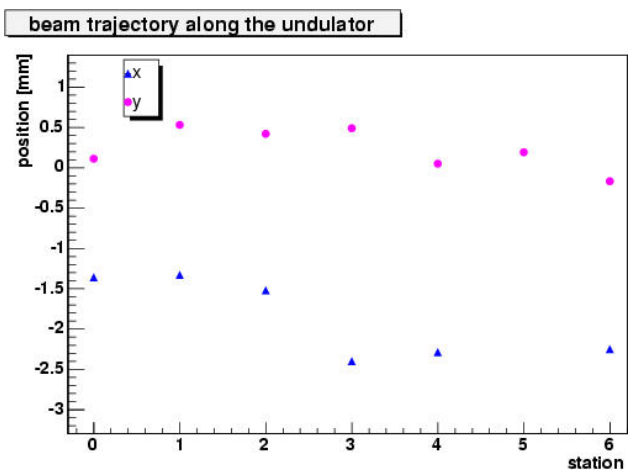

Figure 5: Horizontal and vertical beam trajectories determined by wire scanner measurements along the undulator section.

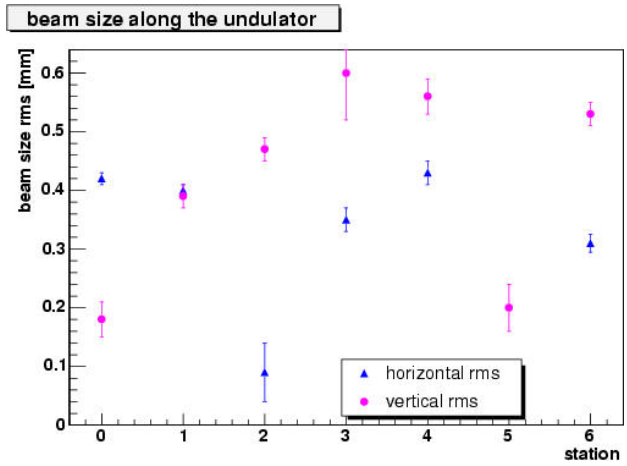

Figure 6: The horizontal and vertical beam size at the position of the wire scanners.

CONCLUSION

A fast wire scanner system was designed and built for the undulator section of VUV FEL at DESY. Seven stations with two wire scanners are in operation now. The beam trajectory along the undulator section as well as the beam size and the beam position are determined. These measurements are used for beam based alignment.

REFERENCES

[1] J. Roßbach, Nucl. Instrum. and Methods A 375, 269 (1996).
[2] K. Wittenburg, Strahlprofilmonitore für den HERA – Protonenring DESY-HERA 1986-06.
[3] U. Hahn, J. Pflueger, G. Schmidt , Nucl. Instrum. and Methods A429 (1999), 276.
[4] G. Schmidt, U. Hahn, M. Meschkat, F. Ridoutt, Nucl. Instrum. and Methods A475 (2001), 545.
[5] J. Pflueger, U. Hahn, B. Faatz, M. Tischer, Nucl. Instrum. and Methods A507 (2003), 228
[6] TESLA Report 2002-06.
[7] Data book, API Portescap.
[8] IP-Stepper, IP-Quadrature Manual, SPS-Greenspring Modular I/O.

IRRADIATION CONTROL OF THE "SPIRAL" TARGET BY MEASURING THE ION BEAM INTENSITY VIA A FAST CURRENT TRANSFORMER

P. Anger, C. Doutressoulles, C. Jamet, T. André, W. Le Coz, E. Swartvagher, M. Ozille
Grand Accélérateur National d'Ions Lourds (GANIL), Caen, France
e-mail : anger@ganil.fr

Abstract

In order to obtain a more precise control on the irradiation of the targets of the "SPIRAL" installation, a new criterion of safety must be respected. To control this latter, an AQ system has been put in operation and more specifically a new device has been set up in order to measure the ion beam intensity and to calculate the number of particules per second. This value can then be integrated over time. This device consists of two Fast Current Transformers integrated in a mechanical unit placed in a vacuum chamber. These sensors reproduce the image of the pulsed beam at 10MHz and we take from the amplified signal of each sensor, the amplitude of the 2nd harmonic. Each one of these amplitudes is detected by a Lock-in Amplifier, which is acquired via a real time industrial controller. The intensity is calculated by the Fourier series relation between the amplitude of the 2nd harmonic and the average intensity. These equipments can be remotely tested by integrating a test turn on the sensors. They are redundant. The accuracy of measurement is estimated taking into account the variation of beam, of the environment and of the installation

INTRODUCTION

The SPIRAL unit generates a radioactive ion beam by irradiating an ECS "Ensemble Cible-Source" *(Target-Ion Source)* with a high energy ion beam. GANIL is a facility submitted to approval, and the irradiation mode of targets is regulated by the safety authorities. At present, the target irradiation is limited by a safety criterion of 15 days of use , independently of the irradiating beam characteristics (ion species, power and risks linked to the operation of the accelerators). A request for modification of this criterion has been formulated to the safety authorities. The maximum irradiation time authorised should depend on the irradiating beam type and of its intensity, the new criterion being that the total number of ions received by the target (integrated flux) should not exceed a certain level, function of the radiological risk.

In order to control this new criterion, the CICS project (**C**ontrôle de l'**I**rradiation de la **C**ible de **S**PIRAL) *(Irradiation Control of the SPIRAL Target)* has been issued: it will require a measurement system and a reliable control of the beam intensity which will, at any time, show both the instantaneous and the integrated beam intensity for each target. The intensity means the number of ions per second.

DESCRIPTION OF THE SYSTEM

The system consists of two sensors measuring the intensity of the primary beam irradiating the ECS *(Target- Ion Source)* and returning an electric signal proportional to the intensity. A dedicated chain of measurement will handle the signal of each sensor so that they can be digitized by a computing system. This dedicated and autonomous computing system will be able to test the two instrumentations and handle any malfunctions. Using an user interface, this computing system will receive the necessary information from the primary beam, the identification of the ECS and the new criterion in order to measure the intensity of the beam, calculate the number of particles per second and integrate the number of ions stopping in the target. The computing system records the data related to the irradiation of each ECS on two reliable and permanent data carriers. It cuts off the beam either when a malfunction occurs or when the target has received the maximum dose (new safety criterion).

PRINCIPLE OF THE MEASUREMENT OF THE BEAM INTENSITY

The beam intensity is obtained by measuring the magnetic field generated by the pulsed beam (fig.1) with a Fast Current Transformer of 10 turns.

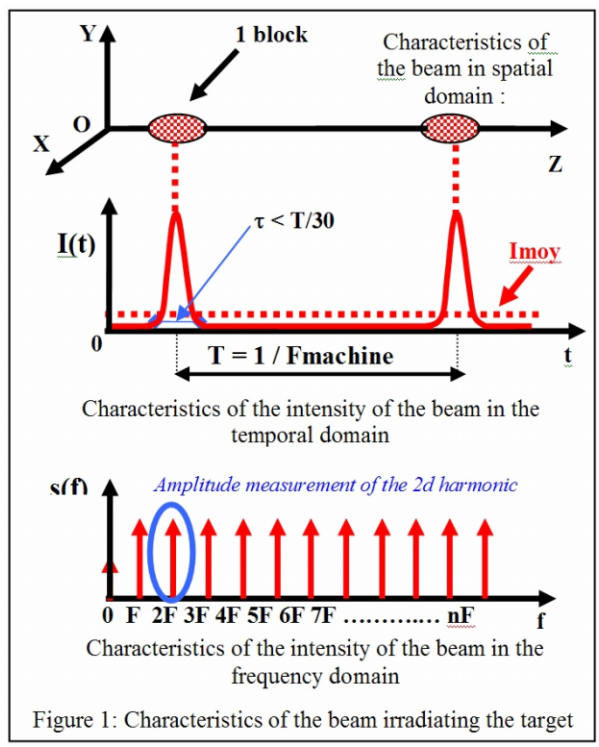

Figure 1: Characteristics of the beam irradiating the target

The current transformer (fig.2, fig.3) generates an image signal of the beam intensity to a treatment chain ; then, the amplitude of the second harmonic of the signal is detected by a Lock-in Amplifier. This Lock-in Amplifier is a Stanford Research Systems "SR844" model (fig.4). This detection is based on the principle of synchronous detection. This amplifier is locked onto the 2nd harmonic by a RF reference in order to measure the module of the 2nd harmonic. The average value of the intensity is calculated by the relation between the 2nd harmonic amplitude and the average value in the Fourier expansion :

$$a_0 = \frac{a_2}{\left(2\frac{\cos(2\pi F\tau)}{1-(4F\tau)^2}\right)} \cong \frac{a_2}{2} \quad \text{if } \tau << \frac{1}{F}$$

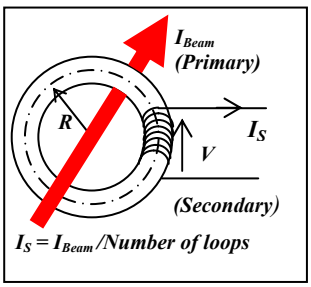

Figure 2: Toric transformer

Figure 3: Picture of 2 Fast Current Transformers BERGOZ FCT-082-10:1-WB

Figure 4: Lock-in Amplifier "SR844"

This measuring equipment is doubled (fig.5) in order to ensure an active redundancy which guarantees the validity of the measurement. The dispersion (D) is calculated and must be lower than a maximum value:

$$|D| = \frac{2\times\left|\overline{I_A(t)} - \overline{I_B(t)}\right|}{\left(\overline{I_A(t)} + \overline{I_B(t)}\right)} \leq D\max$$

The measuring equipment is calibrated in order to establish the global accuracy of the measurement and therefore to deliberatly overestimate, by programming, the calculated intensity :

$$\overline{I(t)} = \left(\frac{\overline{I_A(t)} + \overline{I_B(t)}}{2}\right) \times \left(1 + \frac{\Delta_I}{I}\right)$$

The measurement range of the beam intensity is 10nA/50µA.

An additional test turn was integrated into the Fast Current Transformer to test the measuring equipment (fig.5). Sending a 2F sinusoidal signal allows testing of the availability of the system.

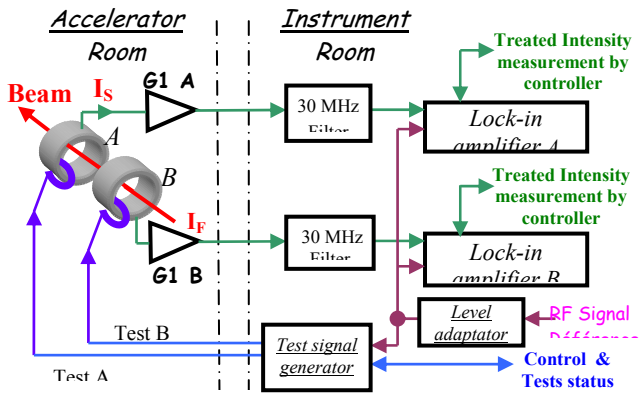

Figure 5 : Instrumentation Synoptic

MECHANICAL INTEGRATION

The sensor is installed in the L4 beam line a few meters in front of the SPIRAL target (fig.6).

The two sensors are integrated in one block which is placed in the vacuum chamber. This mechanical device is operated at a pressure of 10^{-6} Pa and has a leak rate better than 10^{-10}Pa.m^3/s (for He). (fig.7)

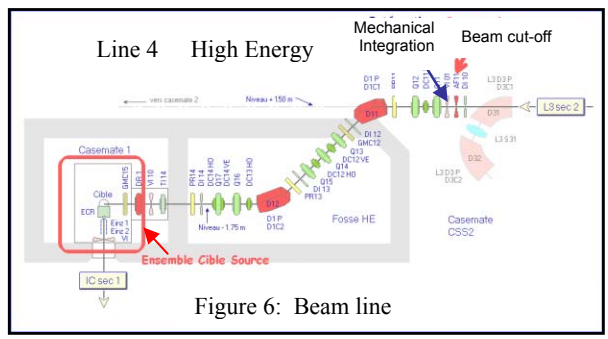

Figure 6: Beam line

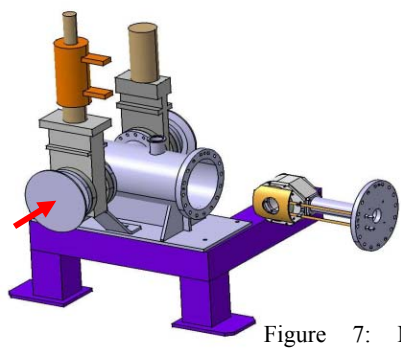

Figure 7: Mechanical assembly of the dual sensor

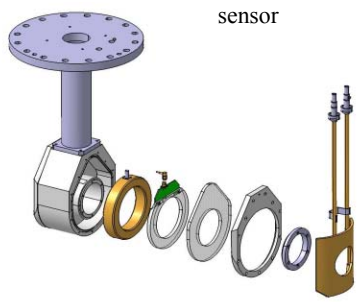

DESCRIPTION OF THE COMPUTING SYSTEM

It is basically composed of a real time industrial controller : Compact Fieldpoint (fig.8) from National Instruments. It is autonomous, has its own operation system and is programmed under Labview. The system must obtain the detected intensity of the beam, calculate the particle fluency, stop the beam with a beam stopper block if the level is exceeded, or in case of malfunction. It will record the irradiation history on a local memory and provide a link to the user PC. The system will also have a user interface in order to configure the system and to keep the users informed (fig.9).

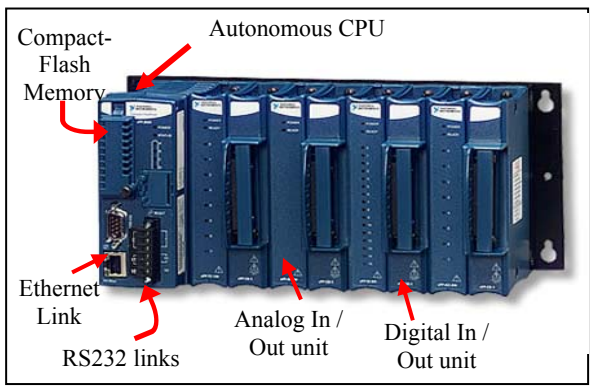

Figure 8: Compact Fieldpoint Controller

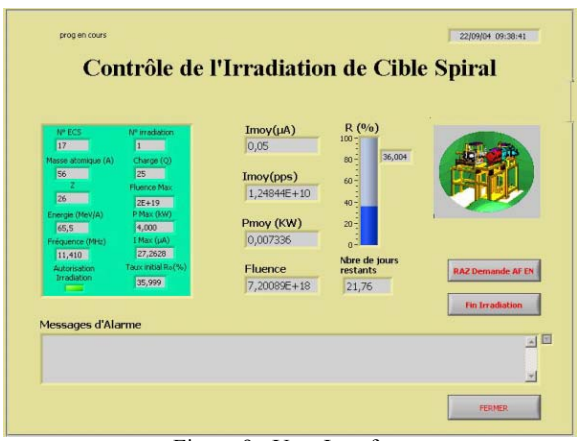

Figure 9: User Interface

QUALITY ASSURANCE

The study, implementation and operation of this system need to satisfy quality requirements in order to control the new safety criterion. The intensity measurement veracity, the malfunction management and the overall reliability were taken into account from the beginning. For example, the uncertainty of the measurement chain will be treated whatever the beam frequency, pulse length, subset operating temperature, and also which units or refills are installed. To calculate the accuracy of each unit, a testing coaxial line was used for FCT (fig.10) and a test bench with a temperature-regulated chamber was developed (fig.11).

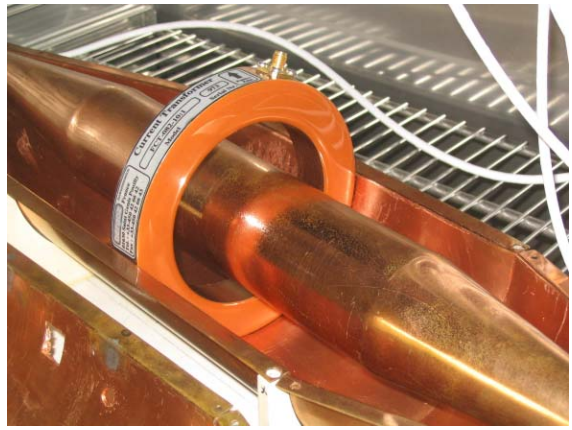

Figure 10: Testing coaxial line for FCT

Figure 11: Temperature testing device

CONCLUSION

This project is nearly completed ; it is awaiting starting-up authorisation for the validation of the concept (control system of the new safety criterion) by the safety authorities. It will allow better management of target irradiation by lowering the number of ECS *(Target-Ion Sources)* used every year. It will also allow us to operate and handle an AQ instrumentation system while assuring absolute accuracy of the measurement.

REFERENCES

[1] S. Faure, *« Limite d'irradiation d'un ECS de SPIRAL »*, GANIL 2003, SPR213B

[2] P. Anger and the Project Team : C. Doutressoulles, M. Ozille, JF. Rozé, B. Jacquot, M. Dubois, S. Faure, F. Bucaille, C. Mauger, JC. Deroy, *« Cahier des Charges et des Clauses Techniques du projet CICS »* GANIL 2003, P-CICS-043-CdCCT-A.

[3] M. Lieuvin et al., Commissioning of SPIRAL, the GANIL radioactive beam facility, 16th Int. Conf. On Cyclotrons and their Applications. Michigan 2001.

SPATIAL AUTO-CORRELATION INTERFEROMETER WITH SINGLE SHOT CAPABILITY USING COHERENT TRANSITION RADIATION

Daniel Sütterlin[1] , Volker Schlott[1], Hans Sigg[1], Daniel Erni[2], Heinz Jäckel[3], Axel Murk[4]
[1] Paul Scherrer Institute, CH-5232 Villigen, Switzerland
[2] Lab. for Electromagnet. Fields and Microwave Electronics, ETHZ, CH-8092 Zürich, Switzerland
[3] Institute of Electronics, ETHZ, CH-8092 Zürich, Switzerland
[4] Institute of Applied Physics, University of Berne, CH-3012 Berne, Switzerland.

Abstract

The polarization dependent intensity distribution of CTR emission has been theoretically and experimentally studied at an optical beam port downstream the 100 MeV SLS pre-injector LINAC. Based on these analyses, a spatial interferometer using the vertically polarized lobes of coherent transition radiation (CTR) has been designed and installed at this location. A successful proof of principle has been achieved by step-scan measurements using a Golay cell detector. The single shot capability of this bunch length monitor is demonstrated by electro-optical correlation of the spatial CTR interference pattern with a Nd:YAG laser pulse.

EMISSION CHARACTERISTICS OF CTR

Step-scan interferometer measurements, such as Martin-Puplett Interferometers offer excellent frequency resolution. One of their major drawbacks however is that a full measurement often takes minutes and averages over many electron bunches. Therefore, the unique emission characteristics of long-wavelength CTR is used to design a novel interferometer producing a spatial auto-correlation of the CTR pulse allowing the determination of the power spectrum in a single-shot. In the following an analytic formalism is presented describing the emission process of CTR.

The result derived by Ginzburg and Frank [1] is valid only for the optical part of the emitted radiation and/or for infinite target diameters. At long wavelengths the transversal extent of the electron field impinging onto the target screen is usually considerably larger than the target dimension. Hence, a model for the emission characteristics of long-wavelength transition radiation has been developed for a finite target screen that is rotated by 45° with respect to the electron trajectory [2,3]. In such a configuration, the metallic target screen acts as a source aperture for the emitted TR. In our formalism the magnetic field of the relativistic electron is inducing a surface current in the thin metallic target, from which the vector potential representation of the radiated field is acquired. When calculating the components of the resulting electrical and magnetic fields a further formalism has been introduced that provides accurate approximations for both cases the far-field and the radiating near-field. A complete description of the proposed analysis will be published elsewhere [3].

The simulated horizontal radiation pattern as depicted in Fig. 1 clearly reproduces the expected angular broadening with increasing wavelengths of the two-lobed emission profile. The asymmetry only occurs in the horizontal direction and vanishes for short wavelengths where our formalism converges with the Ginzburg and Frank model.

As displayed in Fig. 1 the simulations are in good agreement with the corresponding measurements c) and d) at the SLS LINAC. The underlying power spectrum used to model the broadband CTR excitation was measured with a Martin-Puplett interferometer. The discrepancies particularly in the wings of the radiation pattern can be attributed to deviations in the power spectrum (associated to different electron bunches), to the finite detectors size, and the additional diffraction at the vacuum port.

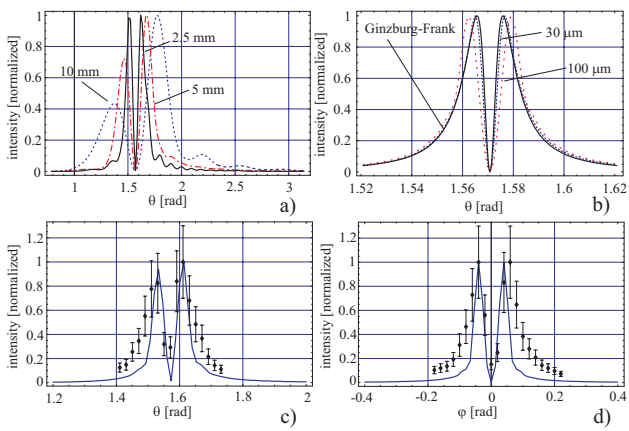

Figure 1: Calculated CTR radiation pattern (single electron of 100 MeV) at a spherical distance of R = 300 mm for a finite target screen with r = 28 mm; a) for millimeter wavelengths; b) for wavelengths in the FIR regime; c) measurements of the horizontal emission pattern for horizontal polarization; and d) measurements of the vertical emission pattern for vertical polarization. The simulations (solid line) are in good agreement.

SPATIAL INTERFEROMETER

Based on above theoretical and experimental analysis effective optics for the spatial interferometer has been designed. Due to the asymmetry in the horizontal emission pattern, we selected to use the vertical polarized component of the emitted CTR using a wire grid

polarizer. The beam splitting has been achieved by reflecting the two vertical lobes in different directions by two plane mirrors. Two toroid mirrors are introduced to refocus the two beams on to the focal plane intersecting at an angle of 60°.

The proof of principle of the interferometer set-up was accomplished using monochromatic cw–sources oscillating in the range between 70 and 120 GHz [4]. The waveguide feed of the source was placed in the nominal focus position. A detector with a similar waveguide feed has been mounted on a xy-scanner in the focal plane. Fig. 2 depicts a 2D scan taken at 100 GHz showing the appearance of the two beam interference fringes. The comparison with the simulation (GRASP) [5] shows very good agreement.

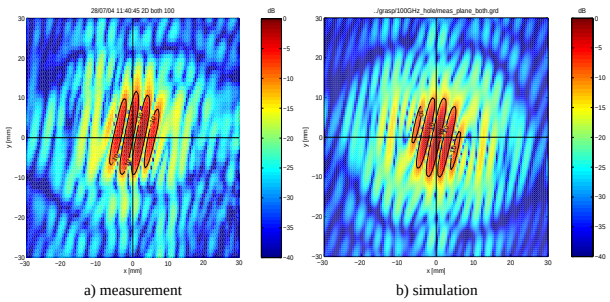

Figure 2: 2D scan of interferometer transfer function at 100 GHz. The tilt of the fringes results from the asymmetric layout of the beam splitters as the beams of the two signal paths intersect the xz-plane from opposite directions; a) measurement b) GRASP simulation.

The set-up was finally installed at the diagnostic station (ALIDI-SM-5) downstream the 100 MeV SLS LINAC. Two off-axis parabolic mirrors transmit the CTR to the entrance focus of the interferometer.

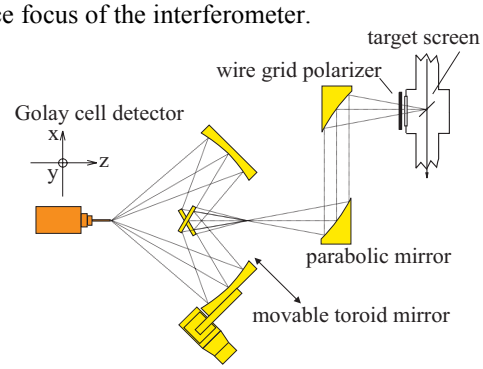

Figure 3: Interferometer test set-up at the SLS LINAC.

A Golay cell detector, sensitive to (sub-) THz radiation, has been mounted on a xyz stage. In a first experiment one of the toroids is displaced to adjust the phase between the two interferometer arms. The interference between the two beam paths has been observed with the detector placed at the interferometer exit focus. The resulting interferogram and the corresponding power spectrum are shown in Fig. 4 a) and 4 b). The sharp edge in the spectrum results from the low frequency cut-off at 80 GHz of the wave guide feed mounted in front of the Golay cell. In a second experiment, the interference pattern in the focal plane has been investigated. At the fixed phase of the interferogram minimum the horizontally distributed intensity is measured by scanning the detector along the horizontal plane. Three consecutives scans are presented in Fig. 4 c) showing up to 50 % interference modulation. The position of the toroid mirror was then altered by 0.5 mm which resulted in a shift of the interference as illustrated in Fig. 4 d).

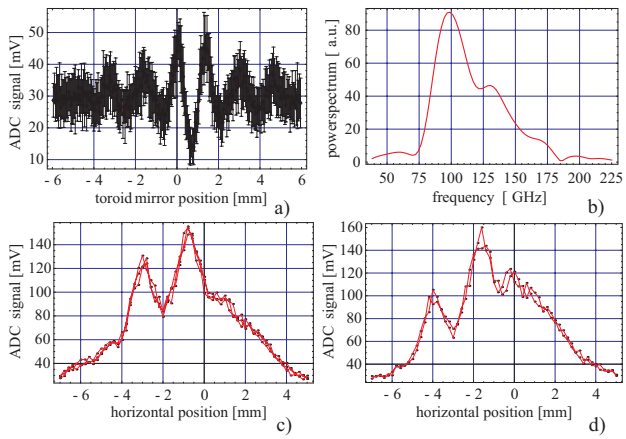

Figure 4: a) Phase scan showing the interference between the two beam paths; b) resulting power spectrum. Horizontal intensity distribution measured in the focal plane of the interferometer; c) at the fixed phase of interferogram minimum; d) at toroid mirror position 0 mm.

As the horizontal interference pattern is generated by each separate radiation pulse, this set-up allows in principle single-shot measurements of the power-spectrum of the emitted radiation. The single-shot readout can be accomplished using electro-optical techniques.

ELECTRO-OPTICAL READOUT

An active-mode-locked Nd:YAG laser (500 ps pulse width) is guided into the radiation bunker of the SLS LINAC and is focused on to a ZnTe crystal (10mmx10mmx1mm), placed in the focal plane of the interferometer. The comparatively (with respect to the CTR pulse) long laser pulse necessitates almost perfect extinction in cross-polarization. Extinction levels of 10^{-6} were achieved using commercially available Glan Laser polarizer. The crystal degrades the total extinction by nearly two orders of magnitude due to strain induced birefringence. The best achieved extinction levels are $4 \cdot 10^{-5}$.

The set-up is depicted in Fig. 5. The laser pulse passes the first polarizer before it is deflected by a small mirror placed between the two signal paths of the interferometer onto the ZnTe crystal in the focal plane. Thus no pellicle beam splitter which is difficult to handle in respect to additional birefringence, is used. After the second polarizer the laser beam is focussed in vertical direction by a cylindrical lens onto the InGaAs linear image sensor (256 pixels, 50 µm pitch).

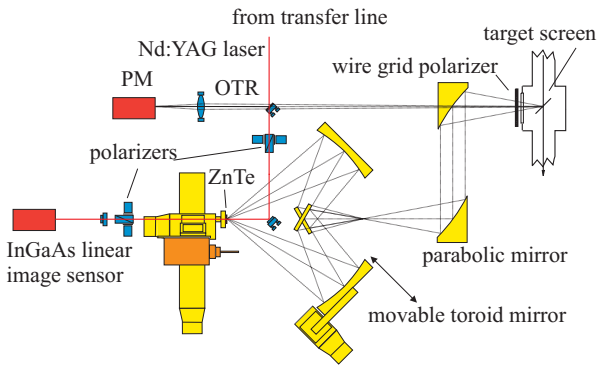

Figure 5: Experimental set-up installed at the ALIDI-SM-5 optical diagnostic port.

Coincidence between the Nd:YAG laser pulse and CTR was reproducibly preset by overlaying OTR and the laser signal measured by a PM tube. When coincidence is obtained, the total signal level rises by a factor of 3 to 5. The signal decreases again when the screen is withdrawn, c.f. Fig 6.

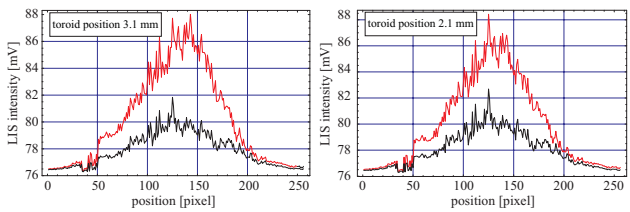

Figure 6: Averaged raw data profiles recorded with the linear image sensor for the target screen inserted and pulled out for two different positions of the toroid mirror.

To resolve the interference pattern, the average over 100 profiles were taken at different phases with and without the target screen. The difference signal between in and out was then normalized and subtracted from the profile taken at a much smaller phase to account for the background. The resulting difference profiles show a pattern which is moving with phase, c.f. Fig. 7. As this behaviour corresponds exactly to the one shown in Fig. 4, the minimum is assigned to the zeroth order fringe and thus is proving the first observation of spatial interference by EO readout. The modulations were not only observable in the averages of the profiles, but also in single profiles, thus demonstrating the single-shot capability of the set-up.

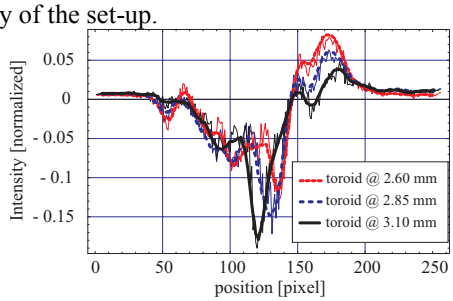

Figure 7: Profiles recorded for different phases. One profile with the toroid mirror placed at 1.35 mm is subtracted as background reference. The minimum corresponding to the zeroth order fringe is displaced with the phase as expected.

CONCLUSIONS

A novel interferometer producing a spatial interference pattern of long wavelength CTR was designed and successfully tested at the SLS pre-injector LINAC. The readout is done using electro-optical techniques. The long pulse of the Nd:YAG probe laser eases synchronization between electron bunch and laser but necessitates excellent levels of extinction in cross-polarization. Coincidence between CTR and laser was reproducibly found, and a modulation of the profile was observed both in averaged and single-shot data. The characteristic minimum of the zeroth order fringe was moving with the phase of the interferometer as expected.

In order to improve the detection of the spatial auto-correlation for single-shot measurements we need to enhance the interference visibility, for example by compensating the asymmetry in the present interferometer set-up.

ACKNOWLEDGEMENT

The authors wish to acknowledge support from the Swiss National Science Foundation.

REFERENCES

[1] V.L. Ginzburg, I. Frank, J. Phys. USSR 9, 353(1945).
[2] D. Sütterlin, et al., "Developement of a Bunch-Length Monitor with Sub-Picosecond Time Resolution and Single-Shot Capability," *DIPAC'03* (Mainz, Germany)
[3] D. Sütterlin, et al., "An analytic formalism for the emission of coherent transition radiation from an oblique finite thin metallic target screen." (in preparation).
[4] A. Murk et al., "Measurements and Simulations of the EOA Optics for SLS," *Research Report No. 2004-06*, Institute of Applied Physics, Dept. of Microwave Physics, University of Berne, 2004.
[5] GRASP „General Reflector Antenna Software Package“, www.ticra.com.

A NEW TV BEAM OBSERVATION SYSTEM FOR CERN

E.Bravin, S.Burger, G.F.Ferioli, G.J.Focker, A.Guerrerro, R.Maccaferri
CERN, Geneva, Switzerland

Abstract

Beam observation, emittance measurements and initial beam steering, are often achieved using scintillating or OTR (optical transition radiation) screens. In the CERN accelerators complex, this system is known as the BTV or MTV system. It consists of an observation camera, an illumination device and a vacuum tank provided of a view port containing the radiator.

More than 100 such equipments, in several different flavours, are installed in the CPS complex, another 50 in the SPS complex and another 50 will be installed in the upcoming LHC.

The newly developed electronics hardware consists of a single VME 64x card. This card is capable of controlling: all the different types of positioning mechanism for the screens, the adjustment of the illumination intensity, the different types of cameras (i.e. CCD or Vidicon tube) and the positioning of optical filters in front of the camera. Apart from the analogue video signal the card provides as output also the digitized image.

A preserie of this new electronics has been installed and tested during the tests of the LHC beam transfer line TI8 last autumn. The production of 300 cards is now underway. These cards will be used for the complete renovation of the MTV system of the CPS complex[1] and for the installations in LHC and its transfer lines.

In this contribution the new system is described with particular emphasis on the new VME card. The performances and limitations are also presented.

SYSTEM OVERVIEW

Figure 1 shows the principle of a TV beam observation system (BTV or MTV), where a radiator screen, attached to an insertion device, an illuminator and a camera represent the basic of the system. The type of radiator depends on the type of beam (sensitivity, dynamic range, linearity and temperature issues) and on the type of measurement to be done. To cope with the problem of the dynamic range of the beam, filters can be used in front of the camera.

The complexity of this system arises mainly from the variety of equipments that were installed over the past 25 years. Now, thanks to the recent unification of different accelerator departments of CERN and to the development of new devices for LHC, all new installations of BTV and MTV systems are made following a standard design, which simplified layout is shown in figure 2. For the new mechanical designs too, as many parts as possible are reused, in particular, all the 50 new BTVs in LHC will share the same type of mechanism. The problem of the many existing different devices is however much reduced now with the installation of the new control hardware.

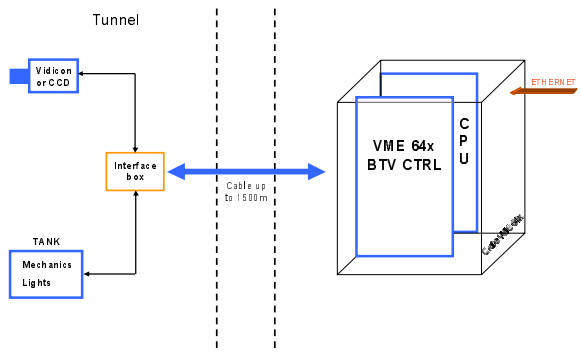

Figure 2: Layout of the new BTV/MTV hardware control system.

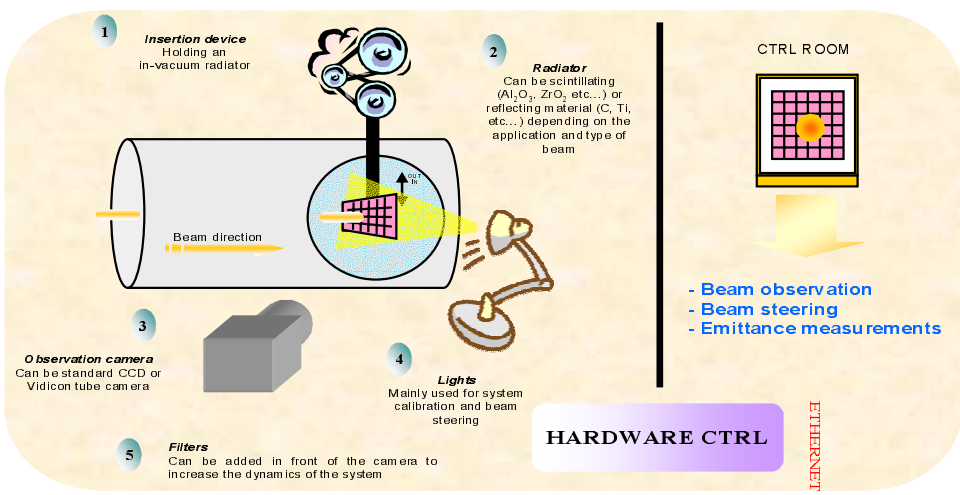

Figure 1: Principle of a BTV or MTV system.

NEW HARDWARE CONTROL

A new VME card for the control of the beam observation system of CERN has been designed. The objective was to redesign completely the system for all new installations, like LEIR and LHC, and taking advantage of this new design to renovate the park of MTVs on the Proton Synchrotron complex.

Specifications

The electronics has to be able to :

- Control CCDs or Vidicon tube cameras
- Transmit the video signals over long distances (up to 1200m)
- Control the intensity of filament light bulbs (24V/5W)
- Control all the existing different types of insertion devices (electric with 2, 3 or 4 positions, Pneumatic with 2 or 3 positions)
- Control the new insertion and filter devices.
- Provide digitalization of the video signal

Moreover, all these features had to be implemented in a single VME64X 6U card (2 or 3 different crates were needed with the old system).

Card insight

The card is based on a 240 pins FPGA from ALTERA. The 175 I/O are used to interface with the VME bus and in general for all the digital circuits of the system (control of power drivers, timings, digitalisation, video processing, etc…). The use of FPGAs allows much more design freedom and reduces space requirements on the PCB, so that all the features can fit on a standard size card.

Two light bulbs are driven independently by a fast switching circuit, synchronised with the horizontal synch. The light intensity is controlled using a DAC (0 to 1V).

The type of insertion device to be controlled is selected via a rotary switch. This indicates to the FPGA which control logic to use. The configuration of the power drivers is made by the mean of straps on the card.

The video receiver includes an amplifier of 26dB that is used only with the Vidicon camera where the signal is small. A set of bits, this time programmable from the VME bus, selects one of 4 different amplification levels for the video signal before being digitized

The digitalisation is made using a 12 bits ADC clocked at 8MHz. The acquisition RAM size is 512x512x16, which allows the storage of 1 image at a time (the useful image area is 500x320).

Some input and output signals have been added directly in the front panel, (veto and ext-TRIG as inputs and screen-OUT as output). The composite video signal is also available on the front panel. A picture of the card is given in figure 3 with its main features highlighted.

Video performances and limitations

The video signal from the camera is transmitted over twisted pair cables to the receiver on the VME card up to 1200m away. After the signal is received on the VME card it is completely reconstructed and the video level adapted.

The video signal is then amplified to 5Vpp and sent to the ADC. For 5V signal, the comparable noise is 50mV, which leads to a S/N ratio equal to 1%.

The signal attenuation over 1200m cables is 20%. Figure 4 shows a video signal sent over 1200m. The S/N ratio is not influenced by the cable length; in fact the main source of noise is the VME crate itself. A typical measurement of a laser beam can be observed in figure 5.

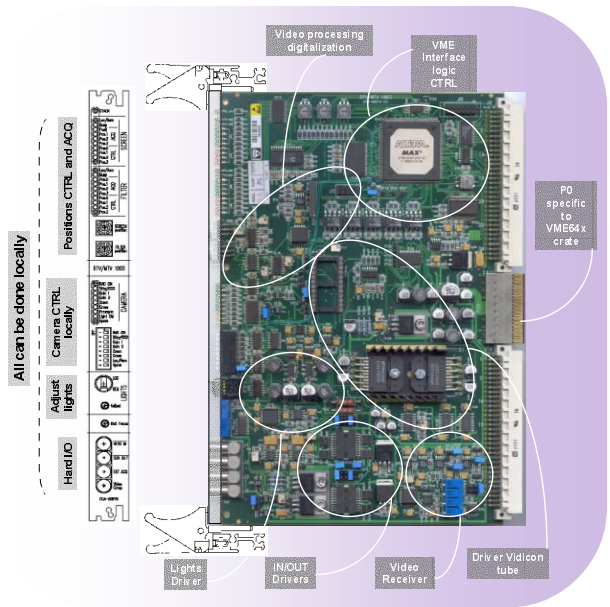

Figure 3: Overview of the VME64x BTV/MTV control card.

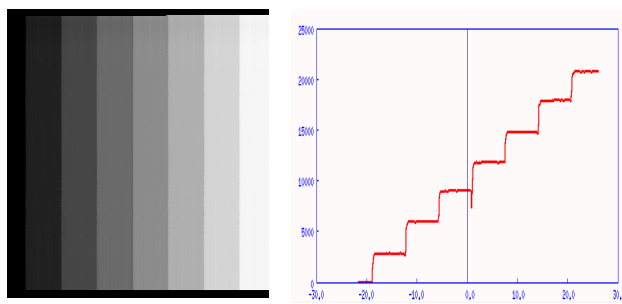

Figure 4: Video image and relative projection showing the linearity of the system (cable length of 1200m).

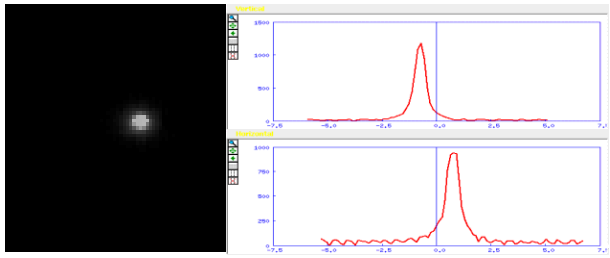

Figure 5: Typical measurement of a BTV or MTV system. On the left 2D: image of the laser beam, on the right: vertical and horizontal profiles.

THE CONTROL CRATE

The VME64x crate is the new standard for the whole accelerator control system. A new hardware environment has been developed around it in order to make the complete BTV/MTV system compact and easy to handle.

The system is composed of the following components:

- VME-64x crate
- Additional specific power supply (lamps, motors, HV) distributed over the P0 connector
- Transition modules to bring the specific power lines to the P0 connector (back and front of crate)
- Transition modules to bring the signals from the BTV/MTV cards to the back of the crate

Up to 8 BTVs can be installed in the same crate. The number of devices per crate is limited by the available space for the connections on the back and by the maximum power of the power supplies and VME bus lines. Figure 6 shows a complete system.

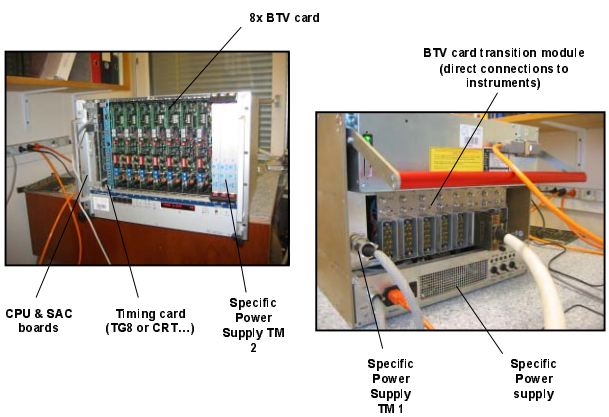

Figure 5: VME 64x crate equipped with the additional hardware needed by the BTV/ MTV systems.

SOFTWARE ENVIRONMENT

The front-end software runs on the VME controller (Power PC). It consists of one real-time task per device and a communication server built using the FESA framework [2], the current AB standard. The FESA framework provides the controls infrastructure (task handling, beam synchronization, middleware…) on top of which the real time behavior and user interface of the equipment is modeled. A graphical user interface (figure 7) accesses remotely the front-end software to display the acquired images and profiles and to provide the status and control registers of the BTVI device.

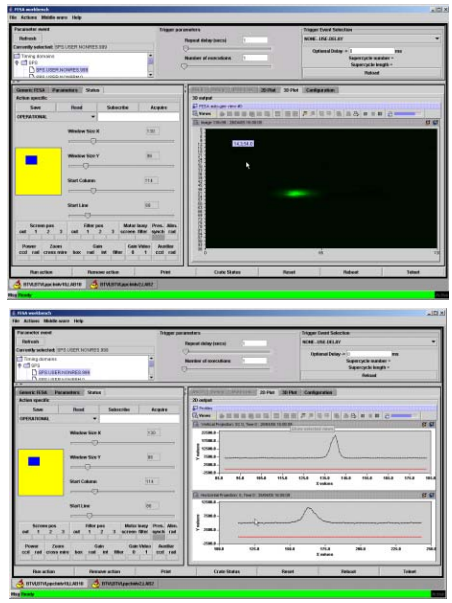

Figure 7: New expert version of the GUI for the BTVs. Top: showing a 2D image of the SPS ejected beam (to LHC). Bottom: the associated horizontal and vertical profiles

STATUS / CONCLUSION

A new VME electronics card for the control and acquisition of the beam observation system (BTV/MTV) has been designed. In September 2004, 13 new BTVs have been installed in one of the transfer lines to LHC (TI8) using this new system. The results have been very positive, achieving all the required specifications. The series production of 300 cards has already been launched. LEIR, the Low Energy Ion Ring will be the next machine at CERN to benefit from this new electronics, followed by CNGS, the remaining of the LHC transfer lines and the LHC itself.

An executive plan has already been prepared for the renovation of all existing MTV systems of the PS accelerators complex and the Clic Test Facility (CTF3).

REFERENCES

[1] S. Burger and R. Maccaferri, “Beam Observation Video Camera System for the PS Complex Status Report”, CERN PS/BD/Note 2002-185, Geneva, October 2002.

[2] ICALEPCS2003

A PROBLEM IN RF SWITCHES OF MULTIPLEXING BPM SYSTEM

T. Fujita, S. Sasaki, M. Shoji and T. Takashima
JASRI/SPring-8, 1-1-1 Kouto, Mikazuki-cho, Sayo-gun, Hyogo 679-5198, Japan

Abstract

At SPring-8, we have been developing a new detection circuit for beam position measurement with a resolution of submicron and a measuring interval of a few milliseconds with high stability. In the circuit, a multiplexing method using RF switches is employed in order for a drift of the circuit to be canceled. To achieve design performance, the switches must have following properties: a short switching time, high repeatability and long lifetime. During the evaluation of components for the new detection circuit, we found that some RF switches made of GaAs had a problem that the output signal changed for a few mdB for seconds after the switches were turned on. A few mdB, which is 1/10000 in voltage ratio, corresponds to a beam position error of a few microns in SPring-8. Such position error is out of the required specifications. We investigated several kinds of RF switches and decided to adopt a CMOS RF switches as the multiplexer. In this paper, we report switching properties of several RF switches and demonstration of beam position measurement using the switches.

INTRODUCTION

We have been developing new detection circuit for COD measurement. The position resolution and the repetition rate of measurement required for the circuit is submicron and hundreds of cycles per second, respectively. Furthermore, a long-term stability of the micron to sub-micron is required. Recently, parallel processing circuits for COD measurement for the sake of high measurement repetition tend to be employed [1, 2, 3], however, we have adopt a multiplexing method, in which four beam signals from one BPM head are multiplexed with RF switches and detected with one detection circuit, in order to increase the long term stability and to reduce the signal amplitude dependence of the detection circuit.

In order to achieve fast repetition of measurement with the multiplexing method, short switching time is required for RF switches. In addition, for the purpose of high stability on beam position measurement, high repeatability of RF switches is required.

Now, we are checking performance of prototype of the circuit. Total performance and that of the circuit downstream of the RF switches will be reported after installation and commissioning. In this paper, we report effect which arises from characteristics of RF switches.

PROTOTYPE

Fig. 1 is a block diagram of prototype of the developing circuit. Three BPMs (total twelve beam signals) are multiplexed with a 12:1 RF switch. After a frequency component of acceleration frequency, which is 508.58 MHz at SPring-8, in the pick-up signals is down-converted to 250 kHz IF frequency, the down-converted signal is digitized with 1MSPS-ADC for 1 ms. The digitized signal is processed with DSP and sent to control system. Thus three BPM data can be obtained every 12ms. When signal from a signal generator of 508.58 MHz is fed to the circuit without RF switches, i.e. BPMs and RF switches in Fig. 1 are replaced with signal generator and power divider, we can obtain the position resolution of 0.2 μm in standard deviation.

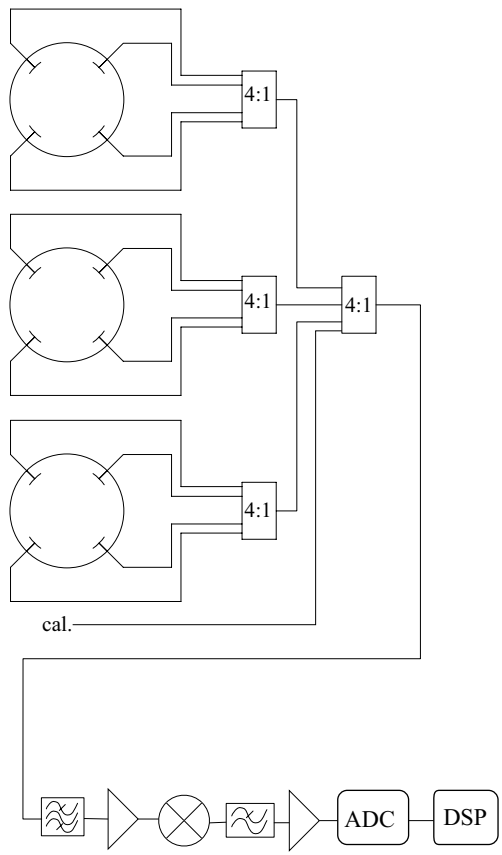

Figure 1: Block diagram of the developing circuit.

SWITCHING TIME

During initial phase of the circuit design, we planned to adopt RF switches made of GaAs. When we measured signal from signal generator with a prototype of the detection circuit equipped with GaAs multiplexer, we observed an unexpected behavior. As shown in Fig. 2, obtained beam position changes asymptotically for a second after

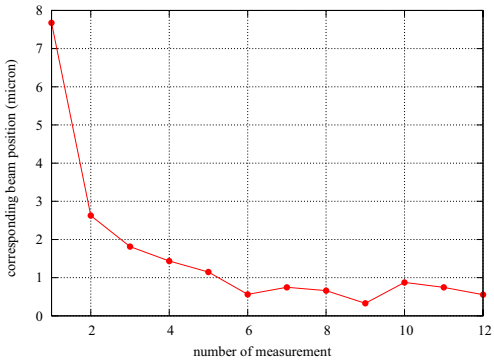

Figure 2: Corresponding beam position obtained with GaAs multiplexer.

the switch was turned on.

The beam position measured with multiplexer depends on the switching pattern, such as the order of the switching the channels and switching rate. We have to eliminate this kind of dependence to obtain the correct beam position data.

We measured switching time of two types of GaAs switches and CMOS type switches using spectrum analyzer (Rohde& Schwartz FSU08) of zero-span mode with its resolution bandwidth set to 100 kHz (Fig. 3). In the figure, absolute RF power is normalized with their final values. The output signal from GaAs switches reached the final values very slowly; it took several hundred milliseconds to read the final values. We did not observe such kind of behavior in the CMOS switch.

The observation of the switching behavior with an oscilloscope cannot recognize this kind of slow ramp of the signal, because the range of the variation is too small to be measured with 8-bit resolution, which correspond to 4×10^{-3}. Although the range of the signal variation is small for normal measurement instruments, the effect of the signal variation to the position values are significant for a beam position measurement with micron to sub-micron resolution.

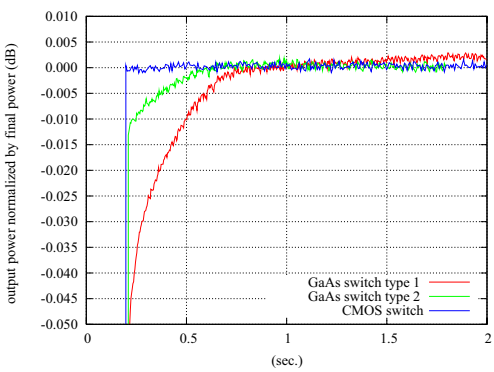

Figure 3: switching behavior observed with spectrum analyzer.

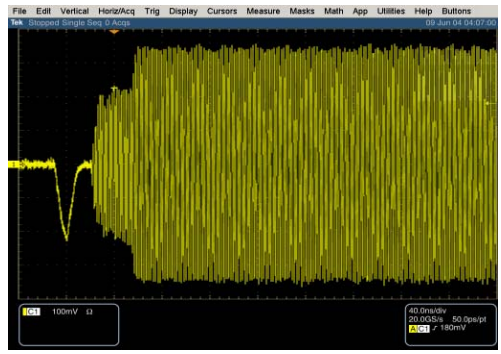

Figure 4: Switching behavior observed with 8bit oscilloscope.

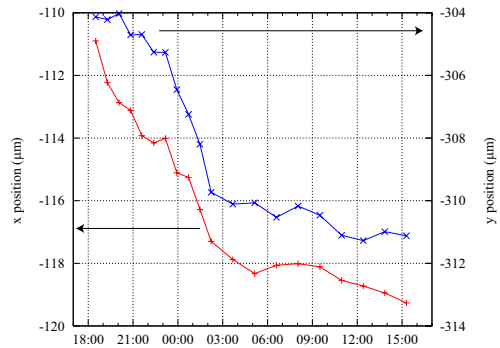

Figure 5: Long time measurement.

REPEATABILITY

For a test of repeatability of CMOS switch, we measured signal from signal generator for about 24 hours. During the measurement, a standard deviation of the calculated x/y position was 0.3 μm. As shown in Fig 5, horizontal and vertical positions drift about 10 μm with 24 hours. The drift of the position might suggest that RF switches drift independently.

MEASUREMENT WITH BEAM

We measured actual beam signal for 15 minutes during user operation at the beam current of 100 mA with top-up operation. Fig 6 is the result of the measurement. As can be seen in the figure, vertical beam position jumped about 2 μm. This jump was also observed with current BPM monitor.

The position resolution observed with actual beam (5.2 and 2.0 μm for horizontal and vertical direction, respectively) is larger than that with signal generator. The source of this deviation might come from a vibration of beam duct and ripple of magnet power supplies[4]. We have to point out the cause of this deviation to take full performance of the circuit.

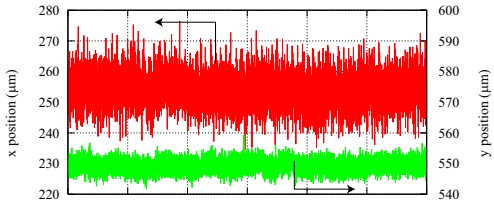

Figure 6: Measurement of actual beam signal.

SUMMARY

In this paper, we reported the problem on RF switches used in multiplexing BPM system. While, RF switches made of GaAs were not appropriate for the multiplexer, as to the switch with CMOS process, switching properties of CMOS process such as switching time and repeatability were suitable. Newly developing BPM circuit with multiplexer was demonstrated briefly with signal generator and actual beam signal.

REFERENCES

[1] K. Hayasaka et. al, UVSOR Activity Report 2001

[2] V. Schlott et. al, "PERFORMANCE OF THE DIGITAL BPM SYSTEM FOR THE SWISS LIGHT SOURCE", DIPAC 2001, Grenoble, France

[3] A. Kosicek, "LIBERA ELECTRON BEAM POSITION PROCESSOR", IWBS2004, Switzerland

[4] T. Yorita et. al, "The optimization for the reduction of the vacuum chamber vibration via structure analysis", IWBS2004, Switzerland

DESIGN OPTIMIZATION OF AN EMITTANCE MEASUREMENT SYSTEM AT PITZ *

L.Staykov†, DESY Zeuthen, Germany;

Abstract

The photo injector test facility at DESY Zeuthen (PITZ) has been built to test and to optimize electron sources for Free Electron Lasers (FEL's). In order to study the emittance conservation principle, further acceleration is required. To increase the electron beam energy up to 30 MeV, a booster accelerating cavity is under commisioning [1]. With this upgrade, the projected normalized transverse emittance less than 1 mm mrad is expected from beam dynamics simulations. To measure such small emittance, an upgrade of the existing Emittance Measurement SYstem (EMSY) is required. EMSY uses the slit mask technique to determine the beam emittance. In this paper, considerations on the physics of the system as well as results from GEANT4 simulations are given. The expected signal to noise ratio, the resolution of the system, and the energy deposition in the slit-mask are presented. EMSY is under construction at INRNE Sofia. Installation and first results are expected by the end of this year.

INTRODUCTION

The careful optimization of the electron source at PITZ has shown that it is possible to achieve small emittance for 1 nC bunch charge. Upgrade on the facility including installation of accelerating booster cavity will increase the energy of the electron beam to about 30 MeV. This requires upgrade of the present Emittance Measurement SYstem (EMSY) Fig. 1. The layout of PITZ is shown on Fig. 2. The electrons are extracted from a photo cathode based RF gun. The minimum beam emittance of $\sim 0.84\ \pi$.mm.mrad expected from the simulations could be achieved by further beam acceleration.

The setup of the emittance measurement system used at PITZ (Fig. 1) is typical for slit measurements. The system consists of two orthogonal actuators which can be inserted separately to penetrate the beam in order to take images or to cut beamlets in the beam transverse planes. The beamlets are observed at some distance L downstream and the normalized emittance ε_n is calculated using the standard formula (Eq. 1).

$$\varepsilon_n = \beta\gamma \cdot \sqrt{\langle x^2 \rangle \cdot \langle x'^2 \rangle - \langle x \cdot x' \rangle^2}. \qquad (1)$$

Here $\langle x^2 \rangle$ and $\langle x'^2 \rangle$ are the rms dimensions of the beam in the so called trace phase space where $x' = \sqrt{\langle p_x^2/p_z^2 \rangle}$ represents the rms divergence of the beam. The rms beam size is measured on an OTR or YAG screen at the position of the slits along the beam axis. The divergence is obtained by analyzing the profiles of the beamlets produced from the slits which drift some distance L downstream where the spatial distribution of the beamlets corresponds to the local divergence, x' can be derived from the size of the beamlet using the formula in Eq. 2.

$$x' = \sqrt{\frac{\langle x_b^2 \rangle}{L^2}}. \qquad (2)$$

Here x_b is the rms size of the beamlet on the screen after distance L. The $\beta\gamma$ is measured using a dispersive arm after EMSY.

EMSY LAYOUT

In general EMSY consists of two orthogonal actuators perpendicular to the beam axis which are holding the components which are inserted in the beam line. Stepper motors are provided to move separately each one of the four axes which give the precise spatial positioning and orientation of the components. On each of the actuators, either an YAG or OTR screen is mounted to observe the beam distribution. A single and a multi slit masks are mounted consecutive to take samples from the transverse phase space of the electron beam. A CCD camera is placed to observe the screens. EMSY was designed and manufactured jointly of Sofia Institute for Nuclear Research and Nuclear Energy and DESY Zeuthen in the period 2000-2001.

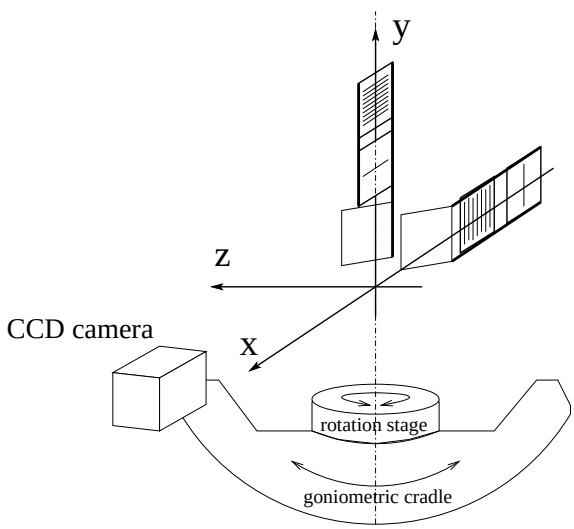

Figure 1: Layout of EMSY.

In the optimization process the components of the existing EMSY were modeled using GEANT4 [2] for the in-

* This work has partly been supported by the European Community, Contract Number RII3-CT-2004-506008, and by the 'Impuls- und Vernetzungsfonds' of the Helmholtz Association, contract number VH-FZ-005.

† Presenting author, e-mail: lazaraza@ifh.de

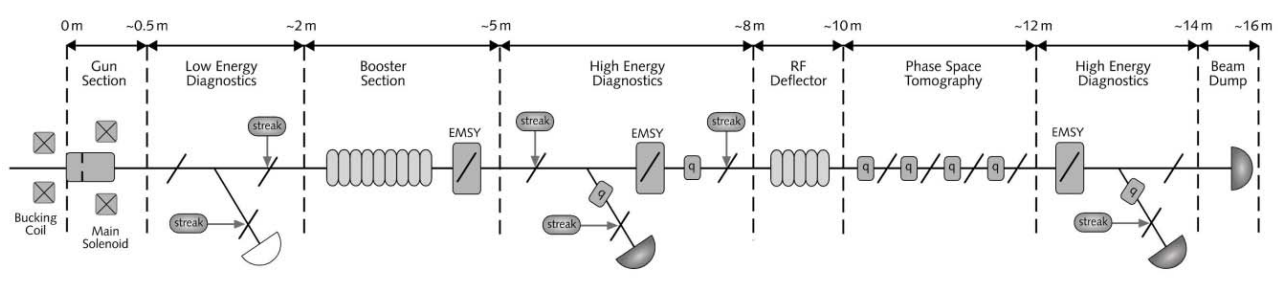

Figure 2: Layout of PITZ.

teractions of the beam with the material of the masks, and ASTRA [3] for detailed beam dynamics simulations.

OPTIMIZATION OF EMSY

Requirements for the system

During the optimization of the system, the following requirements were taken into account [4]:

- The beamlets produced by the slit mask must be emittance and not space charge dominated.
- The contribution of the initial beamlet size to the one measured at the observational screen must be as small as possible.
- The distance betwen the slit mask and the screen must be big enough to resolve small beam divergence.
- The mask thickness must be enough to scatter the residual electrons from the beam in order to produce an uniform background for the beamlets measurements and still it must provide sufficient acceptance angle.

Beam Dynamics considerations

The first requirement can be summarized taking into account formula 3 which is the ratio of the emittance and space charge terms in the envelope equation of a Gaussian beam [5].

$$R_b = \sqrt{\frac{2}{3\pi}} \cdot \frac{I}{\gamma I_0} \cdot \frac{d^2}{\varepsilon_n^2}. \qquad (3)$$

Here I is the beam current, I_0 is the so called Alfvent current and d is the slit width.This ratio must be smaller than 1 when we require emittance dominated evolution of the beamlets after the slit mask. In order to minimize the uncertainty brought by the influence of the space charge forces we set this ratio to be smaller than 0.1 for the design optimization. Since R_b is scaled with $1/\gamma$ it is obvious that for higher energies this is not a dominating parameter. Where the second requirement can be described using Eq. 4 assuming that the beam is at waist.

$$d \leq \sqrt{12} \cdot \frac{L\varepsilon_n}{\gamma\langle x\rangle} \qquad (4)$$

Taking this into account for the wide range of parameters expected in PITZ one ends up with slit width which must be ≤ 10 μm. The result is illustrated on Fig. 3 where a nominal beam is tracked using Astra. The influence from the finite slit size is clearly visible in the case of 50 and 25 μm in comparison with the 10 μm slit width.

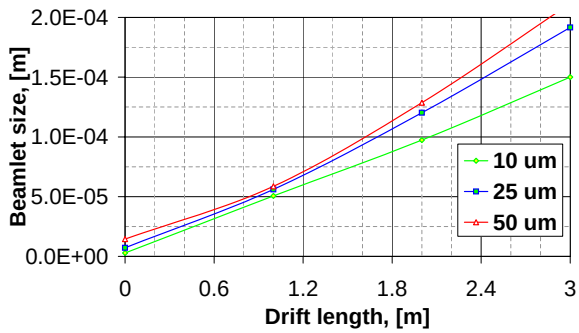

Figure 3: Beamlet evolution along the drift space

GEANT4 simulations

The energy deposition and the signal to noise ratio (S_2N) were estimated using GEANT4. A simplified geometry shown on Fig. 4 was used for the simulations.

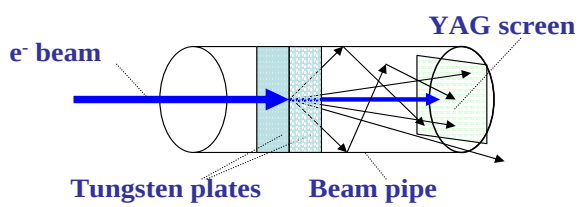

Figure 4: Model applied for the GEANT4 simulations

The mask material and thickens, and the distance between the mask and the observational screen were used as a variables in the optimization procedure. The signal to noise ratio S_2N (Eq. 5) was estimated using the area weighted light output from the YAG screen placed on 1, 2 and 3 meters downstream the slit mask. The signal density

is expressed using $\rho_s = N_s^{ph}/A_b$ where N_s^{ph} is the number of photons produced from the beamlet and A_b is the area from the screen covered by the beamlet, $\rho_n = N_n^p/A_s$ is the noise density where N_n^{ph} is the number of photons produced from the scattered electrons, positrons and photons which are interacting with the screen of area A_s. The screen area is $4 \times 4\ cm^2$.

$$S_2N = \frac{\rho_s}{\rho_n} \tag{5}$$

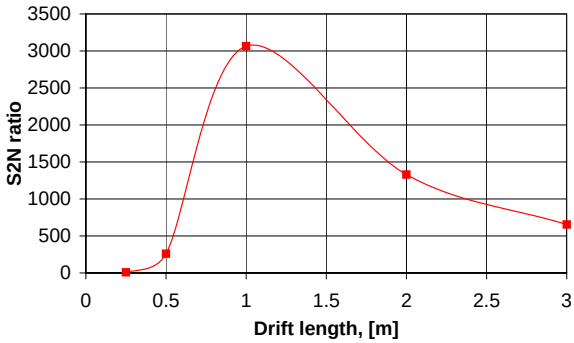

Figure 5: The signal to noise ratio for different drift lengths, mask thickness is 1 mm, slit opening 10 μm

On Fig. 5 one can see that a reasonable signal to noise ratio emerges still after 50 cm downstream from the slit mask and has maximum at $\sim$ 1 m. The image of the beamlet produced from the YAG screen can be seen on Fig. 6 no influence from the scattered radiation is visible.

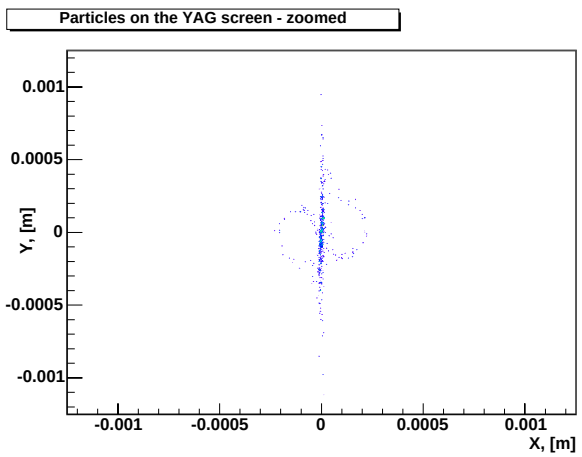

Figure 6: The beamlet image on the YAG screen 1 m downstream, mask thickness is 1 mm, slit opening 10 μm

Heat load of the slits

The energy deposited in the slits (Fig. 7) was used to estimate the heat load of the slits. A 2D numerical model was used to simulate the heat transport trough the tungsten piece. Assuming that no heat is transfered to the other components of the EMSY (which is the worst case scenario in vacuum conditions) we derived the maximum temperature to be reached by the slit components to be smaller than 727 °C.

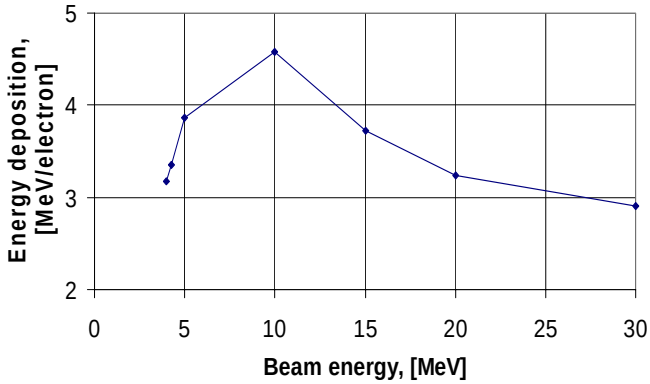

Figure 7: The energy deposition in the components of the mask, mask thickness is 1 mm

CONCLUSIONS

The parametersof the existing emittance measurement system at PITZ were optimized to decrease the uncertainty of the measured emittance smaller then 10 percent in the interval 5-30 MeV. It has been estimated that 1 mm thick tungsten with 10 μm opening for the slit mask must provide reasonable signal to noise ratio after 0.5 m downstream, still for better resolution larger distance from the screen and the slit mask is needed. Big drift length can also be a relief for the optical system of the camera which must resolve beamlet sizes in the interval 0.05 to 1.5 mm.

ACKNOWLEDGMENT

I would like to thank all the people who helped me to optimize the components of EMSY. They are: A.Oppelt, V.Miltchev, M.Krasilnikov and F.Stephan from DESY Zeuthen, I.Tsakov from INRNE Sofia and D.Lipka and D.Richter from BESSY. And all the physicists in PITZ collaboration for the fruitful discussions.

REFERENCES

[1] M. Krasilnikov et al., "Recent developments at PITZ", PAC'05, May 2005, Tennesy USA.

[2] GEANT collaboration, CERN/LHCC 98-44, GEANT4: "An Object Oriented Toolkit for Simulation in HEP"; see also website: http//wwwinfo.cern.ch/asd/geant4/geant4.html

[3] K.Floetmann,ASTRA,http://www.desy.de/ mpyflo

[4] P.Phiot, "Zeroth-Order Considerations for a single slit-based Emittance Diagnostics at the PITZ facility, DESY-Hamburg, April 7, 2000

[5] S.G.Anderson et al., "Space Charge Effects in High brightness electron beam emittance measurements", Phys. Rev. Vol. 5, 2002

PROFILE MONITORS BASED ON RESIDUAL GAS INTERACTION *

P. Forck, A. Bank, T. Giacomini, A. Peters
Gesellschaft für Schwerionenforschung GSI, Darmstadt, Germany, p.forck@gsi.de

Abstract

The precise determination of transverse beam profiles at high current hadron accelerators has to be performed non-interceptingly. Two methods will be discussed based on the excitation of the residual gas molecules by the beam particles: First, the beam induced fluorescence (BIF) where light is emitted from the residual gas molecules (in most cases N_2) and observed with an image intensified CCD camera. Secondly, by detecting the ionization products in an Ionization Profile Monitor (IPM) where an electric field is applied to accelerate all ionization products toward a spatial resolving Micro-Channel Plate. The signal read-out can either be performed by observing the light from a phosphor screen behind the MCP or electronically by a wire array. Methods to achieve a high spatial resolution and a fast turn-by-turn readout capability are discussed.

INTRODUCTION

Various methods for the transverse profile determination are used, most of them are based on energy loss of the beam particles in matter or on nuclear reactions at a target material. But for high current hadron beams, non-intercepting methods are preferred to prevent the risk of material melding by the large beam power deposition. The diagnostics must be non-intersecting in order to monitor the undisturbed properties of a beam stored in a synchrotron at any time during the cycle. Even in a pulsed LINAC it might be important to have access to possible time varying processes during the macro-pulse. Two types of non-destructive methods are described here, based on atomic collisions between the beam ions and the residual gas within the vacuum pipe. These methods are: The detection of single photons from excited levels of the residual gas atoms or molecules by **B**eam **I**nduced **F**luorescence (**BIF**) and the direct detection of ionized residual gas ions or electrons at an **I**onization **P**rofile **M**onitor (**IPM**). In particular IPMs are installed at most hadron synchrotrons and storage rings, but due to the various beam parameters at different laboratories no 'standard realization' is available. The basic features for both methods are discussed and their applicability are compared.

BEAM INDUCED FLUORESCENCE

In most LINACs and transfer-lines N_2 dominates the residual gas composition. Due to the electronic stopping power the molecules are ionized and with a certain probability left in an excited state. A strong fluorescence in the blue wavelength range $390\,\mathrm{nm} < \lambda < 470\,\mathrm{nm}$ is generated by a transition band to the N_2^+ electronic ground state ($B^2\Sigma_u^+(v') \rightarrow X^2\Sigma_g^+(v'') + \gamma$, for vibrational levels v), having a lifetime of about 60 ns [1]. Tests with other gases e.g. Xe were performed, but in this case a lower photon yield in the optical wavelength range was reported [2].

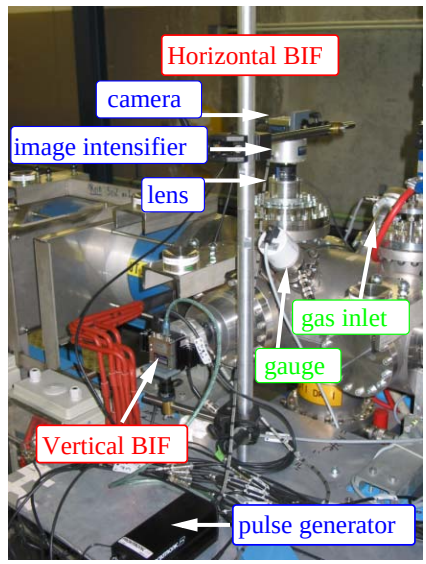

Figure 1: The installation of BIF station at GSI [6].

The low amount of photons can be detected and amplified using an image intensifier. This commercially available device consists of a photo cathode to transform the photons into electrons and amplifies them by a spatial resolving MCP electron multiplier. It is followed by a phosphor screen to create again photons, which are finally monitored by a CCD camera. A single primary photon can be amplified to yield 10^4 to 10^7 detectable photons on the CCD. The photon amplification depends on an adequate choice for the image intensifier components: Various types of photo-cathodes are available offering a different sensitivity with respect to the photon wavelength interval, see e.g. [3]. In general, a photo-cathode sensitive to longer wavelength results in a larger dark current. The photo-electrons can be amplified by a single MCP with typically 10^3 electron-multiplication or a double MCP assembly (Chevron configuration) with typically 10^6-fold multiplication. Due to the enlarged distribution of the secondary electrons on several channels at the second MCP, the light spots on the phosphor screen are about a factor 3 larger compared to an single MCP. Depending on the application the required light detection threshold has to be balanced

* Partly funded by INTAS under Ref. No. 03-54-3931 and by European Union under EU-FP6-CARE-HIPPI

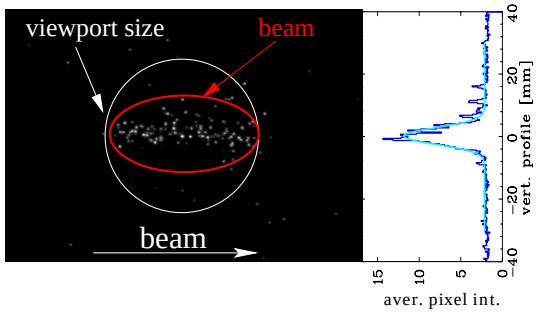

Figure 2: The two dimensional image from the intensifier of a Ar^{10+} beam at 4.7 MeV/u and $I_{beam} = 2.5$ mA recorded during *one* 250 μs long macro-pulse with a vacuum pressure of about 10^{-5} mbar and the projection for the vertical beam profile (right) are shown [6].

with respect to the spatial resolution. Different phosphor screens can be used: Types with fast decay constants of the emitted light of less than 100 ns but lower quantum efficiency (e.g. P47) have to be used if rapid variations have to be monitored. Slower types with typical ms decay times (e.g. P43) offer an increased sensitivity. Instead of using an MCP-phosphor assembly, the BIF-process can also be observed with a segmented photo-multiplier, see e.g. [2, 4].

The hardware set-up, as used for tests at GSI, is displayed in Fig. 1. The BIF-method was pioneered at the Los Alamos proton LINACs [5] for high current dc-beams at MeV energies.

Example for BIF at a pulsed LINAC

The GSI UNILAC is a pulsed heavy ion LINAC with a macro pulse length of about 100 μs to fill the succeeding synchrotron. The beam profile should be monitored within a single macro pulse; therefore the use of a long integration time for an improved signal-to-noise ratio is impossible. Due to the low amount of emitted photons during typically 200 μs integration time, a large amplification of 10^6 is required by a double MCP inside the image intensifier [3]. A P47 phosphor screen with 70 ns decay time is used to monitor fast beam width variations. A raw image is displayed in Fig. 2 together with the vertical profile as yielded from the projection along the beam path [6]. The correspondence of the measured profile to other methods is excellent.

Each of the light spots on the raw image is created by one single photon. Due to the statistical nature of the signal generation, the data quality can be enhanced by data binning or by averaging several images. The resolution of 300 μm/pixel is sufficient for the displayed parameters. A higher resolution can be reached by varying the distance between the beam pass and the camera and by a proper choice of the optics. This flexible adaption for higher resolution is only limited by the required focal-depth for an accurate mapping. By using a regulated gas valve the pressure could be locally (within 1 m) raised up to 10^{-4} mbar. The pressure bump does not show a measurable influence on the ion beam delivered to the GSI synchrotron. For

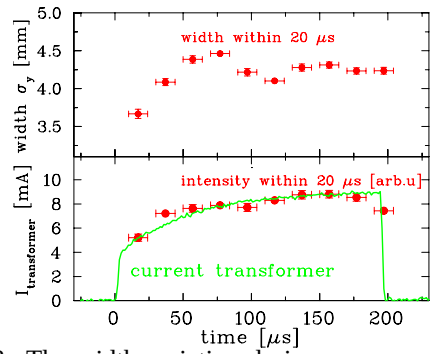

Figure 3: The width variation during a macro-pulse of 8 mA Ar^{10+} at 11 MeV/u is shown. The lower graph compares the normalized image intensity with the beam current [6].

some beam settings a relatively large background was seen, caused by neutrons or γ hitting the photo-cathode. Due to the homogeneous distribution it can be subtracted, but a shielding against neutrons might be required for a fail-save application.

An advanced application is the determination of a possible and in most cases unwanted variation of the beam profile during the macro pulse, as shown in Fig. 3. Within a rise time of $\tau_{rise} = 100$ ns the voltage between the photo-cathode and the MCP can be switched from blocking mode to photo-electron transmission toward the MCP. This can be used to restrict the exposure time during the profile measurement. For the case of Fig. 3 one image of 20 μs exposure time is recorded and these short term measurements are repeated with 10 different trigger delays for consecutive macro-pulses. This time-resolved profile determination is not possible with an intersecting SEM-grid due to the risk of wire melting by the large beam power.

Example for BIF at Synchrotrons

Careful investigations have been performed at the PS-Booster and the PS at CERN for proton beams [2]. Here the wavelength spectrum and photon yield was measured on a wide scale of beam energies from 50 MeV up to 25 GeV. For a N_2 pressure bump the wavelength spectrum is comparable to the results obtained for proton collisions at 200

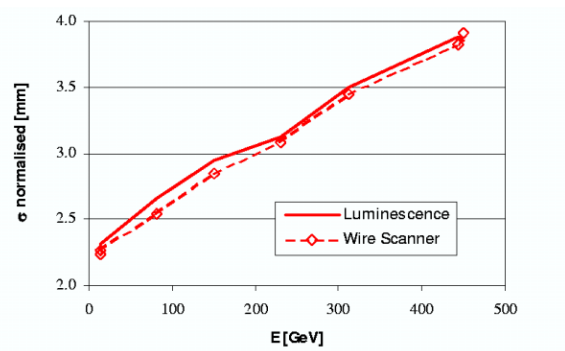

Figure 4: Comparison of the normalized vertical profile width as determined by the BIF-method and a flying wire scanner at CERN-SPS [7].

keV [1]. The lifetime of the excited states was determined using a circulating ~ 5 ns long bunch at 25 GeV energy and observing the decay time using a photo-multiplier. The result of $\tau = 58.0(3)$ ns coincides with the determination for 100 keV. The absolute photon yield in the optical wavelength range coincide with the calculated electronic stopping power as a function of kinetic energy (Bethe-Bloch formula) and is equivalent to the ion's energy loss of about 3.6 keV in N_2. Tests with other gases did not result in a larger photon yield.

A BIF monitor was successfully installed at the CERN-SPS [7]. For a pressure bump of N_2 in the order of 10^{-7} mbar profiles within 20 ms integration time, corresponding to about 900 turns, were recorded with sufficient statistical accuracy. A comparison with the standard flying wire scanner method is shown in Fig. 4, proving the applicability of this method also at high energy synchrotrons.

Example for BIF at ion sources

Behind proton sources, where the protons are only accelerated by the ~ 100 kV potential of the ion source platform these types of measurement are performed in several labs, e.g. [8]. The light yield is large and a long integration time enables careful investigations concerning possible signal broadening processes. A comparison of different gases shows a good correspondence, as displayed in Fig. 5. Taking the different excited levels and lifetimes into account, this result is not evident.

A broadening, in particular at the beam edges was reported [8], therefore the wavelength spectra with varying angles with respect to the beam axis were measured. Due to the angle-dependent Doppler-shift, the fluorescence originating from the residual gas (nearly at rest) and light emitted by the beam particles can be discriminated. The Balmer lines, emitted by the beam protons via recombination $p+e^- \rightarrow H^* \rightarrow H^0+\gamma$ or charge-exchange collisions (like $p + N_2 \rightarrow H^* + N_2^+ \rightarrow H^0 + \gamma + N_2^+$) was detected, as well as lines from neutral and charged hydrogen molecules (H_2, H_2^+, H_3^+). It can be concluded that the applicability of the BIF method has to be carefully checked to prevent misinterpretation due to the complex processes and large residual gas densities close to an ion source. Probably, this problem does not appear after acceleration by a LINAC due to a single composition of beam ions and the decreasing cross section for electron capture processes at energies above a few 100 keV [9]. But for all cases the residual gas density should be low enough to prevent for second order excitation of the gas molecules via electron excitation like $N_2 + e^- \rightarrow N_2^* + e^- \rightarrow N_2 + \gamma + e^-$ [1]. As a rough criterion the mean free path of electrons should be much larger than the beam size, which is only valid for a pressure below $p < 10^{-3}$ mbar.

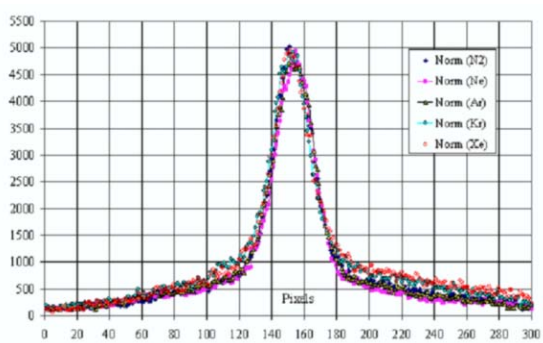

Figure 5: The measured beam profile for different gases determined at the SILHI facility [8].

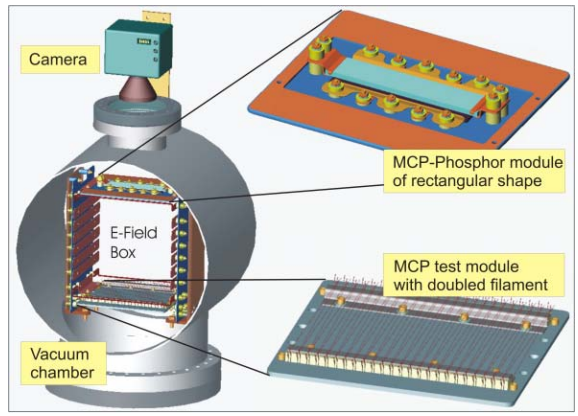

Figure 6: Schematic sketch of an IPM.

IONIZATION PROFILE MONITOR

In most synchrotrons and storage rings the transverse profile of the circulating beam is monitored by detecting the ionization products from the collision of the ions with the residual gas (mainly H_2). Inside the vacuum tube biased electrodes produce an electric field of typically 10 to 50 V/mm to accelerate the secondary electrons or ions toward an MCP, as shown schematically in Fig. 6. In the detection volume below the MCP a large electric field homogeneity is required (typically better than 1 %) to guide the residual gas ions on a straight trajectory toward the MCP resulting in an undistorted beam image. Most IPMs are equipped with a double MCP to yield a $\sim 10^6$-fold electron multiplication for a single particle detection scheme. As stated in the BIF description the spatial resolution is about a factor 3 worse compared to a single MCP. Two different anode readout technologies for the amplified signal are commonly in use:

- *Phosphor screen:* The electrons create light spots on a phosphor screen behind the MCP, which are monitored by a CCD camera, as shown schematically in Fig. 6. A high spatial resolution can be achieved with this readout method, only limited by the ~ 50 μm granularity of the double MCP channel size. Therefore this method is preferred in cooler rings. A typical time resolution is in the order of 10 ms, given by the frame rate of the CCD camera. For a turn-by-turn readout on a μs time scale the CCD camera is too slow. A multi-anode photomultiplier [10] or a photo-diode

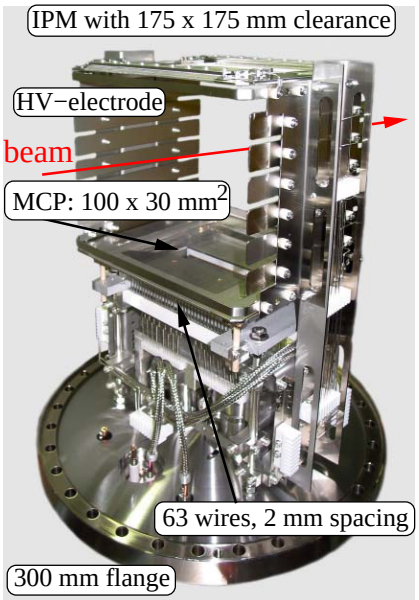

Figure 7: Photo of the IPM at the GSI synchrotron [15].

array [11, 12] has to be installed as a second readout system.

- *Wire array:* An array of wires can be mounted behind the MCP to collect the current of amplified electrons; a technical realization is shown in Fig. 7. The spatial resolution down to 0.5 mm, as given by the distance of the anode wires, is less than for the phosphor screen readout. But it is possible to get a time resolution of $\sim$ 10 ns using sensitive broadband rf-amplifiers [13]. When monitoring a bunched beam, a carefully designed shielding-pass for the beam image current has to be foreseen to prevent for distortions by a capacitive signal pick-up.

The surface-coating inside the MCP-channels shows non-recoverable amplification decrease after reaching a certain irradiation level as caused by the electron bombardment at the exit side of the MCP. To visualize this local non-uniformity of the MCP-amplification a test device has to be foreseen. One can install a filament-array on the HV-electrode opposite to the MCP, which is heated in regular, typically monthly time intervals to emit thermal electrons. Recently, an Electron Generator Plate (EGP) has been used achieve a homogeneous electron emission [14]. Alternatively, the MCP can be illuminated by a UV-lamp [15]. In case of amplification degradation the MCP has to exchanged or a software correction of the sensitivity has to be applied.

Depending on the voltage polarity for the electric field generation IPMs can be operated to detect residual ions or electrons. For low current beam applications residual ion detection is normally chosen and no magnetic field is required. Due to the scattering kinematics a negligible momentum is transfered to the residual gas ions and they are accelerated only on straight trajectories by the external electric field. For beam currents as normally stored in

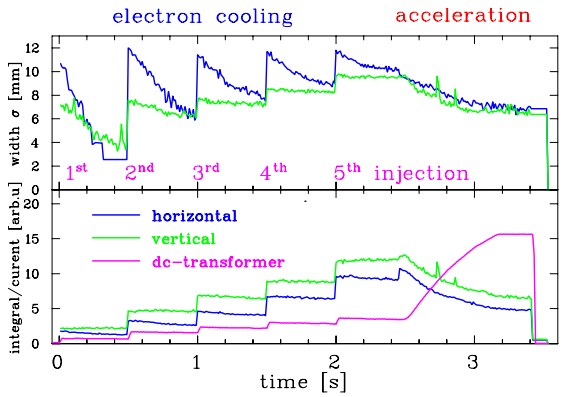

Figure 8: The process of beam stacking by electron cooling of a 11.4 MeV/u U^{73+} beam during 5 injections followed by an acceleration to 400 MeV/u at the GSI synchrotron is monitored. The horizontal and vertical beam width σ during the 3.4 s long cycle is shown on top and the integral of the individual profiles as well as the dc-transformer on bottom. Each 10 ms a profile is recorded [15].

high power synchrotrons, the space-charge field $\mathbf{E}_{SC}$ of the beam is comparable to the IPM electric field. To overcome the influence of $\mathbf{E}_{SC}$ an electron detection scheme is used, where the electrons are guided towards the MCP by a magnetic field of typically $B = 100$ mT. This value is chosen so that the cyclotron radius r_c along a field line is comparable to the resolution of the MCP. The cyclotron radius $r_c = m_e v_\perp / eB$ is mostly determined by the initial electron velocity $v_\perp$ perpendicular to the B-field after the atomic collision. It can be estimated that 90 % of these electrons are emitted with kinetic energies below 50 eV, resulting in $r_c < 100$ μm. A well-defined B-field uniformity is required along the full path of the secondary electrons from the interaction point to the MCP (up to 100 mm) to yield an undistorted image of the beam. To estimate the possible distortion due to the beam space-charge (via $\mathbf{E}_{SC} \times \mathbf{B}$-drift) and the residual B-field non-uniformity, numerical calculations of the electron trajectories are required, see e.g. [12]. Different magnet designs have been realized, using either electro-magnets [10] or permanent magnets [13, 16].

Operating an IPM with an electron detection scheme the residual gas ions hit the electric field electrode opposite to the MCP. Special care has to be taken to prevent surface-emitted electrons reaching the MCP, either by a special electrode-coating by e.g. NEG-material or by installing a negatively biased grid in front of the electrode.

One important application is the alignment of the electron- or stochastic cooling process [15]. As displayed in Fig. 8, electron cooling is applied to stack the beam via iterative injections. Other applications are the monitoring of the beam behavior during emittance blow-up due to intra beam scattering, necessary crossing of tune resonances or a horizontal-vertical coupling due to skew quadrupoles. For these processes significant changes of the transverse profile are slow compared to the revolution period, therefore a time resolution of ms is sufficient and the transverse profile can be averaged over many turns. The high spatial resolu-

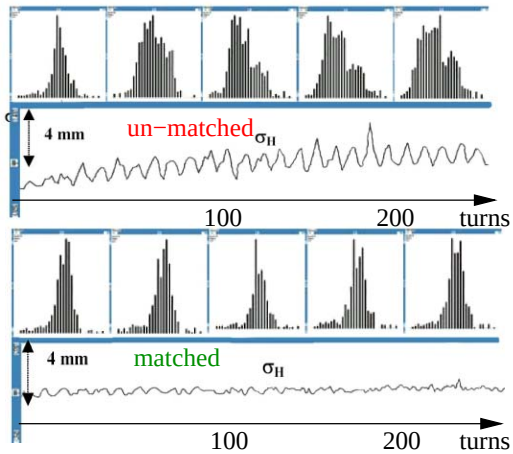

Figure 9: Horizontal beam evolution on a turn-by-turn basis and the associated rms beam width for an un-matched and matched case [10].

tion by a phosphor screen anode and a CCD camera is well suited for this application.

But also fast processes must be monitored on a turn-by-turn basis [10, 13, 16]. An example is the control of the injection matching into a synchrotron as displayed in Fig. 9. If the orientation of the injected transverse emittance (as given by the transfer beam line setting) does not correspond to the values at the synchrotron injection point, damped beam width oscillations occur leading to an emittance blow-up of the stored beam. A matched setting of the transfer line lattice, controlled by the non-destructive IPM, is required to achieve high brilliant beams. For turn-by-turn measurements during the accelerating cycle special HV-switching techniques for the MCP have to be applied to overcome the regular count rate limitation (typically 10^6 counts per second in the stationary case) and enabling a measurement with sufficient statistics of at least 100 events within one turn (i.e. down to 1 μs), see e.g. [16].

At transfer lines the residual density is orders of magnitude larger. In particular, behind a LINAC the ionization rate can be large enough to measure this ionization directly with sensitive current-to-voltage amplifiers. An MCP is not required for this application reducing the mechanical efforts drastically.

COMPARISON BETWEEN BIF AND IPM

The BIF-method detects photons and no mechanical installation inside the vacuum tube is required. Commercial image intensifiers are available, and commercial data acquisition and evaluation systems can be used, reducing the amount of human resources during the development phase. The spatial resolution as given by the optical magnification of the lens system is easily changeable and can be matched to the application. A resolution of 100 μm can be reached and is sufficient for most application at a hadron accelerator. At transfer-lines the residual gas density is relatively large and therefore the amount of detectable photons is higher than at synchrotrons. But compared to the detection of ionization products the photon yield is reduced by at least one order of magnitude because particular levels have to be excited for the emission in the optical range. Only those photons, which are emitted toward the camera can be detected, resulting in a solid angle of only $\Delta\Omega \sim 10^{-4}$. A further reduction is required by a limited iris setting of the optics to ensure a sufficient focal-depth. Background contribution due to neutrons or γs hitting the photo-cathode might occur for some beam settings. The lack of radiation hardness for the CCD camera electronics might be a disadvantage, because for an effective light collection the distance to the beam can not be very large.

The IPM detects all charged residual gas particles due to the applied electric field, but the complex and expensive installation of the electric field generation and the MCP detector inside the vacuum tube is required. For intense beams a magnetic field must guide the residual gas electrons toward the MCP. Its design might be a challenge due to the uniformity requirement and the anomalous large clearance of up to 400 mm. The spatial resolution of $\sim$ 100 μm as given by the MCP channel size is sufficient for most applications at a hadron synchrotron. Resolution limits are presently investigated by the comparison to a wire scanners [17]. At synchrotrons the vacuum pressure has to be much lower compared to transfer-lines. Therefore the $\sim 10^5$ times larger signal strength for the IPM (comparing 'single particle detection' in both cases) is required to enable sufficient time resolution. In particular, IPMs offers the possibility to perform turn-by-turn profile measurements on a μs time scale, which has not been demonstrated with BIF so far.

REFERENCES

[1] R.H. Hughes et al., *Phys. Rev.* **123**, 2084 (1961), L.W. Dotchin et al., *J. Chem. Phys.* **59**, 3960 (1973).
[2] M.A. Plum et al., *Nucl. Instrum. Meth* **A 492**, p. 42 (2002).
[3] see e.g. www.proxitronic.de.
[4] J. Dietrich et al., *Proc. ICFA-Hadron Beams 05,Bensheim* (2004).
[5] D.P. Sandoval et al., *Proc. Beam Instrum. Workshop, Santa Fe, AIP Conf. Proc. 319*, p. 273 (1993).
[6] P. Forck, A. Bank, *Proc. EPAC 02*, Paris, p. 1885 (2002) and A. Bank, P. Forck, *Proc. DIPAC 03*, Mainz, p. 137 (2003).
[7] G. Burtin et al., *Proc. EPAC 2000,Vienna*, p. 256 (2000).
[8] P. Ausset et al., *Proc. EPAC02, Paris*, p. 1840 (2002).
[9] R.H. Hughes et al., *Phys. Rev.* **A 1**, 1424 (1970), R.H. Hughes et al., *Phys. Rev.* **164**, 166 (1967).
[10] G. Ferioli et al., *Proc. DIPAC01*, Grenoble, p. 201 (2001), G. Ferioli et al., *Proc. DIPAC03*, Mainz, p. 116 (2003), C. Fischer et al., *Proc. Beam Instrum. Workshop, Knoxville, AIP Conf. Proc. 732*, p. 133 (2004).
[11] S. Barabin et al., *Proc. EPAC04*, Lucerne, p. 2721 (2004).
[12] D. Liakin et al., *Proc. DIPAC05*, Lyon (2005).
[13] P. Cameron el al., *Proc. PAC99*, New York, p. 2114 (1999), R. Connolly et al., *Proc. PAC01*, Chicago, p. 1297 (2001).
[14] H. Refsum et al., *Proc. DIPAC05*, Lyon (2005).
[15] T. Giacomini et al., *Proc. Beam Instrum. Workshop, Knoxville, AIP Conf. Proc. 732*, p. 286 (2004), T. Giacomini et al., *Proc. DIPAC05*, Lyon (2005).
[16] J.R. Zagel et al., *Proc. PAC01*, Chicago, p. 1303 (2001), J.R. Zagel et al., *Proc. PAC99*, New York, p. 2164 (1999).
[17] C, Fischer et al., *Proc. EPAC04*, Lucerne, p. 2478 (2004).

BEAM DIAGNOSTICS AT THE HIGH POWER PROTON BEAM LINES AND TARGETS AT PSI

R. Dölling, R. Rezzonico, P.-A. Duperrex, U. Rohrer, K. Thomsen, R. Erne, U. Frei, M. Graf, U. Müller, Paul Scherrer Institut, Villigen-PSI, Switzerland

Abstract

The protection of beam lines, targets and target windows from proton beam powers of 0.13 MW (@72 MeV) and 1.1 MW (@590 MeV) is based on beam loss monitors, current measurements at collimators and 4-sector apertures as well as the measurement of the current transmission. The new targets also use harps or an optical observation of the thermally emitted light from a metal sieve in front of the target. Online beam centering using inductively coupled position monitors is needed for continuous operation. Wire profile monitors are used temporarily for setup and tuning. The high radiation background requires radiation hard devices, shielding, a suitable handling of the components and remotely positioned electronics.

INTRODUCTION

High power proton beams of 590 MeV are produced at PSI using two consecutive cyclotrons. The beam current has increased over the years to 1.9 mA. After the passage of the graphite targets M and E for meson production, the remaining ~1.3 mA of beam is transported to the spallation neutron source "SINQ", which uses a solid target of stainless steel and lead. Beam is delivered for ~4800 hours per year for ~400 users [1]. A liquid Pb-Bi target "Megapie" is scheduled for 2006 and an additional beam line with a high power target "UCN" for ultra cold neutron production should start operation in 2007.

Melting of beam line/cyclotron components by mis-steered beam can occur within 10 ms @590 MeV or 1 ms @72 MeV (depending on the beam diameter). Such an event could cause 2 to 300 days of shutdown for replacement, repair or remanufacturing of components, since many built-in parts are not easily accessible or deeply buried under densely packed shielding. Furthermore, there are no spare parts for many components, and sometimes there is a lack of documentation, drawings and the knowledge of exact dimensions. Melting of the Megapie target and window by an overly concentrated beam could also cause a long shutdown. This can occur if the beam misses Target E, while the beam will then not be scattered, resulting in an increase of current density at the target and window by a factor ~25, which will melt after ~170 ms. Hence, redundant systems are needed for the fast (<1 ms) generation of interlocks. Therefore, the detector signals are evaluated in the readout electronics and interlock signals are hard wired to the control system.

26		43	15	1	54	30	wire profiles (1 direction)	x		
10							light profiles (1 direction)	x		
						2	harps (both directions)	x		x
		38	14		31	34	bpms (1 direction)	x	x	
1 (DCCT)		3	2		6	1	current monitors	x	x	x
2	1	3	2	2	1		stoppers/dumps	x		
34	23	32	10	18	33	3	collimators (fixed/movable)	x	(1)	x
		2	2	2	17	6	segmented aperture foils (mostly 4 sectors)	x		x
	8	23	9	14	30	15	ionisation chambers	x		x
	5			5			wire probes	x		
	8	1		13			phase probes	x	x	
	1	1		1			time structure			
					1		glowing sieve			x
								setup & tuning	online beam adjust.	machine protection

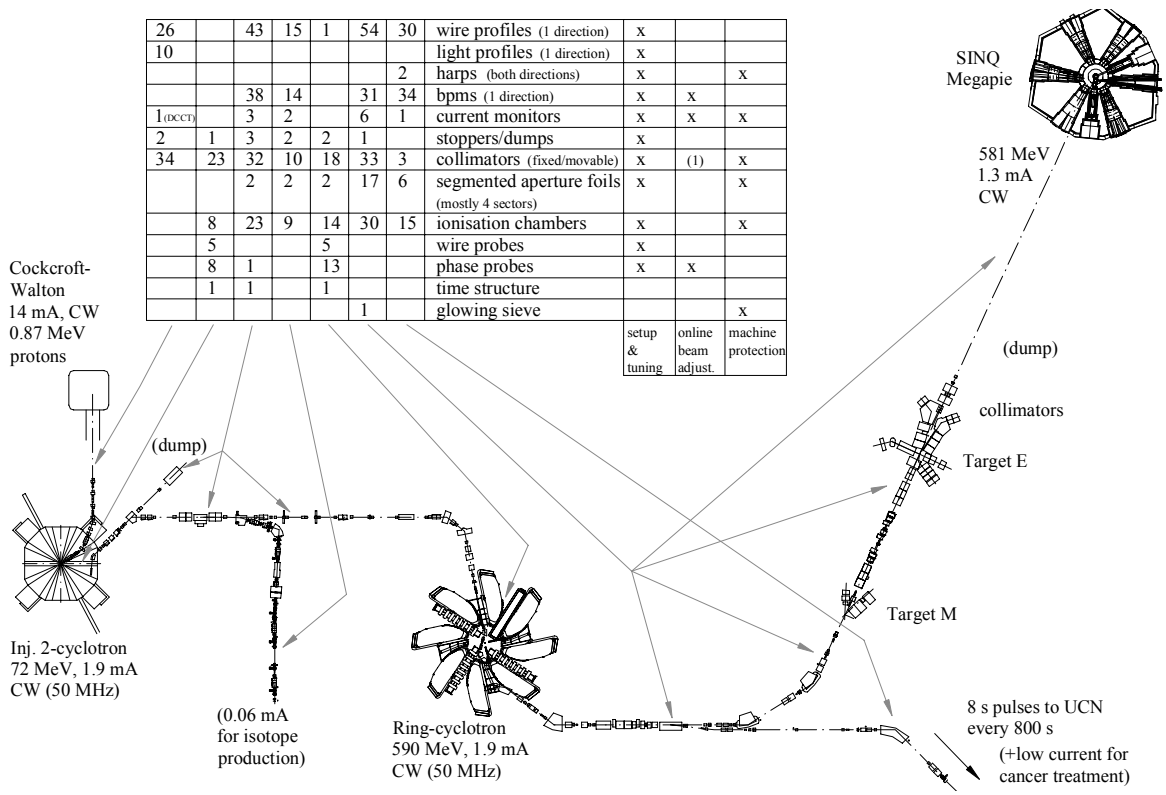

Figure 1: Overview of high power proton facility and diagnostics used.

The diagnostics used for protection, setup and operation are listed in Fig. 1. Most of the systems were introduced decades ago and have since been improved several times.

MACHINE PROTECTION

Collimators and aperture foils

Thick collimators of copper or carbon and thin (mostly 4-segment) nickel or molybdenum aperture foils with current measurements are used for the protection of subsequent components. Additional foils at a bias of +300V are placed adjacent to one or both sides of the foils to remove the secondary electrons (yield ~0.04). The collimators (and sometimes even the vacuum chambers) are cooled if losses occur permanently. The collimators are also used for beam shaping and the signal changes (together with those of the loss monitors) provide useful information for beam setup and tuning.

Loss Monitors

Simple ionisation chambers, formed by two interleaved stacks of metal sheets for high voltage and signal, filled with ambient air are placed next to the beam [2].

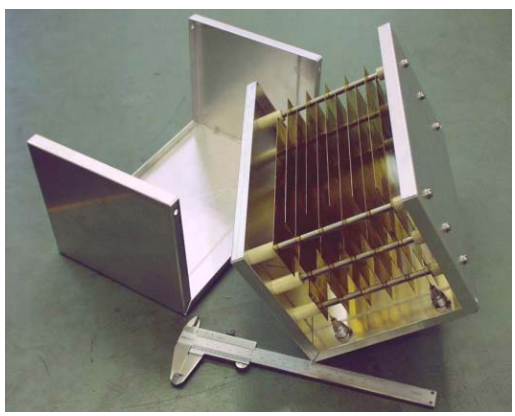

Figure 2: Ionisation chamber (bias +300V, volume 2 liter, separation of sheets 1 cm, 1 nA signal corresponds to a dose rate of ~1.3 Gy/d). Ring-shaped chambers for placement around the beam tube and cylindrical chambers for introduction into concrete shielding are also used.

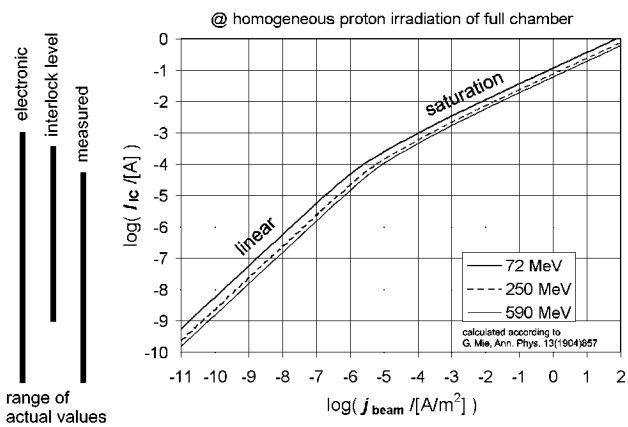

Figure 3: The response of the ionisation chamber is linear in the used regime [3].

Current Monitors and Transmission

Capacitively loaded quarter-wave coaxial resonators working at the double bunch frequency are used as current monitors [4]. The long-term stability of the current reading is limited due to temperature effects in the resonator (±1%), the long cables (±2%) and the electronics (±1%). Hence, calibration to the beam dump current is regularly performed. During this process, the loss monitors are observed in order to ensure that the losses are "correctly low".

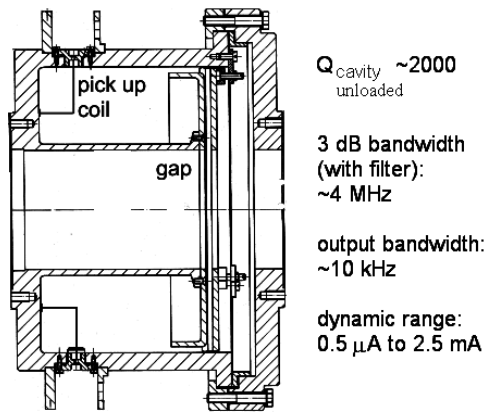

Figure 4: Current monitor.

The transmission is determined by comparing the currents of two or more current monitors (Fig. 5) [5, 6]. The currents are filtered with a current dependent time constant (110 ms to 10 ms for 0 to 1.5 mA) to reduce noise. An interlock is generated if the actual losses deviate significantly from the "usual losses" (Fig. 5, upper left diagram).

In addition, another type of transmission measurement is done around Target E: The signals of the downstream loss monitors are roughly proportional to the beam current and can be used instead of the second current monitor. Hence interlocks are generated if the losses are too low [6]. This system is applied at beam currents above 100 μA and has a response time of ~1 ms.

SPALLATION TARGET PROTECTION

Dispersive Shift onto a Collimator

In the case that the beam misses Target E, the transmission measurements will respond. Another redundant technique was implemented for the same situation: The beam fraction missing the target undergoes no energy degradation. Hence, it follows a different path in a dispersive transport section where it is intercepted by a collimator. The current readings from the collimator and a nearby loss monitor cause an interlock, even if only 0.1% of the beam misses the target [7].

Harps

4 and 8 meters in front of the UCN target, retractable harps will be placed for online supervision of beam size and position. The profiles result from the measured

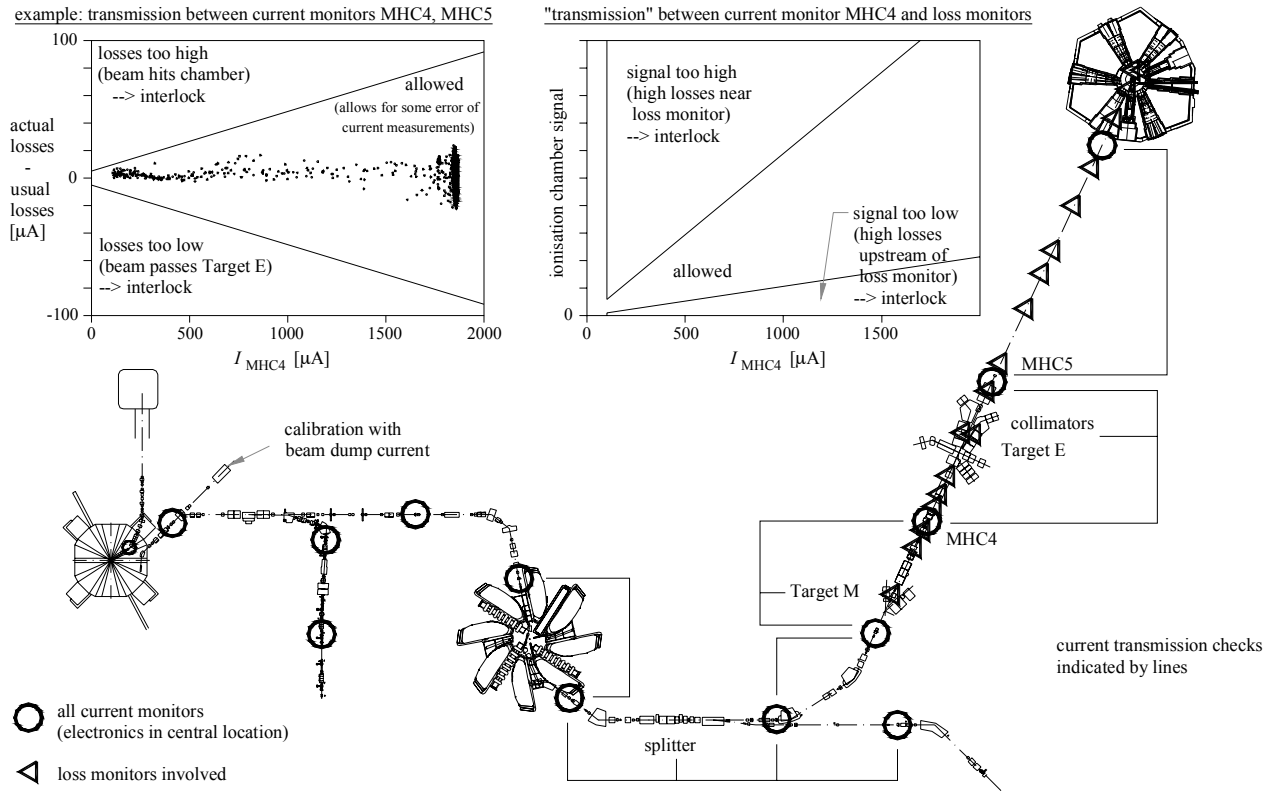

Figure 5: Transmission measurement with current monitors (upper left diagram, which also shows experimental values over a period of 3 hours) and with current and loss monitors (upper right diagram).

secondary emission currents from 16 horizontal and 16 vertical wires. 16 intermediate diagonal wires are biased to +300V for electron pulling. 40 µm molybdenum wires are used although the operation temperature will rise nearly to the onset of thermionic emission.

Glowing Sieve

The most direct control of the beam current density in front of the spallation source target is provided by video observation of the thermal radiation from a tungsten sieve placed in the beam tube and heated by the beam.

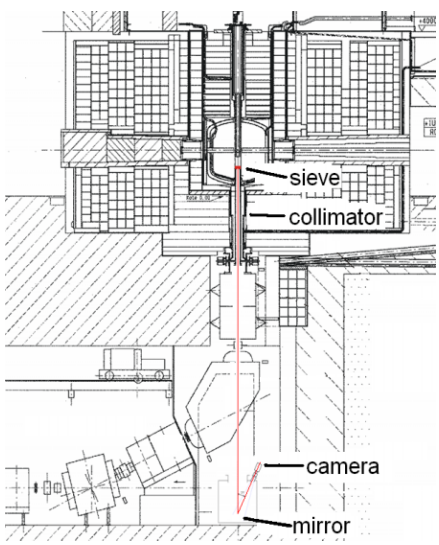

Figure 6: Glowing sieve under the spallation target.

This device has been developed and tested recently [8]. The light from the sieve passes several meters through the beam pipe and is projected by a parabolic mirror, as the only optical element, onto the sensor of a chalnicon radiation hard camera (Fig. 6).

For temperatures above 1000 °C, which are reached already at nominal beam current and size, a signal is detected above the background level which increases rapidly with beam current density (Fig. 8).

Figure 7: Sieve woven from diameter 0.1 mm and 0.3 mm tungsten wire.

Using the total signal, the system is sensitive and fast (~40 ms) enough to protect the Megapie target from an overly concentrated beam. In addition, the position resolution of ~±1 mm is sufficient to detect the beam shift associated with a beam fraction missing the Target E.

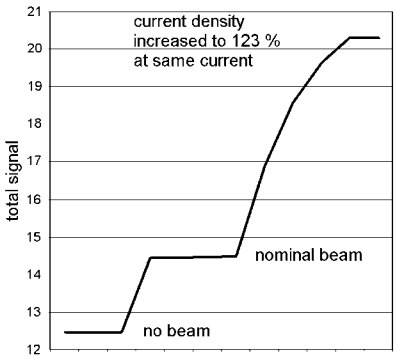

Figure 8: Response to beam current density. The temporal dependency (horizontal axis) stems from the beam adjustment and not from the detector system.

MACHINE OPERATION

BPMs

The frequent (~20 to 500 per day) sparking of the electrostatic septa, used for injection and extraction in the cyclotrons, causes beam trips. The beam is switched off and the current then ramped up in ~20 s. The beam optic is current dependent due to space charge effects and due to the way the beam current is regulated by cutting into the beam with a moving collimator. An automatic beam centering is therefore required and is provided by BPMs and steerers.

The BPMs use single turn coils to couple inductively to the bunched beam (Fig. 9). A preamplifier is located ~1 m from the BPM in the vault. At present, the device works with beam currents above ~5 μA. With an output bandwidth of ~10 Hz, a centering response of ~1 Hz is reached. The position accuracy is ~±1 mm over the full current range. New electronics based on digital receivers are under development with a larger dynamic range down to 0.5 μA and larger bandwidth of ~10 kHz.

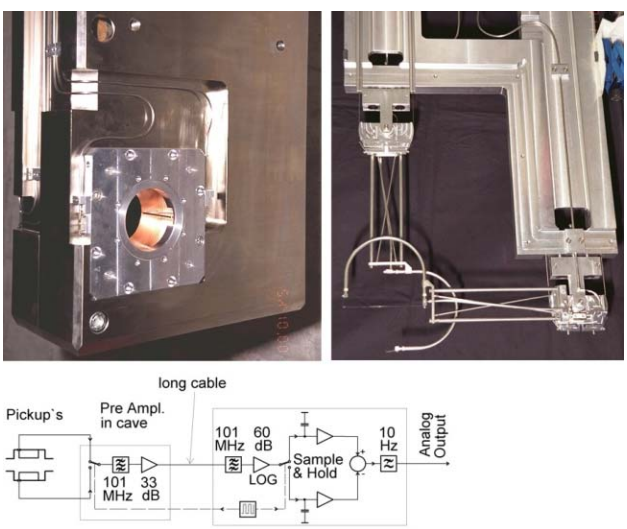

Figure 9: left: BPM, section for the horizontal position (only one coil visible) mounted in shielding. Another section placed behind it is used for the vertical position. The space in between is used for wire monitors (right).

Profile Monitors

The wire monitors measure the secondary emission current from (one or two) 40 μm molybdenum wires, 33 μm carbon fibres or 25 μm molybdenum foils. In the 72 MeV transfer line, thermionic electron emission can occur at small beam diameters, leading to higher signal currents and an interlock to prevent the wire from melting. In the 0.87 MeV injection line, only a 15% duty cycle of the beam is possible without damaging the wires. Here, additional profile monitors based on the fluorescence of the residual gas are used [9].

ELECTRONICS

Nearly all the electronics are located outside the vaults. Hence, no radiation damage occurs and access for service is easy. The drawback is long cables (30 to 300 m).

All the low current measurements are done with logarithmic amplifiers, which, in the newer versions, span a range from 10 pA to 10 mA. The bandwidth is current dependent (from ~30 Hz at 10 pA to ~30 kHz above 10 nA). 16 or 32 channels with up to 4 separate grounds have been realized in single-slot CAMAC or VME modules [10]. Cables with good shielding and low microphonic noise are important as well as the prevention of ground loops [3].

All the newer electronics are divided into dedicated front ends with signal pre-processing and AD-conversion, and universal back ends with digital processing and bus connection. The signals are simultaneously sampled at a rate of the order of 1 to 10 kHz. Evaluation and interlock generation (hardwired to the control system) are performed in the same time. Information on the current status and the last interlock can be read or interlock levels can be changed via bus. Some modules have external and internal trigger functionality and storage and readout of up to 8 ksamples/channel.

RADIATION AND HANDLING

The main beam losses are roughly (@1900 μA): at 72 MeV: 0.5 μA at extraction of Injector 2, 5 μA at the following beam cleaning, 0.5 μA at injection into the ring cyclotron, and at 590 MeV: 0.5 μA at extraction of the ring cyclotron, 0.3 μA (average) at the following splitter, 28 μA at Target M and 560 μA at Target E.

At locations with very high radiation levels during operation, only metal and ceramic parts are used, e.g. helicoflex or aluminium edge seals, mineral insulated cables, etc. It appears that the observed damage to these components is not due to radiation but is of thermal (beam power) or corrosive (cooling water) nature. In accessible places with lower radiation levels, other materials are also in use: epoxy parts, lubricated bearings, motors, potentiometers, scintillators, radiation hard glass windows, viton seals (which get hard but seldom leak if not moved), standard cables (which get brittle).

In the areas accessible for service, the background radiation can be of the order of mSv/h with higher local

hot spots. The background decays to half in approximately 6 hours. Diagnostics, as well as other components, are designed to be fast demountable (few screws, lever mechanisms, guiding rods), easy to handle (no sharp edges, countersunk hexagon socket screws, weak parts guarded, grips, etc.) with a minimum of personnel (local cranes, lifting gear, special trolleys) and easy to clean (smooth surfaces). Nevertheless, reliability is the most important property.

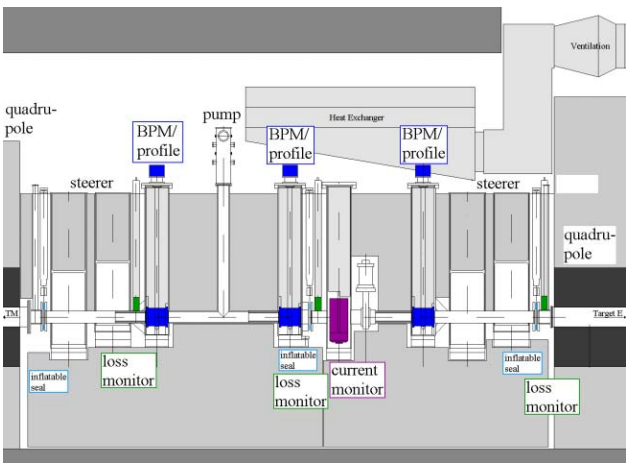

Figure 10: Closely shielded components.

Figure 11: Shielded transport box [11].

In the target regions, the concept of closely shielded components has been applied [12]. After removing 4 m of concrete shielding, access is given to a service level ~2 m above the beam. The diagnostic components are placed under in-vacuum shielding blocks in chimneys (vacuum chambers with seals at the top). The chimneys are densely surrounded by shielding blocks. Drives, feedthroughs, pumps, etc. are located on top and can be easily serviced (Fig. 10).

The components can be extracted vertically into a shielded transport box, after connecting to it with individual adapters (Fig. 11), and transported to a remote handling facility. Even the vacuum chambers, which are connected to each other by inflatable metal seals, can be removed, but this could take some weeks.

REFERENCES

[1] U. Schryber et al., "High power operation of the PSI-accelerators", Proc. Cyclotrons 1995, pp. 32-38

[2] J. Zichy, Ch. Markovits, L. Rezzonico, "The design, assembly and performance of the SIN beam transfer line", Proc. Cyclotrons 1975, pp. 306-311

[3] R. Dölling, "Profile, Current and Halo Monitors of the PROSCAN Beam Lines", BIW04, AIP Conf. Proc. 732, pp. 244-252

[4] R. Reimann M. Rüede, "Strommonitor für die Messung eines gepulsten Ionenstrahls", NIM 129 (1975) pp. 53-58

[5] L. Rezzonico, "Transmissionsmessgeräte für Protonenstrahlen", PSI-Internal Note, April 1, 1996, and P.-A. Duperrex, "Transmissionskontrolle und neues Target E", PSI-Internal Note, October 5, 1996, and U. Müller, "Verbesserungsvorschläge für die bestehenden Strommonitore", PSI-TM 84-05-02, 2002

[6] U. Rohrer, "The multilevel protection system for the vacuum chambers of the high-intensity 590 MeV proton beam lines", PSI Annual Report 2003, Vol. VI, pp. 45-48

[7] U. Rohrer, "First beam tests with the new slit collimator in the proton beam line to SINQ", PSI Annual Report 2004, Vol. VI, pp. 23-26

[8] K. Thomsen, "VIMOS, a novel visual device for near-target beam diagnostics", Proc. ICANS-XVII, Santa Fe, 2005, to be published

[9] L. Rezzonico, SIN Annual Report 1986, p. 7, and "Beam diagnostics at SIN", Proc. Cyclotrons 1987, pp. 457-460, and "A profile monitor using residual gas", Proc. Cyclotrons 1989, pp. 313-316

[10] P.-A. Duperrex et al., "Latest diagnostic electronics development for the Proscan proton accelerator", BIW04, AIP Conf. Proc. 732, pp. 268-275

[11] J. Züllig, A. Strinning, A. Geissler, "A new transport flask for PSI beam line components and the UCN collimator", PSI Ann. Rep. 2004, Vol. VI, pp. 76-77

[12] H. Frei et al., SIN Annual Report 1981, pp. 46-47, and SIN Annual Report 1984, pp. 11-17

BEAM STABILITY IN SYNCHROTRON LIGHT SOURCES*

Glenn Decker
Advanced Photon Source, Argonne National Laboratory
Argonne, IL 60439, USA

Abstract

Numerous third-generation light sources are now in a mature phase of operation, and several new sources are under construction. Submicron beam stability is being achieved routinely at many of these light sources in terms of both AC (rms 0.1 - 200 Hz) and DC (one week drift) motion. This level of stability is a necessary condition for the success of x-ray free-electron lasers such as the Linac Coherent Light Source (LCLS) at Stanford or the European XFEL project. The different methods for addressing this problem at different laboratories—involving various combinations of passive noise identification and suppression, feedback, and feedforward— together with accomplishments to date will be discussed.

INTRODUCTION

In the past ten years, there has been a remarkable increase in the number of accelerator facilities dedicated to the generation of synchrotron radiation. An indicator of this is the recent launch of the web site lightsources.org [1], where 59 separate synchrotron radiation facilities around the world are now listed. The light source beam stabilization field is similarly reaching a mature phase, as evidenced recently by a series of international workshops on beam orbit stabilization [2,3]. Numerous excellent articles have been written on the subject of beam stability in synchrotron light sources [4,5]. The emphasis here will be on trends in third- generation light sources, with indications of what will be expected for future light sources such as x-ray free-electron lasers and energy recycling linacs.

Shown in Table 1 are a set of high-level parameters for the world's operational third-generation light sources (as of June, 2005), defined to be dedicated storage rings having natural emittance below 20 nm-rad. The essential things to notice are that the particle beam tends to be flat, with horizontal beam size σ_x in the range of a few hundred microns, but with vertical beam size σ_y below ten microns in many cases. Since beam stability requirements are typically stated as a fraction like 5 or 10 percent of beam size in a given frequency band, it is clear that submicron stability is a common requirement. The vertical angular divergence of these particle beams is at the few microradian level, approaching the diffraction limit for many of these machines. At the Advanced Photon Source (APS), the goal for vertical pointing stability is to limit beam motion to less than 220 nanoradians rms in a frequency band ranging from 0.016 Hz (i.e., one minute) to 200 Hz, while the long-range pointing stability goal is 0.5 microradians p-p, for time scales extending from one minute to one week.

Table 1: Properties of Operational Third-Generation Synchrotron Light Sources.

	Energy (GeV)	Horizontal Emittance (nm-rad)	Vertical Emittance (pm-rad)	σ_x (mm)	σ_y (mm)	Top-up
SPring-8	8	6	14	390	7.5	yes
APS	7	2.5	25	271	9.7	yes
ESRF	6	4.0	30	380	14	planned
SPEAR-3	3	12 / 18	60 / 90	350 /430	25 / 31	planned
CLS	2.9	15	200	326	30	planned
Pohang LS	2.0 / 2.5	12.1 / 18.9	12 / 19	350 / 434	22 / 27	no
SLS	2.4	5	40	86	6	yes
ELETTRA	2 / 2.4	7 / 9.7	< 70 / 97	241 / 283	15 / 16	planned
ALS	1.5 / 1.9	4.2 / 6.75	200 / 150	240 / 310	27 / 23	planned
BESSY-II	1.72	6	180-240	290 / 76	27 / 17	planned

Beam stabilization efforts in general must account for motions in all six phase-space dimensions, on time scales ranging from the bunch repetition rate up to months. Not only beam centroid motion, but also beam size and even higher-order moments of the phase-space particle distribution must be considered. While historically beam stabilization has been defined in terms of the source, i.e., the particle beam properties, it is becoming clear that many properties of the photon beam cannot be directly controlled using particle beam diagnostics alone. As a

*Work supported by U.S. Department of Energy, Office of Basic Energy Sciences, under Contract No. W-31-109-ENG-38.

result, new photon beam diagnostics have been developed and are increasingly being included in accelerator feedback systems. While a stable source is imperative, many experiments require stability beyond what is possible using traditional particle beam diagnostics and closed- orbit feedback systems. Taken to the logical limit, stability requirements depend in detail on the beamline design and experimental arrangement, which can only be properly studied using detailed ray tracing extending from the source through all beamline optics to the sample [6].

Top-up operation, defined to be operation using injection with beamline shutters open to regulate stored beam current at the level of approximately 1% or better, is also indicated in Table 1. This operating mode is very desirable to synchrotron radiation users since it stabilizes the heating effects on beamline components such as mirrors and monochromator crystals. From the machine side, a similar stabilization of vacuum chamber components exposed to synchrotron light is realized. This technique was pioneered at the APS and first put into operation in the year 2000. Since that time, most existing and planned third-generation light sources use or are planning to incorporate top-up into machine operation. A strong secondary motivation for top-up is that it allows the use of extreme lattices and / or bunch fill patterns with very poor lifetime.

A list of light sources presently under construction is shown in Table 2, including the two hard x-ray free-electron laser projects, which will be moving to a new level of beam stabilization technology. Many new ring-based projects are planned with energies near 3 GeV, which take advantage of new high-quality insertion device technology in order to deliver hard x-rays.

Table 2: Light Sources Under Construction

	Energy (GeV)	**Horizontal Emittance (nm-rad)**
Petra III	6	1
SSRF (Shanghai)	3.5	4
Diamond	3	2.74
Soleil	2.75	3.74
Australian	3	7
LCLS	13.6	0.045
XFEL	20	0.036

SOURCE IDENTIFICATION

Listed in Table 3 are the types of disturbances that every synchrotron light source is subject to, along with approximate time and length scales where they are most pertinent. Ground settlement can be quite large, up to fractions of a millimeter; however, it is primarily short-range differential settlement that impacts photon beam alignment. This is most easily compensated by extending instrumentation out along the beamline, since position monitoring near the source is insensitive to motion of the beamline relative to the accelerator. The effects of earth tides are significant, even for small machines such as the Swiss Light Source (SLS), which must adjust the rf frequency to compensate for variations in the ring circumference.

Table 3: Sources of Beam Motion

Source	**Time Scale**	**Length Scale**
Ground Settlement	weeks to months	10s to 100s of μm / year
Earth Tides	hours	~30 μm / km
Air / Water Temperature	minutes to days	~10 μm / degree C
Beam-induced Heating	minutes to hours	10s of μm / fill from zero
Insertion Device Parameter Changes	10s of ms to 10s of seconds	10s of Gauss-cm
Stray Fields	0.1 seconds to hours	Variable
Magnet Power Supply Noise	10s of μs to 10s of ms	Design-dependent
Ground Vibration	10 ms to 1 second	10s of nm
Magnet Vibration (from resonance)	10 ms to 1 second	100s of nm
RF System	μs to minutes	10s of μm
Impedances / Wakefields	ns to μs	10s of μm

Regulation of water and air temperature at the level of a fraction of a degree C is becoming common and almost mandatory to assure mechanical component stability at the submicron level, since the thermal expansion coefficient of most materials is on the order of 10^{-5} / degree C. In order to reduce susceptibility to small temperature changes, critical component positions can be carefully monitored using detectors placed on stable supports. At ELETTRA, capacitive sensors placed on carbon fiber pillars are used to monitor the position of high-sensitivity small-gap beam position monitor pickup electrodes [7], which are mounted separately. A similar technique is planned for the Diamond machine in the UK.

Synchrotron radiation heating and wakefields account for a very significant potential source of thermally driven component motion. Extensive instrumentation on the girders at the SLS show direct correlations between the amount of stored beam current and beam position monitor location relative to an adjacent quadrupole magnet at the few-micron scale [4]. This effect was eliminated with the advent of top-up operation when the total stored beam current was regulated at the level of +/– 0.15%.

User-variable insertion devices not only produce steering, but in addition are responsible for an edge focusing effect, which disrupts the periodicity of the lattice, causing undesirable beam size changes. Two approaches are generally taken to address the variable bulk properties of insertion devices, and frequently some combination is used. Since these effects are generally

reproducible, feedforward algorithms are used to power nearby steering correctors and / or quadrupole magnets in response to insertion device parameter changes [8]. Extreme care is required in the generation of lookup tables, since systematic errors such as beam position monitor noise can cause problems. The second approach is the use of closed-orbit feedback. Slightly different approaches are required, depending on the time scale of the parameter change. For mechanical variables such as undulator gap changes using motor drives, orbit correction algorithms operating with update rates as low as a few Hz are generally sufficient to compensate for steering effects. Higher-frequency excitations, arising from switched electromagnetic devices for example, require fast feedforward in addition to high-frequency (few-kHz update rate) closed-orbit feedback [9].

In addition to affecting global machine properties such as the closed-orbit and lattice functions, insertion devices produce a local, internal steering effect, which places a fundamental limit on the pointing stability possible using charged particle beam position monitors alone. Shown in Figure 1 are particle beam trajectories derived from numerically integrating Hall probe magnetic field maps of one particular APS insertion device. Data corresponding to four different magnetic field strengths, determined by the device gap, are shown. In each case, the entrance angle (at the left-hand side of the plots) was numerically adjusted to constrain the average slope through the bulk of the device to remain parallel to the horizontal axis. The net result of this is that the angle and displacement of the beam at the exit vary considerably as the gap is varied. What this means is that the photon beam generated by the undulations interior to the device are not colinear with the particle beam trajectory *as determined by rf beam position monitors located external to the device*. Quantitatively, careful fabrication of insertion devices can limit internal trajectory errors at the few-micron / few-microradian level; however, detection of the insertion device photons directly is necessary if one is interested in gap-independent submicroradian-level pointing stability.

The primary sources of stray magnetic fields affecting the beam are magnet power supplies with time variable outputs. Periodic ramping of injector machines produces on-orbit fields in the main storage ring, which are usually difficult to control without orbit feedback. The pulsed injection magnets together with the details of the injection process play a significant role during top-up operation, causing beam size and centroid transients. Careful magnet design and fast feedforward schemes are generally employed to reduce these effects [10,11]. Power supply ripple at harmonics of the mains frequency is generally addressed with special harmonic suppression algorithms built into a fast orbit feedback system [12].

Human-made sources of ground motion generally occur in the frequency range from a fraction of a Hz up to 50 or 100 Hz maximum. These motions have rms amplitudes typically on the order of some 10s of nanometers [13]. An apparently stiff girder assembly can have a vibrational resonance at quite low frequency (7 Hz at ESRF, 10-12 Hz at APS). The effect of this is to amplify ground motion, in some cases by a factor of ten or more. Further aggravating the situation, vibrating quadrupole magnets can result in an additional order of magnitude of particle beam motion, a consequence of the very strong focusing needed for these low-emittance machines. While girder resonances cannot be completely eliminated, the lowest mode frequency can be increased significantly with careful mechanical engineering. Since the spectrum of ground motion generally falls off sharply with increasing frequency, it is expected that raising the lowest mode frequency will reduce particle beam motion accordingly. For the new sources Soleil and Diamond, the lowest mode frequencies have been moved to above 27 Hz [2].

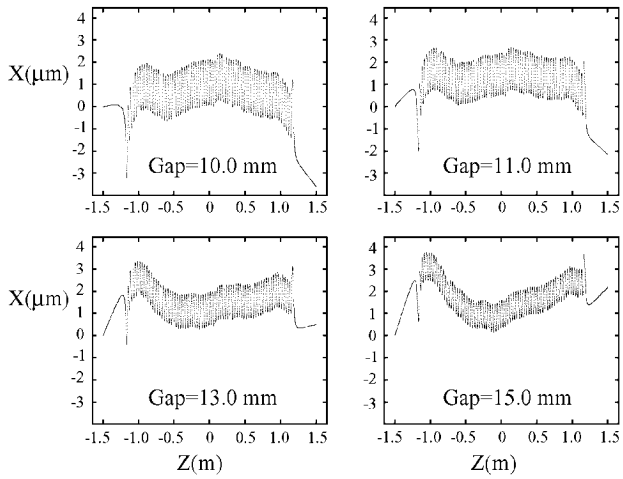

Figure 1: Particle beam centroid trajectory through an undulator as the gap is varied (APS undulator A).

BEAM POSITION MONITORING

Processing electronics for beam position monitoring were advanced significantly by the advent of the Bittner / Biscardi multiplexed receiver in the late 1980s [14]. This design was further developed by J. Hinkson at ALS and K. Unser with Bergoz Instrumentation, from whom a refined version of the design is commercially available [15]. Recent advances in fast sampling and FPGAs have led to systems with micron-scale resolution on a turn-by-turn and even bunch-by-bunch basis [16]. Long-term stability of the electronics is now rivaling and often surpassing the overall mechanical stability of pickup electrode assemblies [17].

Small-aperture capacitive button pickup electrodes are most commonly used for beam position monitoring near the insertion device source points. These are generally placed on stable support structures, sometimes with mechanical position diagnostics added. The "rotated button geometry," shown schematically in Figure 2, is used to maximize signal strength while at the same time providing maximum position sensitivity, albeit with increased nonlinearity in the horizontal response [18]. APS, ESRF, and ELETTRA use this geometry. Inductive matching networks are also sometimes placed at the

button, converting it into a resonant tank circuit to further boost signal strength and reduce reflections [19].

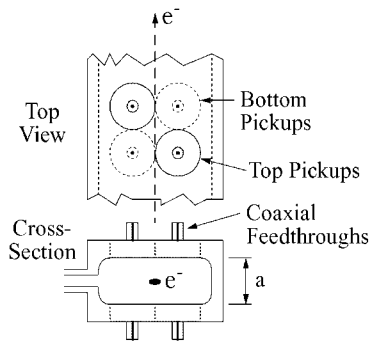

Figure 2: Rotated-button pickup electrode geometry.

For ultrahigh resolution, a cavity BPM based on the excitation of dipole modes will be used for the LCLS x-ray free-electron laser project. This technology, originally developed for linear colliders, should allow submicron resolution and repeatability on a single-pulse basis [20]. Shown in Figure 3 is a cross-sectional view of a recent LCLS design of this type. One of the main advantages of this design is that the signal transmitted through the waveguide is directly proportional to the product of position and intensity, relaxing the need for careful matching of receiver channels, as is commonly required for conventional BPMs based on buttons.

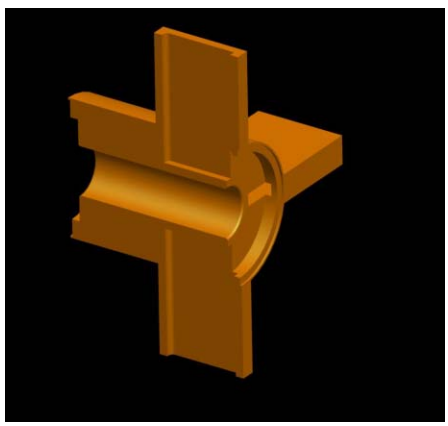

Figure 3: Cavity BPM prototype for the LCLS.

Shown in Figure 4 is a "staggered pair" photoemission-based beam position monitor for detecting bending magnet radiation at BESSY II [21]. Given the top / bottom symmetry of bending magnet radiation, this type of monitor is ideal for high-resolution measurements of the photon beam's vertical position. When placed far from the source point, it provides the best diagnostic to stabilize the vertical beam pointing angle, useful for time scales extending from fractions of a millisecond to weeks.

For insertion device beams, the use of this type of monitor is complicated by several factors, the most important being the presence of stray radiation background signals together with the variable nature of the insertion device radiation due to user-commanded gap changes, for example. The stray radiation background itself can also be variable, because the steering correctors used for orbit correction produce ultraviolet radiation, which can be directed down the insertion device beamline. Small orbit changes through quadrupole and sextupole magnets also contribute.

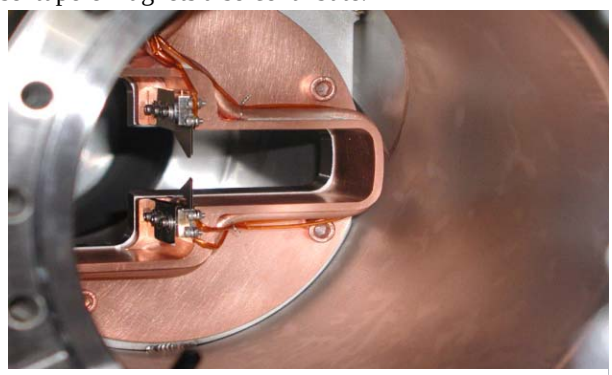

Figure 4: Bending magnet photon BPM (BESSY II).

A number of creative solutions have been implemented for dealing with this problem. One idea employs a relatively complex electron spectrometer-based device to enhance sensitivity to the undulator spectral peaks [22]. For larger machines, a realignment of accelerator components can be used to direct the unwanted stray radiation away from the photon BPM's field of view [23]. This idea has been fully implemented at the APS and is also under investigation for the 6-GeV PETRA-III project at DESY. Use of these monitors allows sub-microradian p-p stability over one-week time scales for fixed-gap operation, limited to several microradians for variable gaps, due to the internal ID steering effect.

ORBIT CORRECTION ALGORITHMS

It is generally recognized that singular value decomposition (SVD), if used correctly, is the best method for dealing with orbit correction for relatively large machines. For a square response matrix with an equal number of monitors and correctors, an "exact" correction is possible, forcing all of the monitor readbacks to be constant. If any of the monitors malfunction, the square matrix technique can actually provide a false sense of security. In this case, only careful study of the amount of activity seen on the steering correctors can be used to diagnose problems with the BPM system. It is generally a good design philosophy to use reliable monitors that are not used by the correction algorithm to validate system performance.

A more common situation occurs when the number of monitors differs from the number of steering correctors. If there are more monitors than correctors, SVD provides a solution that minimizes the rms BPM errors around the ring. If the matrix is poorly behaved, however, it may require very large steering corrector variations to achieve this. By ignoring the most inefficient eigenmodes, i.e., those requiring large effort for little gain, the system can be tuned for best performance. The selection of how many eigenmodes to retain is the essence of the SVD method. If there are more correctors than beam position monitors, SVD can provide a solution that "exactly" corrects the orbit, while at the same time minimizing the

required amount of rms corrector variation around the ring. One is still faced with the question of discerning whether or not any particular BPM is lying when using any "exact" correction scheme.

Singular value decomposition provides a solution to the spatial aspect of orbit correction. For the temporal aspect, an all-digital future is nearly here. Modern closed-orbit feedback systems will involve ultrafast BPM sampling; high-speed data networks; and a combination of local signal processing, centralized algorithm coordination, and the distribution of high-speed correction signals to local power-supply controllers with their own digital regulators. In the past, signal processing and data distribution speed limitations have dictated the construction of two or even three separate feedback systems to deal with different frequency bands. Most facilities employ a "slow" workstation software-based feedback system that uses all available BPMs and correctors, with the full response matrix and a lot of error handling capability. These DC feedback systems are generally limited in operation to have update rates of a few Hz. In addition to the DC system, a "fast" system is often operated in parallel, with an update rate of several kHz [24]. Due to processing limitations, the response matrix for these fast systems is generally much smaller than for the DC correction. Feedforward schemes have been used to prevent the fast and slow systems from interacting with each other, generating unstable performance in the overlapping frequency band [25,26]. The ideal situation is to have one unified system, operating from DC to the full available bandwidth of the steering corrector magnets, with access to all monitors and correctors. Such a system will certainly be seen in the next generation of light sources.

CONCLUSIONS

It is an exciting time to work in the field of light source stability. New facilities with submicron / submicroradian beam stability specifications will likely succeed, given recent experiences at the Swiss Light Source and SPEAR-3. Radio-frequency beam position monitoring electronics has reached a very sophisticated level, with many commercially available options. Photon beam position monitoring is becoming more important due to the advantages of sensing more directly what the experimenter is seeing.

The author would like to thank Hitoshi Tanaka (SPring-8) and Michael Böge (SLS) for initiating and continuing the excellent series of international workshops on beam stability, from which much of the material presented here was taken.

REFERENCES

[1] http://www.lightsources.org
[2] Proceedings of the Third International Workshop on Beam Orbit Stabilization – IWBS 2004, December 6-10, 2004, Grindelwald, Switzerland, http://iwbs2004.web.psi.ch .
[3] M. Green, Transcript of SRI 2001 Beam Stability Workshop, Madison WI (2001), http://src.wisc.edu/meetings/SRI2001/workshops.html .
[4] M. Böge, "Achieving Sub-micron Stability in Light Sources," EPAC '04, Lucerne, Switzerland, July 2004, p. 211.
[5] R.O. Hettel, "Beam Stability at Light Sources," Rev. Sci. Instrum. **73** (2002) 1396.
[6] Michael A. Green et al., "Beam stability: ray tracing requirements and implementations," SRI 2003, AIP Conference Proceedings 705 (2003) 601-604.
[7] D. Bulfone et al., "Exploiting Low-Gap Position Monitors in Orbit Stabilization Feedback and Feed-Forward Systems at ELETTRA", J. Japan. Soc. Syn. Rad. Res. **16** (2003) 4.
[8] T. Nakatani et al., "Scheme for Precise Correction of Orbit Variation Caused by Dipole Error-field of Insertion Device," Rev. Sci. Instrum. **76** (2005) 055105.
[9] O. Singh and S. Krinsky, "Orbit Compensation for the Time-varying Elliptically Polarised Wiggler Operating at 100 Hz," Nucl. Instrum. Methods A418 (1998) 249.
[10] L. Emery, M. Borland, "Top-up Operation Experience at the Advanced Photon Source," PAC '99, New York, NY, March 1999, p. 200.
[11] H. Tanaka et al., "Top-up Operation at Spring-8 – Towards Maximizing the Potential of a 3rd Generation Light Source," EPAC '04, Lucerne, Switzerland, July 2004, p. 222.
[12] D. Bulfone, et al., "Fast Orbit Feedback Developments at ELETTRA," EPAC '04, Lucerne, Switzerland, July 2004, p. 2604.
[13] V. Shiltsev, "Alignment and Stability of Future Machines," EPAC '96, Sitges, Spain, 1996, p. 32.
[14] R. Biscardi, J.W. Bittner, "Switched Detector for Beam Position Monitor," PAC '89, Chicago, IL, March 1989, p. 1516.
[15] Bergoz Instrumentation, http://www.bergoz.com .
[16] A. Kosicek, "LIBERA Electron Beam Position Processor," PAC '05, Knoxville, TN, to be published.
[17] V. Schlott et al., "Performance of the Digital BPM System for the Swiss Light Source," DIPAC '01, Grenoble, France, May 2001, p. 69.
[18] S. Kim, "Optimization of Four-Button BPM Configuration for Small-Gap Beam Chambers," BIW '98, AIP Conference Proceedings 451 (1998) 310-317.
[19] E. Plouviez, F. Uberto, "A Fast Local Feedback System to Correct the Beam Position Deviation in the ESRF Storage Ring," EPAC '96, Sitges, Spain, 1996, p. 1872.
[20] R. Johnson, Z. Li et al., "An X-band Cavity for a High Precision Beam Position Monitor," DIPAC '03, Mainz, Germany, May 2003, p. 196.
[21] K. Holldack et al., "Review of Emittance and Stability Monitoring using Synchrotron Radiation Monitors," DIPAC '01, Grenoble, France, May 2001, p. 16.
[22] A. Galimberti et al., "The Next Generation of Photon Beam Position Monitors for Undulator Beamlines," PAC '01, Chicago, IL, June 2001, p. 544.
[23] G. Decker, O. Singh, "Method of Reducing X-ray Background Signals from Insertion Device X-ray Beam Position Monitors," Phys. Rev. ST. Accel. Beams **2** (1999) 112801.
[24] E. Plouviez, "Upgrade of the Global Feedback of the ESRF Storage Ring," these proceedings.
[25] C. Schwartz, L. Emery, "Compensating the Frequency Deadband of the APS Real-time and DC Transverse Orbit Correction Systems," PAC '01, Chicago, IL, June 2001, p. 1234.
[26] C Steier, "Operational Experience Integrating Slow and Fast Orbit Feedbacks at the ALS," EPAC '04, Lucerne, Switzerland, July 2004, p. 2786.

DETECTION OF HARD X-RAYS IN AIR FOR PRECISE MONITORING OF VERTICAL POSITION & EMITTANCE IN THE ESRF DIPOLES

B.K. Scheidt, ESRF, Grenoble, France

Abstract

The un-used X-rays produced in each of the 64 ESRF dipoles are absorbed in so-called crotch absorbers at the end of the dipole. With 40mm of Copper + 5mm of Steel only 250uW/mrad (out of total power fan of 154W/mrad) traverse the absorber. About 20% of these ~170KeV energy X-rays are converted by a 0.5mm thick Cadmium Tungstenate (CdWO4) scintillator into visible light that is collected and focussed by simple optics on to a commercial CCD camera. This compact monitor operates in air and is situated just behind the crotch chamber. Knowing the small vertical divergence of the 170KeV photons and the distance of the source-point to the scintillator, it possible to calculate precisely the vertical electron beamsize at this sourcepoint. The light yield is enough to measure at >1KHz frequency, with a sub-micro-meter resolution of the beam position, thereby also constituting a powerful tool for beam stability measurement in the vertical plane. The principle, the practical realisation and the results obtained with a prototype since Jan.2005 will be presented.

X-RAYS TRAVERSING THE CROTCH

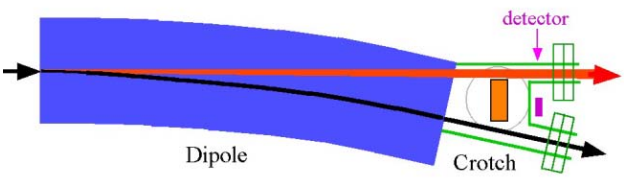

Figure 1: Position of the detector in air just behind crotch

Only 10% of the synchrotron light generated by the ESRF dipole (B=0.86T, E=6GeV) is accepted for possible passage into an X-ray beamline's front-end. The other 90% are dissipated directly by a crotch absorber (fig.1). The dipole's spectral flux characteristics (fig.2 & 3) show,

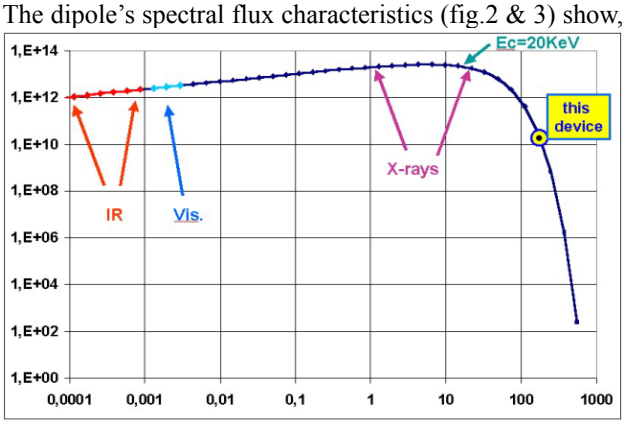

Figure 2: Dipole spectral flux (photons/sec 0.1%bw mrad)

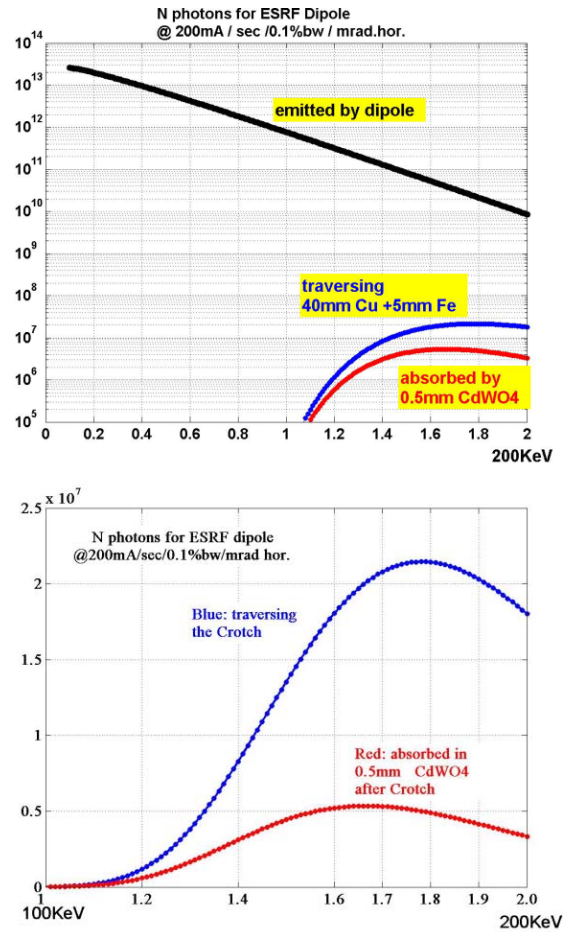

Figure 3: A spectrum of X-rays emitted by the dipole, entering the air and absorbed in the CdW04 scintillator

with respect to 1-20KeV photons typically used for scientific work on a beamline, a reduced intensity of ~3 orders for the 150-200KeV range. The latter are attenuated another factor of ~3 orders by their 40mm path through the copper crotch absorber and 5mm through the steel vacuum chamber. Nevertheless, the fraction that enters the free air after the crotch chamber is still of an intensity of ~2E7 photons per second and per mrad horizontal angle in a 0.1% bandwidth at 200mA current.

The blue curve in the lower graph of fig.3 with a linear scale shows a sort of bandpass shape that is determined at the left-side by the increasing copper attenuation to lower energy photons, and on the right side by the slope of decreasing flux for higher energy photons.

X-RAYS DETECTED BY SCINTILLATOR

Cadmium Tungstenate (CdWO4) is a high-Z crystal of nearly 8gr/cm3 density. [1] Thanks to its mechanical hardness it can be manufactured and polished to a

thickness below 0.5mm. It is transparent to visible light and has a good light yield for the hard X-rays with a short decay time of ~1us. The red curve shows the X-ray spectrum absorbed by a 0.5mm thick CdWO4 screen out of the spectrum that traverses the crotch.

The fig.4 shows the detector with the scintillator screen directly behind the crotch chamber. The light emitted by the screen is deflected upwards by an aluminium mirror just 7mm behind to an achromat pair (f1=50mm, f2=75mm) that collects and focuses an image on the CCD matrix. The entire detector is mounted together and adjusted optically in laboratory before installation. The effective F-number of the optics is ~4. The CCD used is the Sony ST-30 (1/3" format), the pixel size at the source-point is ~4.4um. The optical resolution of the system was assessed in laboratory and estimated at ~10um. It is determined by depth-of-field blurring by the F of the optics and the thickness of the screen.

The schematic does not show the lead shielding of 3mm thickness around the lenses and CCD. The entire assembly is as small and compact as possible since the space behind the crotch-chamber and the flanges just a few cm further down-stream is very limited.

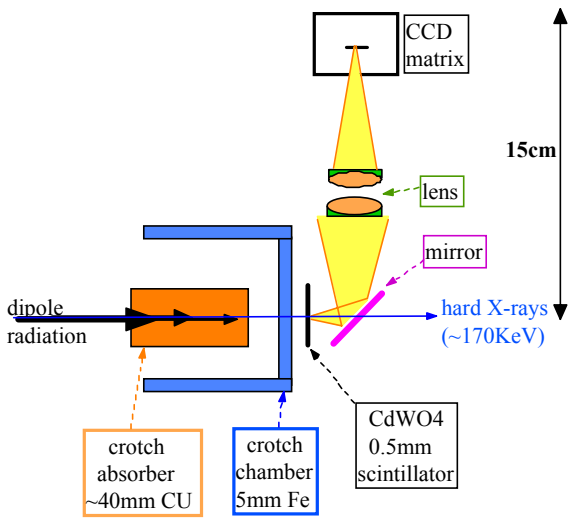

Figure 4: Side-view in the vertical plane of the detector

CALCULATION OF VERTICAL ELECTRON BEAM SIZE

The 170KeV X-rays travel 1.9meter before hitting the screen where they project a stripe-line image. Horizontally this line covers the full-recorded image width because of the horizontal fan of dipole light, and obviously no data of interest can be obtained in this horizontal plane. In the vertical plane however, the relation between the height (h) of the projected image on the screen, and the size of the source-point (i.e. electron beam) can be established in simple and precise terms (see fig.5). Because of the very narrow divergence of the 170KeV photon beam (42urad fwhm, and of gaussian distribution) the projected vertical beam size (h) is only 115um fwhm compared to the vertical electron beam size of 86um fwhm at nominal ESRF emittance of 35pm.rad.

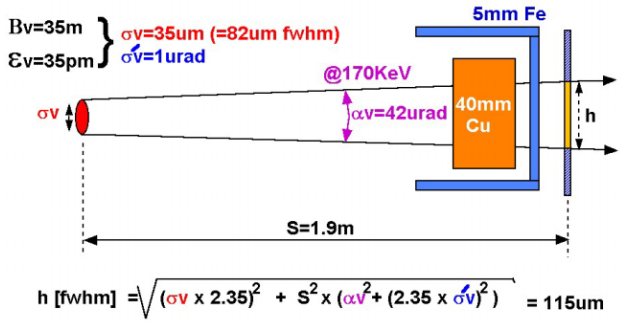

Figure 5: Relation source-point size to projected image size.

The precision of this deconvolution depends on the precision with which the distance (S) and the exact photon beam divergence (αv) can be determined. It can be shown that the uncertainty on both is small and that therefore the precision of the electron beamsize measurement is estimated at better than 2%.

PROTOTYPE RESULTS

A first prototype was installed in Jan-05 and yielded results for only 2 days of operation due to damage by the strong ambient radiation to the CCD camera. This was largely due to a very simple and insufficient lead shielding applied at that time. Nevertheless during some measurements in these 2 days the system provided a clear proof-of-principle with 2 measurements at respectively 23pm and 100pm vertical beam emittance. The ESRF emittance measurements are obtained by an independent emittance measurement system based on an X-ray pinhole camera [2]. The graph in fig.6 shows a curve with the theoretical value for projected vertical size h [um fhwm] versus emittance and the 2 measurements in yellow that are in excellent agreement.

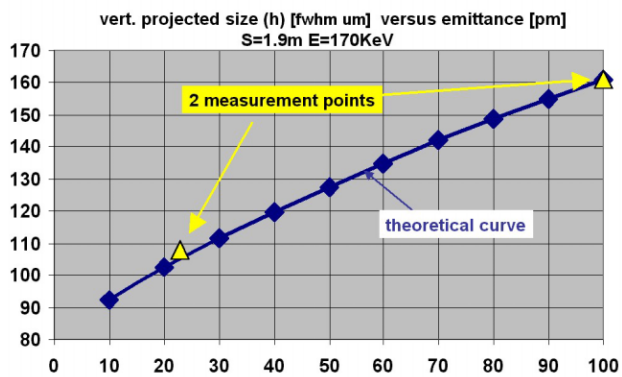

Figure 6: Results of 2 measurements compared to theory

A 2nd prototype was realised with a more rigorous lead shielding structure applied. The average thickness of the lead was 3mm, and the aperture to let the light cone in was reduced to a minimum of 8mm for an optical F of ~4.

The results obtained with the 2nd prototype are shown in fig.7 with an image and a vertical profile plot. The noise in this data is low enough to assess the vertical

stability of the electron beam by measuring precisely the centre of the profiles of a series of measurements.

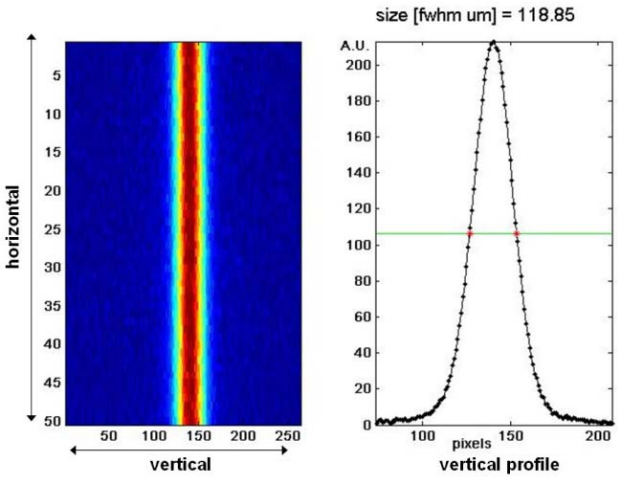

Figure 7: Image results with vertical profile plot

The results of this series of measurements are shown in fig.8 with 60 individual measurements taken with an integration time of 1millisec and at a 1Hz repetition rate. The latter is imposed by the slow transfer rate of the camera and its acquisition system.

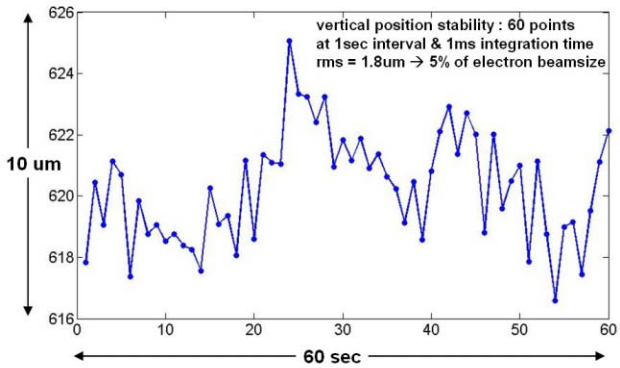

Figure 8: Vertical beam stability measured during 60s

Even with a pixel resolution of 4.4um the low noise of the data allows to see beam displacements of less than a micrometer. The position fluctuations shown in the fig.8 are believed to be caused by the electron-beam itself (with an rms amplitude of 5% of the vertical beamsize) and not by noise in the detector system.

RADIATION SHIELDING

The location of the detector directly behind the crotch implies a strong exposition to radiation caused by particles that are generated inevitably by the interaction of 13KW of high energetic synchrotron light with the crotch absorber. [3]

The lead shielding of the 2nd prototype was sufficient to avoid camera break-down but non-effective in avoiding the blackening of the pair of achromats. Over a run of 2 months the consequent loss of sensitivity was more than a factor 20.

A new type of lead shielding was conceived with 2 additional flat mirrors inside the lead that direct the light cone in a chicane type structure to the lenses. Initial tests over a 2 months period showed that the lenses did not blacken.

CONCLUSION AND PROSPECTS

With a simple, low-cost and compact detector it is possible to detect in air the high-energy photons that traverse the crotch absorbers. The use of a 0.5mm thick CdWO4 scintillator screen results in an effective X-ray detector centred at a 170KeV energy. The precise knowledge of both the distance of the screen to the electron beam and the small divergence of this detected photon beam makes it possible to measure the vertical electron beamsize with very good precision.

With a suitable optical system assembled to it, the whole detector can be kept small and compact and thereby meet the very limited space requirements available just behind the crotch chamber.

The sensitivity of the system allows to measure with simple commercial CCD cameras with integration times as small as 200us without any intensifier device. The future use of a high-transfer-rate camera should then allow measuring the vertical beam stability at frequencies above 1Khz. The resolution with which such stability, at that frequency, can be measured depends on the noise-level of the whole system but results with the prototype indicate that submicro-meter resolution is attainable.

In principle such detector could be implemented on each of the 64 ESRF dipoles and potentially constitute a new device for monitoring vertical beam stability over the full DC-AC frequency range, and possibly serving in a global feedback system.

The strong radiation environment requires an adequate shielding structure to avoid degradation or damage. Initial tests show that this is possible without exceeding the restricted space availability.

REFERENCES

[1] Saint-Gobain Crystals, http://www.detectors.saint-gobain.com/

[2] P. Elleaume et al, "Measuring beamsize and ultra-small electron emittance using X-ray pinhole camera", J. Synchrotron Rad., June 1995 2, 209-214

[3] G. Naylor et al, "Bremstrahlung Detection and Chamber Obstruction Localisation Using Scanning Radiation Detectors", this DIPAC-05 workshop

THE X-RAY BEAM IMAGER FOR TRANSVERSAL PROFILING OF LOW-EMITTANCE ELECTRON BEAM AT THE SPRING-8

S. Takano*, M. Masaki, and H. Ohkuma
Japan Synchrotron Radiation Research Institute, SPring-8, Hyogo 679-5198, Japan

Abstract

The X-ray beam imager (XBI) at the accelerator diagnostics beamline I of the SPring-8 is briefly described. It has been developed for transversal profiling of the electron beam of the SPring-8 storage ring. It comprises a single Fresnel zone plate (FZP) and an X-ray zooming tube (XZT). The spatial resolution is 4 μm (1σ), and the time resolution is 1 ms. The field of view is vignetting-free and is larger than ϕ1.5 mm. With the XBI, we have successfully observed the profiles of the electron beam having vertical emittance smaller than 10 pm•rad.

INTRODUCTION

The SPring-8 is a third generation synchrotron light source operating since 1997. To observe the transverse profiles of the electron beam of the 8 GeV storage ring, we planned the XBI [1]. Our goal is the emittance diagnostics of the SPring-8 with resolution better than 1 pm•rad. The design targets of the XBI are 1) spatial resolution (1σ) in the micron range, 2) time resolution of 1 ms, and 3) vignetting-free field of view larger than ϕ 1 mm on the coordinates of the electron beam. We have constructed the XBI at the accelerator diagnostics beamline I (BL38B2) of the SPring-8 storage ring. The details of the XBI and the results of the measurements will be described elsewhere [2]. In this paper, we give brief descriptions of the XBI and some of the results obtained.

THE X-RAY BEAM IMAGER (XBI)

The schematic layout of the diagnostics beamline I is shown in Fig.1. It has a bending magnet light source with an critical photon energy of 28.9 keV. The optical system of the XBI is shown in Fig.2. All the components of the XBI are in the optics hutch of the beamline. The XBI is based on a single FZP and an XZT. An X-ray image of the electron beam moving in the bending magnet is obtained by the FZP. To avoid the effect of the chromatic aberration of the FZP, monochromatic X-rays are selected by the double crystal monochromator. A 4-jaw slit is used to determine the horizontal width of the white X-ray beam incident on the monochromator to avoid unwanted heat load to the crystals. The magnification factor of the FZP is 0.274. We use an XZT to enlarge the reduced X-ray image of the electron beam. The observing photon energy of the XBI is 8.2 keV, which was determined by considering the .

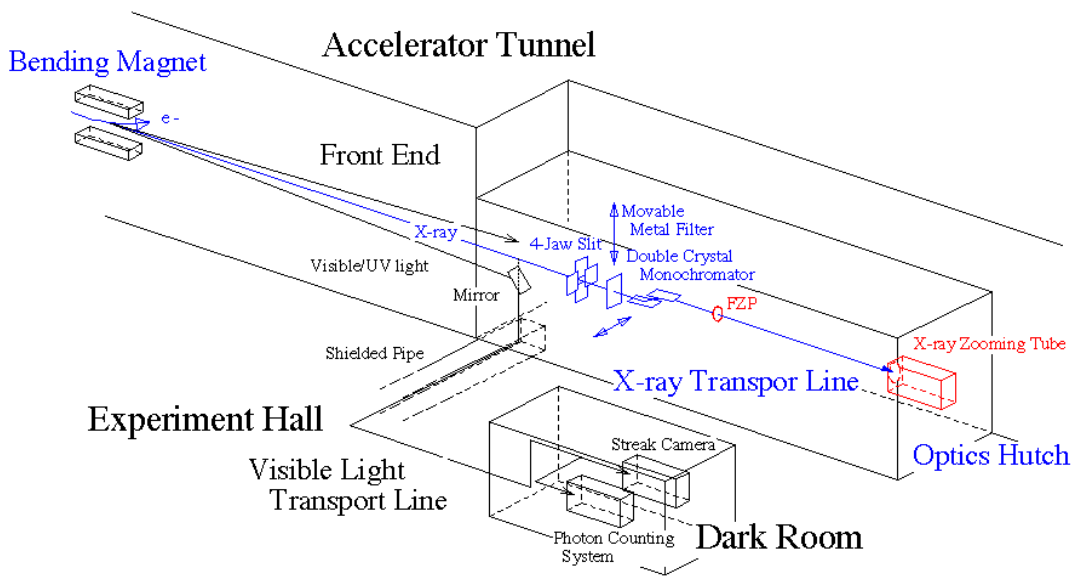

Figure 1: Layout of the SPring-8 accelerator diagnostics beamline I (BL38B2).

* Email:takano@spring8.or.jp

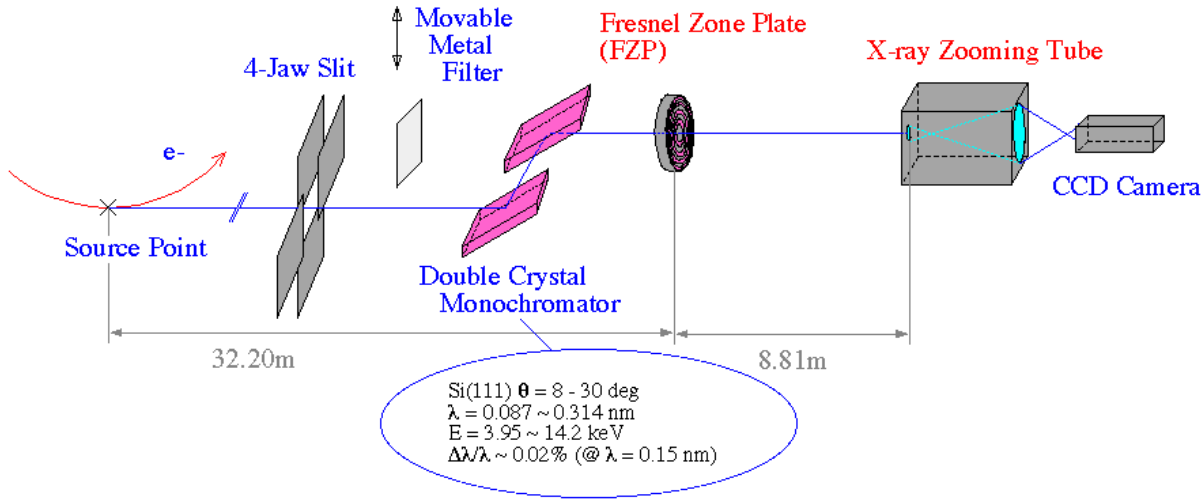

Figure 2: The optical system of the X-ray beam imager (XBI).

spatial resolution and the efficiencies of the FZP and the XZT.

The FZP was fabricated by NTT Advanced Technology Co. The characteristics of the FZP are summarized in Table 1. The width of the outermost zone is 0.75 μm. An FZP with such wide outer zones can be fabricated without difficulties by the existing technologies and promises to achieve theoretical diffraction-limited resolution.

Table 1: Parameters of the FZP

Distance from the source point	32.20 m
Diameter	1.4 mm
Focal length *	6.92 m
Total number of zones	468
Outermost zone width	0.75 μm
Material of absorbing zones	Tantalum (2.0 μm thick)
Diffraction Efficiency *	32 %
Magnification factor	0.274
Spatial Resolution (1σ) * σ_{FZP}	1.5 μm

* Theoretical Value at E = 8.2 keV (λ= 0.15 nm).

The XZT (Hamamatsu Photonics K. K., V4410) is a device which transforms an X-ray image on the input photocathode to a magnified visible light image on the output phosphor screen. The characteristics of the XZT are summarized in Table 2. We set the magnification at 50 for beam profile measurements. The response time of the XZT is predominated by that of the output screen. We have selected the P-47 phosphor as the screen material, because it has a fast decay time of 100 ns (from100 % to 10 %). The contribution σ_{XZT} of the XZT to the spatial resolution of the XBI was determined to be 3.8 μm experimentally [1]. To avoid degradation of the input photocathode of the XZT caused by exposure to

Table 2: Parameters of the XZT

Distance from the source point *	41.01 m
Input photocathode	Cesium iodide (0.3 μm thick)
Output screen	P-47 phosphor
Magnification factor #	50
Spatial Resolution (1σ) & σ_{XZT}	3.8 μm

* The value on the input photocathode.
# The values set at the beam profile measurements.
& Contribution to the XBI determined experimentally.

intense X-ray beams, we use a metal filter made of aluminum foil when the beam current is larger than 10 mA.

The output image of the electron beam from the XZT is observed by a CCD camera (Hamamatsu Photonics K. K., C4742-95). It has an effective area of 8.6mm by 6.9mm in 1280 × 1024 pixels, and the corresponding field of view of the XBI is 1.9 mm by 1.5 mm, which is larger than the design target of ϕ 1.0 mm. The exposure time of the CCD camera can be changed in a range from 0.1 ms to 10 s by an electric shutter. The time resolution of the XBI is at present limited to be 1 ms by the maximum allowable photon flux density on the photocathode of the XZT.

RESULTS

An example of the beam image of the SPring-8 observed with the XBI is shown in Fig. 3. The corresponding horizontal and vertical beam profiles are shown in Fig. 4. The optics of the ring was the so-called low- emittance optics introduced in 2002 [3].The filling pattern of the ring consisted of 1920 bunches in equally spaced twelve trains of consecutive 160 bunches. The total beam current and the current of each bunch were 10

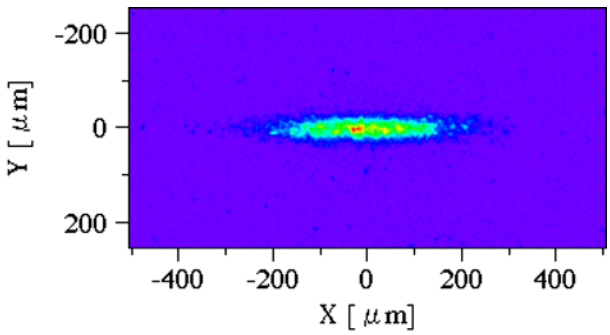

Figure 3: An example of the profile of the electron beam of the SPring-8 storage ring observed with the XBI

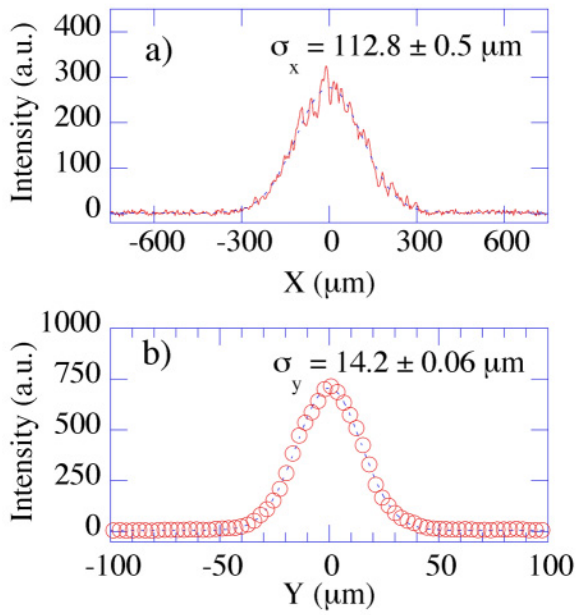

Figure 4: Horizontal and vertical beam profiles observed with the XBI with fitted Gaussian curves (dashed curves).

mA and 5 μA, respectively. The magnet gaps of all the insertion devices were fully opened in to minimize the effects on the beam emittance. No metal filter was used, and the exposure time of the CCD camera was 1 ms. The horizontal and vertical beam sizes were σ_x = 112.8 ± 0.5 μm, and σ_y = 14.21 ± 0.06 μm, respectively, after subtraction of the spatial resolution of the XBI contributed by σ_{FZP} and σ_{XZP}. The errors denote statistical 1σ fluctuations in successive measurements and not including systematic errors.

By using the design values of the betatron and the dispersion functions at the source point and the beam energy spread, we deduced the beam emittances from the beam sizes measured with the XBI. The horizontal and the vertical emittances were 3.29 ± 0.05 nm•rad, 7.26 ± 0.06 pm•rad, respectively. The deduced horizontal emittance is consistent with the design value of 3.4 by taking a 2σ statistical error. The deduced vertical emittance is smaller than 10 pm•rad.

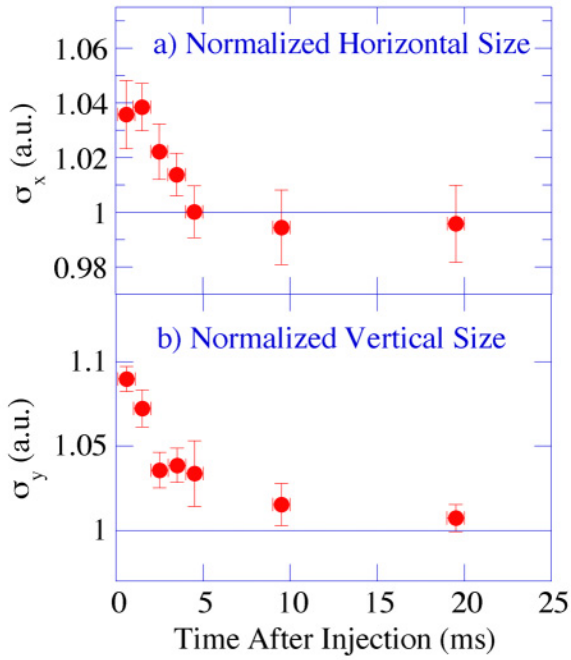

Figure 5: Effective beam sizes as functions of time after injections observed in the top-up operation.

By utilizing the 1 ms time resolution of the XBI, we studied transient behaviors of the effective beam profile after beam injections in the top-up operation [4]. Fig. 5 shows observed time variation of the effective horizontal and vertical beam sizes normalized to those of the unperturbed stored beam. Small but significant increase of beam sizes were found after injections, but they return to the values of the unperturbed beam in a period shorter than injection intervals. It seems that the observed change of the beam sizes induced by injections are tolerable for most user experiments.

FUTURE STEPS

Calibration of the point-spread function of the XBI is necessary to further improve the accuracies of the size measurements. For continuous monitoring of the beam profile, development of a real-time data acquisition system is planned.

REFERENCES

[1] S. Takano et al, DIPAC'01, Grenoble, 2001, p.145.
[2] S. Takano et al, submitted to Nucl. Instr. and Meth. A.
[3] M. Takao et. al., "Progress toward Brightness Improvements at the SPring-8 Storage Ring", APAC'04, Gyeongju, in the press.
[4] H. Tanaka, et al., EPAC'04, Lucerne, 2004, p.222.

PHOTON COUNTING MEASUREMENT IN SINGLE BUNCH OPERATION IN UVSOR-II ELECTRON STORAGE RING

A. Mochihashi, K. Hayashi, M. Hosaka, M. Katoh, J. Yamazaki, UVSOR, Okazaki
Y. Takashima, Nagoya University Graduate School of Engineering, Nagoya

Abstract

In single-bunch operation in electron/positron storage ring for SR light source, it is very important to always keep good single-bunch purity because undesirable spurious bunches can disturb experiments with pulsed SR light. Even though only one main bunch is injected and stored initially, however, spurious bunches can be generated in RF-buckets following the main bunch and gradually grow. Such phenomenon has been understood as a result of Touschek effect in the main bunch; namely, electrons which gain larger momenta than RF-bucket height by scattering process between electrons in the main bunch and go out of the original RF-bucket can be captured again in the following bucket*. We have observed impurity bunches in single-bunch operation in UVSOR-II electron storage ring by using photon counting method which has enough dynamic range to observe both the main bunch and the impurity bunches simultaneously. With the method, we have measured growth of the single-bunch impurity with time and tried to discuss Touschek effect in UVSOR-II.

NO SUBMISSION RECEIVED

BUNCH BY BUNCH CURRENT AND LIFETIME MEASUREMENTS AT DAΦNE

A. Stella, G. Di Pirro, A. Drago, M. Serio, INFN-LNF, Italy

Abstract

A dedicated system, based on digital sampling of beam signals with a commercial oscilloscope, has been developed to measure bunch by bunch current in the DAΦNE collider. It provides an automated tool to equalize bunch filling patterns in the main rings. Individual bunch current and lifetime are simultaneously computed from the sampled data, collected at a 4Hz rate and provided via ethernet to the accelerator control system to control individual bunch injection. System hardware and software data processing are reported, together with performance and results of the measurements obtained during DAΦNE operation.

INTRODUCTION

In the electron-positron collider DAΦNE, the two symmetric rings can be filled with different patterns of maximum 120 bunches, spaced by 2.7ns and with a typical charge of 1÷10nC. Storage of an equal charge in each bunch is crucial to optimize the luminosity.

By monitoring beam induced signals from wide band pickups the less charged buckets are selected for the next cycle of injection in order to obtain an even fill pattern.

This system provides to the accelerator control system an automated tool to perform this task; it is routinely used during the machine runs, being very useful and effective to maintain the average luminosity high and to increase the collider efficiency.

HARDWARE

Sum signals from two beam position monitors (BPMs) installed in the electron and positron ring, are connected to a digital sampling oscilloscope Agilent Infinium 54832B (4GS/s real time sampling rate, 1GHz bandwidth) [1], through a 60m long coaxial cable (Andrew Heliax FSJ-50).

Electrodes used as pickups are of the *button* type with capacitance C_b=3.5pF showing a high pass frequency response. The transfer impedance is that of a time differentiator for frequencies $f<<1/(2\pi R_0 C_b)$=910MHz and of a resistor in the upper frequency range [2].

Each bunch induces a bipolar pulse signal in the button electrodes, whose peak to peak amplitude is proportional to its current. The system bandwidth, including the cable, is such that the peak-to-peak voltage is proportional to the bunch charge irrespective of the bunch length: in our case rms bunch length is less than 200 ps under all conditions.

The bunch pattern of the stored beam current will result, at the end of coaxial cables, in trains of pulses attenuated and stretched by the transfer function of the cable (Fig.1).

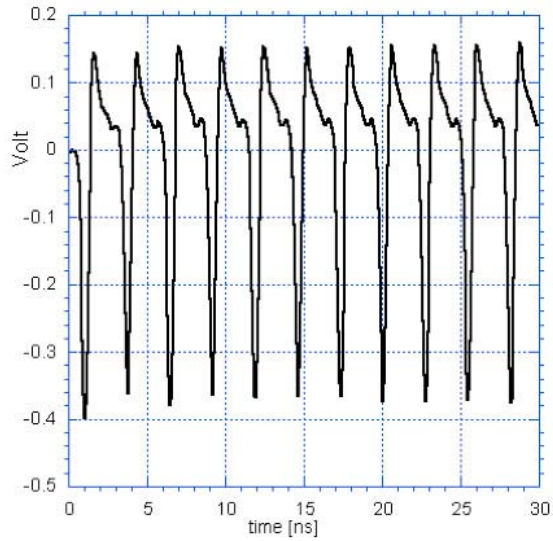

Figure 1: Detail of raw BPM signal waveform.

Due to the lack of DC response of the pickups, the resulting signals display also a significant drift of the base line which must be taken into account during data processing.

The digital oscilloscope samples the whole train of pulses both for electron and positron beams, with a 1GHz analog bandwidth (Fig. 2).

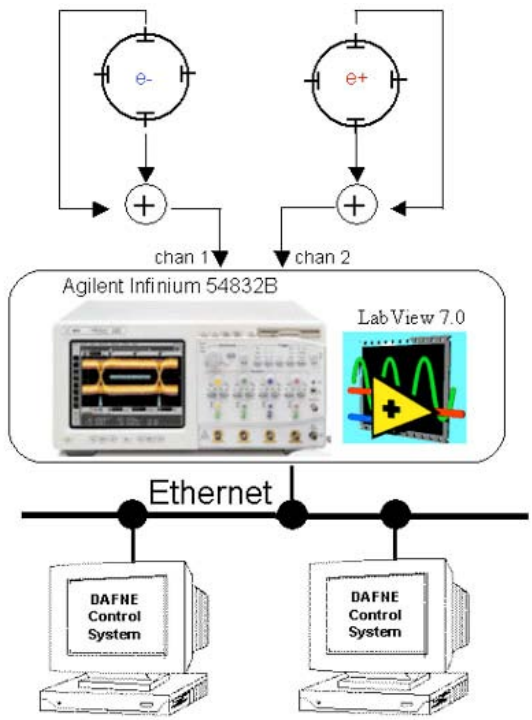

Figure 2: System block schematic.

The resulting waveform, as displayed from the digital oscilloscope, is acquired point by point and software processed to extract the bunch current through peak amplitude measurements of each pulse.

DATA ACQUISITION

Interfacing of the digital oscilloscope with the DAΦNE control system has been realized with a client-server architecture through the TCP/IP protocol.

Server Software

A LabView application, running on the Windows XPpro platform integrated in the Agilent digital scope, works as server.

The server runs in multitasking with the software process provided with the instrument, which controls and manages the oscilloscope. Interaction with it occurs through VISA, the high-level application programming interface widely used to communicate with instrumentation buses [1].

It has been developed to perform the following tasks:

- Setting up of the desired working parameters for the acquisition in connection with the current beam signal characteristics: i.e. sampling rate, acquisition mode, vertical and horizontal scale, channel selection, trigger, etc.
- Collecting the two arrays of data sampled by the scope, representing the electron and positron beam signal waveforms, at fixed intervals of time, through calling of GPIB standard library.
- Sending to the accelerator control system through a TCP/IP connection, upon client request, the two arrays of data together with a time stamp generated by the instrument CPU, identifying when the acquisition has been performed.

Client Software

The client software, fully integrated in the accelerator control system environment, is developed in LabView for Unix Solaris O.S.; it asks to the server for data containing the sampled waveform at a rate of 4Hz and processes it to extract the current of each bunch.

The waveforms collected are fragmented in smaller blocks containing only data sampled in an interval corresponding to the minimum bunch spacing. Individual bunch induced signals are isolated and the absolute values of the two peak amplitudes of each bipolar pulse are measured and summed to deduce the bunch current. By considering both peaks of each pulse signal one can get rid of the drift of the base line.

Peak voltages are normalized to the total beam current through an online calibration with the DC Current Transformers installed on each ring.

Tools to display individual bunch currents of electron and positron beams are also provided (Fig. 3).

Upon operator request a bunch charge equalization procedure is initiated: the buckets in which the current is below a user set threshold (default: average beam current – 3% see Fig. 3) will be selected for the next injection shot [3].

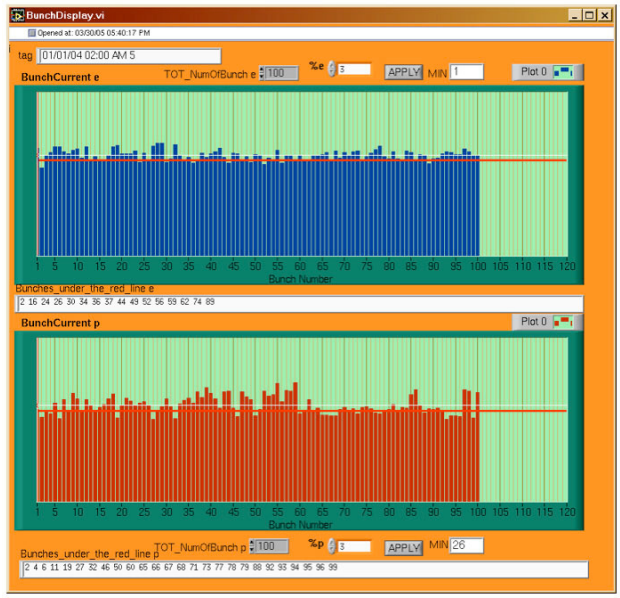

Figure 3: Bunch Current Monitor display for e^- beam (top) and e^+ beam (bottom).

CURRENT MEASUREMENTS

To improve measurements resolution, data are sampled in *equivalent time mode* [1] and averaged, taking advantage of the processing capabilities of the oscilloscope.

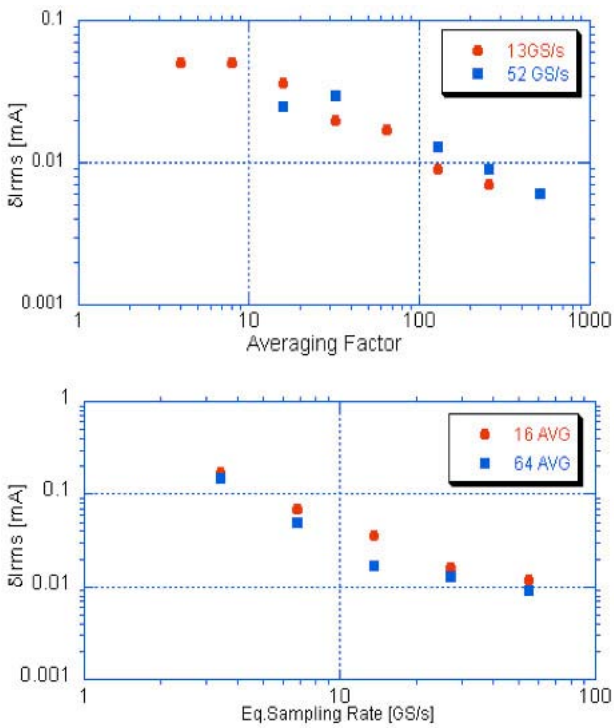

Figure 4: *rms* resolution of current measurements for different averaging factor (top) and sampling rates (bottom).

A limit to the measurement accuracy, i.e. the capability to measure exactly the absolute value of bunch currents, has been found to be due to the excessive length of the coaxial cables carrying the signal to be sampled.

The peculiar decay time of the cable impulse response is longer than the minimum bunch spacing and can overlaps with the following bunch signal. This leakage has been evaluated to be <3% of the bunch current.

RMS resolution δ_I of the current measurements are dependent from the sampling rate and averaging factor used.

Figure 4 reports some results to show system performance.

LIFETIME MEASUREMENTS

Individual bunch lifetime are computed from:

$$\tau_i = \frac{I_i}{\Delta I_i} \cdot \Delta t \qquad (1)$$

where I_i is the bunch current and ΔI_i is the current decay in an interval of time Δt.

An estimate of the relative error δ_τ/τ_i affecting lifetime calculation, due to the resolution of the current measurements is written as:

$$\frac{\delta_\tau}{\tau_i} \approx \frac{\delta_I}{\Delta I_i} \cdot \left(1 + \frac{\Delta I_i}{I_i}\right) \qquad (2)$$

A software routine, implemented in the control system, continuously acquires bunch corrents and stores it in a memory buffer.

Calculation of the bunch lifetimes is performed only when a user configurable ratio $\Delta I_i / \delta_I$ is reached, where δ_I is updated during acquisition.

In the measurements reported, lifetimes for each bunch are evaluated after a current decay $\Delta I_i = 50\delta_I$. Substituting in Eq. (2) it leads to an expected rms relative error ~2%.

For typical values of DAΦNE lifetime during luminosity shifts, one needs interval of times of about one minute to obtain single bunch lifetime measurements with the requested resolution.

A graphic interface allows analysis and display of the lifetime values during machine operation (Fig. 5).

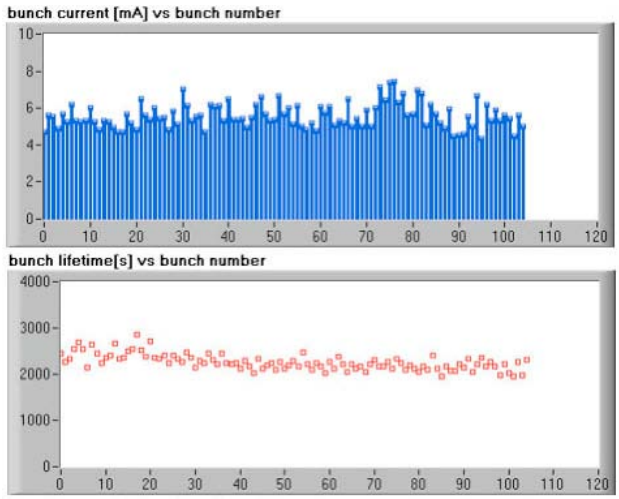

Figure 5: Bunch lifetime monitor display.

ACKNOWLEDGMENTS

The authors wish to thank O. Coiro and D. Pellegrini for technical support.

REFERENCES

[1] Agilent Technologies, “5483xB Series Infiniium Oscilloscopes: Programmer’s Reference Guide”, (2003).

[2] F. Marcellini, M. Serio, A. Stella, M. Zobov: "DAΦNE Broad-Band Button Electrodes", Nuclear Inst. & Meth. in Physics Research A402 (1998).

[3] G. Di Pirro, et al.: "Implementation and Performance of the DAΦNE Timing System", Proc. EPAC Stockholm (Sweden), 1998, p.1661.

THE RENOVATION OF THE ISOLDE INSTRUMENTATION

Gerrit Jan Focker, Enrico Bravin, Stéphane Bart Pedersen, CERN, Geneva, Switzerland

Abstract

The ISOLDE [1] instrumentation [2] is mainly based on mechanical scanners, wire-grids and faraday-cups. Additional items are the “fixed needle beam scanner” (FNBS), the tape-station and a device called the “fast faraday cup”. The control system for these devices is being redesigned and reimplemented in order to be integrated in the standard control system of the CERN accelerators complex. While some devices will still be controlled with "usual" standards (VME), the tape-station and the wire-grids will be controlled using industrial PLC’s. In fact, recently, the automates have become fast enough for these applications. This article will describe the different developments in the control electronics, the improvements of the devices themselves and will finish with a short peek at future projects.

SCANNERS

The mechanical scanners as are used at ISOLDE were initially (1992) controlled by a “front-end computer” (FEC) running on DOS [3].

In 1998 a more intelligent electronic card containing an ADC and local memory to store the data was installed. This card was controlled via a 1Mb/s RS422 from a PC, running Windows NT and programmed in Visual Basic. In 2004 this system was ported to Windows XP.

This system is now being ported to the standard CERN control system based on VME and using a slightly improved version of the RS422 card. The front-end software is ready and this upgrade will be finalised as soon as the console-software is ready.

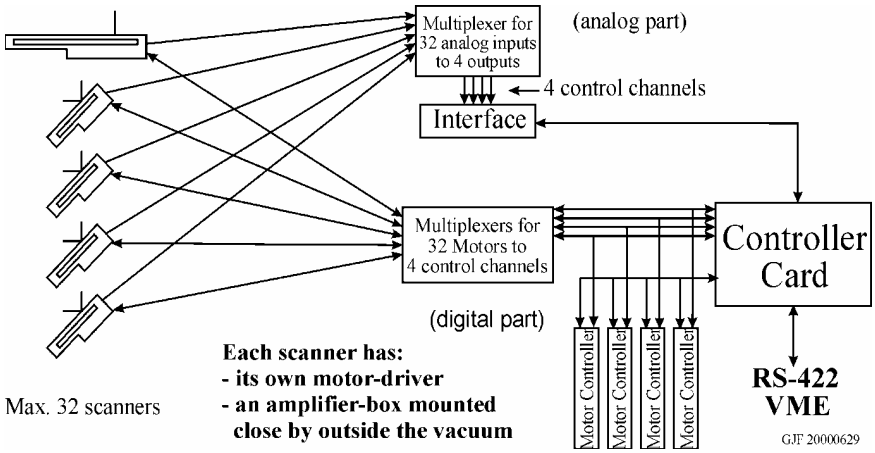

Figure 1: Block-diagram of the ISOLDE Scanner-system

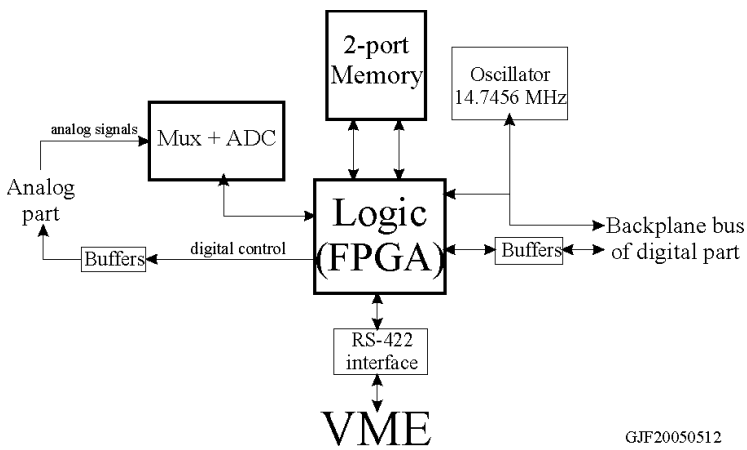

Figure 2: Block-diagram of the RS-422 controller card

WIRE-GRIDS

Choice of Design

The main part of this article is however about the new controls of the ISOLDE wire-grids as it is based on a (for us) new technique. That is to say it is a new technique for taking data. The previous system was based on an obsolete front-end computer running DOS and should be integrated into the standard CERN control system. Adapting the existing electronics with its ISA-bus interface seemed too difficult and we had to look for an alternative. Siemens has in its Simatic program an ADC that has a 52 s conversion time, which is fast enough to read out the wire-grids. They also have a module called “Boolean Processor”, which is an independently running programmable logic device with a time-resolution of 10 s, good enough for controlling the track-and-hold timing and the integration time of the amplifiers which sit on an external chassis. The use of industrial controls is not new to us; the ISOLDE vacuum-controls were already controlled by Simatic somewhere in the eighties. But using them to replace a PC or VME Front-End Computer for data taking is new to us. It should be noted that it is not possible to use Simatic for the ISOLDE scanners as the Simatic-ADC is far too slow for this purpose.

About the Simatic Solution

Simatic PLC's are now an accepted standard for the CERN accelerator control system. But even though the Simatic PLC's connect to Ethernet, the PLC's are not accessed directly by the operators. Operator Consoles connect to a VME-crate acting as a gateway where the data traffic to and from the PLC is treated. Of course the VME may handle many PLC's and this even together with other tasks.

One PLC can handle one amplifier crate with a maximum of 256 input-channels. The system is designed in such a way that it can handle up to 4 Grids.

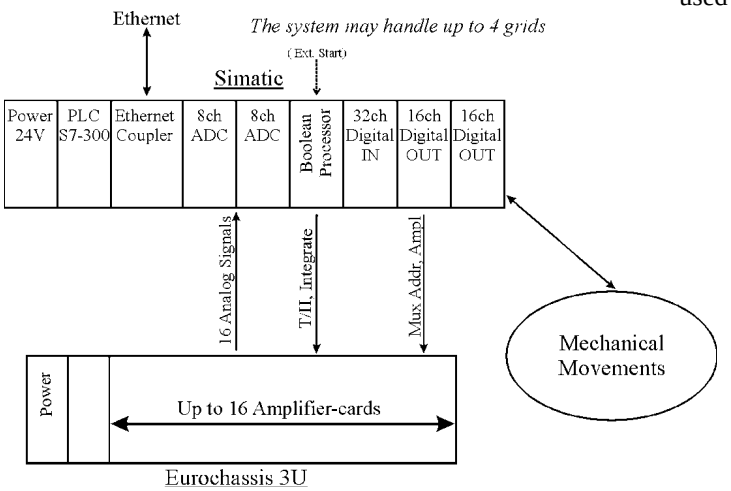

Figure 3: Layout of the wire-grid controls

The system has (up to) 16 amplifier cards and two ADC-modules with 8 inputs each. Each amplifier card is connected to its own ADC-input. In addition each amplifier card has 16 amplifiers and a 16-channel multiplexer. The multiplexers on the amplifier-cards are all controlled in parallel by the same four address-lines. Thus 16 ADC-conversions are necessary to read out all the data.

The ADC's have a conversion-time of 52 s. An ADC-module has 8 inputs; it contains one ADC and an eight-channel multiplexer. An ADC-module will always convert all eight channels (which makes 416 s) and in addition it needs some time to prepare the data before it can be read by the PLC. The result is that conversion takes place with a cycle-time of about 610 s. The ADC-modules cannot be triggered externally and run asynchronously.

The PLC is software based and runs in cycles. At the beginning of a PLC-cycle it reads the input-data, then it executes its program, and finally it refreshes the output-data. When the multiplexers on the amplifier-cards are set to a new address the next ADC-cycle must be discarded! The ADC-modules run asynchronously, so to be sure that they have been able to finish a complete measurement one should wait two times the time of 610 s, i.e. 1.22ms! This necessary delay can be obtained by programming the PLC in such a way that its program skips reading the ADC-data in the PLC-cycle after setting the new multiplexer-address and e.g. checks for mechanical positions or does some other calculations. After this the following PLC-cycle can read the ADC-data and immediately set a new multiplexer-address on the amplifier-cards. As with the used PLC the cycle-time is some 3ms there is no problem, but this means that the 32 cycles necessary to read out all 256 channels take some 100ms.

That is enough for our application, but it isn't really fast. Adding additional software, e.g. for debugging, immediately slows down the system.

The amplifiers have integrators and track-and-hold amplifiers that need a more accurate timing than the standard PLC can offer. Therefore a Boolean processor is used which allows a resolution of 10 s. The Boolean processor contains in fact an FPGA (Field Programmable Gate Array) and is not running in cycles with varying time like the PLC.

Why Use a PLC

The PLC s have slow ADC's and its programming language isn't really made for handling "large" amounts of data. In addition the inputs and outputs work on 24V. This is great for the control of the pneumatic movements, but to control the electronics one will have to convert many signals to and from 5V.

The reason to use a PLC is that we can install it close to the equipment, where space is scarce. If the amplifiers would be made on VME cards we would have been forced to use long cables which would make the system unreliable at low input-currents. And then there is the increase for cabling costs, for the PLC we just need one Ethernet-cable.

The Amplifiers.

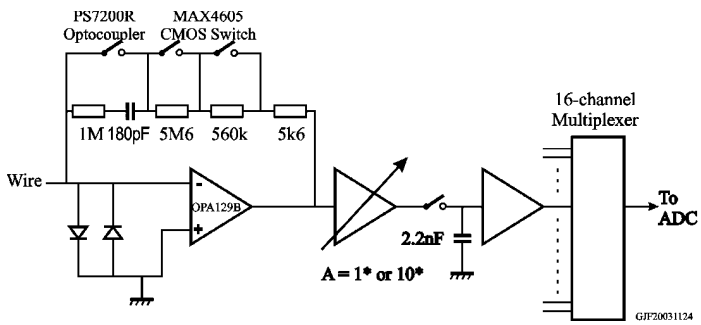

Figure 4: Schematic diagram of the Wire-grid Amplifier

Each channel of the amplifier-card includes a track-and-hold amplifier. There are 16 amplifiers on one Europe-size PCB of 100 by 160mm. For higher currents the amplifier is used as a simple current-to-voltage converter and for smaller currents as an integrator. The reason for this is that precision resistors are easy to find, even in SMD, but not capacitors, especially at large values. For small input-currents it is important to integrate in order to reduce the effect of noise. This integration should preferably be done with a multiple of 20ms to filter out any 50Hz component. To larger currents the noise-problem is less important and therefore don't need

as much filtering. The input-current range is very large: from less than a pA up to 2mA.

The MOSFET opto-coupler used to discharge the integrating capacitor is a delicate issue. It must have a very low "on"-resistance to minimise the amplification-error at 2mA input-current. Most of these switches have 25pF capacitance or more from which the tolerance alone will be too large to be used in parallel with the 180pA capacitor. Then of course the switch should be sufficiently fast. The PS7200R from "Californian Eastern Laboratories" has a capacitance of only 1.1pF, an "on"-resistance of 10 , it switches off in some 0.3ms and even the isolation capacitance is low with 0.3pF. Unfortunately the European distributor (NEC) is not interested to deliver these devices, but thanks to our American colleagues from BNL we could get them.

Due to its special characteristics the switching of the PS7200R isn't that smooth. The light-sensitive switch is made with two MOSFET's. After switching off, the two MOSFET's both create a short discharge. Though these two discharges are of different sign, they don't occur at exactly the same time and are usually not the same size. Tests with a 100pF capacitor in parallel with the switch showed induced voltages of up to 33mV just by switching off the PS7200R. By adding the 1M resistance part of the short discharge-peaks are dissipated lowering the 33mV to a more reasonable 12mV. The final amplifiers show a worst error equivalent to an input-current 0.8pA. (This is with an integration-time of 5s.) This error of maximum 0.8pA is not very repeatable though, it isn't possible to compensate with a constant value. We found the solution in taking two measurements, one just after switching "off" the PS7200 and one at the end of the integration-process. By subtracting the first value from the second we obtain a remaining error of maximum 200fA, which is close to the resolution of 50fA that we have with our ADC.

THE FIXED NEEDLE BEAM SCANNER (FNBS)

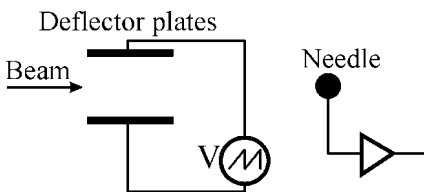

Figure 5: The principle of the FNBS.

The Fixed Needle Beam Scanner is a device where, instead of moving a needle mechanically the beam is deflected electrostatically to a maximum of ±5mm. The needle (actually a 0.1mm wire) doesn't move during the measurement, but can be taken out altogether with a pneumatic movement. The absence of mechanical movement during the measurement allows obtaining higher precision and eliminates the noise caused by microphonics. The FNBS (there is only one at ISOLDE) is still controlled by a DOS-PC. This device will be ported to the new control system and will also be controlled with Simatic. Once the new control system working, we will extend it with a motor-controller and use it to control an Allison Emittance Scanner [4] that will replace the FNBS at a later date.

FUTURE

With the Isolde Tape-station radioactive nuclei can be collected from the beam and measured nearby. This allows to measure beam-intensities of radioactive isotopes too small to be measured otherwise, which allows optimising the Isolde target. Another feature of this device is the measurement of half-lives. The Tape-station has electronics that dates from 1974. The timing control is modern though with a Simatic PLC and "Boolean Processor", but the mechanics and its electronics will be redesigned and replaced.

The Fixed Needle Beam Scanner will be replaced by an Allison Emittance Scanner.

The existing Faraday-Cup measurement system controlling a few dozen of Faraday-Cups is built up with a Keithley Electrometer and a Keithley "Scanner"-box. In the environment of switching over between Faraday-Cups having different input-currents and long cables the readout is not always accurate enough. We will look for a solution to improve this system, either by incrementing the number of Electrometers or by building small local amplifier-boxes controlled by Profibus.

CONCLUSION

The Control of the Isolde Instrumentation is slowly being converted to the standard Control system. The main item of this article is the controls of Grids and FNBS by Simatic. This experience shows that it is possible to use this technique and allows putting the controller close to the equipment. As a drawback the programming of the PLC costs more time than expected.

REFERENCES

[1] E. Kugler, CERN, Geneva, Switzerland, "The ISOLDE Facility", J.C. Baltzer AG, Hyperfine Interactions 129 (2000), p. 23 - 42.

[2] G. J. Focker, F. Hoekemeijer, O.C. Jonsson, E. Kugler, H. L. Ravn, CERN, Geneva, Switzerland, "The Beam Observation System of the ISOLDE Facility", BIW94, Vancouver, 2-6 October 1994. AIP-proceedings Vol. 333, p. 196

[3] O.C. Jonsson, R. Catherall, I. Deloose, P. Drumm, A.H.M. Evensen, G. J. Focker, A. Fowler, K. Gase, E. Kugler, J. Lettry, G. Olesen, H. L. Ravn, CERN, Geneva, Nucl. Instrum. Methods B126 (1997), p. 30

[4] P. W. Allison, J. D. Sherman, and D. B. Holtkamp, IEEE Trans. on Nucl. Sci. NS-30, 2204-2206 (1983).

BEAM PROFILE MEASUREMENTS BY USING WIRE DETECTORS IN J-PARC

H. Akikawa, K. Hasegawa, T. Ohkawa,
JAERI, Ibaraki-ken

H. Hiroki, Y. Kondo, H. Sakaki, S. Sato, M. Tanaka, A. Ueno, H. Yoshikawa,
JAERI/LINAC, Ibaraki-ken

Z. Igarashi, M. Ikegami, S. Lee, K. Nigorikawa, T. Toyama,
KEK, Ibaraki

J. Kishiro,
JAERI/J-PARC, Tokai-Mura, Naka-Gun, Ibaraki-Ken

Abstract

Beam intensity profiles are measured by wire detectors in high intensity proton accelerator J-PARC linac, RCS and MR. A single wire scanner is developed and examined for 20mA, 3 MeV H^- beam in KEK linac. Flying wire methods are also planned for RCS and MR commissioning. In this paper, basic design and preliminary experimental results are discussed.

NO SUBMISSION RECEIVED

LINAC AND TRANSFER LINE BEAM POSITION MONITOR AT ELETTRA

S. Bassanese, M. Ferianis, F. Iazzourene, ELETTRA, Trieste, Italy
V. Verzilov TRIUMF, Vancouver,Canada.

Abstract

A Beam Position Monitor (BPM) system, based on Log Ratio detectors (Bergoz LR-BPM), has been designed, built and commissioned at ELETTRA. Currently, the system is installed on the ELETTRA Linac and Transfer Line and it is integrated in the ELETTRA control system. The system is being used to monitor the trajectory along the Transfer Line; in the Linac, it monitors and controls the Linac beam stability. Furthermore, the Transfer Line BPMs are integrated in the program TOCA for the correction of the trajectory and the optimisation of the injection efficiency. The paper describes the system and the measurements performed both in laboratory and on the ELETTRA electron beam. Future possible applications of the LR-BPM system for the upgraded ELETTRA Linac, to be used for the new seeded FEL source, are here briefly presented.

INTRODUCTION

The old BPM system for the Linac and Transfer Line [5] based on a two GPIB-controlled oscilloscope acquisition system and multiplexer system, has been upgraded.

The system has been developed for the new ELETTRA full energy injector [1] composed by a 100 MeV Linac and a 3Hz cycling Booster synchrotron, up to 2.5GeV. The system will be used for the measurement of the beam position along the Linac and the two new Transfer Lines; it will be integrated in the beam trajectory feedback system for the optimization top up operation.

The single shot acquisitions can be averaged to improve the resolution for the trajectory's optimization. For the injection efficiency evaluation instead, a single shot charge measurement is required.

The main specifications of the system are the acquisition of the position with a resolution of less than 100 μm in a circular vacuum chamber, 40 mm diameter; the minimum beam charge goes down to 50pC, both in single bunch and multi bunch mode.

The theoretical sensitivity [2] of a Log Ratio BPM can be calculated with the following formula referred to Figure 1 and calculated for the dimensions of the actual linac to storage ring transfer line.

$$20Log_{10}\left(\frac{A}{B}\right) = yS_y \cong \frac{160}{Ln(10)}\frac{\sin\left(\frac{\phi}{2}\right)}{\phi}\frac{y}{r} = \frac{160}{Ln(10)}\frac{\sin\left(\frac{\pi/4}{2}\right)}{\pi/4}\frac{1}{22.65} = 1.495dB/mm \quad (1)$$

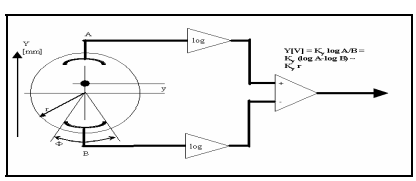

Figure 1: Log Ratio Principle of operation

SYSTEM DESCRIPTION

The system is based on the Bergoz Log Ratio Beam Position Monitor (LR-BPM) electronic board, fitted with sample and hold module to acquire position and charge. Each electronic board can process signals either from orthogonal or rotated pick-ups (user configurable). Two analog outputs, for the x and y position, generate a signal of ±2V. A third analog output gives a signal (sum of logs) the area of which is proportional to charge [3].

There is also a digital output which detects a beam passage, to be used for triggering the A/D converter. The LR-BPM boards are housed in a 19" 3U RF shielded chassis (provided by Bergoz) including 2 power supply units and up to 16 BPM stations, connected to the pick-ups on the rear panel. A custom connection board collecting signals from four BPM stations has been developed to route signals to the A/D converter boards. The A/D converters adopt a CAEN V265 (8 ch.) charge integrating converter and two INCAA VD10 8 ch. 16 bit differential A/D converter. The timing signals to operate the system are provided by a CAEN V462 dual gate generator. All the VME boards are controlled by a Motorola VME5100 CPU, running a server application integrated in the ELETTRA control system, via RPC protocol. Each BPM station, equipped with a CPU, a dual gate board, a charge integrating converter, and two A/D converter boards can manage up to 8 groups of BPM. A group of BPM shares a LR-BPM front-end, and two A/D converter channels via four RF multiplexers that connect the LR-BPM input to each selected pick –up.

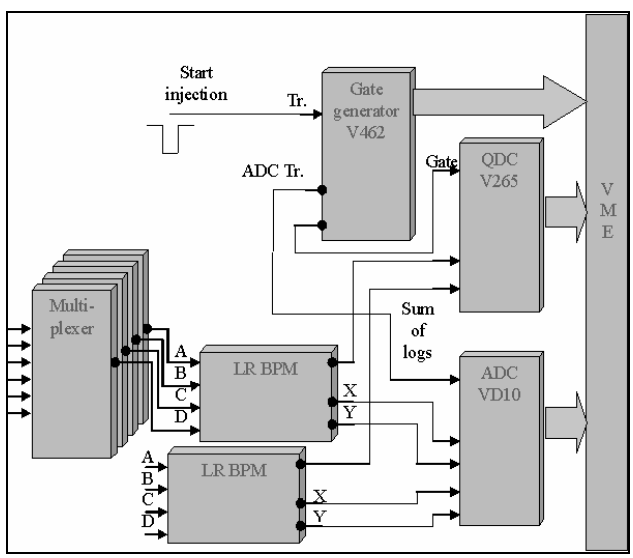

Figure 2: System layout

For each trigger pulse, data are acquired from the selected BPM inside each group.

For a better performance a single pick up for each group has been chosen. For each trigger pulse a complete trajectory is acquired using the same bunch's train in order to check for shot-to-shot stability.

To improve the sensitivity of the system to low charge bunches a set of four amplifier and band pass filters (f_0=500MHz, BW=54MHz) have been inserted between each pick-up's electrode and the LR-BPM input.

SYSTEM CHARACTERIZATION MEASUREMENTS

Bench Top Measurements

Some preliminary measurements have been carried out simulating the beam signal with a generator to check the best performance of the system, in the ideal case of a perfectly stable beam. A series of acquisitions has been done with the system in the final configuration as shown in Figure 3.

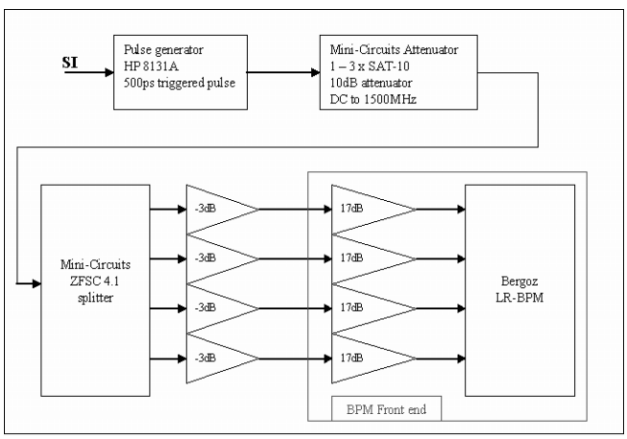

Figure 3: Bench top measurements layout

The acquisitions have been made varying the generator output amplitude to simulate a beam charge variation. The acquired charge and position information show a good linearity for the charge. The RMS of measured position is 75µm and 40µm, for single and multi bunch simulating signal respectively.

Charge sensitivity

A second set of measurements has been performed on the real beam to evaluate the minimum beam charge detectable by the system. The Linac charge, measured with a toroid, has been decreased till the system loosed the trigger with the beam; the measurements were performed both in multi and single bunch. For current injection in multi bunch (MB) mode (70ns macropulse) 500 pC charge is used; the BPM correctly detected down to 25 pC (-26dB from nominal value).

In single bunch (SB) mode only a relative measurement was possible, the toroid being not calibrated. A relative measurement between standard SB beam and the lower detected value also showed a similar dynamic of 28 dB.

Calibration and Position Resolution

To cross-calibrate the system, a series of measurements have been performed acquiring the position of the beam at two consecutive BPMs and a downstream fluorescent screen (FLSC), all located on a drift, while horizontal/ vertical scans were performed using a corrector pair.

The beam positions read by the BPMs and by the FLSC were simultaneously acquired to check for the calibration constant, previously computed. For each beam position, several tens of acquisitions have been stored to a file for off-line processing.

Two derived series of data have been generated averaging respectively five and ten samples. For a fixed number of samples (50) of each of these series the average and rms was computed and then plotted versus the corrector current.

The result of the scan shows a good linearity between the corrector current and the position acquired by the BPM.

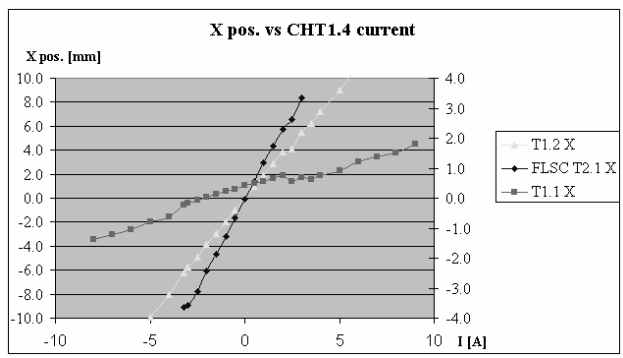

Figure 4 Horizontal beam position read by the BPMs and the fluorescent screen during a horizontal scan. BPMT1.1 is located near the corrector (0.6m) while BPMT1.2 and FLSCT2.1 are at 5.5m and 5.87m respectively. (BPMT1.1 beam position refers to the Y axis on the right of the graph).

The RMS, giving the uncertainty of the measurement, is ≈150µm. Considering the 40µm RMS, due to the electronics, we get a beam position stability of about

$$RMS_b = \sqrt{RMS_T^2 - RMS_e^2} = \sqrt{150^2 - 40^2} = 144\mu m \qquad (2)$$

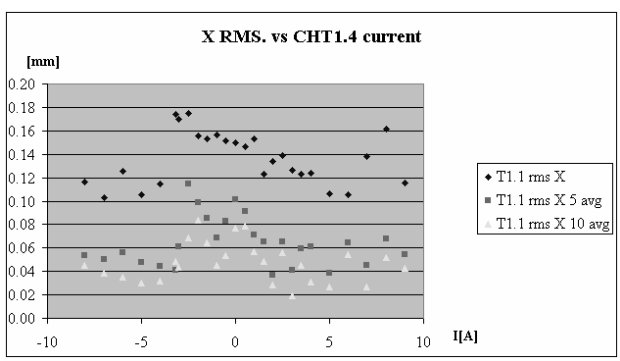

Figure 5 Total measured RMS

TRANSFER LINE TRAJECTORY OPTIMIZATION

The BPM system is installed on the injector Linac and the Linac to Storage Ring Transfer Line. It is used for the monitoring of the Linac beam stability and for the beam trajectory optimization along the Transfer Line.

The data acquired by the system and made available to the ELETTRA control system, via RPC calls, have been used by the application program TOCA [4]; a test has been performed with beam. The response matrix has been measured by the program for both horizontal and vertical planes. The figures below show the beam trajectory before and after a single correction calculated using the measured response matrix.

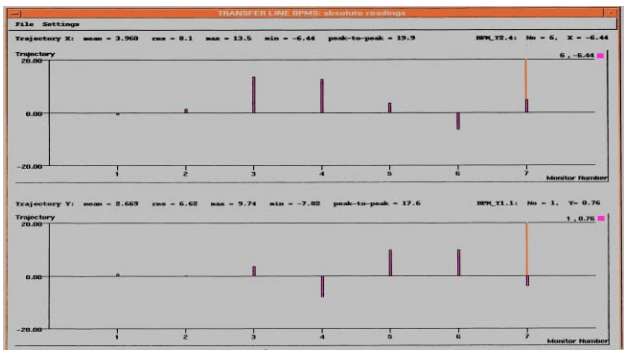

Figure 6: BPM readings before correction. The last BPM orange bar means that the BPM is not reached by the beam due to a beam stopper closed.

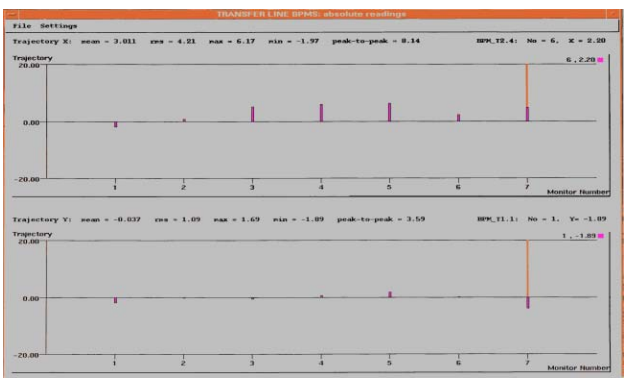

Figure 7: BPM readings after correction.

The vertical trajectory looks better corrected with respect to the horizontal one probably due to an energy variation of the linac beam.

The improvement in the TL trajectory appears evident also by comparing the beam loss monitor (BLM) readings, before and after the correction.

FUTURE APPLICATIONS

The present work on the LR-BPM system will be integrated in the design of an up-graded BPM system, to be used on the up-graded ELETTRA Linac for the new IV Generation Light Source, FERMI@ELETTRA.

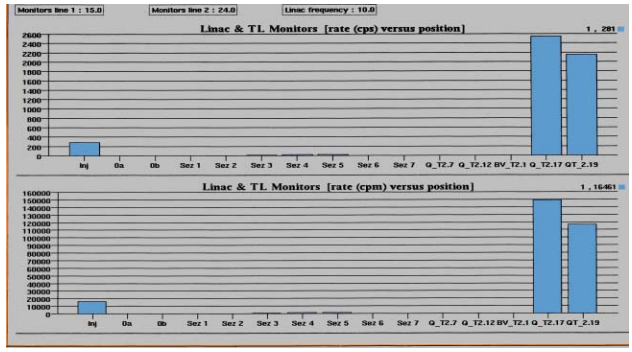

Figure 8: BLM readings before correction.

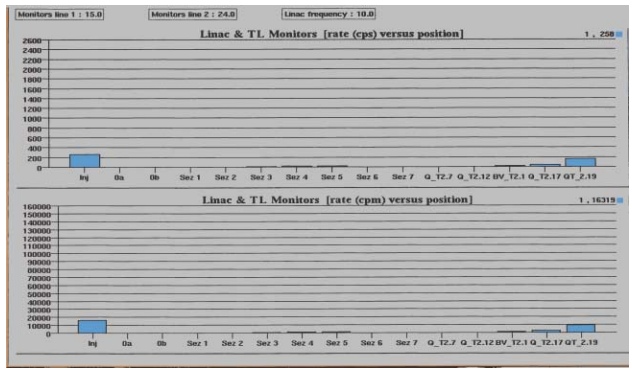

Figure 9: BLM readings after correction.

Equipped with new Photo injector, two bunch compressors and vertical ramp, the 1.2GeV electron beam will feed an Undulator straight section where seeded FEL radiation will be produced. Two sets of BPM will be most probably used for this new machine: an EM pick-up based type for the Linac and a Cavity pick-up based type for the Undulator straight section. The LR detector is a candidate for the first type of BPM although its performance needs to be pushed in order to reach 10-20μm_{RMS} in single shot, single bunch.

REFERENCES

[1] F.Iazzourene, “Update on the Linear and Non Linear Optics of the ELETTRA Full Energy Booster Synchrotron”, EPAC2002.

[2] R.E. Shafer, “Beam Position Monitoring”, AIP Conference Proceedings 212, Upton NY 1989, p.34.

[3] Bergoz Instrumentation: “Log Ratio Beam Position Monitor User’s Manual Rev.2.1.3”.

[4] F.Iazzourene, “TOCA: A highly User Friendly Application program for the Tune, Orbit, Dispersion and Chromaticity Correction.”, PAC 1999.

[5] M. Ferianis et al. “The upgrade BPM systems for the ELETTRA Linac and Transfer Line”, DIPAC 1997 proceedings

FIRST TESTS OF THE MACHINE PROTECTION SYSTEM FOR CTF3

D. Belohrad, CERN, Geneva, Switzerland

Abstract

CTF3, the test facility for the CERN Linear Collider study, is supposed to be operated at intensities and energies which may cause harm to the machine. For this reason there is a need for a machine protection system (MPS). The aim of the article is to describe the preliminary version of this system and to show first results measured in the CTF3 machine at the end of the 2004 running period.

The MPS is based on comparison of particle losses to a given threshold. As the MPS is required to stop the beam production within 1.5μs beam train pulse, very fast response needs to be achieved. Due to that, the losses are evaluated in real time as an amplitude attenuation of the beam current measured at two consecutive wall current monitors (WCM). When losses exceed given threshold, the beam-stop information is transmitted to the CTF3 gun interlock system. This causes inhibition of the beam production within the currently produced beam train. Manual actions are needed in order to recover from the beam-stop state of the MPS.

INTRODUCTION

The MPS protects the CTF3 machine against the consequences of lossy transfer of the particles from CTF3 linac source to PETS, intermediate dumps or spectrometer lines. The system is supposed to recognize two types of losses:

- small repetitive losses, where the loss measured between two consecutive sensors doesn't exceed ~10% of nominal intensity
- a fraction of beam pulse train lost locally

The first case mentioned doesn't damage machine, but it raises personnel radiation hazard. In this case MPS should either decrease or stop the beam production in order to lessen radiation. The response of the MPS to this particular case is not time critical, thus it can be implemented in the software. In the second case, the LINAC source beam production must be stopped inside the present pulse as there is a great risk of damaging the equipment. For this case a very fast response of the system is necessary. For both cases the recovery procedures must be applied and manual actions are needed in order to recover from the beam-stop state.

DESCRIPTION OF THE SYSTEM

Choice of Sensor

With respect to the beam parameters (electron beam of 1.5μs pulse length bunched at 3GHz and accelerated in a Linac working in fully loaded mode, repetition time max. 20ms) and required parameters of MPS, the sensor must satisfy following criteria:

- The intensity measurements must be available at maximum possible places.
- The bandwidth and dynamic range of intensity signal measured must be sufficient to follow fast beam intensity changes and to achieve reasonable precision of the intensity measurement.
- Usage of one measurement device type is advantageous.

A good candidate for the sensor is a wall current monitor (WCM) [1], which is commonly used to observe the time profile of the particle beams. Its high-frequency cut-off reaches 10GHz and the measuring devices are approximately equidistantly spaced in the machine each 10 to 15 metres. As we want to measure the beam intensity instead of observe the internal structure of the beam, we use the output of the WCM's integrator (signal compensated for residual droop of WCM). It provides a

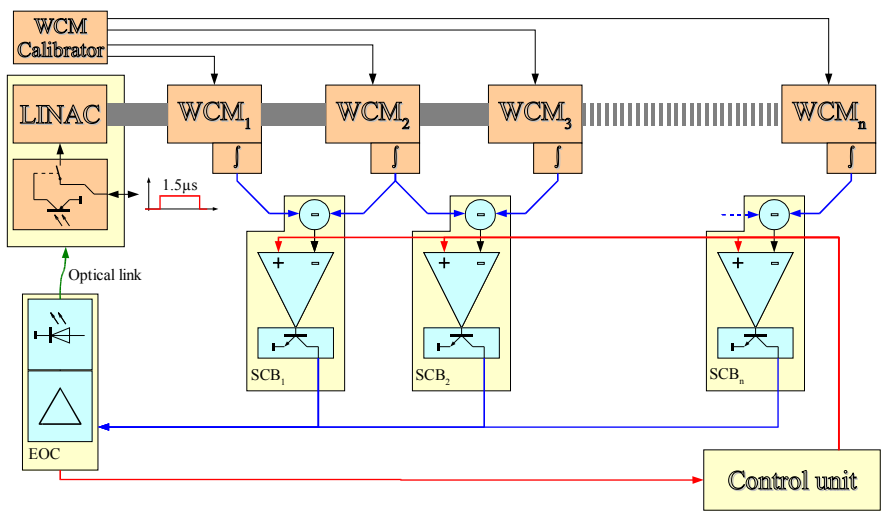

Figure 1: Simplified block schematic of MPS for CTF3

10kHz to 300MHz bandwidth and for maximum beam intensity it gives integrated output voltage of 2V.

Proposed solution

Figure 1 shows the proposed system solution. The core of the MPS is formed by many subtracting comparator blocks (SCB). These blocks compare the difference between actual beam intensities provided by two consecutive wall current monitors to the threshold values of intensity loss. The value of maximum loss permitted is set-up by operators for each SCB block independently. As the information about intensities measured is given in the form of voltage, one can use fast ECL comparators to do comparison of the losses to the threshold in real-time. If a loss occurs, the SCB unit triggers its output to active logic level (open collector output) and by using R-S flip-flop it holds this level until it is manually reset. Each SCB has both positive and negative thresholds implemented.

The real-time comparison assumes very good adjustment of cable lengths to achieve minimum time dispersion of the signals propagating from WCMs to SCBs. The propagation delays of the cables must be matched within 0.5ns for each SCB intensity input, taking into account different time propagation of every WCM's integrator and time of flight of the particles through the vacuum chamber. If this is not the case, the phase difference of intensity signals measured appears as a peak voltage when evaluating the loss signal, causing false triggers.

The outputs of the SCBs form wire-or structure, which transmits the interlock stop-signal into the cage with thermionic electron gun. Due to the high voltage electronics placed in the cage, it is unacceptable to transfer the information about MPS interlock via electrical cables. Thus the electro-optical converter (EOC) converts and transmits the interlock signal via optical link to the thermionic gun electronics.

Thermionic gun interlock system

The thermionic gun electronics provides an optical input for MPS interlock. The signal of interlock acts as a switch gating the signal going from trigger & time width control module to the pulse generator of thermionic gun [2]. Thus, in case of losses, the fastest possible reaction can be achieved. The MPS interlock is level triggered. When losses are detected, the signal of interlock remains active until manual reset is performed.

Control system

The purpose of the control system is to

- set-up appropriate thresholds for all the SCBs installed
- observe current state of the MPS
- provide detailed log and debug facility
- provide RESET control
- provide mechanism to disable certain SCB units

The control system for the MPS is supposed to operate independently of the control system of CTF3, but it must be easily accessible from the control room. It is foreseen to use WWW interface to access the controls of MPS.

Estimation of time-of-reaction

The time of reaction can be approximated from knowledge of the propagation delays of each part of the system. The estimation is based on following criteria:

- distance between monitors ~15 metres
- type of cables installed: HELIFLEX HCA78-50 7/8" coaxial cables with air dielectrics, whose velocity of signal propagation reaches 93% of SoL.
- Velocity of the beam is ~99% of SoL when it reaches first WCM
- assume additional 30% of cable lengths due to installation of the cables via cable supports.
- SCB modules are installed in vicinity of further WCM monitor, seen from direction of beam propagation.

The table 1 summarizes the delays estimated.

Description		***Delay [ns]***
WCM propagation delay	T_{PD1}	8
Estimated SCB propagation delay	T_{PD2}	16
WCM_2 to SCB_1	T_{PD3}	10
SCB_1 to EOC	T_{PD4}	125
EOC prop. delay including delay caused by optical link data transmission to the gun electronics	T_{PD5}	50
WCM_1 to SCB_1	T_{PD6}	To be matched

Table 1: Estimated propagation delays of MPS signals[†]

The table summarizes the best-case delays. For the other SCBs the cable lengths are longer, thus the propagation delay values must be correspondingly adjusted.

Approximated propagation delay from WCM_2, which is the first point where some loss can be detected, to the gun electronics can be expressed as a sum of first five rows from table 1, thus

$$T_{wcm_2,gun} = \sum_{i=1}^{5} T_{PD_i} = 209\,ns$$

When evaluating worst case propagation time for the first two WCMs, thus the case of loss which happens in the vicinity of WCM_2, we have to add additional time of flight of particles from the electron beam source to the WCM_2. This is corresponding to ~20 metres, or $T_{gun,wcm_2} = 67\,ns$ respectively. The worst-case propagation delay – or time-of-reaction – can be expressed as:

$$T_{pe,wc} = T_{wcm_2,gun} + T_{gun,wcm_2} = 276\,ns$$

[†]The cable lengths were estimated from technical drawings of machine layout, elongated about 30% due to installation of the cables into cable distributors.

IMPLEMENTATION

To check the reliability and time-of-reaction of the MPS a preliminary simplified version of the system was installed in CTF3.

It consists of EOC module and one SCB block, thus it supports only first two WCMs (WCM490, WCM823). The WCMs are installed 10 and 22 metres respectively away of the gun. The SCB block is located approximately 1.5 metres away of WCM823, on the side close to the electron gun. To match the propagation delays a cable delay of 3 metres is installed in the path of WCM490 intensity signal. The cables connecting WCMs with the SCB, as well as the interlock signal cable are HELIFLEX 7/8" type.

The control unit was installed in CTF3 main control room. It allows very simple method of setting the threshold voltage and its observation. Because of signal attenuation caused by long cables a small calibration circuitry was added to the control unit to provide correction mechanism for the threshold voltage observation. A low-frequency (10MHz) output signal is provided to observe the difference signal between two WCMs (loss signal).

MEASUREMENTS AND RESULTS

To measure the propagation delay of the system installed we've observed the signals from the outputs of WCMs together with the output of optical link (converted to electrical signal). By knowing the propagation delays of measurement cables and electronics we are able to evaluate the time-of-reaction. The summary of results measured is shown in table 2.

Description		***Delay [ns]***
WCM propagation delay	T_1	8
WCM490 to SCB_1	T_2	94.5
SCB propagation delay	T_3	16.3
SCB_1 to EOC via FLEXWELL	T_4	97
EOC propagation delay	T_5	4
5 metres of optical cable	T_6	25
WCM823 to SCB_1	T_7	44

Table 2: The propagation delays of different parts of the MPS as measured in the machine after installation

As in the previous section, the worst case time-of-reaction is calculated by summing relevant delays and adding the time of flight of particles from electron gun to the WCM823, thus:

$$T_{p,wc} = T_{gun,wcm_2} + \sum_{i=1}^{6} T_i = 311.8\,ns$$

This value approximatively corresponds with estimated $T_{pe,wc}$. The difference comes from different cable length assumptions during estimation of time-of-reaction.

Figure 2 shows the measurement of different signals in SCB. To observe possible problems due to slow slew-rate of the difference signal, a square pulse is passed to one of the inputs of SCB via low-pass filter. Second input of SCB is 50Ω terminated. The green trace corresponds to difference signal of two SCB intensity inputs, red and black traces are corresponding threshold voltages. The blue trace shows the output of ECL comparator just before R-S flip-flop. First positive edge of this signal, freezes the state of the interlock signal on its active level, and it suppresses the beam production until a reset is performed. An influence of slow slew-rate of the input is visible at the comparator's output.

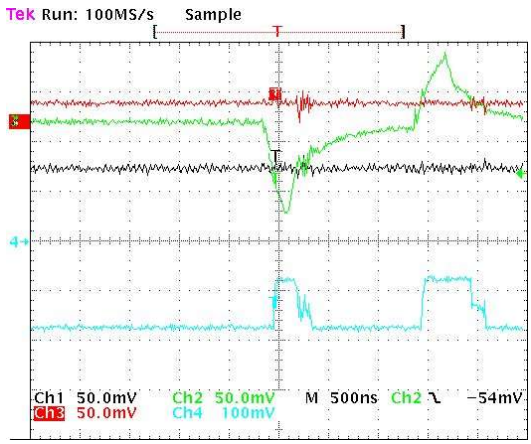

Figure 2: The response of the SCB comparator when losses are detected.

CONCLUSION AND OUTLOOK

The preliminary measurements of the propagation delays show good agreement with the values estimated. It is visible, that major propagation delays are caused by transmission of the signal from SCB to EOC - and for the worst-case also by propagation time of the particles from the gun to the place where the loss occurs. These delays still can be minimized, although it is questionable if it is worth.

The worst-case propagation time $T_{p,wc} \sim 312\,ns$ corresponds to minimum reaction time of the MPS. For the WCMs placed further from the gun the propagation delays must be correspondingly adjusted, but one can assume, that we will be able to stop the beam production within the present pulse train only for first three or four WCMs.

A full version of this system is in the preparation. The new control system based on Rabbit microprocessor and touch screen assures good user interface for the MPS. A digital communication link with the SCBs is used. The SCBs were upgraded to support digital threshold setting and acquisition. Also the possibility of independent masking of SCBs was implemented. The corresponding control software and testing must be done.

REFERENCES

[1] P. Odier, "A New Wide Band Wall Current Monitor", DIPAC'03, Mainz, May 2003, pp. 216-218

[2] G. Bienvenu, M. Bernard, J. Le Duff, H. Hellgren, R. Pittin, L. Rinolfi, "A Thermionic Electron Gun for the Preliminary Phase of CTF3", EPAC2002, Paris, June 2002

LEIR BEAM INSTRUMENTATION

C. Bal, E. Bravin, S. Burger, C. Dutriat, M. Gasior, T. Lefevre, F. Lenardon, P. Odier, U. Raich, L. Søby, J. Tan, G. Tranquille, C. Vuitton, CERN, Geneva, Switzerland

Abstract

The Low Energy Ion Ring (LEIR) is central to the "Ions for LHC" project. Its role is to transform a serie of long low intensity ion pulses from Linac 3, into short high density pulses, which will be further accelerated in the PS and SPS rings, before injection into LHC. To do so the injected pulses are stacked and phase space cooled using electron cooling, before acceleration to the ejection energy of 72 MEV/u. This note describes different types of instruments which will be installed in the LEIR ring and transfer lines.

INTRODUCTION

In addition to proton operation, the LHC machine will run a few weeks per year with ions to provide collisions for heavy ion experiments. The lead ion intensities achievable with the former ion accelerator chain were far below the needs for LHC, and it has been decided to convert the previous Low Energy Antiproton Ring (LEAR) into a low energy ion ring, dedicated to accumulate and cool ions, in order to reach the required beam brilliance for LHC. The installation of the LEIR machine is underway and commissioning will start soon. A typical LEIR cycle is shown in Figure 1. At the end of each multi turn injection of 200µs of PB^{54+} the beam is electron cooled and stacked. After 4-5 injections the beam is bunched and accelerated to the ejection energy, where two bunches of 4.5 10^8 ions each are created and transferred to the Proton Synchrotron (PS). The main machine parameters are resumed in Table 1.

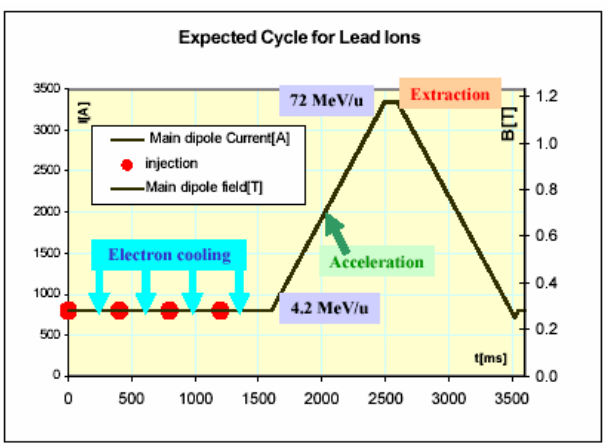

Figure 1: A typical production cycle.

Table 1: LEIR parameters.

Circumference	78.54m
Relativistic beta	0.095-0.37[1]
Energy	4.2-72 MeV/u
Rev. Frequency	0.36-1.41 MHz
Q_H, Q_V	1.82, 2.72
Intensity range	2E8-2E11 Charges
Injection pulse	200us 50uA
Ejection bunch	2* 200ns 50mAp
Vacuum	10^{-12} Torr
Bake out temp.	300 ˚C

INJECTION LINES

The injection line from LINAC3 consists of 3 segments: ITE, ETL which is common with the ejection line and the IE line just before the ring, see Figure 2.

Position

A total of 10 scintillating screens and cameras (MTV's) will be installed in the LEIR transfer lines. Seven are used to steer the injected beam, from which four can also be used at ejection.

Heavy ions at low energy are stopped within a few µm and all the energy is deposited in a very small volume. Different types of screen materials were tested in Linac3 [2], in order to find a material capable of withstanding this energy deposit. The material often used in high energy accelerators Al_2O_3, showed degradation and reduced sensitivity after a few hours of beam. ZrO_2 for which a degradation of the material was visible, showed no reduction in sensitivity, and has been chosen as screen material.

A new MTV electronics hardware, consisting of a single VME 64x card, has been developed. This card is capable of controlling: all the different types of positioning mechanism for the screens, the adjustment of the illumination intensity, the different types of cameras (i.e. CCD or Vidicon tube) and the positioning of optical filters in front of the camera. Apart from the analog video signal the card provides also the digitized image.

Intensity

Three old transformers will be re-used and installed in the ETL and EI lines refurbished with new magnetic shielding and water cooling system according to the PS standard model. New front end electronics have been

[1] Will be extended to 0.9 for light ions, but not before 2009.

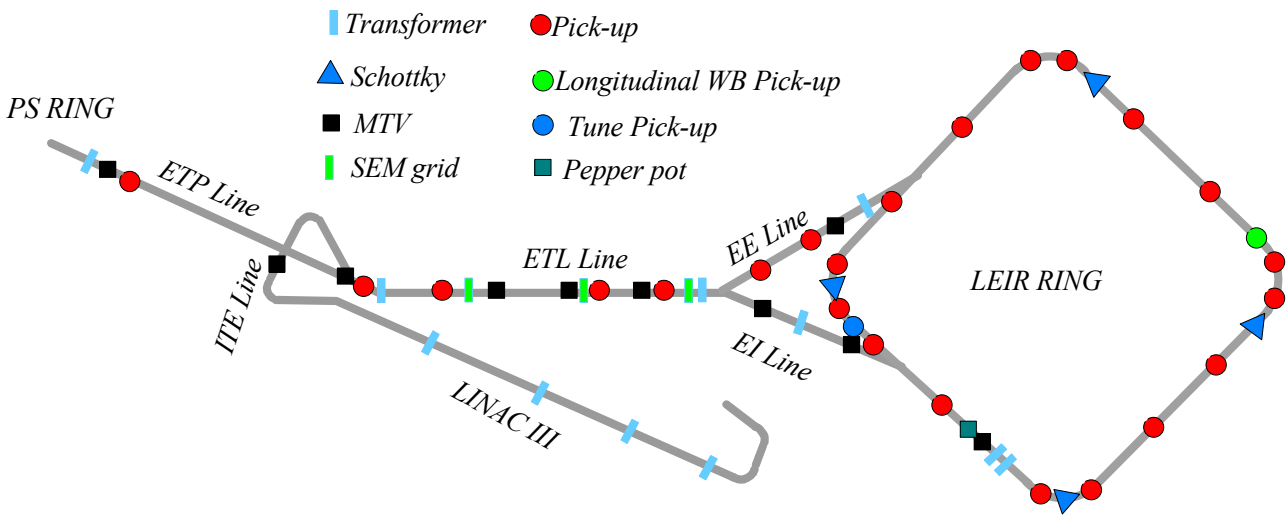

Figure 2: Layout of the LEIR complex and instruments.

developed which will in the near future be used to standardize all the transformers of the PS complex.

The two transformers installed in the ETL line, which will also have to measure the current of the two ejected bunches, will be equipped with 2 sets of electronics, one slow and one fast.

After amplification by the front end electronics and transmission to the control room the signals will be digitised with a 12 bit, 10MS/s FADC followed by digital baseline restoration and integration.

INJECTION

Injection Efficiency

For the measurement of the multi turn injection efficiency (T_{rev} =2.7μs), a special semi fast transformer is requested. It will allow measuring every injection pulse (200μs) with a droop less than 1%, but will also have a time constant short enough to measure the next injection 200ms later, without any current offset. This means a frequency bandwidth from 8 Hz to 500 kHz.

Schottky

The Schottky pick-ups are non perturbation measurement tools which provide a large set of informations for either coasting or bunched beams. With a spectrum analyser one can deduce: the tune, the emittance, the momentum distribution and the revolution frequency. Two existing systems, inherited from the former LEAR machine will be brought back to operation. Both consist of a succession of short strip-line pick-ups. Two of them will be connected as travelling wave pick-ups suitable only for low energy particles at injection (b = 0.095). The two other pick-ups are used in a parallel configuration, which will work at all particle velocities. There are two Schottky pick-ups per transverse plane but the horizontal ones also yield longitudinal informations.

Emittance

The emittance and matching of the beam injected into LEIR will be measured by means of a "pepper pot" device. This device consists of a molybdenum mask, in which a square matrix of 0.17mm holes with 1mm spacing is drilled.

The surviving particles will be observed on a scintillating screen located some 30cm further downstream and digitized using a CCD camera. By measuring the width and the center of the distribution of each beamlet, it is possible to reconstruct the transverse phase space distributions of the injected beam.

ELECTRON COOLING

Trajectory

Two H+V electrostatic pickups placed at each end of the drift space are foreseen to measure the electron and ion trajectories separately. The expected resolution is 0.1mm so as to insure that electron and ion beams are aligned within an angle lower than 1mrad.

Profiles

For the measurement of the ion beam transverse profiles and the electron cooling efficiency, two Beam Ionisation Profile Monitors (BIPM) will be installed. Both monitors consist of electrodes separated by alumina plates and a two-stage multi-channel plate (MCP) for the amplification of the ionisation signal. This amplified signal is collected on a strip readout having a resolution of 1mm.

Despite the expected ultra-high vacuum in the LEIR ring (2 x 10-12 torr), given the increased number of lead ions available from the source, it should be possible to obtain enough signal to measure profiles every 20 ms thus enabling a very precise evaluation of the electron cooling time in the horizontal and vertical planes.

ACCELERATION

Orbit

In the ring 32 ceramic based electrostatic PUs are foreseen. Eight horizontal and eight vertical shoebox type will reside inside the bending magnets, and eight combined horizontal and vertical cylindrical PUs in the straight sections, of which 2 are inside the electron cooler.

The orbit measurement system consists of head amplifiers (3 gains), which generates the Δ and Σ-signals, distribution amplifiers and an analogue normaliser module, whose output is proportional to the average beam position. These 32 signals are then fed to a multiplexing ADC.

Tunes

The LEIR system will be equipped with a strip line kicker, which can deliver large kicks needed for machine non linearity studies. Betatron oscillations will be observed on a dedicated electrostatic pick-up.

The acquisition system will be based on the Direct Diode Detection (3D) method [1], where the beam pulses from the pick-up are stretched in time, in order to increase the betatron frequency content in the base band. This can be accomplished by a simple diode detector followed by an RC low pass filter, as used in the common envelope detection technique for demodulating AM signals. The circuit can increase the betatron signal level by orders of magnitude compared to classical systems. In addition, it suppresses the revolution frequency content by a few tens of dB, which would be very difficult to achieve by other means, due to some two octaves of frequency swing.

Intensity

For the measurement of the circulating beam current, the continuous current transformer (DCCT) employed in the previous LEAR will be reused and installed in straight section 12. A new magnetic shielding is designed and the water-cooling system, needed during the bake-out, is renovated. An electronic similar to that one used in the PSB and PS will be adapted to the existing transformer, which is from a previous generation.

The ß normalization will be based on the 1 Gauss B-train counting and on look-up tables calculated for the various types of ions foreseen. 3 ranges available in parallel will cover the intensity. The acquisition of the 3 ranges will be made, during all the time the beam is circulating, with a 1 kHz sampling rate by a 12 bit ADC. A post-acquisition selection is performed to choose the best range, i.e. the highest non-saturated range. A resolution of 2uA and temperature drift of 5uA per deg. C is foreseen.

Longitudinal Profile

The existing 300MHz wide band pick-up will be used for measuring the longitudinal bunch shape. The pick-up consists of a stainless steel ring (length=200mm, diameter=120mm) mounted on ceramic isolators.

The signal induced by capacitive coupling will be amplified and monitored with a fast digital oscilloscope.

EJECTION

Trajectory

In the LEIR ejection lines, 7 horizontal and 7 vertical electrostatic PUs will be installed.

The cylindrical PUs exists in three different diameters, and are made of stainless steel (316 LN) sheets. One annular electrode provides the intensity signal, and the difference signal is derived from a v-cut cylinder, forming two semi-sinusoidal electrodes.

The acquisition system consists of a head amplifier mounted close to the PU, followed by differential transmission to the control room. Here the signals are split to several users, among others a 12 bit 200MS FADC based digital acquisition system, which will digitise the position and intensity signals.

Intensity

A total of four fast transformers are used to measure the ejected beam intensity. For the fast extraction pulses 200MS FADC's are used to digitise and integrate the ejected bunches.

Profiles

As mentioned earlier four of the MTVs used to steer the injected beam will also be used at ejection. Another two will be installed in separate parts of the ejection line. Since the trajectory will be measured by the PUs, the main purpose of the MTVs will be profile measurements. Frame grapper software provides this from the digitized images.

To measure the emitance of the ejected beam three SEM grids will be installed in the ETL line. They consist of 1mm thick ceramic grids onto which 30 wires of 40um gold coated tungsten, have been soldered every 1.5mm. Each detector consists of 2 such grids mounted on independent arms, which are controlled by pneumatic motors. The acquisition system consists of 30 integrators followed by sample and hold system and ADC's.

CONCLUSION

This note describes the beam measuring instruments foreseen for the LEIR commissioning which will start in June 2005 and continue until mid 2006. Injection of lead ions into LHC is foreseen for the beginning of 2008. Results and performances of the LEIR beam diagnostics will be presented on next years conferences.

REFERENCES

[1] M.Gasior, R.Jones, "High Sensitivity Tune Measurement by Direct Diode Detection", this conference.

[2] C. Bal, E. Bravin, T. Lefèvre, R. Scrivens, M. Taborelli, Scintillating Screens Study for LEIR/LHC Heavy Ion Beams, this conference.

HARDWARE SIMULATION KIT FOR BEAM INSTRUMENTATION

Arkady Lokhovitskiy, Danil Kortchaguin, JINR, Dubna, Russian Federation
Michael Ludwig, CERN, Geneva, Switzerland

Introduction

For beam instrumentation front-end software consolidation in the CERN-PS AB-BDI-SW section has launched a campaign in collaboration with the Joint Institute for Nuclear Research (JINR) in Dubna (Russia). This consolidation is to a large extent re-engineering of legacy front-end software of the running CERN-PS machine. This raises the following issues: standardization, simulation of non active timing events, simulation of non available hardware, and backward compatibility. This paper describes a beam instrumentation hardware simulation, which is used to develop, test and validate instrumentation software, which are disconnected from the real hardware and machine timings.

CONSOLIDATION

The aim of this consolidation is to replace instrumentation servers in our front-end computers (FECs) which have reached the end of their lifecycle after more than a decade by completely re-engineered instrument servers for the LHC Injector chain. Directly affected are 15 FECs for beam current measurements hosting in total 279 devices and 8 FECs for beam position measurements with 357 devices, all of which are "24h/7d" mission critical. The new servers have to cover all functionality of the existing software, provide a high degree of backward compatibility in order to avoid software incompatibility in the client application layer, and provide subscription, structured properties, a data subset selection mechanism, object oriented design and code generation using graphical design tools. All these new features are needed to satisfy the increased demands of the LHC era. New servers are test-deployed and validated on a per-FEC basis under operational conditions with beam in dedicated software machine development sessions: this is normally the first time a new server runs with real hardware.

CONSTRAINTS

Standard Framework

The Front-End Software Architecture (FESA) framework [1] is the new framework which is used to overcome the current diversity in the LHC injector chain front end equipment software domain and pave the way towards LHC for efficient development, diagnostic and maintenance in this area. All data retrieving and processing is going through two types of actions: real-time (RT) actions and communication (COMM) actions. RT actions are scheduled according to timing maps and manage control and acquisition data flows between the hardware and a common shared memory region called FESA device. COMM actions are scheduled according to users' requests and transmit data to client applications.

Instrument Functional Model

An instrument server generally performs many acquisitions from different hardware modules at different moments during the production of a type of a beam[*], processes them according to the logic of the measurement and then publishes the results for each type of beam separately[†]. The result data must be available and consistent for at least the duration of one cycle (of a given type), so that the application client can pick it up before it is overwritten by the next cycle of the same type.

Backward Compatibility

FESA is not fully backward compatible with the present control system (referred to as **g**eneral **m**odules **GM**) and existing naming conventions [1]. The GM type software clients are interfaced to FESA using a system of special GM classes for each instrument which connect to a set of FESA properties for this instrument (FESA2GM adapter). Each GM class provides full inheritance to the GM super classes at the same time. Thereafter, the GM-specific communication channels: local GM access in the FEC, the common middleware servers (CMW) and the remote procedure calls (RPC) servers can be used transparently. Correspondence maps between old and new properties and devices, which provide also many-to-one relationships, are used to overcome naming incompatibilities and to regroup devices in the re-engineered instruments.

STANDARDIZATION

In the context of the consolidation project [3] we deal with a lot of hardware module types and different coding principals. At the same time there are no common patterns to standardize and simplify hardware module calls as the FESA does with an instrument design. This requires finding some solution to provide an abstraction as a standardized approach to HW interaction design in FESA, including instrument simulation. The abstraction has to solve the following issues:

- Support a vastly heterogeneous structure of equipment and coding technologies present in CERN.

[*] A beam is produced during a cycle. A sequence of several (usually different) cycles forms a supercycle.

[†] The results are multiplexed in pulse-to-pulse (=cycle) modulation (PPM) slots of the device memory.

- Reuse efficiently existing code/design and provide high expansibility to work with new hardware module types at a later time.
- Simulate a hardware module behaviour to test and validate instruments, which are disconnected from the real hardware. Exclude an instrument rebuilding at switching on/off the simulation mode.
- Ensure compatibility with FESA framework and device drivers installed on FECs of the LHC complex.

HARDWARE SIMULATION KIT

The hardware simulation kit represents a layer between the FESA framework and hardware application programming interface HW-API (see Figure 1). It's based on an object oriented approach to closely link the software to the hardware module [4][5] and allow its real control or its simulation. In addition it allows us to switch from the real world to simulation and vice-versa in a transparent manner, just by configuration.

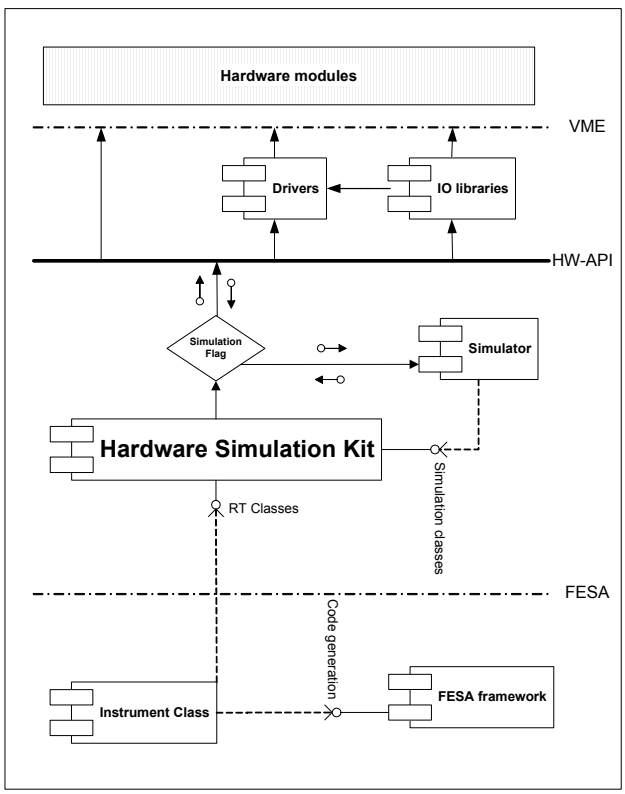

Figure 1: Component cooperation diagram. Here, a dashed line means a relation, a solid line with an arrow – an invocation, a solid line with a circle – a public interface, a circle with an arrow – data flow direction.

It provides:

- standardization of hardware interaction design within the FESA framework,
- the simulation functionality to efficiently develop and test instrumentation servers which are partially or entirely disconnected from real hardware,
- an extension interface to develop specific classes for new hardware module types and thus extend the simulation toolkit .

The hardware simulation kit implements pairs of related classes for each hardware module type with a set of default methods to perform read/write or in/out actions: one class is to be used in an RT process to both modes working with real hardware and simulation, the second one is to design an instrument specific simulator that has to be a separate process running on the same FEC where instrument binaries were deployed. All the methods calling a real hardware are virtual and can be redefined in derived classes in course of an instrument development

Beside read/write and in/out all other types of actions controlling hardware (initialize, restart, start and stop scanning, etc.) can have unpredictable function and coding principals. As described above the standardization nevertheless requires giving an interface to extend a base class functionality adding instrument specific actions. To solve this problem in the hardware simulation kit they have been excluded from a device class scope and implemented as an independent branch of the class hierarchy (see Figure 2 – Device command components).

The hardware simulation kit also contains a set of abstract template classes imposing a protocol to add new types of hardware modules. They are a public interface of Abstract Template Classes component (see Figure 2). Have implemented all the abstract methods in a derived class for a new hardware module type will get available for end-users.

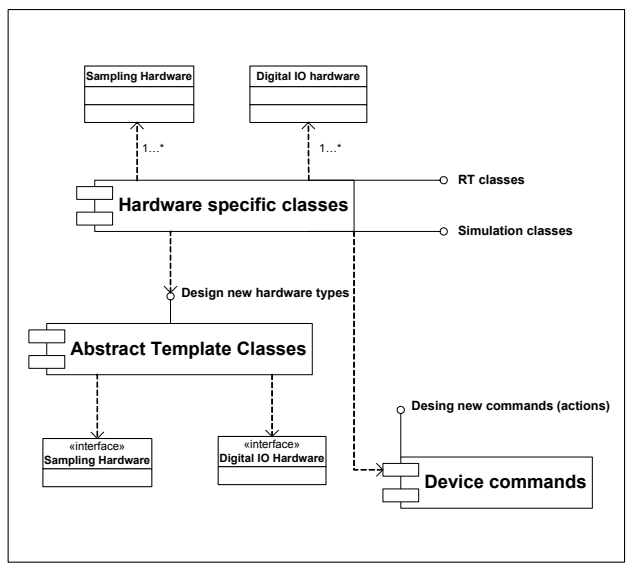

Figure 2: The hardware simulation kit component diagram (a dashed line means a relation (1…* - one-to-many), a solid line with a circle – a public interface).

SUMMARY

Simulation of instrumentation hardware (including timing [6]) is essential in order to efficiently develop and test instrumentation servers within the consolidation scenario for the LHC injector chain. The constraints of standardization, backward compatibility and instrument functionality are addressed, so that the consolidated instrument can be deployed on a per-FEC basis with minimized impact on operations.

At present a few instrument servers based on the hardware simulation kit are in progress. They measure or simulate a beam current and orbits using the following types of standard hardware modules: MPV908, SIS3300, DPRAM, and ICV196. They allow us to access the efficiency of the proposed implementation.

REFERENCES

[1] "FESA Essentials", http://project-fesa.web.cern.ch/

[2] "Guidelines and Conventions for Defining Interfaces of Equipment Developed Using FESA", AB-Note, CERN, 2005.

[3] "Consolidation Programme for CERN Accelerators", P. Bonnal, R. Forrest, J. Poole, AB-Note-2005-018, CERN, 2005.

[4] "MPV908 Operating Manual – Analog I/O Series ", Pentland System LTD, 1996.

[5] "General Sampler Class Specifications", C.H. Sicard, F. di Maio, PS-CO-Note-94-62, CERN, 1994.

[6] "The 8ESA Simulation Timing Event Source", M. Ludwig, CERN, 2005.

ACCURACY OF THE SPS TRANSVERSE EMITTANCE MONITORS

F. Roncarolo, B. Dehning, C. Fischer, J. Koopman, CERN, Geneva, Switzerland

Abstract

A campaign of studies and measurements has been carried out with the aim of establishing the SPS transverse profile monitors resolution, reproducibility and accuracy. The studies regarded systematic dependencies of the SPS Wire Scanner (WS) monitors on the operation setups and on the beam parameters, like beam intensity, bunch spacing and beam size. The emittance increase due to multiple Coulomb scattering during the linear WS operation has been measured and compared with the theoretical model prediction. Numerical simulations estimate the errors introduced by the limited resolution of the imaging systems and by excessive electronic noise of the detectors. The experimental measurements have been carried out with a wide range of beams, from the low intensity pilot bunch to the LHC nominal beam. At first the different SPS WS are compared during simultaneous measurements. The SPS IPM vertical profiles have been compared to the WS while tracking the beam emittance from 26 to 450 GeV. The IPM resolution improvements from 2003 to 2004 are pointed out.

WS MEASUREMENTS

The CERN SPS is equipped with ten WS monitors (five for each transverse plane) mounting $30\,\mu m$ diameter Carbon wires. Four of them are based on a mechanism that drives the wire *linearly* along a direction orthogonal to the beam trajectory with a maximum speed of $1\,m/s$. The remaining six monitors are based on a rotational mechanism which drives the wire at a maximum speed of $6\,m/s$.
All the WS measurements presented below were carried out with two or three instruments simultaneously, with a time jitter of $1\,ms$. For all the plots and tables which will be presented hereafter, the emittances are intended at one sigma and normalized to the beam energy.

Linear WS Calibration

The result of the simultaneous operation of two linear WS (measuring the vertical beam size) during seventeen SPS cycles is shown in Fig. 1. Each time slot (horizontal axis on the plot) refers to one cycle and consequently to the injection of new particles that do not necessary have the same emittance as in the previous cycle. Two scans per cycle are performed with each instrument: at $t = 0.5\,s$ after the protons injection the wires move in a forward direction (*IN scan*, from the bottom to the top of the beam pipe) and at $t = 1.5\,s$ they move backward (*OUT scan*). Both instruments detect a systematic emittance increase during

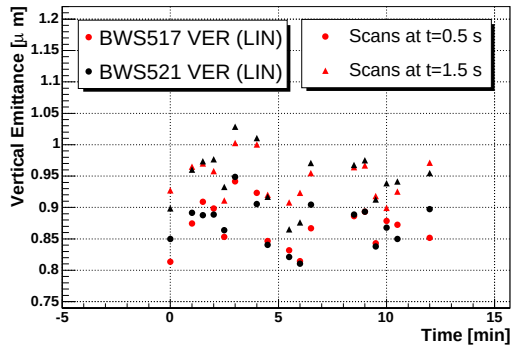

Figure 1: Comparison between two linear WS during simultaneous measurements with TOTEM beam injected every 30 s in the SPS and circulating at 26 GeV for 4.5 s.

the two scans. This is due to Coulomb scattering between the beam and the wire material, the OUT scan detects the emittance increase generated by the IN scan [3].

The standard deviation of the measured emittance increase, divided by $\sqrt{2}$ (since the increase is detected by two scans), assesses the monitors *repeatability*. In terms of beam size the repeatability results in 6 and $10\,\mu m$ for the considered instruments. The mean value of the differences between the emittances measured by the two linear monitors determines the relative WS *accuracy*. The relative average difference results well below $1\,\%$ of the small vertical emittance characterizing the measured beam ($\approx 0.9\,\mu m$).

Cross Calibration Between Linear and Rotational WS

The three rotational WS monitoring the vertical beam size have been operated in synchronization with a linear device (labelled 517V) used as a reference. Table 1 and Fig. 2 summarize the comparisons, including the one between the two linear WS described in the previous paragraph. The IN and OUT scans are analyzed separately and in the table μ, σ and σ_μ are the differences mean value, standard deviation and error on the mean ($= \sigma/\sqrt{N_m}$) over N_m measurements. The figure also refers to the "IN/OUT correction".
A post-processing of the values of the wire position during the rotational WS operation is in fact necessary. The measured angular position of the wire is projected on the transverse coordinate by an algorithm. A systematic error in the angular position arises from a low pass filter used to reduce the electronic noise on the potentiometer. Such filter introduces a delay in the time domain between the measured and the real angle, which results in an opposite

Table 1: Vertical normalized emittance differences between the linear WS labelled V517 and the other four SPS WS, separating the IN and OUT scans. (R) stands for "Rotational" and (L) for "Linear".

Monitors	N_m	Relative Emittance Difference [%]					
		Scan IN			Scan OUT		
		μ	σ_μ	σ	μ	σ_μ	σ
414V(R)	14	4.0	1.9	7.1	-3.7	2.3	8.7
416V(R)	5	-32.7	2.1	4.7	-37.9	2.2	4.9
519V(R)	7	10.4	2.7	7.1	-0.8	4.1	10.8
521V(L)	17	0.3	0.6	2.3	0.1	0.6	2.5

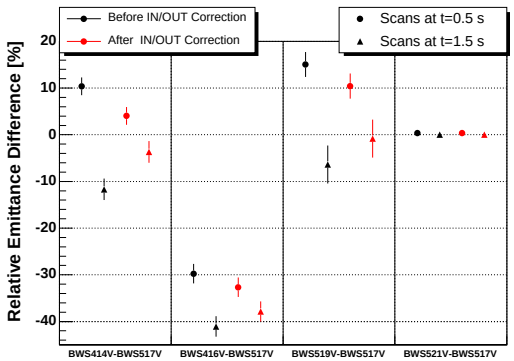

Figure 2: Normalized emittance relative differences between couples of WS monitors.

sign offset in the angular domain for opposite movement directions. Even if the wire speed is constant, the measured transverse beam size is distorted, due to the non linearity of the wire position projection on the transverse coordinate. Hence, without any off-line correction, the emittance measured during the IN scan systematically results about $10\,\%$ higher then the one measured during the OUT scan. The off-line correction reduces the error to below $3\,\%$ [2].
Reconsidering now the comparisons summary of Table 1, the error on the mean σ_μ, expression of the accuracy of this set of measurements, has a maximum value of $4\,\%$ (for the monitor labelled 519V, OUT scans). The *repeatability* of the differences follows from the repeatability of the compared instruments. With the assumption that all the monitors are characterized by the same statistical fluctuations in measuring the beam size, the repeatability would be the standard deviation of the differences divided by the square root of 2. However it is not known a priori if the repeatability of the rotational WS is equal to the one of the linear devices. Profiting of the considerations of the previous paragraph, we can take $r_{517V} = 10\,\mu m$ as the repeatability of the reference wire scanner in terms of beam size. This corresponds to a variation of $10\,nm$ of the absolute emittance. In terms of relative emittance the repeatability of BWS517V is $r_{\epsilon 517v} = 1.1\,\%$. This value, together with the statistical fluctuations of the differences between couples of instruments can be used to calculate the repeatability of the other monitors according to:

$$r_{dif,i} = r_{i-517V} = \sqrt{r^2_{\epsilon 517V} + r^2_{\epsilon i}}$$

Table 2: Repeatability in terms of beam size of the five SPS WS monitoring the vertical plane.

Monitor	Repeatability $[\mu m]$			
	Scan IN	Scan OUT	Average	RMS
414V (R)	29.9	36.8	33.4	4.9
416V (R)	32.6	36.8	33.4	1.0
519V (R)	33.1	50.6	41.8	12.4
517V (L)	10			
521V (L)	12.8	14.3	13.6	1.0

$$\Rightarrow \qquad r_{\epsilon i} = \sqrt{r^2_{dif,i} - r^2_{\epsilon 517V}} \quad \text{with i=414V, 519V, 521V}$$

where the values $r_{dif,i}$ are the standard deviations σ of the differences in terms of relative emittance. From each value $r_{\epsilon i}$ the repeatability in terms of absolute beam size can be calculated, after denormalizing for the betatron function and the beam energy. The repeatability values determined for the five WS are summarized in Table 2, where the average and RMS values are calculated from the IN and OUT scans.

CROSS CALIBRATION BETWEEN WS AND IPM

The SPS Ionization Profile Monitor (IPM) [4], designed to monitor the vertical emittance has been calibrated with respect to the WS, after several adjustments and upgrades during the year 2003 [5]. We will present the IPM-WS comparisons in measuring all the LHC type beams accelerated in the SPS in 2004 and confront the results with the ones obtained in 2003.
Unlike the previous measurements with the SPS WS, where the different monitors have been compared simultaneously on the same beam, the comparison between IPM and WS has been carried out over long periods. In such a way it was possible to assess the IPM repeatability with different gain settings and its reproducibility with different beam conditions. During the considered periods the beam emittances measured by the IPM and the WS are determined by averaging a number of profiles. The averages which will be presented in the plots and tables are computed from all the profiles at a fixed time in the cycle for several cycles. The error bars on the plots indicate the error on the mean. The cross calibration has been carried out during the acceleration in the SPS of the LHC *pilot*, the *75 ns bunch spacing* and the *LHC nominal* beams, differing in intensity and bunch spacing and beam size. Fig. 3 displays the vertical emittance as function of time in the cycle, as measured by the IPM and WS monitors with the nominal LHC beam in 2003 and 2004. The particles circulate at 26 GeV until $t = 10.8\,s$, when the acceleration starts. The energy flat-top at 450 GeV begins at $t = 18.5\,s$. In 2003 the IPM overestimated of about $17\,\%$ the emittance measured at top energy by the WS. The discrepancy dropped below $2\,\%$ in 2004. This demonstrates the improved resolution obtained after the upgrade of the imaging system [5]. Table 3 summarizes the IPM-WS comparisons carried out in 2004

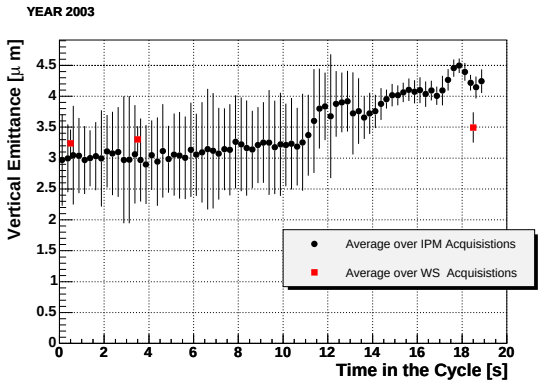

(a)

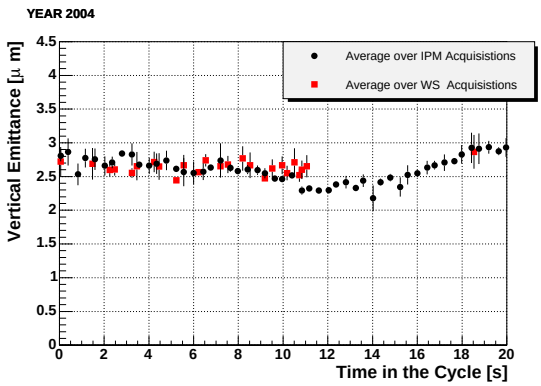

(b)

Figure 3: Vertical normalized emittance measured by the IPM with LHC nominal beam and comparison with the WS: (a) year 2003, (b) year 2004.

with the three different beams. Fig. 4 displays the absolute difference between the beam size σ_{IPM} measured by the IPM and the expected value at the IPM location σ_{WS}, derived from the WS measurements. The difference is plotted as function of σ_{WS} for the various measured beams. The largest discrepancy between IPM and WS is with the smallest beam, the pilot bunch at 450 GeV. Expressing the IPM *beam size error* as $\delta\sigma = \sqrt{\sigma_{IPM}^2 - \sigma_{WS}^2}$, $\delta\sigma$ resulted in about $350\,\mu m$ in 2003 and $250\,\mu m$ in 2004. For an expected beam size of $224\,\mu m$ at the IPM location (see last line in Table 3), the IPM *beam size overestimation* ($\sigma_{IPM} - \sigma_{WS}$) was about $240\,\mu m$ in 2003 and decreased to $140\,\mu m$ in 2004. These two values are very close to the $\mu m/pixel$ factors achieved in the two years with the different optical imaging systems.

SUMMARY AND OUTLOOK

During the acceleration in the SPS of low intensity, low emittance beams the wire scanner monitors were operated simultaneously. The linear WS, have been considered as a reference and the rotational compared to them. The systematic difference between two linear WS is below 1 % in terms of normalized emittance. The difference between the rotational and linear monitors emittance varies from 3 to

Table 3: IPM resolution with different beam conditions and comparison with parallel wire scanner measurements. Measurements taken during the SPS 2004 run. σ^e_{IPM} is the beam size expected at the IPM location, derived by the WS measurements.

Beam	E_b $[GeV]$	$\sigma^{\mathbf{m}}_{\mathbf{IPM}}$ $[mm]$	$\sigma^{\mathbf{e}}_{\mathbf{IPM}}$ $[mm]$	$\epsilon_{\mathbf{IPM}}$ $[\mu m]$	$\epsilon_{\mathbf{WS}}$ $[\mu m]$	$\mathbf{\Delta}\epsilon$ $[\%]$
LHC	26	3.097	3.085	2.770	2.750	0.7
Nomin.	450	0.762	0.755	2.900	2.850	1.8
75 ns	26	2.209	2.201	1.410	1.400	0.7
	450	0.583	0.535	1.700	1.430	18.9
Pilot	26	0.985	0.911	0.280	0.240	16.7
	450	0.361	0.224	0.650	0.250	160.0

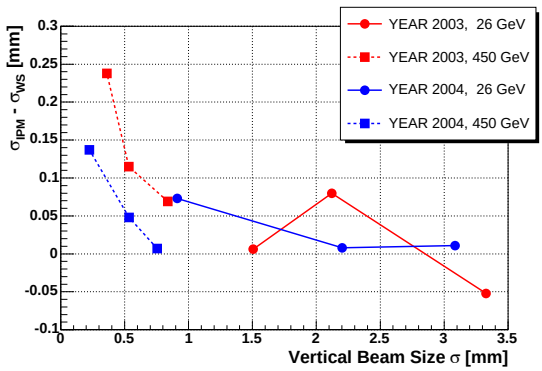

Figure 4: Comparison between IPM and WS derived from all the available measurements, in terms of beam size differences.

38 % (in terms of normalized emittance). The SPS Ionization Profile Monitor has been optimized and tested under several beam conditions and the measured normalized vertical emittance has been compared with the one measured with the WS. The IPM overestimates the width of low intensity, low emittance beams. Such effect is attributed to the limited resolution of the imaging system. Improvements were observed in the year 2004 with respect to the year 2003, but the relative disagreement between IPM and WS remains above 20 % in terms of normalized emittance when the beam size at the IPM location is below $400\,\mu m$.

REFERENCES

[1] G. Moliere, Z.Naturforscher 2a (1947) 133; 3a (1948) 78.

[2] F. Roncarolo, Accuracy determination of the emittance monitors for LHC, PHD thesis, to be published.

[3] F. Roncarolo, B. Dehning, Transverse Emittance Blow-Up Due to the Operation of Wire Scanners, Analytical Predictions and Measurements, Proceedings of the Particle Accelerator Conference, 2005, Knoxville, Tennessee.

[4] C. Fischer et al., Design and Tests of a New Rest Gas Ionisation Profile Monitor Installed in the SPS as a Prototype for the LHC, CERN-AB-2004-031-BDI.

[5] B. Dehning et al., Design and Test Measurements of the Imaging System of the Ionisation Profile Monitor, These Proceedings

SRAM-BASED PASSIVE DOSIMETER FOR HIGH-ENERGY ACCELERATOR ENVIRONMENTS

D. Makowski, M. Grecki, B. Świercz, A. Napieralski, DMCS, Łódź, Poland
B. Mukherjee, S. Simrock, DESY, Hamburg, Germany

Abstract

This paper reports on a novel Non-Volatile Random Access Memory (NVRAM)-based neutron dose equivalent monitor (REM counter). The principle of this device is based on the radiation effect initiating the Single Event Upsets (SEUs) in high density memories. Several batches of NVRAMs from different manufactures were examined in various radiation environments, i.e. ^{241}Am-Be (α, n) and Linear accelerator, produced radiation fields. A suitable neutron moderator was used to enhance the detector's sensitivity. Further experiments were carried out in a linear accelerator VUV-FEL. A separate batch of SRAM was irradiated with ^{60}Co-gamma source risen up to a dose of about 1.1 kGy. The proposed detector could be ideal for a neutron dose measurement produced by a high-energy electron linac, including synchrotron and Free Electron Laser (FEL) facilities.

INTRODUCTION

During the operation of high energy linear accelerators bremsstrahlung gamma and photoneutrons are produced [1]. Both gamma and neutrons pose a real threat to electronic devices installed in an accelerator tunnel. Therefore radiation measurement plays a crucial role to assure the reliable operation of accelerators. A large number of gamma detectors is currently available [2]. One can use photomultipliers, ionization chambers, scintillation counters and semiconductor-based dosimeters. Conversely to gamma, neutrons are uncharged particles, that have only a few interactions with matter, thus their detection is much more complicated than gamma. Neutrons are only detectable through measurements of secondary particles or a secondary phenomena [2, 3]. Superheated emulsion (bubble) and thermoluminescent (TLD) dosimeters can be used for sensitive neutrons measurement. Superheated emulsion dosimeters have a flat-response characteristic, however require an arduous bubble-counting process. TLD must be calibrated before the measurement.

The pulsed generation of neutrons in the high gamma background is difficult to measure. Gamma radiation has always an influence on the measured neutron fluence [2]. Only bubble dosimeters are able to measure neutrons fluence without gamma interaction.

Radiation present in linear accelerators, like the VUV-FEL or Linac II located at DESY, is produced because of the unwanted collision of the electronbeam with high Z materials in the beam line [1]. The amount of gamma is a few orders of magnitude higher than the neutrons' dose.

PRINCIPLE OF NEUTRON DETECTION

The basic idea of the SRAM-based dosimeter is to count the number of SEU induced in the memory during the measurement. SEU can be generated only by charged particles, which have relatively high Linear Energy Transfer (LET). Neutrons can be only detected from the secondary charged particles generated in the material (e.g. α, protons) [7].

The presented passive dosimeter uses Non-Volatile Random Access Memory instead of the classical SRAM device as a dosimeter, which is depicted in Fig. 1. SRAM devices

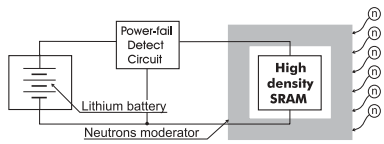

Figure 1: NVRAM-based neutron detector

cooperate with a lithium battery that provides a supply voltage when the memory is disconnected from the main power. An additional power supervisory circuit was implemented to detect a sudden disconnection from the main supply voltage and reconnect a back-up battery to avoid the accidental memory data corruption.

SEU in SRAM are generated by thermal neutrons which generate alpha particles present in accelerators, [5, 7]. Alpha particles have very high LET [7]. The energy is deposited along the ionising particle track, therefore electron-hole pairs are created. SEU is generated in the SRAM chip when a critical charge is deposited near the drain electrode of the MOS transistor [2]. The standard SRAM cell, presented in Fig. 2, consists of six MOS transistors, however only four are used to store a binary value. Solely, disabled transistors T_2 and T_3 are sensitive to SEU effect.

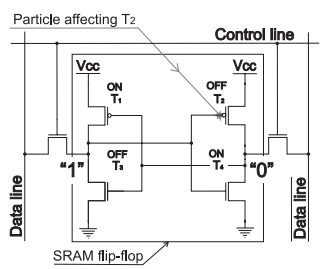

Figure 2: A single SRAM cell affected by ionising particle

The number of SEU induced in SRAM chips is proportional to the neutron fluence [3, 5]. However, the applica-

tion of SRAM as neutrons dosimeter requires a high sensitivity and linear response for a wide spectrum of detected particles. An appropriate neutron moderator assure a flat characteristics response for a wide spectrum of neutrons and allows to increase the detector sensitivity, see Fig. 1.

Design of Appropriate Moderator

All common neutron sensors (detectors), including SRAMs exhibits a high sensitivity to thermal neutrons. However, in all practical situations neutrons are not thermal but of much higher energy. The moderator is an entity which reduces the energy of the impinging neutrons to lower energies (process called thermalisation).

During the moderation process a part of the neutrons is also absorbed in the moderator. Therefore, a larger moderator reduces the neutron energy and absorbs a certain part of it, acting as a neutron shield. The experiments carried out in DESY Research Center in Hamburg proved that the sensitivity of the detector can be improved by the usage of higher density memories. The results of the experiment are presented in the following section. Memories designed for the operation with lower voltages (e.g. 3,3 V) are more susceptible to SEU. Moreover, SEU were detected in high density memories working on the ground level. Therefore, Error Correction Codes are implemented in modern high-density memories to avoid unwanted SEU in electronics. These type of SRAM chips are not good candidates for a neutron detector because of a very poor sensitivity to neutron generated SEUs.

A DEDICATED NVRAM READER

The contents of the NVRAM device can be read and written with a dedicated programmer. Configuration and reference data must be written to the memory before the first usage. This process is called memory formatting. The reference data can be programmed with a desired pattern. The application of a few different patterns allows to choose the most sensitive one. This pattern should be used for future measurements.

The configuration data are written to the memory starting from the address 0 up to 0x3FF. The data written with a repeated redundancy describe: memory density, its configuration, pattern used for the measurement, calibration factor, memory signature, date and the accumulated dose from the first usage. Some of these data are obligatory to calculate the neutron fluence during the irradiation (e.g. memory density, calibration factor), other can be used for diagnostic purposes. SEU generated in both main and configuration memories can be as well used to calculate neutron fluence.

The schematic diagram of the reader is shown in on Fig. 3. Data read from the memory can be displayed on LCD or sent to a PC computer. The device is able to operate 3.3 V and 5 V chips. The calibration factor read from the configuration memory of the chip is used to calculate the absorbed dose after the measurement. Fig. 4 presents

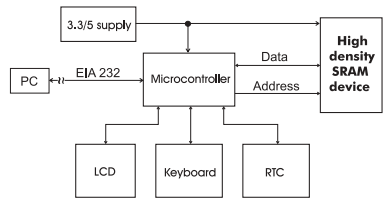

Figure 3: Schematic diagram of the SRAM reader

the Graphical User Interface (GUI) and some results for the measurement carried out in Linac II accelerator.

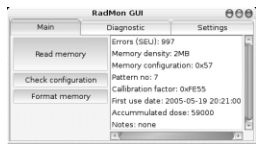

Figure 4: GUI interface of the dedicated NVRAM reader

RESULTS AND DISCUSSION

NVRAM chips fabricated by Texas Instruments and Dallas were used during the experiment. The devices were calibrated with a standard neutron source ^{241}AmBe during 24 hours. The source was moderated with the use of deionised water in order to imitate the energy spectrum of the linear accelerator [6]. Cross-sections for the memories, used during the experiment and Calibration Factors (CFs) are shown in Fig. 5. CFs allow to calculate neutrons fluences relying on induced in SRAMs SEUs.

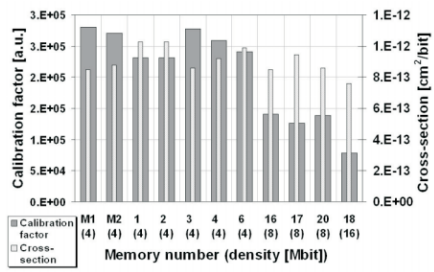

Figure 5: CFs and cross-sections for the memories irradiated from AmBe

Measurements in VUV-FEL

Previously investigated memories with additional bubble and TLD dosimeters were irradiated within 48 hours in the VUV-FEL accelerator. The devices with numbers 1 and 2 were placed 50 cm from the bunch compressor 2, the memories 3, M2, 6, 4, 17 were placed along the accelerating module 1, from input to output of the module. However chips 16, 18, 20, 21 were attached to the tunnel's

wall, opposite to the modules 4 and 5. The cross-sections and neutron fluences calculated for the memories are presented in Fig. 6. The memories 16 and 18 were covered

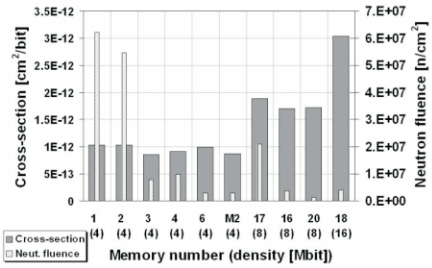

Figure 6: Cross-sections and fluences for the irradiated memories in VUV-FEL

in a polyethylene moderator, with the dimension equal to 6 cm, however chips 20, 21 were irradiated directly with no moderated neutrons. The results are presented in table 1. Neutron fluence calculated for the memory 20 is very

Table 1: Results obtained for 1 and 2 MB NVRAMs

No	Memory density [Mbit]	Induced SEU	Neutron fluence [n/cm^2]	Additional Moderator
20	8	10	1387522	no
21	16	21	1358192	no
16	8	26	—	yes
18	16	53	—	yes

close to the value obtained from the memory 21. The superheated emulsion dosimeter generated 44 bubbles. This result corresponds to 956 μSv. The dose of gamma radiation registered by TLD was equal to 3178 μSv. The devices were irradiated in VUV-FEL tunnel without the moderator. Memories 16 and 18 were packed in a polyethylene moderator. The number of SEU registered for these devices is two and a half times higher than SEUs generated, respectively, in memories 1 and 2. The lack of calibration factors for memories with moderators prevents the calculation neutron fluences.

High Gamma Dose Irradiation

Two batches of 256 kB memories were irradiated with a strong cobalt ^{60}Co gamma source, within 31 days. The dose of radiation absorbed by the memory was equal to 1.1 kGy. No SEU was registered in the memory contents. This validates, that gamma radiation has a negligible effect to trigger SEU in the SRAM.

SUMMARY AND CONCLUSIONS

High gamma background and pulsing neutron fields present in linear accelerators requires the usage of dedicated dosimeters to measure neutrons fluence. SRAM-based detector, insensitive to gamma radiation can be used as a neutron dosimeter. Experiments, carried out in VUV-FEL tunnel and with ^{241}AmBe proved that the sensitivity of the detector can be increased more than ten times. Another method to improve sensitivity is to use selected memories as regards to density and supply voltage.

The application of repeated redundancy allows to keep all necessary parameters of the memories in SRAM cells, therefore decreases the reading time and simplifies its operation. There is no need to set the memory density before reading of the irradiated chip. The number of generated SEU in memories of the same density was different, therefore NVRAM devices require individual calibration.

ACKNOWLEDGMENTS

We acknowledge the support of the European Community-Research Infrastructure Activity under the FP6 “Structuring the European Research Area“ program (CARE, contract number RII3-CT-2003-506395), and Polish National Science Council Grant “138/E-370/SPB/6.PR UE/DIE 354/2004-2007“.

THE AUTHORS

Dariusz Makowski*, Mariusz Grecki, Bartłomiej Świercz are affiliated to the Department of Microelectronics and Computer Science, Technical University of Łódź, Poland.

Bhaskar Mukherjee, Stefan Simrock are affiliated to the Deutsches Elektronen–Synchrotron DESY, Germany
e-mail: *dmakow@dmcs.p.lodz.pl

REFERENCES

[1] B. Mukherjee, D. Makowski, S. Simrock, “Dosimetry of high energy electron linac produced photoneutrons and the bremsstrahlung gamma rays using TLD-500 and TLD-700 dosimeter pairs”, NIM A, 2005.

[2] J.Barthe,“Electronic dosimeters based on solid state detectors”,NIM B , May 2001.

[3] F. Errico, M. Luszik-Bhadra and T. Lahaye, “State of the Art of Electronic Personal Dosimeters for Neutrons”, Symposium on radiation Measurements and Applications, Mai 2003.

[4] D. Makowski, M. Grecki, B. Mukherjee, S. Simrock, B. Swiercz and A. Napieralski, “The application of SRAM chip as a novel neutron detector”, Nanotech 2005, May 2005.

[5] D. Makowski, B. Mukherjee, M. Grecki and S. Simrock, “SEE induced in SRAM operating in a superconducting electron linear accelerator environment”, XIV IEEE-SPIE, May 2004.

[6] B. Mukherjee, D. Makowski, A. Kalicki, D. Rybka, M. Grecki and S. Simrock,“A neutron irradiation device for the testing of microelectronic components to be used in the radiation environment of high-energy particle accelerators at DESY”, MIXDES, June 2005.

[7] B. Mukherjee, D. Makowski, D. Rybka, M. Grecki and S. Simrock, “Interpretation of the Single Event Upset in Static Random Access Memory chips induced by low energy neutrons”, MIXDES, June 2005.

BEAM POSITION MONITOR FOR THE J-PARC MAIN RING SYNCHROTRON

T.Toyama*, D.Arakawa, Y.Hashimoto, S.Lee, T. Miura, H.Nakagawa, KEK, Tsukuba, Ibaraki, Japan
N.Hayashi, R.Toyokawa, JAERI, Tokai, Ibaraki, Japan

Abstract

A BPM system has been developed for the J-PARC Main Ring Synchrotron. A diagonal-cut 'electrostatic' pick-up and a processing circuit with an analog amplifier, attenuator, filter and ADC are adopted. The system expects no active devices in the tunnel to avoid radiation damage. The system aims at a position accuracy of ±0.1 mm. The test using whole system except a cable at the KEK-PS shows good system performance with the position resolution better than ±20 μm. The position accuracy will be attained with careful installation and beam based calibration.

INTRODUCTION

J-PARC 50 GeV Main Ring Synchrotron will feed 3.3×10^{14} protons per pulse (typically in 3.6 s), corresponding to an average current of 12.4 - 12.8 A and a peak current of 41.3 - 220 A as shown in Table 1[1]. Main features of this machine are: (1) high intensity, (2) main frequency components are localized less than a few 10 MHz, (3) a beam size is large both in transverse and longitudinal. To fit these characteristics the following design principle is adopted: (a) electrostatic pickup with diagonal-cut cylinder for linear response to the position, (b) no active devices (semiconductors) will be installed in the tunnel.

Signal processing is performed using a 14 bit - 80 MSPS ADC with 10 MHz LPF. The data acquisition and module control will be accomplished using a control software tool-kit, EPICS, in principle. Large data will be exceptionally handled with ftp [2]. The dynamic range of the system should meet the following conditions: (1) initial beam commissioning will be done with 1/100 of the design intensity [3], (2) the peak beam current is expected as 41 - 220 A.

The precise position measurements and COD correction is crucial to prevent beam losses at the injection flat bottom [4]. Therefore the goal is set at the position accuracy of ±0.1 mm and the resolution of ±10 μm. The alignment between the quadrupole and BPM pair will be achieved by making use of beam based calibration.

Table 1: Parameters of the 50 GeV MR

Parameter		Unit
Peak beam current	41.3 - 220	A
Average beam current	12.4 - 12.8	A
Speed of the beam	0.9712 - 0.9998	
Bunch length	360 - 67	ns
Bunching factor	0.3 - 0.058	
Revolution frequency	186 - 191	kHz
RF frequency	1.67 - 1.72	MHz

*takeshi.toyama@kek.jp

BPM PICK-UP

Electrostatic pickup with diagonal-cut cylinder is adopted because of its linear response to the position [5]. One BPM set consists of one horizontal and one vertical electrode pairs (Fig. 1). The electrodes and chamber are made of stainless steel, SUS316L and the SMA coaxial vacuum feed through is made of SUS316L brazed with alumina ceramics. The electrodes are supported and insulated with small ceramic block positioned in grooves of the inner surface of the chamber. The coupling impedance is very small. The electrode capacitance is ~210 pF.

Calibration of the position response is going on with a copper wire of ϕ 0.4 mm and the position resolution of ±10 μm. The linear position response, deviation of less than 0.1 mm within $r < 40$ mm was obtained. The lower cut-off frequency was ~17 MHz (Fig. 2), which differentiates the beam signals. The frequency response of the position sensitivity:

$$\kappa = (L-R)/(L+R)/x$$

is plotted in Fig. 3, where L and R are the output voltage from the left and right electrodes, x is the horizontal displacement of the wire. Reduction of position sensitivity κ at $f > \sim 5$ MHz is considered due to capacitive coupling between the opposite electrodes. The calculation with this assumption agrees with the measured data (Fig. 4) [5]. This will not affect the COD measurement because the detection frequency is the RF frequency, ~1.4 or ~3.4 MHz.

The wire calibration will be planned for all pickups in this year. Overall position offset relative to the quadrupole center will be identified by beam-based calibration.

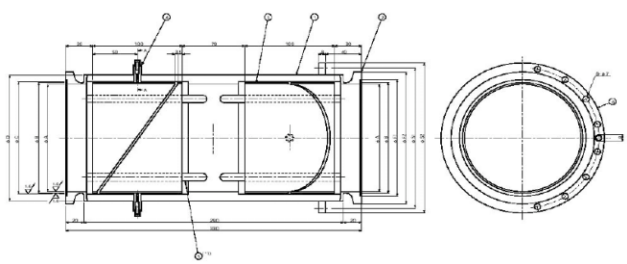

Figure 1: Drawing of the pick-up.

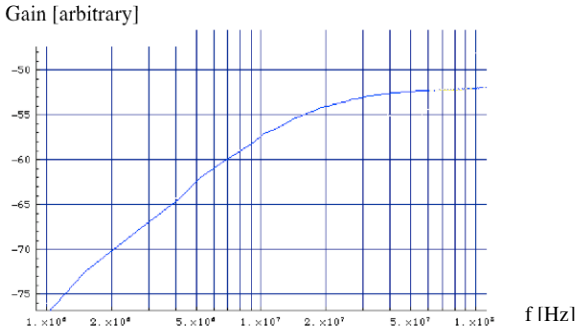

Figure 2: Pick-up response in the frequency domain.

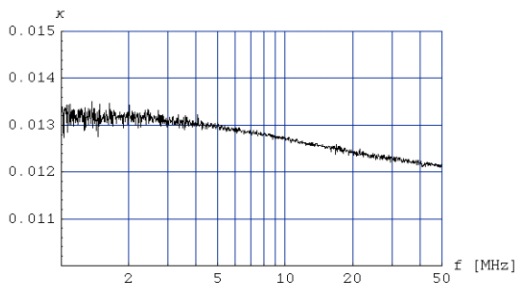

Figure 3: Position response κ measured by the wire method in the frequency domain.

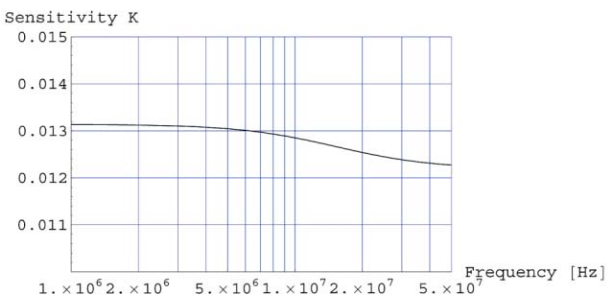

Figure 4: Calculated position response in the frequency domain.

SIGNAL PROCESSING

Four signals from one BPM set are sent to one processing module, which consists of a power supply, analog circuit, 14 bit, 80 MSPS ADC, FPGA and PC in an independent chassis. Five pole Butterworth low pass filter of 10 MHz, provides anti-aliasing. Noise level is < 10 digit without amplification (0.05% of the full scale). Noise with the amplifications are measured as shown in Fig. 5.

Three alternative processing is possible: COD measurement, one pass position measurement and waveform measurement. In the COD measurement, the tailored signals are digitized, 1024 data are fast Fourier transformed using FPGA, then a peak at the RF frequency is obtained. Then Δ/Σ is calculated in an EPICS IO controller (IOC). One pass position is detected with scanning peak and bottom of the digitized signal, then calculating Δ/Σ at every bunch.

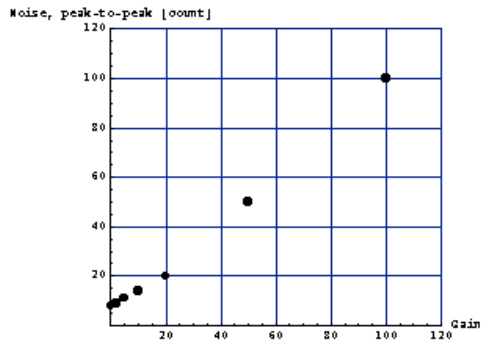

Figure 5: Measured noises of the amplifiers in the processing module. Input was terminated with 50 Ω.

BEAM TEST

To demonstrate the system performance, the pickup and processing circuit was tested with the proton beam at the KEK 12 GeV PS. The beam intensity was $4x10^{11}$ protons per bunch, one hundredth of the design value. The frequency of the RF is 6 MHz, nearly four times larger than J-PARC MR. The COD measured at the injection flat bottom are shown in Figs 1 and 2. Spike-like displacements are due to the leakage fields of the injection pulse septa. Small wiggle is due to ripples of magnets and BPM noise.

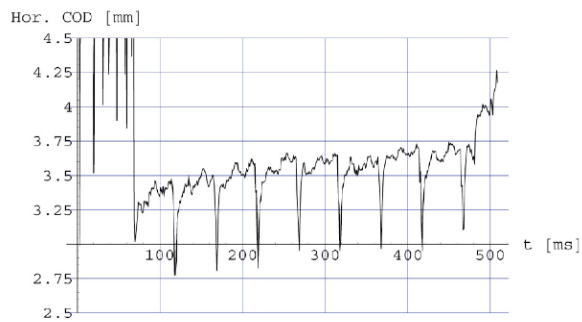

Figure 6: Horizontal COD measurement at the KEK-PS.

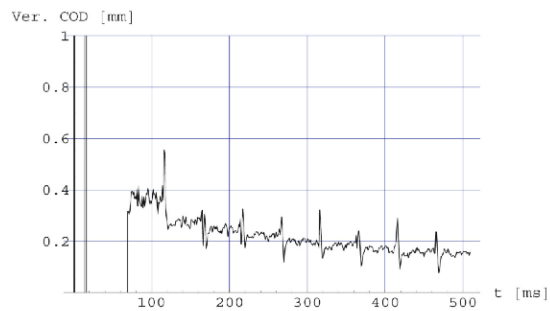

Figure 7: Vertical COD measurement at the KEK-PS.

In the J-PARC MR, 1024 data with 80 M sampling per second is insufficient to achieve enough frequency resolution. Higher frequency resolution, i.e. longer time window at the same data length, 1024, is realized by decimation with a digital low pass filter.

Turn-by-turn position is also measured successfully with a single bunch just after injection as shown in Figs 8 and 9. The betatron tunes ν_x, ν_y, are also successfully obtained by FFT of these data.

Deterioration of performance due to noise is serious problem. Especially the system without front-end electronics has a great risk. One effect observed during the study is noise at the rf frequency. Figure 10 indicates the error occurs only at the RF frequency, 6 MHz in the position sensitivity plot. In this case the cables from the pickup to the processing circuit were 5D2V. Using better cables, 9D-HFBE [7] and common mode choke coils, the noise effect at the rf frequency almost disappeared (Fig. 11). Estimating electromagnetic environment at J-PARC is in progress: EMI from power supplies utilizing IGBT switches, leakage of electromagnetic fields surrounding beams from gaps between vacuum ducts and so on.

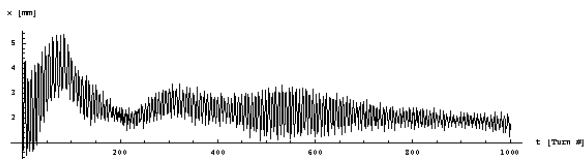

Figure 8: Horizontal turn-by-turn measurement.

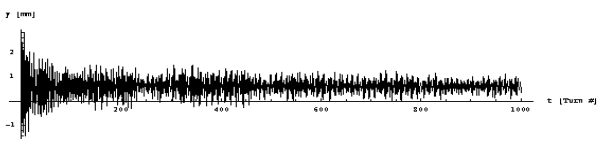

Figure 9: Vertical turn-by-turn measurement.

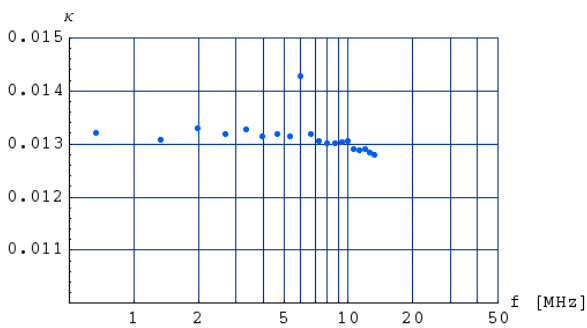

Figure 10: κ measurement at the KEK-PS. The cable was 5D2V, screening effectiveness not sufficient. κ deviates due to the noise at the RF frequency, 6 MHz.

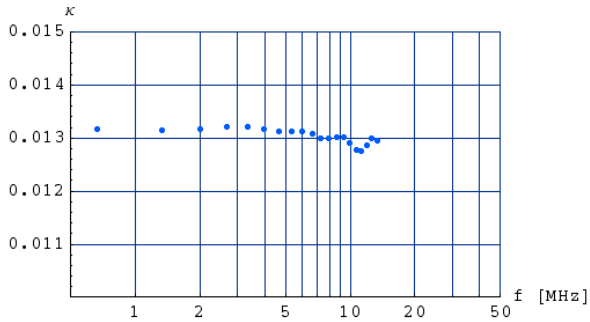

Figure 11: κ measurement at the KEK-PS. With the high screening effectiveness cable, 9D-HFBE.

CONCLUSION

BPM, electrostatic pick-up with diagonal-cut cylinder and processing circuit based on 80 MSPS 14 ADC, was successfully developed. Position accuracy of the pickup within ±0.1 mm is proved with the wire calibration. The processing circuit has enough SNR, 0.05% FS in time domain. Three operational mode, COD measurement, one pass position measurement and waveform measurement, was realized. The preliminary beam test using the KEK-PS shows satisfactory results.

Noise suppression is one of the most important task. Sufficiently high screening-effectiveness cable is now under investigation, compromising between performance and cost. Grounding method is another big issue.

Over all accuracy of BPM setting, ±0.1 mm, will be realized with beam based calibration.

ACKNOWLEDGMENT

The authors thank to S. Hiroki, A. Nakamura, Y. Teruyama for developing pick-up, T. Kato, J. Odagiri, G. Shen, N. Yamamoto for controlling the BPM system, Y. Yamamoto, Y. Saito and M. Uota for vacuum techniques, H. Kobayashi, Y. Mori for proceeding this project.

REFERENCES

[1] Y. Yamazaki, *eds*, Accelerator Technical Design Report for High-Intensity Proton Accelerator Facility Project, J-PARC, KEK-Report 2002-13; JAERI-Tech 2003-044.

[2] J. Odagiri et al, . Proc. of ICALEPCS 2003, 494.
G. Shen et al, submitted to PCaPAC 2005.

[3] S. Machida, memorandum of the beam commissioning group.

[4] S. Machida, submitted to ICFA-HB2004.

[5] T. Toyama et al, Proc. of 14th Symp. Accel. Sci. and Tec., (2003) 470 (Japanese).

[6] N. Hayashi et al, Proc. of 14th Symp. Accel. Sci. and Thec., (2003) 515 (Japanese).

[7] Used for the KEKB BPM. Four coaxial cables (9D-HFBE) are covered with a metal tape and braid.

FIRST STEPS TOWARDS THE INTEGRATION OF PHOTON BEAM POSITION MONITOR SIGNALS INTO THE SLS FAST ORBIT FEEDBACK

T. Schilcher, M. Böge, B. Keil, R. Kramert, J. Krempaský, P. Pollet, V. Schlott,
Paul Scherrer Institute, Villigen, Switzerland

Abstract

So far, photon beam position monitor (PBPM) signals at the SLS are mainly used to verify the performance of the fast orbit feedback (FOFB), which is based on RF BPM position readings. Additionally, a slow high level PBPM feedback compensates systematic effects of the digital BPM electronics. The development of a new PBPM signal processing electronics allows the synchronization of the PBPM signals with the 4 kHz sampling rate of the FOFB. Subsequent integration of the photon beam position data into the FOFB system will be achieved by signal distribution through fibre optics links (Rocket I/O) based on the generic VME PMC carrier board (VPC) and on mezzanine receiver modules on the FOFB DSP board. The integration of PBPM signals based on the new electronics concept is explained.

INTRODUCTION

User operation of the SLS requires the reproduction and stabilization of a defined reference orbit within 1/10th of the electron beam size. In addition, the growing number of insertion devices (IDs) with their needs to change the gaps transparently to all other users and the increasing sensitivity of the experiments demanded a fast orbit feedback system (FOFB) to stabilize the beam to the required level. Such a FOFB has been foreseen at the design stage of the SLS [1] to correct orbit perturbations in the relevant frequency range up to 100 Hz to provide μm orbit stability. After the commissioning phase [2] the FOFB has replaced the former high level based slow orbit feedback in November 2003. Table 1 summarizes the improvements of the beam stability at the SLS with the FOFB running compared to the situation without feedback. The values still contain the noise contribution of the DBPM system, which has been measured to be $<$0.13 μm within the bandwidth up to 100 Hz.

Table 1: Integrated beam position temporal rms values with FOFB off and on measured at the tune BPM. The values are normalized to the beta function $\beta_{x/y}$ ≈12/17 m and reflect the situation for fixed ID settings.

	horizontal		vertical	
FOFB	**off**	**on**	**off**	**on**
1−100 Hz	0.83 μm	0.38 μm	0.40 μm	0.27 μm
100−150 Hz	0.08 μm	0.17 μm	0.06 μm	0.11 μm
1−150 Hz	0.83 μm	0.41 μm	0.41 μm	0.29 μm

In addition to the digital RF BPMs (DBPM), photon beam position monitors (PBPM) are important tools for beam-line and machine diagnostics. Several PBPMs have been installed and commissioned at the SLS [3]. They feature high resolution in the range of 0.5 μm rms ($<$0.5 Hz bandwidth). Due to the long lever arm PBPMs are excellent devices to judge the electron beam stability at the location of the photon beam source point beyond the resolution of any RF BPM. Moreover, PBPMs measure the photon beam movement and therefore allow to discriminate perturbations caused by the electron beam from those caused along the beam-line up to the experimental station. However, position measurements with PBPMs are subject to systematic effects like background radiation from the bending magnets, changes in the ID radiation spectrum during gap changes (for ID PBPMs) and/or varying PBPMs blade response due to thermal effects. Therefore, these systematics of PBPMs have to be understood for the desired ID settings before any conclusion can be drawn from their readouts. At the SLS, the in-vacuum undulators of two protein crystallography (PX) beam-lines and the wiggler of the material science (MS) beam-line are mostly operated at fixed gap positions. The PBPMs at the mentioned beam-lines are well understood and calibrated.

PBPM FEEDBACK ALGORITHM

If PBPM readouts are calibrated they can be integrated into the global orbit correction scheme. The underlying PBPM feedback algorithm changes the orbit reference of the DBPMs adjacent to the IDs in such a way to keep the photon beam position constant at the PBPMs. If only one PBPM is available, the photon beam position change is compensated by a pure angle variation of the orbit at the source point. Eq. 1 allows to calculate the reference change of the two DBPMs 1 and 2 ($d_1,\ d_2$) adjacent to the ID for a desired reading of the PBPM (see Fig. 1).

$$\begin{pmatrix} d_1 \\ d_2 \end{pmatrix} = \frac{1}{a} \begin{pmatrix} -c_{\alpha_x} \cdot l_1 \\ c'_{\alpha_x} \cdot l_2 \end{pmatrix} \cdot x_1 \qquad (1)$$

The factors c_{α_x}, c'_{α_x} translate the purely geometrical offsets for an asymmetrical bump to the required offsets at the location of the DBPMs for a given optics. In case of two available PBPMs, the corresponding necessary angle and offset change can be calculated according to Eq. 2. Similar as in Eq. 1 the factor c_x allows to map a geometrical transverse shift to the necessary transverse offsets at the DBPMs for a given optics. In both cases, the calcu-

lated offset (d_1, d_2) is subtracted from the orbit reference of DBPM 1 and 2. The new reference settings are fed into the FOFB loop as new set-points.

$$\begin{pmatrix} d_1 \\ d_2 \end{pmatrix} = \begin{pmatrix} c_{\alpha_x}\frac{l_1}{b} + \frac{c_x}{2} & -c_{\alpha_x}\frac{l_1}{b} + \frac{c_x}{2} \\ -c'_{\alpha_x}\frac{l_2}{b} + \frac{c'_x}{2} & c'_{\alpha_x}\frac{l_2}{b} + \frac{c'_x}{2} \end{pmatrix} \cdot \begin{pmatrix} x_1 \\ x_2 \end{pmatrix} \quad (2)$$

The PBPM feedback will only be active if gaps are closed and below predefined thresholds. It is foreseen that no user input is required to activate the PBPM feedback. The above mentioned criteria are sufficient to automatically start the feedbacks. The reference position of the PBPM is initialized when the ID gap is closed below the threshold and kept constant for a certain time (∼10 s). Once the reference position is defined it is kept until the gap is raised above the threshold.

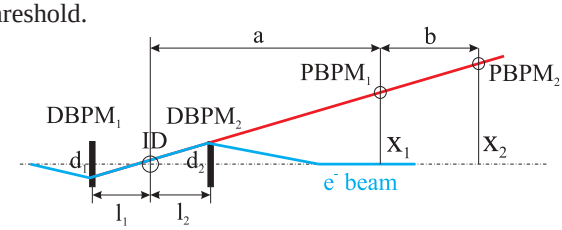

Figure 1: Schematic view of the PBPM and DBPM layout at an ID.

SLOW PBPM FEEDBACK PERFORMANCE

Although the FOFB confines the closed orbit to the reference positions of the involved DBPMs to within less than 1 μm the reference of these BPMs is not perfectly static. The analysis of PBPM data revealed a bunch pattern (intensity) dependence in the RF front-end of the 4-channel DBPM electronics [3]. The implementation of a bunch pattern feedback finally eliminated this effect [4]. Nevertheless remaining systematic effects, like a small temperature dependence of the DBPM electronics in the technical gallery and movements of the DBPM blocks in the storage ring caused by varying heat load on the vacuum chamber or by temperature fluctuations in the SLS tunnel for example due to a beam loss, may still lead to a change of the FOFB reference on the μm level. In order to tackle the problem, presently three slow (≈0.5 Hz bandwidth) feedback loops have been implemented involving PBPMs located at a distance of ≈8.6 m from the IDs of two PX beam-lines featuring in-vacuum undulators and one wiggler based MS beam-line. The feedbacks, which are by default only activated for gaps <8.5 mm in order to minimize the photon beam profile dependence of the PBPM readings, only involve one PBPM according to Eq. 1. Fig. 2 depicts the variation of the horizontal and vertical reference of the upstream DBPM together with the corresponding stabilized PBPM readings at one of the PX beam-lines over ≈85 h of continuous FOFB and "top-up" operation. The resulting temporal distributions of the photon beam positions exhibit rms values of σ_x = 0.37 μm and σ_y = 0.5 μm for frequencies <0.5 Hz.

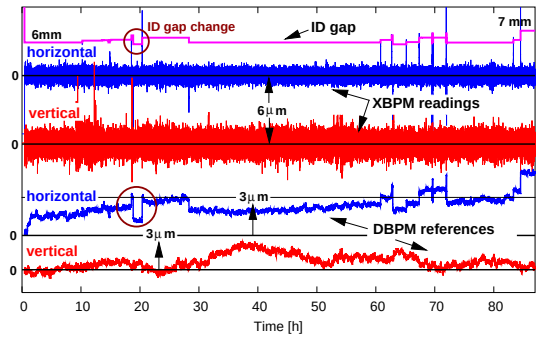

Figure 2: Slow PBPM feedbacks provide sub-μm rms in-loop stability of the PBPM reading at the first optical elements of presently three beam-lines (exemplified by the data taken at a PX beam-line over 85 h of FOFB and "top-up" operation).

FAST PBPM READOUT

Recently the synchronous readout of the PBPM blade photo current at one of the PX beam-lines has been upgraded to 1 kHz using the existing hardware. Although the PBPM readout is not yet synchronized to the DBPM readings it allows to study the performance of the FOFB down to the millisecond range. The presently uncalibrated horizontal and vertical power spectral densities in Fig. 3 document the significant improvement of the photon beam stability up to the 0 dB point with active FOFB. Although

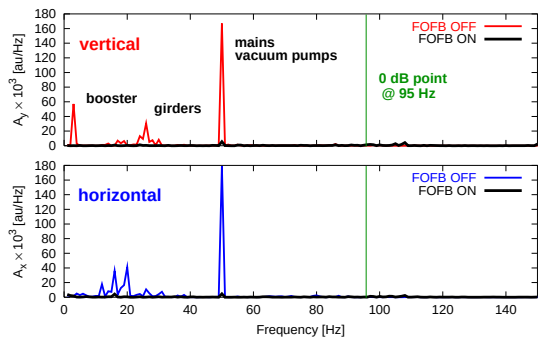

Figure 3: The uncalibrated vertical and horizontal power spectral densities taken at the PBPM of a PX beam-line document the significant improvement of the photon beam stability up to the 0 dB point with active FOFB (black curves).

the preliminary results are still subject to further investigations to clarify the perturbation reduction factors it confirms the successful suppression of perturbations originating from the electron beam which are also seen by DBPMs. As a consequence, it provides the possibility to integrate PBPMs into the global orbit feedback system. This, of course, is only the case for PBPMs at IDs with well defined operation modes and for vertical PBPMs at bending magnet beam-lines.

FOFB UPGRADES

The FOFB will be upgraded for two reasons. Firstly, it will be extended by an additional DBPM in the FEMTO insertion [5] and corresponding adjacent correctors. Secondly, additional interfaces will be implemented to allow the integration of several PBPMs into the FOFB loop.

The extension to include an additional DBPM and horizontal/vertical corrector pair is necessary to provide proper fast beam steering at the entrance of the in-vacuum undulator which is part of the partially completed FEMTO insertion. Adding a DBPM/corrector pair to the present FOFB layout with its 72 DBPMs and 72 correctors in each plane will brake the symmetry. As a consequence it is foreseen to introduce 7 DBPMs/sector in order to maintain the present structure where 11 of them remain "virtual" for the time being.

As a second step it is foreseen to adapt and synchronize the fast PBPM blade current readouts to the DBPM/FOFB sampling rate of 4 kHz. In order to achieve this goal a new current digitizer hardware is under development which will replace the presently used 4-channel low current asymmetry detector. The new electronics is based on the generic VME PMC carrier board (VPC) [6] which will become the standard platform for diagnostic devices at PSI. The clock rate for the PBPM ADCs is derived in the same way as in case of the DBPM system. The main RF frequency of 499.651 MHz is divided by the harmonic number to get the revolution frequency of 1.04 MHz. A further decimation by a factor of 256 will result in the same clock rate as in the FOFB case. Since all clock signals will be derived from the main RF frequency they will be locked to each other. An external trigger input from the timing system will provide the possibility to start the decimation of all PBPMs synchronously to the decimation of the DBPMs. The PBPM electronics will be connected to a Gigabit fibre optic ring (Rocket I/O) network with a dedicated interface to the multi-processor bus on the DBPM/FOFB digital signal processor board (Fig. 4). In this way, several PBPMs can be integrated into the FOFB, which gives the flexibility to include one or two PBPM at each ID and/or PBPMs at the bending magnet beam-lines. The additional position information of the PBPMs will then be available to the FOFB in the same way as it is the case for all DBPMs which are provided as memory mapped readings on the DSP multiprocessor bus.

STATUS AND CONCLUSION

Integration of slow PBPM feedbacks into the FOFB has provided excellent medium term photon beam stability at the position of the first optical elements of the beam-lines. Recent power spectral density measurements with PBPMs have demonstrated that photon monitors are promising candidates to stabilize the photon beam beyond the stability performance obtained by a fast orbit feedback based exclusively on DBPMs. It is therefore foreseen to make PBPM readings directly available to the FOFB.

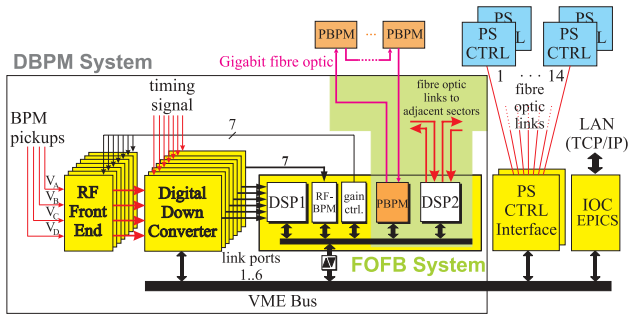

Figure 4: Schematic view of the PBPM integration into the FOFB. An additional interface from the Gigabit fibre optic ring network which connects all PBPMs maps the photon position readings on the DSP multi-processor bus of the present DBPM/FOFB system.

Presently, the DSP interface hardware for the integration of an additional DBPM and for the Gigabit ring network is tested under laboratory conditions. As a first priority, a 7th DBPM will be included into the DBPM system in one of the twelve sectors within the next three months in order to provide the required beam stability in the FEMTO insertion. As soon as the new PBPM readout electronics becomes operational the fibre optic ring connecting all PBPMs in one sector will be closed. Thus, PBPM readings will be available synchronously to all DBPMs at a rate of 4 kHz. As a first step, the three high level PBPM feedbacks for the MS beam-line and for the two PX beam-lines will be implemented in the low level DSP software. These beam-lines operate in well defined modes, the PBPMs are well understood and therefore ideal candidates for testing the integration of PBPMs in the fast global orbit correction scheme. In a second step, new PBPM feedbacks can be added to the FOFB to accommodate the needs of upcoming bending magnet beam-lines and for ID based beam-lines with calibrated PBPMs for a restricted parameter space of the IDs.

REFERENCES

[1] M. Böge et al., "Fast Closed Orbit Control in the SLS Storage Ring", PAC'99, New York, March 1999.

[2] T. Schilcher et al., "Commissioning of the Fast Orbit Feedback at SLS", PAC'03, Portland, May 2003.

[3] J. Krempaský et al., "The Use of Photon Monitors at the SLS", EPAC'04, Lucerne, July 2004.

[4] B. Kalantari, T. Korhonen, V. Schlott, "Bunch Pattern Control in Top-up Mode at the SLS", EPAC'04, Lucerne, July 2004.

[5] G. Ingold et al., "FEMTO Project: Status of the FEMTO Insertion", PSI Scientific Report 2003, Vol. VII, 2003.

[6] B. Keil et al., "The PSI 'VPC' Board - First Applications of a Common Digital Back-End for Electron and Proton Beam Instrumentation at PSI", DIPAC'05, Lyon, these proceedings, June 2005.

INVESTIGATION OF PHOTO NEUTRALIZATION EFFICIENCY OF HIGH INTENSITY H^- BEAM WITH Nd:YAG LASER FOR J-PARC

T. Tomisawa, H. Akikawa, K. Hasegawa, Y. Kondo, H. Oigawa, S. Sato, A. Ueno
JAERI/LINAC, Ibaraki-ken

M. Ikegami, S. Lee, T. Toyama, I. Zenei
KEK, Ibaraki

Abstract

The photo neutralization method with Nd:YAG laser for negative hydrogen ions has been considered as an available candidate for beam intensity profile monitor and charge exchange procedure for Accelerator-Driven-System (ADS) in J-PARC. An electron of H^- beam can be stripped by fast and intense Nd:YAG (1064nm) laser with non-destructive, and laser system have advantages of maintenance and radiation hardness in high intensity proton accelerators. In this paper, an experimental set-up and preliminary results of photo neutralization method for linac H- beam in KEK DTL1 are described.

NO SUBMISSION RECEIVED

INVESTIGATION OF PHOTO NEUTRALIZATION EFFICIENCY OF HIGH INTENSITY H⁻ BEAM WITH ND:YAG LASER IN J-PARC*

T. Tomisawa, H. Akikawa, S. Sato, A. Ueno, Y. Kondo, H. Oigawa, T. Sasa and K. Hasegawa
JAERI, Tokai, Naka, Ibaraki, 319-1195, Japan

S. Lee, I. Zenei, T. Toyama and M. Ikegami, KEK, Tsukuba, Ibaraki, 305-0801, Japan

Abstract

The photo neutralization method with Nd:YAG laser for negative hydrogen ions has been expected as an available candidate for the transverse beam profile measurement. The fraction of photo detached electron can also be used for charge exchange procedure to extract very low power proton beam for Transmutation Experimental Facility in J-PARC. The laser system has advantages of maintenance and radiation hardness in high intensity proton accelerators. In order to establish the low power beam extraction system and beam profile monitor, the photo neutralization efficiency must be surveyed in practical beam line with high intensity H⁻ beam. In this paper, an experimental set-up and preliminary results of photo neutralization method for intense H⁻ beam in J-PARC MEBT1 are described.

INTRODUCTION

The J-PARC linac aims to provide high intensity negative hydrogen ion beams of peak current 50mA, kinetic energy 181/400MeV, pulse width 0.5mA and repetition rate 25Hz [1]. The goal of 133 kW beam power and hand-on maintenance will place significant demands on the performance and operational reliability of accelerator diagnostics systems. Beam diagnostics system is required to verify proper transverse focusing and matching of the magnetic focusing lattice of the linac. The transverse beam profile is one of the most important parameter for beam commissioning and/or tuning, and currently measured by single wire scanner in linac [2]. However, the interaction mechanism between thin wire and H⁻ ions for various beam energies should also be investigated to clarify beam profiles. The photo neutralization method with Nd:YAG laser has been considered as an available candidate for beam intensity profile monitor. The photo neutralization technique is also expected as a beam extraction method for Transmutation Experimental Facility (TEF) in J-PARC [3]. The laser charge exchange method is an essential technique to extract very low power and narrow pulse width proton beam from intense H⁻ beam as shown in Fig.1.

Thus, the neutralization efficiency should be investigated experimentally. This paper reports the development of a laser based beam profile monitor system. The MEBT1 beam diagnostic system to measure photo neutralization efficiency is also described in detail.

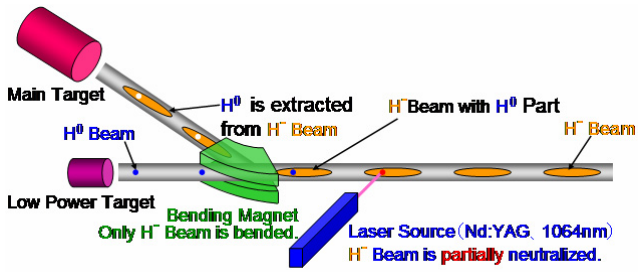

Figure1: Schematic view of low power beam extraction

EXPERIMENTAL SET-UP

The experimental device is composed of ion source, RFQ, MEBT1 and the laser system. A photo interaction chamber of laser profile monitor was installed in the MEBT1 (Fig. 2).

Ion Beam Line:

0.5ms long, 30mA pulse beam in the MEBT-1 consists of micro bunch of <0.5ns pulse width. The H⁻ ion beam is accelerated by 324MHz radio frequency quadrupole linac (RFQ) up to the beam energy of 3MeV.

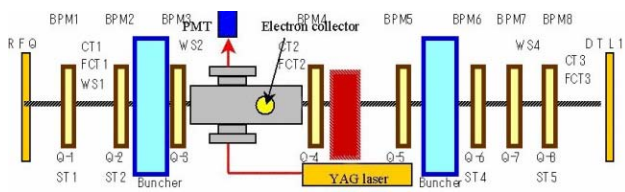

Figure 2: Laser profile monitor in MEBT1

Laser System:

Commercial Nd:YAG laser can produce pulse width of 20ns long, maximum pulse energy of 500mJ, wavelength of 1064nm at repetition rate of 25Hz. Laser beam size was formed to horizontal width of 6mm and height of 0.8mm at the H⁻ beam line by a pair of 80mm focal length cylindrical lenses. Stripped electrons were deflected 90degree by an electromagnetic dipole and collected to a Faraday cup.

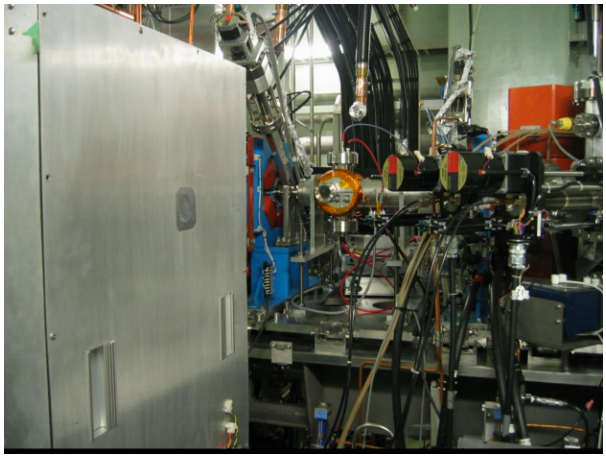

Figure 3: Layout of the laser injection port (center) and an optical beam guide box (left).

EXPERIMENTAL RESULTS

The beam current was also monitored by using a fast current transformer (FCT, ~324MHz) at downstream of laser diagnostic box [4].

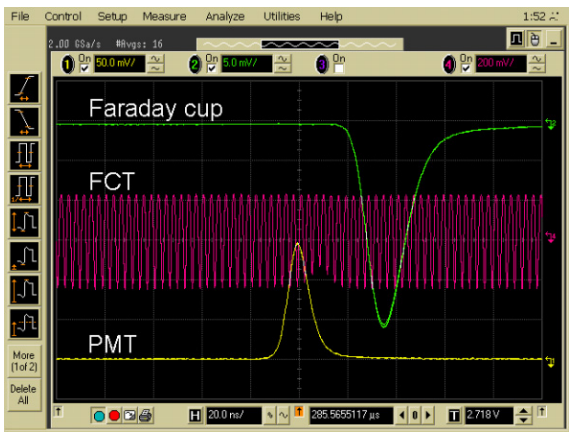

Figure 4: Example of Faraday cup, PMT and FCT signals during the laser injection timing.

The beam current notch was also measured in FCT signal at downstream of laser photo neutralization point. The notch depth corresponds to the photo neutralized beam component. For example, about 25% decreasing of 15mA H^- beam equivalent to about 30mV Faraday cup signal by taking account of the total 31% through rate of electron reppeler and shield mesh, 3dB reduction of low pass filter and 50ohm input impedance of oscilloscope. As shown in Fig. 5, the consistent beam current notch level with neutralized electron signal was confirmed.

The radial profile after Abel inversion is also calculated and rms width of the Gaussian fitted vertical profile is σ=2.2mm, the width of the laser beam of 0.8mm intercept about 25% particles at beam center line. Thus the almost complete photo neutralization fraction for a 130mJ (repetition frequency of 5Hz) 1064nm Nd:YAG laser pulse on a 15mA, 3MeV H^- beam could also be confirmed.

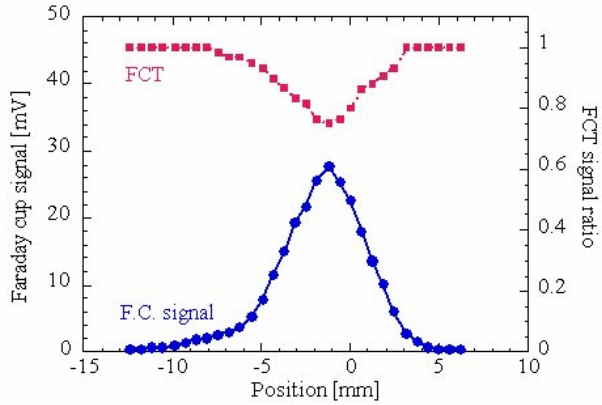

Figure 5: Faraday cup signal and FCT reduction profile in vertical direction (beam current 15mA). The FCT notch signal corresponds to stripped electron signal..

PHOTO NEUTRALIZATION EFFICIENCY

The fraction of beam ions neutralized by passing through the laser beam is,

$$f = 1 - e^{-\sigma(E)Ft}$$

Here σ(E) is the energy-dependent cross section, F is the photon flux, and t is the time during which the ion is in the laser light. For ion beam energies up to about 200MeV the cross section changes very little [1]. For example, the laser on the MEBT1 experiment produces a 20ns-long pulse with an output energy of 130mJ (repetition rate of 5Hz and taking into account the reduction of optical elements). It is formed to a laser spot 0.8mm hight by 6mm along the beam. The approximate variation of neutralization fraction with beam energy of this laser is shown in Fig.6.

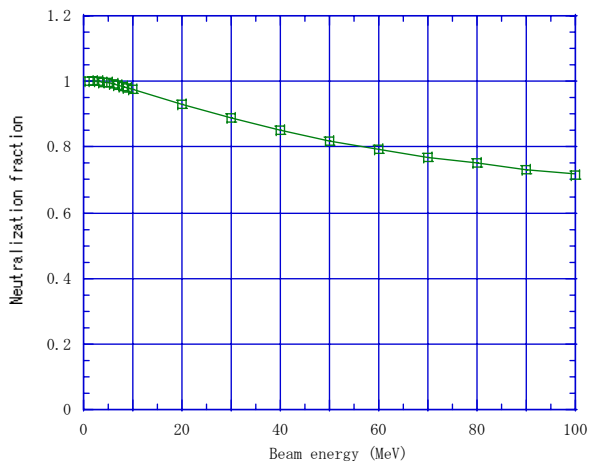

Figure 6: Calculated neutralization fraction as a function of beam energy for 20ns-long, 130mJ laser pulse focused to a spot size of 0.8mm x 6mm.

SUMMARY

The laser wire scanner using a pulse width of 20nsec, beam energy of 500mJ (repetition rate of 25Hz) Nd:YAG laser have been installed in J-PARC MEBT1 to measure current profile of high intensity H^- beam. It was confirmed that the photo stripped electron signal corresponds to the reduction of FCT current signal at downstream. The results of transverse profile measurements are also consistent with wire scanner signals of upper and downstream. The H^- beam components intercepted by 0.8mm height laser beam have been estimated by transverse profile measurement, and agree with photo detached fraction (Faraday cup and FCT reduction signal). The calculation results also show the complete neutralization ratio with 130mJ Nd:YAG laser for 3MeV H^- beam. Thus the almost complete photo neutralization fraction for a 130mJ (repetition frequency of 5Hz) 1064nm Nd:YAG laser pulse on a 15mA, 3MeV H^- beam could be confirmed practically. The difficulty of practical construction of laser system, for example the stability of optical transport line and/or laser oscillator, should be investigated in future.

REFERENCES

[1] R. E. Shafer, "Laser Diagnostic for High Current H^- beams", Proc. 1998 Beam Instrumentation Workshop (Stanford). A.I.P. Conf. Proceedings, (451), 191.

[2] Y. Yamazaki, eds. *Accelerator Technical Design Report for J-PARC,* KEK Report 2002-13.

[3] K. Tsujimoto *et al.,* "Conceptual Study of Transmutation Experimental Facility" JAERI-Tech 2003-085.

[4] S. Lee *et al.,* Proc. of LINAC2004, TUP74.

THE LHC BEAM LOSS MONITORING SYSTEM'S REAL–TIME DATA ANALYSIS CARD

C. Zamantzas, B. Dehning, E. Effinger, G. Ferioli, G. Guaglio, R. Leitner
CERN, Geneva, Switzerland

Abstract

The BLM (Beam Loss Monitoring) system has to prevent the superconducting magnets from being quenched and protect the machine components against damages making it one of the most critical elements for the protection of the LHC. The complete system consists of 3600 detectors, placed at various locations around the ring, tunnel electronics, which are responsible for acquiring, digitising, and transmitting the data, and surface electronics, which receive the data via 2km optical data links, process, analyze, store, and issue warning and abort triggers. At those surface units, named BLMTCs, the backbone on each of them is an FPGA (field programmable gate array) which treats the loss signals collected from 16 detectors. It takes into account the beam energy and keeps 192 running sums giving loss durations of up to the last 84 seconds before it compares them with thresholds uniquely programmable for each detector. In this paper, the BLMTC's design is explored giving emphasis to the strategies followed in combining the data from the integrator and the ADC, and in keeping the running sums updated in a way that gives the best compromise between memory needs, computation, and approximation error.

INTRODUCTION

Around 3600 *Ionization Chambers* are the detectors of the system. A set of up to 8 of them can be connected to each of the tunnel cards. In those tunnel cards, called *BLMCFCs*, the digitisation of the detector signal is done by using *CFCs* (current-to-frequency converters) and *ADCs*. An *Anti-Fuse FPGA* [1] acquires the digitised data and transmites them at the surface using the GOLs (*Gigabit Optical Links*) [2]. There, the data analysis cards, named *BLMTCs*, receive those data. The surface *FPGA* will analyse by keeping a history of those data and decide whether or not a dump request should be initiated. Each surface card receives data from 2 tunnel cards, which means that it can treat up to 16 channels (see Fig.1).

ANALYSIS CARD (BLMTC)

The data analysis card is based on the general purpose PCB that was implemented for the whole instrumentation group, named DAB64x [3]. It is comprised from an Altera Stratix™ [4] FPGA, an Altera MAX™ CPLD [5] for power-on configuration and VME functionality, and three SRAM memories. The functionality of the system is realised by using different firmware on the FPGA and CPLD devices, and different mezzanine cards that can be placed on either of the six general-purpose connectors.

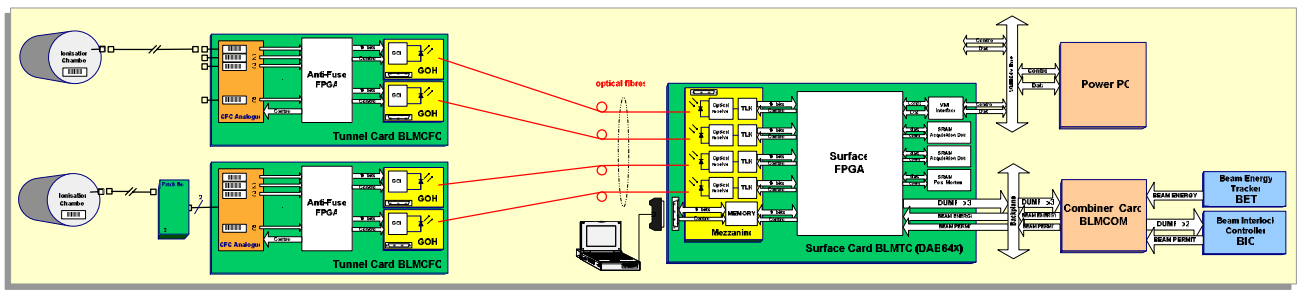

Figure 1: Overview of the complete BLM System for the LHC.

The BLM mezzanine card [6] includes all necessary components for the four gigabit optical receivers and a Mbit of Flash memory for system specific data.

PROCESSES RUNNING IN THE FPGA

The surface FPGA has 41,000 LE (logic elements), 615 user I/O pins, and 400KBytes of internal memory as available resources for the system to be built from.

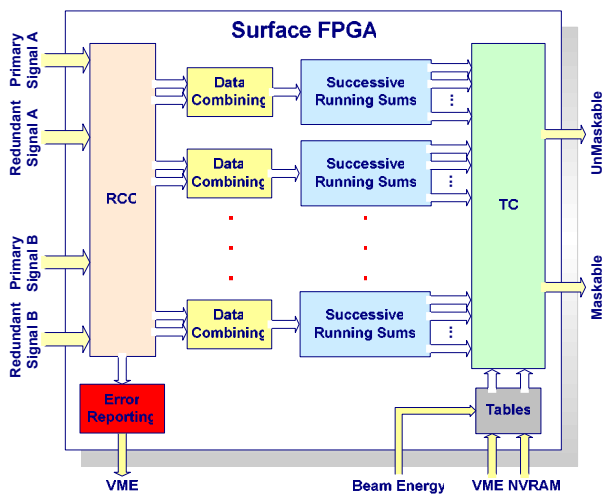

Figure 2: Block diagram of processes related to data analysis running in the surface FPGA.

A description of each of the system blocks related to the data analysis process follows (see Fig.2).

Transmission Check (RCC Block)

In the *BLM* system, for reliability reasons, many parts were decided to have redundancy. The communication link was one of them. A comparison of the two could trigger a dump of the beam in the case of a difference. By including, some digital techniques, like the 8b/10bit and the CRC (Cyclic Redundancy Check), a more sophisticated receiver part was produced that achieves even higher data reliability and system availability.

Table 1: Decision Table for the Signal Select Block.

CRC Check A	CRC Check B	Compare A to B	Output	Remarks
Error	Error	Error	Dump	Both signals have error
Error	Error	OK	Dump	CRC generation or check is wrong
Error	OK	Error	Signal B	Error at CRC part
Error	OK	OK	Signal B	Error at data part
OK	Error	Error	Signal A	Error at CRC part
OK	Error	OK	Signal A	Error at data part
OK	OK	Error	Dump	One of the counters has error
OK	OK	OK	Signal A	Both signals are correct

With the 8b/10b encoding before transmission, the complete frame is split into 8-bit blocks and each of them is encoded into a 10-bit block. On receipt, the reverse procedure (i.e. decoding) is used. It serves two purposes. First, it makes sure there are enough transitions in the serial data stream so the clock can be recovered easily from the embedded data. Second, because it transmits the same number of ones as zeros, it maintains a DC balance.

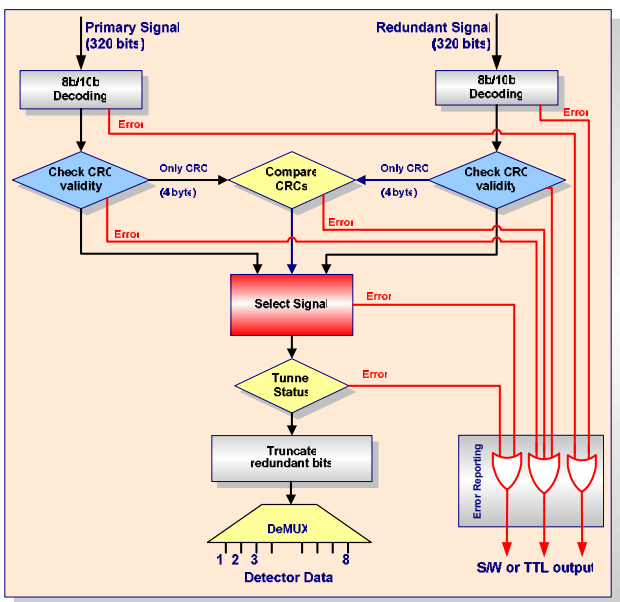

Figure 3: Transmission Check (RCC) Block Diagram.

The *CRC*, a polynomial arithmetic based algorithm, is widely used as error detection scheme. In this system, the redundant bits it introduces are not only used to detect transmission errors but also to find any difference between the two signals.

The "*Signal Select*" block receives the outputs of the checks and the comparison and gets the responsibility of selecting the error free signal to convey on the stages below. By using efficiently all information it is expected to increase the availability of the system (see Table 1, cases 3 to 6). Additionally, its error reporting features can also indicate problematic areas and failing components in the tunnel installation (see Fig.3).

CFC & ADC Data Combining

Based on the fact that the two types of data acquired for each detector are different, a pre-processing is needed for them to be combined seamlessly. The measurement with a counter of the frequency produced by the *Current-to-Frequency Converter* relates to the average current between the two last acquisitions. On the other hand, the voltage measured by the *ADC* is the voltage of the CFC integrator at the time of the counter readout. It represents then the fraction remained between the last count and the first from the next acquisition.

In order to combine those data the difference of the last two *ADC* measurements is needed. It will then correspond to the counter fraction of the last 40 µs and thus could be added to the counter value. Of course, since the difference could be a negative number, signed number arithmetic is used for the addition (see Fig.4).

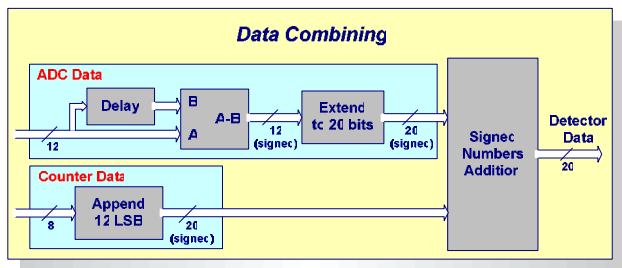

Figure 4: Data Combining Block Diagram.

Using this scheme, the usage of resources and computation effort is minimised since it is concentrated in this beginning stage. All later stages are just exploiting those combined values.

Successive Running Sums

The *Running Sums* can be produced simply by adding the newly acquired value to a register and subsequently subtracting from it a value coming delayed by a number of cycles in a shift register. A similar configuration is used in the *BLMTC* where, in order to increase the efficiency in resources, it is making use of the multipoint shift registers available on the Stratix devices. It is simply adding the difference of those two values, the new and the delayed, to an Accumulator.

Another scheme of resource sharing is employed for reaching higher integration time with relatively small in

length shift registers. It makes use of the already calculated sums in order to calculate bigger in length running sums with the only expense of some additional latency (see Fig.5).

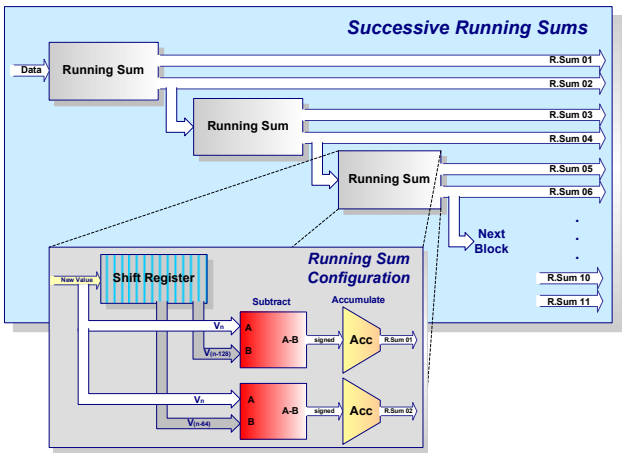

Figure 5: Production of Successive Running Sums.

The latency introduced has little effect to the optimal approximation accuracy though since it varies between them. More specifically, the running sums that span to the low range (fast losses) have zero or very small additional latency and gradually increases reaching up to 1.3s for the 21 and 83s time range (see Table 2).

Table 2: Integration Time-Windows Configuration.

The red coloured RSs (running sums) outputs, i.e. RS1, RS4, RS6, and RS8, represent their additional utilisation as inputs for the adjacent SRs (shift registers), i.e. SR2, SR3, SR4, and SR5.

Range		Refreshing		Shift Reg. Name	Signal Name
40 µs steps	ms	40 µs steps	ms		
1	0.04	1	0.04		RS0
2	0.08	1	0.04		RS1
8	0.32	1	0.04	SR1	RS2
16	0.64	1	0.04		RS3
64	2.56	2	0.08	SR2	RS4
256	10.24	2	0.08		RS5
2048	81.92	64	2.56	SR3	RS6
8192	327.68	64	2.56		RS7
32768	1310.72	2048	81.92	SR4	RS8
131072	5242.88	2048	81.92		RS9
524288	20971.52	32768	1310.72	SR5	RS10
2097152	83886.08	32768	1310.72		RS11

This gained efficiency was necessary for this system to be applicable in a configuration with relatively very low memory available. In a "normal" configuration of this system, the running sums would need to hold approximately 3 million values for each of the 16 detectors to achieve the same approximation error. That means a total of approx. 150MBytes. Instead, by using the successive running sums the system is using only some of the FPGA internal memory since it does not need more than 100KBytes.

Threshold and Masking Tables (TC Block)

The quench and damage levels are time and energy dependent [7, 8]. For this reason, from each detector's data, as it was shown, this system calculates 11 *Running Sums*. Every *Running Sum*, after every new calculation, is compared with its corresponding *Threshold* value that was chosen by the beam energy reading at that moment. If found to be higher, the *Comparator* will initiate the necessary dump request (see Fig. 6).

All requests are being gathered by a *Masking* block with the purpose of distinguishing between "Maskable" and "Unmaskable" channels. The tables are stored on the BLM Mezzanine's non-volatile memory and can be unique for each detector. For added functionality both of them can be loaded locally either by the frond-panel's connector or by the Power-PC.

Finally, all outputs will be summed and collected by the "Combiner Card" which will forward them to the "Beam Interlock System".

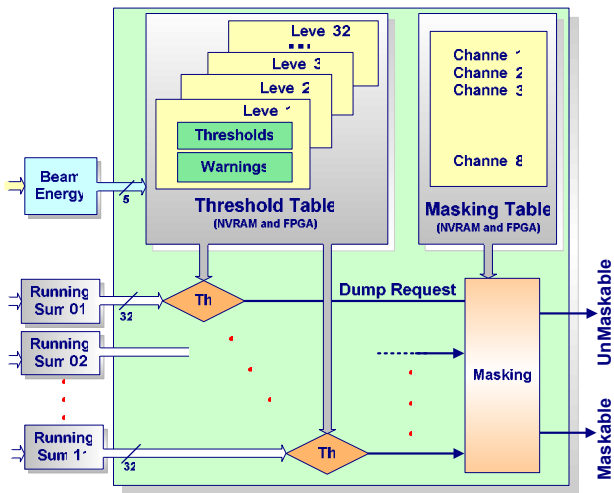

Figure 6: Threshold Comparator (TC) Block Diagram.

REFERENCES

[1] Actel Antifuse Devices SX-A/ SX, *http://actel.com/*

[2] P. Moreira, G. Cervelli, J. Christiansen, F. Faccio, A. Kluge, A. Marchioro, T. Toifl, J. P. Cachemiche and M. Menouni "A Radiation Tolerant Gigabit Serializer for LHC Data Transmission", *Proceedings of the Seventh Workshop on Electronics for LHC Experiments,* Stockholm, Sweden, 10-14 September 2001

[3] R. Jones, "VME64x Digital Acquisition Board for the LHC Trajectory and Closed Orbit System", *LHC Engineering* Specification, *LHC-BP-ES-0002*.

[4] Altera Stratix Device Family Overview, *www.altera.com/ /products/devices/stratix/overview/stx-overview.html*

[5] MAX 3000A CPLD Family Overview, *www.altera.com/ /products/devices/max3k/overview/m3k-overview.html*

[6] Schematic files of the BLM Mezzanine Card (version 2), *https://edms.cern.ch/item/EDA-00780*

[7] J.B. Jeanneret, D. Leroy, L. Oberli and T. Trenkler, LHC Project, "Quench levels and transient beam losses in LHC magnets", *LHC Report 44, CERN, July 1996.*

[8] A. Arauzo-Garcia et al., "LHC Beam Loss Monitors", *5th European Workshop on Diagnostics and Beam Instrumentation DIPAC 2001, Grenoble, France.*

THE DIGITAL CAMERA APPLICATION IN THE TAIWAN LIGHT SOURCE

C. H. Kuo, Y. T. Yang, J. Chen, S. Y. Hsu, D. Lee, K. H. Hu, C. J. Wang, K. T. Hsu

NSRRC, Hsinchu 30076, Taiwan

Abstract

Digital camera has been adopted for the booster, storage ring and transport-line diagnostic recently at the Taiwan Light Source. The system provides low image distortion transmission over long distance. The system is integrated with control system. Each screen monitor equip with a digital camera. These screen monitors are used for beam profile measurement and help injection condition optimization. Wider dynamic range and highly flexibility of the digital gated camera provide various functional enhancements. System configuration and present status will be summary in this report.

INTRODUCTION

Using a fully digital camera has two major advantages over analog CCD camera. First, the A/D conversion is performed closer to the CCD/CMOS sensor, keeping the amount of electronic noise to a minimum degree. Once the digitized signal is immune to noise, we can implement long haul (10 m ~ 10^3 m) applications in accelerator researching field. Various long hops solution is supported by the IEEE1394A/B interface. Noise immunity and isolation provided by this solution must be welcome in the accelerator environment. Second, unlike analog camera systems, digital systems do not suffer from pixel jitter. Each captured pixel value corresponds to a well-defined pixel on the CCD/CMOS chip. The IEEE1394 interface is a hot swappable and self-configuring, high performance serial bus interface that is capable of 400 Mbit/sec data transmission and will be enhanced to 3.2 Gbit/s for next generation products. The interface support asynchronous (guaranteed delivery) and isochronous (guaranteed bandwidth and latency) data transfers. By using digital IEEE1394 camera system [1,2], we are able to eliminate the frame-grabber stage of processing and directly transfer data at maximum rates of 400 MB/sec. IEEE1394 general purposed CMOS cameras (Prosilica CV640, 659 x 494 by 4.65 μm square pixels) [1] were chosen for screen monitor application. Progressive scan interline CCD camera (Q-Imaging QICAM, 1392 x 1040 4.65 μm square pixels) [2] are used for synchrotron radiation monitor with 12-bit digital output. There is no frame grabber or additional power supply required. Frame rates of up to 100 fps can be achieved with adequate binning and ROI selection.. Intensify gated CCD camera are also used for low light applications.

Imaging applications in the accelerator community are most often utilized to measure beam profile and interference fringes. The beam profile may convert form fluorescence, various optical diagnostics [3]. Usually, fluorescence screen/OTR and synchrotron light source radiation monitor is used to measure size of beam profile in order for performance optimization, routine operation, and various beam physics studies in the accelerator. This tool has been useful for characterizing properties of electron beam analysis. For example, the beam emittance is calculated from the measured beam size.

SYSTEM STRUCTURE

There are about fifteen IEEE-1394 cameras [4] were installed for the screen monitor of the transport line and storage ring. All of these cameras are distributed in a large area beyond copper wire can cover, three to four near-by cameras are grouped and connected to central hub by IEEE-1394B fiber link for long distance transmission. To simply cabling, multiple nearby cameras are cascading together. Only one camera is active in the cascading chain, transmission bandwidth is shared by all cameras in cascading when system is initializing. All screen monitor are controlled by one computer. Since only one camera is used, the main bus bandwidth in used by only camera. Synchrotron radiation monitor for the booster synchrotron and storage ring are stand alone station to acquire image and to do analysis.

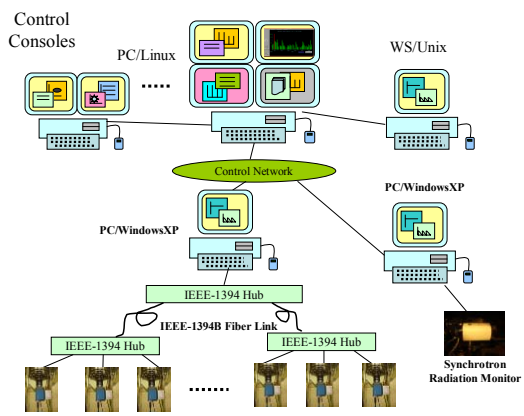

Figure 1: Topology of the IEEE-1394 camera installation.

The copper cable is suffered for longer distance transmission especially near the pulse magnet power supplies. Data stream is deteriorated sharply by the operation of pulse magnets for the cameras nearby. The camera may hang and need power reset to assume its operation occasionally. After this problem was identified, the topology of the camera array has been changed slightly to ensure the reliable operation of the whole system. Camera radiation damage is similar with analog

camera. Some damage pixels are observed due to radiation [5]. Thin lead enclosure is help to keep from this slightly damage.

Based upon experience during last two years, major disadvantage of IEEE-1394 based camera are the noise immunity of form pulse magnet operation. Short cable is preferred. Multiple nearby cameras are cascading together by the simple cabling. Transmission bandwidth is shared by all cameras in the cascading bus.

Several 1394 hubs are applied in this install as shown in the Figure 1. The main issues are from 1394 copper cable specification and installation environment. The standard 1394 copper cable is defined up to 5 meter. This cable length isn't enough to real situation. The cameras are divided to several groups with the hub and optical fiber transceiver in the transport line. This layout also keeps from kicker pulse magnetic field interference.

Since the camera is comply with DCAM (IIDC 1.31) digital camera standard. The protocol defines the exchange of data with IEEE 1394 cameras. However, DCAM isn't only defined in the video stream provided by the camera, but is also the camera parametric control (for instance brightness, shutter, white balance, exposure time, …etc.). This DCAM driver based on windows PC is upgraded from 1.30 to 1.31 by to improve functionality which is lake in the old driver 1.30. The old driver is supported in the plug and play operation. The existent devices are automatically renamed to a new device name if there is any device is failed or disappeared in the bus. This mechanism leads uncomfortable form maintenance point of view. The new driver overcomes these problems.

SYNCHROTRON RADIATION MONITOR FOR THE BOOSTER SYNCHROTRON

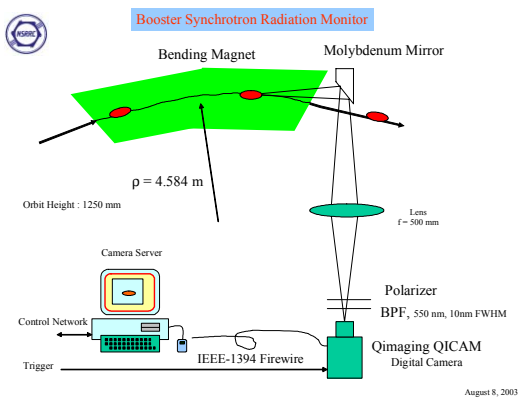

Figure 2: The system block diagram of the booster synchrotron radiation monitor.

Since the booster synchrotron is a 10 Hz machine, the injected beam is accelerated from 50 MeV to 1.5 GeV within 50 ms. Exposure time should be as short as possible for energy revolving measurement. External trigger of the camera is synchronized to the booster 10 Hz clock. By adjusting 10Hz delay times, the different beam energy profile is captured by the camera. Available tools can adjust 10 Hz delay time, camera exposure time, beam size analysis and provide networking service. Remote consoles can access all information by client program. This system layout is shown in Figure 2. An example of the measurement is also shown in Figure 3. The vertical beam size is reduced when energy increased due to synchrotron radiation damping. Multiple exposures can be used at low energy to measured low intensity synchrotron radiation light. Multiple exposures are also increase dynamic range without scarified linearity especially for low light application.

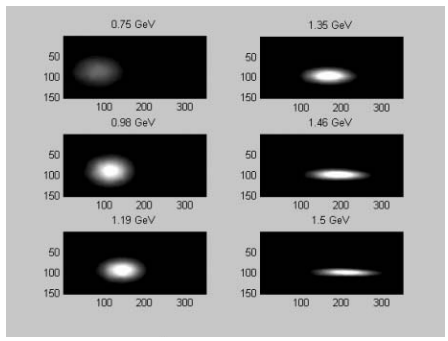

Figure 3: An example of observed beam profiles during ramping with various energies. With 2x2 binning, the pixel size is 9.4 μm x 9.4 μm. Exposure time is 0.5 ms.

APPLICATION FOR TRANSPORT LINE BEAM EMITTANCE MEASUREMENT

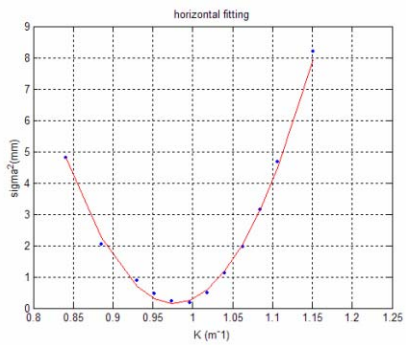

Figure 4**:** Example of transverse beam emittance measurements at transport line by using quadrupole scan method. Fitted parameter of A = 255.22, B = 0.98, C = 0.15, giving emittance ε_x = 238 nm-rad.

Transport line screen monitor have been upgraded to IEEE-1394 cameras. All cameras are external trigger by the timing system. The exposure time of the camera can be adjusted according beam intensity. Multiple exposures are also support for low light applications. Emittance of the transport line was measured by quadrupole scan method. Measured horizontal beam size as function of quadrupole strength is shown in Figure 4. The data are fitted by the quadratic fitting function in following form [6]:

$$\Sigma_{11} = A(K-B)^2 + C$$

Where A, B, C are fitted parameters, K is the quadrupole strength. Emittance can be calculated by the relationship

$\varepsilon = \sqrt{AC} / S_{12}^2$. Figure 4 showed the measured beam size as function of quadrupole setting. The fitted A,B,C parameters are also calculated. Fitted emittance is 238 nm-rad.

PERTURBATION OF INJECTION KICKERS ON THE STORED BEAM OF THE STOARGE RING

Intensified gated camera was used to measure turn-by-turn beam profile at synchrotron radiation port of the storage ring to investigate the bump closure of the injection local bump produced by four injection kickers. In the figure 5, shows the beam profile image of consecutive 5 turns with stored beam during kickers fired. Image are spread about 4 mm in horizontal direction and 1 mm in vertical direction by this non-closure bump. This diagnostics system may be used as the injection kickers tuning complementary tools. The injected beam can also observed by this tools for optimize the injection conditions.

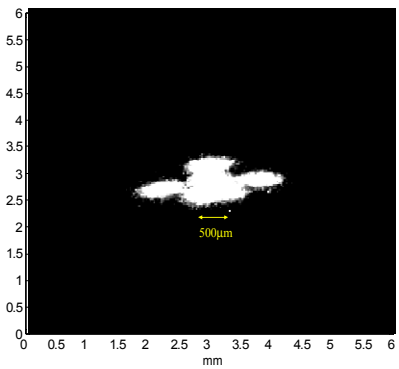

Figure 5: The turn-by-turn beam profile of the stored beam was observed by the synchrotron light monitor. This monitor is outside the local bump form by the injection kickers. The bump is not a closure bump.

GAP VOLTAGE MODULATION STUDY

Intensified gated CCD camera [2] was used for low light application. Here is an example to observe turn-by-turn beam profile of the storage ring after setting RF gap voltage modulation magnitude to double of the synchrotron frequency ($2f_s \approx 50$ kHz), that help to relief the effect from high order mode (HOM) of the cavity and to stabilize the stored beam. Modulation depth is about 5% of the total 800 kV RF gap voltage. For turn-by-turn observation, the exposure time of camera was set to 400 ns that is the revolution time of stored beam. Trigger input to CCD camera is synchronized with the RF gap voltage modulation source. Different delay times after trigger were observed and shown as in the Figure 6. The horizontal beam size is at minimum when the RF gap voltage is minimal, and maximal beam size occurs at maximal gap voltage setting; also the period value is the same as modulation frequency. Stable horizontal beam size is obtained by low speed imaging system that enables the integration procedure performed effectively.

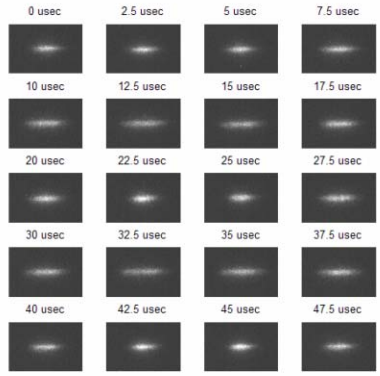

Figure 6: Observed beam profile at difference phase of RF gap voltage modulation cycle. Period of the modulation signal is about 20 μsec (50 kHz ≈ 2 f_s).

SUMMARY

The preliminary results have been shown that the functionality of the imaging system with improved performance are all accomplished by the new generation IEEE-1394 CCD camera. Developing of various application programs to support new imaging system is underway and it will also provide user-friendly interface for all kind of applications

REFERENCES

[1] http://www.prosilica.com.
[2] http://www.qimaging.com.
[3] M. Ferianis, "Optical Techniques in Beam Diagnostics", Proceeding of the EPAC'98 and reference therein, 1998, pp. 159-163.
[4] C. J. Wang, et. al., AIP Conf. Proc. 732 (2004) 462.
[5] G. Rehm, AIP Conf. Proc. 732 (2004) 407.
[6] M.G. Minty, F. Zimmermann, "Measurement and Control of Charged Particle Beams", Springer-Verlag, Berlin, Heidelberg, New York, 2003.

RESONANT STRIP LINE BPM FOR ULTRA LOW CURRENT MEASUREMENTS

M. Dehler,
Paul Scherrer Institut, CH-5232 Villigen PSI, Switzerland
e-mail: Micha.Dehler@psi.ch

Abstract

Proton beams used in proton therapy facilities like PROSCAN have extremely small currents of an order of nanoamperes, which create a challenge for a precise beam position measurements due to their extremely low signal level and subsequent bad signal per noise ratios. For suitable power levels with these currents, pickups need to have a high shunt impedance, something, which is difficult to design for wide band devices. So for a new strip line BPM design, the coupling of the signal outputs to the electrode was deliberately mismatched to create a resonance at the second harmonic of the RF frequency at 145 MHz. The optimum Q-factor to use is given by the coupling between the BPM electrodes leading to to a Q of 50, an overall shunt impedance of 2.9 kOhms and power output levels of an order of -120 dBm at the design current of 1 nA. A prototype of the device has been manufactured, first measurement results will be presented.

INTRODUCTION

The PROSCAN project at PSI aims at the development and construction of a dedicated facility for proton therapy. It consists of a supra conducting 250 MeV cyclotron built by ACCEL Instruments GmbH and will allow the treatment of interior tumors with protons [1].

Due to the extremely small beam currents, the conventional measurement of position and beam profile using ionization chambers must be performed outside vacuum, which limits its application [2]. Furthermore the measurement always introduces some degradation of the beam due to its intrusive character. To overcome these restrictions, it was decided to adapt the design of the strip lines in the SLS transfer lines, which have increased signal levels due to a non conventional resonant layout and so are more suitable for low current measurements. Adding a low noise RF front end and a sophisticated digital receiver should allow a performance suitable for PROSCAN.

With bunch trains in the order of seconds, the signal to be measured is essentially mono frequent and the bandwidth of the system can be chosen at convenience. The design current is 1 nA, for minimum interference and crosstalk a center frequency twice of the RF frequency of 72.7 MHz was defined. A further requirement was to have 100 mm clear space for the beam.

BASIC DESIGN CONSIDERATION

The central figure of merit in a beam position device is the obtainable signal to noise ration. With the position dependent difference part of the signal Δ and the independent sum part Σ, the beam offset computed from these signals can be written as

$$x = C\frac{\Delta}{\Sigma}, \tag{1}$$

where C is the inverse device sensitivity. Linearizing the equation with respect to the sum gives

$$x \approx C\Big(\frac{\Delta}{\Sigma_0} - \frac{\Delta}{\Sigma_0^2}\delta\Sigma\Big),$$

so that one can get the statistical variance of the position reading as

$$\sigma_x^2 = C^2\frac{\sigma_\Delta^2}{\Sigma_0^2}\Big(1 + \frac{\sigma_\Sigma^2}{\Sigma_0^2}\Big) \tag{2}$$

With the sum signal noise $\frac{\sigma_\Sigma}{\Sigma_0}$ typically being small, the optimum device has a high sensitivity (low factor C), low noise in the difference signal (mostly determined by thermal noise) and high signal levels Σ_0.

One option for the BPM would be to use a pair of cavities as a BPM, one using a dipole resonance to procure the position dependent signal and monopole resonant cavity for the sum signal. The Q factors and so the bandwidth could be optimally adapted to the beam spectrum. The problem with this would have been the relatively high temperature variations in the measurement location, which would have led to frequency drifts and subsequent accuracy problems. So it was decided to go for a strip line design, which has been designed in a similar way already used for the transfer lines of the swiss light source (SLS).

A conventional strip line design, as shown in the upper part of figure 1, consisting of strip line shorted on one side and perfectly matched to the output coupler, has a FIR pulse response consisting of two peaks giving a transfer impedance of

$$Z_T = \frac{U_{out}}{I_{beam}} = jZ_l e^{-j\omega\tau}\sin\omega\tau$$

with $\tau = l/c$ as the electrical strip line length and Z_l the characteristic impedance of strip line and coupling. The first idea of changing the characteristics consists in introducing a deliberate mismatch by lowering the strip line impedance Z_s with respect of that of the coupler. The transfer impedance becomes

$$Z_T = Z_l\frac{1 + e^{-2j\omega\tau}}{1 + Z_l/Z_s + e^{-2j\omega\tau}(1 - Z_l/Z_s)}.$$

The method has two drawbacks, the first having to realize mechanically very low characteristic strip line impedances

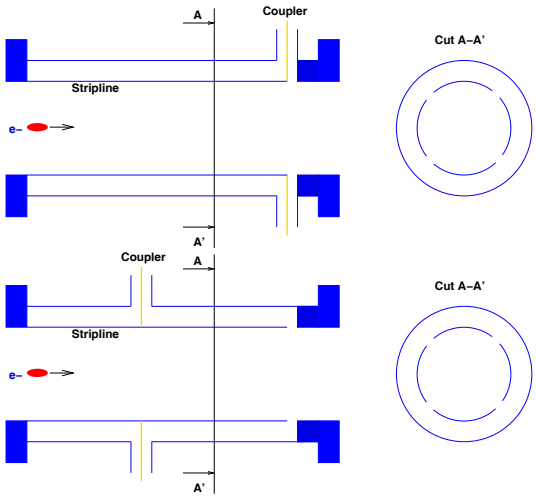

Figure 1: Strip line designs with conventional coupling at strip line end (upper figure) and changed coupling

in order to reach small bandwidths and the second, more important, the impedance maximum is given by impedance of the coupler (i.e. that of the connecting coaxial cable) and does not change at all with bandwidth

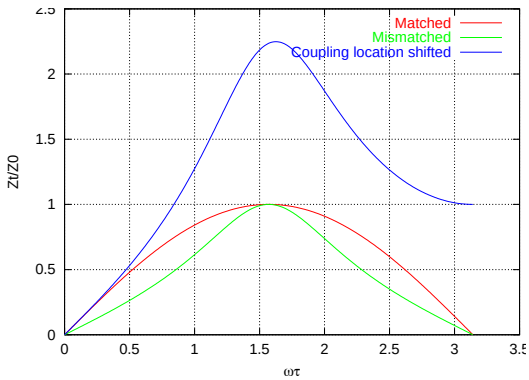

Figure 2: Transfer impedances $Z_T = U_{out}/I_{beam}$ for conventional matched strip line design, effect of introducing mismatch (strip line impedance is half the coupler impedance and shifting the coupler location into middle of strip line.

Only the second method, that of changing the location of the coupler itself has a simultaneous effect on bandwidth and impedance maximum as the impedance of coupler and shorted strip line is transformed to higher values seen at the gap. As can be seen in figure 2, shifting the location from the end of the strip line to its middle increases the peak impedance by a factor 2.2, shifting the coupler further to the shorted end leads to further improvements.

Given the non negligible coupling between the strip lines, there are three different resonant frequencies inside the structure, the the monopole/sum resonance, the difference/dipole resonances and a quadrupole resonance. The central frequency of the measurement should lie in between the monopole and the dipole resonances and, interestingly,

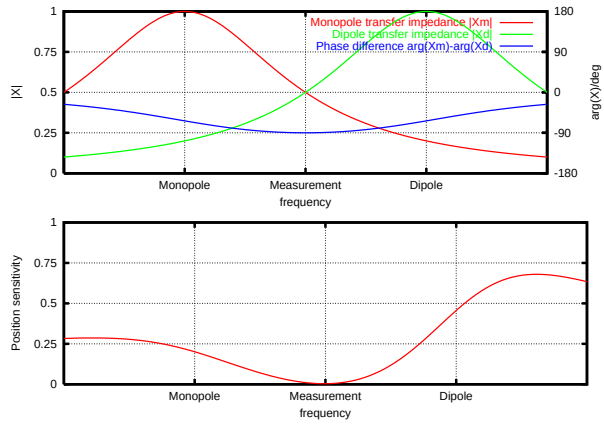

Figure 3: Example of dysfunctional choice of resonant frequencies and Q factors: At measurement frequency, resonances combine with a 90 degree phase difference, so that position sensitivity of output signal goes to zero.

it is not the extreme Q factors, which gives the best results, but the one, where monopole and dipole resonance overlap with the measurement frequency, as can be seen in the upper plot of figure 3.

A second condition on the choice of the Q factor comes from the way of the post processing. The individual electrode signal contains a mix of monopole and dipole components:

$$V_e = V_m + \Delta x V_d = \frac{C_m}{j\omega - j\omega_m + \alpha} + \Delta x \frac{C_d}{j\omega - j\omega_d + \alpha}$$

In our case, each electrode signal passes the RF front end, mixer and demodulator channel and only at the end, the absolute values of the electrode signal are used to determine sums and differences. Now the electrode signal is a sum of two complex phasors, so phase differences have an important influence on the variation of the absolute signal levels. Figure 3 shows a pathological case in that respect. The bandwidth of the monopole and dipole resonance are chosen so, that we obtain a 3 dB drop in the middle between both frequencies, which at first glance seems to be the best setting. But the problem lies in the phases of monopole and dipole parts, which are at 90 degree offset versus each other. Adding a small dipole amplitude at 90 degrees phase offset to the big monopole one will create negligible changes in the overall electrode signal, so that in this case, the sensitivity of the BPM would be zero! As a conclusion, an even lower Q and larger bandwidth is required.

LAYOUT AND MEASUREMENTS

Figure 4 gives a view of the inner layout of the BPM. In order to have a minimum distance between monopole and dipole frequency, the coupling between the electrodes is minimized via metallic shielding plate, located between the strip line blades. The theoretical characteristic impedance of the blades is 66 Ohms, when driven in the monopole

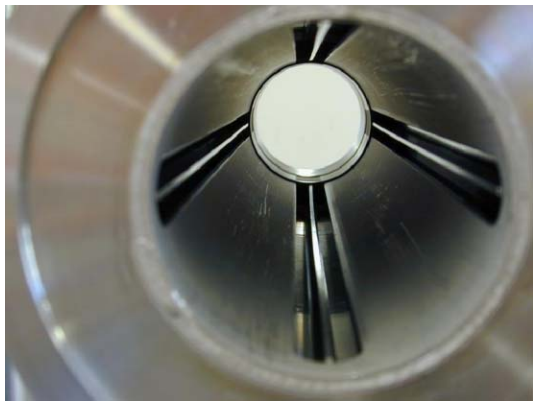

Figure 4: View into BPM showing strip line with shielding fins

mode (all blades being in phase) and 57 Ohms in the dipole mode. Going higher in impedance would have resulted in mechanical problems like impractical dimensions and e.g. the shielding plates having to stick into the beam cross section. The big part of the resonant enhancement comes from the location of the coupler. With a complete length of the strip line blades of 500 mm, output coupling takes place at 35 mm from the shorted and, giving a theoretical loaded Q of 53 for the monopole and 57 for the dipole mode. The overall shunt impedance of the monopole resonance comes out to as 2.9 $k\Omega$ corresponding to an output power level of about -120 dBm at 1 nA beam current.

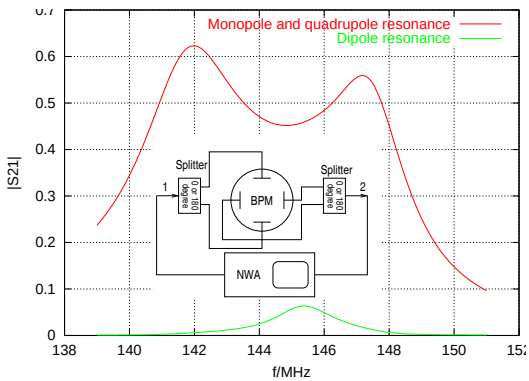

Figure 5: Transmission between pairs of strip line blades revealing monopole, dipole and quadrupole spectra

A prototype of the structure has been manufactured and measured in the laboratory in order to check the electrical properties and to prepare the structure for tests with the beam. A first set of measurements concentrated on identifying the modal spectrum inside the BPM. As shown in figure 5, either one pair of opposite electrode were connected to zero degree power splitters and the transmission from one splitter to the next was measured using a network analyzer. With opposite electrodes driven at even phase, this will excite only the monopole and quadrupole modes, which can be seen clearly in the plot at approximately 142 and 147 MHz.

In a second step, the zero degree splitters are replaced by 180 degree splitters, so that (assuming ideal splitters) only dipole modes are excited. Since the two dipole modes (horizontal and vertical) are decoupled, one would expect no transmission in theory. In reality however, there are slight asymmetries leading to some signal showing the dipole at 145.5 MHz.

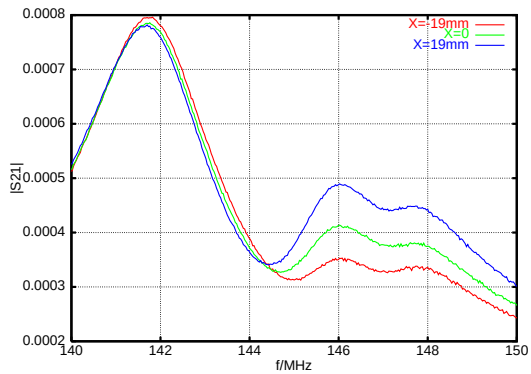

Figure 6: Transmission from on axis antenna inside BPM to BPM output coupler as a function of frequency and antenna offset

In figure 6, a small antenna was inserted on the axis of the BPM and the transmission to the electrodes were measured with the network analyzer for different offsets. As has been shown in the preceding paragraph, the sensitivity does not simply follow the curve of the dipole resonance, since also complex phase changes play a role. The overall sensitivity parameter comes out to be approximately 75 mm.

CONCLUSION

A new strip line beam position monitor has been developed for ultra low current operation. The structure employs a resonant design to maximize shunt impedance and so also the transfer impedance. The obtainable maximum is given by the modal spectrum within the structure, in turn determined by the mutual coupling between the strip line blades. A prototype has been built and characterized in laboratory measurements. Further tests with the proton beam will follow in summer during the commissioning of the PROSCAN facility.

REFERENCES

[1] J.M. Schippers, J. Duppich, M. Jermann, H. Reist, et al, “The SC cyclotron and beamlines of the PROSCAN project at PSI accepted for publication in Proc. of 17th International Conference on cyclotrons and their applications”, Tokyo, October 2004

[2] R. Dölling, “Profile, Current and Halo Monitors of the PROSCAN Beam Lines”, 11th Beam Instrumentation Workshop (BIW04), Knoxville, Tennessee, USA, May 3-6, 2004, to be published in AIP Conf. Proc. 732, p. 244-252

TURN-BY-TURN AND BUNCH-BY-BUNCH DIAGNOSTICS AT NSRRC

K. H. Hu, Jenny Chen, C. J. Wang, Y. T. Yang, Demi Lee, C. H. Kuo, K. T. Hsu

NSRRC, Hsinchu 30076, Taiwan

Abstract

Turn-by-turn and bunch-by-bunch diagnostic systems were set up to support various studies. The beam oscillation signals were detected by transverse and longitudinal bunch signal detectors, and were digitized by a transient digitizer or oscilloscope. The signal data thus obtained were analyzed to extract information concerning the bunch oscillation on a turn-by-turn and bunch-by-bunch basis. The analytical results of this study are summarized herein.

INTRODUCTION

Turn-by-turn and bunch-by-bunch store beam parameters are useful in many studies [1]. Parameters which can be extracted for the data include the filling pattern, multi-bunch oscillation modes, ion instability, pseudospectrum growth and instability damping time. In this study, a system with this capability was setup up for measurement and analysis. Similar system have been set up and proved useful in many accelerator institutes. We set up the system accompany with the development of multi-bunch feedback system. Current effort is to improve the system to support study beam stabilities improvement.

SYSTEM DESCRIPTION

The turn-by-turn and bunch-by-bunch diagnostics are based upon transient digitizers. Time domain diagnostic tools with transient capability are useful for studying the multi-bunch instability and turning of a multi-bunch feedback system. A transient digitizer and feedback electronics are applied to record the bunch-by-bunch and turn-by-turn beam signal as shown in Fig.1. The digitizer acquires data from a transverse bunch oscillation detector and a longitudinal bunch phase detector [2]. The CompuScope 82G digitizer [3] was specified for this study because it provides a friendly application development environment (SDK for LabVIEW and MATLAB). Simple MATLAB scripts were applied to access transient digitizer hardware to enable capture data. These scripts were designed to be easily integrated with analytical scripts. The system supports transient domain data capture. A trigger signal and a feedback switch was used to capture the transient signal for 30 msec for all bunches without decimation.

Intensity gated CCD cameras with an IEEE-1394 interface were also set up to observe the oscillation of bunches. Single turn observation was performed to observe longitudinal stability of the stored beam. The cameras support triggering by revolution clock, adjustable exposure time and multiple exposure are supported.

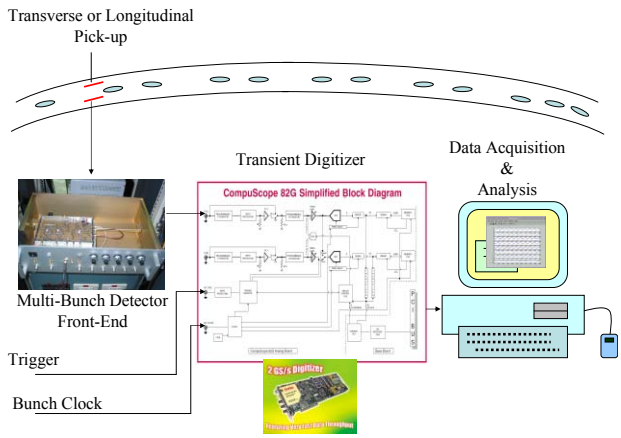

Figure 1: Transient signal capture system.

TIME DOMAIN DIAGNOSTIC

The acquired data can be arranged according to bucket address and bunch ID to reconstruct the individual bunch oscillation. Fig. 2 illustrates the captured data. The oscillation of each bunch is illustrated in Fig. 3. This study aims to use the proposed system to measure growth time and damping accompany with the multi-bunch feedback system.

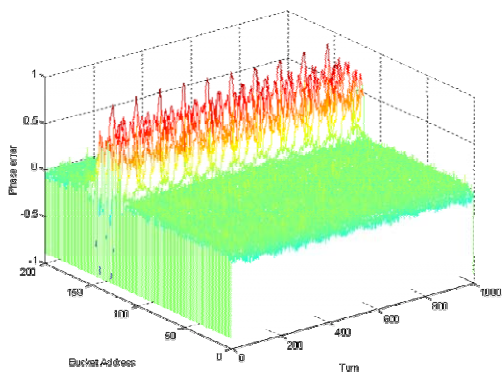

Figure 2: Turn-by-turn and bunch-by-bunch signal captured.

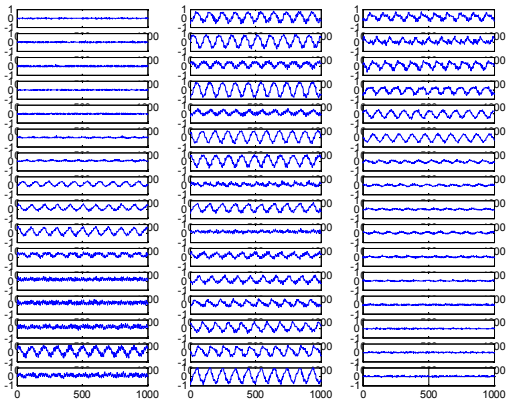

Figure 3: Oscillation of individual bunch is shown on the figure.

FREQUENCY DOMAIN DIAGNOSTIC

Fourier analysis was conducted on the acquired data, generating a high-resolution pseudospectrum, which is the beam spectrum without revolution harmonics, calculated from the digitized data. Typical beam pseudospectrum with the RF gap voltage modulation On and Off are shown in Fig. 4. The sharp peak near 190 MHz is the result of a HOM in the Doris cavity. The 2nd plunger of the Doris RF cavity is tuned to keep the magnitude of this peak. The RF gap voltage modulation further reduces the strength of the instability to provide stable beam [4]. The beam spectrum is much cleaner after the superconductor RF (SRF) upgrade than before it. However, residues transverse and longitudinal instabilities still exist. The transverse instabilities are much more severe due to the very high bunch charge density after the SRF upgrade. A transverse feedback system is needed to solve the instability problem. Fig. 5 illustrates the beam pseudospectrum with and without transverse feedback loop. The spectrum is clean when feedback is applied. The loop effectively suppressed instabilities.

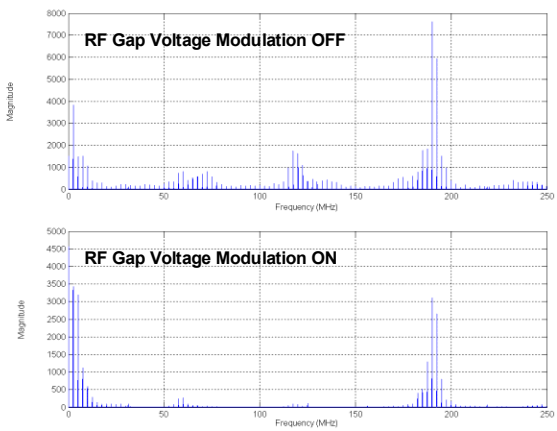

Figure 4: Longitudinal pseudospectrum of the stored beam without/with RF gap voltage modulation.

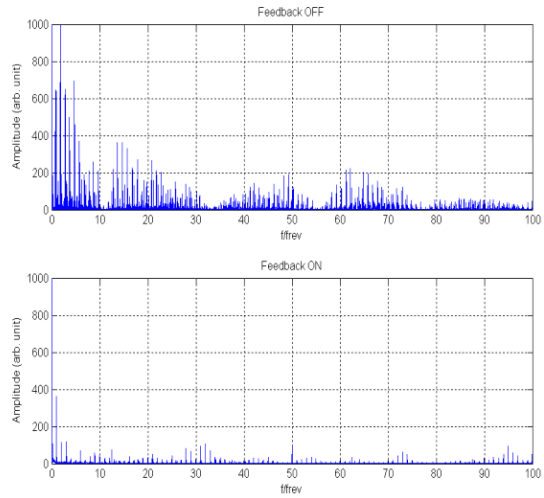

Figure 5: Transverse pseudospectrum of the stored beam without/with transverse feedback loop.

SINGLE TURN SYNCHROTRON RADIATION DIAGNOSTIC

Intensified gated CCD cameras were used adopted to observe the low-light turn-by-turn profile variation in different operation conditions [5]. The source point of the synchrotron radiation monitor located at the dispersion region) and the energy oscillation contributed to the horizontal beam size change of the observed profile. If the longitudinal is stable, then the energy oscillation is small, and the variation of horizontal beam size can be negligible. The high order mode of the Doris conventional cavities was severe, and the energy oscillation was unstable. RF gap voltage modulation was applied to help relieve the effect of the high order mode (HOM) of the DORIS conventional cavities and to stabilize the stored beam before the SRF upgrade. The modulation frequency and depth were twice the synchrotron frequency ($2f_s \approx 50$ kHz) and 5% of the total 800 kV RF gap voltage, respectively. For a single turn beam profile observation, the camera exposure was set to 400 ns, which is the revolution time of the stored beam. The trigger input to the CCD camera is synchronized with the RF gap voltage modulation source. Different post-trigger delay times were observed, as shown in Fig. 6. The horizontal beam size was smallest when the RF gap voltage was smallest, and the beam size was largest at the maximum gap voltage setting. Additionally, the period value was the same as modulation frequency. A stable horizontal beam size was obtained by a low speed imaging system, allowing the integration procedure to be performed effectively. Without this gap voltage modulation, the measured profile fluctuated, implying that the beam stability deteriorated severely because of the longitudinal instabilities. To improve the beam stability and double the maximum stored beam current, the two Doris conventional cavities were replaced by one CESR superconducting RF cavity in late 2004. Success commissioning was performed last December. This

upgrade produced longitudinal stable beam, making the RF gap voltage redundant. The measured single-turn beam profile was much more stable than it was before the upgrade, as shown in Fig. 7. The variation of horizontal beam size because of longitudinal coupled bunch oscillation in the SRF cavity was much less than that in the Doris cavities due to the almost HOM-free nature of the SRF cavity.

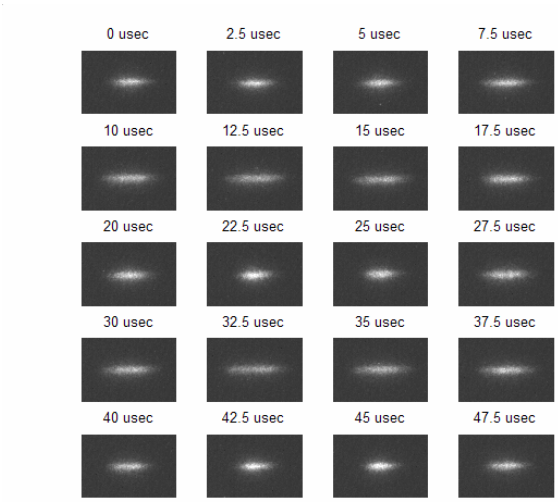

Figure 6: Observed beam profile at difference phase of RF gap voltage modulation cycle. Longitudinal stable beam is obtained by the aid of RF gap voltage modulation. Period of the modulation signal is about 20 μsec (50 kHz ≈ 2 fs).

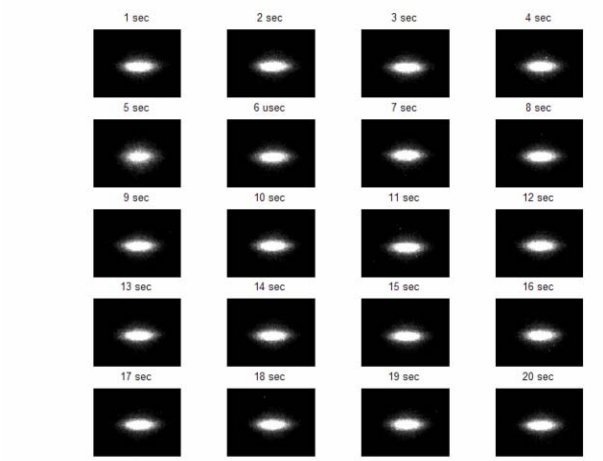

Figure 7: Single turn profile observation after SRF system upgrade during 20 sec observation time. The time on the top of each profile image is the elapse time after start of image acquisition. Longitudinally stable beam was observed.

SUMMARY

Turn-by-turn and bunch-by-bunch diagnostic systems were set up to support various studies. Preliminary results confirm that various stored beam phenomena are useful to observe. The analytical tools for these diagnostic systems are being further developed.

REFERENCES

[1] S. Prabhakar, "New Diagnostics and Cure for Coupled-Bunch Instabilities", SLAC-Report-554, Feb 2000.
[2] http://www.i-tech.si.
[3] http://www.gage-applied.com.
[4] M. H. Wang, S.Y. Lee, "RF Voltage Modulation and Coupled Bunch Instabilities", J. of App. Phys. 92, 555 (2002).
[5] C. J. Wang, et al., AIP Conf. Proc. 732, 462 (2004).

BPM SYSTEM AND ITS DEVELOPMENT FOR THE STORAGE RING OF NSRRC

Jenny Chen, K. H. Hu, Y. T. Yang, C. J. Wang, C. H. Kuo, Demi Lee, K. T. Hsu

NSRRC, Hsinchu 30076, Taiwan

Abstract

About 60 BPMs were installed in the storage ring of an NSSRC. High precision closed orbits were measured by Bergoz's MX-BPMs. Data were acquired by multi-channel 16-bit ADC modules. The orbit data was sampled every millisecond. Fast orbit data were shared by reflective memory network to support fast orbit feedback. The Averaged data were updated to control database at a rate of 10 Hz. Turn-by-turn beam position signals were processed by several Bergoz's log-ratio BPMs and recorded by a transient digitizer to support various beam physics study. Digital BPMs were installed at the storage ring to improve the BPM system functionality at the storage ring, supporting routine operation and study of beam physics. A preliminary test of Instrumentation Technologies' Libera digital BPM is ongoing. The system structure, software environment and performance of the BPM system are summarized in this report.

INRODUCTION

The storage ring of an NSRRC is a 1.5 GeV synchrotron light source. Orbit stability and multi-bunch stability are both very important for user service. The storage ring consists of six super-period triple-bent achromatic lattices. Multi-bunch instability was eliminated using the SRF cavity and multibunch feedback systems. Eight BPMs one wiggler, two conventional undulators (U5 and U9), one elliptical polarised undulator (EPU5.6), one superconducting wavelength shifter and one superconducting multi-pole wiggler were installed in each section. Extra BPMs were installed at the upstream and downstream the insertion devices to guarantee micro-level stability, except thermal, water flow measure. A BPM and orbit feedback system is essential to guarantee good orbit performance, especially when operating the undulator gap change and the EPU phase during an experimental scenario.

MULTIPLEXING BPM SYSTEM

A total of 58 button-type BPMs were installed. The orbit signal was process with Bergoz's MX-BPM [1]. The measured performance was around one micron for a 10 Hz orbit update rate. All MX-BPMs were synchronized externally with a common clock source to avoid the alias effect resulting from synchrotron sideband. To achieve μm level stability, the ambient environment of the BPM electronics was also monitored. The control system interface of the MX-BPM system and its relationship with corrector control and orbit feedback is illustrated in Fig. 1. The BPM server VME crate acquired orbit data every 1 msec. These fast orbit data were shared with an orbit feedback VME crate and a corrector control VME crate with a dedicated reflective memory network. The average slow orbit was updated to control the database every 100 msec. The orbit feedback node read the fast orbit data and compared them with the reference orbit data to execute the control rule, locking the orbit into in-loop BPMs. A typical orbit in a user shift is illustrated in Fig. 2. The beam position can be maintained at the μm level by an orbit feedback system even when undulator parameters are changed.

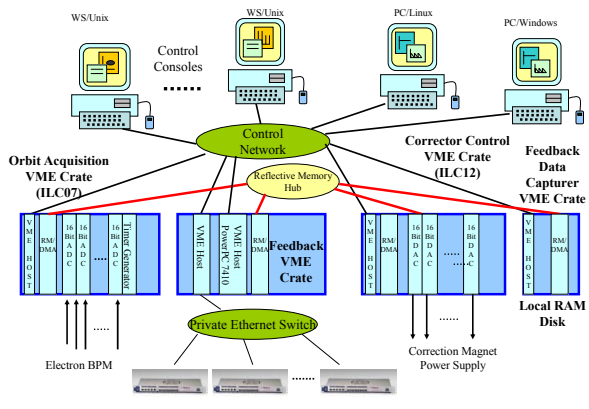

Figure 1: Software environment for BPM data access.

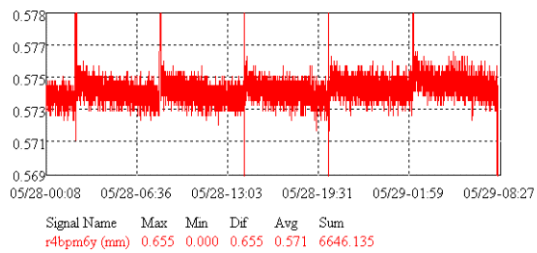

Figure 2: Typical long term beam position measured by in-loop MX-BPM, root mean square is less than 1 μm by the help of orbit feedback loop.

LOG-RATIO BPM

To measure the turn-by-turn beam position, several Bergoz's log-ratio BPM processors [1] were installed at the storage ring accompany with a digitizer to capture the turn-by-turn beam position data. The digitizer was clocked by the machine revolution clock, and triggered by the timing system to synchronize with the external excitation source. The system support mechanism has

been widely studied during last several years [2, 3]. Resolutions better than 100 μm have been achieved.

DIGITAL BPM DEVELOPMENT

A digital BPM test-bed was set up at the storage ring to improve the functionality of the BPM system and support routine operation and various beam physics study [4]. The purpose of this test-bed is to measure and explore the potential and performance of the new technology for storage ring beam diagnostics.

Commercial DBPM2 products [5] were used for the first test. The experimental system comprised a multi-channel coherent down-converter and VME64x crate equipped with multi quad-digital receivers boards (QDR). Preliminary experimental results show that the system achieved micron resolution in the closed-orbit mode and high resolution in the turn-by-turn mode. Promising results were obtained from the test bed. To meet various operation conditions and measure the functionality and performance, the integrated system includes multi-channel access, channel calibration, gain control, and parameter control. The DBPM system must be programmable to calculate the multi-mode high precision beam position, turn-by-turn beam position, tune and other diagnostic measurements. A control system interface was implemented to support the DBPM system operation. A new architecture was designed to improve the integration and functionality of the digital BPM system. Libera products [5] were chosen as the DBPM integration candidates. Since the TLS is the operation user's facility, all functionality is in the operation. Providing seamless integration is necessary for the light source already in operation. Since the existing BPM system needs support routine operation and orbit feedback system, the integration and software environment emphasizes compatibility. The control system interface is separated into two layers. The front-end layer is a VME64x created with a PowerPC module running the real time operation system LynxOS. The user interface layer is located at a workstation/Unix and PC/Linux control console, supporting commercial software programs Matlab and LabVIEW. The VME host receives control parameters from the user interface via Ethernet. The user interface displays the DBPM data are transmitted on after receive a software trigger is received from the Ethernet. Fig. 3 shows the software environment. The DBPM test-bed is seamlessly integrated with the existing system. The preliminary operation environment for Libera is illustrated in Fig. 4. One VME crate is connected to a private network to acquire a low-precision orbit. The embedded server program running in Libera is interfaced with the firmware by a Control system programming interface (CSPI). Data in a slow orbit are updated at 10 Hz. Data from Libera in the turn-by-turn or post-mortem modes are accessed from the Linux server to simplify the programming effort. The fast orbit is connected to the VME crate directly via the fibre link with SFP interface in future. The fast data are then shared with existing BPM system using reflective memory.

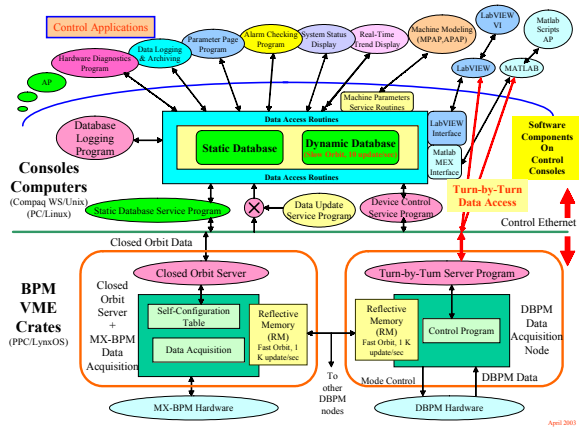

Figure 3: Software environment for DBPM data access.

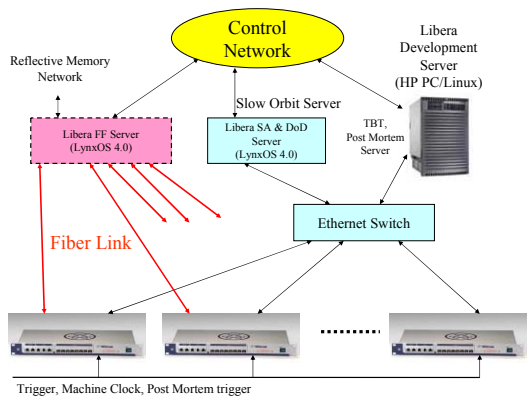

Figure 4: Block diagram of Libera data access.

PRILIMINARY TEST OF LIBERA BPM PROCESSOR

Preliminary tests were performed on the Liberal BPM processor. Most preliminary tests were performed on the integration environment and the functionality evaluation. A Libera processor is a multi-mode device which supports turn-by-turn, sub-micron precision beam position and tune monitoring. The control system need to various software packages to support the digital BPM operation. The features of the new BPM system include analog multiplexing BPM and user-transparent digital BPM. Seamless integration of these features is the most difficult task. Fig. 5 shows the typical response of the beam position when a kicker magnet is fired (K1 @ 3 KV, ~ 1.5 mrad kick). The top diagram in Fig. 5 illustrates the damped horizontal betatron oscillation. A small regular synchrotron oscillation signal rides on the envelope of the damped oscillation, because of residue longitudinal instability probably from the vacuum component of the storage ring. Vertical signal excitation was also observed; and may be due to the imperfection of the field distribution in injection kicker or machine coupling. Fig. 6 illustrates the horizontal phase space

portrait of two BPM separated about π/2 phase advanced near fourth order resonance.

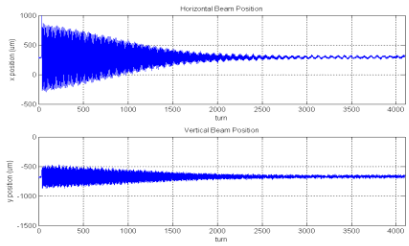

Figure 5: Turn-by-turn beam position measured by new digital BPM; upper is the horizontal beam position, and the lower figure is the vertical beam position.

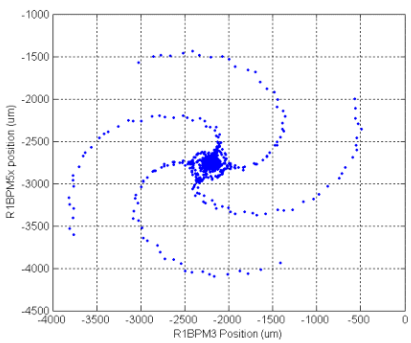

Figure 6: Horizontal phase space portrait of two BPM separated about π/2 phase advanced near 4th order resonance.

TUNE MONITOR

A dedicated tune monitor was implemented by using Libera. The proposed monitor is based on the Fourier analysis of the turn-by-turn data from the Liberas based on various beam excitation levels. Fig. 7 shows the system block diagram. The stored beam was excited by a narrow-band white noise or kicker. The excitation level was controlled by the software. The tune was extracted by Fourier analysis of the turn-by-turn beam position data. Very small beam sizes were magnified under adequate pink noise excitation. It may be compatible with a user not checking the beam condition.

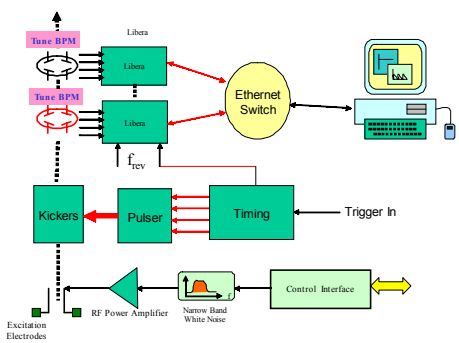

Figure 7: The block diagram of the tune monitor.

The clean tune spectrum is easy to obtain as shown in Fig. 8. The upper part of Fig. 9 displays the 128K-turn data captured by the Libera device on its large internal memory. The data show some beam instabilities in the vertical direction. An instantaneous tune extracted by the numerical analysis of fundamental frequency (NAFF) method is illustrated in the lower part of Fig. 9, showing no evidence of power line cycle tune variation. These findings demonstrate that the main storage ring power supplies ring have acceptable ripple values.

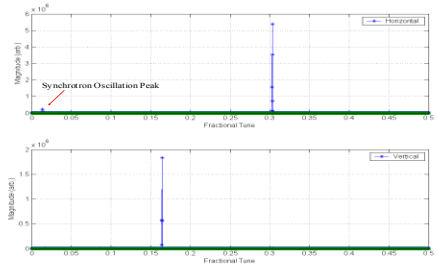

Figure 8: Tune spectrum obtained by Fourier analysis of data set in Figure 7.

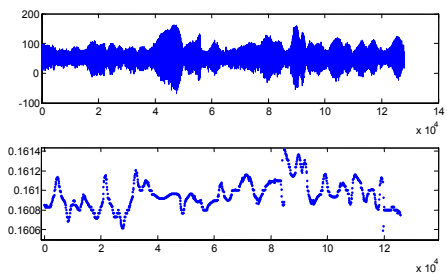

Figure 9: 50 msec turn-by-turn beam position measured data in y direction and its instantaneous tune extracted by NAFF method.

SUMMARY

This report summarizes the status and development of the beam position monitoring system at NSRRC. The short-term goals of this study were to improve the performance and reliability of the existing BPM system. New BPM electronics are being integrated with the monitoring system to improve its functionality. More testing is needed to verify the performance and the operation environment or the hybrid BPM system. Existing BPM and Libera systems are currently being combined to improve their performance and functionality.

REFERENCES

[1] http://www.bergoz.com.
[2] K.H. Hu, et al., "LR-BPM", Proceeding of PAC2001 , 546, 572 (2001).
[3] C.C. Kuo, et al., "Nonlinear Beam Dynamic Experiments at the NSRRC", Proceeding of PAC2001, 1767 (2001).
[4] C. H. Kuo, et al., "The Operation of Digital Beam Position Monitor in NSRRC", Proceeding of EPAC 2004, Vienna, Austria, 1809 (2004).
[5] http://www.i-tech.si.

DIAGNOSTICS FOR THE 1.5 GeV TRANSPORT LINE AT THE NSRRC

K. H. Hu, Jenny Chen, C. J. Wang, Demi Lee, C. H. Kuo, Y. T. Yang, K. T. Hsu

NSRRC, Hsinchu 30076, Taiwan

Abstract

Electron beams at 1.5 GeV were extracted from a booster synchrotron and transported via a transport line and injected into a storage ring. This booster-to-storage ring transport line was equipped with stripline beam position monitors, integrated current transformers, fast current transformer and screen monitors. Commercial log-ratio BPM electronics were adopted to process the 500MHz bunch signal directly. The position of the passing beam was digitized by VME analog interface. An integrated current transformer was applied to measures the transmission efficiency. Screen monitors were used to support routine operation. This study summarizes the system architecture, software tools and performance of the BTS diagnostic system.

INTRODUCTION

A 1.5 GeV electron beam was extracted from a booster synchrotron and transported via a 70 m long transport line before being injected into a storage ring. Various diagnostic devices were installed along the transport line, as illustrated in Fig. 1. These devices included seven stripline type beam positions monitors, three integrated current transformers (ICT) [1], a fast current transformer (FCT) [1] and seven screen monitors. Commercial log-ratio beam position monitor (LR-BPM) electronics [1] were adopted to process the 500MHz bunch signal directly. The passing beam position was digitized by VME analog interface. The transmission efficiency was measured by an integrated current transformer. Screen monitors were applied to support routine operation. Several test screen monitors equipped with a short decay time, a YAG:Ce scintillator and an optical transition monitor with an aluminium file were also installed for various R&D tests.

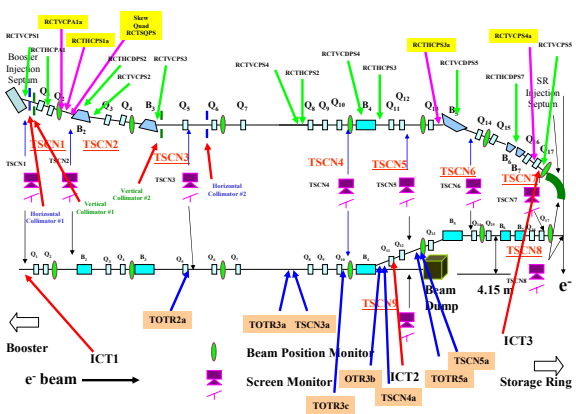

Figure 1: Transport line diagnostic devices layout

BEAM POSITION MONITOR

Seven stripline type BPMs were installed in the transport line to measure the beam trajectory, as shown in Fig. 2. The stripline was mounted on the circular vacuum chamber with a 63 mm inner diameter. The stripline was 10 mm wide and 150 mm long. The beam intercept angle was around 10°. Each BPM had a sensitivity was about 1 dB/mm near the beam pipe centre.

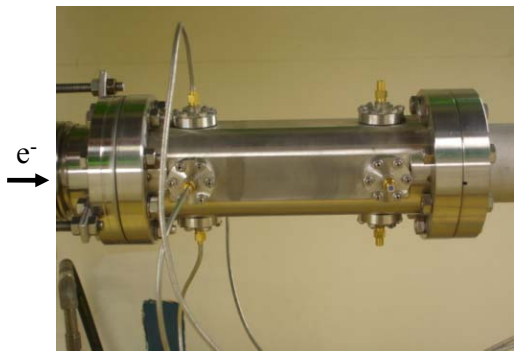

Figure 2: Stripline type beam position monitor

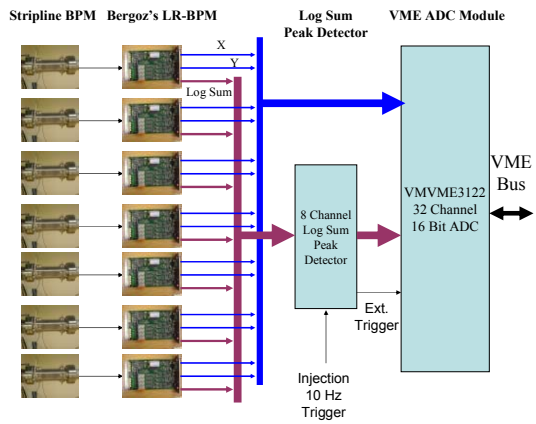

Figure 3: Data Acquisition System for the BTS LR-BPM

Log-ratio BPM electronics were used to measure the beam position in the BTS of the NSRRC [2]. The log ratio processor was a two-channel device. This module consisted of a low-pass filter, a band-pass filter, a log-ratio amplifier and sample & hold (S&H) circuits. The S&H circuits were a timing control circuit, and a position and an intensity signal processing circuit. The transport line beam position data acquisition system, with a 32-channel, 16-bit VME ADC module acquired data from seven LR-BPMs, is illustrated in Fig. 3. The S/H position data are held on the on the LR-BPM module, and a log

sum output signal is also available. An in-hosed made peak detector module in VME form factor was used to ensure that the total log output was at least 100 msec. A PPC CPU module running LynxOS and controlled the operation of the VME crates. The collected data were transmitted to a control database every 100 msec to be displayed and fed to various applications. The LR-BPM in S&H mode with self-beam trigger is considered to be working correctly when the signal is strong enough to activate the trigger circuitry. The LR-BPM indication is given whether the trigger occurs. To consider the problem of data correctness, the position data were validated using the log sum signals. If the log sum signal exceeds a given presentable level, then the LR-BPM is working properly and can provide reliability data. The application software can easily perform this check in the control system.

A beam test was conducted to verify the functionality of the BTS LR_BPM system. Fig. 4 shows the log sum of LR-BPMs along the beam transport line of a routine injection scenario. The trigger of electron gun stops immediately when the storage ring stored beam increases to 200 mA in 170 seconds, corresponding to the machine cycle near 120. The intensity variation of the transport line reveals the performance of the booster synchrotron. The log sum, even if it is not very accurate,, together with the screening, can optimize the operating conditions of the transport line and the extraction conditions of the booster synchrotron. The log sum can also be used to measure the loss of the beam along the transport line. The input current of the correct magnet power supply controls the beam position. HC1 denotes the first horizontally correct power supply, and VC1 denotes the first vertically correct power supply. Fig. 5 illustrates the results of varying HC1 with the position of X. Fig. 6 illustrates the results of varying VC1 with the position of Y.

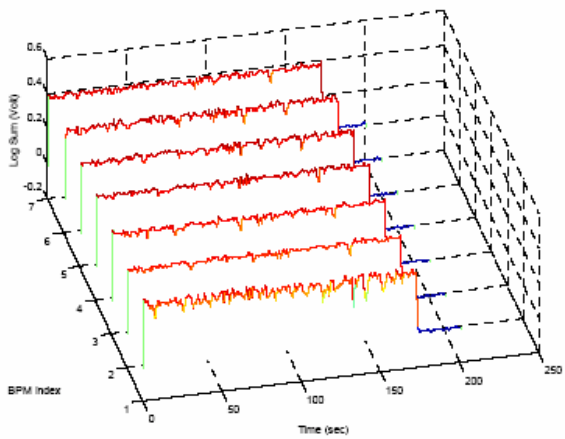

Figure 4: The BTS beam intensity (log sum) distribution as function of time in a routine injection scenario. This figure is shown the log sum output or BTS LR-BPM during injection, the stored beam current of the storage ring is started form 0 mA accumulated to 200 mA about 170 seconds.

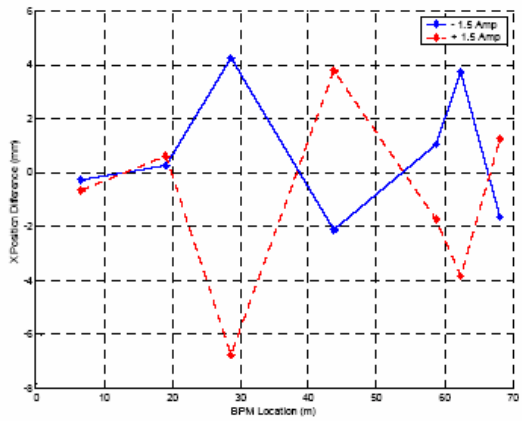

Figure 5: Horizontal trajectory difference when the HC1 change ± 1.5 A.

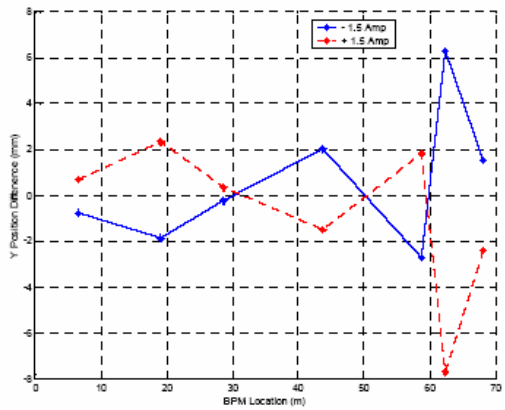

Figure 6: Vertical trajectory difference when the VC1 change ± 1.5 A.

The LR-BPM transport line system non-destructively measures the beam trajectory. LR-BPM can simultaneously measure the position and intensity of the BTS in the injection period. The intensity information also measures the loss of the beam along the transport line. The log sum complements the optimized transport line operating conditions and the booster synchrotron extraction conditions, improving the injection efficiency. The system was recently integrated and tested, with further ongoing improvements. This measurement system is expected to help optimize the transport line for routine and top-up mode operation in the near future.

INTENSITY MONITOR

Two fast current transformers (FCT) and three integrated current transformer (ICT) was installed to measure the beam intensity and to characterize transmission efficiency of the transport line. One FCT was installed at the booster synchrotron, and the other was installed at the upstream of the transport line. The two FCTs were used to measure the booster synchrotron extraction efficiency. The measured results are illustrated in Fig. 7. The upper trace represents the stored beam at the booster synchrotron, and the lower trace represents the extracted beam. The ripple baseline is the interference

from the extraction kicker. The extraction efficiency can be calculated from the shape of the beam signal. To measure the transport line transmission efficiency, three ICTs were installed at the upstream and downstream of the transport line and in the middle of the vertical achromatic section around the middle of the transport line. The first and second ICT measured waveforms are illustrated in Fig. 8. The transmission efficiency of the first half of the transport line was nearly 100%.

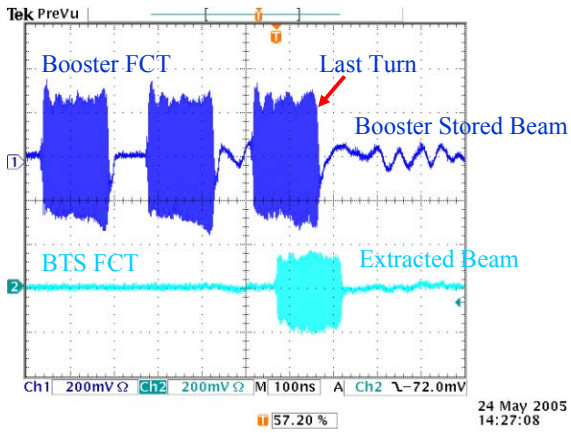

Figure 7: In-flange integrated current transformer

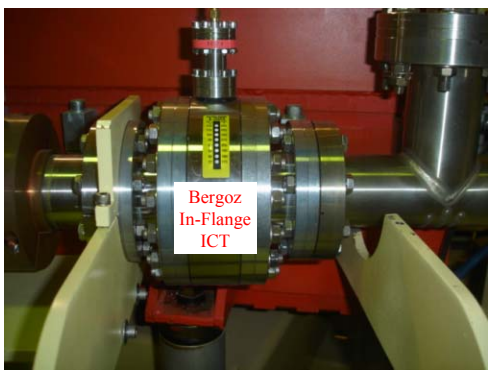

Figure 8: In-flange integrated current transformer

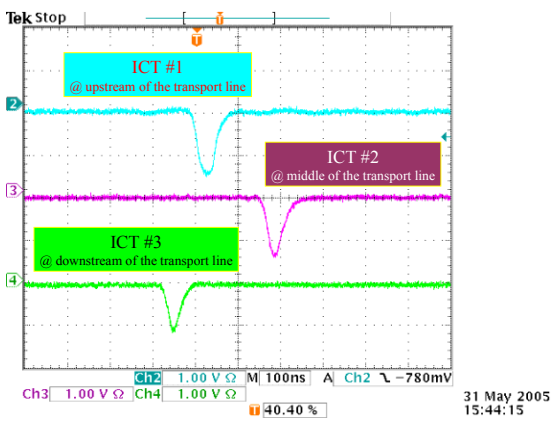

Figure 9: Typical output of the integrated current transformer

SCREEN MONITOR

Eight fluorescent screen monitors were installed at the transport line. Several optical transition monitors and YAG:Ce screen monitors were also installed for testing and evaluation. IEEE-1394 digital cameras were used as the fluorescent screen monitors [3, 4]. The long distance transmission with the digital interface eliminates image distortion, and eliminates the need for a frame grabber in the computer. All cameras can be triggered with the extraction timing. The exposure time is user programmable, providing flexibility when using monitor screens. The emittance was measured by quadrupole scan methods. The measured emittance was around 230 nm-rad, which was consistent with the theoretical value.

SUMMARY

This study summarizes transport line diagnostics, describes devices and functionality, and presents the results of beam testing.

REFERENCES

[1] http://www.bergoz.com
[2] K. H. Hu, et al., “Beam Position Monitoring System fir the 1.5 GeV Transport Line of NSRRC”, Proceeding of the PAC 2003 2554 (2003).
[3] C. J. Wang, et al., “Applications of the IEEE-1394 CCD Camera for Beam Diagnostics in NSRRC”, AIP Conf. Proc. 732, 462 (2004).
[4] C. H. Kuo, et al., “The IEEE-1394 Digital Camera Application in the Taiwan Light Source”, Proceedings of PAC 2005.

TOWARDS A ROBUST PHASE LOCKED LOOP TUNE FEEDBACK SYSTEM

Rhodri Jones, CERN, Geneva, Switzerland
Peter Cameron, Yun Luo, Brookhaven National Laboratory, Upton, NY 11973, USA

Abstract

Attempts to introduce a reliable tune feedback loop at RHIC (BNL) [1] have been thwarted by two main problems, namely transition crossing and betatron coupling. The problem of transition crossing is a dynamic range problem, resulting from the increase in the revolution content of the observed signal as the bunch length becomes short and from the fast orbit changes that occur during transition. The dynamic range issue is being addressed by the development of a baseband tune measurement system [2] as part of the US LHC Accelerator Research Program (US-LARP). This paper will focus on the second problem, showing how a phase locked loop (PLL) tune measurement system can be used to continuously measure global betatron coupling, and in so doing allow for robust tune measurement and feedback in the presence of coupling.

INTRODUCTION

There are two main difficulties associated with utilizing a PLL tune measurement and feedback system in the presence of coupling. The first arises from the fact that in a coupled machine the excitation from one plane shows up in the other. A PLL therefore has the possibility to become confused regarding which signal is associated with a given measurement plane, which causes problems for both PLL measurement and tune feedback.

The second difficulty arises when a tune feedback system tries to maintain the tunes at their 'set' tune values in the presence of coupling. When the coupling amplitude becomes larger than the difference in the unperturbed tunes (the value of the tunes for a completely decoupled machine), then no amount of quadrupole adjustment can diminish this minimum tune split and restore the tunes to their desired 'set' values. This again leads to a breakdown in the tune feedback loop.

As these obstacles to tune measurement and feedback became evident at RHIC, the need for improved coupling measurement became clear, and the PLL was re-configured to permit measurement of the projections of both eigenmodes in both planes. The excellent quality of the data obtained by this method motivated the development of a proper formalism [3, 4] for its interpretation.

MEASUREMENT OF COUPLING PARAMETERS USING A PLL TUNE TRACKER

This section will discuss the use of a phase locked loop tune tracker to measure the betatron coupling amplitude and phase.

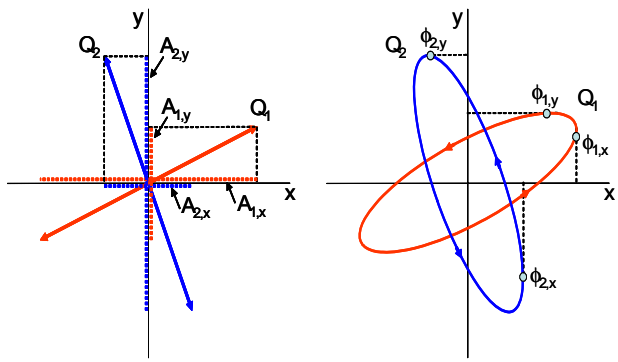

Figure 1: Schematics showing the two eigenmodes rotated with respect to the horizontal and vertical planes due to coupling.

Equations of Interest

For a linearly coupled circular accelerator the observed displacement on turn n in the horizontal (x) and vertical (y) planes are a combination of the projections of two eigenmodes (see e.g. [3]). This is illustrated in Fig. 1 and can be expressed as

$$\begin{cases} x(n) = A_{1,x}\cos(2\pi Q_1 n + \phi_{1,x}) + A_{2,x}\cos(2\pi Q_2 n + \phi_{2,x}) \\ y(n) = A_{1,y}\cos(2\pi Q_1 n + \phi_{1,y}) + A_{2,y}\cos(2\pi Q_2 n + \phi_{2,y}) \end{cases} \quad (1)$$

The eigenmode frequency of Mode 1 is denoted by Q1, while $A_{1,x}$ and $A_{1,y}$ represent the amplitudes of this mode in the horizontal and vertical plane respectively. Similarly $\phi_{1,x}$ and $\phi_{1,y}$ represent the phases of this mode in the horizontal and vertical plane respectively. The same notation applies for Mode 2.

Using Hamiltonian perturbation theory in the absence of intentionally strong local couplers, it is possible to define the following relationships [3]

$$\begin{cases} r_1 = \dfrac{A_{1,y}}{A_{1,x}} = \sqrt{\dfrac{\beta_y}{\beta_x}} \cdot \dfrac{|C^-|}{2\nu + \Delta} \\ r_2 = \dfrac{A_{2,x}}{A_{2,y}} = \sqrt{\dfrac{\beta_x}{\beta_y}} \cdot \dfrac{|C^-|}{2\nu + \Delta} \end{cases}, \begin{cases} \Delta\phi_1 = \phi_{1,y} - \phi_{1,x} = \chi \\ \Delta\phi_2 = \phi_{2,x} - \phi_{2,y} = \pm\pi - \chi \end{cases} \quad (2)$$

Here Δ is the difference between the fractional part of the unperturbed tunes, $\beta_{x,y}$ the beta functions at the

observation location, $|C^-|$ and χ the coupling amplitude and phase respectively and

$$\nu = \frac{1}{2}\sqrt{\Delta^2 + |C^-|^2}$$

It is also possible to write the following relations for the eigenmode frequencies, Q_1 and Q_2

$$\begin{cases} Q_1 = Q_{x,0} - \frac{1}{2}\Delta + \frac{1}{2}\sqrt{\Delta^2 + |C^-|^2} \\ Q_2 = Q_{y,0} + \frac{1}{2}\Delta - \frac{1}{2}\sqrt{\Delta^2 + |C^-|^2} \end{cases} \quad (3)$$

Solving for Δ and $|C^-|$ one obtains

$$|C^-| = \frac{2\sqrt{r_1 r_2}\,|Q_1 - Q_2|}{(1 + r_1 r_2)} \quad , \quad \Delta = \frac{|Q_1 - Q_2|(1 - r_1 r_2)}{(1 + r_1 r_2)} \quad (4)$$

which are independent of the beta functions at the observation location.

Configuring a PLL tune tracker to measure betatron coupling parameters

In the classical PLL tune tracker implementation, the horizontal plane is configured to track one eigenmode (assumed to be eigenmode 1), while the vertical tracks the other (eigenmode 2). If, instead, the vertical detection frequency is forced to be the same as that of the horizontal, then the vertical acquisition chain will observe the projection of eigenmode 1 in the vertical plane (see Fig. 2). By duplicating the number of channels the same principle can be applied to eigenmode 2.

The amplitude and phase measured by each of these channels are then the same amplitudes and phases described in Eq. (1). Since the PLL kicker is the same for a given eigenmode, its gain and the beta-function at its location do not have to be taken into account when computing the ratios r_1 & r_2 of Eq. 2. This is not true for the receiver gains, which can be different for each channel.

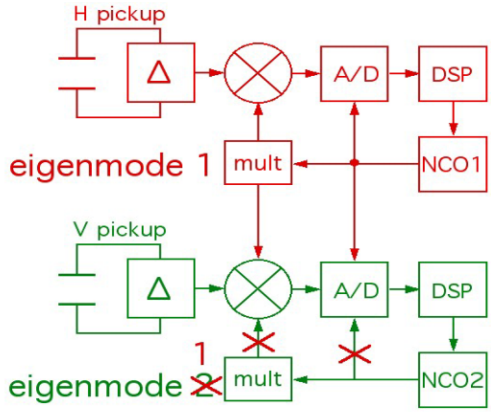

Figure 2: Schematic representation of the RHIC PLL system as modified for coupling measurement

When the PLL is locked, to first order $\phi_{1,x} = \phi_{2,y} = 0$ and hence the coupling phase, χ, is simply given by $\phi_{1,y}$ (or $\pm\pi$ - $\phi_{2,y}$). The coupling amplitude, $|C^-|$, and unperturbed tune difference, Δ, can be obtained using Eqs. (4). In addition the unperturbed tune values $Q_{x,0}$ and $Q_{y,0}$ can be calculated using Eqs. (3). Hence by reconfiguring the PLL as shown in Fig. 2 it is possible to provide all the necessary information to measure coupling [4]

RESULTS OF COUPLING MEASUREMENTS USING A PLL TUNE TRACKER AT RHIC

To perform continuous coupling measurements during the acceleration ramp, the RHIC PLL tune tracker was configured as shown in Fig. 2. Since the measurement required doubling the number of acquisition channels it could only be performed for one ring. The yellow ring PLL was therefore used in its standard configuration to acquire eigenmode 1 (horizontal) and eigenmode 2 (vertical), while the blue PLL system was used to

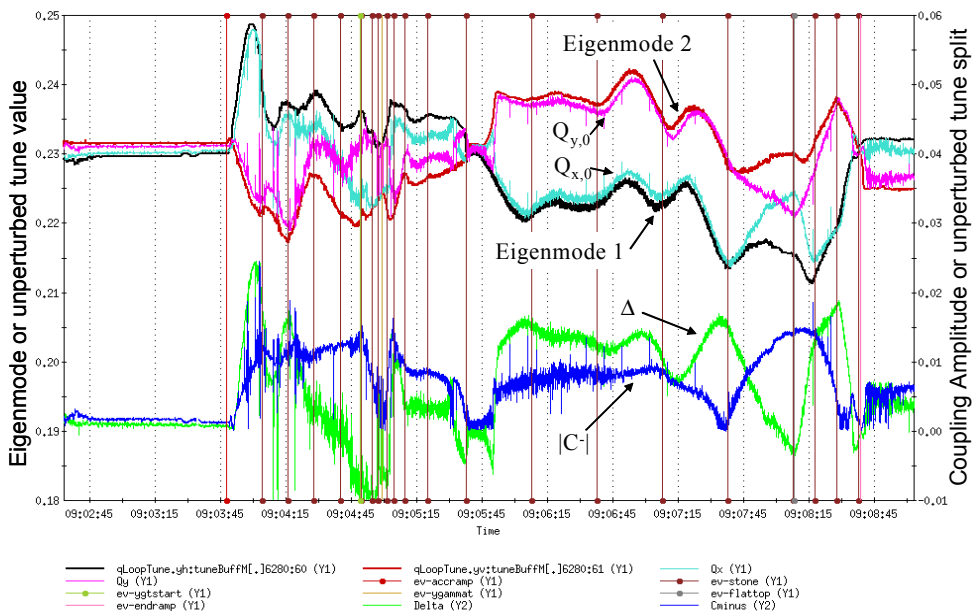

Figure 3: Continuous coupling amplitude measurement using the PLL tune tracker during a RHIC ramp.

acquire the projection of yellow eigenmode 1 in the vertical and that of yellow eigenmode 2 in the horizontal.

Fig. 3 shows the results of one such measurement taken during Cu run number 6280. The coupling is seen to be well adjusted during injection, but becomes large near transition and again towards the end of the ramp. When considering only the usual PLL tune data (eigenmodes 1 and 2) the tune would seem to be well adjusted during the early part of the ramp. Looking at the unperturbed tunes ($Q_{x,0}$ and $Q_{y,0}$) as calculated from $|C^-|$ and Δ using Eq. (3), one can clearly see that this is not the case. The unpertubed tunes actually cross during this time, something which was confirmed by the kicked tune measurement system (ARTUS) from a similar, earlier ramp (the kicked tune system was left off during ramp 6280 to minimize beam loss due to emittance blowup). This is a good example of where the PLL will continue to track a given eigenmode, even though its major projection is now in the other plane. Incidentally, this leads to a negative Δ at these locations, since the amplitude ratios r_1 and r_2 become larger than 1 due to the fact that the PLL is now tracking the eigenmode with the smallest projection amplitude in both planes. In addition, if the tune feedback loop were closed, it would become unstable in this coupling condition.

MAKING A PLL TUNE TRACKER ROBUST IN THE PRESENCE OF BETATRON COUPLING

By tracking a single eigenmode in each plane, as is typically done by most PLL tune measurement systems, it is very easy for the PLL to become confused when the unperturbed tunes are close together and the coupling amplitude becomes large. This can lead to the PLL in both planes tracking the same eigenmode, or with one of the planes losing lock altogether.

The addition of the information related to the projection of the excitation in the other plane allows the PLL to know the state of its current eigenmode with respect to that being tracked by the other plane. This means that if the unperturbed tunes cross, then the horizontal and vertical PLLs can be forced to change from one eigenmode to the other. In this way they keep track of the eigenmode with the largest amplitude projection in their respective planes, reducing the chance of losing lock should the coupling amplitude decrease.

As was shown in the previous section, if a robust tune tracker can be successfully implemented during the ramp, then coupling is automatically measured. Taking this one step further one could imagine performing direct coupling feedback using the parameters measured by the PLL.

MAKING PLL TUNE FEEDBACK ROBUST IN THE PRESENCE OF BETATRON COUPLING

It has been shown how it is possible to configure a PLL tune tracker to continuously measure the coupling parameters. By knowing $|C^-|$ and Δ and the two eigenmode frequencies Q_1 and Q_2 it is possible to determine the unperturbed tunes, $Q_{x,0}$ and $Q_{y,0}$, that would be measured in the absence of betatron coupling. The nice thing about the unperturbed tunes is that they remain constant for any value of the coupling amplitude. This means that these values could be used in a tune feedback loop without giving rise to the problems encountered when feeding back on the eigenmode frequencies.

In practice this would imply that the set tunes requested by the tune feedback loop would be the unperturbed tunes rather than the actual oscillation frequencies (eigenmodes) undertaken by the beam. The feedback loop would therefore be stable in the presence of coupling, but would not prevent the beam from oscillating on or near resonances were coupling to become large. By performing tune feedback in this manner, however, the problems of coupling and tune correction become two separate issues rather than being interdependent.

CONCLUSIONS

Results from RHIC have shown that continuous betatron coupling measurements can be obtained throughout the acceleration ramp by appropriately configuring a PLL tune tracker. Not only does this provide the coupling amplitude, but also the coupling phase, both of which are required for successful coupling correction. The ability to measure the coupling parameters gives a PLL tune tracker two added advantages: the ability to track tunes in the presence of betatron coupling, and the ability to provide the necessary quantities for an 'unperturbed' tune feedback system in the presence of betatron coupling. All of this greatly enhances the power of a PLL tune measurement system, and points the way to a robust tune feedback system for RHIC and future hadron machines.

So far the effect of local coupling on the measurements has not been studied, but future beam experiments will attempt to verify that the observed quantities do indeed allow for global betatron coupling correction or eventual feedback.

REFERENCES

[1] P. Cameron et al, "RHIC Third Generation PLL Tune Measurement System", PAC 2003. http://epaper.kek.jp/p03/PAPERS/ROAB009.PDF

[2] M. Gasior and R. Jones, "High Sensitivity Tune Measurement by Direct Diode Detection", DIPAC 2005. http://cern.ch/dipac2005/default.htm

[3] Y. Luo, P. Cameron, S. Peggs, D. Trbojevic, "Possible phase loop for the global betatron decoupling", BNL-C-A/AP/174. http://www.agsrhichome.bnl.gov/AP/ap_notes/ap_note_174.pdf

[4] R. Jones, P. Cameron, Y. Luo, "Towards a Robust Phase Locked Loop Tune Feedback System", BNL-C-A/AP/204. http://www.agsrhichome.bnl.gov/AP/ap_notes/ap_note_204.pdf

BEAM LOSS POSITION MONITOR USING CERENKOV RADIATION IN OPTICAL FIBERS

W. Goettmann, F. Wulf, HMI, Berlin, Germany
M. Körfer*, DESY, Hamburg, Germany
J. Kuhnhenn, FhG-INT, Euskirchen, Germany

Abstract

The VUV FEL in TESLA technology at DESY provides Giga-Watt output power in laser pulses. The SASE single pass Free Electron Laser (FEL) has been developed for high-brightness user applications. At the design parameters the average power of the electron beam is about 72 kW. To avoid vacuum breakdown and high radiation levels caused by electron losses a machine protection system is required. Collimators are installed upstream of the radiation sensitive undulators [1]. However, the proper operation of the collimator system needs to be measured with a beam loss monitor. Conventional radiation sensor systems are not suited for the VUV-FEL undulators, because of the restricted free space in the undulator gap. A Beam Loss Position Monitor (BLPM) based on Cerenkov light in optical fibers allows real time monitoring of loss location and loss intensity. Electrons with energies above 175 keV generate Cerenkov light during their penetration of the optical fiber. The fast response of the Cerenkov signal is detected with photomultipliers at the end of the irradiated fibers. The reconstruction of the particle loss trace in 3 space dimensions became possible with four sensors.

INTRODUCTION

Since September 2004, the VUV-FEL has been in operation and will soon used by synchrotron radiation user. The accelerator consists of an rf-laser gun, the acceleration modules, each containing eight 9-cell super conducting (SC) cavities, two bunch compressors, collimators and a 30 m long permanent magnet undulator section comprising six 4.5 m long undulator units. The final electron beam energy is 1.0 GeV. Dark current electrons caused by field emission from the normal conducting rf gun and generated in the first acceleration module are transported along the beamline. Electrons outside the phase space acceptance of the accelerator will be lost anywhere. Moreover, the electron bunches suffer unavoidable beam emittance growth from space charge effects in the gun and bunch compressors.

Lost electrons hit the vacuum chamber and create a shower of secondary particles. These showers penetrate an optical fiber and generate Cerenkov radiation. Using four parallel sensors radial to the vacuum pipe along the section of interest the electron loss traces can be determined in transversal and longitudinal direction. Thus a Beam Loss Position Monitor BLPM is used at the VUV-FEL for online analysis of particle losses. During machine commissioning and routine operation the online optimisation of collimator efficiency and studies concerning electron losses are performed.

CERENKOV RADIATION

Cerenkov radiation is emitted whenever charged particles pass through dielectric matter with a velocity exceeding the velocity of light in the medium (fiber). Cerenkov emission is immediately generated by recombination effects in the material. The response time is negligible compared to light propagation time in the fiber or rise time in photomultiplier electronics. The intensity of Cerenkov light increases inverse to the cube of the wavelength. Consequently, in the visible spectrum the blue colour dominates.

The propagation of Cerenkov light in the fiber depends on the particle shower geometry, particle and fiber properties. The shower angle with respect to the fiber axis and the shortest distance (Stoss-Parameter) between particle trajectory and the center of fiber cross-section are important for the coupling of Cerenkov light into the fiber. The modelling of Cerenkov-effects in fibers is documented in [2-5]. For electrons, the lowest energy for emitting Cerenkov light in pure quartz fibers (n=1.46) is about 175 keV. The opening angle of Cerenkov radiation in the fiber scales with the energy of non-relativistic electrons. Above 6 MeV electron energy the light intensity is given only by the number of electrons hitting the fiber and their path length inside the material.

BEAM LOSS POSITION MONITOR

Some publications about fibre optic radiation monitoring systems for accelerators based on the generation of Cerenkov light by relativistic charged particles appeared recently [6-9]. Using one fiber, a particle loss trace can be detected only within a small radial angle. Using four (or more) parallel fibers in equidistant radial space, similar to the arrangement of beam position monitor (BPM) sensors, the loss trace can be measured in transverse and longitudinal dimensions. The Cerenkov light is detected with photomultipliers (PMT's) at the end of the sensor fibers. The response of the PMT is monitored with a fast scope (ACQIRIS-Card). Measuring the time of light propagation in the fiber by

* corresponding author: markus.koerfer@desy.de

using a trigger signal from the bunch clock, the position of the secondary shower can be determined. The scheme of the BLPM is shown in figure 1.

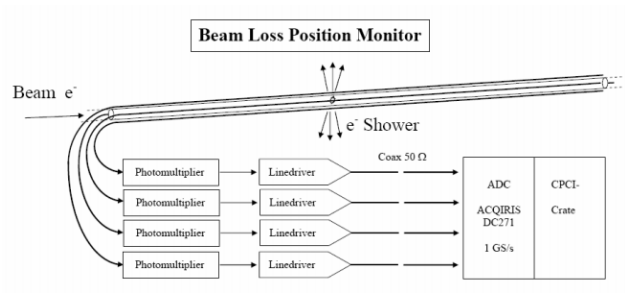

Figure 1: Scheme of the Beam Loss Position Monitor. Four fibers in equidistant radial arrangement allow the measurement of secondary particle showers along the beam line. The photomultiplier is followed by a line driver and a fast ADC (1G/s) card. The transverse loss trace can be calculated from the photomultiplier signals.

The precise location of the secondary shower with respect to the beam line layout can be figured out by movable vacuum components, e.g. OTR screens or wire-scanners. Consequently, the allocation of the accelerator layout and signal time structure can be checked. Due to the fact, that the speed of relativistic electrons in vacuum (~ c) is higher than the light propagation in the fiber (~ 0.66 c), the chronological order of detected losses generated by one bunch / halo can be mixed up. In order to keep the chronologic order of loss events, the beam needs to pass first the PMT position and afterwards the sensor fiber. In other words: with respect to the beam direction the PMT position is always upstream of the sensor position. In this case, the detected time difference t_D^* of two Cerenkov pulses in the fiber (within one trigger event) is $t_D^* = 5/2\ t_D$ with reference to the time difference t_D of two beam-loss occurrences. The time scale stretching by a factor of 2.5 implies a higher local resolution on the scope. While the scope sample rate of one nanosecond covers a distance in vacuum of about 300 mm, the in fact supervised distance is only 120 mm. In the case, that the PMT would be downstream of the sensor fiber the detected signals can be mixed up and the time difference t_D^* is a factor 5 shorter.
An important issue for analysing the data is the clear allocation of losses to a bunch clock trigger. The overlap of different Cerenkov light pulses generated by different clock triggers can be avoided when the time space of two consecutive trigger signals is larger than the time of light propagation in the total fiber length. At the VUV-FEL at DESY the time space of bunch triggers in a bunch train varies between 1 μs and 111 ns, respectively the fiber sensor length could vary between 120 m and 13 m. The sections downstream of the collimator are equipped with the BLPM system using a maximum sensor length of 36m for a beamline upstream of the undulators and 35m for the undulators itself.

Fiber Properties

The detection system needs a radiation resistant optical fiber extending the working periods without fiber replacement. Unfortunately, the highest Cerenkov intensity appears in a spectrum-range where the radiation induced losses are high. The radiation hardest commercial fibers for visible light and light of shorter wavelength are multi-mode step-index fibers with pure silica core of high OH-content. A sensor fiber with a 300 μm core diameter drawn from a Heraeus Tenevo SSU preform was used. To increase the signal to noise ratio the fiber was shielded by black Nylon buffer against ambient light. The light output of the sensor scales linear with the diameter, but a larger diameter reduces the bandwidth and limits the local resolution. The spectrum of the output signal depends strongly on the spectral attenuation of the fiber. In agreement with theoretical predictions the maximum intensity was measured in the wavelength range around 550 nm after penetrating a fiber length of 35 m.

Photomultiplier

For all fiber sensors selected photomultipliers (Hamamatsu H6780-02) are used. Every single PMT was tested to obtain the gain characteristics depending on PMT control voltage and wavelength. The relative comparison of the PMT's to each other was done with a red laser (pulse width 40 ns). The PMT output-signal was amplified depending on different control voltages to approve its linearity. To ensure that all photomultipliers are working with the same amplification the individual control voltage settings of PMT's are saved in a look-up table. A LabView Software ensures comparable output signals at different amplification levels for all PMT's in use.

MEASUREMENT

The system allows a sensitive loss measurement along the beam path. A typical loss pattern in the Temporary-Beamline Seeding is shown in figure 2. The losses are generated by an inserted OTR-screen (3SUND1). The loss shower intensity started smoothly and was rapidly increased downstream of the (first) quadrupole. The local minima in the signals are due to the transverse distance variation of the fiber with respect to the vacuum pipe center. The distances at screens, pumps and quadrupoles are increased by roughly a factor of three. An envelope curve (not shown in the plot) of the signal maxima corresponds to the loss profile with equidistant space between fiber and transverse chamber center. However, losses at places with larger fibre distances will probably lead to false detection of the shower origin.

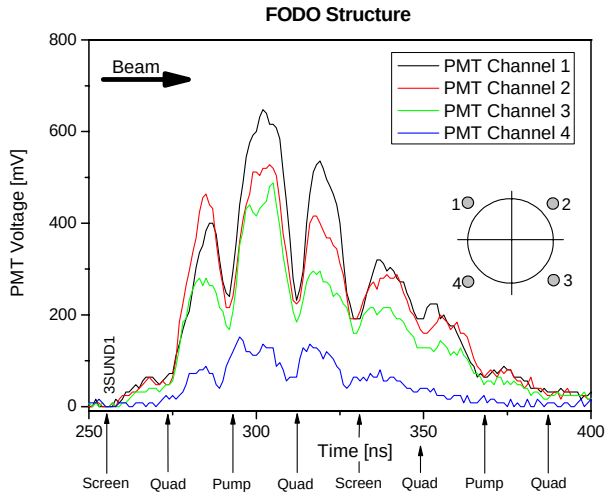

Figure 2: Cerenkov light in optical fibers detected with photomultipliers. The online monitor system allows the measurement of electron losses along the sensor. Due to bypassing the fiber at several enlarged vacuum components along the beam line (screens, quadrupoles, pumps) the transverse distance varies and influences the signal height. The minima allow the reconstruction of the beam line design. The time axis scaling is 8.2 ns/m.

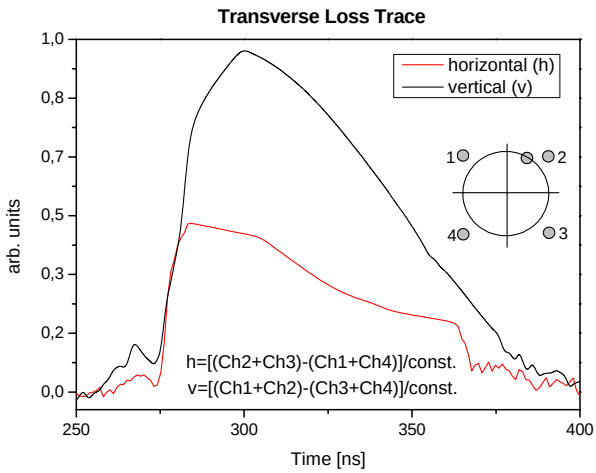

Figure 3: Transverse particle loss trace along the beam line. The envelope of the calculated horizontal and vertical loss trace is shown. Losses are dominated in the first quadrant of the vacuum chamber.

The transverse loss traces are calculated from the PMT signals. In figure 3 the minima due to local shielding have been omitted. Then the envelopes reveal the loss trace for both planes. With respect to the beam direction the losses are on top (vertical) and on the right side (horizontal) of the beam path. The loss trace amplitude for each plane is different because of the asymmetric beam halo (measured by profile monitors). In an untypical case, that the signals measured at the four fibers are equal in amplitude and time the loss trace in figure 3 would become zero. So, by observing the PMT signals and the loss trace one can easily figure out the transverse position of the loss shower.

The same principle of the BLPM System with four fibers was also adapted to an optical fiber dosimeter system based on the Optical Time Domain Reflectometer [10] technique.

CONCLUSIONS

A real time sensing system measuring the local origin of electron losses and collimator "leaks" has been developed and operated during the VUV-FEL commissioning and routine operation run. The advantages of an optical fibre BLPM system are:

- It enables the operator to control radiation emission in transverse and longitudinal dimensions.
- The losses can be measured in narrow slits, which are inaccessible for conventional online dosimeter systems. The radiation hard bare fibre is shielded with nylon and has a diameter of only 800 µm.
- Beam losses can be tuned continuously.
- Malfunction of active components (rf, magnets) and operator errors can be verified by electron losses.
- Fast switch off for machine protection system is possible.

REFERENCES

[1] V.Balandin, N.Golubeva and M.Körfer, Studies of the collimation system for the TTF FEL , Nucl. Instr. and Meth. A483, 340-344, 2002

[2] G. Anzivino et al, Quartz fibre calorimetry – Monte Carlo simulation, Nucl. Inst. Meth. A357 (1995) 380-385

[3] P. Gorodetzky et al, Quartz fibre calorimetry – Monte Carlo simulation, Nucl. Inst. Meth. A361 (1995) 161-179

[4] Yao-Cai Wang et al, Passive optical fibre sensor based on Cerenkov effect, SPIE Proceedings 1572/74 (1991) 32-37

[5] B.L.Pruett et al, Gamma-Ray to Cerenkov-Light Conversion Efficiency for Pure-Silica-Core Optical Fibers, SPIE Proceedings 506 (1984) 10-16

[6] T. Kawakubo et al, Fast-response beam loss monitor, Proceedings of ICANS-XV, 15th Meeting of the International Collaboration on Advanced Neutron Sources, November 6-9, 2000, Tsukuba, Japan

[7] R. Naka, et al., Radiation Distribution Sensing With Normal Optical Fiber, IEEE Trans Nucl. Sci., Vol. 48, No. 6, pp. 2348-2351, 2001

[8] R. Nishiura, N. Izumi, Radiation Sensing System Using an Optical Fiber, Mitsubishi Electronic ADVANCE, pp. 25-28, Sept. 2001

[9] E. Janata, Determination of location and intensitiy of radiation through detection of Cerenkov emission in optical fibers. Part 1. method and experimental, Nucl. Instr. Meth. Phys. Res. A 493, pp. 1-7, 2002

[10] H. Henschel, M. Körfer, J.Kuhnhenn, U.Weinand, F.Wulf, Fibre optic radiation sensor systems for particle accelerators, Nucl. Instr. and Meth. A526, 537-550, 2004

BEAM POSITION MONITOR AND KICKER FOR THE SPRING-8 TRANSVERSE BUNCH-BY-BUNCH FEEDBACK

T. Nakamura, JASRI/SPrig-8, Mikazuki-cho, Hyogo, Japan

Abstract

A high-resolution beam position monitor and a wideband kicker for the SPring-8 transverse bunch-by-bunch feedback system are developed. To avoid the increase of effective emittance by unwanted kicks by a feedback driven by noise, the monitor is designed to have high position resolution of the order of micro meters for single pass of 0.25nC bunch by adopting shorted stripline structure. Also a kicker for the feedback and the experience of those are described.

INTRODUCTION

A transverse bunch-by-bunch feedback is in operation to suppress the instabilities in the SPring-8 storage ring. The parameters of the ring are shown in a Table 1. The vertical emittance is small and the beam size at the feedback is 9μm(rms). The allowable amplitude (rms) of the motion driven by the feedback should be less than 10% of that and is ~1 μm.

Table 1. Parameters of the SPring-8 Storage Ring

Energy	E	8 GeV
Average Current	I	100 mA
RF Frequency	f_{RF}	508.58 MHz
Harmonics	h	2436
Bunch current at multi-bunch operation (2000 bunches)	I_b	0.24 nC
Revolution Period	T_0	4.8 μs
Emittance / Coupling	ε / κ	6.6 nm / 0.2 %
Beta function †	β_H / β_V	25 m / 6 m
Beam size †	σ_H / σ_V	400 μm/ 9 μm
Beam Pipe Radius (elliptic shape)	r_H / r_V	45 mm / 20 mm
Transverse Radiation Damping Time	τ_β	8.3 ms
Feedback Damping Time	τ_{FB}	~ 1ms

† : Values at BPMs and kickers for feedback

REQUIREMENT FOR BPM

Effective Emittance Degradation by Noise

The analysis of the effect of the random error/noise in measured beam position signal on the beam quality is performed. This shows that the random error drives a feedback and kicks a beam and increases the effective emittance with the relation as

$$\sigma_x = \sqrt{\varepsilon\beta} = \frac{\sqrt{T_0 \tau}}{\tau_{FB}} \sigma \qquad (1)$$

where, T_0 is a revolution period and τ and τ_{FB} are a total damping time with feedback and other effects and a damping time only with feedback, and σ is the rms position resolution of a BPM. This relation shows that the increase of the effective emittance is larger for larger ring and faster feedback damping. And the bunch charge of the ring at multi-bunch operation is smaller than the other rings and the vertical size of beam pipe also larger, the requirement on the resolution of BPM is more severe.

Position Resolution

The relation in Eq.1 is $\sigma_x = 0.07\ \sigma$ for the SPring-8 feedback of which damping time is 1ms. The vertical beam size (rms) is 9μm, hence, the requirement for the vertical position resolution of the BPM is 13 μm for one pass of 0.24 nC bunch if the allowable degradation of the beam size is less than 10%.

From the result of the button type BPMs for C.O.D. measurement[2], shows that the resolution of the button type BPM is one order smaller than requirement.

Carrier Frequency

For the ease of the handling, the RF acceleration frequency, 508.58MHz, is chosen as the carrier frequency. A 933MHz Bessel type low pass filter is inserted to the signal from the monitor to reject unnecessary higher frequency signals.

POSITION MONITOR

To fulfill the requirement, we developed a new monitor for the feedback. The design of the monitor is performed with MAFIA.

Shape

A shorted stripline type monitor is adopted to obtain higher voltage signal to fulfill the requirements described in previous section. The shape of the BPM is shown in Fig. 1, 2 and 3.

Its advantages over button type BPMs are

(1) compact : It is difficult to make large button type BPM because of its complicated structure.

(2) easy to fit to elliptical shape of the beam pipe of the ring.

Disadvantage over stripline type is that its impedance seen from ports is zero by shorted structure, while the impedance of stripline is matched to cables. This makes a unwanted signal to feedback.

Independent in Horizontal and Vertical

To make RF signal processing stage simple, a pair of stripline electrodes are placed horizontally and vertically

to detect the position of those direction independently. This is realized by the advantages of shorted stripline structure.

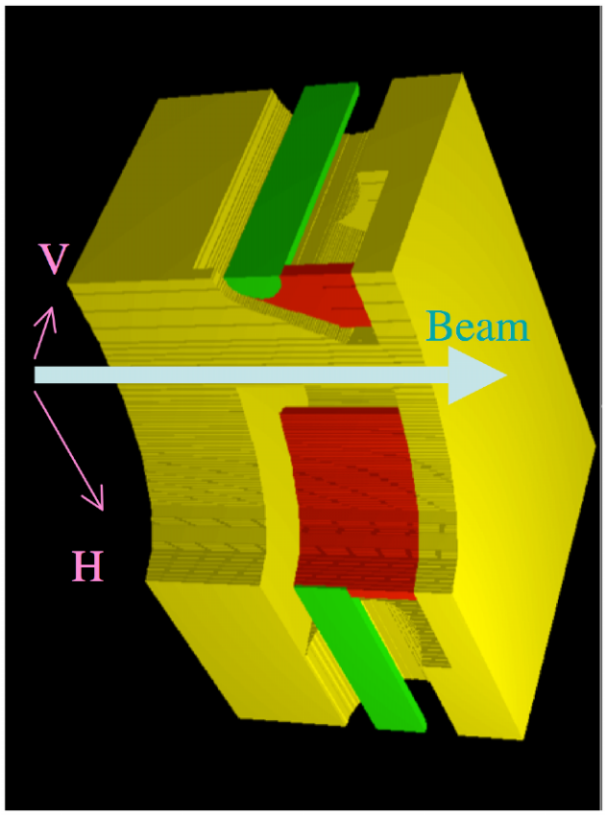

Figure 1: The structure of the position monitor. One quarter is shown and arrows show a beam axis and vertical and horizontal directions.

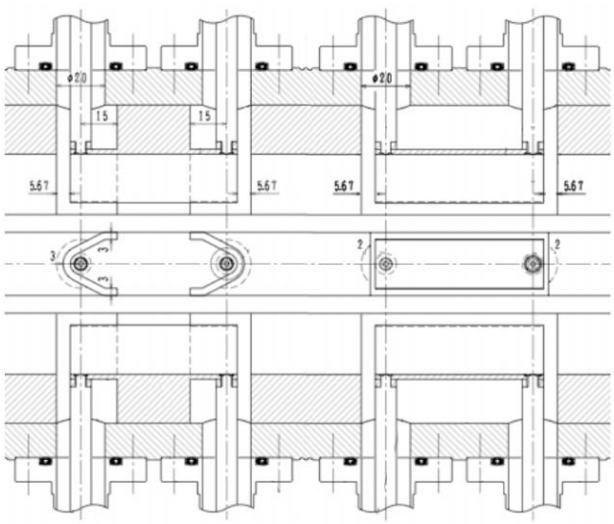

Figure 2: View of upper part of the chamber from the beam (top-bottom: horizontal, depth : vertical, left-right : beam axis). Left two sets of shorted striplines are the BPMs and right striplines are 7cm kickers. The beam pipe is a ellipse of diameter 90mm(H) × 40mm(V)

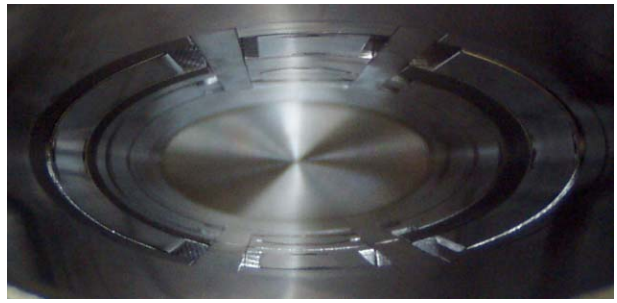

Figure 3: View from a beam port. 7cm striplines for kickers(near side) and shorted stripline type monitors (far side) are seen.

Signal Level

A gap of monitors scrapes a field of a beam and produces a signal of voltage s(t). At a stripline, a half of the scraped field propagates to an output port and the other half along with stripline. The field along with stripline is reflected by shorted wall and reverses the sign of its voltage, then propagates back to gap and then to the output port. A button type structure scrapes the field at upstream part and downstream part of a round shape gap. Both case, the produced signal is s(t)–s(t+d/c) where d is the scale of the twice of radius of button or the twice of the length of shorted stripline. The strength of the signal produced by the scraped field is proportional to the longitudinal width of gap(g) and transverse width of gap(w). At frequency of which wavelength is much longer than d/c, the voltage level of the signal s(t)–s(t+d/c) is proportional to d. Table 2 is the comparison of the dimensions and the signal level with the button type monitor. Table 2 shows the dimension of the monitors and measured signal level.

Table 2. Comparison with Button Type

	Shorted stripline	Button
Longitudinal gap width (g)	3 mm	0.5 mm
Transverse gap width or Diameter (w)	20 mm	10 mm
Length or Radius (d)	20 mm	5 mm
Horizontal offset from the beam axis	0 mm	14 mm
Horizontal monitor signal level† (normalized to button)	18	1
Vertical monitor signal level† (normalized to button)	8	1

† : after 933MHz Bessel type low pass filter

Resonances

Low Q resonance at ~1.5GHz can be seen in the monitors. However, the damping time of the horizontal monitor is 1ns and is faster than the bunch spacing, 2ns, and the build up of the signal is negligible. In vertical, the taper structure is attached at the end of the stripline as seen in Fig. 1 and 2 and this enhances the damping and

the damping time is two times faster than that of horizontal.

Sensitivity

The sensitivity of the monitor is obtained from the calculation with MAFIA and is

$$x/\mathrm{mm} = \frac{1}{0.08}\frac{V_1 - V_2}{V_1 + V_2} \quad \left(= \frac{1}{0.07}\frac{(V_1 + V_4) - (V_2 + V_3)}{V_1 + V_2 + V_3 + V_4}\right)$$

$$y/\mathrm{mm} = \frac{1}{0.07}\frac{V_3 - V_4}{V_3 + V_4} \quad \left(= \frac{1}{0.05}\frac{(V_1 + V_2) - (V_3 + V_4)}{V_1 + V_2 + V_3 + V_4}\right)$$

where $V_{1,2,3,4}$ are the voltage from a pair striplines or a set of button monitors. Those values are almost the same as the button type BPM for C.O.D. shown in bracket[2].

Reduction of Reflection

A signal produced at the stripline of the monitor is lead to the feedback system with cables using connectors. Mismatches at connectors reflect a signal at some amount and send back to the monitor. The impedance of the shorted stripline type monitor is intrinsically zero and the monitor reflects back signals with 100% reflectivity to the feedback system. At the feedback, signals from pair of the striplines are subtracted each other to produce the difference signals of them (Fig. 4) and the voltage of this signal is proportional to the beam position. The reflected signals that come to the feedback have some delay and some amplitude usually uncontrollable amount and the subtraction is not performed and produces comparable or larger signals that has no position information. This causes the offset in the position signal and its reduction is necessary. To reduce this, two 6dB attenuators are used. One is placed at the monitor and one is placed before the feedback as shown in Fig. 4.

Position Resolution

At the input to ADC of the feedback system, which is placed after RF amplifier, down converter and base band amplifier, the position resolution is 5μm and is fulfill the requirements, 9 μm. No observation of the degradation of the emittance caused by the feedback is reported by users of synchrotron light.

KICKER

New 7cm stripline type horizontal and vertical kickers are also installed in the same chamber as BPMs. The same cross sectional shape as the monitor is used as shown in Fig. 2. The feedback also uses three 45cm long stripline kickers that are also used to shake a beam for tune measurement and its transit time factor at 250MHz is 0.3. The feedback have to suppress an instability driven by higher order mode of acceleration cavities at ~200 MHz. If long stripline is used, the unnecessary gain at low frequency arises and may produces increase of the effective emittance. To avoid this, the shorter stripline kicker is also installed.

The length of the kicker is 7cm and the transit time factor has flat frequency response to $f_{RF}/2$.

COUPLING CANCELER

To save the length, the monitors and the 7cm kicker are placed side-by-side in a single vacuum vessel (Fig. 2). This produces the coupling between the vertical monitors and vertical kicker through the beam pipe. This coupling is less than -90dB between the kicker and the monitor at far side. The monitor signal is down converted to be base band signal at front-end RF circuits of the feedback, and this eliminates the coupling in principle. However the gain of the feedback is so high and the even stray coupling in the feedback system drives positive feedback loop.

To reduce this coupling to suppress this positive feedback, a circuit to suppress the coupling is attached as shown in Fig. 4. The coupling between the kicker and the monitor at near side is higher than the monitor at far side and the subtraction of signal of the near side monitor with proper attenuation from the signal from the far side monitor to cancel the signal by coupling. The feedback gain can be rise +20dB with the coupling canceller.

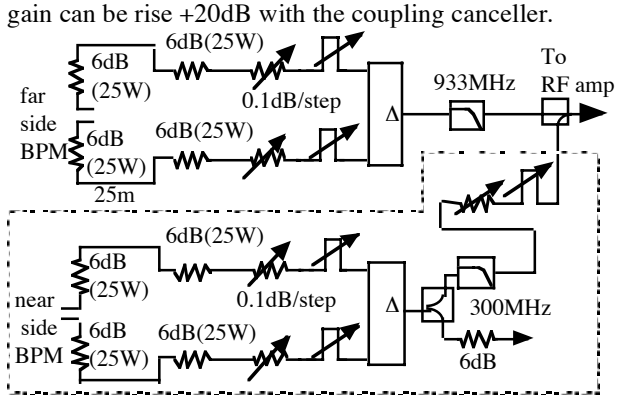

Figure 4: Front-end circuits for BPM with coupling canceller(inside of dotted line). The output of the circuits is send to an RF amplifier.

SUMMARY

The beam position monitor of micro meter resolution for a single passage of 0.24 nC bunch is developed to suppress the increase of the effective emittance driven by noise to the feedback. Also stripline kickers and the coupling canceller are developed. No increase of the emittance of the beam is reported by users of synchrotron light.

ACKNOWLEGEMENT

The auther thanks to Dr. Sasaki for helpful discussion on BPMs and to Dr. Shoji and Dr. Ohkuma for their help at making and installation of the monitors and kickers.

REFERENCES

[1] T. Nakamura, S. Date, K. Kobayashi, T. Ohshima, "Transverse Bunch-by-bunch Feedback System for the SPring-8 Storage Ring", EPAC'04, Lucerne, June 2005, p. 2649.

[2] by S. Sasaki (SPring-8)

LOW ENERGY HIGH BRIALLANCE BEAM CHARACTERIZATION

J. Bähr, DESY, Zeuthen, Germany

Abstract

Low energy high brilliance beam characterization plays an important role for electron sources and injectors of Free Electron Lasers (FELs) and electron linear accelerators as for example the future ILC project. The topic is discussed basing on solutions of the PITZ facility (Photo Injector Test facility Zeuthen) which are compared with methods applied at other facilities. The properties of an electron beam produced at a laser driven rf-gun is mainly influenced by characteristics of the laser beam and the electron gun itself. Therefore aspects of diagnostics will be discussed for the laser, laser beam line and gun as well. The main properties of the electron beam are transverse and longitudinal phase space and emitted charge. Measurement of transverse beam size and position, transverse emittance, charge and longitudinal phase space will be discussed in detail. At PITZ the measurement of the longitudinal phase space is based on a correlated measurement of the momentum spectrum and the temporal characteristics of the electron bunch.

INTRODUCTION

Low energy high brilliance beam characterization will be discussed at the example of PITZ (Photo Injector Test facility Zeuthen) [1] at DESY. PITZ is a dedicated facility for the optimization of electron sources for FELs. The energy range of PITZ1 (until fall 2004) was 4.5 MeV, the energy range of PITZ2 [2] just under commissioning will increase to 30 MeV in 2005-2006. The nominal bunch charge is 1 nC. The discussion of the characterization will cover mainly the transversal phase space, the longitudinal phase space and charge as well. Further diagnostics topics as the characterization of processes at the cathode and in the electron gun, the relative phase between laser and rf and properties of the photocathode laser beam will be discussed shortly as well. Further examples of diagnostics of other facilities will be discussed in the momentum range up to 130 MeV/c. The production and characterization of polarized beams is not matter of this paper.

PITZ

The sketch of the beam line of PITZ1 is shown in fig.1. The facility consisted of three sections: the cathode section, the gun section and the diagnostics section. PITZ1 was dismounted in the beginning of 2005. The upgrade, PITZ2, is under commissioning now and will be completed in several steps until end of 2006. Fig. 2 shows schematic of the beam line of PITZ2.

The electron source of PITZ is a normal conducting 1.5 cell laser-driven rf-cavity. The rf-frequency is 1.3 GHz. The active cover of the photo cathode is Cesium Telluride. Main topics of the upgrade for PITZ2, are the use of a booster cavity to demonstrate the emittance conservation principle [3] and the increase of the field gradient in the gun to improve the electron emittance from the beginning. The diagnostics beam line will be essentially extended.

TRANSVERSE PHASE SPACE

Beam Size and Beam Position

The characterization of beam position and beam size is a standard task at every particle accelerator. There are invasive and non-invasive devices in use:

- Flourescence screens (e.g.YAG)
- Optical Transition Radiation (OTR) screens
- Beam position monitors (BPM)
- Wire scanners

The YAG (Yttrium-Aluminium garnet) transforms part of the beam energy in visible light. This light is usually imaged on the sensor of a TV-camera. Two kinds of YAG

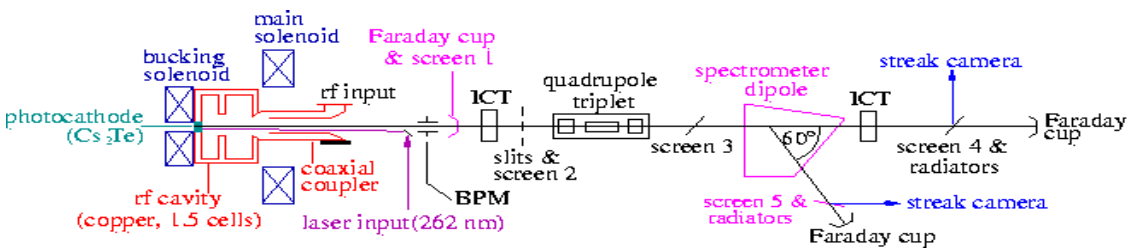

Figure 1: Schematic of PITZ 1.

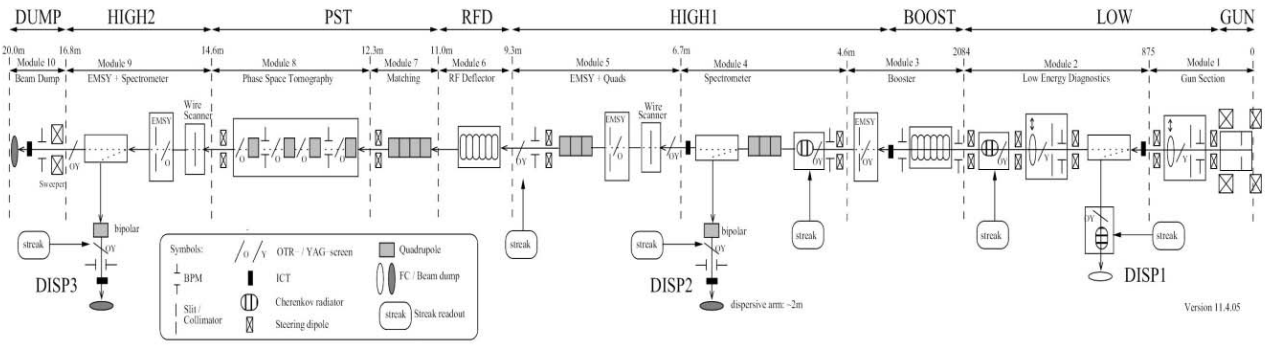

Figure2: Schematic of PITZ2

are commonly in use, polycrystalline and Cerium-doped mono-crystals.

Several kinds of TV-cameras and optical systems are applied at the various facilities. CCD type cameras are mostly chosen. Analogous and digital read-out modes are distinguished. At PITZ [4] an analogous camera with non-interlaced read-out, external trigger and remotely controlled gain is applied. The optical scheme of the TV system is optimized such, that the camera does not need to stay near to the beam line. One of the major problems is the low radiation hardness of common CCD-cameras. At PITZ the cameras are shielded by lead bricks. The TV systems contain an illumination for the screens, and a calibration unit. Using a movable mirror a calibration grid is imaged onto the camera sensor. Magnification and resolution can be measured and calibrated.

OTR screens are based on the effect of Optical Transition Radiation (OTR). The charged particle beam causes a light cone emitted from a metallic screen. Examples for such screens are aluminium coated capton or aluminium coated Silicon. The half angle of the emission cone is the inverse of the relativistic -factor. Therefore there is a lower threshold for the use of OTR. OTR is commonly used for electron energy > 10 MeV.

Beam position monitors (BPM) are based on an antenna principle. Their use is widely discussed on DIPAC conferences (for example DIPAC 2001, [5] and others). Therefore it will not be discussed in this paper.

Wire scanners [6] are used for the measurement of the beam diameter, halo and position. A thin wire (O(50 microns) is moving fast through the particle beam. A system of scintillation detectors is detecting part of the created gamma quanta. By measuring the signals of several scintillation detectors and measuring the position of the wire accurately at the same time the beam profile and position can be reconstructed. A wire scanner for one coordinate was used in PITZ1. Two wire scanners with a two-coordinate measuring system will be used at PITZ2. Several wire scanner stations are in use at the VUV-FEL at DESY [7].

Measurement of Transverse Emittance

The measurement of the transverse emittance will be discussed using three examples:

- EMSY [8] at PITZ
- The emittance-meter at SPARC [9]
- A 4-screen method at the VUV-FEL [10]

At PITZ1 and PITZ2 the transverse emittance is measured using the Emittance Measurement System (EMSY). The apparatus contains several tungsten masks (single slit, multi-slit, pepper pot) which can be moved in four degrees of freedom (two transverse, two rotational). The electron beam hits the masks and most of the beam is scattered. But also undisturbed beam-lets are produced. The beam-lets are analyzed using a YAG screen in a distance of about 1 m, see fig.3. The transversal beam

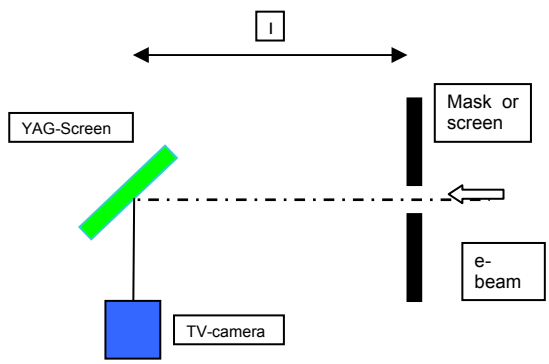

Figure 3: Schematic of emittance measurement

distribution is also measured in the plane of the masks. Fig. 4 shows an example of results of autumn 2004 [11].

At SPARC an emittance meter is under commissioning. The goal of this device is the coordinate dependent measurement of the transverse emittance in a range of about 1.5m along the beam direction, see fig.5. It is foreseen to do a first commissioning of this device with beam measurement at PITZ.

The transverse emittance at the VUV-FEL was measured recently at 130 MeV based on a 4-screen method. The

four quadrupoles are situated behind the first bunch compressor. The readout is realized using OTR-screens.

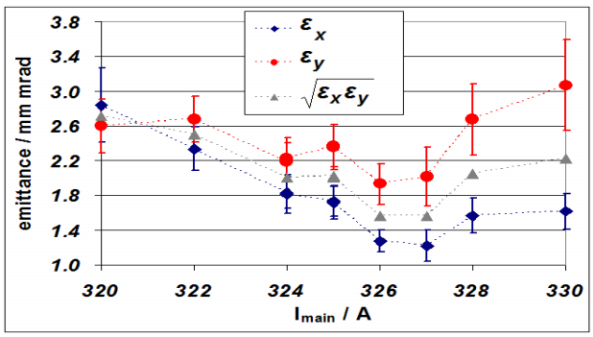

Figure 4: Emittance results vs. solenoid current

Measurement of the Complete Longitudinal Phase Space

A measurement of the complete longitudinal phase space was performed at PITZ. This includes a measurement of the momentum spectrum and the bunch length as well as their correlation. Fig. 6 shows the principle of the measurement [14]. The measurement of the bunch length at PITZ is performed using a streak camera [15]. The electron beam hits a Cherenkov radiator. The best light output compared to OTR and a quartz plate was reached using Silica aerogel (refractive index 1.03 and 1.05) as Cherenkov radiator. The light is transmitted by a 27 m long optical transmission line [16]. It is mainly constructed of telescopes consisting of achromatic lenses. The bunch length measurement is possible for the uncorrelated case in the straight section and for the correlated measurement in the magnet spectrometer. For the correlated measurement the light distribution representing the momentum spectrum has to be imaged exactly onto the entrance slit of the streak camera. The

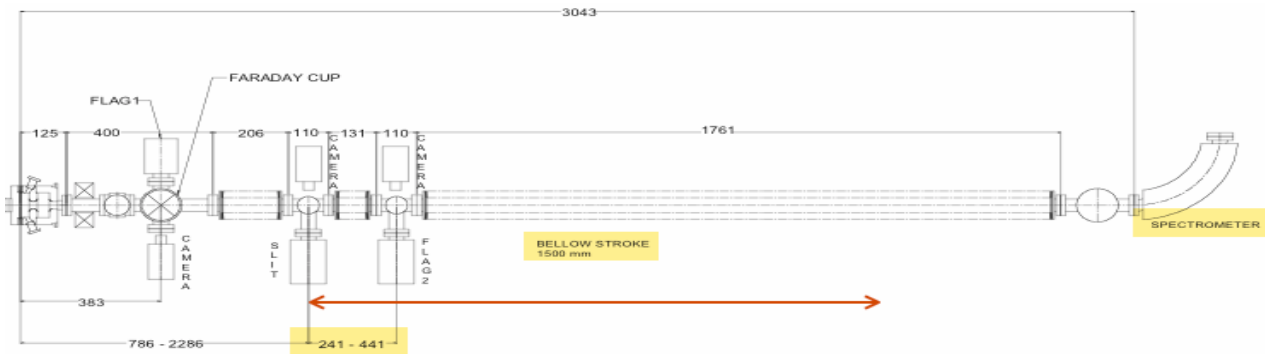

Figure 5: Emittance meter from the SPARC collaboration

LONGITUDINAL PHASE SPACE

The longitudinal phase space is spanned by the momentum, the bunch length. Besides the properties also the correlation between these properties is important

The measurement of the beam momentum is usually realized in magnet spectrometers using dipole magnets. A special case of a 180-degree spectrometer will be used at PITZ2 and at the ELBE facility [12] in the near future. They have several advantages what can be easily derived by analyzing the transport matrix of the dipole [13]:

- Influence of divergence at entrance of the dipole is zero
- Dispersion is maximized resulting in optimum resolution
- The resolution is independent of transverse emittance
- Space economy
- No turning of image needed for streak camera readout.

dimensions of the image have to fit to both slit dimension, the image has to be focussed into the slit plane and to be parallel to the slit.

One example of the results of the measurements for 1nC bunch charge and a temporal flat top laser pulse is shown in table 1[17]. For all 4 properties the results of the measurements agree with the simulation within the error range.

Table 1: Results of long. phase space measurement

	measured	Astra
FWHM / ps	SS: 25.2 +/- 1.3; DA: 28.5 +/- 3.3	25
long. emittance / π keV mm	32.7 +/-6.8	26,6
momentum / MeV	5.19 +/- 0.06	5,19
momentum spread / keV	46.0 +/- 5.1	42,2

A deflecting cavity for the measurement of single bunches is used at the VUV-FEL at DESY in Hamburg. The device of 3.6 m length is part of a DESY-SLAC collaboration and a contribution of SLAC [18]. The goal

is to reach a time resolution of about 10 fs. The principle sketch is shown in fig.7. A pre-selected bunch gets a kick by the rf-field of 25 MV and 18 MW. The transverse kick is 40 microns in the plane of a screen. The created light distribution is imaged onto a camera sensor. Similar devices are foreseen for example at SPARC and PITZ2.

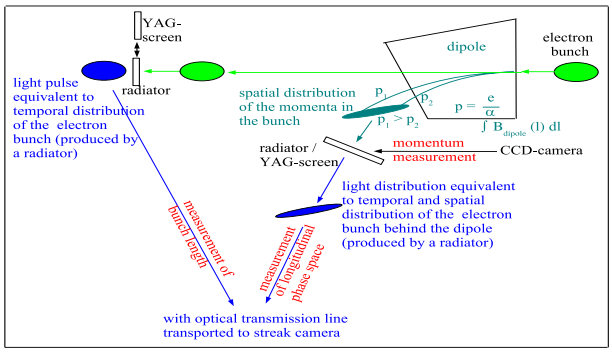

Figure 6: Schematic of measurement of longitudinal phase space

Electro-optical sampling

The refractive index of electro-optical crystals (for example ZnTe) can be changed by the electric field of the electron bunch . Such a crystal can be mounted inside the

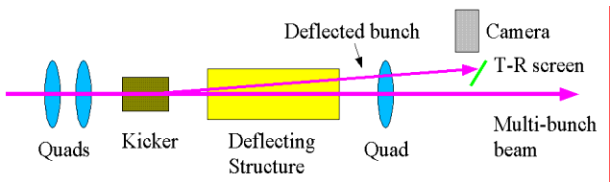

Figure 7: Deflecting rf-cavity at VUV-FEL

beam pipe near to the electron beam. The read-out is realized by a laser beam (for example Ti:Sa) with short pulse length (< 1ps). Different schemes of optical analysis are published [19]. The reached resolution is about 100 fs.

CHARGE AND CURRENT

Charge and current of single bunches and bunch trains can be measured by Faraday cups, integrating current transformers (ICT) and wall gap monitors. These techniques are well known and will be not discussed widely in this paper. Faraday cups are sensitive down to charges of about 1 pC whereas the sensitivity threshold of commercially available ICTs measured at PITZ is about 100 pC.

PROCESSES AT CATHODE AND RF-GUN

The gun cavity at PITZ is a 1.5 cell normal conducting copper cavity running at 1.3 GHz. A proper tuning of the eigen-frequency of the cavity has to be guaranteed for stable running with stable gradient. The fine tuning of the gun is realized by a powerful cooling system which controls the gun temperature on the level of 0.1 degree water temperature.

Dark current is a phenomenon which can limit the performance of an injector or accelerator essentially. One main source is field emission at the cathode, at the gun corpus or at contures of the cathode fixing mechanics. Investigations of the dark current are described in [20].

The photo cathodes at PITZ are produced at INFN Milano [21]. The sensitive cathode substance is Cesium Telluride. The quantum efficiency QE and its temporal behavior is an essential quality factor of an electron source. Cesium Telluride is very sensitive to vacuum, therefore a high vacuum of about $>10^{-10}$ mbar has to be maintained in the gun cavity. The measurement of the quantum efficiency is done by two methods at PITZ. The first method is in-situ. The extracted charge created by a laser pulse of known pulse energy is measured. The second method is based on a dedicated setup consisting of a high pressure mercury lamp and a pico-amperemeter. The light intensity is measured absolutely. A typical QE of freshly produced cathodes is about 10 percent. During operation it decreases down to about 1 percent.

PHASE

The phase between rf-system and the photocathode laser is an essential property of every laser driven rf-gun. The behavior of the gun shows several characteristic points varying the phase over the active range of about 100 degrees, for example the phase of maximum mean energy gain and the phase of maximum charge.

At PITZ three methods of phase measurements are applied [22]. The first is the usual phase scan. The phase is varied over the full range and the charge is measured. Both other methods are in use to measure the phase of the maximum mean energy gain. This can be done by measuring the momentum of the particles in the bunch using the spectrometer. Alternatively the phase of highest energy is estimated by measuring the electron beam diameter on a YAG screen as function of the phase. It has been shown [23] that the phase of the maximum mean energy gain is very close to a maximum or minimum of the beam diameter depending on the setting of the focussing solenoid.

LASER

The photo cathode laser is one of the deciding sub-systems of a laser-driven rf-gun determining to a large extent the quality of the electron beam. The photo cathode laser of PITZ is developed by the
Max-Born-Institute Berlin [24]. Flat-top laser pulse profiles in time and space are necessary to reach the needed low transverse beam emittance. Furthermore, the stability of several parameters like laser pulse energy and phase has to be guaranteed. Therefore, dedicated diagnostics tools have to be provided. The transverse beam profile (see fig.8) is monitored by two virtual cathodes, working in different

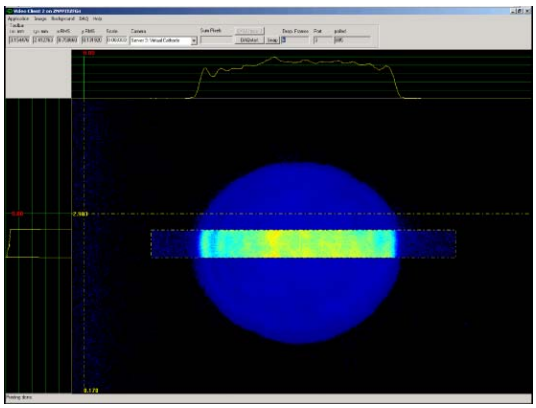

Figure 8: Transverse laser beam profile

ranges of laser pulse train energy. These virtual cathodes are realized by CCD-cameras which are UV sensitive and in a position corresponding to the photo cathode in the gun. The laser pulse energy monitoring by photomultiplier is under commissioning at PITZ. The monitoring of direction, position and transverse profile of the laser beam for PITZ will be realized by a TV system. It is in preparation on the laser table and will be realized by two cameras for the near and far field. The longitudinal laser pulse profile is monitored using a streak camera.

CONCLUSION

An overview about methods of diagnostics for low energy high brilliance electron beams is presented based on the diagnostics scheme of the PITZ facility and facilities in further accelerator centers.

ACKNOWLEDGEMENT

I want to thank my colleagues of the PITZ collaboration for their support, especially J. Roensch, S. Khodyachykh, V. Miltchev and F. Stephan for fruitful discussions.

REFERENCES

[1] F. Stephan et al., Proc. FEL2000, Durham
[2] A. Oppelt et al., Linac 2004 Lübeck
[3] M. Ferrario et al., LNF-00-004(P)
[4] J. Bähr et al., DIPAC 2001, Grenoble
[5] L. Farvacque et al., DIPAC2001,Grenoble
[6] A.B.El-Sisi, DIPAC2003, Mainz, p.131
[7] M. Sachwitz et al., DIPAC2005, Lyon
[8] K. Abrahamyan et al., DIPAC 2003 Mainz, p.225
[9] D.Alesini et al., "Virtual beam dynamics experiments at SPARC, ICFA workshop 2005, Zeuthen
[10] K. Honkavaara et al., Measurements of Transverse Emittance at TTF VUV-FEL, ICFA workshop 2005, Zeuthen
[11] L. Staykov et al., DIPAC 2005, Lyon
[12] Th. Kamps, ICFA workshop 2005, Zeuthen
[13] S. Khodyachykh, Internal paper, PITZ 2005
[14] J. Rönsch, Diploma Thesis, Univ. of Hamburg 2005
[15] D. Lipka, PhD Thesis, Berlin 2004
[16] J. Bähr et al., DIPAC 2003, Mainz, p.98
[17] J. Rönsch, "Measurement of the Longitudinal Phase Space at the Photo Injector Test Facility at DESY in Zeuthen (PITZ) DIPAC 2005, Lyon
[18] C.O'Connell et al., "Bunch Longitudianl Profile Diagnostics using a Transverse Deflection cavity (LOLA) at the TTF", ICFA workshop 2005, Zeuthen
[19] Berden et al., DIPAC 2003, Mainz , p.25
[20] J.H. Han et al., PAC 2005, Knoxville
[21] D. Sertore et al., Proc.EPAC 2004, p.408
[22] M. Krasilnikov, PAC2005, Knoxville
[23] M. Krasilnikov, PAC2005, Knoxville
[24] I. Will et al., Nucl. Instr. Meth. A472(2001), p.79

HIGH SENSITIVITY TUNE MEASUREMENT BY DIRECT DIODE DETECTION

M. Gasior, R. Jones, CERN, Geneva, Switzerland

Abstract

The fractional part of the betatron tune for a circular accelerator can be measured by observing beam oscillations on a position pick-up. In frequency domain the betatron frequency is seen as sidebands on either side of the revolution harmonics. Usually beam signal pulses from the pick-up are very short with respect to the revolution period, resulting in a broadband spectrum. Classical tune measurement systems filter out just one of the betatron sidebands. As a consequence, most of the betatron energy is lost and only a very small fraction remains for further processing. This paper describes a new method, referred to as Direct Diode Detection (3D). It is based on the idea of time stretching beam pulses from the pick-up in order to increase the betatron frequency content in the baseband. The 3D method was recently tested in the CERN SPS and PS, BNL RHIC and FNAL Tevatron machines. Results from all these machines [1, 2, 3, 4] show that this method can increase the betatron signal level by orders of magnitude as compared to classical systems, making it possible to observe tunes with no explicit excitation. Frequency resolution in the order of 10^{-5} and amplitude sensitivity in the order of 10 nm has been achieved with this very simple hardware.

3D PRINCIPLE AND THE HARDWARE

The crucial part of a 3D-based tune measurement system is the peak detector. Two such detectors connected to opposing electrodes of a beam position pick-up (PU) (see Fig. 1) yield the amplitude modulation envelope of the beam signals. Such signals, depicted in Fig. 2, are superimposed on a DC voltage related to the bunch amplitude (revolution frequency content). The signal difference, shown in Fig. 3 for single bunch in the machine, contains almost the whole bunch modulation amplitude, with a DC component related to the beam offset from the centre of the pick-up. Since the DC content can be easily suppressed by series capacitors, most of the corresponding revolution frequency (f_r) background can be removed by the peak detectors before the first amplifying stage. In Fig. 4 the f_r attenuation characteristic is shown assuming single bunch in the machine, which is the most difficult case to deal with. For a detector time constant $\tau = R_f C_f$, which is larger than the machine revolution period $T=1/f_r$, the suppression of the revolution line goes as $4\tau/\mathrm{T}$ [1]. This makes it possible to obtain f_r attenuation in the order of 50 dB for $\tau \approx 100$, which is easily achievable in practice.

The 3D circuit in Fig. 1 can be also understood as two sample-and-hold blocks, sampling bunch signals close to their maxima at the bunch repetition rate, downmixing the wideband bunch spectrum into the baseband.

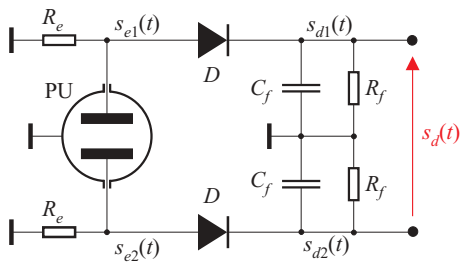

Figure 1: Direct Diode Detection principle.

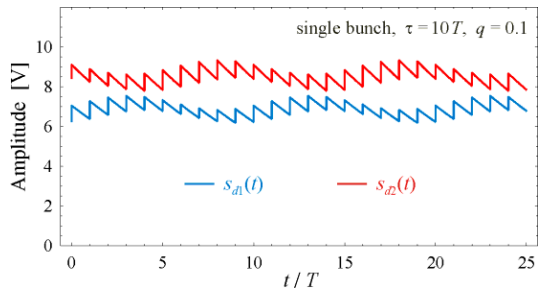

Figure 2: An example of peak detector voltages.

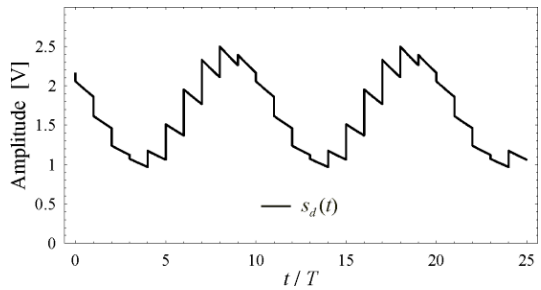

Figure 3: Difference of the signals in Fig. 2.

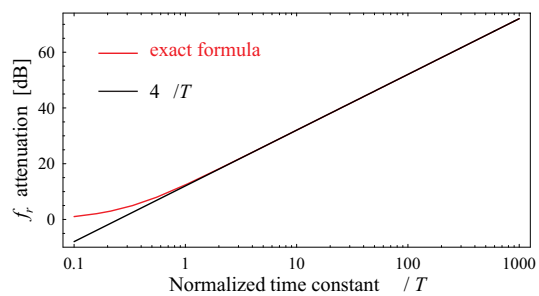

Figure 4: 3D circuitry revolution frequency attenuation.

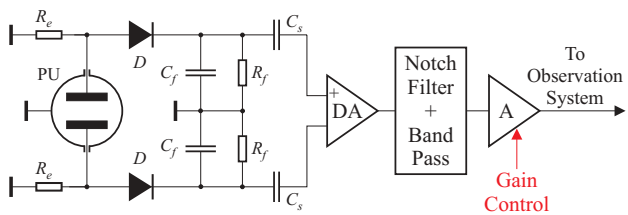

Figure 5: Block diagram of a 3D-BBQ system.

A block diagram of a 3D Base-Band Q (BBQ) measurement system is depicted in Fig. 5. The peak detector voltages with the DC content removed by the series capacitors are subtracted by the differential amplifier (DA), further increasing the suppression of f_r for beams close to the PU centre and improving the interference immunity. A notch filter attenuates f_r by another large factor, in the order of 100 dB [1]. The high cut-off frequency of the band pass filter is $0.5 f_r$, as for all possible tune values one betatron sideband is always present in the band $(0, f_r/2)$. The typical low cut-off is $0.1 f_r$, which means that the observation system only has to process frequencies between 0.1 and $0.5 f_r$. For large machines, therefore, the 3D-BBQ output signal can be digitised with a 24-bit audio ADC at the revolution frequency, requiring relatively little processing power to yield a signal spectrum through an FFT, or to build a tune tracker based on a digital phase-locked loop (PLL) [2].

Notice that a 3D-BBQ system is 'low frequency' only after the detectors, due to the 'time stretching' of the short beam pulses. Before the detectors the processed bandwidth can easily be as high as a few hundred MHz. In the detection process the spectral content from this wide bandwidth is converted to the baseband, resulting in a very high sensitivity.

3D-BBQ prototypes according to the block diagram of Fig. 5 have been installed on four machines, namely SPS ($f_r \approx 43$ kHz), PS ($f_r \approx 477$ kHz), RHIC ($f_r \approx 78$ kHz) and Tevatron ($f_r \approx 48$ kHz) (chronological order). All prototypes were based on very similar hardware, with only the notch and band-pass filters adjusted for the machine f_r.

A detailed comparison of the 3D and classical tune measurement methods are given in [1], together with a quantitative estimate of the signal to noise improvement given by the 3D method operated on a machine with a single bunch. This factor is in the order of 30 dB for the PS, 40 dB for RHIC and Tevatron, 50 dB for the SPS, and 60 dB for the LHC.

RESULTS

All installed prototypes were sensitive enough to observe betatron oscillations with no explicit beam excitation. Such oscillations, with amplitudes in the μm range, were seen to be almost always present in the beam.

Examples of such measurements made with the SPS BBQ prototype and no intentional beam excitation are shown in Fig. 6 and 7. Figure 6 shows the horizontal tune path for the lowest intensity SPS beam of $\approx 5 \cdot 10^9$ protons in a single bunch at 26 GeV, during a programmed tune change of $\approx 5 \cdot 10^{-3}$. Figure 7 shows the SPS horizontal tune variations induced by the jaws of an LHC collimator prototype as it was cycled between a fully opened position and a gap of 1.96 mm. This measurement was performed with a single bunch at 270 GeV and formed part of a series used to evaluate impedance-induced tune changes introduced by LHC collimators [5]. Tune variations as small as a few Hz could be resolved in this

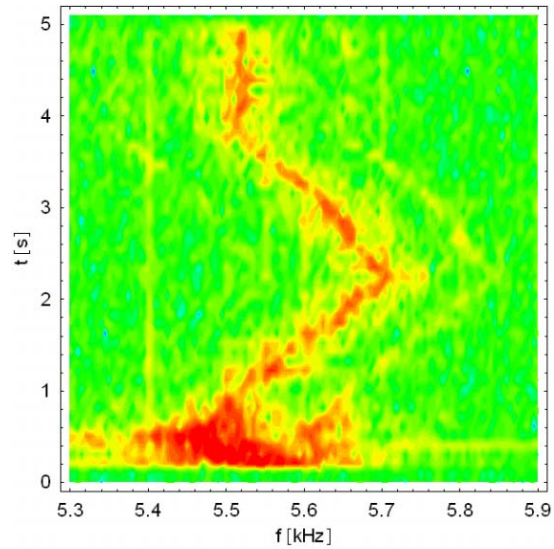

Figure 6: SPS, single bunch LHC pilot beam ($\approx 5 \cdot 10^9$ p^+).

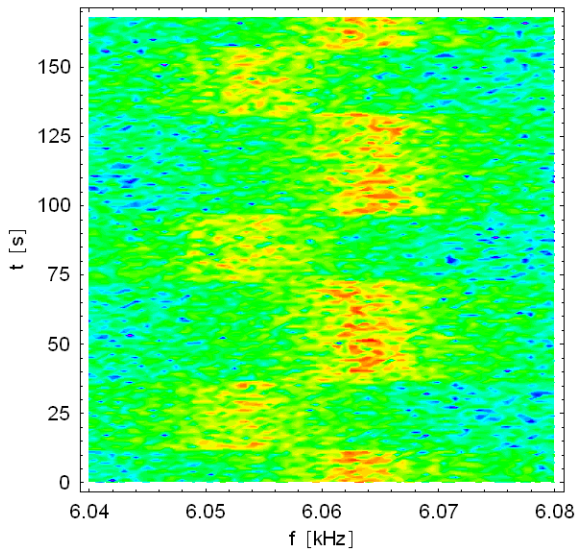

Figure 7: SPS, single bunch LHC beam ($\approx 10^{11}$ p^+).

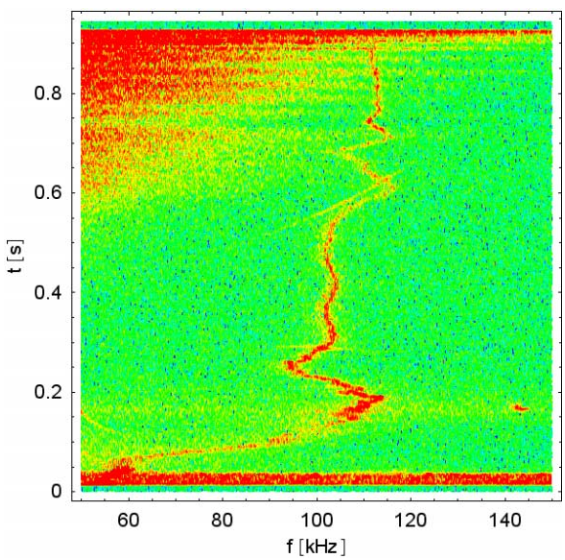

Figure 8: PS, AD beam (4 bunches, $\approx 4 \cdot 10^{12}$ p^+/b).

way, with the tune resolution in the order of 10^{-5}. These SPS measurements were acquired using a low cost 24-bit PC sound card followed by off-line spectral analysis.

Figure 8 shows the horizontal tune evolution measured by the PS BBQ prototype with no explicit excitation for a beam destined for the Antiproton Decelerator (AD), and accelerated from 1.4 to 26 GeV. The noise-like components appearing from the middle of the record onwards result from the RF beam gymnastics performed for this type of PS beam.

Figure 9 shows a vertical plane time record from the RHIC 3D-BBQ prototype, with the corresponding frequency spectra shown in Figure 10. The largest amplitude signals correspond to beam oscillations caused by high voltage sweeps, related to the operation of an Ionization Profile Monitor (IPM). Each excitation consists of a burst of a hundred pulses, applied every 100th revolution. If either of the tunes happen to be a multiple of $f_r/100$, then these kicks resonantly excite the beam, as seen in the spectra for frequencies around 17.1 kHz ($0.22 f_r$, close to the horizontal tune) and 17.9 kHz ($0.23 f_r$, vicinity of the vertical tune).

Mains harmonics are clearly visible around the betatron tune paths throughout the RHIC acceleration cycle. These lines increase considerably once the main ramping power supplies are turned on around 26 s from the beginning of the record. The corresponding increase in the time domain signal can be seen in Figure 9. The presence of mains harmonics in the beam spectrum is reported in detail in [3] and is thought to be caused by magnetic field ripple in the main RHIC dipoles. Similar phenomenon was observed with the 3D-BBQs on the SPS, PS and Tevatron.

A comparison at RHIC between spectra from calibrated, million turn BPM data and that of the 3D-BBQ data has quantified the noise floor of the RHIC BBQ prototype at less than 10 nm. This is an order of magnitude better than most existing tune measurement systems.

CONCLUSIONS

This paper has introduced the principle of tune measurement using Direct Diode Detection. It has been shown to be highly sensitive while using simple, cheap and robust hardware. Prototypes recently installed on four machines, namely the CERN SPS and PS, BNL RHIC and FNAL Tevatron, have given very good results and are in the process of being converted into fully operational systems. Due to the many advantages of this method, 3D baseband tune measurement systems will be gradually introduced on all circular machines at CERN. This includes the LHC, where it is hoped to use the 3D-BBQ as part of a PLL tune tracking system, for the measurement of tune, chromaticity and coupling [5], with the ultimate aim of providing reliable tune feedback.

The 3D method is still under development and its full potential has probably not yet been fully realised. Extensive studies will therefore continue on this technique.

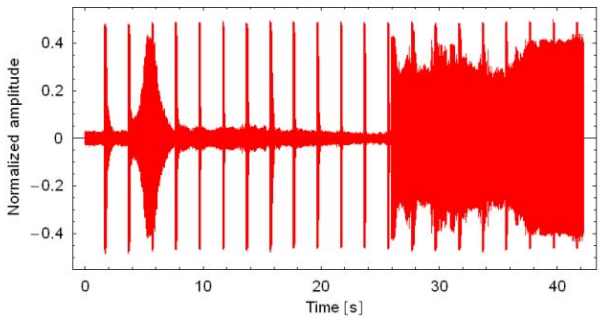

Figure 9: RHIC, a 3D-BBQ signal sound card record.

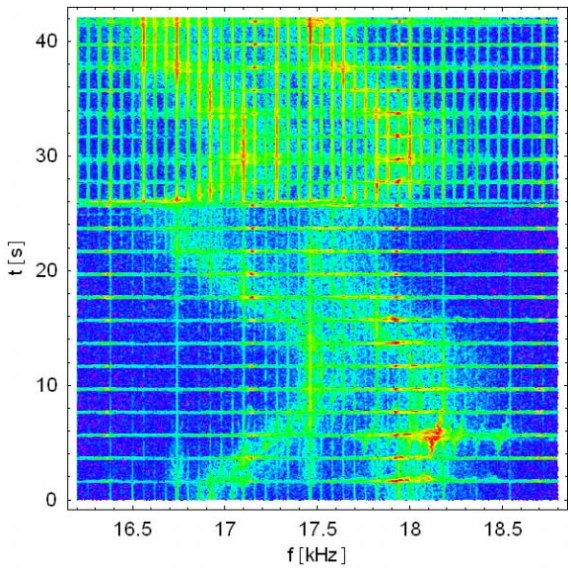

Figure 10: RHIC, spectra of the signal in Fig. 9.

ACKNOWLEDGMENTS

We would like to thank P. Cameron and J. Belleman for their help throughout the whole development as well as C.-Y. Tan for testing the BBQ prototype on the Tevatron.

REFERENCES

[1] M. Gasior, R. Jones, "The Principle and First Results of Betatron Tune Measurement by Direct Diode Detection", CERN-LHC-Project-Report-8XX.

[2] P. Cameron et al., "Advances Towards the Measurement and Control of LHC Tune, Chromaticity, and Coupling", these proceedings.

[3] P. Cameron, M. Gasior, R. Jones, C.-Y. Tan, "The Effects and Possible Origins of Mains Ripple in the Vicinity of the Betatron Spectrum", this proceedings.

[4] C.-Y. Tan, "Novel Tune Diagnostics for the Tevatron", PAC 2005.

[5] H. Burkhardt et al., "Measurements of the LHC Collimator Impedance with Beam in the SPS", PAC 2005.

[6] P. Cameron, M. Gasior, R. Jones, Y. Luo , "Towards a Robust Phase Locked Loop Tune Feedback System - The Continuous Measurement of Global Betatron Coupling Using a Phase Locked Loop Tune Measurement System", these proceedings.

RADIATION TESTS ON SOLID STATE CAMERAS FOR INSTRUMENTATION

S. Hutchins, M. Facchini, E. Tsoulou, CERN, Geneva, Switzerland

Abstract

Technological advances in solid state camera design have provided a wider choice of equipment for beam diagnostics, but following simulations of the expected radiation environment in the LHC knowledge of their radiation tolerance was required. Several cameras have been progressively exposed to a 60MeV proton beam and their performance degradation monitored. Following these results, further simulations have been carried out on the level of shielding needed to ensure satisfactory operation in the LHC.

OBJECTIVES

Previous experience with CCD based cameras has shown that the performance degrades with as little as 10Gy, which limits the areas in which they can be used and imposes the use of local radiation shielding[1]. It will be very difficult to provide shielding in the LHC, given the high energy of the secondary particles, which are generated by the interaction of the beam with residual gas in the vacuum chamber.

Resolution and Contrast

In order to get quantifiable data on the degradation of the sensors a simplified testing method was used. Rather than using resolution test targets to establish the Contrast Transfer Functions [2] at each radiation test point, a checker-board pattern was used as the target.

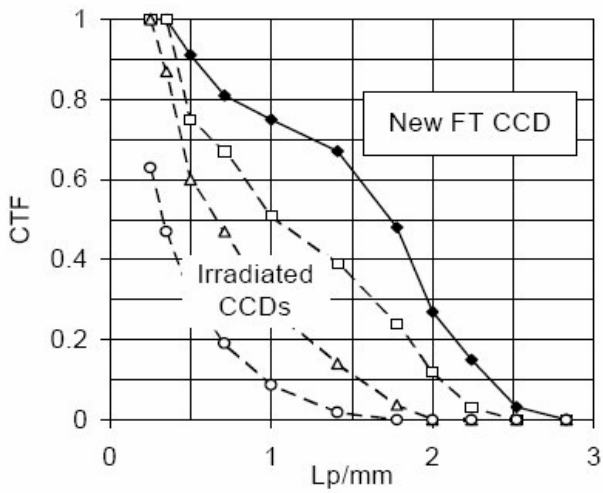

Figure 1: Contrast Transfer Function

It is assumed that the main effect of radiation damage is the loss of contrast, so that by ensuring that each square would correspond to many pixels on the sensor, problems of single pixel damage, optical resolution and speckle would be avoided. Sensors having different pixel sizes can be tested with the same equipment, each pixel in the stored bitmap image would be analyzed and a histogram produced for each radiation level, to show the loss of contrast due to radiation effects. The cameras were also to be tested under operational conditions so that Single Event Upsets (SEU's) could be noted and the risk of damage due to the devices being powered was of interest.

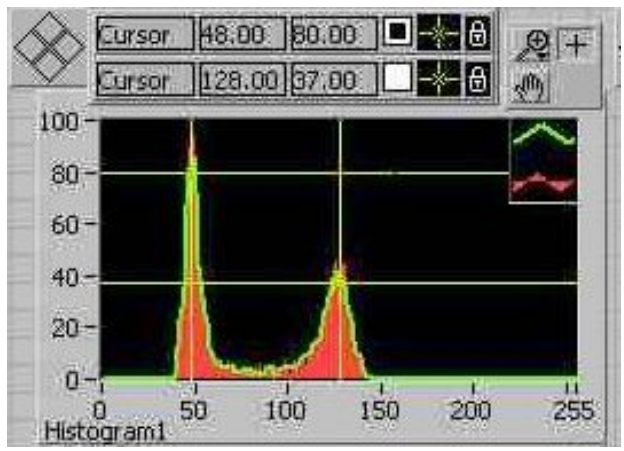

Figure 2: Histogram of pixel brightness for an area of the checkerboard pattern

Radiation Damage

Any semiconductor device operating in a radiation field can undergo degradation due to radiation damage effects. Energetic particles incident on the semiconductor bulk lose their energy to ionising and non-ionising processes as they travel through a given material. The ionising processes involve electron-hole pair production and subsequent energy deposition (dose) effects. The non-ionising processes result mainly in displacement damage effects, i.e. displaced atoms in the detector bulk and hence defects in the semiconductor lattice like vacancies and interstitials.

The solid state arrays use a structure of metal-dielectric-semiconductor that makes them sensitive to ionising radiation due to energy deposition in the gate dielectric and displacement damage in the semiconductor substrate.

Ionization effects refer to the transient effects due to energy deposition in the gate dielectric and silicon bulk. The gate dielectric in the CCD imagers is usually a silicon oxide. 3.6 eV for the silicon and 17-18 eV for the silicon oxide are needed in order to create an electron-hole pair. Electron-hole pairs are created all along the charged particle track, which may be trapped in the silicon oxide or the silicon oxide/silicon interface, swept away by the applied electric field or recombine. The processes taking place are quite fast (in the picosecond range) and depend

on irradiation time, temperature, electric field and manufacturing technology.

The main consequences of the ionising processes are changes in the bias voltages applied to the devices (flatband voltage) and increase in the (surface) dark current.

The displacement damage effects are the most important source of CCD malfunction after irradiation with energetic hadrons. The hadrons interact with the atoms of the semiconductor material resulting in the displacement of some of them from their lattice positions and the creation of vacancies and interstitials. The primary defects are usually quite unstable and mobile at room temperature. This reordering might lead to recovery of some defects (annealing) or to the formation of more stable and complex ones, depending on the doping, temperature and excess carrier concentration.

These complex vacancies are the source of (bulk) dark currents in every pixel of a CCD imager. The dark current is non-uniform along the silicon array leading to random telegraph signals and charge transfer inefficiency [3-5].

During the ionisation process (electron-hole pair creation), the electron-hole recombination can be prevented by intrinsic, strong, internal electric fields. This can generate an electrical pulse large enough to disrupt normal device operation. The result can be a non-observable effect, a transient disruption of circuit operation, a change of logic state or a permanent damage to the device or integrated circuit [6,7].

High energy charged hadrons cause SEU through the highly ionising secondary fragments they produce when they collide with silicon nuclei. Neutrons do not create direct ionisation, but randomly interact with silicon nuclei producing charged secondary particles, which will further cause ionisation and possibly SEUs [6]. In general, neutrons at all energies can induce SEU in circuits. Protons seem to be harmless below an energy threshold, but SEUs might increase rapidly with increasing proton energy and finally level off at energies above 60-100 MeV. The energy threshold to induce a SEU has decreased to 20 MeV in the current technologies (in respect with that of 50 MeV at early 1990s) and tends to be further decreased to below 10 MeV due to the continuous decrease of the critical charge (lower applied voltage, smaller charge-collection volumes, increased device density per chip) [6]. As a result, SEU are expected to be one of the main future concerns related to radiation effects.

Radiation Effects in the LHC Tunnel

In the LHC tunnel and close to the beam lines (where cameras are foreseen to be installed) we expect a great variety of particles with energies of up to a few TeV (figure 2). These particles cannot be effectively shielded to protect the silicon arrays. Electronic equipment is expected to suffer the basic radiation effects, i.e. total dose effects, displacement damage and hadron-induced SEU [8].

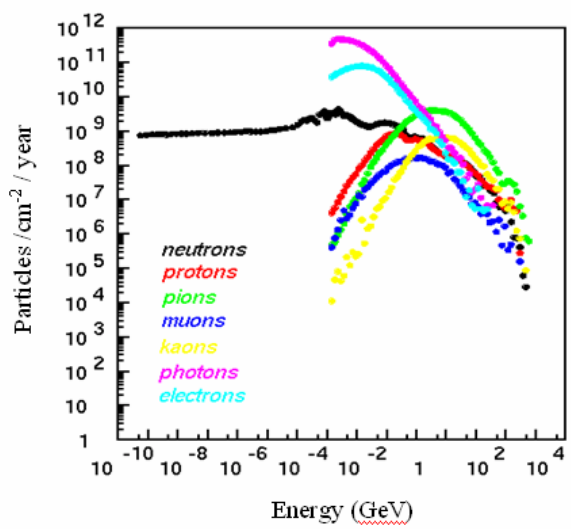

Figure 3: Annual hadron fluence in the LHC tunnel, at the region of the CCD cameras in Point 4, as calculated by Monte Carlo simulations.

Results E2V emCCD Camera

The emCCD camera was progressively irradiated starting with the sensor area but initially keeping the memory and charge amplifiers sections shielded. The gain was set 500x for the tests, which were performed at PSI (CH) using 60MeV protons. However, the 1 cm thick copper shielding used could not stop secondary neutrons that were in the beam, so all sections were exposed to some radiation all the time, including the amplifiers.

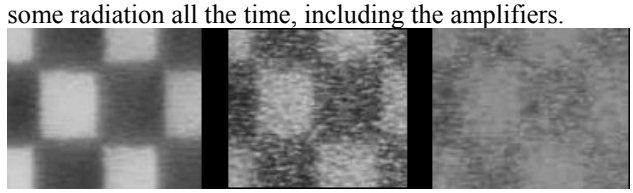

Figure 4: Degradation of the Checker-board pattern with progressive level of radiation: 0, 25 & 73Gy.

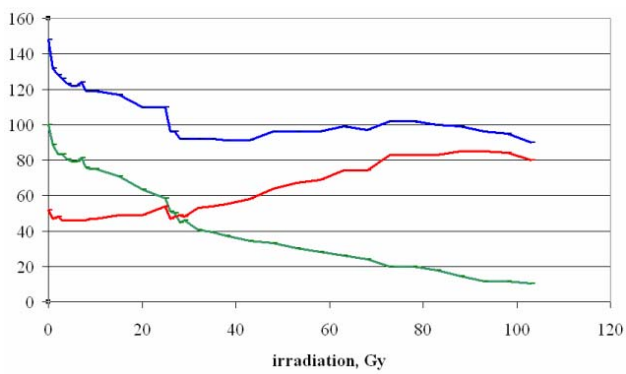

Figure 5: Loss of contrast with increasing radiation dose

The result of the analysis shows that the camera is very sensitive to radiation damage, in particular when the charge amplifier sections were first exposed there was an immediate loss of gain, seen at 25Gy. With radiation damage the contrast and resolution in the image become a function of the gain setting, as, a low gain the contrast and

resolution are nearly restored to the pre-irradiation level. However, the conclusion must be that after only 10-20Gy the level of damaged pixels and the loss of gain made the camera unsuitable for use in the LHC as a measuring instrument without suitable radiation shielding.

"Radiation-Hard" Camera Tests

We simulate LHC conditions with 60MeV protons, at Louvain-la-Neuve (BE), using a high flux rate: 7.7 10^8 p/ cm^2 / s. The devices are powered up and working during test, during which we found the image quality with and without beam to be nearly the same.

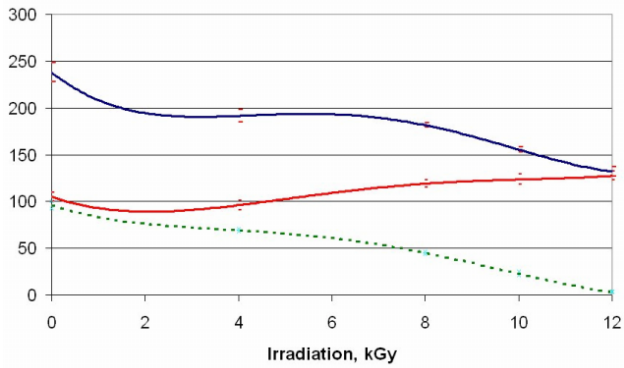

Figure 6: Spectra-Physics CID8712 Camera

The camera is rated to be operational to 1MRad: it was exposed to 1.2 MRad , SEU were not observed, the only effect was a progressive loss of contrast with increasing radiation. The camera has accessible gate bias voltage which can be adjusted to compensate for some of the lost contrast, which is due to the PMOS gate thresholds moving to the off state when irradiated.

The Fill-Factory Star 250 sensor was then irradiated in the same beam up to an integrated dose in silicon of 6MRad, the loss of contrast is almost entirely due to the loss of brightness, the dark levels observed to be quite stable. The SIRA APS250 camera based on this device has variable gain which can partially compensate for this loss of contrast.

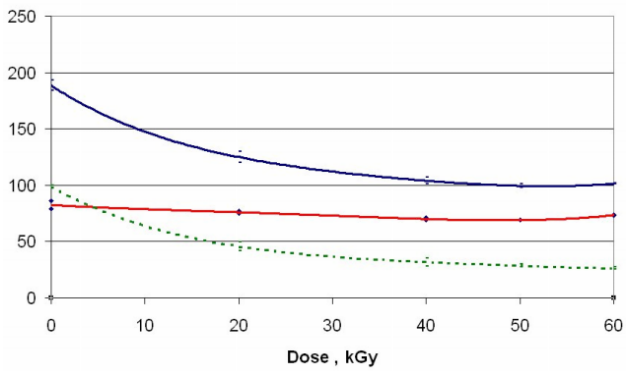

Figure 7: Star 250 Active Pixel Sensor

CONCLUSION

Both cameras have remote control box at ~30m from head, which is not Rad-tolerant. Advanced features such as selectable region of interest are not available on these cameras, but the CID8712 can be synchronized and triggered, while the SIRA APS250 camera, based on the Star250 sensor, will have a simple video output.

Shielding layouts have been simulated, resulting in a protection for the BSRT which reduces the incident radiation to acceptable levels, however this has required reorganization of the vacuum chamber layout to move the radiation sources away from the telescope, which is placed under the vacuum chambers protected by a 10cm thick steel plate supported by 1m thick steel blocks at the ends. These solutions are not easily implemented for other equipment which needs to be closer to the beam-pipes..

ACKNOWLEDGEMENTS

The authors wish to thank R.Jung for his help and encouragement in this work and G.Burger (LLN) and R.Brun (PSI) for their help in setting-up the radiation testing.

REFERENCES

[1] K.Tsoulou: Simulation of Radiation levels and shielding studies at the BDI positions in IR4, LHC Note 367, 2005.

[2] R. Jung: Image Sensor Technology for Beam Instrumentation, BIW 1998, CERN SL 98-061 BI

[3] J. R. Stour, C. J. Marshall, P. W. Marshall, Review of displacement damage effects in silicon devices, IEE Trans. Nucl. Sci., 50 (3), June 2003.

[4] M. S. Robbins, "High energy proton-induced dark signal in silicon Charged Coupled Devices", IEEE Trans. Nucl. Sci., 47 (6), pp. 2473 – 2479, 2000.

[5] C. J. Dale, P. W. Marshal, E. A. Burke, G. P. Summers, G. E. Bender, " The generation life time damage factor and its variance in silicon", IEEE Trans. Nucl. Sci., 36, pp. 1872 – 1881 (1989).

[6] H. H. K. Tang, K. P. Rodbell, "Single event upsets in microelectronics: fundamental physics and issues", MRS Bulletin, pp 111-116, February 2003.

[7] P. E. Dodd, L. W. Massengill, "Basic mechanisms and modeling of Single-Event Upset in digital microelectronics", IEEE Trans. Nucl. Sci., 50 (3), June 2003.

[8] G. R. Hopkinson, C. J. Dale, and P. W. Marshal, Proton Effects in Charge-Coupled Devices, IEEE Trans. Nucl. Sci., 43 (2), Apr. 1996.

List of Authors

Italic papercodes indicate primary authors

Institutes List

ANL
Argonne, Illinois
- Decker, G.

BESSY GmbH
Berlin
- Hartrott, M.V.
- Lipka, D.
- Richter, R.

BINP SB RAS
Novosibirsk
- Bogomyagkov, A.
- Gurko, V. F.
- Khilchenko, A.D.
- Kiselev, V.
- Meshkov, O.I.
- Muchnoi, N.Yu.
- Selivanov, A.N.
- Zhuravlev, A. N.
- Zubarev, P.V.

BNL
Upton, Long Island, New York
- Ben-Zvi, I.
- Cameron, P.
- Cupolo, J.
- D'Imperio, N.
- Degen, C.
- Della Penna, A.
- Hoff, L.T.
- Kewisch, J.
- Litvinenko, V.
- Luccio, A.U.
- Luo, Y.
- MacKay, W.W.
- Mead, J.
- Sikora, R.

CEA/DSM/DAPNIA
Gif-sur-Yvette
- Napoly, O.
- Paparella, R.

CERN
Geneva
- Bal, C.B.
- Bart Pedersen, S.
- Belleman, J.M.
- Belohrad, D. B.
- Braun, H.-H.
- Bravin, E.
- Burger, S.
- Caspers, F.
- Castro, M.E.
- Chritin, N.C.
- Corsini, R.
- Dehning, B.
- Dutriat, C.D.
- Effinger, E.
- Facchini, M.
- Ferioli, G.
- Fischer, C.
- Focker, G.J.
- Gasior, M.
- Gras, JJ.
- Guaglio, G.
- Guerrero Ollacarizqueta, A.
- Hutchins, S.C.
- Jensen, L.K.
- Jones, O.R.
- Jung, R.
- Koopman, J.
- Koutchouk, J.-P.
- Kramer, D.
- Kroyer, T.
- Lefevre, T.
- Leitner, R.
- Lenardon, LF.
- Ludwig, M.
- Maccaferri, R.
- Moles, M.
- Odier, OP.
- Raich, U.
- Refsum, H.H.
- Roncarolo, F.
- Schmickler, H.
- Schulte, D.
- Scrivens, R.
- Serrano, J.
- Soby, L.
- Taborelli, M.
- Tan, JT.
- Tecker, F.
- Tranquille, G.
- Tsoulou, E.
- Vuitton, VC.
- Welsch, C.P.
- Zamantzas, C.

DEEI
Trieste
- Boscolo, A.

DESY Zeuthen
Zeuthen
- Abrahamyan, K.
- Asova, G.
- Bähr, J.W.
- Dimitrov, G.
- Grabosch, H.-J.
- Han, J.H.
- Khodyachykh, S.

- Krasilnikov, M.
- Liu, S.
- Lüdecke, H.L.
- Miltchev, V.
- Oppelt, A.
- Petrosyan, B.
- Riemann, S.
- Sachwitz, M.
- Staykov, L.
- Stephan, F.
- Thom, H.

DESY
Hamburg
- Baboi, N.
- Bähr, J.W.
- Braeuer, M.
- Castro, P.
- Fischer, R.
- Franz, H.
- Hahn, U.
- Kim, Y.
- Knaack, K.
- Körfer, M.
- Kreps, G.
- Kube, G.
- Mukherjee, B.
- Schlarb, H.
- Simrock, S.
- Wendt, M.
- Wittenburg, K.

Diamond
Oxfordshire
- Abbott, M.G.
- Morgan, A.F.D.
- Rehm, G.
- Thomas, C.A.

ELETTRA
Basovizza, Trieste
- Bassanese, S.
- Ferianis, M.
- Iazzourene, F.

ESRF
Grenoble
- Joly, B.
- Koch, J.M.
- Meyer, J.M.
- Naylor, G.A.
- Perron, T.
- Plouviez, E.
- Pons, J.L.
- Robinson, D.
- Scheidt, B.K.
- Uberto, F.

ETH
Zurich
- Erni, D.
- Jäckel, H.

FOM Rijnhuizen
Nieuwegein
- Berden, G.
- Redlich, B.
- van der Meer, A.F.G.

FSU Jena
Jena
- Nawrodt, R.
- Neubert, R.
- Nietzsche, S.
- Vodel, W.

FZJ
Julich
- Dietrich, J.
- Mohos, I.

Fermilab
Batavia, Illinois
- Tan, C.-Y.

FhG
Euskirchen
- Kuhnhenn, J.

GANIL
Caen
- Andre, T.A.
- Anger, P.
- Baelde, J.L.
- Doutresssoulles, C.
- Ducoudret, B.
- Jamet, C.
- Le Coz, W.LC.
- Ozille, O.M.
- Petit, E.
- Swartvagher, E.

GSI
Darmstadt
- Bank, A. B.
- Dorn, C.
- Forck, P.
- Galatis, A.A.
- Giacomini, T.
- Hoffmann, T.
- Kaufmann, W.
- Kowina, P.
- Peters, A.
- Reeg, H.

- Schölles, J.
- Schwickert, M.

HMI
Berlin
- Göttmann, W.
- Wulf, F.

Heriot-Watt
Edinburgh
- Buller, G.S.
- Gordon, K.J.
- Pellegrini, S.

INFN Genova
Genova
- Conte, M.

INFN-Roma
Roma
- Valente, P.

INFN-Trieste
Trieste
- Vallazza, E.

INFN/LNF
Frascati (Roma)
- Buonomo, B.
- Di Pirro, G.
- Drago, A.
- Mazzitelli, G.
- Quintieri, L.
- Serio, M.
- Stella, A.

IPN
Orsay
- Ausset, P.
- Berthelot, S.
- Coacolo, J.-L.
- Lesrel, J.
- Maymon, J.N.
- Olivier, A.
- Rouviere, N.
- Solal Cohen, M.
- Vatrinet, L.
- Yaniche, J.-F.

ITEP
Moscow
- Barabin, S.V.
- Belyaev, G.E.
- Liakin, D.A.
- Roudskoy, I.
- Sergeeva, O.
- Skachkov, V.

JAEA
Ibaraki-ken
- Akikawa, H.
- Hasegawa, K.
- Ohkawa, T.

JAEA/J-PARC
Tokai-Mura, Naka-Gun, Ibaraki-Ken
- Hayashi, N.
- Kishiro, J.
- Toyokawa, R.

JAEA/LINAC
Ibaraki-ken
- Akikawa, H.
- Hasegawa, K.
- Hiroki, H.
- Kondo, Y.
- Oigawa, H.
- Sakaki, H.
- Sato, S.
- Tanaka, M.
- Tomisawa, T.
- Ueno, A.
- Yoshikawa, H.

JASRI/SPring-8
Hyogo
- Fujita, T.
- Masaki, M.
- Masuda, T.
- Nakamura, T.
- Ohkuma, H.
- Sasaki, S.
- Shoji, M.
- Takano, S.
- Takashima, T.
- Yamashita, A.

JINR
Dubna, Moscow Region
- Kortchaguin, D.
- Lokhovitskiy, A.E.

Jefferson Lab
Newport News, Virginia
- Bevins, M.E.
- Day, A.R.
- Degtiarenko, P.
- Dotson, D.W.
- Freyberger, A.
- Popov, V.P.
- Saha, A.
- Slachtouski, S.

KEK
Ibaraki
- Arakawa, D.A.
- Fukuma, H.
- Haga, K.
- Hashimoto, Y.
- Honda, T.
- Igarashi, Z.
- Ikegami, M.
- Lee, S.
- Mitsuhashi, T.
- Miura, T.
- Nakagawa, H.
- Nigorikawa, K.
- Obina, T.
- Tadano, M.
- Toyama, T.
- Zenei, I.
- Cheng, W.X.

LBNL
Berkeley, California
- Goldberg, D.A.

MIT
Middleton, Massachusetts
- Franklin, W.A.
- Ihloff, E.
- Zwart, T.

MPI-K
Heidelberg
- Bauer, C.
- Schmelling, M.T.

MSL
Stockholm
- Paal, A.

MSU
Moscow
- Skachkov, Vic.
- Vetrov, A.A.

NASU/IM
Kiev
- Karengin, V.G.
- Perevertailo, V.L.

NASU/INR
Kiev
- Aushev, V.E.
- Fedorovitch, O.A.
- Mikhailenko, A.V.
- Prystupa, S.V.
- Pugatch, V.M.
- Pylypchenko, Y.V.

NSRRC
Hsinchu
- Chen, J.
- Hsu, K.-T.
- Hsu, S.Y.
- Hu, K.H.
- Kuo, C.H.
- Lee, D.
- Wang, C.-J.
- Yang, Y.-T.

Nagoya University Graduate School of Engineering
Nagoya
- Takashima, Y.

ORNL
Oak Ridge, Tennessee
- Shea, T.J.

PSI
Villigen
- Boge, M.
- Dehler, M.
- Duperrex, P.-A.
- Dölling, R.
- Erne, R.
- Frei, U.P.
- Gamma, G.G.
- Graf, M.
- Janser, G.
- Keil, B.
- Kramert, R.
- Krempasky, J.
- Müller, U.
- Pollet, P.
- Rezzonico, L.
- Rohrer, U.
- Schilcher, T.
- Schlott, V.
- Schlumpf, N.
- Schmid, E.
- Sigg, H.
- Spuhler, P.
- Sütterlin, D.
- Thomsen, K.

Politecnico/Milano
Milano
- Cova, S.
- Ghioni, M.
- Gulinatti, A.
- Labanca, I.
- Rech, I.

RRC Kurchatov Institute
Moscow
- Moiseev, V.I.

Rutgers University, The State University of New Jersey
Piscataway, New Jersey
- Gilman, R.

SESAME
Amman
- Varnasseri, S.

SLAC
Menlo Park, California
- Frisch, J.C.
- McCormick, D.J.
- Ross, M.C.
- Smith, T.J.

SOLEIL
Gif-sur-Yvette
- Cassinari, L.
- Denard, J.-C.
- Dohou, F.
- Hubert, N.
- Leclercq, N.L.
- Nadji, A.
- Nadolski, L.S.N.
- Pedeau, D.

Strathclyde University
Glasgow
- Jamison, S.P.

TRIUMF
Vancouver
- Verzilov, V.A.

TU Darmstadt
Darmstadt
- Zoubir, A.M.

TUL-DMCS
Lodz
- Grecki, M.K.
- Makowski, D.R.
- Napieralski, A.
- Pawlik, P.
- Swiercz, B.P.

U. Kassel
Kassel
- Becker, W.J.
- Hape, M.
- Ricken, W.

UAD
Dundee
- MacLeod, A.

UVSOR
Okazaki
- Hayashi, K.
- Hosaka, M.
- Katoh, M.
- Mochihashi, A.
- Yamazaki, J.

Uni HH
Hamburg
- Honkavaara, K.
- Loehl, F.
- Rönsch, J.R.

Univ. Insubria and INFN Milano
Como
- Bulgheroni, A.
- Cappellini, C.
- Foggetta, L.G.
- Mozzanica, A.
- Prest, M.

University of Dundee
Nethergate, Dundee, Scotland
- Gillespie, W.A.

University of Berne, Institute of Applied Physics
Berne
- Murk, A.

YerPhI
Yerevan
- Arutunian, S.G.
- Bakshetyan, K.G.
- Dobrovolski, N.M.
- Mailian, M.R.
- Poghosyan, L.A.
- Sinenko, I.G.
- Soghoyan, H.E.
- Vasiniuk, I.E.

iThemba LABS
Somerset West
- Botha, A.H.
- Conradie, J.L.
- Delsink, J.L.G.
- Fourie, D.T.
- Kormany, Z.
- Mansfield, P.T.
- Rohwer, P.F.
- Sakildien, M.

Participants List

— A —

Michael **Abbott**
Diamond Light Source
michael.abbott@diamond.ac.uk
Great Britain

Ake **Andersson**
PSI
ake.andersson@psi.ch
Switzerland

Ivan **Andrian**
Elettra Trieste
ivan.andrian@elettra.trieste.it
Italy

Pascal **Anger**
GANIL
anger@ganil.fr
France

Suren **Arutunian**
Yerevan Physics Institute
femto@yerphi.am
Armenia

Brigitte **Azzara**
GSI
B.Azzara@gsi.de
Germany

Patrick **Ausset**
IPNO
ausset@ipno.in2p3.fr
France

— B —

Nicoleta **Baboi**
DESY-Hamburg
nicoleta.baboi@desy.de
Germany

Andreas **Bäcklund**
Svedberg Laboratory
andreas.backlund@tsl.uu.se
Sweden

Jürgen **Bähr**
DESY-Zeuthen
baehr@ifh.de
Germany

Isabelle **Bailly**
CEA
isabelle.bailly@cea.fr
France

Cathelijne **Bal**
CERN
cathelijne.bal@cern.ch
Switzerland

Silvano **Bassanese**
Elettra Trieste
silvano.bassanese@elettra.trieste.it
Italy

Jeroen **Belleman**
CERN
jeroen.belleman@cern.ch
Switzerland

David **Belohrad**
CERN
david.belohrad@cern.ch
Switzerland

Giel **Berden**
FOM Institute Rijnhuizen
g.berden@rijnh.nl
Netherlands

Julien **Bergoz**
Bergoz Instrumentation
bergoz@bergoz.com
France

Michel **Bernard**
LAL CNRS
bernard@lal.in2p3.fr
France

Christian **Boccard**
CERN
christian.boccard@cern.ch
Switzerland

Thierry **Bogey**
CERN
thierry.bogey@cern.ch
Switzerland

Antonio **Boscolo**
DEEI Trieste Univ.
boscolo@univ.trieste.it
Italy

Enrico **Bravin**
CERN
enrico.bravin@cern.ch
Switzerland

Sasa **Bremec**
i-Tech
sasa@i-tech.si
Slovenia

Bruno **Buonomo**
INFN-LNF
bruno.buonomo@lnf.infn.it
Italy

Stephane **Burger**
CERN
stephane.burger@cern.ch
Switzerland

— C —

Eva **Calvo Giraldo**
CERN
eva.calvo.giraldo@cern.ch
Switzerland

Peter **Cameron**
BNL
cameron@bnl.gov
USA

John **Carwardine**
ANL
carwar@aps.anl.gov
USA

Lodovico **Cassinari**
Synchrotron SOLEIL
lodovico.cassinari@synchrotron-soleil.fr
France

Maria Elena **Castro Carballo**
CERN
maria.castro.carballo@cern.ch
Switzerland

Madeleine **Catin**
CERN
madeleine.catin@cern.ch
Switzerland

Marie-Emmanuelle **Couprie**
CEA-DRECAM
Couprie@drecam.cea.fr
France

— D —

Glenn **Decker**
APS-ANL
decker@aps.anl.gov
USA

Christophe **Defrance**
Bergoz Instrumentation
defrance@bergoz.com
France

Michael **Dehler**
PSI
micha.dehler@psi.ch
Switzerland

Bernd **Dehning**
CERN
bernd.dehning@cern.ch
Switzerland

Raffaele **De Monte**
Elettra Trieste
demonte@elettra.trieste.it
Italy

Jean-Claude **Denard**
Synchrotron SOLEIL
jean-claude.denard@synchrotron-soleil.fr
France

Dominique **Deslandes**
CEA
dominique.deslandes@cea.fr
France

Jürgen **Dietrich**
Forschungszentrum Jülich
j.dietrich@fz-juelich.de
Germany

Rudolf **Doelling**
PSI
rudolf.doelling@psi.ch
Switzerland

Christoph **Dorn**
GSI
c.dorn@gsi.de
Germany

Pierre-André **Duperrex**
PSI
duperrex@psi.ch
Switzerland

— E —

Ewald **Effinger**
CERN
ewald.effinger@cern.ch
Switzerland

Jonathan **Emery**
CERN
jonathan.emery@cern.ch
Switzerland

— F —

Mario **Ferianis**
Elettra Trieste
mario.ferianis@elettra.trieste.it
Italy

Gianfranco **Ferioli**
CERN
gianfranco.ferioli@cern.ch
Switzerland

Claude **Fischer**
CERN
claude.fischer@cern.ch
Switzerland

Gerrit Jan **Focker**
CERN
gerrit.focker@cern.ch
Switzerland

Vincenzo **Forchi**
Elettra Trieste
vincenzo.forchi@elettra.trieste.it
Italy

Peter **Forck**
GSI
p.forck@gsi.de
Germany

Dirk **Fourie**
iThemba LABS
dirk@tlabs.ac.za
South Africa

Arne **Freyberger**
Jefferson Laboratory
freyberg@jlab.org
USA

Takahiro **Fujita**
JASRI/Spring-8
tfujita@spring8.or.jp
Japan

Hitoshi **Fukuma**
KEK
hitoshi.fukuma@kek.jp
Japan

— G —

Andreas **Galatis**
GSI-TUD
a.galatis@gsi.de
Germany

Marek **Gasior**
CERN
marek.gasior@cern.ch
Switzerland

Tino **Giacomini**
GSI
T.Giacomini@gsi.de
Germany

Jose Luis **Gonzalez**
CERN
jose.luis.gonzalez@cern.ch
Switzerland

Hans-Jürgen **Grabosch**
DESY-Zeuthen
grabosh@ifh.de
Germany

Jean-Jacques **Gras**
CERN
jean-jacques.gras@cern.ch
Switzerland

David **Guilhem**
CEA
david.guilhem@cea.fr
France

— H —

Markus **Häpe**
Universität Kassel
markus.haepe@uni-kassel.de
Germany

Tobias **Hoffmann**
GSI
t.hoffmann@gsi.de
Germany

Eva Barbara **Holzer**
CERN
barbara.holzer@cern.ch
Switzerland

Katja **Honkavaara**
Hamburg University
katja.honkavaara@desy.de
Germany

Laurent **Hourdin**
CEA
laurent.hourdin@cea.fr
France

Kuotung **Hsu**
NSRRC
kuotung@nsrrc.org.tw
Taiwan

Nicolas **Hubert**
Synchrotron SOLEIL
nicolas.hubert@
synchrotron-soleil.fr
France

Steve **Hutchins**
CERN
steve.hutchins@cern.ch
Switzerland

— J —

Stephen **Jackson**
CERN
stephen.jackson@cern.ch
Switzerland

Christophe **Jamet**
GANIL
jamet@ganil.fr
France

Lars **Jensen**
CERN
lars.jensen@cern.ch
Switzerland

Benoit **Joly**
ESRF
bjoly@esrf.fr
France

Kevin **Jordan**
Jefferson Lab
jordan@jlab.org
USA

— K —

Peter **Karlsson**
CERN
peter.karlsson@cern.ch
Switzerland

Boris **Keil**
PSI
boris.keil@psi.ch
Switzerland

Eiji **Kikutani**
KEK
kikutani@post.kek.jp
Japan

Klaus **Knaack**
DESY-Hamburg
klaus.knaack@desy.de
Germany

Jean-Marc **Koch**
ESRF
jmkoch@esrf.fr
France

Markus **Körfer**
DESY-Hamburg
markus.koerfer@desy.de
Germany

Danil **Korchagin**
CERN
danil.korchaguin@cern.ch
Switzerland

Piotr **Kowina**
GSI
p.kowina@gsi.de
Germany

Gero **Kube**
DESY
Gero.Kube@desy.de
Germany

— L —

Seishu **Lee**
KEK
seishu.lee@kek.jp
Japan

Simon C. **Leemann**
PSI
simon.leemann@psi.ch
Switzerland

Thibaut **Lefevre**
CERN
thibaut.lefevre@cern.ch
Switzerland

Hervé **Lefort**
IPNO
lefort@ipno.in2p3.fr
France

Tor **Lofnes**
Uppsala University-Sveldberg L
tor.lofnes@tsl.uu.se
Sweden

Arkady **Lokhovitskiy**
CERN
arkady.lokhovitskiy@cern.ch
Switzerland

Andrei **Lounine**
PSI
andrei.lounine@psi.ch
Switzerland

Hartmut **Lüdecke**
DESY-Zeuthen
luedecke@ifh.de
Germany

Dmitry **Lyakin**
ITEP/GSI
d.liakin@gsi.de
Germany

— M —

Dariusz **Makowski**
DMCS
dmakowdmes.p.lodz.pl
Poland

Christophe **Mariette**
SC Synchrotron Soleil
christophe.mariette@
synchrotron-soleil.fr
France

Jean-Gabriel **Marmouget**
CEA
jean-gabriel.marmouget@cea.fr
France

Oleg **Meshkov**
Budker Inst. Of Nucle.Physics
O.I.Meshkov@inp.nsk.su
Russia

Toshiyuki **Mitsuhashi**
KEK
toshiyuki.mitsuhashi@kek.jp
Japan

Akira **Mochihashi**
UVSOR Facility
mochi@ims.ac.jp
Japan

Istvan **Mohos**
Forschungszentrum Jülich
i.mohos@fz-juelich.de
Germany

Alun **Morgan**
Diamond Light Source
alun.morgan@diamond.ac.uk
Great Britain

— N —

Takeshi **Nakamura**
JASRI/Spring-8
nakamura@spring8.or.jp
Japan

Graham **Naylor**
ESRF
naylor@esrf.fr
France

— O —

Takashi **Obina**
KEK
takashi.obina@kek.jp
Japan

Patrick **Odier**
CERN
patrick.odier@cern.ch
Switzerland

— P —

Francis **Perez**
ALBA Synchrotron/CELLS
perez@cells.es
Spain

Thomas **Perron**
ESRF
perron@esrf.fr
France

Andreas **Peters**
GSI
a.peters@gsi.de
Germany

Eric **Plouviez**
ESRF
plouviez@esrf.fr
France

Patrick **Pollet**
PSI
patrick.pollet@psi.ch
Switzerland

John **Poole**
CERN
john.poole@cern.ch
Switzerland

Virginia **Prieto**
CERN
virginia.prieto@cern.ch
Switzerland

Valery **Pugatch**
KINR/NASU
pugach@kinr.kiev.ua
Ukraine

Yuriy **Pylypchenko**
KINR/NASU
yupy@kinr.kiev.ua
Ukraine

— Q —

Lina **Quintieri**
INFN-LNF
Lina.quintieri@lnf.infn.it
Italy

— R —

Uli **Raich**
CERN
uli.raich@cern.ch
Switzerland

Günther **Rehm**
Diamond Light Source
guenther.rehm@diamond.ac.uk
Great Britain

Bernard **Rischmann**
PMB
bernard.rischmann@pmb-mt.com
France

Juliane **Roensch**
Hamburg University
jroensch@ifh.de
Germany

— S —

Martin **Sachwitz**
DESY-Zeuthen
martin.sachwitz@desy.de
Germany

Angela **Salom Sarasqueta**
ALBA Synchrotron/CELLS
asalom@cells.es
Spain

Volker RW **Schaa**
GSI
v.r.w.schaa@gsi.de
Germany

Kees Bertus **Scheidt**
ESRF
scheidt@esrf.fr
France

Thomas **Schilcher**
PSI
thomas.schilcher@psi.ch
Switzerland

Hermann **Schmickler**
CERN
hermann.schmickler@cern.ch
Switzerland

Jürgen **Schölles**
GSI mbh
j.schoelles@gsi.de
Germany

Mario **Serio**
INFN-LNF
mario.serio@lnf.infn.it
Italy

Javier **Serrano**
CERN
javier.serrano@cern.ch
Switzerland

Thomas **Shea**
ORNL
shea@sns.gov
USA

Stefan **Simrock**
DESY-Hamburg
stefan.simrock@desy.de
Germany

Lars **Soby**
CERN
lars.soby@cern.ch
Switzerland

Maurice **Solal**
IPNO/CNRS
solal@ipno.in2p3.fr
France

Jens **Spanggaard**
CERN
jens.spanggaard@cern.ch
Switzerland

Lazar **Staykov**
DESY-Zeuthen
lazaraza@ifh.de
Germany

Angelo **Stella**
INFN-LNF
angelo.stella@lnf.infn.it
Italy

Daniel **Sütterlin**
PSI
daniel.suetterlin@psi.ch
Switzerland

— T —

Shiro **Takano**
JASRI/Spring-8
takano@spring8.or.jp
Japan

Gianni **Tassotto**
FNAL
tassotto@fnal.gov
USA

Cyrille **Thomas**
Diamond Light Source
cyrille.thomas@diamond.ac.uk
Great Britain

Daniel **Treyer**
PSI
daniel.treyer@psi.ch
Switzerland

— U —

Klaus **Unser**
Bergoz Instrumentation
unser@bergoz.com
France

— V —

Seadat **Varnasseri**
SESAME
s.varnasseri@unesco.org.jo
Jordania

Jean-Luc **Vignet**
Ganil/CEA
vignet@ganil.fr
France

Wolfgang **Vodel**
Friedrich Schiller University
wolfgang.vodel@uni-jena.de
Germany

— W —

Matthias **Werner**
DESY-Hamburg
Matthias.Werner@desy.de
Germany

Kay **Wittenburg**
DESY-Hamburg
kay.wittenburg@desy.de
Germany

Naomi **Wyles**
CCLRC Daresbury Lab.
n.g.wyles@dl.ac.uk
Great Britain

— Z —

Christos **Zamantzas**
CERN
christos.zamantzas@cern.ch
Switzerland

Production Notes

The DIPAC2005 proceedings volume was produced using tools of the JACoW Collaboration (http://www.jacow.org). The SPMS database (Scientific Program Management System, author: Matt Arena, FermiLab) has been used for abstract and paper submission.

The contents of the database has been exported to XML, providing all data necessary for the batch production of the abstract booklet, proceedings and consistent conference web pages. The generated XML file consisted of 20 720 lines of meta data describing each paper contribution. The PERL script `spms2batch` read this XML file and transformed it to `<html>`, \ConTEXt, \LATEX, and command files. With the script `scan-keywords` all pdf-files submitted by the authors were transformed to text files, which then were scanned for keywords given by a reference list. The five top-most keywords were used for the keyword list.

One script run produced 552 pages for the conference web site (http://bel.gsi.de/dipac2005/). These pages consist of lists for *Sessions*, *Classification*, *Authors*, *Keywords*, and *Institutes* with all available cross links. All these pages are coded in UNICODE (UTF8), making greek characters and small math formulas in abstracts possible, as well as showing the correct writing of names with accented characters. For alphabetic sorting of author names a rule based method is used honoring accented letters, umlauts, etc.

The script generated 103 pdfTEX wrappers for each single raw pdf-file, and one for the proceedings file. *Raw* pdf-files are papers conforming to the JACoW (Joint Accelerator Conferences on Web) editor's guideline without page numbers, running title, and session names (see http://www.jacow.org). A pdfTEX wrapper transforms the raw pdf-file into one that has all hidden fields (*Title*, *Subject*, *Author*, *Keywords*) filled, in addition to page numbering, classification names, and conference details.

The final printed proceedings required minimal manual intervention. Embedding of preface material, lists of authors, institutes, participants, papers, and affiliation details were controlled by means of a configuration file. The proceedings pdf-file, which can be downloaded from the proceedings web site (http://bel.gsi.de/dipac2005/papers/proceed.pdf), features a completely cross-linked document including table of contents, list of authors, and list of institutes, as well as the papers themselves. The final version of the proceedings was made using pdfLATEX (version `1.21a`) with macro packages *pdfpages* (version `v0.3e`), *fancyhdr* (version `v2.1`), and *thumbpdf* (version `v3.8`).

All tools and scripts are available from the JACoW site under the GNU license.

November 2005
Volker RW Schaa